University of Strathclyde Department of Naval Architecture and Marine Engineering

Component Mode Synthesis for Ship Structures:

Investigation into an Alternative Approach

Petrus Gosse Zoet

A thesis presented in fulfilment of the requirements for the degree of Doctor of Philosophy

2013

This thesis is the result of the author's original research. It has been composed by the author and has not been previously submitted for examination which has led to the award of a degree.

The copyright of this thesis belongs to the author under the terms of the United Kingdom Copyright Acts as qualified by University of Strathclyde Regulation 3.50. Due acknowledgement must always be made of the use of any material contained in, or derived from, this thesis.'

Signed: *Date:*

Acknowledgements

I would like to thank first of all my wife Tineke for her patience and understanding and support during my research work and the writing of the thesis. I would like to express my gratitude to Professor Atilla Incecik, Professor Osman Turan and Professor Peiling Zhou for giving me and my wife the opportunity to live and work in Scotland, which has been a wonderful experience so far.

I would also like to thank my colleagues and friends Serkan Turkmen, Olgun Hizir and Cagan Diyaroglu for their support and helping me painstakingly putting together the geometry of the LNG carrier into the FEM software using only hard copy drawings and a ruler.

Last, but certainly not least, I would like to specially thank my supervisor Professor Osman Turan for his great support, the great Christmas diners we had at his house with his family, and the wonderful travel companion he was with our many trips to the various EU FP7 project meeting for the SILENV project in Europe.

Contents

1 Abstract 1

2 Aims and Objectives 2

3 Introduction 3

3.1 Background 3

3.1.1 Noise and Vibrations and Global Developments 3

3.1.2 Modelling Challenges 5

3.2 Structure of the Thesis 7

4 Critical Review 10

4.1 Controlling the Excitation Characteristics 11

4.1.1 Propeller Excitation 12

4.1.2 Diesel Engine Excitation 18

4.2 Controlling Structural Response 20

4.2.1 Hull Girder Approach 21

4.2.2 Finite Element Modelling 27

4.2.3 Mode Superposition 30

4.2.4 Spectral Element Modelling 31

4.2.5 Statistical Energy Analysis 33

4.2.6 Component Mode Synthesis Techniques 35

4.3 Conclusion and Summary Critical Review 41

4.3.1 Excitation Forces 41

4.3.2 Response Modelling Techniques 43

5 Measurement Results 48

5.1 Vibration and Noise Measurements on a Gas Carrier 49

5.1.1 Measurement Conditions, Locations and Procedure 50

5.1.2 Propeller induced Vibration and Noise 51

5.1.3 Evaluation of Measured Propeller Vibrations 55

5.1.4 Evaluation of measured Propeller Noise 56

5.2 Vibrations and Noise Measurements on a Fishery Research Vessel 57

5.2.1 Measurement Conditions, Locations and Procedure 58

5.2.2 Evaluation and Identification of Propeller Induced Vibrations 59

5.2.3 Identification and Evaluation of Diesel Engine Induced Vibrations ... 60
5.3 Vibrations on Board a ROPAX Vessel ... 63
5.3.1 Evaluation of Propeller Induced Vibrations ... 63
5.3.2 Evaluation of Diesel Engine Induced Vibrations ... 65
5.4 Summary of Measurement Result Evaluation ... 66
6 Theory of Structural response Simulation ... 68
6.1 Introduction: Choosing the Modelling Techniques ... 69
6.2 The wave and mode approach ... 70
6.2.1 The Wave Approach ... 71
6.2.2 The Mode Approach ... 78
6.3 The Principles of Finite Element Modelling ... 79
6.4 Solving the Equations of Motion ... 82
6.4.1 Full Analysis: Row Reduction. ... 84
6.4.2 Mode Superposition ... 85
6.4.3 Mode Superposition with Residual Compensation ... 88
6.5 Component Mode Synthesis (CMS) ... 90
6.5.1 Fixed Interface CMS: the Craig-Bampton Method ... 90
6.5.2 Free Interface: the McNeal and Rubin's Method ... 100
6.5.3 Reducing the Interface Degrees of Freedom ... 107
6.6 Summary and Discussion ... 114
7 Modelling Vibrations of the Aft-ship of an LNG Carrier ... 115
7.1 Vessel Properties, Measurements and Simulation Locations ... 117
7.2 Properties of the Structural Models ... 119
7.2.1 The full finite element model ... 119
7.2.2 The CMS Model ... 123
7.3 Excitation Characteristic and Response Calculation Method ... 124
7.4 Comparison of Simulation Results with Measurement Results ... 129
7.5 Sensitivity of the Model ... 134
7.5.1 Effect of the Boundary Conditions, Added Mass and Damping ... 134
7.5.2 Excitation characteristic ... 144
7.5.3 Number and Type of Elements ... 145
7.6 The Contribution from Hull Girder Modes ... 146
7.7 Correlation of Simulation Results ... 147

7.8 Evaluation of FE and CMS Performance 149
7.8.1 Accuracy of CMS results 150
7.8.2 Required CP Time for CMS Calculations 152
7.9 Summary and Conclusion 153
7.9.1 Comparison with Measurement Results 153
7.9.2 Evaluation of Simulated Excitation Characteristics 154
7.9.3 Choice of Boundary Conditions 154
7.9.4 Element Size 155
7.9.5 Evaluation of Component Mode Synthesis (CMS) Techniques 155
8 Methodology of an Alternative Approach to Classical CMS 156
8.1 Introduction 156
8.2 Interface stiffness and mass matrix 160
8.3 Proposed Reduction Technique 164
8.4 The Zoet Method with Boundary Residual Flexibility 167
8.5 Eliminating Residual Flexibility Modes from the Zoet Method 175
8.5.1 Compiling the Total Boundary Mobility Matrix 177
8.5.2 Eliminating Interface Displacement Degrees of Freedom 178
8.5.3 Overcompensation of Residual Flexibility 181
8.6 The Rubin–Zoet Method 183
8.7 Comparing Required Calculation Time 185
8.7.1 Estimating Calculation Time: Floating Point Operations 186
8.7.2 Required Number of FLOPS for Zoet's Method 187
8.7.3 Required Number of FLOPS for the Rubin-Zoet Method 190
8.8 Discussion of Performance of the Proposed CMS Techniques 192
8.8.1 Formulating Matrices 193
8.8.2 The Zoet Method without Residual Boundary Modes 194
8.8.3 The Zoet Method with Boundary Residual Flexibility Modes 194
8.8.4 Zoet Method versus Rubin-Zoet Method 195
8.8.5 Comparing CMS with Mode Superposition 197
8.9 Conclusions 199
9 Case Study: Evaluating Zoet's Method 201
9.1 Properties of the Test Model 202
9.1.1 Size types of Elements, and Properties of the Substructures 203

9.1.2 Excitation Characteristic 204
9.1.3 Damping and Added Mass 205
9.1.4 Boundary Conditions 205
9.2 Software Used 206
9.3 Evaluation of the Zoet Method 206
9.3.1 Relevance of Residual Boundary Flexibility Modes 207
9.3.2 Results for Individual Pairs of Substructures 208
9.3.3 Results with Multiple Coupled Structures 212
9.3.4 Evaluation of Required Computation Time 214
9.3.5 Consequences of Overcompensation on LNG Carrier 217
9.4 Residual Interface Flexibility and Overcompensation: a Discussion 220
9.4.1 The Effect of the Need for Residual Boundary Flexibility Modes 221
9.4.2 Overcompensation of Residual Flexibility 224
9.5 Conclusion 229
9.5.1 Evaluation Rubin-Zoet Method 230
9.5.2 Evaluation Zoet Method with Residual Compensation 231
9.5.3 Evaluation Rubin Method with Interface Modes 233
9.5.4 Evaluation Mode Superposition Method 234
9.5.5 Using CMS for Time-Domain Analysis 235
10 Discussion 237
10.1 Recap of the thesis 237
10.1.1 Aim of This Work 238
10.1.2 Critical Review and Selection of Modelling Techniques 238
10.1.3 Modelling of the Structural Response of a LNG Carrier 239
10.1.4 Problems Encountered with the Full Harmonic Analysis 240
10.1.5 Advantages of a Sub-Structural Approach 241
10.1.6 Identified Problems with Classical Sub-Structural Approaches 241
10.1.7 Development of the Zoet Method 243
10.1.8 Zoet Method with Residual Interface Flexibility 243
10.1.9 The Rubin-Zoet Method 244
10.2 Contributions and Achievements 245
10.2.1 Decreasing Effort Required for Building the Model 246
10.2.2 Building More Accurate Models 246
10.2.3 Reducing Required Computer Memory 246

10.2.4 Reducing Required Computation Time 247
10.3 Shortcomings and Limitations of the Zoet and Rubin-Zoet Methods ... 251
10.3.1 Increase of Required Cut-Out Frequency 251
10.3.2 Analysing a Lower Number of Frequencies 252
10.3.3 Analysing over a Smaller Frequency Range 253
10.3.4 Using Zoet and Rubin-Zoet for Time-Domain Analysis 255
10.4 Future Work 256
11 Final Concluding Remarks 258

Appendix number	Appendix Title	Page
Appendix I	Equipment Used for Noise and Vibration Measurements	264
Appendix II	Full Girder Approach	271
Appendix III	Formulation of the Beam Element	276
Appendix IV	Formulation of the Plate Element	289
Appendix V	Residual Compensation for Free Floating Structures	296
Appendix VI	Sparse Matrix Solver: Row Reduction Technique	300
Appendix VII	Results FEM for Different Boundary Conditions	308
Appendix VIII	Comparing Simulation Results with Measurement Results	315
Appendix IX	Substructures LNG carrier CMS	324
Appendix X	Results Full FEM, Fixed Interface CMS and Free Interface CMS	333
Appendix XI	Simulated Deflection Shapes for Model Constrained at Frame 25	339
Appendix XII	Simulated Deflection Shapes for Model Constrained at Frame 21	344
Appendix XIII	Comparing Correlated Simulated Spectra With Measurement Results	350
Appendix XIV	Matrix-Vector Calculus and Number of Required Floating Point Operations	353
Appendix XV	Steps and Estimated Number of Matrix Operation Mode Superposition	357

Appendix XVI	Steps and Estimated Number of Matrix Operation Classic Rubin's Method	359
Appendix XVII	Steps and Estimated Number of Matrix Operations Rubin's Method using Interface Modes	366
Appendix XVIII	Steps and Estimated Number of Matrix Operations Zoet's Method	376
Appendix XIX	Steps and Estimated Number of Matrix Operations Rubin-Zoet Method	386
Appendix XX	Calculation of the Number of FLOPS for Mode Superposition Method	394
Appendix XXI	Calculation of the Number of FLOPS for Rubin's Method Applied on the LNG Carrier	396
Appendix XXII	Required Number of Flops for Application of the Zoet Method on the CMS Model of the LNG Carrier	404
Appendix XXIII	Required Number of Flops for Application of the Rubin- Zoet Method on the CMS Model of the LNG Carrier	416
Appendix XXIV	CMS Results of the Case Study Model According to ANSYS	429
Appendix XXV	Test Case Substructure Division for the Zoet Method	437
Appendix XXVI	Test Case Results Zoet Method Individual pair of Substructures	440
Appendix XXVII	Evaluation of the Effect of Residual Interface Flexibility on the Results of Zoet's method	445
Appendix XXVIII	Test Case Results Zoet Method Total Dynamic Behaviour A, B, C and D Coupled	449
Appendix XXIX	Reduced Test Case Results Zoet Method, Substructures A, B and C Coupled	458
Appendix XXX	Rubin's Method With Interface Modes for PHD Test Case	465
Appendix XXXI	Computation Time for Different Methods PHD Test Case	471
Appendix XXXII	Computation Time for Zoet and Rubin-Zoet Method for the LNG Carrier with Increased Number of Normal Modes	480

1 Abstract

The main aim of this work is to help the shipbuilder to effectively assess a ships' structural design for its vibratory behaviour. For that purpose state of the art structural modelling techniques are reviewed for the validity of their basic principles, accuracy, practicality and required computation time when applied on typical marine structures. Full finite element modelling has been applied on a part of the structure of an LNG carrier on board which the author has taken vibration and noise measurements. Also fixed interface (Craig-Bampton) and free interface (Rubin's method) component mode synthesis sub structuring techniques have been applied. The aim of the analysis is to evaluate the effectiveness of finite element modelling through evaluation with measurement results, evaluate the accuracy of the sub structuring modelling techniques and to identify short comings of any of the tested methods.

Two alternative component synthesis modelling sub structuring techniques are proposed in order to reduce required computation time; Zoet's method and the Rubin Zoet method. The Zoet method is tested using a section of the LNG carrier's structural model. The method is evaluated for accuracy (comparing obtained results with the results obtained through the full harmonic finite element analysis) and required computation time through comparison with the required computation time for:

- full harmonic analysis
- the classical modal reduction and mode superposition technique
- the classical Rubin free interface component mode synthesis
- and Rubin's method with interface reduction according to the IRS method (see section 6.5.3)
- the Rubin-Zoet technique

2 Aims and Objectives

The aim of this research work to develop an effective accurate methodology to asses a ships structural design on its structural dynamic behaviour as early as possible in the design stage in order to prevent noise and vibration problem occurring once the ship has been built. The following objectives have been set:

- Understanding the general mechanism leading to ships' vibrations and noise through noise and vibration measurement results taken on board a bulk carrier, gas carrier and fishery research vessel which are used together with available information on the structural geometry.
- Identifying gaps with most commonly used state of the art structural modelling techniques considering the mechanisms that have been identified as typically occurring on board ships.
- Proposing a practical modelling technique and approach that makes assessing the structural design of ships for noise and vibrations easier.

3 Introduction

In this section an introduction is given explaining both the background (context) of the thesis and the structure of the thesis.

3.1 Background

In this section the context of the thesis is described set against the background of the current global developments in the marine industry, through which the increasing need for reliable and practical tools for evaluation of marine structure's dynamic response is demonstrated. With the global developments in mind, the modelling needs are described on which the approaches to structural modelling in this work are based.

3.1.1 Noise and Vibrations and Global Developments

Many problems occur in the shipping industry related to noise and vibrations. The biggest nightmare of ship operators concerning vibrations is failure of structures and machinery due to material fatigue. Failure of machinery and structures poses a huge threat to the ships' safety and usually also leads to huge loss of revenue due to unplanned downtime. In addition, high vibration levels, just like high noise levels, also affect crew and passengers' health and wellbeing. Particularly for passenger ships and ferries the impact of noise and vibrations on human comfort compromises the earning capability of the ship as people may chose not to travel with that ship in the future again.

Although above concerns have already lead to numerous rules, regulations and guidelines issued by class societies and other regulatory bodies, recent research on ship noise and vibrations carried out for the European Union is likely to result in even more (stringent) requirements in the near future. This resent research has focused on the impact of noise and vibrations on crew comfort and performance as well as the impact on people living close to harbours and seaways and the effect on the underwater environment (marine mammals).

Unfortunately, there any many powerful vibration sources on board a ship. The most dominant sources are the propeller and the (diesel) engines, which produce the high amplitude fluctuating forces to which the ship's structure is subjected. In addition, the dynamic structural behaviour of ships (particularly structural parts above water) is strongly characterised by the low damping properties of the material (typically steel) the structure is built of. These low damping values combined with typically high amplitudes of harmonic components found in propeller and (diesel) engines forces, may result in destructively high vibration levels when excitation frequencies are close, or coincide with resonance frequencies.

Adding to the likelihood of structural fatigue damage occurring is the increasingly hostile environment under which offshore equipment has to operate. Raising oil and gas prices for instance mean that winning oil and gas from increasingly difficult and dynamically challenging locations becomes economically viable, which means that equipment is pushed to their limits.

Raising fuel prices and current global economic circumstances also push the need for efficiency of operation, flexibility of operation (option for slow steaming) which sparks the development of new design concepts, new ship geometries, the application of new materials (sandwich panels, visco-elastic materials, piezo-electric materials), increase of scale, and increasing propeller and engine loads. This means that under the present global circumstances the shipbuilding industry design concepts become more revolutionary as opposed to evolutionary, which has always been the best fitting term through to characterise the nature of progress in the industry.

As ships and equipment are designed further outside the traditional design envelop than ever, relying on tradition and history for selecting machinery components and developing structural geometry becomes very questionable, as different dynamic mechanisms may start playing a role and extrapolation curves outside the design envelop may not linear. In addition, economy also forces designers to decrease the design margins, which leaves less space for errors.

All above considered, a full understanding of the characteristics of the forces acting on ship's structure and machinery, together which a full understanding of the

corresponding structural and machinery dynamic response mechanisms is required when designing a ship and minimising impact of vibrations and noise. Modelling tests, full scale measurements in combination with (practical) deterministic modelling techniques are needed more than ever. On top of that, the validly of traditional modelling approaches need to be questioned based on a thorough understanding of the modelling principles and the nature of the excitation characteristics and natural response behaviour. Particularly statistical approaches need to be questioned, as the outcome is based on a population of the state of the art design concepts at best, and may not be representative for new design concepts which go **beyond** the state of the art.

3.1.2 Modelling Challenges

As described above, theoretically estimating structural and machinery dynamic behaviour on ships has become very important considering the development of many new innovative design concepts in a quest for saving fuel, or being able to deploy equipment that stays operative under the increasingly dynamically hostile environment under which the offshore industry operates. Modelling structural response, even with state of the art modelling techniques, is already a challenge, and will become even more challenging in the future.

Problems with modelling structural vibrations typically experienced in the marine sector are:

- **Labour intensity of generating the mathematical model.** Describing the typically complex ship's structural geometry for structural modelling purposes is often very time consuming and labour intensive (as experienced in this work). Although the ship geometry may be imported into a structural modelling software package from drawings generated through CAD designing software packages, many problems still arise with generating a suitable mesh (in case of finite element modelling) or with connection between different parts of the geometry, or with the describing complex curves.

- **Require memory time and computation time**. Due to the size and complexity of ship structures, problems are experienced with the related required computer memory and computation time for running the structural model. Required memory and computation time increases further with the excitation frequency order number. As mode shapes involved in the corresponding structural response become more complex, a higher number of degrees of freedom is required in order to be able to accurately enough describe these mode shapes.
- **Uncertainty about correctness of the applied boundary conditions**. Although analysis at the higher order frequencies requires more detailed models, not the entire structure needs to be modelled at that level of detail, if one would be focussing on only a particular part of the structure. A far more practical and feasible approach adopted is to model only local parts of a ship's structure. However, the main challenge with that approach is finding the appropriate boundary conditions. Global, courser models may be required for modelling the rest of the ship structure in order to evaluate the transmission behaviour of vibrations through the ship structures.
- **Uncertainty of modal parameters (damping and added mass) and excitation characteristics**. Particularly with the analysis at increasing excitation frequency order numbers, a correct estimation of material properties, (hydrodynamic) damping and added mass properties is important.

Considering new design concepts are developed, new materials are applied, flexibility in operation is required (for slow steaming) and amplitudes of alternating (and impulse) forces acting on a structure increase, evaluating dynamic structural and machinery response characteristics becomes even more difficult:

- Predicting structural response over a **range** of operational conditions, and not just at nominal speed. Not only is this required for estimating the sensitivity of the model, but also for estimating the vibration response when machinery is running off design in case of slow steaming (a trend in the shipping industry in order to save fuel) and manoeuvring. This increases computation time and required computer memory for the output files.

- Predicting the response to impulse loads, which is particularly required for evaluation of robustness of offshore structures and the evaluation of structural response to (propeller) cavity implosions in case of violent cavitation. Time domain simulation is required which requires much more computation time than the traditional harmonic analysis considering that numerical integration requires solving the equations of motion for a great number of time steps.
- Considering modelling local vibration behaviour, bigger parts of the ship structure may have to be modelled as uncertainty may arise about how to define boundary conditions with new (revolutionary) structural design concepts or application of new types of material. This means that generating the structural model becomes even more labour intensive.

The aim of this work is to help the shipbuilding industry to build ships for low noise and vibration levels by proposing an approach to modelling that will help overcome above described problems.

3.2 Structure of the Thesis

Figure 1 shows the outline of the thesis. The thesis starts with section 4 “

Critical Review”, where a review of the state of the most commonly adopted approaches to theoretically estimating excitation characteristics and structural response is presented.

In section 5 “Measurement Results” vibrations and noise measurement results taken on board different ships are analysed. Together with the critical review and the analysis of the measurement results, the most promising modelling techniques are selected for modelling the structural dynamic behaviour of the aft ship of a gas tanker, one of the ships on board which the author has performed vibration measurements. In section 6, “Theory of Structural response Simulation”, the theory behind the selected structural modelling techniques is presented more in depth.

Following the conclusion of section 4 “

Critical Review", section 5 "Measurement Results" and deeper analysis of the modelling techniques in section 6, Finite element modelling and component mode synthesis modelling techniques are evaluated in section 7 "Modelling Vibrations of the Aft-ship of an LNG" through a case study. In this case study, vibration levels are simulated over a range of frequencies for a number of locations on the steering gear deck and mooring deck of an LNG carrier, on board which the author has performed the vibration measurements presented in section 5. The following is covered in section 7 "Modelling Vibrations of the Aft-ship of an LNG"

- Vibration simulation through a full finite element harmonic analysis.
- Evaluation of full harmonic analysis through measurement results.
- Evaluation of changing boundary conditions on simulation results
- Evaluating results obtained through free interface and fixed interface component mode modelling techniques. Results are evaluated through comparison with the results obtained through the full analysis.
- Estimating and comparing required computation time for:
    - Full harmonic analysis
    - Mode Superposition
    - Free Interface Component Mode Synthesis (Rubin's Method)
    - Fixed Interface Component Mode Synthesis (Craig-Bampton)

Following the findings from section 7 "Modelling Vibrations of the Aft-ship of an LNG", an alternative approach to the classical component mode synthesis technique is proposed in section 8 "Methodology of an Alternative Approach to Classical CMS". This approach is evaluated through a case study presented in section 9 "Case Study: Evaluating Zoet's Method", using a part of the structural model studied in section 7. Comparison of simulation time required for all above listed techniques is again carried out. As interface modes and corresponding natural frequencies have been calculated for the test case model, the achieved reduction of computation time using an already existing interface reduction technique according to the IRS method is also calculated and compared to the reduction in computation time achieved through the newly proposed reduction techniques. The thesis ends with a discussion, summary, conclusions and recommendations for future work.

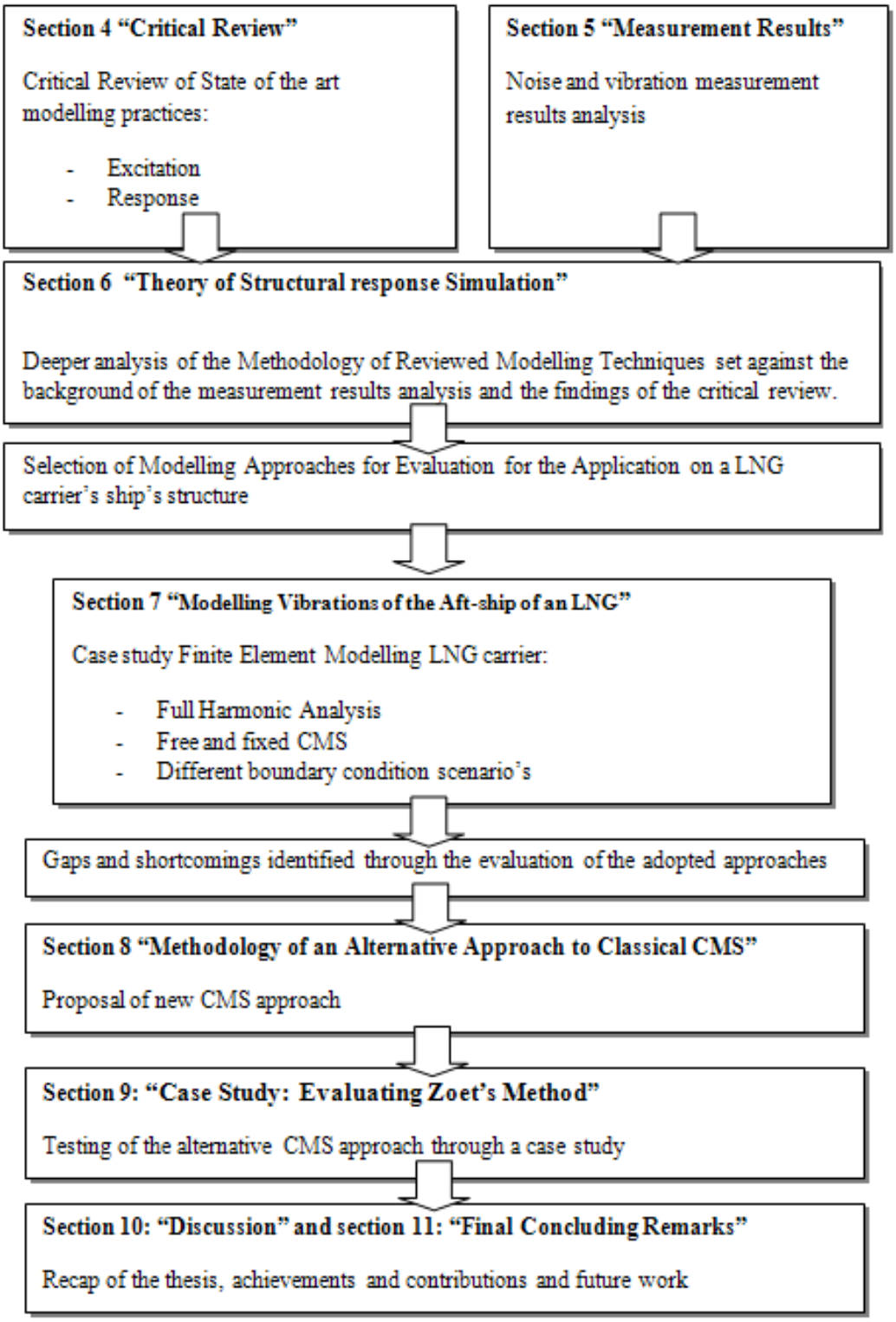

Figure 1 ***Structure of this thesis***

4 Critical Review

Many problems occur in the shipping industry resulting from the dynamic behaviour of structures and drivelines acting as mass spring systems. One of the most dangerous aspects of mass spring behaviour is that shock, impulse and harmonic excitation may case large alternating deformation of that structure. This alternating deformation may be perceived as vibrations by those touching the structure or standing on it and may have a profound impact on human wellbeing and health. These alternating deformation also result in alternating stresses in the structure, which may lead to fatigue damage.

In addition, vibrations may also cause the air surrounding a structure to vibrate which results in audible air borne noise. Transmission of noise to the underwater environment also takes place through that mechanism. Through that route, propeller and onboard machinery noise not only cause health and wellbeing problems for people on board, but also affect the heath of the underwater life.

The important question that needs to be asked is what determines the level of these structural vibrations that result in alternating stresses in the ship's structure, onboard noise and underwater noise. In that discussion it is very important to realise that the level of vibration is the result of a combination between the nature of the excitation and the natural response characteristics of the structure that is subjected to that excitation. Considering the low damping factors of steel, the main concern is not the amplitude of the excitation, although it naturally does have an impact. More important parameters are the frequencies of alteration that are within the excitation force characteristics and more precisely, the relation between these frequencies and the structures' natural dynamic behaviour. This natural dynamic behaviour is strongly characterised by a structure's resonance (natural) frequencies. A relatively low amplitude excitation force with a frequency close to any of the structure's resonance frequencies may already result in destructively high vibration levels. This is particularly the case with lightly damped structures, what ship structures typically are.

In order to prevent problems related to noise and vibrations it is important to have access to tools to estimate/simulate ship's structural dynamic behaviour in relation to the excitation characteristic that may be expected from the main excitation sources such as the propellers and on board machinery. This work focuses on the challenges of modelling ship's structural dynamic response. However, as it is the relation between the excitation characteristic and the response characteristic of a structure that determines the resulting noise and vibration levels, knowing the excitation characteristic is just as important. This section, the critical review, therefore starts with a brief review of the characteristics of the main ship excitation sources (propellers and diesel engines) and methods generally used to estimate these characteristics. This will provide the context for the critical review of the most commonly used methods for modelling structural response.

4	Critical Review
4.1	Controlling the Excitation Characteristics
4.1.1	Propeller Excitation
4.1.2	Diesel Engine Excitation
4.2	Controlling Structural Response
4.2.1	Hull Girder Approach
4.2.2	Finite Element Modelling
4.2.3	Mode Superposition
4.2.4	Spectral Element Modelling
4.2.5	Statistical Energy Analysis
4.2.6	Component Mode Synthesis Techniques
4.3	Conclusion and Summary Critical Review
4.3.1	Summary and Conclusions Review Excitation Forces
4.3.2	Summary and Conclusions Review Response Modelling Techniques

Paragraph structure chapter 4 'Critical Review'

4.1 Controlling the Excitation Characteristics

With the inventory of different sources for vibrations first a definition of the word 'vibrations' as used in this work should be given. With the definition of vibrations it has to be kept in mind that the focus of this work is on dynamic structural behaviour where both inertia forces (kinetic energy) and structural deformation forces (potential

energy) play an important role. This is the type of structural dynamic behaviour where dangerous resonance phenomena may occur. Resonance, or near resonance, may result in a situation that very low excitation forces may already result in high vibration levels that not only cause problems with health and well being for people working with or on that structure, but may also lead to structural fatigue damage resulting from high alternating material stresses.

On board ships there are many sources of alternating load, with many different frequencies of alteration. Forces induced on the ship's structure by sea going behaviour, ship loading condition and alternating power demands are low frequency alternating forces with periodicities ranging from a couple of times per minutes to a couple of times per month. Propellers and engines produce alternating forces with frequencies ranging from a couple of Hz to a couple of kHz.

Considering the main concern in this work is the consequences of structural resonance occurring, alternating stresses induced by **harmonic** seagoing behaviour, changing ship loading conditions and alternating power demand (manoeuvring for instance) are less relevant as the frequencies of these load alterations are outside the range of typical ships' structural resonance frequencies. For that reason, the review of excitation sources and modelling techniques has been narrowed down to propeller excitation and main and auxiliary machinery (diesel engines) excitation.

4.1.1 Propeller Excitation

One of the most powerful excitation sources resulting in ship vibrations and structure borne noise is the propeller. Through different hydrodynamic mechanisms the propeller generates alternating forces and couples on the shafting systems and transmits an underwater fluctuating pressure field which results in onboard noise and vibrations and underwater radiated noise [1, 2].

In order to control these propeller generated alternating loads, propeller excitation simulation tools are required so that aft ship and propeller geometry design choices can evaluated based on the resulting propeller excitation characteristic. Different tools and methods are available and much research is still carried out particularly in

understanding the inception of tip vortex cavitation through which broadband propeller excitation is generated. [3, 4].

4.1.1.1 Types of Propeller Excitation

Propeller excitation is a result of the following hydrodynamic phenomena [2]

- Unsteady blade lift
- Blade thickness effect (mainly local vibrations).
- Cavitation (sheet, bubble and tip vortex cavitation).

Unsteady lift

Thrust of a propeller is generated through the lift that is generated by the propeller blades. The lift generated by a propeller blade is determined a combination of two water velocity components. These components are [2]:

- Relative velocity component tangential to the rotation of the propeller. This velocity component is a result of the rotation of the propeller.
- Water inflow speed axial to the propeller disc. This speed is related to the speed of the ship through the water.

The combination of both velocity components determine the angle of incidence of the water flow relatively to the propeller blade profile which determines the lift generated by the propeller.

The wake is however is not constant over the propeller disc. The wake factor at the upper segment of the propeller disc is generally higher than at the lower segment as the water flow closer to the hull is generally more retarded than the flow further away from the hull. This means that the axial water velocity component to the propeller disc is not equally distributed over the propeller over the propeller disc area either.

As the axial velocity component, together with the rotation speed of the propeller, determines the incident angle to the propeller, the lift force generated by a propeller

blade, and all other related forces and couples, is not constant over time and varies with the position of the blade in the wake field.

Main concern in relation to the irregularity of these couples and forces is the excitation of torsional and lateral propeller shaft vibrations. Ship structural vibrations are only excited indirectly through transmission of shaft bending vibrations through the propeller shaft bearings. This is why these forces and couples related to the unsteady lift are referred to in the literature as the bearing (excitation) forces.

The unsteady lift excitation spectrum consist of distinct tonal peaks that are typically multiples of the blade passing frequency where the amplitudes of the frequency components rapidly decrease with the order number [1, 2].

Blade Thickness Effect

A more effective (local) hull vibration excitation source is through the hull pressure pulses generated through the displacement effect of passing propeller blade tips. This effect is further amplified when sheet cavitation occurs, through which the effective blade thickness (displacement) is increased and the resulting hull pressure pulses are amplified.

Because this type of excitation can best be described as a passing by of an area of low pressure right next to a high area of pressure, this type of excitation has the characteristics of a dipole source [5]. Dipole sources generate hull fluctuating pressure fields that are characterised by a large phase variation over the hull surface area[1]. Because of this phase variation, this type of excitation is mainly known for exciting local vibrations (appendices, smaller plate areas of the hull etc). Similar to the unsteady lift force generated excitations, the blade thickness induced excitation pressures are strongly characterised by frequency components that are multiples of the propeller blade passing frequency where the first blade passing frequency is the strongest and amplitudes decrease with the order number.

Sheet Cavity Volume Variations

A far more effective mechanism for global (hull) vibrations excitation is through the hull pressure fluctuations induced by fluctuating and collapsing sheet cavitaties. Change of volume of the cavities is related to changing pressure on the propeller blades whilst rotating through the wake field. The alternating propeller blade pressure is both related to the unequal distribution of wake at the propeller disc and the differences in hydrostatic pressure with the blade rotated to the upper segment of the propeller disc and the blade rotated to the lower segment of the propeller disc.

This type of cavitation is characterised as a monopole fluctuating pressure source resulting in an alternating hull pressure field that is largely in phase over the hull surface area [1]. Even though the actual pressure pulse amplitudes from blade thickness effects are higher, this source of excitation is still far more effective in exciting global hull vibrations because of above described phase characteristic of the generated pressure field [5].

The fluctuating cavity volume variation induced excitation spectrum consist of distinct tonal peaks that are typically multiples of the blade passing frequency where the amplitudes of the frequency components rapidly decrease with the order number.

Tip Vortex and Bubble Cavitation

Through cavitation of tip vortices and bubble cavitation propellers also generate a broad band excitation. Collapse of both sheet, bubble and tip vortex cavities is considered to behave as a broadband excitation source at frequency ranges typically from 50 Hz to 100 kHz [6]. Although it is up to now mainly addressed in navy applications where the resulting underwater radiated noise is of great concern, there is a growing concern for these phenomena in the merchant shipping as well both from a cavitation erosion damage point of view and from the underwater and on board radiated noise point of view [3, 4].

4.1.1.2 Developments in Evaluating Propeller and Aft-ship Design

The amplitude of excitation generated by a propeller resulting in onboard noise and vibrations and underwater radiated noise, can be controlled through carful design of propeller and aft ship geometry. For the evaluation of propeller generated excitation, first the wake distribution at the aft ship of a given geometrical design needs to be estimated. Both model test and CFD calculations techniques are used for that purpose [7] . From there, the greatest part of the tonal excitation components from the propeller can be theoretically calculated through following the very well established lifting line or lifting surface theories [8].

Estimating the effect of broadband cavitation induced by tip vortices and bubble cavitation is far more complex. Particularly the inception of tip vortex cavitation is considered one of the most complex phenomena occurring on a ship propeller [9]. Although it is up to now mainly addressed in navy applications where the resulting underwater radiated noise is of great concern, there is a growing concern for these phenomena in the merchant shipping as well both from a cavitation erosion damage point of view and from the underwater and on board radiated noise point of view [3, 4].

4.1.1.3 Propeller Excitation Control

Main issues that are addressed when trying to control the propeller excitation are:

- Wakefield at the aft ship
- Pressure distribution on the propeller blades (tip unloading)
- Increasing Tip Clearance

Wake distribution at the aft ship

A very important factor affecting the nature of propeller induced alternating bearing forces and hull pressure fields is the wake distribution at the aft ship. With an evenly distributed wake, no distinct tonal excitation would have come from the propeller except from the highly localised pressure pulses due to the blade thickness effect [2]. Unfortunately, for a maximum cargo capacity, particularly bulk carriers, tankers and

trailing suction hopper dredgers have a typically full aft ship geometry characterised by rapidly converging curves and steeply rising lines of the underwater part of the aft ship, where the propeller is. This geometry leads to a rapidly diverging water flow round the aft ship, resulting in unevenly distributed axial water velocities with strongly retarded velocities particularly close to the aft ship's hull.

For low propeller pressure pulses it is important to design the aft ship geometry that will induce a wake distribution at the propeller that is as evenly distributed as possible. Gradually rising and converging curves in the aft ship geometry will result in a smoother inflow of water and a far more equal distribution of axial water speed into the propeller compared to an aft ship that is characterised by steeply rising and rapidly converging curves and ends abruptly.

Propeller Blade Tip Loading

An important factor determining the amplitude of the propeller induced pressure pulse is the load distribution of the propeller tip. High propeller tip loads are beneficial for the propeller efficiency. However, a high tip load also leads to a deeper contrast between the high and low pressure area side of the propeller blade increasing cavitation volumes and increases changes of shedding effects and violent bubble implosions occurring [1, 2].

Tip-Hull Clearance

Another strategy for reducing propeller tip loads is by increasing the tip-hull clearance. Vorus argues [2] that it is a common misconception that increasing tip-hull clearance is most effective because of the resulting reduction in the refraction effect. The most important factor increasing propeller excitation with small tip clearance according to [2] is that the wake gradient increases strongly with a decreasing distance from the hull. This means that not only the propeller tip load will be higher closer to the hull, but also the fluctuations of cavity volumes will be stronger resulting in higher amplitudes of alteration of the induced hull pressure field [3].

4.1.2 Diesel Engine Excitation

The main and auxiliary engines on board a ship are also major sources of excitation playing an important role in structure borne noise and vibrations propagating throughout the ship's structure. Two types of excitation are generated by the engine. Alternating forces and couples are generated through the irregularity of the cylinder gas pressure (gas forces) and through the acceleration and deceleration of the translating and rotating masses such as cranks, pistons and connecting rods (inertia and rotary forces)[10-12].

Both gas force and rotary and inertia forces excitation are mainly of a tonal nature. Inertia forces generated excitation spectra exhibit tonal frequency components that are multiples of the crankshaft rotation frequency. The first and second order crankshaft rotation frequencies are the two most dominant excitation frequencies resulting from inertia and rotary dynamic phenomena. Higher order frequencies also occur, but their amplitudes rapidly decrease with an increasing order number.

4.1.2.1 Characteristics of Gas Forces Induced Excitation

The first type is the excitation generated by the unsteady cylinder gas pressures. The irregularity of the cylinder pressure, which is related to the different stages of the combustion process, results in an unsteady, irregular vertical gas force [13].

The vertical gas force, through the geometry of the crankshaft and connecting rod, results in an irregular driving torque and, as a reaction to the irregular torque, in irregular transversal piston or guide forces. The irregularity of the driving torque is of concern for the torsional vibratory behaviour of the driveline. The irregular transversal piston or guide reaction forces try to force the engine into a rolling motion (H-couple) through which engine vibrations are transmitted to the ship's structure. Gas forces also force the engine's A-frame to periodically deform through the resulting so called X-couple. This is mainly of concern for slow running 2-stroke engines of which the A frame is relatively flexible. The vertical gas force irregularity also induces high alternating loads in the engine's components, but do not directly transmit engine vibrations to the ship's structure. Vibrations induced by vertical gas

forces are only indirectly transmitted through the projection of the connecting rod forces in transversal direction (guide forces) which result in the above mentioned H-couple and X-couple [14].

Gas forces excitation spectra exhibit harmonic tonal components that are multiples of halve order or first order crankshaft rotation frequency, depending whether it is a four stroke or two stroke engine respectively. Distinctive dominant peaks in the excitation spectrum occur at multiples of the firing frequency, with the amplitude rapidly decreasing with order number.

4.1.2.2 Characteristics of Inertia Forces Induced Excitation

Force characteristics generated through the acceleration and deceleration of translating and rotating masses exhibit distinct tonal frequency components that are multiples of the (crank)shaft rotation frequency [12]. The first and second order crankshaft rotation frequency are the two most dominant excitation frequencies resulting from inertia and rotary dynamic phenomena. Higher order frequencies also occur, but their amplitudes rapidly decrease with the order number [12, 15]. Both X and H couples are generated in the same way as explained for the gas forces induced X and H couples. In addition to the X and H couple, inertia and rotary forces also induce a couple that tries to force the engine into a pitching couple [15].

4.1.2.3 Estimating Engine Excitation Characteristics

Theoretically estimating the excitation characteristics from a particular engine depends on the quality of data provided by the engine manufacturer. From gas force induced tangential effort harmonic components the gas forces induced transversal cylinder or guide reaction forces can be calculated. From these transversal forces the X and H couples can be deduced. These tangential effort curves are available from engine manufacturers as they serve as excitation input for the class compulsory drive line torsional vibration analysis [11, 16-18].

Excitation couples and forces are also available from engine manufacturers. They can also be deduced from information of the reciprocating and rotating weights and

the properties of the rotary masses used for the first and second moment compensation [15].

4.1.2.4 Controlling Engine Excitation

Direct reduction of excitation is done through applying rotating balancing weights. Through installing rotating balancing weights at the forward and aft end of the engine first and second moment inertia induced excitation moments are partially, and sometimes even fully compensated [10, 15].

Reducing engine induced vibrations is indirectly done trough applying flexible mounting systems through which dynamic isolation between the engine and ship foundation is achieved [18]. Recent development has also been focussing on applying active mounting systems [19].

4.2 Controlling Structural Response

A very important factor determining the level of vibrations and the related consequences is the structural response to the excitation characteristics. Particularly for steel structures which typically contain very little damping, high vibration levels may already occur at relatively low excitation amplitudes with excitation frequencies close to structural resonance frequencies. Being able to evaluate the impact of design choices of the response characteristic of a structure or drive line is very important when designing a ship, which has also been demonstrated through simulation tests carried out for the fp7 EU project SILENV [18, 20]. In these publications it has been demonstrated that in case of (near) resonance, reducing the response to acceptable levels through reduction of excitation (through optimising propeller design) is very difficult. The simulation results have also demonstrated the benefits of estimating the structural response of a ship's over a frequency **range,** rather than for just a few harmonic components. Simulating results over a frequency range will not also show where the sensitive response frequencies are, but also at what frequencies the mobility of the structure is the lowest. This way structural response and excitation frequencies can be deliberately tuned for an as low as possible vibratory response.

In this section the available state of the art structural response simulation tools are critically reviewed for their practicality and validity as tools for simulating ship vibrations. The following methods are discussed:

- Application of the beam theory (hull girder vibrations)
- Finite element modelling (FEM)
- Spectral element method (SEM)
- Statistical energy analysis (SEA)
- Mode Superposition and Component Mode Synthesis Techniques (CMS)

4.2.1 Hull Girder Approach

A much used well validated method used for calculating ship vibrations is through modelling the ship hull as a uniform continuous beam [2, 21]. The beam is supported by a uniformly distributed spring stiffness *K* representing the buoyancy effect of the water (see Figure 2). This uniformly distributed spring has a uniformly distributed damping coefficient *C* representing the hydrodynamic damping of the water surrounding the hull girder. The uniform beam-mass per unit length μ represents the mass of the ship (plus cargo) plus the hydrodynamic added mass. The uniform stiffness of the beam itself is according to Hooks law equal to EI where E is the elasticity modulus of the hull material and I is the average cross sectional moment of inertia of the vessel. The engine and propeller excitation loads on the hull are modelled as concentrated loads (couples or forces, $M_{(t)}$ or $F_{(t)}$).

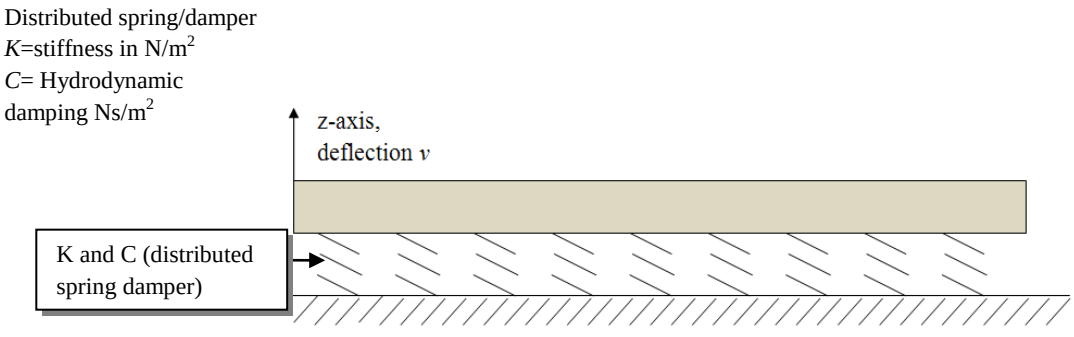

Figure 2 ***Representation of a ship hull as a beam. The beam is supported through a distributed springs with stiffness properties K representing the buoyancy effect of the water and damping C representing hydrodynamic damping.***

Since for normal ships the shear centre for horizontal and torsional vibrations and the centroid for longitudinal and vertical vibrations are roughly located at the centre of gravity, no coupling is assumed between horizontal and torsional (hull twisting) modes. Therefore these modes are all treated separately [21]. The ship's response acting as a hull girder is calculated by modelling vibrations as set of interacting travelling waves, following the Euler-Bernoulli beam theory.

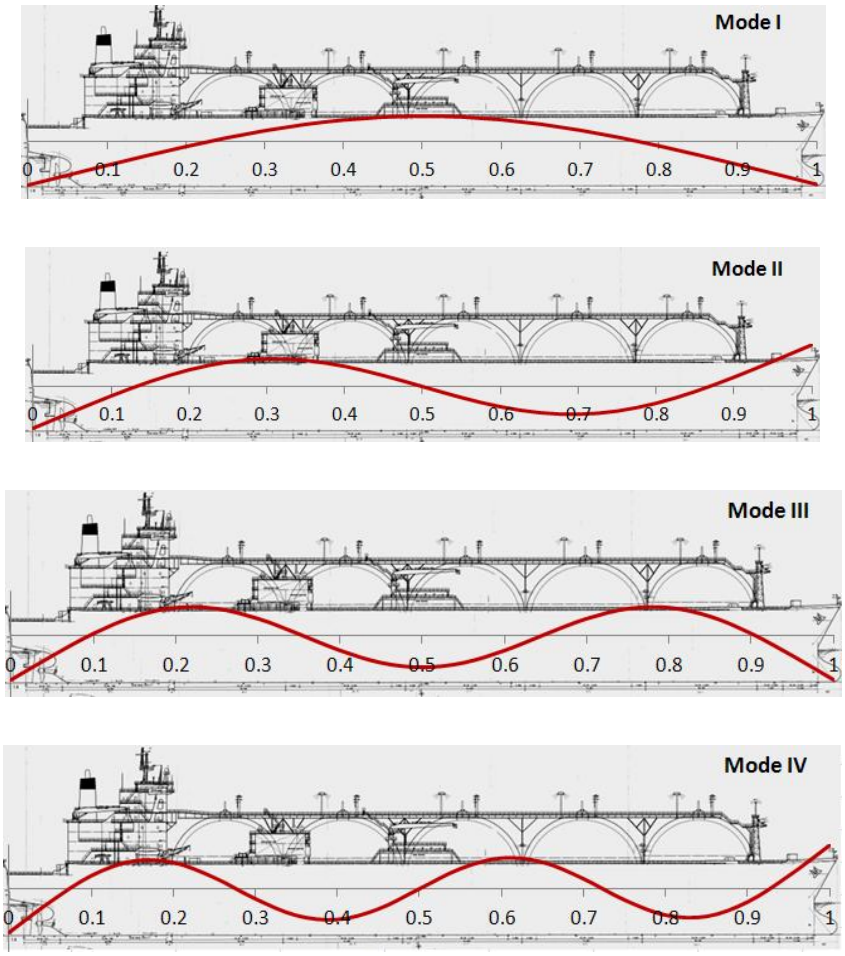

Figure 3 ***The first four modes shapes as they will look like modelling the ship as an Euler beam***

Although Figure 2 shows stiffness and damping effect due to hydrodynamic interaction with the hull girder vibrations, these contributions to the mass elastic behaviour is considered very small and is normally omitted, which simplifies the model further. The effect of added mass to the natural frequencies corresponding

with the hull girder modes is however considerable. Different methods have been developed for estimating the hydrodynamic mass as presented in [2].

4.2.1.1 Limitations and Latest Developments in the Hull Girder Approach

With the calculation of the natural frequency and mode shapes of a ship hull the Euler beam approach is used, which is a very practical approach. However, to be able to use the Euler beam approach the following assumptions are made:

- The cross section of the beam remains normal to the deflection line, i.e. no shear deformation takes place.
- No rotary inertia effect of the cross-sectional area is taken into account assuming it to be negligible relatively to the vertical inertia effect.
- No coupling between bending and hull girder torsion is assumed as the location of the centre of gravity, centroid for longitudinal and vertical vibrations and the shear centre are assumed to coincide [21].

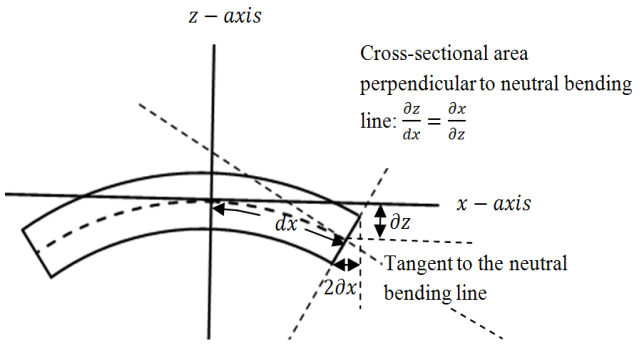

Figure 4 ***Perfect bending where the tangent of the neutral bending line is perpendicular to the cross-sectional area, i.e. no shear deformation of the cross-sectional area takes place (Euler beam theory)***

This means that there are limitations to the wavelength related to the mode shape for which the natural frequency can safely calculated using the Euler beam theory. In the literature a minimum wavelength of 10 times the height of the beam (in this case the depth = freeboard plus draft) is recommended [22]. The shorter the wavelength, the less valid the approach will be. Considering the wavelength involved with the mode shape decreases with the mode number, errors in estimating natural frequencies increase with mode number as well. Considering the minimum requirement of the wavelength to be at least 10 times the depth of the vessel, the wavelengths for mode

numbers higher than 2 (see Figure 3) will for most vessels not fulfil these requirements. Although this can still be overcome by adding the inertia and shear deformation effect to the Euler beam (through which the beam becomes a Timoshenko beam), the fact that the ship's mass-stiffness distribution has been simplified to a continuous model will still decrease the validity of the model with increasing mode number.

Another shortcoming of this approach is that no coupling between horizontal and torsional mode-shapes is assumed as the location of the centre of gravity, centroid for longitudinal and vertical vibrations and the shear centre are assumed to coincide [21], so that all mode shapes can be analysed separately. However, with ships with large hatch openings (such as large container vessel), the shear centre is typically located outside the cross section (below the keel) which implies that there will be a coupling between the hull torsional vibration mode and bending modes [21].

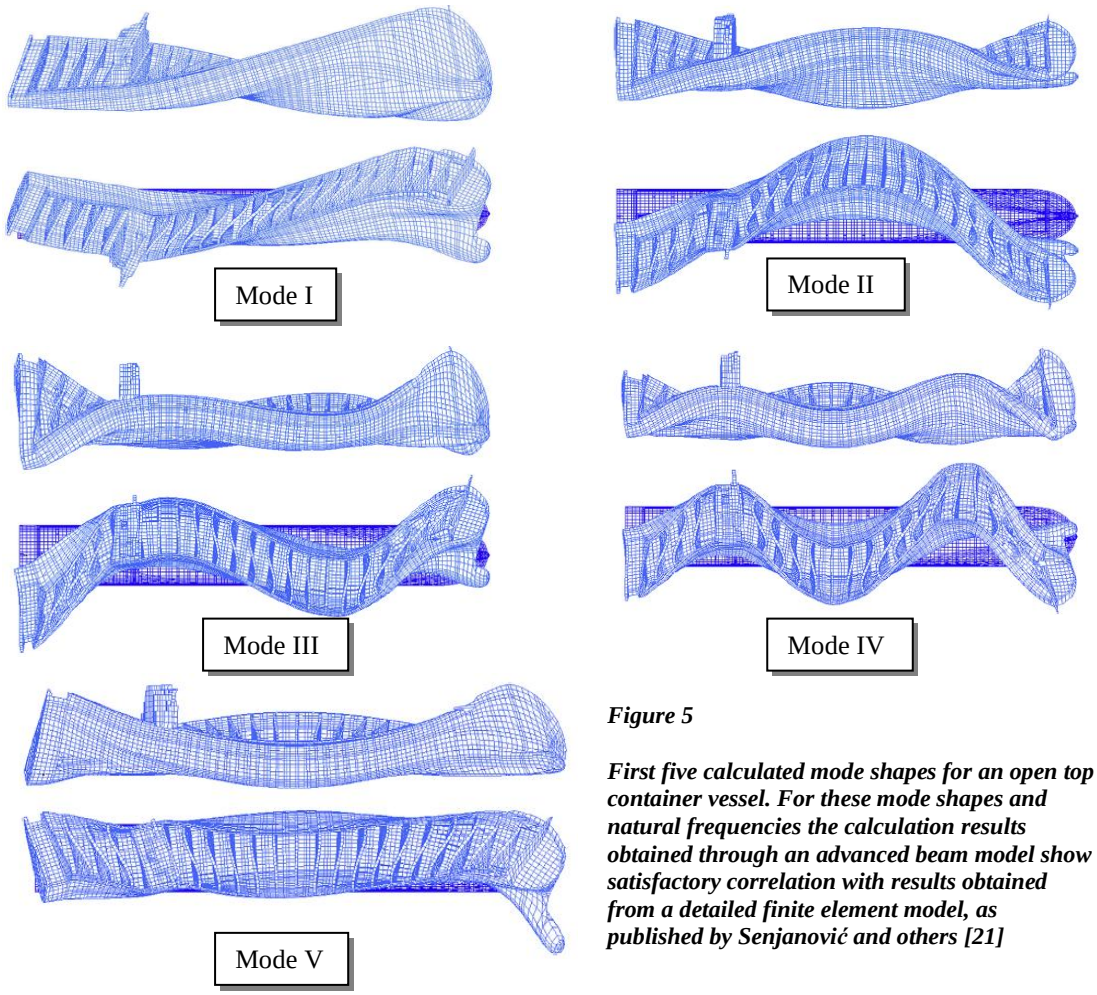

Figure 5

First five calculated mode shapes for an open top container vessel. For these mode shapes and natural frequencies the calculation results obtained through an advanced beam model show satisfactory correlation with results obtained from a detailed finite element model, as published by Senjanović and others [21]

As a result, warping will also be constrained, resulting in added shear force which affects the mode shapes and corresponding natural frequencies.

Senjanović and others [21] propose a generalised and improved solution to the classical thin walled hull girder theory and suggest using a beam finite element modelling techniques (1D FEM) for calculating hull girder vibration modes. In the beam elements used, all effects of the location of the centroid, shear centre and centre of gravity are taken into account. Tests with an open container carrier has showed good correlation up to the 5th mode between the 1D FEM model and a 33072 node/84076 element 3D finite element model (see Figure *5*).

4.2.1.2 The Relevance of the Hull Girder Approach

Estimating hull girder natural frequencies is particular of importance for ships for which propeller and machinery excitation frequencies are expected to be in the same range as the hull girder natural frequencies. Empirical data originally presented by Johannessen and Skaar have been presented in [2] and are shown in Figure 6. Also empirical formulas are available such as the Kumai's Formula presented in [2] for estimating the 2 node vibration natural frequency (mode I in Figure 3):

$$N_{2v} = 3.07e6\sqrt{\frac{I_v}{\Delta_i L^3}} \quad \textbf{(4.1)}$$

Where:

$\Delta_i = \left(1.2 + \frac{1}{3}\frac{B}{T_m}\right)\Delta$

Δ_i= ship's displacement including virtual added mass of water

Δ = ship's displacement

I_v = cross-sectional moment of inertia

B = midship breath

T_m = mean draft

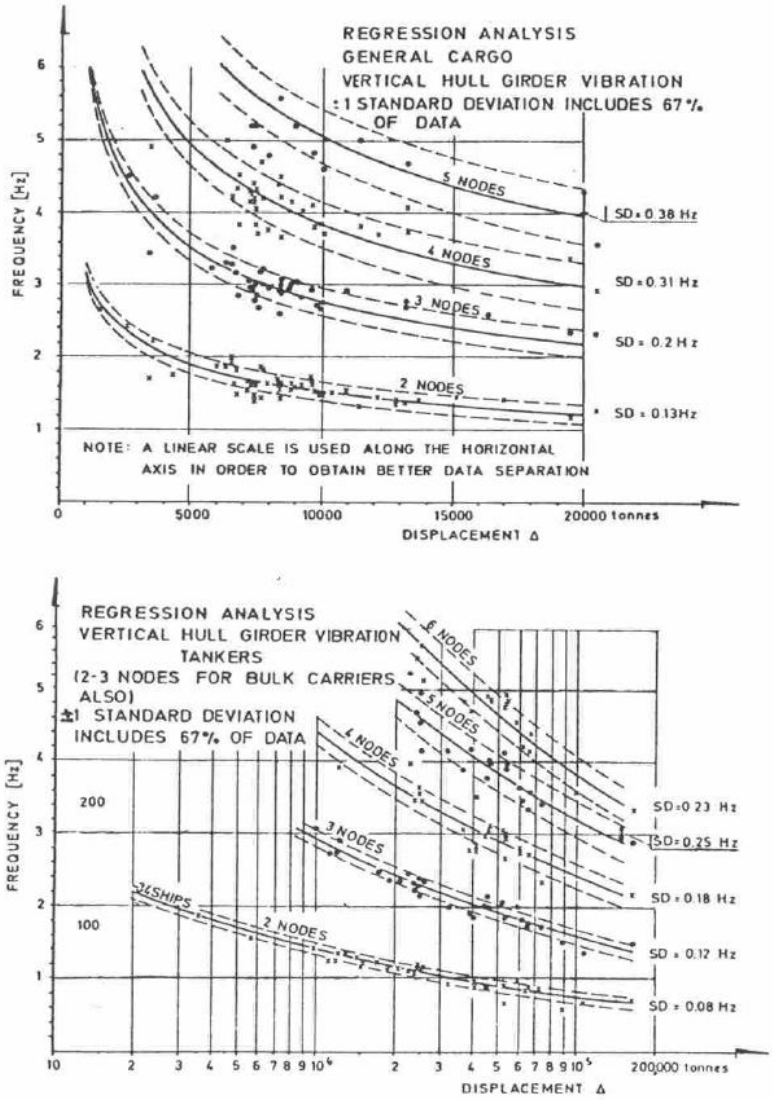

Figure 6 ***Empirical data originally presented by Johannessen and Skaar for vertical hull bending vibrations***

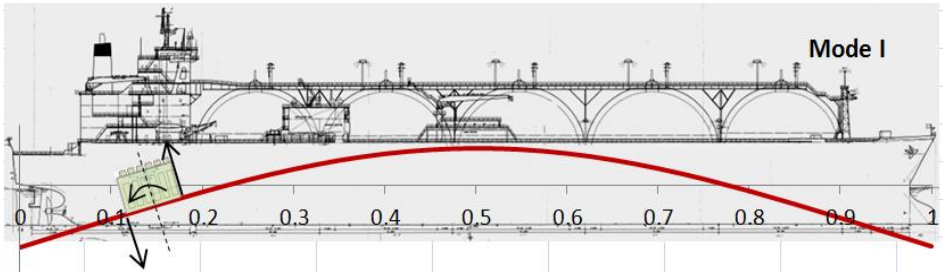

Figure 7 ***Excitation of hull bending vibrations through the pitching engine couple***

Considering the empirically obtained data presented in Figure 6 it can be demonstrated that excitation frequencies from slow running four stroke engines may

be in the range of hull girder natural frequencies corresponding with the first 5 modes. Figure 7 shows that the pitching couple generated by the engine's inertia couple fits very well onto the first mode hull bending vibration.

In addition, considering a 100 rpm diesel engine, alternating pitching couples of the 1^{st} and 2^{nd} order crankshaft rotation frequency occur at 1.7 and 3.3 Hz, which are frequencies that are right into the range of natural frequencies corresponding with the first 5 hull girder modes, as can be seen in Figure 6. If any of these hull girder natural frequencies should be close the engine pitching moment frequencies, special attention may has to be given to the balancing arrangement on these types of engines.

However, there will be many vessels for which the first couple of hull girder bending frequencies are well below the dominant excitation frequencies, which may be particularly the case for vessels with medium to high speed engines. Even though hull girder vibrations are not directly excited at their natural frequencies, they may still play an important role in the transmission of vibration energy from propellers and machinery to area's where local resonance may occur. This local resonance may involve vibration modes of the superstructure, decks or bulkheads. As propeller cavity volume fluctuation results in a very effective in-phase fluctuating pressure field at the aft ship through which hull bending, even though not at resonance, is excited very effectively. As hull bending vibrations are global vibrations, they are felt throughout the vessel and are therefore capable of inducing indirectly local resonance phenomena. In order to be able to estimate the relevant higher order natural frequencies and corresponding more complicated mode shapes, much more detailed models are required in order to overcome the difficulties with the fact that a hull does not behave as a slender beam with an evenly distributed mass and stiffness.

4.2.2 Finite Element Modelling

Although in theory the natural frequencies and mode shapes of any structure can be calculated considering vibrations the result of interaction between waves travelling through the structure, this approach is not practical for more complex structures [12]. As demonstrated above, there is a practical value to this approach as long as a ship is

considered a continuous homogeneous beam. However, the penalty paid for this simplification of the ship's structural properties becomes larger with increasing mode number. A more precise description of the complex ship's structure is required. This means that the ship's structure needs to be subdivided in many sections with different (homogeneous) properties. Mathematically describing the interface condition for each section according to the wave approach becomes very complex in this case and makes the beam theory approach a highly unpractical choice for analysing higher frequency vibrations.

4.2.2.1 Principles of Finite Element Modelling

For complex structures discrete finite element models are used. These models are based on a modal approach. The value of this approach for modelling hull girder vibrations has already been demonstrated in [21], where beam elements were used to model the ship hull and calculate the hull girder mode shapes and natural frequencies.

With a finite element model a (complex) structure's mass spring distribution is described through a collection of discrete points (nodes) connected to each other by elements. These elements represent a mathematic description of the relation between the lateral and angular displacement of the nodes (translation and rotation), the deformation of the element, and the resulting reaction load in the nodes. Through the formulation of the equilibrium requirements for all nodes at each degree of freedom, a set of coupled equations is obtained equal to the number of degrees of freedom of the model. Displacement of the nodes due to (harmonic) external forces is calculated, through which deformation of the elements and related element stresses are obtained as well.

As mentioned above, the properties of a element are described through the relation between displacement and reaction loads on the nodes. This requires a description of the relation between the displacement of the nodes and the deformation of the element. The deformation of the element is described as a polynomial with a degree equal to the number of degrees of freedom of the element, i.e., the elements deformation is described through a superposition of a finite number of modes of

deformation, equal to the number of degrees of freedom of the element. As the equations of motions are composed based on a finite number of assumed deformation modes, the approach to vibrations adopted by the finite element modelling technique is referred to as the so called modal approach to vibrations. The equations of motion are obtained through substituting the mathematical description of these modes (shape functions) into the energy relation based on d' Alembert, Hamilton and Lagrange equations [12, 22, 23]. The connection of many simple elements forms the description of the complex structure.

As this approach quickly leads to a large number of equations that needs to be solved (one for each degree of freedom, i.e. the number of equations required is at least equal to the number of nodes), the principle only become interesting for application on larger scale with the development of computer technology in the 1960ties. With the sharp increase of computer capacity over the last decades, the finite element modelling technique has also become accessible for analysis of the structural response of complex marine structures, and has become a widely used method.

4.2.2.2 Ship Structures and Gaps in Finite Element Modelling

For complex structures, a minimum number of elements is required in order to accurately enough describe the elastic behaviour of the structure. In the past, the degree of complexity of ship structures quickly lead to models requiring long computation times and required too much computer memory to run, which made the simulations either too expensive or highly unpractical.

Although developments in the computer technology has made it possible and affordable to run FEM models representing considerable parts of a (complex) ship structure, problems still occur with size and running time of simulation, particularly when trying to simulate the propagation of structure borne noise. At higher frequencies mode shapes corresponding with the high mode numbers of concern become increasingly complex. In order to be able to accurately enough describe these mode shapes (deformation shapes), an increasing number of elements is required. In the literature, the number of elements required is often related to the wave length of the structural vibrations. Guidelines for selecting element size vary in the literature

where it is recommended that the distance covered by 6 to 12 times the element length should not exceed the wave length [24] [22]

Different modelling techniques have been developed to overcome problems experienced with Finite Element Modelling related to required computer memory and computation time. The techniques reviewed in this section are:

- Mode Super position Techniques
- Spectral Elements Method [25]
- Statistical Energy Analysis
- Component mode synthesis techniques

4.2.3 Mode Superposition

In order to speed up calculation time, mode superposition is used through which the number of equations that need to be solved, is decreased.

4.2.3.1 Principles of Mode Superposition

This technique is based on calculating the response as a superposition of the contributions of a reduced number of vibration modes. These contributions are expressed through modal coordinates. These modal coordinates are calculated through reduced stiffness and mass matrices obtained through so called modal reduction. With modal reduction the full stiffness and mass matrices are reduced by projecting those onto the subspace spanned a truncated set of eigenvectors, i.e. mode shapes. These number of eigenvectors chosen to serve as a reduction basis is based on the relation between their corresponding natural frequencies and the response (excitation) frequencies of interest. Usually the cut-out frequency, i.e. the upper limit of the frequency range within all modes are selected that are to be retained, is 1.5 times the frequency of interest (according to Rubin's criterion [26]).

4.2.3.2 Ship Structures and Gaps in the Mode Superposition Approach

Through applying the mode superposition technique, the total set of equations of motion has been reduced considerably and with that, the computation time required to find the response modal amplitudes. However, the time required to calculate the

natural frequencies and mode shapes for the retained mode numbers has to be added to the time required to solve the reduced set of equations of motion. Unfortunately, the time required to calculate the mode shapes and natural frequencies increases exponentially with an increasing number of required modes [22]. The impact of computation time required for calculating mode shapes and natural frequencies may, particularly with the analysis at higher frequencies, be the most dominant factor in the total required computation time. The calculation time required to produce the forced vibration solution may even exceed the computation time required for generating the forced vibration solution through full harmonic analysis. This is also demonstrated later in this work.

4.2.4 Spectral Element Modelling

A different approach to overcome problems with model size and computation time is the application of the Spectral Element method. With spectral element analysis a similar approach is chosen with compiling the stiffness and mass matrices as with Finite Element Modelling, but using much bigger elements representing homogeneous parts of a structure, and using a travelling wave approach to vibrations.

4.2.4.1 Principles of Spectral Element Modelling

This method uses elements of which the dynamic behaviour is described following a wave approach as also adopted for the hull girder calculations as explained in section 4.2.1. Where the finite element method uses a frequency independent polynomial shape function for describing the deformation of an element, with spectral elements the shape function is frequency dependant and is based on the wave equations. As the wave equation approach gives the exact mathematical description of the form relations of a continuous structural element, the thus obtained total dynamic stiffness matrix of an entire structure is also referred to as the exact stiffness matrix [24, 27, 28].

Advantage of this modelling technique is that a huge reduction of elements is obtained. Elements may now represent an entire part of a structure that may be considered homogeneous of nature, such as a beam or a plate section, as the

frequency dependant deformed shape obtained through the wave approach is the exact shape of deformation of the element. As a result, the number of elements does not need to be increased with a decreasing wavelength (increasing frequency). This is unlike the Finite Element Modelling technique, as described in section 4.2.2, where the number of elements needs to be increased with decreasing wave length (increasing frequency) as a consequence of the frequency independent non-exact polynomial approximation of the shape function.

4.2.4.2 Ship Structures and Gaps in the Spectral Element Modelling Approach

As described above, spectral elements are elements covering parts of a structure that are considered homogeneous of nature so that the wave approach to vibrations can be safely adopted. Unfortunately, a ship structure does not contain many large portions that could be safely considered homogeneous. Research has been carried out into developing spectral elements representing stiffened plate fields by Ajith [27], but still, all beams, brackets and plate sections should be modelled as separate spectral elements. This problem has been described by Lee [28] as ‘not knowing the exact wave solution for most complex multidimensional problems’. This is certainly the case when considering a double bottom of a ship as a homogeneous structure.

Another problem is the relation between the size of structural elements and wave length of the vibration. Adopting a wave approach implies that vibrations are modelled as waves transmitted from one element to another element through bending, axial shear or torsional deformation. Considering the size of homogeneous elements in a ship structure, combined with typically relatively low excitation frequencies, transmission of vibration energy between elements does not take place just through flexural deformation of the elements, but mainly through rigid body movement of these elements. As is demonstrated later in this work, dominant (tonal) vibrations excited by propeller and engine induce typical alternating structural deformations involving wave lengths largely exceeding the maximum possible size of a homogeneous spectral element. As vibration propagation takes place through vibration deformation patterns involving larger parts of the structure, the rigid

movement of the relatively small element play a major role, but is not taken into account as a consequence of the adopted wave approach.

4.2.5 Statistical Energy Analysis

An approach adopted in order to overcome problems occurring with finite element modelling when analysing higher frequency response is the Statistical Energy Analysis approach (SEA). With statistical energy analysis a structure is divided in subsystems. These subsystems have the same function as the elements used in finite element modelling. The big difference is that subsystems are much larger than the elements used in FE modelling. As the number of elements for statistical energy analysis models is much smaller than for finite element models the number of equations that need to be solved is a lot lower as well, which is a huge advantage.

4.2.5.1 Principles of Statistical Energy Analysis

The main properties of Statistical Energy approach [29-32]:

- It is an energy approach: vibrations and noise are represented as quantities of energy travelling between subsystems
- It is a broad band approach. Quantities of energy are given as the total quantity of energy content over a broad frequency bandwidth. Octave and 1/3 octave bandwidths are typically used. No narrowband tonal information can be extracted from the calculation results.
- The necessary dynamic properties of subsystems are estimated for the subsystems in resonance. Dynamic subsystem interaction factors (coupling loss factors) and energy loss factors (internal loss factors) are expressed as energy exchange factors between the resonance modes of neighbouring subsystems.
- It is a frequency and modal average approach. The dynamic properties of a subsystem are frequency average properties for the bandwidth of concern. The properties of subsystems necessary to calculate the energy flows and

energy contents of subsystems are the coupling and internal loss factors and are taken to be the same for each resonance mode (modal equipartition condition). Each resonance mode within a substructure is also assumed to contribute the same amount of vibration energy to the total stored vibration energy of a subsystem.

- It is a modal average approach. All resonance modes in a particular subsystem contain the same amount of energy. The total energy of a subsystem for a particular bandwidth is equal to the number of natural frequencies in that subsystem in that particular bandwidth times the modal energy of any individual mode.

- It is a spatial average approach i.e. no information is available of how the energy is distributed within the subsystem. Excitation is also assumed to be spatially equally distributed so that each mode shape receives the same amount of energy.

- The effect of global mode shapes (for instance mode shapes of which the wavelength exceeds the length of a subsystem) are not taken into account.

The following conditions need to be met in order for the statistical energy approach to work:

- Preferably a broadband excitation over the analysed frequency bandwidth. This way all natural mode shapes within the frequency band are fully excited, the condition for which the coupling loss and internal loss factors are estimated for a substructure.
- The higher the number of resonance frequencies within an analysed frequency bandwidth, the more reliable the results become. This is where the term ‘statistical’ refers to. With a high number of resonance frequencies within a bandwidth, the total energy content of the subsystem is calculated as a sum of the average energy contributions from all these resonance mode shapes. The higher the number of resonance mode shapes involved (the

bigger the population) the better the deviations from the average values are averaged out.

- A uniformly spatially divided excitation source is ideally required to ensure equipartition of modes.

4.2.5.2 Ship Structures and Gaps in the Statistical Energy Analysis Approach

The following remarks can be made about typical marine structures and excitation characteristics in relation to the requirements for statistical energy analysis:

- Ship structures are highly complex. Subsystems will therefore show little uniformity in structural behaviour corresponding with the different resonance frequencies. This decreases the chance that there is actual mode equipartition [33].
- Excitation sources are of a highly tonal nature. This also decreases the chance that there is actual mode equipartition.
- Some excitation sources are spatially unequally distributed. This also decreases the chance that there is actual mode equipartition.

Statistical energy analysis could however still be used as a tool for a qualitative approach to propagation of structure borne noise for some types of ships. particularly for high speed crafts with high turbulent flow excitation and light structures with high modal densities. However, considering above, this technique is unsuitable for simulation of propagation of vibrations induced by the tonal sources such as the propeller blade passing harmonics and diesel engine crankshaft rotation and firing frequency related harmonic components.

4.2.6 Component Mode Synthesis Techniques

One of the attractive aspects of statistical energy analysis is that the calculation of dynamic behaviour is based on subdividing a structure in coupled substructures and calculating assembled structural behaviour based on the individual dynamic behaviour of the uncoupled substructures. As a ship's structure consists of many

repeating structural sections, the dynamic properties (mode shapes and natural frequencies) of only one of a series of repeating substructures would be required for the calculation of the total dynamic structural behaviour of the total assembled system. This saves computation time and required computer storage space for the model. Also symmetry of ship structures can be used to reduce the number of calculations required.

In the 1960ties a modelling techniques called Component Mode Synthesis (CMS) has been developed also allowing a sub-structural approach which, unlike SEA, can be used for simulating narrowband vibration response of highly complex structures. CMS is mostly used based on a finite element model. The model is reduced by applying a mode superposition technique on the individual substructures. Modal information of the substructures is usually obtained through finite element analysis.

As calculation time required for obtaining mode shapes and natural frequencies decreases exponentially with the size of the model, the total required computation time for obtaining all relevant modal information for each individual substructure will be a lot less than the time required for obtaining modal information for the total assembled structure, which is an advantage relatively to the classical mode superposition method.

4.2.6.1 Principles of Component Mode Synthesis

The Component Mode Synthesis (CMS) approach has been proposed for the first time by Craig and Bampton in 1968 [34] and has been used a lot since for large structures such as airplane fuselages and civil engineering applications. Variations on the method have been developed by, amongst others, MacNeal and more recently, by Rixen [35, 36].

Some of the key advantages recognised in the literature and presented as the motivation for developing the method are [37-39]:

- Reduction of required computer time. Computer time increases exponentially (depending on the eigenvalue extraction method and nature of the structure) with the number of degrees of freedom. As a result, analysing the complete

assembled structure requires more time than the combined time required doing the analysis of the individual substructures [35].

- Further reduction of the model is obtained through using a limited number of eigenvectors (mode shapes) as a reduction basis.
- The computation method allows separate teams of engineers to work independently on the design of parts of the structure. This saves time enabling the engineering teams to work parallel setting up the dynamic stiffness matrices of the individual substructures. These matrices will be compiled together for the calculation of the dynamic behaviour of the complete structure.
- Modification of the design of a structure does not require changing and re analysing the complete model. Only the substructure containing the part that is redesigned needs to be analysed for mode shapes and natural frequencies again.
- Through component mode synthesis the dynamic behaviour of a structure can be evaluated through measurements once the individual substructures (in the shipping industry these could be ship sections) have been constructed, even though these sections have been manufactured at different locations.

4.2.6.2 Fixed and Free Interface CMS

Two types of CMS techniques are distinguished:

- Fixed interface CMS
- Free interface CMS

With fixed interface CMS the dynamic behaviour of the substructures is described through elastic modes and constraint modes. Elastic modes are calculated for the substructures with the interface lines (lines connecting a substructure to adjacent substructures) constrained. The alternating displacement of the interface nodes is described through constraint modes, which are in fact static modes representing the static deformation of the substructure as a result of the interface forces occurring due to the interaction between sub structures. These constraint modes represent an important contribution to the total dynamic behaviour of the ship's structure.

With free interface CMS the dynamic behaviour of the substructures is also described through elastic modes and constraint modes. Elastic modes are calculated for the substructures with the interface lines or points free.

Comparison between free and fixed CMS is presented in Table 1

	Fixed interface CMS	**Free interface CMS**
Dynamic response calculated through	Elastic modes and constraint modes	Elastic modes and constraint modes
Number of elastic modes required for accurately describing dynamic displacement field	Requires less elastic modes than the free interface CMS method for accurately describing a substructure's elastic behaviour	More modes required as un-constrained model contains more degrees of freedom
Importance of Static modes	Important for describing displacement field. Need to be expanded for obtaining total dynamic displacement field.	**Not** important for describing displacement field. Expanding only the elastic modes gives an accurately enough representation of the dynamic displacement field.

Table 1 ***Comparison fixed and free CMS methods***

The difference between fixed and free interface CMS is that the displacement of the interface modes and the internal modes is already sufficiently described by the elastic modes. This means that unlike the fixed CMS method, the static modes don't need to be expanded for the sake of the accuracy of the calculated displacement field. For typical ship structures, this will reduce the number of required floating point operations required for generating the results. The reason for that is the high number of interface nodes usually involved in CMS models of typical ship structures, as the substructures are connected to each other through interface lines. The number of static constraint modes involved is therefore high as well, as this number is equal to the number of degrees of freedom on the interface lines. The number of elastic modes required to describe the dynamic displacement field of a substructure

accurately enough is however higher than for the fixed CMS model, as the increased number of degrees of freedom also increases the modal density, particularly at lower frequency ranges.

Although expanding static mode does not add a lot to the accuracy of the calculated displacement field, they are however very important for the accuracy of the description of the equilibrium relations, and therefore for the accuracy of the calculated modal coordinates representing the structures assembled dynamic response. Element stress and therefore the resulting reaction forces acting on the interface nodes are extremely sensitive to errors in nodal displacement [22, 39]. See also section 6.5.2 “Free Interface: the McNeal and Rubin’s Method”.

Another advantage of free interface CMS modelling is a more practical approach when evaluation of substructures modal properties takes place through modal measurements in the field. If these actual substructures are sections of ships that are waiting to be assembled, these sections will in most case be supported by a number of support points (blocks) which means that the interface boundaries of the section will be free, i.e. unconstrained. This is an advantage also mentioned for application in the aeronautical industry in [35].

4.2.6.3 Ship Structures and Gaps in CMS Approach

Although there are a lot of advantages of applying Component Mode Synthesis (CMS) modelling for ships, problems may arise with required computation time when applying CMS on typical ship structures. Although the CMS total set of equations (matrix size) is a lot lower than the number of equations obtained following the full harmonic analysis, the ratio between the number of non zeros /number of zeros in the CMS matrix is a lot higher (denser matrix). As a result a situation may arise that the number of non zeros in the CMS matrix is higher than the number of non zeros in the full dynamic stiffness matrices used for full harmonic analysis. Such a situation may easily occur when applying CMS on structures containing many interface nodes, as is the case with typical ship structures. Ship structures are continuous of nature and substructures are therefore coupled to each other through coupling lines which have to contain a certain number of nodes, in

order to accurately enough describe the deformation at these interface lines. Classic CMS approaches are based on describing the interaction between substructures through setting up equations of equilibrium and compatibility for each interface node. With a high number of interface modes, the number of equations required for describing compatibility and equilibrium may be higher than the number of normal modes required for accurately enough expressing the displacement field. In that case, the size of the CMS matrix is dominated by the number of interface degrees of freedom.

Through the relatively high number of required CMS equations for typical ship structures, combined with the high density, this situation may arise that a CMS matrix contains more non zeros than the full matrix used for classical harmonic analysis, which also means that more time is required for solving the CMS equations of motion than the time required for solving the classical harmonic finite element matrix equation.

Recent work has been carried out for a more efficient mathematical formulation of the compatibility and equilibrium relations [35, 36]. Reference has been found addressing problems with increased calculation times due to the density of the reduced CMS matrices resulting from high number of coupling nodes. Reference [40] addresses this problem typically occurring when coupling a structural domain to a fluid domain.

Tran [41] has carried out test for evaluation of a interface reduction technique based on the procedure developed by O'Calligan [42] called the improved reduced system method (IRS method). This method is based on describing the static displacement of a substructure due to interface displacement through superposition of Ritz vectors (interface modes). These Ritz vectors are obtained through solving the eigenvalue problem involving a reduced mass and stiffness matrix. These reduced matrices are obtained through projecting the full stiffness and mass matrix of the subsystem onto the Guyan reduction basis. This enables describing the interface displacements through a number of mode shapes smaller than the number of interface degrees of freedom. Reduction in computation time at around a factor 3.5 compared to the

classical CMS approaches has been reported. The cut-out frequency used for selecting the number of interface modes however had to be increased from $1.5f_{max}$ (according to Rubin's criterion) [26]) to $3.5f_{max}$ in order to get an accurate enough description of the interface displacement.

In this work he also referrers to Bourquin [43] and Craig and Chang [44] who also present interface reduction techniques and suggest using Guyan Modes for describing the reduced interface displacement vector.

4.3 Conclusion and Summary Critical Review

In this section the nature of dominant on board excitation characteristics have been reviewed through literature study. The most dominant sources of alternating forces leading to vibrations and structure borne noise are considered to be the propeller and the engine. The excitation forces produced by engines and propellers contain very dominant tonal components with frequencies ranging from a couple of Hz for low speed engines, to multiples of 100 Hz for high speed engines and higher speed propellers.

These findings formed a basis for the review of the most commonly used structural response modelling techniques and the recent developments in these techniques.

4.3.1 Excitation Forces

In the section above a brief review of the major ship vibration excitation sources is given. The excitation characteristic generated by the diesel engine can be easily be estimated during the design stage in order to generate the input for the structural response model for the simulation of the ship's vibratory behaviour. The tangential effort cylinder pressures are often available serving as excitation input values for the driveline torsional vibration calculation. With the tangential effort harmonic information the gas forces induced H and X-couple can be directly deduced.

	Nature of Excitation	Evaluation and control
Diesel engine Excitation	Tonal components at frequencies that are multiples of 0.5 or 1st order crankshaft rotation frequency for a two stroke or four stroke engine respectively. Most dominant frequencies are the 1st and 2nd order crankshaft rotation frequencies (inertia forces), and multiples of the firing frequencies (induced by gas forces) Amplitudes decrease with order number	**Control of diesel engine excitation**
		Applying flexible or active mounting systems reduces transmission of vibrations from engine to ship. Applying rotating balancing weights may reduce or even completely eliminate inertia generated excitation forces
		Theoretical Evaluation of Excitation Characteristic
		Excitation characteristics are relatively easy to estimate or to obtain.
Propeller excitation	Tonal components at frequencies that are multiples of the propeller blade passing frequency. Amplitudes of excitation decreases with order number. Generally up to the third order blade passing frequency is considered relevant Between 50 and 100 Hz broad band cavitation induced excitation occurs	**Control of propeller excitation takes place through**
		Unloading of the blade tip through propeller geometrical design A high as possible blade tip-hull clearance Introducing an a uniform as possible wake field at the propeller through careful geometrical aft ship design
		Theoretical Evaluation of Excitation Characteristic
		CFD modelling techniques, lifting line theory and towing tank test are used for estimating propeller excitation characteristics

Inertia forces induced H and X couples can also be easily estimated through reciprocating masses together with information about the balancing arrangement and engine connecting rod and crankshaft geometry given by the engine manufacturer.

Excitation properties from the propeller however are harder to estimate. Calculation of excitation amplitudes requires an estimation of the wake field to start with, which can be obtained through CFD modelling or through model towing tank testing.

With the estimated wake field, the propeller blade pressure distribution variations can be calculated through well established lifting line or lifting surface theories.

Predicting broadband cavitation induced by collapsing of sheet, bubble and tip vortex cavities is considered the most complex excitation form. Understanding and predicting this behaviour is still subject of ongoing research.

For both the propeller and the diesel engine excitation characteristics it can be concluded from the review that most of the excitation energy is concentrated in very distinct tonal frequency components. For the propeller excitation the relevant frequencies are generally assumed to be the first three blade passing harmonic. Diesel engine excitation generally produces a tonal excitation characteristics induced by the oscillation of the translating masses (inertia forces) (1^{st} and second order crankshaft rotation frequency) and the gas forces (multiples of the engine's firing frequency.

4.3.2 Response Modelling Techniques

An important aspect of ship noise and vibrations is the combination of the excitation characteristics (source characteristics) and the natural response of the structure that is subjected to this particular excitation. Through careful design of propeller blade and aft ship geometry, and through applying flexible or active machinery supporting system, excitation amplitudes can be very well controlled. However, no matter what excitation mitigating technique is applied, resonance or near resonance of the ship's structure or machinery may still easily result in destructively high vibration levels, even though the excitation amplitudes are perfectly acceptable.

Consciously tuning the structural response and excitation frequencies is very important when designing a ship for low noise and vibration levels. Therefore, estimating the impact of structural design choices on the response characteristic of the ship's structure for a given excitation characteristics is very important, and is a huge challenge.

With the critical review, finite element modelling has been recognised as the most suitable modelling tool for evaluating ship's structural design considering the nature of ship's structures and excitation characteristic from diesel engines and propellers. However, particularly when taking large parts of the ship structure into account, problems may still arise with require computer memory and computation time.

The principles of the Spectral Element Modelling approach have been reviewed as a possible solution to reduce required computer memory and analysis time. Although this method has great potential to reduce computation time at high frequencies, its practical value is questioned for modelling the typically relatively low frequency excitation forces typically encountered on ships. These low frequencies induce vibrations involving global structural deformation. Considering the nature of ship structures, the size of spectral elements has to be chosen relatively small. Considering the nature of the structure, and considering the typical excitation characteristics, the wavelength of mode shapes that play an important role in ship vibrations largely exceeds the size of the spectral element. This means that rigid body modes of the spectral elements play and important role in the propagation of vibrations. These rigid body mode shapes are not taken into account with this approach. In addition, considering the complex nature of the stiffened ship structures, a lot of uncertainty arises about choosing the correct wave functions.

The principles of statistical energy analysis (SEA) have also been studied for practicality and validity for simulating propagation of vibrations through ships. The advantage of SEA is that the mathematical description of the structural dynamic behaviour is much simpler than for the FE method. However, broadband excitation, high modal density and statistically uniform modal behaviour are required for reliable results. Statistical energy analysis could however still be used as a tool for a

qualitative approach to propagation of structure borne noise for some types of ships, particularly for high speed crafts with high turbulent flow excitation and light structures with high modal densities. However, considering above, this technique is unsuitable for simulation of propagation of vibrations induced by the tonal sources such as the propeller blade passing harmonics and diesel engine crankshaft rotation and firing frequency related harmonic components.

In order to reduce computation time and computer memory requirement whilst still be able to apply a finite element approach, the principles of component mode synthesis have been reviewed. With this method the ship's structure is divided in well manageable substructures. Reduction of the model takes place by applying modal reduction onto the individual substructures. Calculation time required for obtaining mode shapes and natural frequencies for all individual substructures is a lot smaller than the calculation time required to obtain the mode shapes and natural frequencies of the total assembled structure, as required for the classical mode superposition technique.

Through component correlation of the theoretical model to the real structure can already start very early in the design stage. Modal information of already finished ship sections can be obtained through measurements. By modelling these sections as substructures, these theoretical substructures can be correlated to the measured data through which the confidence in the simulation results is increased.

However, due to high number of required interface nodes typically seen on ship structures, a situation may arise, particularly when subdividing a ship structure into many (repeating) ship structures, that solving the total assembles CMS matrix requires more computation time than solving the matrix equations following classical full harmonic finite element analysis.

Modelling Technique	Pro	Con
Hull Girder Beam Approach	Simple hand calculation approach. Particular valid for estimating propagation of vibrations forced by low speed two stroke engines (and sometimes also the first blade passing frequency from the propeller)	As assumptions and simplifications of the model only allow analysis up to the 5^{th} mode shape, this approach becomes invalid for estimating vibration propagation induced by medium and high speed engines and propeller excitation.
Finite Element Modelling	Suitable for modelling geometrically complex structure that ships are.	Modelling large part of typical complex ship structures results in model requiring much computer memory and computation time. Number of required elements increases further with increasing required response frequencies
Mode Superposition	Reducing computation time mainly at lower frequencies	At higher frequencies, calculation time required for calculating the relevant mode shapes and natural frequencies increases exponentially.
Spectral Element Modelling	Reducing computation time considerably at higher frequencies. Exact solution, works well for high frequencies.	Still many elements are required for typical ship structures, due to the non homogeneous nature of typical ship structures. Global modes play an important role in the vibrations of a ship considering the frequency of excitation and the nature of the ship's structure. Due to the non homogeneous nature of the global ship structure, it is not possible to know the exact wave solution

Modelling Technique	Pro	Con
Statistical Energy Analysis	Reducing computation time considerably at higher frequencies.	- Requires high modal density. This is a condition not met with typical ship structures. - Requires broadband and spatially evenly distributed excitation. Propeller and diesel engine excitation is of a tonal nature and spatially concentrated - Global mode shapes are not taken into consideration, but play an important role in vibration propagation on board ships.
Component Mode Synthesis	Reduction of Required Computer Memory and possible reduction of Computation time Allows a Finite Element Approach Sub structural approach allows correlation of modal parameters to take place through measurements whilst the ship is being built	High number of coupling modes typically encountered with continuous ship structures may increase the total computation time and undo the reduction of computation time obtained through modal reduction

5 Measurement Results

In this section vibration and noise measurement results are reviewed. Through the vibration measurement results the nature of propeller and diesel engine excitation and the corresponding structural response is.

5	Measurement Results
5.1	Vibration and Noise Measurements on a Gas Carrier
5.1.1	Measurement Conditions, Locations and Procedure
5.1.2	Propeller induced Vibration and Noise
5.1.3	Evaluation of Measured Propeller Vibrations
5.1.4	Evaluation of measured Propeller Noise
5.2	Vibrations and Noise Measurements on Board a Fishery Research Vessel
5.2.1	Measurement Conditions, Locations and Procedure
5.2.2	Evaluation and Identification of Propeller Induced Vibrations
5.2.3	Identification and Evaluation of Diesel Engine Induced Vibrations
5.3	Vibrations on Board a ROPAX Vessel
5.3.1	Evaluation of Propeller Induced Vibrations
5.3.2	Evaluation of Diesel Engine Induced Vibrations
5.4	Summary of Measurement Result Evaluation

Paragraph structure of chapter 5 'Measurement Results'

Measurement results from measurements campaigns carried out for the FP7 EU research project SILENV have been used. For two vessel analysed in this work, these measurements have been performed by the author of this work (a fishery research vessel and a LNG carrier). Also measurement results taken on board a ROPAX ferry, carried out by a Spanish consultancy company TSI, have been used. These measurements have also been carried out for the EU research project SILENV.

The main aim of SILENV was the formulation of a green label for shipping. This green label was to contain recommendations of noise and vibration limit values based on:

- Human response (work quality impairment and comfort)
- Response of marine mammals.
- Response of people working and living close to waterways and harbours
- Technical feasibility

The green label also was to contain guidelines for designing ships in order to achieve the proposed more stringent recommended noise and vibrations limits.

To serve the aims of the SILENV project, on board noise and vibration measurements have been carried out as well as underwater noise measurements in some cases. Also questionnaires have been distributed among passengers and crew through which the impact of noise and vibrations on working performance and perception of comfort is measured.

5.1 Vibration and Noise Measurements on a Gas Carrier

One of the ships the author of this work has performed Noise and Vibration Measurements on was a 260 m long LNG carrier with a gross tonnage of 111459 tons and a displacement of 84491 tonne (see Figure 8). For the development of the green label for the fp7 project SILENV as described above, onboard noise and vibration measurements have been carried out by the author. At the same time, underwater noise measurements have been carried out by project partner CETENA, so that noise and vibration levels on board could be related to the resulting under water noise radiation.

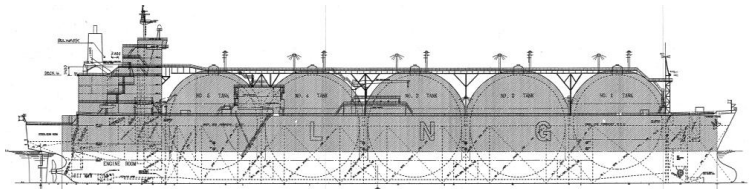

General Properties		
Max. Length waterline	260	m
Max. Beam Waterline	45	m
Maximum Speed	19	kn
Draft During Trials	9.4 m aft, 9.4 m fwrd	
Propeller		
Power	21500	kW
Maximum Revolutions	80	rpm
Nominal Revolutions	75	rpm
Number of Blades	4	
Pitch	fixed	
Main engines		
1 low pressure steam turbine (LP) and 1 high pressure steam turbine (HP)		
Total Power	21550	kW
Revolutions	5800 rpm (HP) and 3970 rpm (LP)	

Figure 8 ***Properties of the gas carrier of which the vibration measurements have been shown in Figure 10 and some noise measurement results are presented in***

As this ship is equipped with steam turbines, the most dominant vibration and noise source was found to be the propeller.

5.1.1 Measurement Conditions, Locations and Procedure

An important aspect of all the measurement results collected was the identification of the noise and vibration sources and the mechanism behind the transmission of noise and vibrations from theses sources through the ship itself, and to the underwater environment.

In order to be able to identify the contributions of the main noise sources vibration measurements and noise measurements had to be carried out in such a way that they can be related to each other. With that in mind, vibration measurements were carried out on parts of the ships structure as close to main sources of structure borne noise as possible.

The most dominant sources are considered to be:

- Propeller (measurement positions plate fields deck steering gear room and aft deck)
- Main steam turbines (measurement positions turbine feet and founds)
- Gearbox (measurement positions on foundations)
- Auxiliary sets (measurement positions on foundations)
- Feed water pumps (measurement positions on foundations)

Measurements took place at four different operational conditions:

- Ship at anchor
- Ship with propeller running at 31 rpm (7 knots)
- Ship with propeller running at 50 rpm (9 knots)
- Ship running at full speed (75 rpm) (19 knots)

As the ship is equipped with steam turbines, the main focus in this work is on the vibrations above the propeller and on the steering gear deck.

Spectra of the vibration measurements are produced over a frequency range from 0.16 Hz up to 1 kHz. The spectrum bandwidth was 0.16 Hz. A hand held B&K 2250 vibration/noise meter has been used as further described in Appendix I. With this meter both noise and vibrations were measured. The meter had logging options

which enables logging of both spectra and raw signals, so that post processing could be carried out afterwards. Being able to record spectra and time signals over a longer period is convenient, particularly when measurement reading fluctuate over time. Linear averaging of vibration and noise spectra also had to take place considering the irregularity of the vibrations levels. Particularly at the steering gear deck sailing at full speed cavitation occurred and the highly irregular noise and vibration levels sometimes required averaging times longer than one minute, before the reading become stable.

5.1.2 Propeller induced Vibration and Noise

Figure 10 and Figure 11 show some of the vibration measurement results taken on the steering deck plating directly above the propeller on board a gas carrier [18, 20]. The measurements have been carried out using accelerometers and hand held equipment (shown in Appendix I). The spectra show the FFT analysis results that have been transformed from 0 to peak acceleration levels [mm/s^2] to 0 to peak velocity levels [mm/s] through dividing the acceleration spectrum through the frequency in rad/s.

The spectra presented in Figure 11 and Figure 12 present the 0 to peak maximum amplitudes of the frequency components measured over roughly one minute, with no weighting function applied. In the legend of the graphs, also the total average and total maximum RMS values measured during that minute are presented, applying a weighting function according to EU directive 2002/44/EC.

Identification of propeller induced vibration took place by plotting lines of multiples of the blade passing frequency into the spectrum. These blade passing harmonics have been estimated through the estimated propeller rotation speed obtained from the readout of the on-board revolution meter.

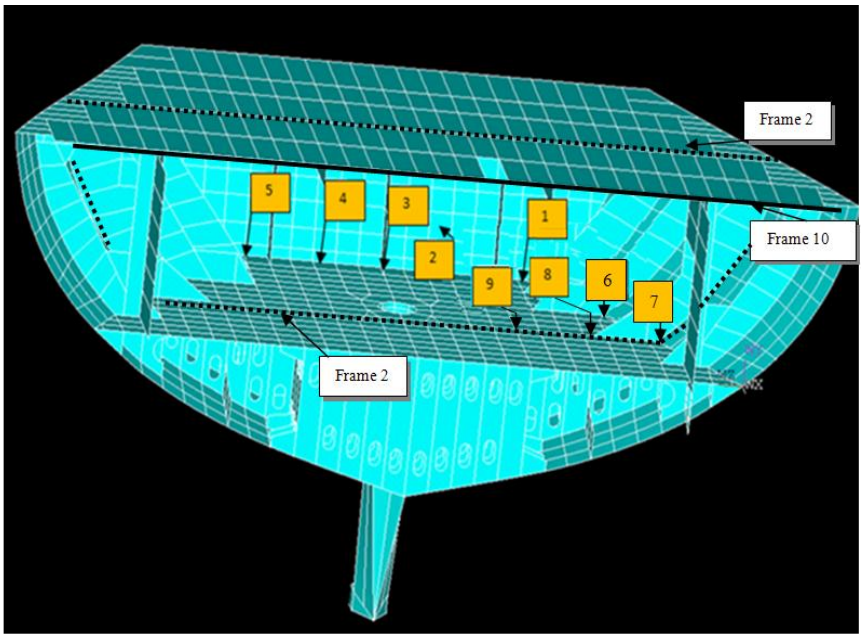

Figure 9 ***Some of the measurement locations on the steering gear deck shown plotted in a 3D representation of the aft ship cut open at frame 10***

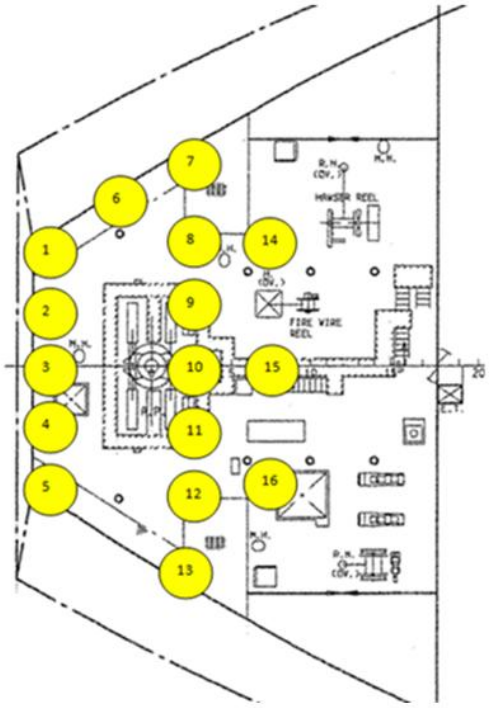

		conventional propeller reponse 0 to peak [mm/s]	
peak values	limit	Steering gear deck 3	Steering gear deck 5
1 blade passing frequency	4 mm/s	1 mm/s	0.77 mm/s
2 blade passing frequency	4 mm/s	1.5 mm/s	1.72 mm/s
3 blade passing frequency	4 mm/s	2.2 mm/s	2.04 mm/s
4 blade passing frequency	4 mm/s	4.4 mm/s	2.93 mm/s
5 blade passing frequency	4 mm/s	0	1.43 mm/s
	limit	Steering gear deck 3	Steering gear deck 5
total weighted RMS [mm/s]	4.4 mm/s	5.5 mm/s	4.75 mm/s

Figure 10 ***Measurement locations and results for location 3 and 5, the location where the highest vibration levels have been measured. The table shows the maximum 0 to peak velocity amplitudes at each blade passing harmonic frequency component from the 1st to the 5th order. The bottom line shows the maximum overall RMS value. Limits given in the table are prelimenry limits formulated in the SILENV project for evaluation of vibration spectra.***

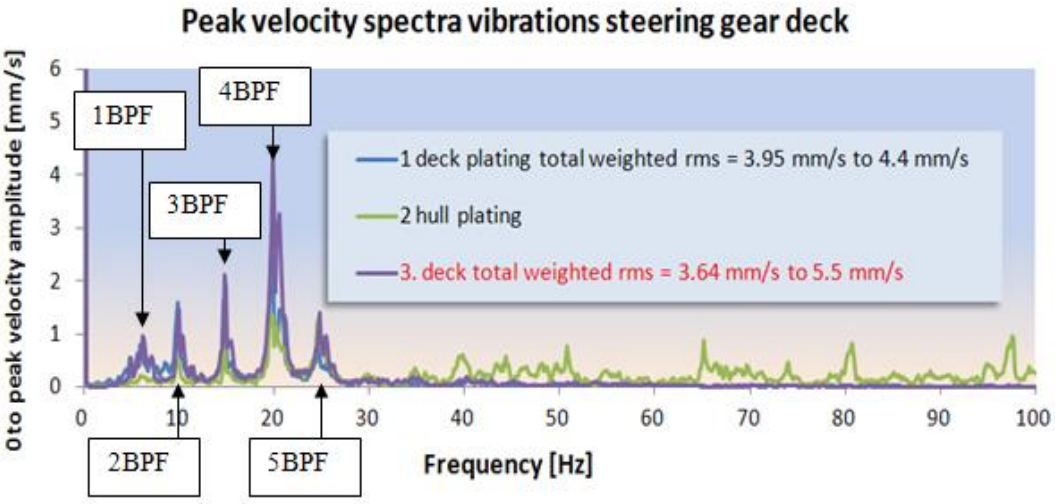

Figure 11 ***Spectra of measurement results taken at location 1 to 3.Amplitudes are given in mm/s 0 to peak values and are the maximum values measured. During the approximately one minute over which the measurement results were averaged, total RMS values were within the bandwidth indicated in the legend of the graph (from 3.95 mm/s to 4.4 mm/s for location 1 for instance). Indicated in the figure are the multiples of the blade passing frequencies (BPF).***

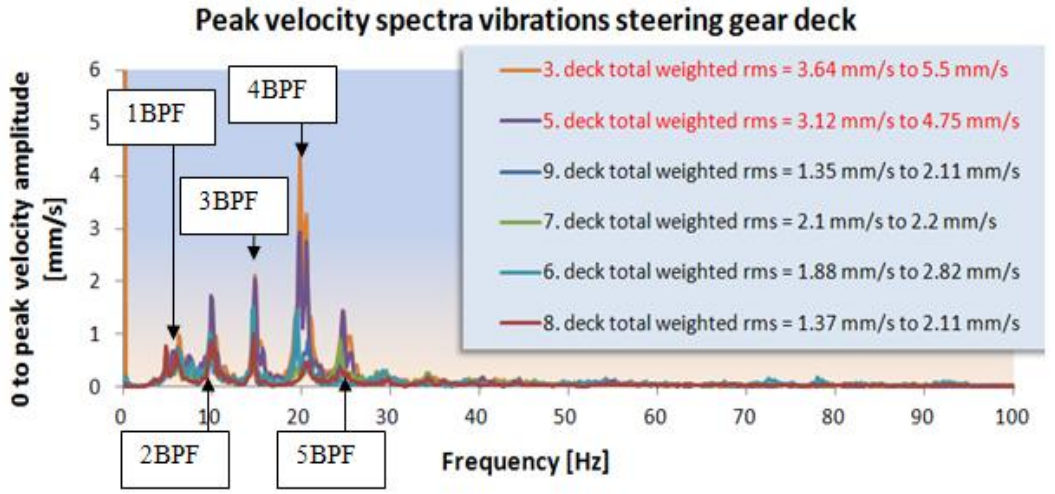

Figure 12 ***Spectra of measurement results taken at various locations. Amplitudes plotted in the graph are given in mm/s 0 to peak values and are the maximum values measured. During the approximately one minute over which the measurement results were averaged, total RMS values were within the bandwidth indicated in the legend of the graph (between 3.64 mm/s and 5.5 mm/s for location 3 for instance). Indicated in the figure are the multiples of the blade passing frequencies (BPF).***

In the table of Figure 10 the maximum measured 0 to peak velocity amplitude values are listed for the first 5 blade passing harmonic frequency components for locations 3 and 5. At these two locations the highest vibration levels have been measured. The

limits given in the table are the preliminary vibration limits formulated at the start of the SILENV project in order to be used for assessment of vibration measurement results.

In Figure 13 the noise measurement results taken at two locations under different operational conditions are plotted in one graph. These measurements have been presented in this way in order to understand the propagation mechanism of structure borne noise.

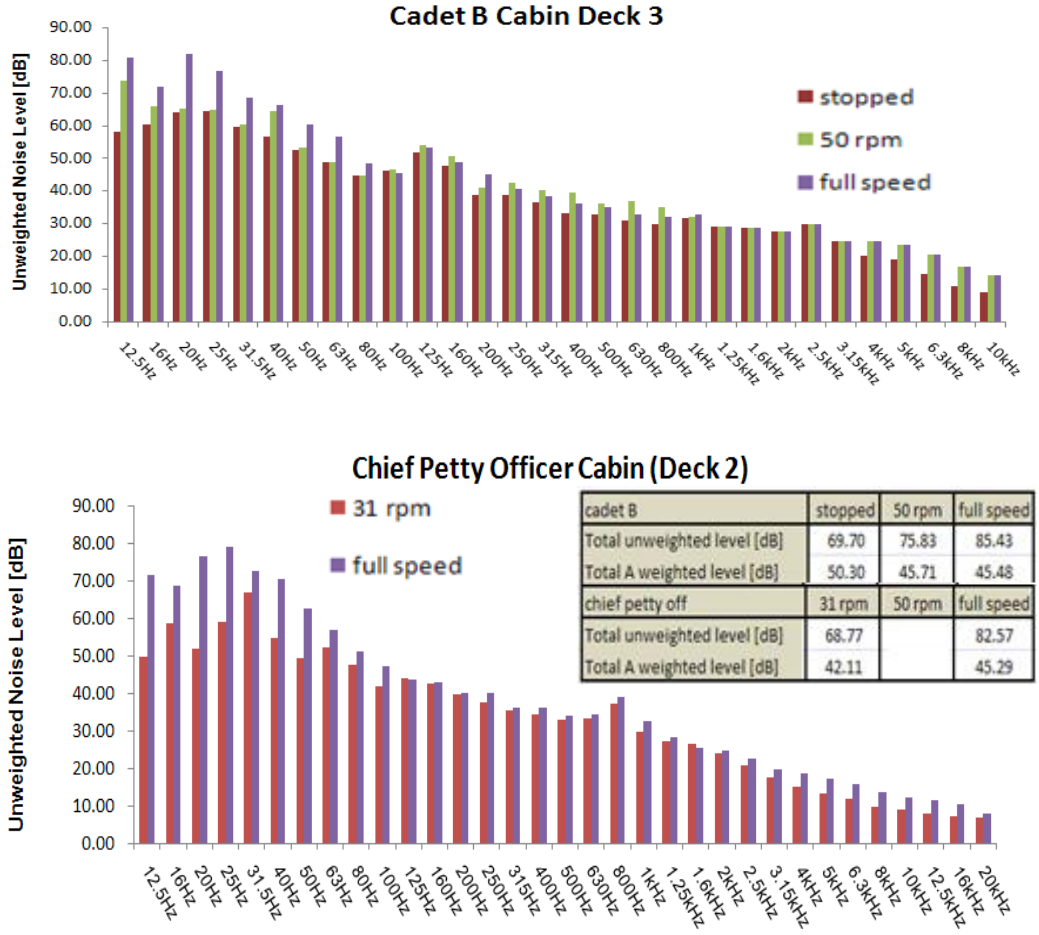

Figure 13 ***1/3 octave band spectra of noise measurement results with no weighting curve applied, taken on board the gas tanker with properties shown in Figure 10. Noise at Cadet B cabin has been measured with the ship stopped, propeller running at 50 rpm (9 knots) and at full speed (19 knots). Noise in the Chief Petty Officer Cabin has been measured at propeller speed 31rpm (7 knots) and at full speed (19 knots).***

5.1.3 Evaluation of Measured Propeller Vibrations

The vibration measurement results shown in Figure 10 suggest a concentration of propeller vibration energy below the 30 Hz. Frequencies up to the 5th order blade passing frequency have been clearly identified through the FFT analysis. It has also been established that all the vibration energy under 100 Hz is mainly coming from the propeller. Figure 14 shows measurement results taken close to machinery in the engine room of the vessel. These vibration levels are considerably lower than the levels measured on the steering gear deck (compare with Figure 12).

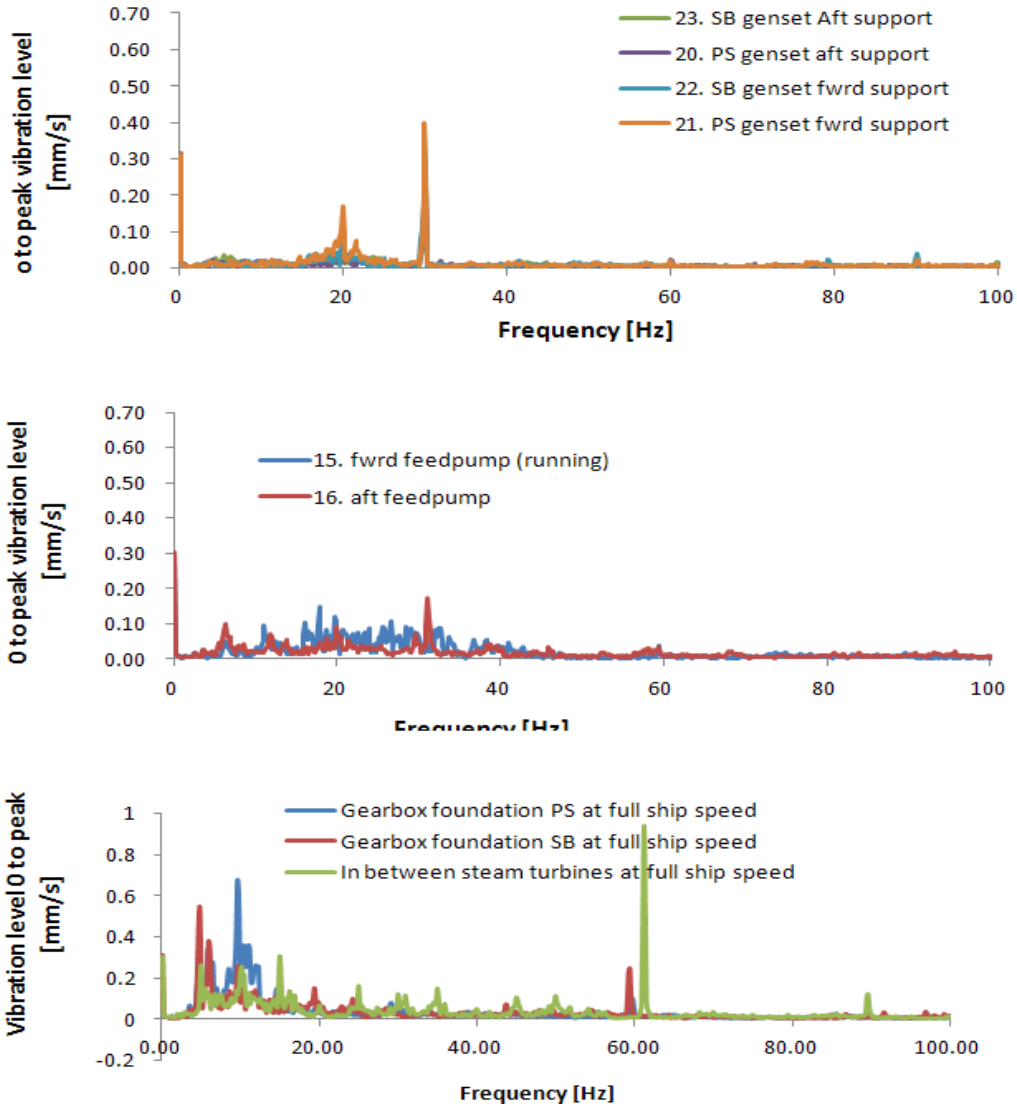

Figure 14 ***Spectra of measurement results taken on close to auxiliary and main machinery (steam turbines) in the engine room of the of the LNG carrier***

Also some broad band effect seems to be present round about the 20 Hz and round about the 1st blade passing frequency.

The clear presence of blade harmonic components above the 3rd order is mainly due to the shape of the aft ship. As mentioned in section 4“

Critical Review” it is normally assumed in the literature that propeller blade passing excitation amplitude decreases with order number and is assumed to be negligible above the 3rd order. However, the literature also mentions that with a full aft ship such as the LNG carrier’s aft ship, characterised by rapidly converging lines, a high degree of non uniformity of wake distribution at the propeller can be expected, which may lead to blade passing harmonics above the 3rd order to be relevant as well.

Another important aspect when evaluating the relation between amplitudes at different harmonics is the fact that through accelerometers not an excitation amplitude is measured, but a response amplitude. This means that the structural response characteristics may also result in certain harmonic components being more dominant than others (for instance, when certain blade harmonics are close to a natural frequency)

As mentioned before, a broad band response has been identified close to 20 Hz. Although there may be the effect of smearing of higher harmonics due to time variation of the wake distribution (as described by [3]), the broadband excitation is suspected to have been mainly induced by cavity collapse on the hull considering the observed impulse like nature of the vibrations at the aft ship that could best be described with the metaphor of the aft ship being machine gunned with marbles. These violent time varying cavitation phenomena also resulted in a huge fluctuation in vibration levels as can be seen from the range between the maximum and minimum measured (weighted) RMS velocity values quoted in the legends of the graphs in Figure 11 and Figure 12.

5.1.4 Evaluation of measured Propeller Noise

The concentration of vibration energy below 30 Hz is further confirmed through the un weighted noise spectra of noise measurement results at different propeller speeds

shown in Figure 13. In Figure 13 the 1/3 octave band spectra at different propeller revolutions at one location have been plotted in one figure. These graphs have been produced for identification of the contribution of the propellers structure borne noise to the total airborne noise in the cabin in question. From the spectra can be seen that changing the propeller revolutions and load only affects the noise spectrum shape below the 50 Hz. As according to the A-weighting curve the sensitivity of humans to noise at these frequencies is very low, the differences in the total A-weighted noise levels, measured at different ship speeds therefore are very small, particularly at the higher decks being situated further away from the propeller. The main contributor to cabin noise is general was found to be the air conditioning [20].

5.2 Vibrations and Noise Measurements on a Fishery Research Vessel

Following the same procedures as on the LNG carrier described above, Noise and vibration measurements have been carried out on board a fishery research vessel by the author of this work for the FP7 EU research project SILENV. Also underwater noise measurements have been performed by one of the SILENV project partners.

The Fishery Research vessel is equipped with two main diesel engines driving one controllable pitch propeller, as shown in Figure 15.

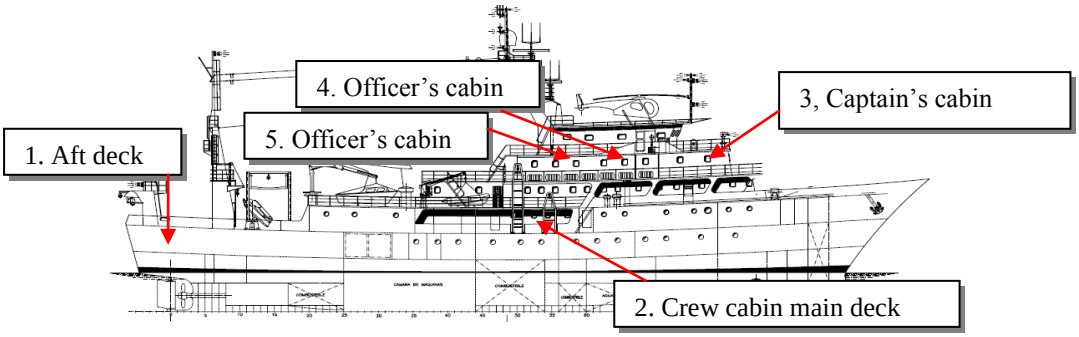

General Properties		
Max. Length waterline	66.7	m
Max. Beam Waterline	15.5	m
Maximum Speed	11.5	kn
Draft During Trials	4.7 m aft, 5.0 m fwrd	
Propeller		
Power	2000	kW
Maximum Revolutions	303	rpm
Number of Blades	4	
Pitch	controllable	
Main engines		
one 6L diesel engine and one 12V engine		
Total Power	2000	kW
Revolutions	750	rpm

Figure 15 ***Properties of the Fishery Research vessel, the second vessel on which the author has performed vibration and noise measurements supporting the FP 7 research project SILENV***

5.2.1 Measurement Conditions, Locations and Procedure

Vibration and noise measurements have been carried out under different operational condition:

- Vessel stopped, propeller running with zero Pitch
- Propeller running at 50% Pitch
- Propeller running at 100% Pitch

Vibration and noise measurements have been taken close to the main sources, which were considered to be the diesel engines and propellers. Vibration and noise measurements have also been taken at cabins and various other locations away from the sources, so that propagation mechanisms can be studied.

A hand held B&K 2250 vibration/noise meter has been used as further described in Appendix I and has been used in a similar manner as described for the measurements

for the LNG carrier above where the amount of averaging time required for obtaining a spectrum depended on how long it took before a reading was stable.

5.2.2 Evaluation and Identification of Propeller Induced Vibrations

Figure 16 shows the vibration measurement results at 50% pitch and show that most of the vibration energy is concentrated below 150 Hz [33]. In Figure 16 and Figure 17 can be seen that most of the vibration energy is concentrated under 150 Hz. In the vibration measurement spectra at the aft ship, closest to the propeller (Figure 16) the first and second blade passing harmonic tonal components (1st BPF and 2nd BPF) can be clearly distinguished at 20 Hz and 40 Hz. In line with the findings presented in the critical review of the excitation sources, no noticeable response at blade passing frequencies with order numbers higher than 2 can be found in the spectra presented. The 6th blade passing harmonic can also be distinguished from the graph at about 120 Hz. The response around that frequency seems to suggest a broad band like excitation characteristic, but response amplitudes are low.

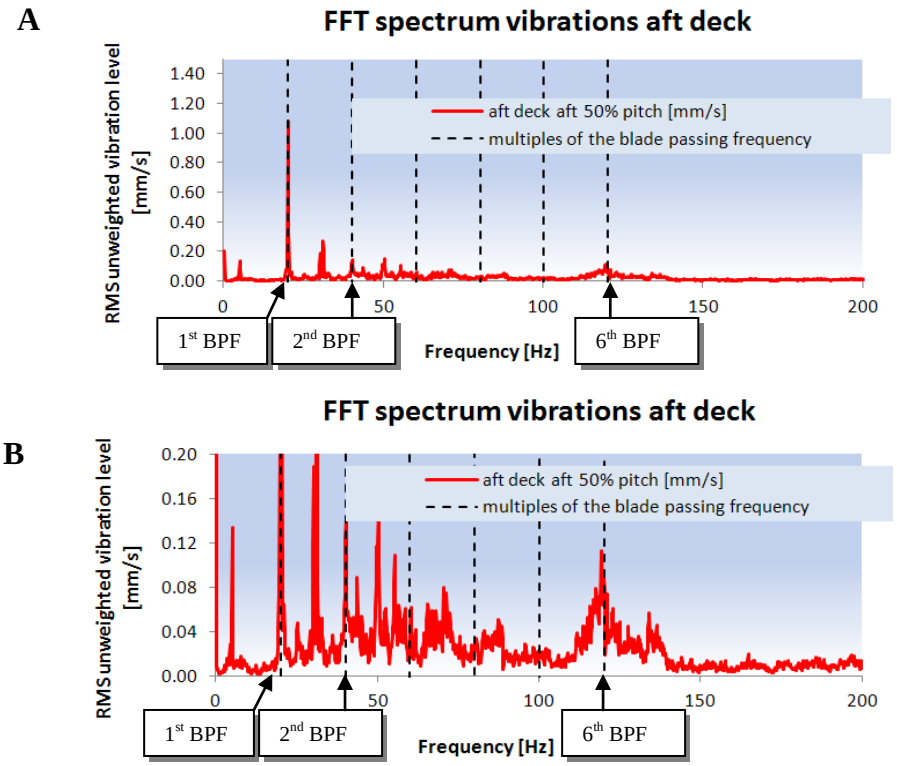

Figure 16 ***Vibration measurement results on the aft deck directly above the propeller. Graph B in a zoomed in version of graph A. BPF = propeller blade passing frequency.***

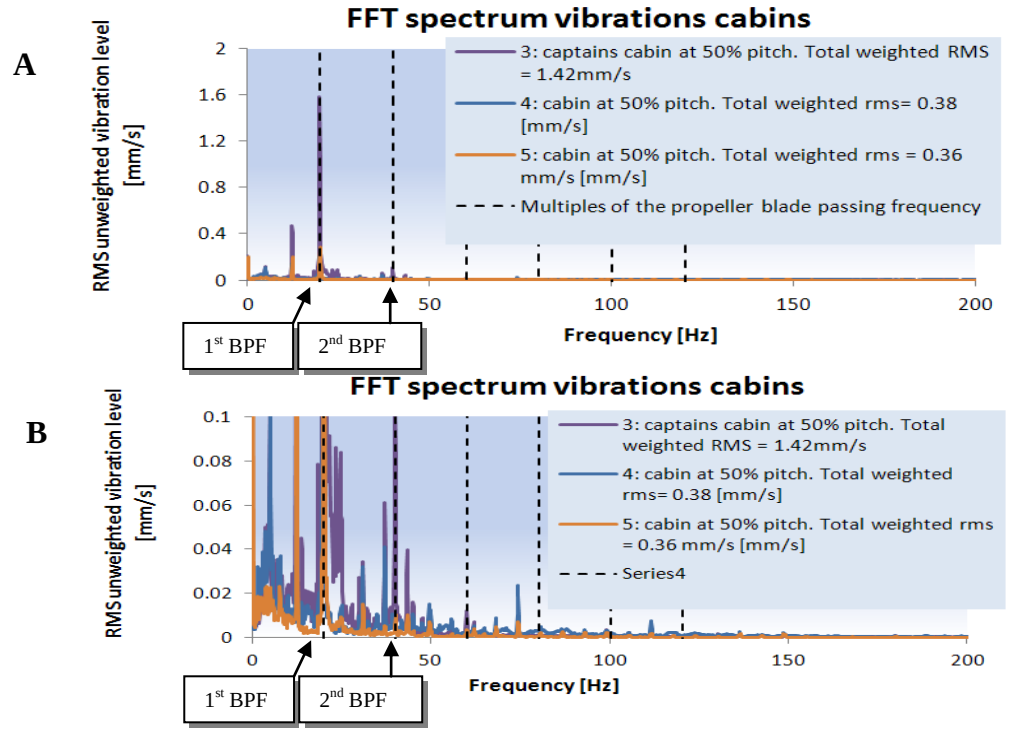

Figure 17 ***Vibration measurement results in cabins. Graph B in a zoomed in version of graph A. BPF = propeller blade passing frequency***

In Figure 17 can be seen that only the first propeller blade passing frequency really comes through to the cabins at the captain's deck. Local resonance has been established of the captain's cabin's deck which explains the amplification of the blade passing frequency amplitude relatively to the amplitude measured at the aft ship, the closest to the source.

5.2.3 Identification and Evaluation of Diesel Engine Induced Vibrations

Spectra of vibration measurement results taken on the engine foundation of the fishery research vessel (Figure 15) are shown in Figure 18. Also plotted in the spectrum of Figure 18 are dotted vertical lines representing multiples of 0.5th crankshaft rotation frequency (CRF), which is the ground harmonic of a 4 stroke engine. As can be seen from Figure 15 the vessel is equipped with a 6L and a 12V engine both running at a constant speed of 750 rpm.

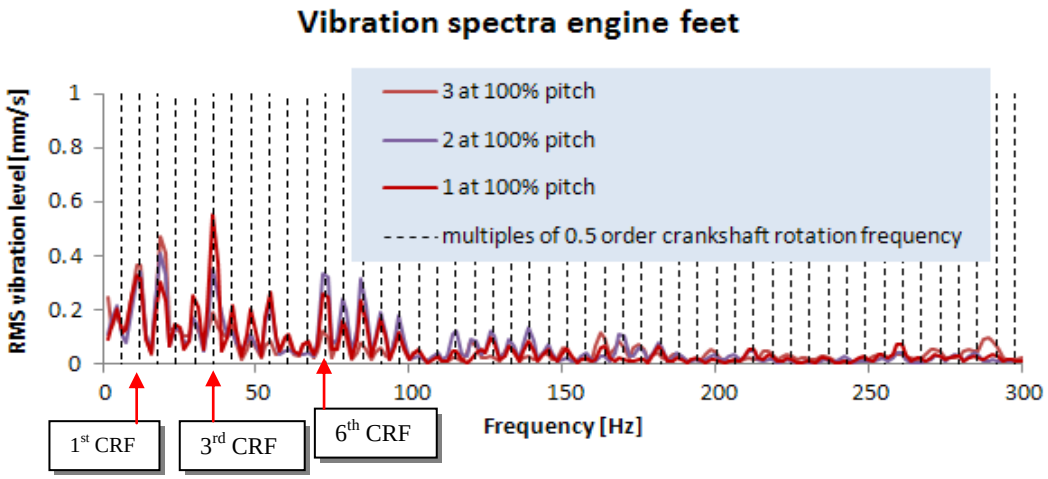

Figure 18 ***Spectra of vertical vibration measurement results taken on a 12V engine running at 740 rpm. (Fishery research vessel). The 3rd and 6th CRF (crankshaft rotation frequency) are the firing frequency of the 6L and 12V engine respectively.***

Specifically indicated in the graph in Figure 15 are the 3rd and 6th order CRF components. They are usually dominant in a 12V engine as they represent the firing frequency of one cylinder bank (behaving like a 6L engine) and the firing frequency of all 12 cylinders [18] together respectively. In addition, a 6L engine was running synchronously this 12V engine right next to it, both driving one propeller through a common gearbox. That would further amplify the 3rd order crankshaft rotation

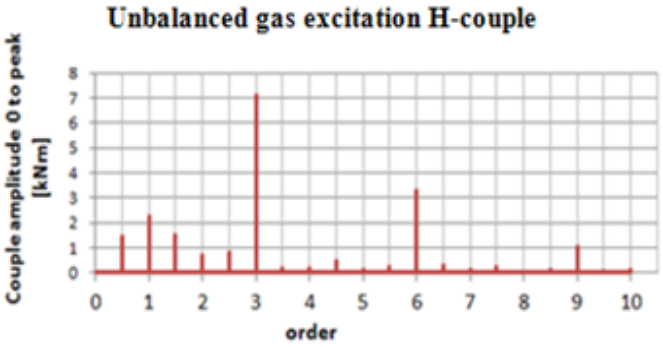

Figure 19 ***Simulated total H-couple for the 12V engine of the fishery research vessel specified in Figure 15.***

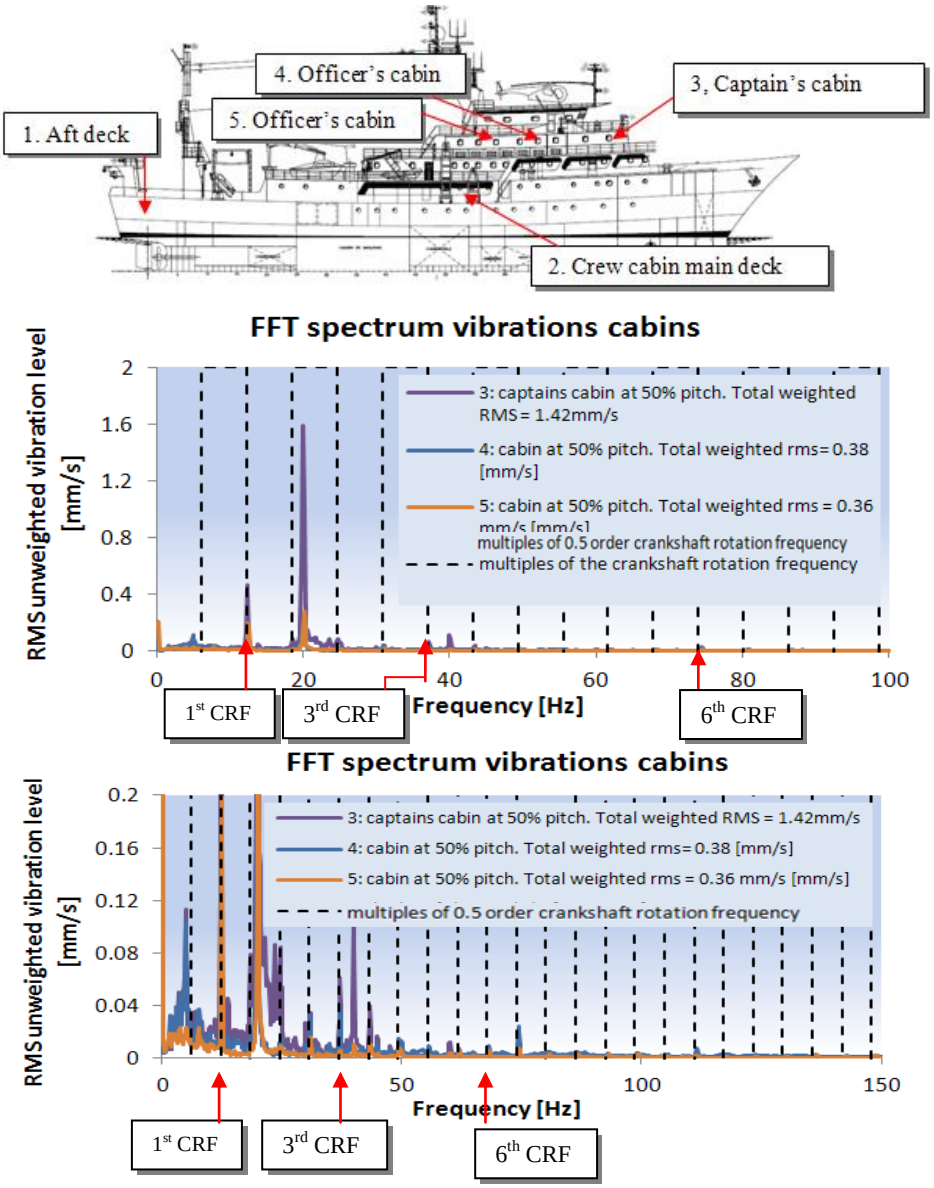

Figure 20 ***Spectra of vertical vibration measurement results taken at various locations on board. CRF= crankshaft rotation frequency.***

frequency. Although theoretically only these firing frequencies should be present in the excitation spectrum, many more tonal components related to the engine's ground harmonic can be distinguished up to 200 Hz in Figure 18. The harmonic components outside the multiples of the firing frequencies can be found as a result of unequal distribution of thermodynamic cylinder load, and as a result of the unequal timing of the firing of the cylinders relatively to (dynamic) top dead centre. With the simulation of the gas force induced H-couple excitation characteristic simulated by

the author of this work in reference [18], the on board measured exhaust gas temperatures have been used to estimate the load distribution of the cylinders.

The resulting total H-couple characteristic is shown in Figure 19 and shows that the unbalanced distributed load particularly results in frequency components under the 3rd order (firing frequency one cylinder bank).

Figure 20 shows the vertical spectra measured at locations further away from the engine. Apart from the first order crankshaft rotation frequency the engine crankshaft rotation related frequencies can only be distinguished very faintly. The dominant 1st order crankshaft rotation frequency has been considered a result of mass unbalance in the engine's driveline in combination with local resonance phenomena.

5.3 Vibrations on Board a ROPAX Vessel

In this section measurement results taken on board a ROPAX ferry, carried out by the Spanish noise and vibrations consultancy company TSI, are reviewed. Figure 23 and Figure 24 show the vibration measurement result spectra taken on board this ROPAX vessel (Figure 22).

5.3.1 Evaluation of Propeller Induced Vibrations

Figure 23 shows the vertical vibration measurement results on deck plating closest to the propeller. As can be seen, amplitudes of vibrations with frequencies that are a multiple of the blade passing frequency rapidly decrease with the order number.

This is therefore also the case with the harmonics found in the vibration measurement results taken further away from the propeller. Figure 24 shows the vibration spectra measured on the bridge and at public spaces at the highest deck right above the propeller. It can be seen that the effect of the 2nd and 3rd blade passing frequency is decreasing the further the receiver location is from the source. The first blade passing frequency however is dominant throughout the vessel. This had been contributed to resonance phenomena, which can be concluded from the amplification of the amplitude at the first blade passing frequency relatively to the first blade passing frequency measured close to the propeller (see Figure 23). The vibration

measurement results do not suggest any broad band component in the excitation characteristic.

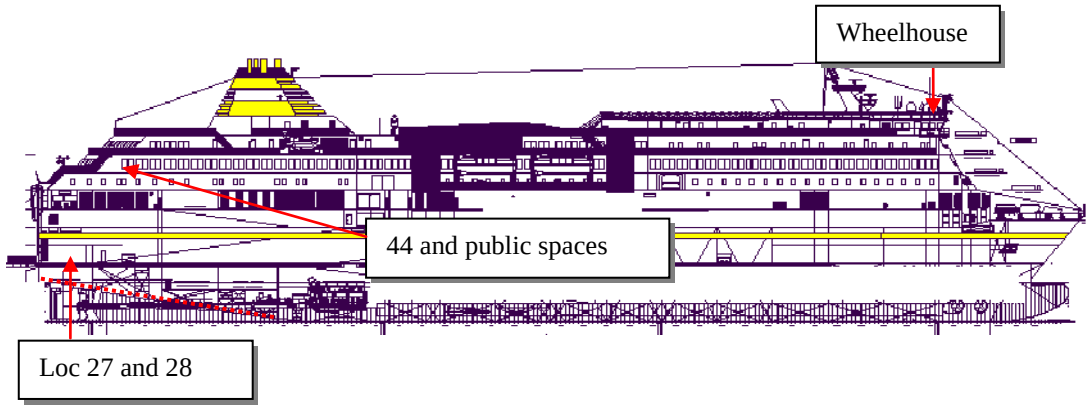

Figure 21 ***Layout ROPAX vessel on which measurements were carried out for the FP7 project SOLENV***

General Properties		
Max. Length waterline	157	m
Max. Beam Waterline	26.2	m
Maximum Speed	23.5	kn
Displacement	16556	t
Propellers		
Power	2 × 9100	kW
Maximum Revolutions	184	rpm
Number of Blades	4	
Pitch	controllable	
Main engines		
4 × L8 diesel engines		
Total Power	2 × 4550	kW
Revolutions	500	rpm

Figure 22 ***General information ROPAX vessel***

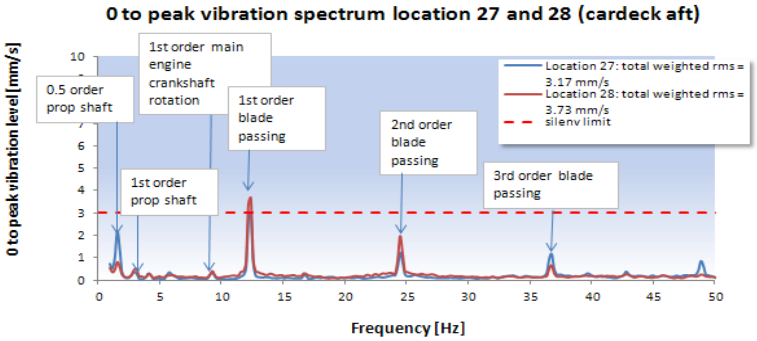

Figure 23 ***Measurements on plating above the propellers of a RO-PAX vessel (location 27 and 28 as shown in Figure 21)***

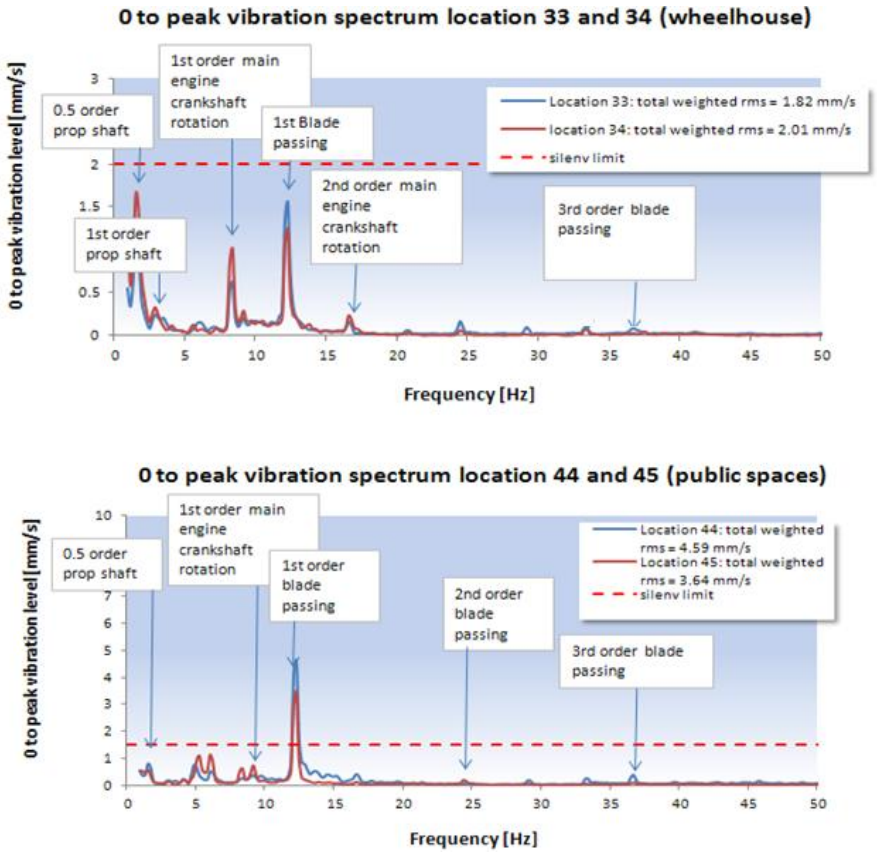

Figure 24 ***Vertical Vibration measurement results ROPAX vessel (see also (see Figure 22 and Figure 23). Weighting curve according to EU directive 2002/44/EC has been used for calculating the total weighted RMS values quoted in the legends.***

5.3.2 Evaluation of Diesel Engine Induced Vibrations

Vibration measurements taken close to the engines on board the ROPAX vessel (see Figure 22 and Figure 23) are shown in Figure 25. As for the fishery research vessel in Figure 19 and Figure 20, the measurement results suggest a tonal engine excitation characteristic. Again, as for the fishery research vessel, apart from the firing frequency (± 33 Hz) many more other engine ground harmonic related frequencies can be identified in the spectrum which is a result of the fact that cylinder gas loads are never perfectly equally distributed and the crank angle of firing of the cylinders relatively to their top dead centres is not exactly equal either.

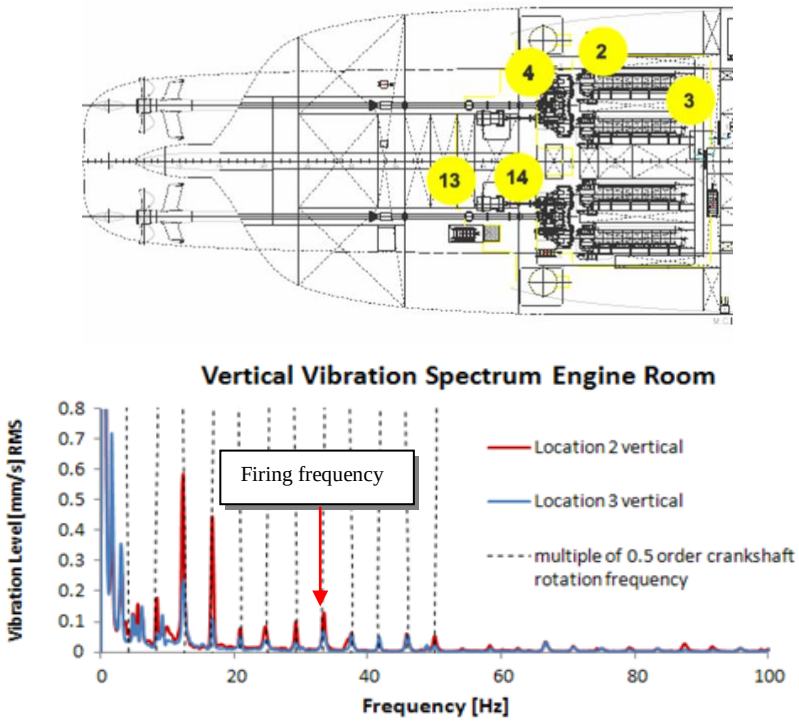

Figure 25 ***Measurement locations and results taken close to the engine feet***

As can be seen from Figure 24 apart from the first order crankshaft rotation frequency hardly any vibration energy from the engine is coming through to the selected measurement positions of Figure 22, which is also down to the fact that the engines are flexibly mounted. The amplification of the first order crankshaft rotation frequency (compare engine room spectrum which accommodation spectrum) is an indication of local resonance phenomena occurring, which has been confirmed by the TSI team that carried out the measurements.

5.4 Summary of Measurement Result Evaluation

The mechanisms and characteristics of diesel engines and propeller excitation forces identified from the measurement results above are in line with the findings of the literature review of excitation source characteristics presented in section 4 “Critical Review“. Above shown vibration measurement results suggest that from a vibration point of view the propeller should indeed mainly be regarded as a very dominant tonal excitation source. Frequency tonal response components up to the 3rd blade passing frequency were found in the measurement results taken on the ship

structures. Higher order blade passing harmonic components were found to be dominant as well in the vibration measurement results taken on board an LNG carrier. This is also in line with the findings from the literature research presented in section 4 “Critical Review“, were it has been mentioned that dominant higher order blade harmonics typically occur with vessels such as the LNG carrier with a typical ‘full’ aft ship geometry characterised by rapidly converging and rising lines. This type of aft ship results in a highly irregular wake distribution at the propeller, through which violent cavity volume fluctuations and cavity implosions occur, which is exactly as experienced on board the LNG carrier during the measurement campaign. All measurement results considered, the propeller induced vibration energy and therefore the structure borne noise was mainly found to be concentrated below the 100 Hz in all cases.

From the measurement results taken from a ROPAX vessel and a Fishery Research vessel can be seen that the excitation from diesel engines is of a tonal nature and contains many tonal frequency components typically a multitude of the 0.5 order crankshaft rotation frequency which is the ground harmonic of a four stroke engine. Most of the vibration energy seems to be concentrated in the frequency band between 0 and 200 Hz.

6 Theory of Structural response Simulation

In this work state of the art state of the structural modelling techniques are evaluated. The first step of this evaluation is a critical review of the existing most commonly used structural modelling techniques. In this critical review presented in section 4, the validity and practicality of these modelling techniques are assessed considering the nature of typical ship structures and most dominant ship vibration excitation characteristics (propeller and diesel engines). Further assessment of the nature of excitation and response characteristics is done through analysing measurement results, presented in section 5.

Based on the findings from the literature study and the tonal structural response measured on the ship's structure close to engines and propellers, finite element based modelling techniques are considered the most suitable modelling techniques for ship vibrations.

6	Theory of Structural response Simulation
6.1	Introduction: Choosing the Modelling Techniques
6.2	The wave and mode approach
6.2.1	The Wave Approach
6.2.2	The Mode Approach
6.3	The Principles of Finite Element Modelling
6.4	Solving the Equations of Motion
6.4.1	Full Analysis: Row Reduction.
6.4.2	Mode Superposition
6.4.3	Mode Superposition with Residual Compensation
6.5	Component Mode Synthesis (CMS)
6.5.1	Fixed Interface CMS: the Craig-Bampton Method
6.5.2	Free Interface: the McNeal and Rubin's Method
6.5.3	Reducing the Interface Degrees of Freedom
6.6	Summary and Discussion

Paragraph structure of chapter 6 'Theory of Structural response Simulation'

The next step in evaluating structural modelling techniques is applying some of these finite element modelling techniques on a structural model representing the aft ship of the LNG carrier on board which the author has performed vibration measurements (see section 5, Figure 8). Assessment of the modelling techniques will be based on accuracy of results and required computation time (in measured CP time or calculated number of floating point operations).

In this section the mathematical background of the selected modelling techniques is presented before applying these techniques on the aft ship model of the LNG carrier, which will be done in section 7. Understanding the different calculation steps required to obtain the results is important in order to develop an expression through which the number of floating point operations can be estimated for each step. The number of floating points required for the analysis is a direct indication of the number of computation time required for the analysis. Understanding how each calculation step contributes to the computation time is important in order to develop the alternative component mode synthesis approaches suggested in section 8.

6.1 Introduction: Choosing the Modelling Techniques

A very important aspect of controlling noise and vibrations is the ability to assess structural geometry design choices on their impact on natural structural dynamic behaviour related to the relevant excitation characteristics. Both structural response modelling techniques and techniques to estimate the characteristics of the most dominant ship vibration excitation sources are needed.

In the first part of section 4 “

Critical Review” the state of the art is reviewed of the methods available for estimating the nature of these excitation characteristics. Measurement results taken on board vessels by the author have been studied in section 5 “Measurement Results” for evaluation of the nature of the excitation characteristic. From the literature study of section 4 and the measurement results in section 5 the excitation characteristic from both propellers and diesel engines was found to be predominately tonal of nature and the vibration energy was in all cases found to be concentrated below 200 Hz.

In the second part of section 4 “

Critical Review” the state of the art in modelling structural response is reviewed. For assessing the validity and practicality of the different approaches available the nature of the excitation characteristic needs to be considered. Having established in the first part of the critical review that propeller and diesel engine excitation characteristics

are predominantly of a tonal nature, with vibration energy content rapidly decreasing with blade passing or crankshaft rotation frequency related harmonics, statistical energy analysis and spectral element methods have been considered unsuitable or unpractical for modelling the structural response of ship structures such as the LNG carrier. As the findings of the study of the measurement results presented in section 5 confirm the findings about the typical nature of propeller and diesel engine excitation characteristics, presented in the critical review, finite element based modelling techniques have been selected as the most suitable modelling techniques for modelling vibrations on ships. The most suitable techniques considered are:

- Full Harmonic Finite Element Modelling Technique
- Mode Superposition Technique
- Component Mode Synthesis Techniques

Later in this work, some of these finite element based modelling techniques are assessed by using them for the simulation of vibration spectra of the aft ship of the LNG carrier on board which the author has performed noise and vibration measurements (as presented in section 5, see Figure 8). The simulation results presented in section 7 will focus on propeller generated vibrations alone, as the ship is equipped with steam turbines for generation of both main and auxiliary power, and only very little contribution from the steam turbines have been found in the measurement results [20].

In preparation of the evaluation of these techniques, the mathematical background of these techniques are presented in the following sections.

6.2 The wave and mode approach

When vibrations are modelled mathematically, two main approaches to vibrations can be adopted:

- The wave approach
- The mode approach

Through the wave approach the shape of deformation of an object is described as a superposition of travelling waves. Vibrations are modelled as waves travelling from the source and spreading through the structure and waves that are reflected at the boundaries and are travelling back into the structure. The interference of these waves result in a standing waves. These standing waves are most effectively formed at certain frequencies, where the phase relation between incident and reflected waves is such, that these waves amplify each other. In that case, little energy is required to generate a vibratory response. These frequencies are the resonance frequencies and the standing waves are the corresponding mode shapes. In this approach the modelling of the wave reflecting from the boundaries (phase shift and amplitude) is very important and is done through the mathematical formulation of the boundary conditions.

When structures become geometrically more complicated, the wave approach becomes unpractical. Particularly the mathematical definition of the boundary conditions becomes complicated as these conditions are formed by a complex combination of dynamic properties of the structures attached to all the boundaries. In this case a modal approach is adopted which is based on approaching vibrations as a superposition of a number of assumed mode shapes, which are substituted into the energy equations through which the equations of motion are formulated. This approach is adopted in finite element modelling techniques

6.2.1 The Wave Approach

With the wave approach a structure is modelled as an elastic continuum through which different type of waves propagate:

- Compressional waves
- Flexural waves (transverse or bending)
- Shear waves
- Torsional waves

Of these types of waves the flexural wave is the only type of wave that produces perceivable vibrations and noise for the reason that the particle velocity (structural

displacement) is perpendicular to any object or person that is in contact with the structure and is also perpendicular to the air or water that is surrounding the structure, through which airwaves or underwater waves are generated which is perceived as noise.

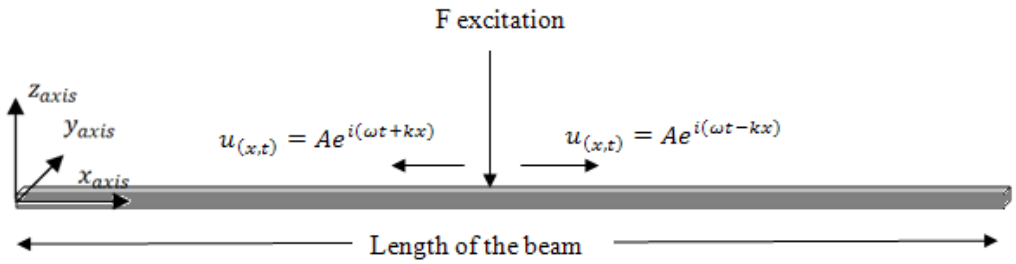

Figure 26 ***Beam with a travelling wave***

The wave approach, as already explained in section 4.2.1 “Hull Girder Approach”, is successfully adopted for the estimation of the natural frequencies corresponding with the first 4 or 5 bending modes of a ship’s hull. The hull is considered a slender homogeneous beam. The principle of the approach to vibrations according to the wave approach is therefore demonstrated with a slender beam as shown in Figure 26.

This beam is excited at half the length by a force *F* at a frequency *ω*. As a result a wave travels from the point of excitation both to the right and to the left (opposite directions). Two types of velocity can be distinguished for both waves: the velocity of propagation of the wave (disturbance) through the material (horizontally), and the alternating velocity perpendicular to the propagation direction (vertically).

The vertical velocity of the particle (point) on the structure is expressed through the frequency of alteration normally expressed through the radian frequency $\omega = \frac{2\pi}{T}$ (T is the time required for a point on the structure to move from the equilibrium position to the positive maximum amplitude, to the negative maximum amplitude and back to equilibrium position again = 1 cycle).

The propagation speed is expressed through the wave number and is also a function of the radian frequency of the vertical wave motion of a point on the beam:

$$c = \frac{\omega}{k} \quad \textbf{(6.1)}$$

$$k = \frac{2\pi}{\lambda} \quad \textbf{(6.2)}$$

Where:

c = the speed in which the disturbance propagates through the structure (wave velocity)

k = the wave number also expressed as a function of the wave length λ

The particle displacement is expressed through the following complex representation:

$$v_{(x,t)} = Ae^{i(\omega t - kx)} \quad \textbf{(6.3)}$$

Where:

$v_{(x,t)}$ is the vertical displacement at point x on the beam at time t

A is a complex constant

ω is the frequency of alteration of the excitation force (and therefore the vertical motion of the particle) in rad/s

k = the wave number through which the phase difference between the wave motion at x=0 and x=x is expressed.

The complex constant A is evaluated through the force balance equations. These force balance equations are based on the formulation of the relation between curvature of bending and the resistance against bending, and the vertical acceleration of a particle due to the bending motion and the resulting inertia forces.

Through the description of the relation between the curvature of bending and the bending moment the shear force of an infinitively small beam can be described [23, 45].

$$D = \frac{\partial M}{\partial x} \quad \textbf{(6.4)}$$

$$M = EI\frac{\partial^2 v}{\partial^2 x} \quad \textbf{(6.5)}$$

Where:

D= the shear force in a beam alement of a length ∂x

M = bending moment

$\frac{\partial^2 v_{(x,t)}}{\partial^2 x}$ = the curvature of the beam

$v_{(x,t)}$= vertical deflection of the beam as a function of time t and x = coordinate in the direction of length of the beam

E= elasticity modulus (2.11e11 Pa for steel)

I = is the moment of inertia of the cross-sectional area of the beam = $\int_A z^2 dA$

Where:

dA= infinitively small crosssectional area

z= vertical distance neutral bending line of the beam and the infinitively small cross sectional area dA

Inertia forces of a beam are expressed as the mass times vertical acceleration of beam section ∂x

$$\rho A dx \frac{\partial^2 v_{(x,t)}}{\partial t^2} \quad \textbf{(6.6)}$$

Where

A = the cross-sectional area of the beam.

$\frac{\partial^2 v_{(x,t)}}{\partial t^2}$ = the vertical acceleration of the mass particle $\rho A dx$ where t = time

Combining Euler's law with Newton's law, the total equation of motion according the equilibrium of forces becomes:

$$\rho A dx \frac{\partial^2 v_{(x,t)}}{\partial t^2} + EI \frac{\partial^4 v_{(x,t)}}{\partial^4 x} dx = 0 \tag{6.7}$$

$$\left(\frac{\rho A dx}{EI dx}\right) \frac{\partial^2 v_{(x,t)}}{\partial t^2} + \frac{\partial^4 v_{(x,t)}}{\partial^4 x} = 0$$

$$\left(\frac{\rho A}{EI}\right) \frac{\partial^2 v_{(x,t)}}{\partial t^2} + \frac{\partial^4 v_{(x,t)}}{\partial^4 x} = 0$$

$$-\left(\frac{\rho A \omega^2}{EI}\right) v_{(x,t)} + \frac{\partial^4 v_{(x,t)}}{\partial^4 x} = 0 \tag{6.8}$$

Where equation (6.8) represents the wave equation according to Euler and is a classical differential equation. This equation is however only valid for a slender beam where:

- The normals remain normal to the x axis when the beam is bending due to the wave motion.
- No effect of the rotary inertia is taken into account.

Considering a solution for the amplitude as a function of *x* and *t* in the form as shown in (6.3):

$$v_{(x,t)} = A e^{i(\omega t - kx)}$$

, and substituting into (6.8) gives the homogeneous solution of the differential equation (6.8). Four solutions for the wave number k are found:

$$A\left(k^4 - \omega^2 \frac{\rho A}{EI}\right) e^{(i\omega - ikx)} = 0 \tag{6.9}$$

For the non trivial solution:

$$\left(k^4 - \omega^2 \frac{\rho A}{EI}\right) = 0$$

$$k_1 = \sqrt[4]{\left(\omega^2 \frac{\rho A}{EI}\right)}$$

$$k_2 = -\sqrt[4]{\left(\omega^2 \frac{\rho A}{EI}\right)} = -k_1$$

$$k_3 = i\sqrt[4]{\left(\omega^2 \frac{\rho A}{EI}\right)} = ik_1$$

$$k_4 = -i\sqrt[4]{\left(\omega^2 \frac{\rho A}{EI}\right)} = -ik_1$$

This means that there are four wave types possible that propagate through the structure simultaneously. The expression for the solution to the differential equation (6.8) shows these four wave types all with their own participation factor A_n:

$$\hat{v}_{(x,t)} = (A_1 e^{kx} + A_2 e^{-kx} + A_3 e^{ikx} + A_4 e^{-ikx}) e^{i\omega t} \quad \textbf{(6.10)}$$

The interpretation of the general solution is that there are two propagating wave motions $A_1 e^{(\omega t + kx)}$ and $A_2 e^{(\omega t - kx)}$ and two non propagating decaying wave motions $A_3 e^{(\omega t + ikx)}$ and $A_4 e^{(\omega t - ikx)}$. The two propagating wave motions are waves travelling in each other's opposite direction. The general solution is also expressed as:

$$\hat{v}_{(x)} = A_1 cos(kx) + A_2 sin(kx) + A_3 cosh(kx) + A_4 sinh(kx) \quad \textbf{(6.11)}$$

Through substitution of this equation for the vertical beam displacement (6.11) into the force equilibrium equation (6.8), and applying the boundary conditions at the end of the beams, an expression for the natural frequencies and corresponding mode shapes is obtained. In Appendix II it is demonstrated how this is done for a free floating beam, representing the hull girder properties of a vessel (see Figure 27)

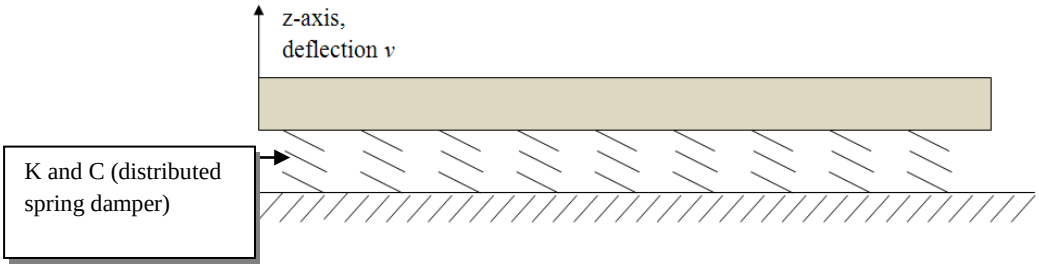

Figure 27 ***Representation of a ship hull as a beam. The beam is supported through a distributed springs with stiffness properties K representing the buoyancy effect of the water and damping C representing hydrodynamic damping.***

For the beam equation used for calculating the hull girder vibration response of ships however, the wave number *k* is derived in a slightly different manner in order to be able to accommodate for the distributed stiffness that is representing the buoyancy effect of the water the ship is floating in and the hydrodynamic mass (Figure 27). The wave equation (6.8) becomes:

$$\frac{\partial^4 v_{(x,t)}}{\partial^4 x} + \left(K - \omega^2 \left(\frac{\mu}{EI}\right)\right) v_{(x,t)} = 0 \qquad \textbf{(6.12)}$$

K = distributed stiffness representing buoyancy effect of the water

μ = continuous distributed mass of the ship per unit length. This mass includes hydrodynamic added mass of the water, mass of the cargo and mass of the ship's structure.

Expression (6.9) becomes:

$$\left(k^4 + \left(K - \omega^2 \left(\frac{\mu}{EI}\right)\right)\right) e^{\lambda x} = 0 \qquad \textbf{(6.13)}$$

Through which the values for k are calculated:

$$k = \sqrt[4]{\left(-K + \omega^2 \left(\frac{\mu}{EI}\right)\right)} = \frac{(n + \frac{1}{2})\pi}{L}$$

Although in above equations stiffness and damping effect due to hydrodynamic interaction with the hull girder vibrations have been included, these contributions to the mass elastic behaviour is considered very small and is normally omitted, which simplifies the model further. The effect of added mass to the natural frequencies corresponding

6.2.2 The Mode Approach

In section 4.2.1, 6.2.1 and in Appendix II approaching the ship's structural dynamic behaviour through a wave approach (Euler beam theory) is discussed. Through the mathematical description of the boundary conditions natural frequencies and mode shapes are formulated.

As described above, the beam approach to a ship is based on two major assumption which implies that the approach would only be valid for estimating the first two natural frequencies corresponding with the first two mode shapes. These assumptions are:

- The equations are valid only for a slender beam which means that no shear deformation and rotary inertia effect has been taken into account.
- The ship is considered a structure which a continuous mass stiffness distribution,

Beam equations can still be formulated in such a way that shear deformation and rotary inertia effects can be taken into account (Timoshenko beam), but that complicates the mathematical description and has therefore not been demonstrated in this work. The second assumption still remains a problem for analysing higher mode shapes. In addition, local vibration modes start to play an important role when considering excitation frequencies which are in the range of most of the engine excitation characteristics and multiples of typical propeller blade passing frequencies.

Theoretically the wave approach could still be adopted for models which are not continuous. One could subdivide the ship's structure into a limited number of structures that could be regarded continuous and are couples to each other. However, describing the boundary conditions of the individual continuous structures in coupled condition becomes more complicated resulting in mathematically unpractical formulations of the natural frequencies and corresponding mode shapes [12].

A more practical way of describing the mass spring system is through the finite element method. A finite element model consists of a finite number of elements through which the mass stiffness distribution of a structure is described. One such element represents the mathematical description between the deformation of such an element and the resulting reaction loads at the boundaries of the elements. This mathematical description (equation of motion) is obtained through substituting a number of predefined deformation shapes (mode shapes) into a suitable formulation of the equilibrium relations.

Important to note is that the equilibrium relations used in the finite element description of an element are the same as those used for the beam theory where the wave approach has been used. However, the difference is that the finite element approach uses a finite number of predefined mode shapes relating the deformation of the element to the translations and rotations of the elements boundaries. The form of this relation is formulated as a polynomial:

$$v(x) = a_1 + a_2 x + a_3 x^2 + \cdots a_n x^{(n-1)} \quad \textbf{(6.14)}$$

Where $v(x)$ is the displacement of the element at coordinate *x*

$a_n x^{(n-1)}$ is the contribution to the element displacement distribution on the x-axis from mode shape *n* where $x^{(n-1)}$ is the mode shape and a_n the modal coordinate of the n^{th} mode shape. The number of mode shapes through which the deformation of the element can be described depends on the number of degrees of freedom of the element. A beam for instance with two nodes (one at each end) has four degrees of freedom (rotation and translation of end *p* and rotation and translation of end *q*). Therefore the displacement function can be described as a superposition of 4 mode shapes.

6.3 The Principles of Finite Element Modelling

As described in 6.2.2 “The Mode Approach” the application of a wave approach to ship structural vibration modelling is not practical. The beam theory is applied for estimating the natural frequencies and response of low mode number bending mode

shapes of the ship hull. However, the frequency range within which powerful tonal excitation frequency components exist coming from propellers and diesel engines exceed the frequency range where typically the first four hull bending mode shape's natural frequencies are to be found. Higher order mode shapes become important, for which a more precise description of the ship's structural geometry is required. Although through a wave approach, theoretically, the response behaviour of any structure could still be obtained, but due to the complex nature of the structure, this approach is not very practical.

Therefore, finite element modelling is in this work considered the most practical approach to modelling structural vibrations of a ship's structure such as the aft ship of the LNG carrier which is used as a study object in this work. As explained above in section 6.2.2 "The Mode Approach", with a finite element model the distribution of stiffness and mass of a structure is described through a series of discreet masses and spring, i.e., a finite number of elements. When considering describing a ship's structure with a finite element model, the two most commonly used element types are beam elements (for stiffeners) and plate elements (for the hull plating).

The displacement of the nodes of the elements is calculated through the equations of motion formulated for each degree of freedom for each node an element consists of. A beam element, as used in the case study for this work, consists of two nodes (one at each end) with each 6 degrees of freedom (along the x,y and z axis and rotation about x, y and z axis). The square plate elements used in this this work's case study consist four nodes (one on each corner) with each 6 degrees of freedom (along the x,y and z axis and rotation about x, y and z axis).

The equations of motion for each degree of freedom are based on the formulation of the equilibrium between external forces and internal forces. The external forces are the excitation forces acting on the nodes, and the internal forces are the reaction forces on the nodes resulting from the deformation of the element (strain forces) and the acceleration of the elements mass (inertia forces).

This equilibrium is described according to d' Alembert's principle in the form

$$M\ddot{u} + C\dot{u} + Ku = F \quad \textbf{(6.15)}$$

where M, C, K are the mass, damping, and stiffness matrices and F is the excitation force vector.

Defining the equation of motion lays in the formulating the mass, damping and stiffness matrix (M, C, K) in such a way that they represent accurately enough the physical relation between the alternating displacements (inducing element strain forces on the nodes), acceleration (inducing inertia forces on the nodes) and velocity (inducing damping forces on the nodes), and the resulting reaction forces in the nodes.

Through applying the principle of virtual work, the Lagrange equation has been formulated, which is in fact a convenient reformulation of Hamilton's principle, particularly useful for obtaining equations of motion for continuous structures subjected to alternating dynamic loads. With the Lagrange equation the equation of motion is expressed in quantities of energy:

$$\frac{d}{dt}\left(\frac{\partial T}{\partial \dot{u}}\right) + \frac{\partial U}{\partial u} + \frac{\partial D}{\partial \dot{u}} = f \quad \textbf{(6.16)}$$

Where:

T = the kinetic energy

U= is potential energy (in our case strain energy)

D is the dissipation function = $\frac{1}{2}c\dot{u}^2$

u is the displacement

$\dot{u}$ is velocity

c = damping factor

In order to obtain the mass matrix and stiffness matrix through the Lagrange equation, an expression is required for the relation between nodal displacement of an element, kinetic energy of the elements, and strain energy of the element. These relations are expressed through the energy expressions of the element.

An important aspect of the formulation of the energy expression is the formulation of the displacement function which needs to be substituted into the energy expression. As described above, the formulation of the equations of motion which finite element modelling is based on a modal approach, i.e. the displacement function is expressed through a polynomial series (6.14) which is in fact a superposition of assumed shapes of deformation or mode shapes.

The two most used types of elements for the simulation of the structural response of a ship's structure are the plate elements and the beam element. Appendix III and Appendix IV show how the stiffness and mass matrices are composed for the two node beam element and the four node plate element. These are both the types of elements selected for modelling the aft ship of the LNG carrier presented in the case study of this work.

6.4 Solving the Equations of Motion

From the stiffness mass and damping matrices of the elements, the stiffness K, mass M and damping matrix C of the total structure is composed. Through these matrices the equation of motion is formulated:

$$F_e = M\ddot{u} + C\dot{u} + Ku \quad \textbf{(6.17)}$$

Where

u, $\dot{u}$, and $\ddot{u}$ are the vectors representing the displacement, velocity and acceleration of a nodal degree of freedom.

Solving the equations of motion can be done in time domain, or in frequency domain. The calculation of the displacement vector in time domain relies on

numerical integration techniques and requires solving the set of equations of motion for every time step *dt*.

Vibration problems however are in most cases solved in frequency domain. The excitation force is assumed to be of a harmonic nature and is described through a superposition of harmonic components written in the form:

$$F(t) = \sum_{1}^{n} F_n \cos(\omega_n t + \varphi_n) \quad \textbf{(6.18)}$$

Where:

F_n = force amplitude of harmonic *n*

ω_n = frequency of harmonic *n* in rad/s

φ_n = phase angles for harmonic *n* in radians

n = the number of relevant tonal harmonic components through which the excitation force $F(t)$ is described

As most of the excitation sources are of a harmonic nature, the harmonic approach to calculating the response is very appropriate. The focus of this work will therefore be on harmonic analysis (steady state).

As the excitation is described as a superposition of harmonic components (equation (6.18)), the response displacement of the structure is also described as a superposition of responses calculated for each of these harmonic excitation components:

$$u(t) = \sum_{1}^{n} \hat{u}_n \cos(\omega_n t + \varphi_{un})$$

$u_n(t) = \hat{u}_n \cos(\omega t + \varphi_{un})$ = response deflection to the nth harmonic **(6.19)**

$\dot{u}_n(t) = -\omega \hat{u}_n \sin(\omega t + \varphi_{un})$ = response velocity to the nth harmonic.

$\ddot{u}_n(t) = -\omega^2 \hat{u}_n \cos(\omega t + \varphi_{un})$ = response acceleration to the nth harmonic.

Where

$\hat{u}_n$ the amplitude displacement vector for harmonic *n*.

φ_{un} is response phase angle for harmonic *n*.

ω_n= frequency corresponding with harmonic *n* in rad/sec

Considering the calculation of the response to a single frequency *n*, the general complex notation of the equations of motion is:

$$F = (-\omega^2 M + \omega C i + K)u \quad \textbf{(6.20)}$$

Where $(-\omega^2 M + \omega C i + K)$ is also referred to as the dynamic stiffness matrix

In this work, two methods of calculating the response of a structure are discussed:

- Full solution method by directly solving $F = (-\omega^2 M + \omega C i + K)u$
- Mode superposition method, only taking the response contribution of a limited number of mode shapes into account.

6.4.1 Full Analysis: Row Reduction.

The most direct way of solving the set of equations of motion shown in equation (6.20) is through solving the equations of motion directly. In the finite element method used in this work (ANSYS), equation (6.20) is solved through the so called sparse solver which applies the row reduction technique, as demonstrated in Appendix VI. In this appendix also the number of required floating point operations is estimated required for each step of the row reduction technique.

The first step in obtaining the solution of equation (6.20) is the factorisation of the sparse dynamic stiffness matrix into a lower triangular matrix. This factorisation is characterised by two distinct phases: the forward phase (or forward substitution) of row reduction and the backward phase (backward substitution) of row reduction. The forward phase is the stage in the factorisation where elementary row operations are performed to transform the sparse dynamic matrix in a triangular matrix. The backward phase is the stage where through row operations the above obtained

triangular matrix is reduced. The pivots are first all transformed into 1. From there it easy to transform all numbers above the pivots into zeros with reduces the size of the matrix. From the thus obtained triangular reduced matrix the results are very easy to obtain starting from the bottom row working upwards.

Appendix VI demonstrates how the system matrix is factorised considering a mass spring system consisting of four masses and of 200 kg and four springs of 4e6 N/m as shown in Figure 28. All masses have only one degree of freedom in horizontal direction and no damping assumed to be present. Consider the following stiffness matrix K, mass matrix M and the excitation load vector F:

$$K = \begin{bmatrix} 4e6 & -2e6 & 0 & 0 \\ -2e6 & 4e6 & -2e6 & 0 \\ 0 & -2e6 & 4e6 & -2e6 \\ 0 & 0 & -2e6 & 4e6 \end{bmatrix}$$

$$M = \begin{bmatrix} 200 & 0 & 0 & 0 \\ 0 & 200 & 0 & 0 \\ 0 & 0 & 200 & 0 \\ 0 & 0 & 0 & 200 \end{bmatrix}$$

$$F = \begin{bmatrix} 60 \\ 0 \\ 0 \\ 0 \end{bmatrix}$$

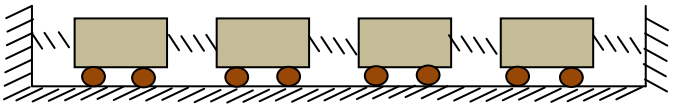

Figure 28 **Mass spring system**

Consider the excitation frequency to be 10 Hz:

$\omega = 62.8\ [\frac{rad}{s}]$ = (10Hz)

6.4.2 Mode Superposition

The response of a structure can be described as a superposition of a set of mode shapes with their modal coordinates:

$$\begin{bmatrix} \varphi_1 & \varphi_2 & \dots & \varphi_n \\ \vdots & \vdots & \dots & \vdots \end{bmatrix} \begin{bmatrix} a_1 \\ a_2 \\ \vdots \\ a_n \end{bmatrix} = \begin{bmatrix} u \\ \vdots \end{bmatrix} \quad \textbf{(6.21)}$$

Where:

a_1 to a_n are the modal coordinates (participation factors) corresponding to mode shapes φ_1 to φ_n

$\begin{bmatrix} u \\ \vdots \end{bmatrix}$ is the total displacement vector (the physical coordinates).

Calculating the response through mode superposition reduces the required analysis time (CP time), as only the mode shapes with corresponding natural frequencies and within a certain bandwidth of the excitation frequencies are calculated and used. This approach is justifiable considering that contributions from mode shapes decrease the further the corresponding natural frequency is from the excitation frequencies. Usually the first set of modes are selected of which the natural frequencies are within a bandwidth between 0 and $1.5\,f$ (according to Rubin's principle [26]), where f is the frequency for which response calculations are required.

The first step in obtaining results through mode superposition is the calculation of natural frequencies and mode shapes. These natural frequencies and mode shapes are obtained, starting with the formulation of the natural behaviour of a structure, i.e., the behaviour of the structure with no external loads acting on it.

As damping factors are usually low for steel structures, for simplification of the calculation procedure, usually un-damped natural frequencies and mode shapes are used. This means that the equation of motion (6.20) is written as follows:

$$(-\omega^2 M + K)u = 0$$

$$[K - M\omega^2] = 0 \quad \textbf{(6.22)}$$

Through formulating the determinant of $[K - M\omega^2]$ and stating that the determinant should be zero, the non trivial solutions for ω^2 are found. Through the square root of the thus obtained values for ω^2, the natural frequencies are found. A number of

values for ω^2 is found equal to the number of rows or the number of columns the matrix $[K - M\omega^2]$, consists of, i.e. equal to the number of degrees of freedom the theoretical structure has been given through the finite element formulation.

Through calculation of the eigenvectors of $[K - M\omega^2]$ corresponding with the above calculated values for ω^2, the theoretical mode shapes are found corresponding with the calculated eigenvalues (natural frequencies) ω^2.

Through the mode shapes obtained, the matrix Φ is formulated:

$$\Phi = \begin{bmatrix} \varphi_1 & \varphi_2 & \cdots & \varphi_n \\ \vdots & \vdots & \cdots & \vdots \end{bmatrix}$$

This matrix is used as the basis for reducing the full stiffness, mass and damping matrices, and excitation force vector (K, M, C and F) to the reduced stiffness, mass and damping matrices, and excitation force vector ($\bar{K}$, $\bar{M}$, $\bar{C}$ and $\bar{F}$). These reduced matrices are calculated as follows:

$$\bar{M} = \Phi^T M \Phi \quad \textbf{(6.23)}$$
$$\bar{K} = \Phi^T K \Phi$$
$$\bar{C} = \Phi^T C \Phi$$
$$\bar{F} = \Phi^T F$$

Through these reduced matrices a reduced set of equations of motion is formulated based on the modal coordinates, instead of the physical coordinates (equation (6.42) and (6.43)). Through this equation of motion the modal coordinates a are calculated and expanded into the physical coordinates according to equation (6.21)

Substituting equation (6.23) into (6.20) and using the relation of equations (6.19) , we can write:

$$\Phi^T M \Phi \ddot{a} + \Phi^T C \Phi \dot{a} + \Phi^T K \Phi a = \Phi^T F$$
$$(-\omega^2 \Phi^T M \Phi + \Phi^T C \Phi \omega \mathrm{i} + \Phi^T K \Phi) a = \Phi^T F \quad \textbf{(6.24)}$$

$$-\omega^2 \bar{M} a + \bar{C} \omega \mathrm{i} a + \bar{K} a = \bar{F} \quad \textbf{(6.25)}$$
$$(-\omega^2 \bar{M} + \bar{C} \omega \mathrm{i} + \bar{K}) a = \bar{F}$$

In Appendix XV "Steps and Estimated Number of Matrix Operation Mode Superposition" the number of floating point operations required for each step of the modal reduction technique is presented. The number of steps required for solving equation (6.25) in order to obtain the modal coordinate vector a are explained in Appendix VI "Sparse Matrix Solver: Row Reduction Technique".

Further simplification of the solution of equation (6.43) is obtained by normalising the eigenvectors Φ to the mass matrix. This means that

$$\Phi^T M \Phi = \bar{M} = 1$$

And by using the relation

$$\frac{\bar{K}}{\bar{M}} = \Lambda$$

Where Λ is a diagonal matrix with the squared natural frequencies ${\omega_0}^2$ on the main diagonal and the rest of the matrix is zero.

$$(-\omega^2 \bar{M} + \bar{C}\omega\mathrm{i} + \bar{K}) = \bar{M}\left(-\omega^2 + \frac{\bar{C}}{\bar{M}}\omega\mathrm{i} + \frac{\bar{K}}{\bar{M}}\right) = (-\omega^2 + \bar{C}\omega\mathrm{i} + \Lambda)$$

$$a = (-\omega^2 + \bar{C}\omega\mathrm{i} + \Lambda)^{-1}\bar{F} \qquad \textbf{(6.26)}$$

For an individual modal coordinate corresponding with mode number *n* we can write:

$$a_n = \frac{{\varphi_n}^T f}{(-\omega^2 + {\varphi_n}^T \mathrm{C} \varphi_n \omega\mathrm{i} + \omega_\mathrm{n})} \qquad \textbf{(6.27)}$$

6.4.3 Mode Superposition with Residual Compensation

Results obtained through modal reduction can be improved by including the static contributions from the omitted modes. Calculating the static contribution from all modes is simply done by solving the following relation [22, 39]

$$Ku_{static} = F$$

$$u_{static} = K^{-1}F \quad \textbf{(6.28)}$$

Where

K = the stiffness matrix of the analysed structure

u_{static} = the static displacement vector

F= the excitation force

G_c = the flexibility matrix K^{-1}

Through subtracting the static contributions of the retained modes from the static contribution from all modes (expressed through equation (6.28) the static contribution of the omitted modes is obtained.

The static contribution of the retained modes is the response of these modes at 0 rad/s frequency. Considering equation (6.26) and setting ω to 0 gives:

$$a_s = \Lambda^{-1}\bar{F} \quad \textbf{(6.29)}$$

Where

a_s = modal coordinates expressing the static contribution from the retained mode shapes

$\bar{F}$= reduced force vector $\Phi^T F$

Residual compensation is therefore formulated as:

$$u_{residual} = u_{static} - \Phi a_s \quad \textbf{(6.30)}$$

$$u_{residual} = u_{static} - \Phi\Lambda^{-1}\Phi^T F \quad \textbf{(6.31)}$$

The displacement vector obtained through modal expansion including residual flexibility is written as:

$$u = \phi a + K^{-1}F - \phi\Lambda^{-1}\phi^T F \quad \textbf{(6.32)}$$

Reformulating equation (6.29) gives

$$u = \phi a + [K^{-1} - \phi\Lambda^{-1}\phi^T]F = \phi a + G_{res}F \quad \textbf{(6.33)}$$

Where:

$\left[K^{-1} - \phi\Lambda^{-1}\phi^T\right]$ is the residual flexibility matrix G_{res}

The inverse of the stiffness matrix K^{-1} is in fact the flexibility matrix G_c. The residual flexibility is written as:

$$G_{res} = G_c - \phi\Lambda^{-1}\phi^T \quad \textbf{(6.34)}$$

Residual flexibility can also be calculated for free floating, unconstrained structures. As the calculation of the residual compensation requires inverting the stiffness matrix, the residual compensation for free floating structures cannot be obtained directly through equation (6.38) as the stiffness matrix is singular. In Appendix V the formulation of G_{res} for free floating structures is given.

6.5 Component Mode Synthesis (CMS)

As mentioned in the critical review (section 4.2.6 "Component Mode Synthesis Techniques") dynamic sub structuring has some very attractive advantages for modelling marine structures' vibratory behaviour. Assembled dynamic behaviour is described through the modal properties of individual uncoupled sections of the total structure is subdivided in. Different mathematical methods have been developed to describe the interaction between different structures. In this section the principles of the original method presented by Craig an Bampton [34] are described together with some variations of this method proposed by H. MacNeal and Rubin [26, 35].

6.5.1 Fixed Interface CMS: the Craig-Bampton Method

The earliest developed method of dynamic sub structuring is the Craig-Bampton method which has been developed in the 1960ties [34, 37, 38]. The Craig-Bampton method is based formulating the dynamic behaviour of a subsystem as a result of two force vectors. One force vector is the force vector representing the external excitation

force acting on the sub structure (propeller or machinery excitation). This represents the dynamic behaviour of the uncoupled substructure. The other force vector represents the forces on the nodes that are shared with other substructures and are a result of the dynamic interaction between the sub structures. The latter force vector is also very appropriately called the interface force vector. The equation of motion for one coupled substructure is written as:

$$M\ddot{u} + Ku = F_e + F_b \quad \textbf{(6.35)}$$

Where

M = Mass matrix of the substructure

$\ddot{u}$ = second derivative of the displacement vector (acceleration)

K = stiffness matrix of the subsystem

u = displacement vector

F_e = external excitation force (propeller or machinery excitation)

F_b = forces acting on the interface between substructures resulting from the dynamic interaction.

By forcing the geometrical compatibility relations on the equations of motion, the reduced mass and stiffness matrices of the total assembled system are found through which total assembled natural frequencies and mode shapes are calculated and forced vibration calculations can be performed.

6.5.1.1 The Formulation of the Reduction Basis

Reducing calculation time through CMS is based on the application of modal reduction for the description of the mass and stiffness properties of the uncoupled individual substructures. The reduction basis formulated for the Craig-Bampton method consists of elastic modes and so called constraint modes.

Elastic and Rigid Body Modes

With fixed interface CMS the elastic modes are the normal modes of an uncoupled individual substructure with the interface or boundary nodes (where the substructure in connected to other substructures) constrained. Usually these elastic modes and

natural frequencies are calculated through finite element models. Modes shapes and natural frequencies are obtained through solving the eigenvalue problem formulated through the equations of motion of the uncoupled individual substructures (with fixed interfaces) with no external forces acting on it:

$$(K - \omega_n^2 M)\varphi_n = 0 \quad \textbf{(6.36)}$$

Where

K = Subsystem's stiffness matrix with the interface boundaries constrained
M= Subsystem's mass matrix with the interface boundaries constrained
$\omega_n{}^2$ = the square of the natural frequency of mode number n $[rad^2]$
φ_n = normal mode shape corresponding with mode number n

The eigenvalues represent the natural frequencies and the corresponding eigenvectors represent the corresponding mode shapes

Constraint Modes (Static Modes)

When two substructures are coupled to each other through their interface nodes, these initially constrained interface nodes will perform an alternating displacement as a result of the dynamic interaction between the two substructures. Through the so called constraint modes or static modes, the alternating displacement at the interface boundaries is described. Through the constraint modes the relation between a static displacement distribution along the interfaces and the resulting static displacement of the interior nodes of the substructure is expressed. This expression is obtained through the so called Guyan reduction technique [42].

The first step in obtaining the constraint modes is rearranging the stiffness matrix in such a way that the reaction force at the interface nodes of the substructure is separated from the external force acting on the other nodes of the substructure (excitation force).

Therefore the stiffness matrix of an individual substructure is partitioned as follows:

$$\begin{bmatrix} F_b \\ F_e \end{bmatrix} = \begin{bmatrix} k^{BB} & k^{BI} \\ k^{IB} & k^{II} \end{bmatrix} \begin{bmatrix} u^b \\ u^{si} \end{bmatrix} \quad \textbf{(6.37)}$$

Where

F_b = Reaction forces acting on the boundary of the substructure resulting from the dynamic interaction between this substructure and the adjacent substructures (also referred to as interface forces).

F_e = External excitation force vector.

k^{BB}, k^{BI}, k^{IB}, k^{II} = the four subsections of the substructure's stiffness matrix resulting from grouping the interface node forces.

u^b physical displacement vector interface nodes (at the nodes coupling the subsystem to the rest of the total structure). These interface nodes are also referred to as master nodes.

u^{si} physical static displacement vector of the interior nodes (displacement vector representing the displacement of the rest of the substructure). The interior nodes are also referred to as slave nodes.

In order obtain the constraint modes, F_e is set to 0 as this force is related to the normal mode response. An expression is obtained of the relation between the displacement at the interface nodes and the resulting static displacement of the interior nodes:

$$[u^{si}] = -[k^{II}]^{-1}[k^{IB}][u^b] \quad \textbf{(6.38)}$$

$$[u^s] = \begin{bmatrix} u^b \\ u^{si} \end{bmatrix} = \begin{bmatrix} I \\ -[k^{II}]^{-1}[k^{IB}] \end{bmatrix} [u^b] = [\phi^c][u^b] \quad \textbf{(6.39)}$$

Where

$[u^s]$ = the complete static displacement vector containing both interface and internal degrees of freedom displacements

ϕ^c = the constraint mode matrix = $\begin{bmatrix} I \\ -[k^{II}]^{-1}[k^{IB}] \end{bmatrix}$ **(6.40)**

Also,

$$\phi^c = \begin{bmatrix} I \\ \phi^{ci} \end{bmatrix}$$

Where ϕ^{ci} are the internal degrees of freedom (slave nodes) of the constraint modes

6.5.1.2 Reducing Stiffness and Mass Matrices

The reduction basis used for the Craig-Bampton technique is obtained through the combination of elastic modes and constraint modes. The response of one substructure is written as:

$$\begin{bmatrix} u_A^b \\ u_A^i \end{bmatrix} = \begin{bmatrix} I & 0 \\ \phi_A^{ci} & \phi_A \end{bmatrix} \begin{bmatrix} u_A^b \\ a_A \end{bmatrix} \quad \textbf{(6.41)}$$

$$R = \begin{bmatrix} I & 0 \\ \phi_A^{ci} & \phi_A \end{bmatrix} \quad \textbf{(6.42)}$$

Where:

u_A^b are the physical coordinates (displacements) at the interface degrees of freedom of subsystem A.

u_A^i are the physical coordinates (displacements) at the internal degrees of freedom of subsystem A.

ϕ_A^{ci} is the constraint mode matrix of substructure A calculated according to equation (6.40) $\phi^{ci} = -[k^{II}]^{-1}[k^{IB}]$.

ϕ_A is the normal mode matrix of the uncoupled substructure calculated according to equation (6.36).

a_A are the modal coordinates of the normal modes of the uncoupled substructure A.

R is the reduction basis

For two systems together the equations of motion are written as:

$$\begin{bmatrix} M_A & 0 \\ 0 & M_B \end{bmatrix}_{n\times n} \begin{bmatrix} \ddot{u}_A \\ \ddot{u}_B \end{bmatrix}_{n\times 1} + \begin{bmatrix} K_A & 0 \\ 0 & K_B \end{bmatrix}_{n\times n} \begin{bmatrix} u_A \\ u_B \end{bmatrix}_{n\times 1} = \begin{bmatrix} F_{eA} + F_{bA} \\ F_{eB} + F_{bB} \end{bmatrix}_{n\times 1} \quad \textbf{(6.43)}$$

Where:

M_A and M_B are the mass matrices of substructure A and B respectively

K_A and K_B are the stiffness matrices of substructure A and B respectively

F_{eA} and F_{eB} are the external excitation forces acting on substructure A and B respectively.

F_{bA} and F_{bB} are the interface forces acting on substructure A and B respectively as a result of the dynamic interaction between substructure A and B.

$\ddot{u}_A$ and $\ddot{u}_B$ are physical coordinates presenting the accelerations of the degrees of freedom of substructure A and B respectively.

The deflection vector u can be written according to equation (6.41) as:

$$[u_A] = \begin{bmatrix} u_A^b \\ u_A^i \end{bmatrix} = \begin{bmatrix} I & 0 \\ \phi_A^{ci} & \phi_A \end{bmatrix} \begin{bmatrix} u_A^b \\ a_A \end{bmatrix}$$

For the total deflection vector for substructure A and B:

$$\begin{bmatrix} u_A \\ u_B \end{bmatrix} = \begin{bmatrix} u_A^b \\ u_A^i \\ u_B^b \\ u_B^i \end{bmatrix} = \begin{bmatrix} I & 0 & 0 & 0 \\ \phi_A^{ci} & \phi_A & 0 & 0 \\ 0 & 0 & I & 0 \\ 0 & 0 & \phi_B^{ci} & \phi_B \end{bmatrix} \begin{bmatrix} u_A^b \\ a_A \\ u_B^b \\ a_B \end{bmatrix} \quad \textbf{(6.44)}$$

The reduction basis R of substructure A and B together has become:

$$R = \begin{bmatrix} I & 0 & 0 & 0 \\ \phi_A^{ci} & \phi_A & 0 & 0 \\ 0 & 0 & I & 0 \\ 0 & 0 & \phi_B^{ci} & \phi_B \end{bmatrix} \tag{6.45}$$

Substitution of (6.44) into (6.43) and noting that according to (6.37)

$$\begin{bmatrix} K_A & 0 \\ 0 & K_B \end{bmatrix} = \begin{bmatrix} k_A^{BB} & k_A^{BI} & & \\ k_A^{IB} & k_A^{II} & 0 & \\ & & k_B^{BB} & k_B^{BI} \\ & 0 & k_B^{IB} & k_B^{II} \end{bmatrix} \tag{6.46}$$

and therefore

$$\begin{bmatrix} M_A & 0 \\ 0 & M_B \end{bmatrix} = \begin{bmatrix} m_A^{BB} & m_A^{BI} & & \\ m_A^{IB} & m_A^{II} & 0 & \\ & & m_B^{BB} & m_B^{BI} \\ & 0 & m_B^{IB} & m_B^{II} \end{bmatrix} \tag{6.47}$$

And pre-multiplying with R^T gives the reduced equation of motion for the coupled substructures A and B:

$$\begin{aligned} R^T \begin{bmatrix} m_A^{BB} & m_A^{BI} & & \\ m_A^{IB} & m_A^{II} & 0 & \\ & & m_B^{BB} & m_B^{BI} \\ & 0 & m_B^{IB} & m_B^{II} \end{bmatrix} R \begin{bmatrix} \ddot{u}_A^b \\ \ddot{a}_A \\ \ddot{u}_B^b \\ \ddot{a}_B \end{bmatrix} \\ + R^T \begin{bmatrix} k_A^{BB} & k_A^{BI} & & \\ k_A^{IB} & k_A^{II} & 0 & \\ & & k_B^{BB} & k_B^{BI} \\ & 0 & k_B^{IB} & k_B^{II} \end{bmatrix} R \begin{bmatrix} u_A^b \\ a_A \\ u_B^b \\ a_B \end{bmatrix} = R^T \begin{bmatrix} F_{bA} \\ F_{eA} \\ F_{bB} \\ F_{eB} \end{bmatrix} \end{aligned} \tag{6.48}$$

Where

$$R^T \begin{bmatrix} m_A^{BB} & m_A^{BI} & & \\ m_A^{IB} & m_A^{II} & 0 & \\ & & m_B^{BB} & m_B^{BI} \\ & 0 & m_B^{IB} & m_B^{II} \end{bmatrix} R = \bar{M} \tag{6.49}$$

Is the reduced mass matrix

$$R^T \begin{bmatrix} k_A^{BB} & k_A^{BI} & & 0 \\ k_A^{IB} & k_A^{II} & & \\ & 0 & k_B^{BB} & k_B^{BI} \\ & & k_B^{IB} & k_B^{II} \end{bmatrix} R = \overline{K} \quad \textbf{(6.50)}$$

Is the reduced stiffness matrix

6.5.1.3 Describing the Interaction between Substructures

In the previous section (section 6.5.1) it has been demonstrated how the dynamic behaviour is represented through the sum of limited number of retained modes and the sum of a number of constraint modes that is always equal to the number of interface degrees of freedom. However, the sets of equations of motions for subsystem A and subsystem B are still independent from each other considering the upper lower left and upper left parts of the matrices (6.49) and (6.50) are zero. Therefore, no coupling has been described mathematically between the two substructures. The mathematical dependency between the two matrices is obtained by forcing the compatibility relations and the equilibrium relations on the set of equations.

- The compatibility relations simply state that the displacement of the interface of substructure A is equal to the interface displacement of the coinciding interface nodes of substructure B.

$$u_A^b = u_B^b \quad \textbf{(6.51)}$$

- The local equilibrium requirements state that the connection forces at the interface nodes should be equal and in opposite direction so that at the interface nodes equilibrium of forces is obtained:

$$F_{bA} = -F_{bB} \quad \textbf{(6.52)}$$

Forcing compatibility and equilibrium can be done through the interface displacement approach or through the interface force approach.

The description of the interaction between the matrices of the uncoupled systems can be either obtained though primal assembly or dual assembly.

Primal Assembly

In the matrix shown in equation (6.48) no coupling exists between the set of equations related to the degrees of freedom of substructure A and substructure B. For the classic Craig-Bampton formulation of the compatibility and equilibrium relations, the primal assembly method is used. The primal assembly method is based on describing the assembled dynamic behaviour of the substructures through interface displacements through which the compatibility relations (see equation (6.51)) are satisfied a priory [37]

$$u_A^b - u_B^b = 0 \tag{6.53}$$

Through this mathematical relation one of the set of interface nodes is made redundant through which the set of equations of motions (6.48) will be reduced. From equation (6.48) (6.53) can be rewritten as:

$$u_A^b - u_B^b = [I \quad 0 \quad 0 \quad 0]\begin{bmatrix} u_A^b \\ a_A \\ u_B^b \\ a_B \end{bmatrix} - [0 \quad 0 \quad I \quad 0]\begin{bmatrix} u_A^b \\ a_A \\ u_B^b \\ a_B \end{bmatrix} = 0$$

$$u_A^b - u_B^b = [I \quad 0 \quad -I \quad 0]\begin{bmatrix} u_A^b \\ a_A \\ u_B^b \\ a_B \end{bmatrix} = Bu = 0 \tag{6.54}$$

u_A^b is in this case going to be made redundant by describing $\left[u_A^b\right]$ as a function of $\begin{bmatrix} u_A \\ u_B^b \\ u_B \end{bmatrix}$.

$$[I][u_A^b] = -[0 \quad -I \quad 0]\begin{bmatrix} a_A \\ u_B^b \\ a_B \end{bmatrix} \qquad [u_A^b] = -[I]^{-1}[0 \quad -I \quad 0]\begin{bmatrix} a_A \\ u_B^b \\ a_B \end{bmatrix}$$

$$\begin{bmatrix} u_A^b \\ a_A \\ u_B^b \\ a_B \end{bmatrix} = \begin{bmatrix} -[I]^{-1}[0 & -I & 0] \\ & I & \end{bmatrix} \begin{bmatrix} a_A \\ u_B^b \\ a_B \end{bmatrix} \tag{6.55}$$

In the literature the $\begin{bmatrix} -[I]^{-1}[0 & -I & 0] \\ & I & \end{bmatrix}$ matrix is referred to as the *L* matrix and is used to further reduce the stiffness matrix making one set of interface nodes redundant.

The reduced matrix (6.48) is written as:

$$R^T \begin{bmatrix} M_A & 0 \\ 0 & M_B \end{bmatrix} R \left\{ L \begin{bmatrix} \ddot{a}_A \\ \ddot{u}_B^b \\ \ddot{a}_B \end{bmatrix} \right\} + R^T \begin{bmatrix} K_A & 0 \\ 0 & K_B \end{bmatrix} R \left\{ L \begin{bmatrix} a_A \\ u_B^b \\ a_B \end{bmatrix} \right\} = R^T \begin{bmatrix} F_{bA} \\ F_{eA} \\ F_{bB} \\ F_{eB} \end{bmatrix}$$

For further description of the coupling between the two systems the equilibrium condition needs to be satisfied which is also done through satisfying the following relation:

$$F_{bA} + F_{bB} = 0$$

$$[L]^T R^T \begin{bmatrix} F_{bA} \\ F_{eA} \\ F_{bB} \\ F_{eB} \end{bmatrix} = \begin{bmatrix} \bar{F}_{eA} \\ 0 \\ \bar{F}_{eB} \end{bmatrix}$$

This brings the total equation of motion to

$$[L]^T \bar{M} [L] \begin{bmatrix} \ddot{a}_A \\ \ddot{u}_B^b \\ \ddot{a}_B \end{bmatrix} + [L]^T \bar{K} [L] \begin{bmatrix} a_A \\ u_B^b \\ a_B \end{bmatrix} = [L]^T R^T \begin{bmatrix} F_{bA} \\ F_{eA} \\ F_{bB} \\ F_{eB} \end{bmatrix} = \begin{bmatrix} \bar{F}_{eA} \\ 0 \\ \bar{F}_{eB} \end{bmatrix} \tag{6.56}$$

Dual Assembly

The difference between the primal and dual assembly method is that the assembled dynamic behaviour is described through interface forces instead of the interface displacements. In other words, the full assembled equations of motion is obtained through inserting the equilibrium condition into the uncoupled equations of motion whereas with the primal assembly method the compatibility relation is added to the

individual uncoupled equation of motion through which the coupling is mathematically obtained. With the dual assembly method the compatibility relations are added explicitly and with the primal assembly method the equilibrium conditions are added explicitly [37]. In section 6.5.2 the dual assembly technique is demonstrated as applied for the Rubin and MacNeal method.

6.5.2 Free Interface: the McNeal and Rubin's Method

Calculating the assembly dynamic behaviour according to the Craig-Bampton method described above uses the normal elastic modes of the substructures with **constrained** interface boundaries combined with the static (constraint) modes for the description of the vibratory displacement distribution of the substructure. Rubin and McNeal have developed a sub structuring method using normal modes calculated for the subsystem with **free** interface boundaries. Also residual attachment modes are used. The advantages of this method are (see section 4.2.6.2 "Fixed and Free Interface CMS")

- Expansion of results requires less floating point operations as expansion of only elastic modes gives an accurately enough representation of the dynamic response of the structure.
- Substructures dynamic behaviour with free interface boundaries reflects the actual ship sections' structural behaviour a lot better, as interface boundaries of a stored section are seldom fixed. This makes it easier to correlate modal information of the mathematical substructure to the modal information of the physical substructure obtained through modal measurements.

6.5.2.1 McNeal's Method

The Rubin and McNeal Method start with a dual formulation of the coupled substructures analogue to (6.35) [35-37]

$$M\ddot{u} + Ku + Cu = F_e + F_b \qquad \textbf{(6.57)}$$

Where:

F_e = external excitation force

F_b = forces acting on the interface boundaries resulting from the dynamic interaction (also referred to as interface forces)
M, K, and C are the mass, stiffness and damping matrices respectively

With both the Rubin and McNeal's method three types of modes are considered for the description of the displacement field:

- Normal modes (with free (unconstrained) interfaces)
- Residual flexibility attachment modes (static modes)
- Rigid body modes (if structure is not constrained, i.e. free floating)

The displacement field u of a substructure is therefore described as:

$$u = a_e \phi_e + a_r \phi_r + G_{res} F_b \quad \textbf{(6.58)}$$

Where:

a_r and a_e are the modal coordinates of the rigid body modes and the retained elastic modes respectively. The retained normal modes are calculated with free interface boundaries

$G_{res} F_b$ is the static residual response of the flexible system to the forces occurring in the substructure resulting from the interaction with the other substructure. These are also referred to as the residual flexibility attachment modes. F_b is a force vector presenting the interface forces for the interface degrees of freedom and 0 for the internal degrees of freedom.

G_{res} is the residual flexibility matrix representing the boundary residual flexibility modes. The residual flexibility matrix is expressed through the inverse of the stiffness matrix corrected for the static contributions from the retained flexible modes. The reason for this correction is that the static response of the retained elastic modes is already included in the contribution from the elastic modes.

Following section 6.4.3 we write for the residual flexibility matrix:

$$G_{res} = K^{-1} - \phi\Lambda^{-1}\phi^{T} \quad \textbf{(6.59)}$$

Where:

K^{-1} is the inverse of the substructure's stiffness matrix.

ϕ is the retained elastic mode matrix

Λ is a diagonal matrix with the squared natural frequencies ${\omega_0}^2$ on the main diagonal.

Selecting the columns of the G_{res} matrix related to the interface degrees of freedom gives the G_{resb} matrix.

Through equation (6.58) an expression for the interface displacements is obtained and serves as the reduction basis:

$$u_b = a_e\phi_{eb} + a_r\phi_{rb} + G_{resb}F_{boundary} \quad \textbf{(6.60)}$$

Where:

u_b = interface displacement vector

ϕ_{eb} and ϕ_{rb} are the elastic and rigid mode shape vectors containing only the interface (boundary) degrees of freedom.

$F_{boundary}$ is the interface force vector containing only the interface degrees of freedom forces.

Further rearranging equation (6.58) gives an expression of the interface forces:

$${G_{resb}}^{-1}(u_b - a_e\phi_{eb} - a_r\phi_{rb}) = F_{boundary} \quad \textbf{(6.61)}$$

Consider $\phi = [\phi_r \quad \phi_e]$ and $a = [a_r \quad a_e]$. Substituting (6.61) into (6.57) gives:

$$M\phi\ddot{a} + K\phi a = F_e + {G_{resb}}^{-1}(u_b - a\phi_b) \quad \textbf{(6.62)}$$

Where ϕ_b is the set of retained normal modes (rigid and elastic modes) representing only the boundary (interface) degrees of freedom.

Multiplying (6.62) with ϕ^T gives

$$\phi^T M\phi\ddot{a} + \phi^T K\phi a = \phi^T F_e + \phi^T {G_{resb}}^{-1}(u_b - a\phi_b)$$

Enables the equation of motion to be further simplified to

$$I\ddot{a} + \phi^T K\phi a - \phi^T {G_{resb}}^{-1}(u_b - a\phi_b) = \phi^T F_e$$

Considering $\phi^T M\phi = I$, i.e. the mode shapes are normalised to the mass matrix

$$\begin{bmatrix} I & 0 \\ 0 & 0 \end{bmatrix}\begin{bmatrix} \ddot{a} \\ \ddot{u}_b \end{bmatrix} + \begin{bmatrix} {\phi_b}^T {G_{resb}}^{-1}\phi_b + \phi^T K\phi & -{\phi_b}^T {G_{resb}}^{-1} \\ -{G_{resb}}^{-1}\phi_b & {G_{resb}}^{-1} \end{bmatrix}\begin{bmatrix} a \\ u_b \end{bmatrix} = \begin{bmatrix} \phi^T F_e \\ F_b \end{bmatrix} \quad \textbf{(6.63)}$$

6.5.2.2 Rubin's Method

Rubin's method has been developed to improve the Mac Neal method. With the Mac Neal's method the stiffness matrix and mass matrix are not reduced with the same basis. The difference between the reduction basis of the stiffness matrix and the mass matrix is that with the mass matrix, unlike with the stiffness matrix, no coupling is formulated between the interface deformations and the internal deformations and displacement due to the subsystem's flexible and rigid body modes. Rubin reformats the reduction basis used by Mac Neal for the stiffness matrix, and uses this reformatted basis for the reduction of both the stiffness and the mass matrix. This increases the accuracy of the calculation results, particularly at higher frequencies [37]. The free interface CMS applied in ANSYS is based on Rubin's method. In order to be able to compare different methods later on in this work (section 8.7), the Rubin method is described through performing 5 steps as listed in Appendix XVI.

The reduction basis formulated in (6.61) is transformed from a formulation based on interface forces to a formulation based on interface displacements. The reduction basis is a combination of normal modes and constraint modes. The first step distinguished in this work (step 1) is the calculation of the constraint modes through

which the relation between static interface displacement and the displacement and the internal displacement of the nodes is described (see equations (6.40), (6.39) and (6.38)):

$$[u^I] = \left[\phi^{ci}\right][u_b\ ] \tag{6.64}$$

The total displacement field is described as:

$$[u^I] = \left\{\left[\phi^{ci}\right][u_b\ ] - \left[\phi^{ci}\right][\phi_{eb}]a_e - \left[\phi^{ci}\right][\phi_{rb}]a_r\right\} + [\phi_e]a_e + [\phi_r]a_r \tag{6.65}$$

Where:

u^I = vector representing the internal (slave) degrees of freedom displacements
ϕ^{ci} = constraint modes internal degrees of freedom as shown in equation (6.40)
u_b physical displacement vector interface point (at the points coupling the subsystem to the rest of the total structure).
ϕ_{eb} = elastic mode shapes displacements for the interface degrees of freedom
ϕ_{rb} = rigid body mode shape displacements for the interface degrees of freedom
a_e and a_r are the elastic modal coordinates and the rigid modal coordinates

Where $\left[\phi^{ci}\right][\phi_{eb}]a_e$ and $\left[\phi^{ci}\right][\phi_{rb}]a_r$ represent the contribution of the elastic and rigid body modes to the static displacement of the internal (slave) nodes. The reason why these two terms are subtracted from the equation of displacement is to compensate for the fact that these factors are already included in $\left[\phi^{ci}\right][u_b\ ]$, as $[u_b\ ]$ represents the displacement of the interface nodes as a result of all retained normal, rigid and static modes. The static (internal) residual deformation induced by interface line displacement, representing the compensation of the contributions from the omitted normal modes, should be written as:

$$u_{static} = [u_b\ ] - \ [\phi_{eb}]a_e - [\phi_{rb}]a_r$$

Considering $\left[\phi^{ci}\right]$ is expressed through $-[k^{II}]^{-1}[k^{IB}]$ (see equation (6.37), (6.38), (6.39) and (6.40)), equation (6.65) can be written as:

$$[u^I] = \{-[k^{II}]^{-1}[k^{IB}][u_b\,] + [k^{II}]^{-1}[k^{IB}][\phi_{eb}]a_e + [k^{II}]^{-1}[k^{IB}][\phi_{rb}]a_r\} + [\phi_{ei}]a_e + [\phi_{ri}]a_r$$

(6.66)

Where

k^{BB}, k^{BI}, k^{IB}, k^{II} = the four sub sections of the substructure's stiffness matrix resulting from grouping the interface node forces as shown in equation (6.37).

u_b physical displacement vector interface point (at the points coupling the subsystem to the rest of the total structure).

a_e and a_r are the elastic modal coordinates and the rigid modal coordinates respectively

u^I physical displacement vector of the internal (slave) degrees of freedom.

ϕ_{eb} and ϕ_{ei} are the normal elastic mode shapes displacements for the interface degrees of freedom and for the internal (slave) degrees of freedom respectively

ϕ_{rb} and ϕ_{ri} are rigid body mode shape displacements for the interface degrees of freedom and for the internal (slave) degrees of freedom respectively

The reduction matrix R can be deduced through:

$$\begin{bmatrix} u^b \\ u_i \end{bmatrix} = R \begin{bmatrix} a_r \\ a_e \\ u_b \end{bmatrix} = \begin{bmatrix} 0 & 0 & I \\ [\phi_{ri}] + [k^{II}]^{-1}[k^{IB}][\phi_{rb}] & [\phi_{ei}] + [k^{II}]^{-1}[k^{IB}][\phi_{eb}] & -[k^{II}]^{-1}[k^{IB}] \end{bmatrix} \begin{bmatrix} a_r \\ a_e \\ u_b \end{bmatrix}$$

So R becomes:

$$R = \begin{bmatrix} 0 & 0 & I \\ [\phi_{ri}] + [k^{II}]^{-1}[k^{IB}][\phi_{rb}] & [\phi_{ei}] + [k^{II}]^{-1}[k^{IB}][\phi_{eb}] & -[k^{II}]^{-1}[k^{IB}] \end{bmatrix} \quad \textbf{(6.67)}$$

The calculation of R forms the second step of the Rubin CMS method process as described in Appendix XV. Calculating the reduced stiffness and mass matrices is done in step 3 (see again Appendix XV):

(6.68)

$$\bar{K} = R^T K R$$

$$\bar{M} = R^T M R$$

As demonstrated above, the displacement of the interface line is described taking residual compensation into account through expressing the displacement at the interface line as shown in equation (6.66). However, the static response of the internal nodes to the interface displacement is expressed as the sum of:

- The static response of the constraint modes to the total interface displacement:

$$\{-[k^{II}]^{-1}[k^{IB}][u_b\,] + [k^{II}]^{-1}[k^{IB}][\phi_{eb}]a_e + [k^{II}]^{-1}[k^{IB}][\phi_{rb}]a_r\}$$

- The response of the normal modes

$$[\phi_{ei}]a_e + [\phi_{ri}]a_r$$

This means that in the response calculation the contribution from the retained normal modes to the static deflection of all nodes of the substructures has been taken into account twice: first through the calculation of the response of the constraint modes, and the second time through the response of the normal modes. An improved version of the Rubin's method has been formulated correcting for that, which is the Rubin's method with residual compensation.

If residual compensation is taken into account, the displacement is expressed through the normal modes, rigid modes and residual flexibility attachment modes. According to equation (6.59) the residual flexibility attachment modes G_{res} are expressed according to:

$$G_{res} = K^{-1} - \phi\Lambda^{-1}\phi^T$$

Where $\phi\Lambda^{-1}\phi^T$ represents the contribution to the static deformation from the normal modes, which are already accounted for through the expression $[\phi_{ei}]a_e + [\phi_{ri}]a_r$

Dividing G_{res} is partitions:

$$\begin{bmatrix} u_b \\ u_i \end{bmatrix} = \begin{bmatrix} {G_{res}}^{BB} & {G_{res}}^{BI} \\ {G_{res}}^{IB} & {G_{res}}^{II} \end{bmatrix} \begin{bmatrix} F_b \\ 0 \end{bmatrix} \quad \textbf{(6.69)}$$

According to the upper line of the matrix (6.69) we can express the interface force F_b as a function of u_b:

$$[F_b] = \left[{G_{res}}^{BB}\right]^{-1}[u_b] \tag{6.70}$$

Substituting (6.70) into the lower line of matrix (6.69) an alternative (better) expression of u_i as a function of interface displacements is obtained:

$$[u_i] = \left[{G_{res}}^{IB}\right]\left[{G_{res}}^{BB}\right]^{-1}[u_b] \tag{6.71}$$

This expression is a more accurate expression of the residual flexibility modes, as this expression includes correction for the fact that the static response from the retained modes is already represented in the response of the normal flexibility modes.

Substituting $\left[\phi^{ci}\right]$ in equation (6.65) for the expression in (6.71) gives:

$$u^I = \left\{[{G_{res}}^{IB}][{G_{res}}^{BB}]^{-1}[u^b] - [{G_{res}}^{IB}][{G_{res}}^{BB}]^{-1}\left[\phi_{eb}\right]a_e - [{G_{res}}^{IB}][{G_{res}}^{BB}]^{-1}\left[\phi_{rb}\right]a_r\right\} + \left[\phi_e\right]a_e + \left[\phi_r\right]a_r$$

Resulting in the reduction matrix written as:

$$\boldsymbol{R} = \begin{bmatrix} \mathbf{0} & \mathbf{0} & \boldsymbol{I} \\ [\boldsymbol{\phi_{ri}}] - [{\boldsymbol{G_{res}}}^{\boldsymbol{IB}}][{\boldsymbol{G_{res}}}^{\boldsymbol{BB}}]^{-1}[\boldsymbol{\phi_{rb}}] & [\boldsymbol{\phi_{ei}}] - [{\boldsymbol{G_{res}}}^{\boldsymbol{IB}}][{\boldsymbol{G_{res}}}^{\boldsymbol{BB}}]^{-1}[\boldsymbol{\phi_{eb}}] & [{\boldsymbol{G_{res}}}^{\boldsymbol{IB}}][{\boldsymbol{G_{res}}}^{\boldsymbol{BB}}]^{-1} \end{bmatrix} \tag{6.72}$$

In Appendix XVI "Steps and Estimated Number of Matrix Operation Classic Rubin's Method" the expression and description of the matrix operations for each step of the classic Rubin's method (without residual flexibility modes) is listed together with an expression of the number of floating point operations required for each step. (see also Appendix XIV "Matrix-Vector Calculus and Number of Required Floating Point Operations"). The Rubin's method without residual compensation is the method used in this work with the calculation of response according to the free interface CMS.

6.5.3 Reducing the Interface Degrees of Freedom

As discussed in the critical review (section 4) through the reduction process adopted in all classical CMS modelling techniques discussed above, high density matrices are

produced. With high numbers of connection nodes, which typically occurs with ship structures, the numbers of non-zeros in the total assembled CMS matrices may exceed the non-zero entries of the dynamic stiffness matrix generated following the full harmonic analysis. Hence calculation time required for calculating the dynamic structural behaviour according to classical CMS methods is higher as well, compared to the traditional full harmonic analysis.

In an attempt to overcome this problem, techniques for reducing the interface have been developed.

6.5.3.1 Introducing Interface Modes

As explained above, the problem with classical Component Mode Synthesis (CMS) is that static contribution from the displacement of the interface lines is expressed through the Guyan reduction technique (static condensation) through which the internal nodal displacement is expressed through a number of static modes equal to the number of degrees at the interfaces. In order to reduce the number of modes through which internal static displacement can be described, a procedure for an improved reduced system (IRS) is proposed in 1989 by o' Callanhan [42].

The technique starts with producing a reduced mass and stiffness matrix of a substructure, which is obtained through projecting the full stiffness and mass matrices onto the Guyan reduction basis. The Guyan reduction basis is derived from the description of the static displacement of all the degrees of freedom of a substructure, obtained through static condensation:

$$[u_A^s] = \begin{bmatrix} I \\ \phi_A^{ci} \end{bmatrix} [u_A^b] = [\phi_A^c][u_A^b]$$

$$R_G = \begin{bmatrix} I \\ \phi_A^{ci} \end{bmatrix}$$

Where

u_A^s = static displacement of all the degrees of freedom of substructure A

$[\phi_A^c]$ = constraint modes representing all degrees of freedom of a substructure

ϕ_A^{ci} = internal degrees of freedom of the constraint modes according to equation (6.37) to equation (6.42) = $\phi_A^{ci} = -[k^{II}]^{-1}[k^{IB}]$

R_G = Guyan reduction basis

Reduced stiffness and mass matrices K_G and M_G become:

$$K_G = {R_G}^T K R_G \text{ and } M_G = {R_G}^T M R_G \quad \textbf{(6.73)}$$

From these reduced matrices the eigenvalue problem is formulated according to:

$$K_G \emptyset_{interface} = M_G \emptyset_{interface} \omega^2 \quad \textbf{(6.74)}$$

Where $\emptyset_{interface}$ is the matrix containing the interface modes.

From the eigenvalue problem shown in equation (6.74) eigenvectors are calculated representing mode shapes through which the static deformation of the entire substructure (interface modes), as a result of interface displacement, is expressed. Corresponding natural frequencies are also calculated. The number of interface mode retained, is based on the proximity of the natural frequencies corresponding with the interface modes, to the excitation frequencies.

Tran [41] suggests than selecting the number of eigenvectors required for an accurately enough representation of the interface degrees of freedom should be based on applying a cut-out frequency of 3.5 times the maximum frequency analysed. These findings are based on simulation result produced for a 12 bladed disc where each bladed was modelled as a substructure. For the selection of the normal modes of the substructures, he applied a cut-out frequency of 1.5 times the maximum frequency of interest, according to Rubin's criterion.

The retained eigenvectors are represented through the $\emptyset_{interface}$ matrix. The interface displacement is expressed through (see (6.39):

$$\begin{bmatrix} I \\ -[k^{II}]^{-1}[k^{IB}] \end{bmatrix}[u^b] = \begin{bmatrix} I \\ \phi^{ci} \end{bmatrix}[u^b] = \begin{bmatrix} u^b \\ u^{si} \end{bmatrix} = \emptyset_{interface} a_b \quad \textbf{(6.75)}$$

Where:

$\emptyset_{interface}$ is the matrix containing the set of retained eigenvectors representing the interface displacement

a_b is the vector containing the interface modal participation factors.

u^{si} is the internal static displacement due to displacement at the interface line

Considering (6.67), the reduction basis for Rubin's method is written as:

$$\begin{bmatrix} u^b \\ u_i \end{bmatrix} = \begin{bmatrix} 0 & I \\ [\phi_i] + [k^{II}]^{-1}[k^{IB}][\phi_b] & -[k^{II}]^{-1}[k^{IB}] \end{bmatrix} \begin{bmatrix} a \\ u_b \end{bmatrix}$$

Which forms the reduction basis for the Rubin's method. Alternatively written as:

$$\begin{bmatrix} u^b \\ u_i \end{bmatrix} = \begin{bmatrix} 0 & I \\ [\phi_i] - [\phi^{ci}][\phi_b] & [\phi^{ci}] \end{bmatrix} \begin{bmatrix} a \\ u_b \end{bmatrix} \quad \textbf{(6.76)}$$

Where

ϕ^{ci} = constraint modes at internal degrees of freedom = $-[k^{II}]^{-1}[k^{IB}]$

ϕ_i is the normal modes presenting only the internal (slave) degrees of freedom

ϕ_b is the normal modes presenting only the interface degrees of freedom

a is the modal participation factors vector (modal coordinates) of the normal modes (rigid and elastic modes of the substructure

The skyline of the reduction matrix $\begin{bmatrix} 0 & I \\ [\phi_i] - [\phi^{ci}][\phi_b] & [\phi^{ci}] \end{bmatrix}$ is as follows:

$$\begin{bmatrix} 0 & I \\ [\phi_i] - [\phi^{ci}][\phi_b] & [\phi^{ci}] \end{bmatrix} =$$

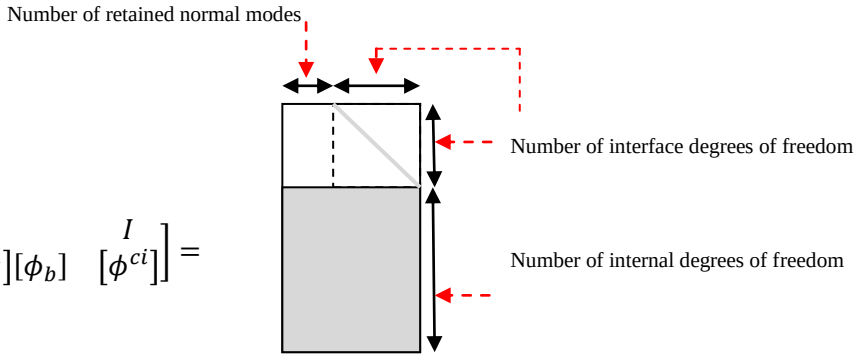

Figure 29 Skyline of the reduction matrix used for the classic Rubin method

Substituting equation (6.75) into equation (6.76) gives:

$$\begin{bmatrix} u^b \\ u_i \end{bmatrix} = \begin{bmatrix} 0 & [\emptyset_{interface\ b}] \\ [\phi_i] - [\phi^{ci}][\phi_b] & [\emptyset_{interface\ i}] \end{bmatrix} \begin{bmatrix} a \\ a_b \end{bmatrix} \quad \textbf{(6.77)}$$

Gives a new reduction basis:

$$R_{IRS} = \begin{bmatrix} 0 & [\emptyset_{interface\ b}] \\ [\phi_i] - [\phi^{ci}][\phi_b] & [\emptyset_{interface\ i}] \end{bmatrix}$$

Where:

$\emptyset_{interface\ b}$ = the interface degrees of freedom of the retained number of interface modes

$\emptyset_{interface\ i}$ = the internal degrees of freedom of the retained number of interface modes

a = vector of normal modal participation factors (modal coordinates)

a_b is the modal participation factors (modal coordinates) of the interface modes

The skyline of the reduced reduction basis $R_{IRS} = \begin{bmatrix} 0 & [\emptyset_{interface\ b}] \\ [\phi_i] - [\phi^{ci}][\phi_b] & [\emptyset_{interface\ i}] \end{bmatrix}$ is as follows

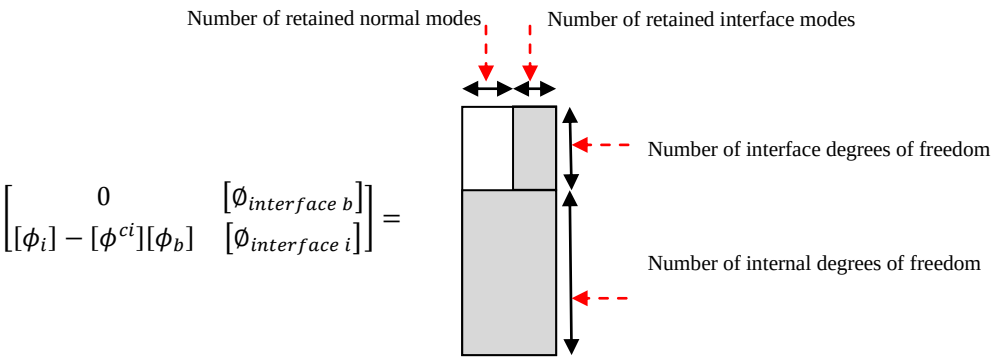

$$\begin{bmatrix} 0 & [\emptyset_{interface\ b}] \\ [\phi_i] - [\phi^{ci}][\phi_b] & [\emptyset_{interface\ i}] \end{bmatrix} =$$

Figure 30 ***Skyline of reduced reduction matrix applying interface modes for the formulation of the reduction basis following Rubin's method***

Through which, parallel to equation (6.68), the reduced stiffness and mass matrices $\bar{K}$ and $\bar{M}$ are calculated:

$$\bar{K} = {R_{IRS}}^T K R_{IRS}$$
$$\bar{M} = {R_{IRS}}^T M R_{IRS} \quad \textbf{(6.78)}$$

6.5.3.2 Describing the Compatibility Relations

Similar to the method described in 6.5.1.3 the compatibility relation can be written as:

$$u_A^b - u_B^b = \begin{bmatrix} {\emptyset_{interface\ b}}^A & 0 & 0 & 0 \end{bmatrix} \begin{bmatrix} a_A^b \\ a_A \\ a_B^b \\ a_B \end{bmatrix} - \begin{bmatrix} 0 & 0 & {\emptyset_{interface\ b}}^B & 0 \end{bmatrix} \begin{bmatrix} a_A^b \\ a_A \\ a_B^b \\ a_B \end{bmatrix} = 0 \quad \textbf{(6.79)}$$

Where:

u_A^b and u_B^b are the physical displacement coordinates at the shared interface degrees of freedom of sub structure A and B respectively

a_A^b and a_B^b are the interface modal participation factors (modal coordinates) of sub structure A and B respectively

${\emptyset_{interface\ b}}^A$ and ${\emptyset_{interface\ b}}^B$ are the retained interface modes for substructure A and B respectively representing **only the interface degrees of freedom**.

a_A and a_B are the normal modal coordinates of sub structure A and B respectively

$$u_A^b - u_B^b = \begin{bmatrix} {\emptyset_{interface\ b}}^A & 0 & -{\emptyset_{interface\ b}}^B & 0 \end{bmatrix} \begin{bmatrix} a_A^b \\ a_A \\ a_B^b \\ a_B \end{bmatrix} = Bu = 0 \quad \textbf{(6.80)}$$

a_A^b can now be made redundant by describing $[a_A^b]$ as a function of $[a_B^b]$

Considering the upper line in the matrix of equation (6.80):

$$\left[\emptyset_{interface\ b}{}^{A}\right][a_A^b] = -\begin{bmatrix}0 & -\emptyset_{interface\ b}{}^{B} & 0\end{bmatrix}\begin{bmatrix}a_A\\ a_B^b\\ a_B\end{bmatrix}$$

Multiplying with $\left[\emptyset_{interface\ b}{}^{A}\right]^T$ gives

$$\left[\emptyset_{interface\ b}{}^{A}\right]^T\left[\emptyset_{interface\ b}{}^{A}\right][a_A^b] = -\left[\emptyset_{interface\ b}{}^{A}\right]^T\begin{bmatrix}0 & -\emptyset_{interface\ b}{}^{B} & 0\end{bmatrix}\begin{bmatrix}a_A\\ a_B^b\\ a_B\end{bmatrix}$$

$$[a_A^b] = -\left[\left[\emptyset_{interface\ b}{}^{A}\right]^T\left[\emptyset_{interface\ b}{}^{A}\right]\right]^{-1}\left\{\left[\emptyset_{interface\ b}{}^{A}\right]^T\begin{bmatrix}0 & -\emptyset_{interface\ b}{}^{B} & 0\end{bmatrix}\right\}\begin{bmatrix}a_A\\ a_B^b\\ a_B\end{bmatrix}$$

$$\begin{bmatrix}a_A^b\\ a_A\\ a_B^b\\ a_B\end{bmatrix} = \left[\underbrace{-\left[\left[\emptyset_{interface\ b}{}^{A}\right]^T\left[\emptyset_{interface\ b}{}^{A}\right]\right]^{-1}\left\{\left[\emptyset_{interface\ b}{}^{A}\right]^T\begin{bmatrix}0 & -\emptyset_{interface\ b}{}^{B} & 0\end{bmatrix}\right\}}_{I}\right]\begin{bmatrix}a_A\\ a_B^b\\ a_B\end{bmatrix}$$

(6.81)

Where is the L matrix used to connect the substructures together in a similar way as described in equation (6.56):

$$L = \left[\underbrace{-\left[\left[\emptyset_{interface\ b}{}^{A}\right]^T\left[\emptyset_{interface\ b}{}^{A}\right]\right]^{-1}\left\{\left[\emptyset_{interface\ b}{}^{A}\right]^T\begin{bmatrix}0 & -\emptyset_{interface\ b}{}^{B} & 0\end{bmatrix}\right\}}_{I}\right] \quad \textbf{(6.82)}$$

$$[L]^T\overline{M}\,[L]\begin{bmatrix}\ddot{a}_A\\ \ddot{u}_B^b\\ \ddot{a}_B\end{bmatrix} + [L]^T\overline{K}[L]\begin{bmatrix}a_A\\ u_B^b\\ a_B\end{bmatrix} = [L]^T R^T\begin{bmatrix}F_{bA}\\ F_{eA}\\ F_{bB}\\ F_{eB}\end{bmatrix} = \begin{bmatrix}\bar{F}_{eA}\\ 0\\ \bar{F}_{eB}\end{bmatrix}$$

Where $\overline{K}$ and $\overline{M}$ are the reduced mass and stiffness matrices obtained according to equation (6.73) to (6.78), using R_{IRS} as the reduction basis.

In Appendix XVII “Steps and Estimated Number of Matrix Operations Rubin’s Method using Interface Modes” the different steps are presented required for running an analysis according to the Rubin’s method using interface modes. For each step an expression is given through which the number of real floating point operations can be estimated.(see also Appendix XIV “Matrix-Vector Calculus and Number of Required Floating Point Operations”).

6.6 Summary and Discussion

In section 4 the different available, most used, state of the art structural modelling techniques are reviewed for their validity and practicality considering a typical diesel engine and propeller excitation characteristics and the nature of the geometry of marine structures. Through the critical review and considering the analysis results of measurement results, finite element based modelling approach has been recognised as the most suitable modelling technique. In order to reduce computation time and required computer memory, mode superposition and component mode synthesis have been considered as reduction techniques. In this section, the mathematics behind the simulation techniques have been presented. Through understanding each calculation step for each modelling technique, an expression can be formulated for the estimation of the required number of real floating point operations, which is a direct indication of the require computation time. These expressions are listed for the different modelling techniques in the appendices Appendix XV to Appendix XVII. Through understanding the mathematical steps required for solving a matrix according to the row reduction technique, a table of required number of floating point operations for each step is presented in Appendix VI.

In the next section, a finite element model of a part of the aft ship on which measurements have been carried out by the author is used in order to test the different modelling techniques. The assessment of these techniques is based on accuracy, and the number of floating point operations required for generating the results. With the given properties of the finite element model, the number of number of floating points operations required for generating the solution will be calculated according to the findings from this section listed in Appendix XV to Appendix XVII.

(see also Appendix XIV “Matrix-Vector Calculus and Number of Required Floating Point Operations”)

7 Modelling Vibrations of the Aft-ship of an LNG Carrier

From the critical review and the deeper study of the mathematical principles behind the different structural modelling techniques, finite element modelling has been identified as the most appropriate modelling technique for simulating ship's structural vibrations. Study of the excitation mechanisms and measurement results from the field presented above suggest that the most dominant sources of excitation are predominately of a tonal nature, concentrated at relatively low frequencies. This further confirms the findings from the critical review and supports the choice of finite element based models as the most suitable vibration simulation technique for ships.

In this section simulation results are presented performed with a finite element model that represents of a part of the aft ship of the LNG carrier on board which the author has carried out vibration and noise measurements (see section 5, Figure 8 and Figure 31). The aims of carrying out the different simulations are:

- Evaluating finite element modelling as a tool for simulating structural vibrations for a typical aft-ship of LNG and bulk carrier. The analysis results are evaluated through measurement results taken on board this particular vessel by the author (see section 5, "Measurement Results").
- Identify the effect of chosen boundary conditions, damping and added mass assumptions on the calculated vibration levels at the steering gear deck and mooring deck.
- Evaluate the accuracy of the free and fixed boundary CMS techniques using the full FEM results as reference.
- Compare the required computation time of the different analysis techniques.

In Table 2 the structure of this section is presented.

7.1 Vessel Properties, Measurements and Simulation Locations	
7.2 Properties of the Structural Models In this section the properties of the model are presented	**7.2.1The full finite element model** Type and number of elements used and the boundary conditions of the model are discussed
	7.2.2The CMS Model In this section the way in which the structure has been subdivided in substructures for the Component mode synthesis analysis is discussed
7.3 Excitation Characteristic and Response Calculation Method	The simulation results of the propeller excitation characteristics are discussed. Also the method used in this work for obtaining the forced vibration response is presented.
7.4 Comparison of Simulation Results with Measurement Results	
7.5 Sensitivity of the Model	**7.5.1Effect of the Boundary Conditions, Added Mass and Damping** In this subsection the effect of the boundary conditions and assumption on added mass and damping on the modelling results is discussed
	7.5.2 Excitation characteristic
	7.5.3 Number and Type of Elements Number and type of elements used for this simulation are evaluated
7.6 The Contribution from Hull Girder Modes	
7.7 Correlation of Simulation Results	
7.8. Evaluation of FE and CMS Performance	**7.8.1. Accuracy of CMS results**
	7.8.2. Required CP Time for CMS Calculations
7.9 Summary and Conclusion	

Table 2 Structure of presentation of results

7.1 Vessel Properties, Measurements and Simulation Locations

In Figure 31 the properties of the vessel are shown for which the structural response simulations are carried out. The finite element model represents the part of the ship's structure indicated with the red dotted line in Figure 32. The aft ship has been modelled up to frame 25, which is 4 frames forward from the engine room bulkhead. Figure 33 shows a cut-out of the model showing the locations where measurements were taken. For these locations the finite element harmonic analysis results are presented and evaluated. Simulation results of the vibrations on the mooring deck (locations presented in Figure 34) are also presented.

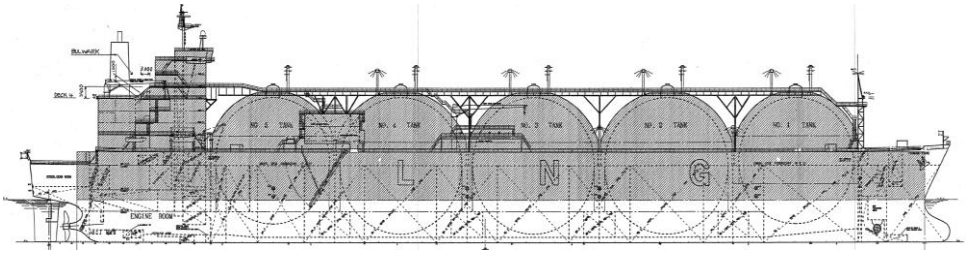

General Properties		
Max. Length waterline	260	m
Max. Beam Waterline	45	m
Maximum Speed	19	kn
Draft During Trials	9.4 m aft, 9.4 m fwrd	
Propeller		
Power	21500	kW
Maximum Revolutions	80	rpm
Nominal Revolutions	75	rpm
Number of Blades	4	
Pitch	fixed	
Main engines		
1 low pressure steam turbine (LP) and 1 high pressure steam turbine (HP)		
Total Power	21550	kW
Revolutions	5800 rpm (HP) and 3970 rpm (LP)	

Figure 31 Properties of the gas carrier

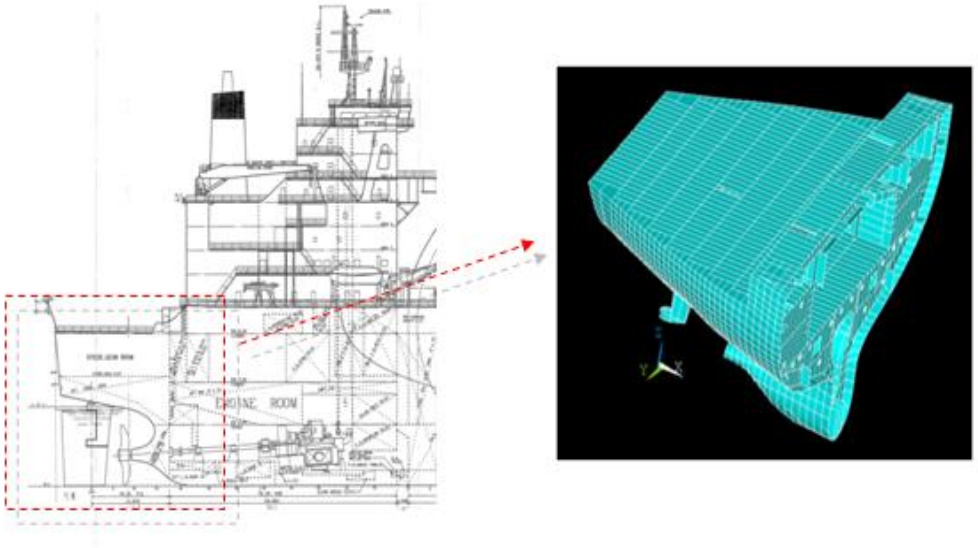

Figure 32 *Part of the ship's structure modelled.*

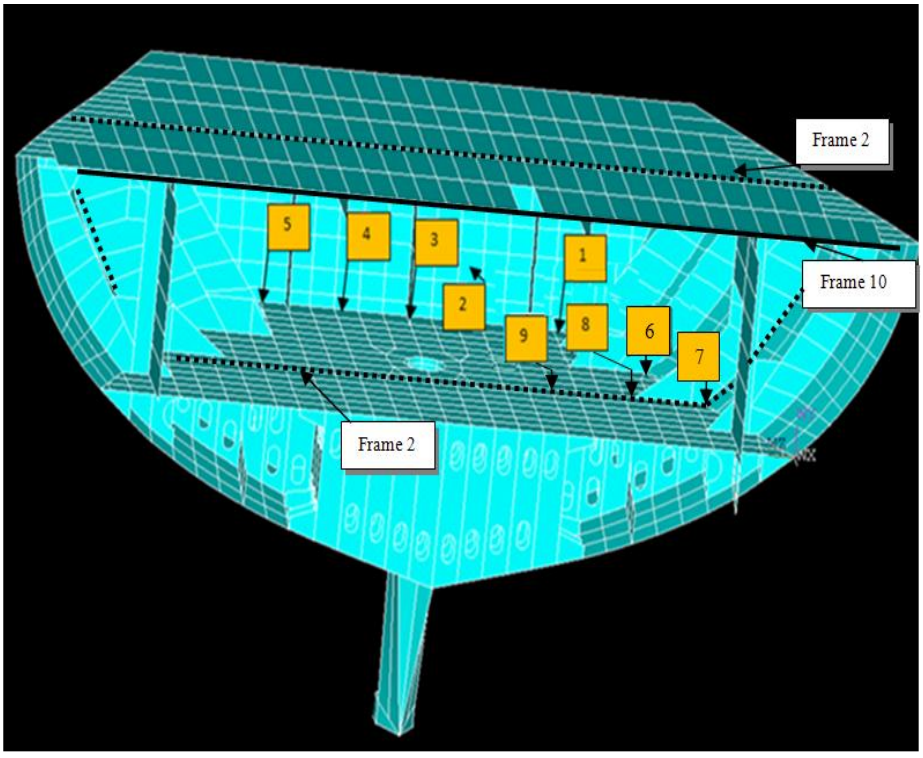

Figure 33 *Locations on the steering gear deck for which simulation results are presented in this work*

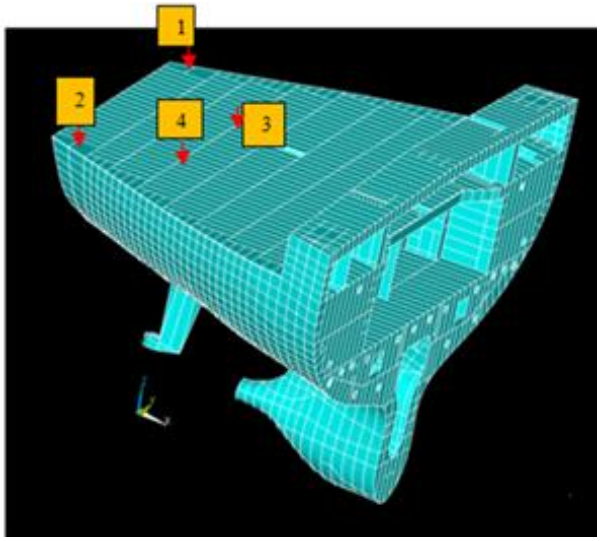

Figure 34 Locations on the mooring deck for which simulation results are presented in this work

7.2 Properties of the Structural Models

FEM software by ANSYS 13.1 has been used to generate the geometry, generate the mesh and calculate the structural response. Due to the size of the result files generated through solving the full set of equations of motion, problems occurred with generating a representation of the deflection shapes. A visual presentation of this deflection shape is important for understanding the structural mechanism s. Free boundary and fixed boundary component mode synthesis modelling techniques (CMS) have been used. Deflection shapes of the complete model are obtained by pasting the deflection shapes of the individual substructures together as shown in Appendix XI and Appendix XII. As the ship is equipped with steam turbines, only excitation from the propeller has been taken into account. The fluctuating pressure field distribution used for this simulation has been calculated for the first three blade passing frequencies for the FP 7 project SILENV.

7.2.1 The full finite element model

Figure 35 shows the full finite element model together with a part of the model showing in more detail the nature of the mesh used.

7.2.1.1 Types of elements used and size of the model

Two types of elements have been used, shell181 elements for modelling hull and deck plating and BEAM188 elements for modelling stiffeners and girders.

The shell181 is a four node plate element as described in Appendix IV and is therefore suitable for thin to moderately thick plates. Rotary inertia effect is taken into account.

The BEAM188 element has been selected for representing the effect of the stiffeners, as it is recommended by ANSYS for slender to moderately stubby beams. The element is based on the Timoshenko beam theory and takes into account rotary inertia and shear deformation effects as described in Appendix III. The element also provides an option for restraining warping, through which a 7^{th} degree of freedom is added to the beams nodes. This option has not been used for this model as torsion of girders is not expected to play a big role in the propagation of vibrations through the ship. In addition, adding a 7^{th} degree of freedom for each node attached to a beam would increase the size of the model considerably.

The validity of application of the beam element has been tested by calculating the slenderness ratio of the beam, which should be higher than 30, as recommended by ANSYS.

$$Slenderness\ ratio = \frac{GAL^2}{EI}$$

Where:

G = the shear modulus

A is beam's cross-sectional area

L is the length of the beam

E = the elasticity modulus

I = second moment of inertia

As can be seen from Figure 35, the longitudinal girders (stiffeners) are approximately twice as high as the veridical stiffeners. For calculating the slenderness ratio for the

vertical beams, the length considered is the distance between two longitudinal girders. For calculating the slenderness ratio for the longitudinal beams, the length considered is the distance between two main frames. (see Table 1 for the calculated slenderness ratio's)

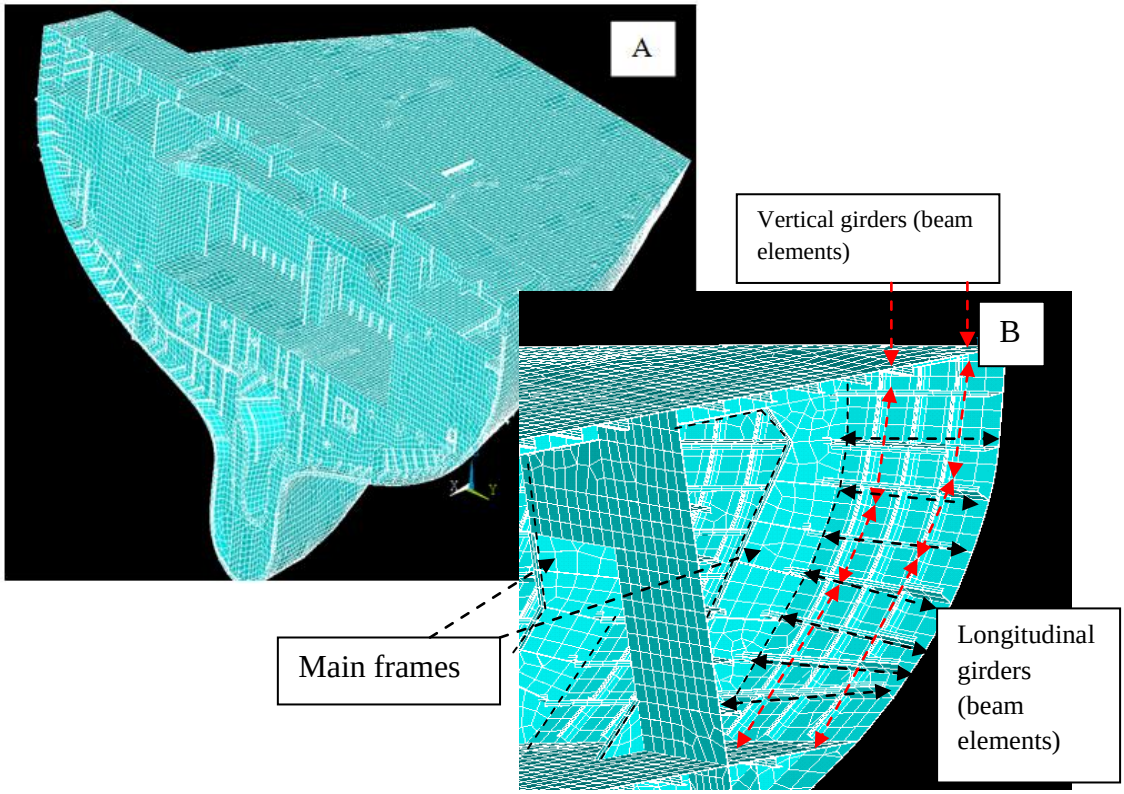

Figure 35 ***Complete finite element model (A) and a part of the finite element model (B)***

Longitudinal Girders		
L	3	m
G	7.89E+10	Pa
A	0.010232	m^2
E	2.10E+11	Pa
I	2.57E-04	m^4
Slenderness ratio	135	

Vertical Girders		
L	0.8	m
G	7.89E+10	Pa
A	0.0029	m^2
E	2.10E+11	Pa
I	1.23E-05	m^4
Slenderness ratio	57	

Table 1 ***Calculated slenderness ratio's for the longitudinal girders and vertical girders***

The propeller mass has been added as two point masses attached to the stern tube. Each of these masses is 23 tons adding up to the total mass of the propeller of 46 tons. The mass of the rudder has been modelled as two separate concentrated masses as well. The model consists of

- 7171 key points
- 12252 lines
- 5132 areas
- 69345 nodes
- 84100 elements

7.2.1.2 Damping and Added Mass

A relative damping coefficient (loss number ϵ) of 2% has been used, a value typically adopted for steel structures. No extra hydro dynamic damping due to the water surrounding the hull has been taken into account. Nor has the effect of added mass of the water been taken into account. The model represents the ship's bare steel structure.

7.2.1.3 Boundary Conditions

Three different boundary conditions have been tested:

- Constrained at frame 25: all degrees of freedom of the nodes on the lines bordering to the rest of the ship's structures have been constrained.
- Constrained at frame 21: all degrees of freedom of the nodes on the lines bordering to the rest of the ship's structures have been constrained.
- No boundary conditions: ship is free floating in space.

For indication of the location of the different frames see Figure 36.

For all boundary condition scenarios no stiffness effect of the buoyancy has been taken into account.

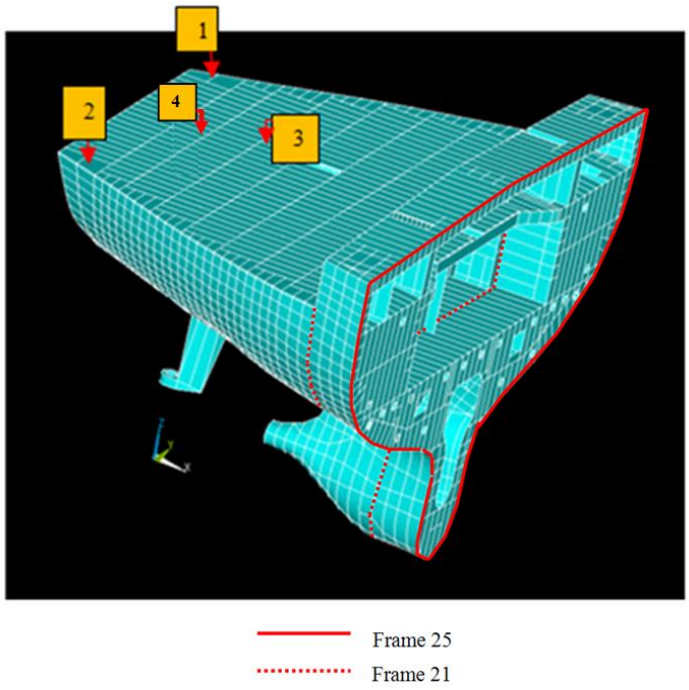

Figure 36 ***Frames in the model where constraints have been applied***

7.2.2 The CMS Model

In Appendix IX and Table 3 the substructures are presented of which the CMS models used of the LNG carrier consists (see also Table 6). With the fixed CMS method in ANSYS the classical Craig-Bampton's method (see section 6.5.1) is used and results using free boundary CMS are obtained according to Rubin's method (see section 4.2.6.2) without residual compensation taken into account. Table 3 the number of mode shapes retained for each substructure for calculating the assembled response is listed. This number is obtained applying a cut-out frequency of $1.5 \times f_{max}$ following Rubin's Priciple [26]. This means that all modes have been retained of which the corresponding natural frequency are within the frequency range between 0 and $1.5 \times f_{max}$, where f_{max} is the maximum to frequency for which results are generated. As most of the vibration energy at the aft ship was found to be between 0 and 40 Hz according to the measurement results, the frequency range of the solutions is chosen to be between 0 and 40 Hz. This means that f_{max} is 60 Hz and all the normal modes with natural frequencies between 0 and 60 Hz have been retained for both the free and fixed boundary CMS models.

LNG vessel FE model	Number of nodes	Number of boundary nodes	Number of boundary degrees of freedom	Number of modes required*	Required CP for calcuating eigenvectors and	Required time generation pass
PartHfixedcms	5819	348	2088	181	18.5	22.8
PartHfreecms				257	24.5	52.5
PartGfixedcms	6675	250	1500	373	29.8	40
PartGfreecms				419	39	100.8
PartFfixedcms	6675	250	1500	373	29.8	40
PartFfreecms				419	39	100.8
PartEfixedcms	10728	1198	7188	213	30	46.6
PartEfreecms				323	61	174
PartDfixedcms	11118	1140	6840	162	29.14	53.6
PartDfreecms				336	95	328
PartCfixedcms	14393	854	5124	195	38.11	68.13
PartCfreecms				335	75	225.7
PartBfixedcms	11705	633	3798	138	29.4	47.7
PartBfreecms				231	53	138.3
PartAfixedcms	7168	263	1578	91	18.8	25.4
PartAfreecms				154	24.6	53.3

Table 3 ***Table of properties of the substructures shown in Appendix IX. The number of retained mode shapes are also presented for each substructure together with the CP time required to calculate these mode shapes***

7.3 Excitation Characteristic and Response Calculation Method

As this vessel is equipped with steam turbines, only propeller excitation has been taken into consideration with the calculation of the response of the ship's structure. Steam turbines generate very little vibration excitation forces and through the study of the vibration measurement results in section 5.1.1 (see

Figure 9, Figure 10 and Figure 13) it has been established that the propeller is by far the most dominant vibration excitation source.

Frequency	Original	Modified	Factor of change
1x blade freq. (kPa) = 5 Hz	3.3138	2.7591	-17 %
2x blade freq. (kPa) = 10 Hz	1.8093	1.046	-42%
3x blade freq. (kPa) = 15 Hz	0.3831	0.56357	+47%

Table 4 ***Maximum predicted pressure amplitude at full propeller speed and full power(75 rpm)***

In Table 4 the pressure fluctuation calculation results are presented which have been calculated for the propeller as installed on the LNG carrier, and as calculated for a propeller optimised for low vibration levels. The calculations have been carried out

by SSPA for the EU project SILENV as a part of research into mitigation of propeller induced vibrations [18, 20, 46].

The wake distribution at the propeller disk has been estimated through CFD calculations. With the calculated wake distribution, blade pressure distribution has been calculated following the vortex lattice method. Through this method also the sheet cavitation volume fluctuation is calculated. The resulting effects on the pressure field on the hull is calculated through HULLFPP (Hull Field Point Potential), a postprocessor to MPUF3a that calculates the pressure field by calculating the field point potential induced by a propeller and solving the diffraction potentials on the hull [18, 46].

The first results (original) are for the propeller as it was mounted on the LNG carrier during the measurements. The second set of results is for a similar propeller designed for low pressure pulses. Through this alternative propeller geometry design, the pressure pulse reduction has been achieved through reduction of propeller tip load.

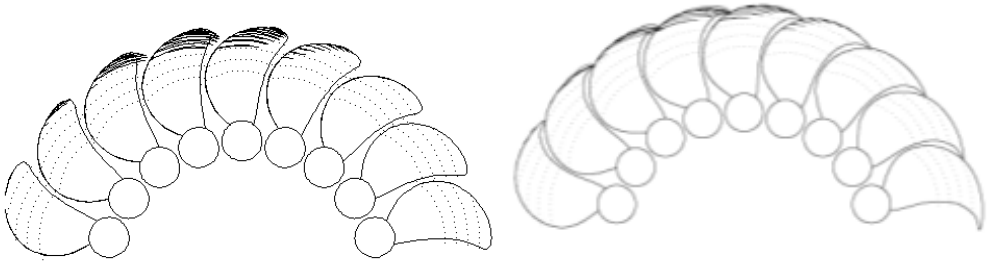

Figure 37 ***Visualisation of the effect of propeller blade tip unloading on the sheet cavitation area according to calculation results [46]***

Through that route the extend of sheet cavitation has been reduced (see Figure 37) leading to lower 1st and 2nd order blade passing frequency excitation amplitudes.

For the simulation in this work, the excitation characteristic simulated for the original propeller has been used. The distributed alternating (complex) pressure over a grid of points on the aft ship hull plating has been produced by SSPA through their simulation software. These pressures have been recalculated into node forces and

have been adapted for the mesh of the FE model (see Figure 38) and have been introduces to the structural model as harmonic forces.

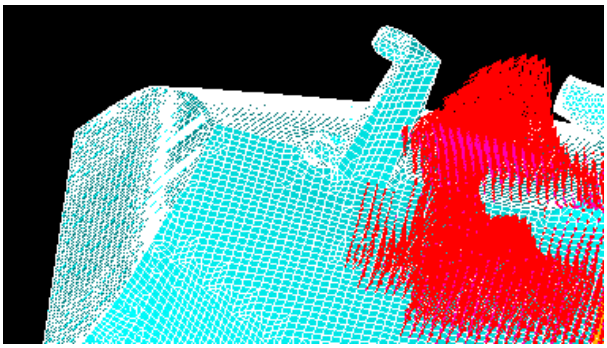

Figure 38 ***Red vectors show the downwards pointing excitation force amplitude distribution as applied for the harmonic analysis of the LNG carrier.***

Considering the measurement results presented in section 5.1, most of the vibration energy was found to be concentrated between 0 to 40 Hz. Over a range between 1to 40 Hz, harmonic analysis results have been produced with a step size of 0.5 Hz. Considering that the propeller has 4 blades, 0.5 Hz represents a step of 6 rpm.

The run-up simulation has been carried out using the first blade passing frequency fluctuating pressure distribution calculated by SSPA. By using the same excitation load for each frequency step, the relevant sensitive (resonance) frequencies are identified.

From a design point of view the advantage of a frequency range simulation is that excitation frequencies or response behaviour may be tuned in such a way that minimum vibration levels occur [20].

Of particular interest for this work, simulation results over a frequency range also helps understanding why the modelling results may deviate from the measurement results, as it shows the sensitivity of the model.

For the evaluation of the simulation results, measurement results taken at full speed (75 rpm propeller speed) and full power are used. Also for obtaining the simulation results at full power and full speed, above mentioned simulation results over the range from 1 to 40 Hz have been used. As the fluctuating pressure field simulation

results calculated for the (first) blade passing frequency have been used for these simulations, the thus obtained response amplitudes at the multiples of the blade rate frequency higher than 1, need to be corrected. As vibrations amplitudes are assumed to be low enough that the structure behaves linearly (i.e, the relation between excitation and response is linear), the response is corrected by multiplication with the ration between the ratio:

$$\frac{maximum\ presdicted\ pressure\ amplitude\ at\ blade\ rate\ n}{maximum\ presdicted\ pressure\ amplitude\ at\ the\ first\ blade\ rate}$$

These maximum predicted pressure amplitudes are presented in Table 4. This means that the following ratios are obtained for the original propeller (as was mounted during the trials):

Ratio for the 2nd order blade passing frequency:

$$\frac{1.8093}{3.3138} = 0.55$$

Ratio for the 3rd order blade passing frequency:

$$\frac{0.3831}{3.3138} = 0.12$$

Important to note is that through this approach the higher blade passing order pressure fields are obtained by only adjusting the pressure amplitudes, and not the relative spatial distribution of pressure fluctuation over the aft ship.

As can be seen from Table 4, no alternating pressure field harmonic components higher than 3 times the blade passing frequency are presented. This is because (as can also been seen from Table 4) the amplitudes of blade passing frequency related pressure pulses decreases rapidly with increasing order number. Producing harmonic amplitudes at order higher than three did not seem relevant. However, measurement results show that the 4th and 5th order blade passing harmonic frequencies are very dominant in the response. In order to estimate the response amplitudes obtained through simulation, the excitation amplitude at the 4th and 5th order are assumed to be

equal to the amplitudes given for the 3rd blade passing harmonic. Figure 39 visually explains how the response amplitudes at the different blade passing frequency harmonics have been obtained.

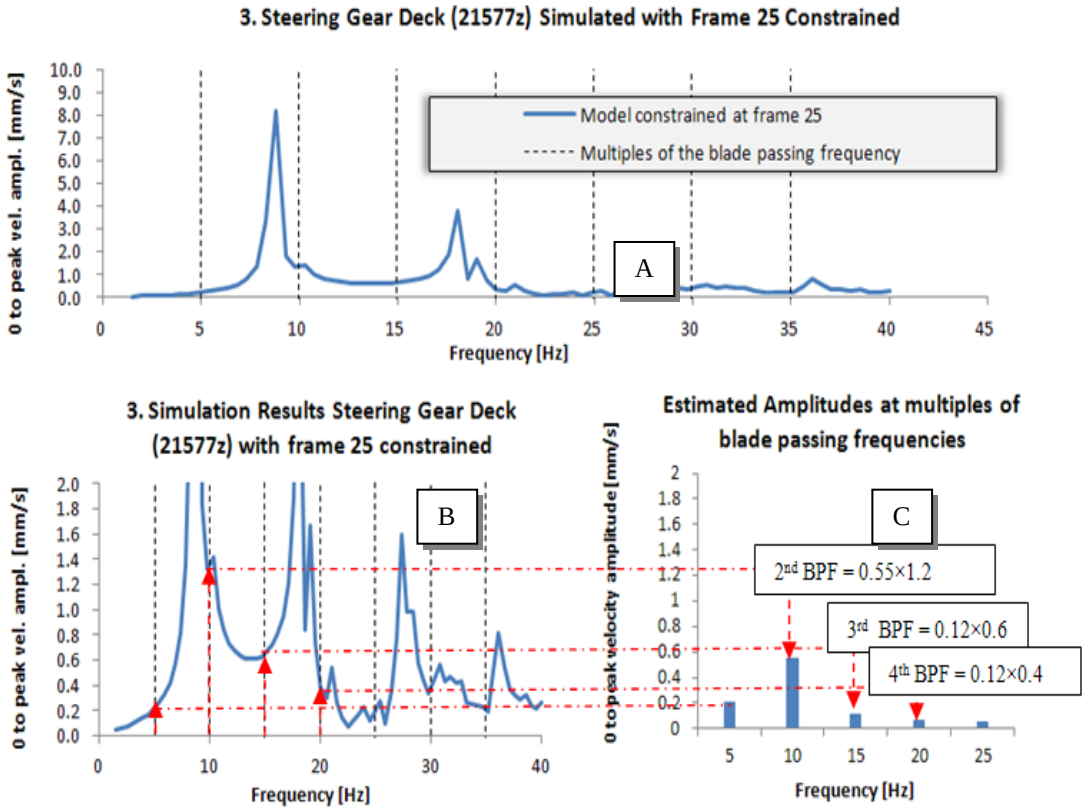

Figure 39 ***Example of how response amplitudes at blade passing frequencies have been obtained. Graph B is a zoomed in version of graph A.***

7.4 Comparison of Simulation Results with Measurement Results

Referring to Figure 36 simulation results have been produced applying the following boundary conditions:

- Constrained at frame 25: all degrees of freedom of the nodes on the lines bordering to the rest of the ship's structures have been constrained.
- Constrained at frame 21: all degrees of freedom of the nodes on the lines bordering to the rest of the ship's structures have been constrained.
- No boundary conditions: ship is free floating in space.

Response amplitudes have been calculated for 80 frequencies covering a frequency range from 0 to 40 Hz, at locations where also measurement results have been obtained from the field. In Appendix VII these results obtained at all frequencies applying different boundary conditions have been plotted in graphs. As can be seen from Figure 40 and Figure 41 the choice of how to define boundary conditions has a huge impact on the simulations results.

From the curves presented in Appendix VII and Figure 41 and Figure 40 below, the response amplitudes are calculated following the method described in section7.3. In Appendix VIII and Figure 42 to Figure 44 simulation results are compared with measured results taken with the vessel operating at full speed (nominal propeller revolutions = 75 rpm). With these results can be seen that the choice of boundary also affects the calculated response amplitudes at the blade passing frequencies. The general trends observed are:

- The measured response amplitude at the first blade passing harmonic roughly coincides with the average of all amplitudes obtained at the first blade passing frequency for all different boundary conditions.
- The response amplitude at the second blade passing frequency is extremely sensitive to the choice of boundary condition. There is a high risk of hugely over predicting the vibration levels at any location at the 2^{nd} blade passing frequency.

- The finite element model hugely under-predicts the amplitudes at blade passing harmonic 3 and higher.

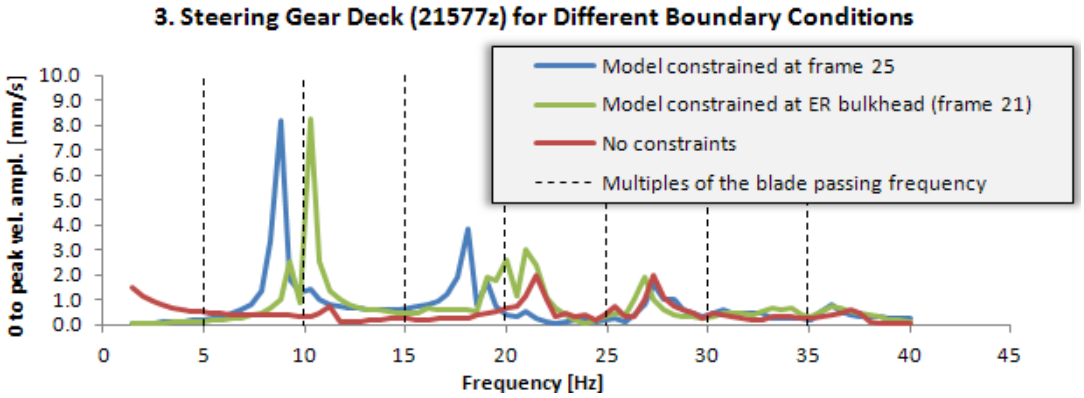

Figure 40 ***Simulation results for the vertical vibration levels on the steering gear deck, extreme aft PS corner (at measurement location 1 in Figure 33). Results obtained applying different boundary conditions have been plotted in one graph (see also Figure 36 for the location of the constrained frames)***

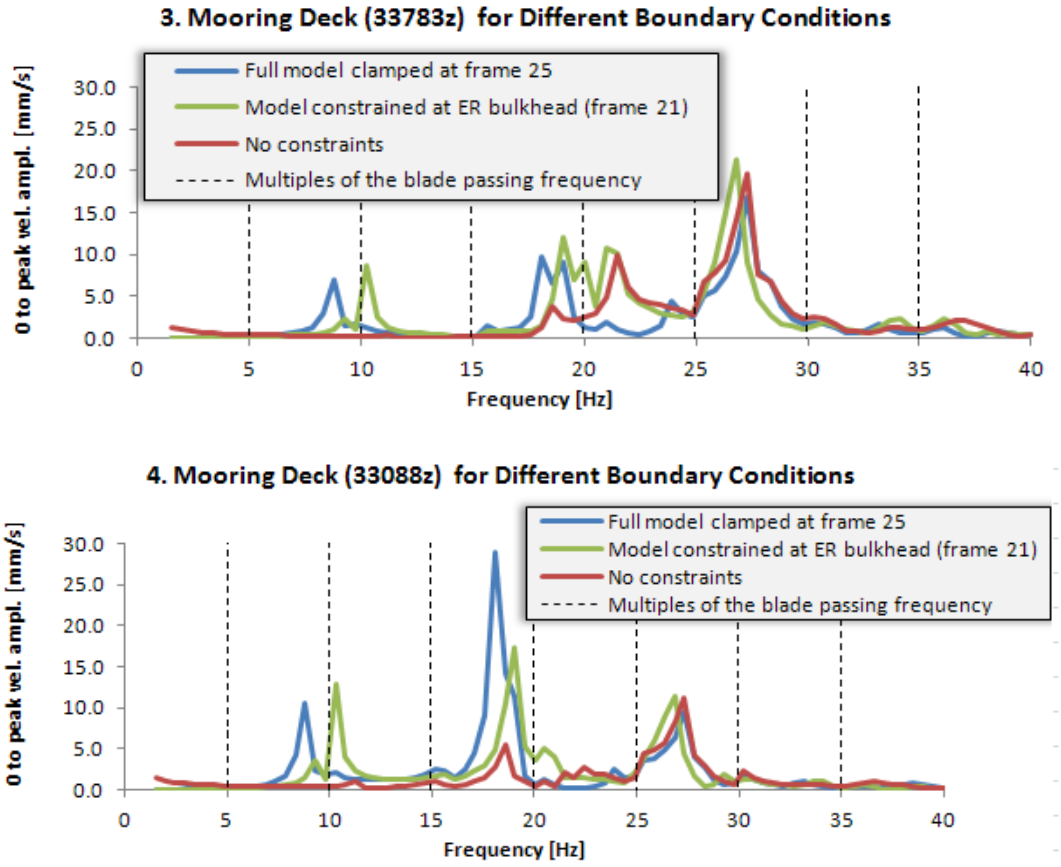

Figure 41 ***Simulation results for the vertical vibration levels on the mooring deck, extreme aft PS corner and at the middle of the deck (at measurement location 3and 4 in Figure 33). Results obtained applying different boundary conditions have been plotted in one graph (see also Figure 36 for the location of the constrained frames)(see also Appendix VII)***

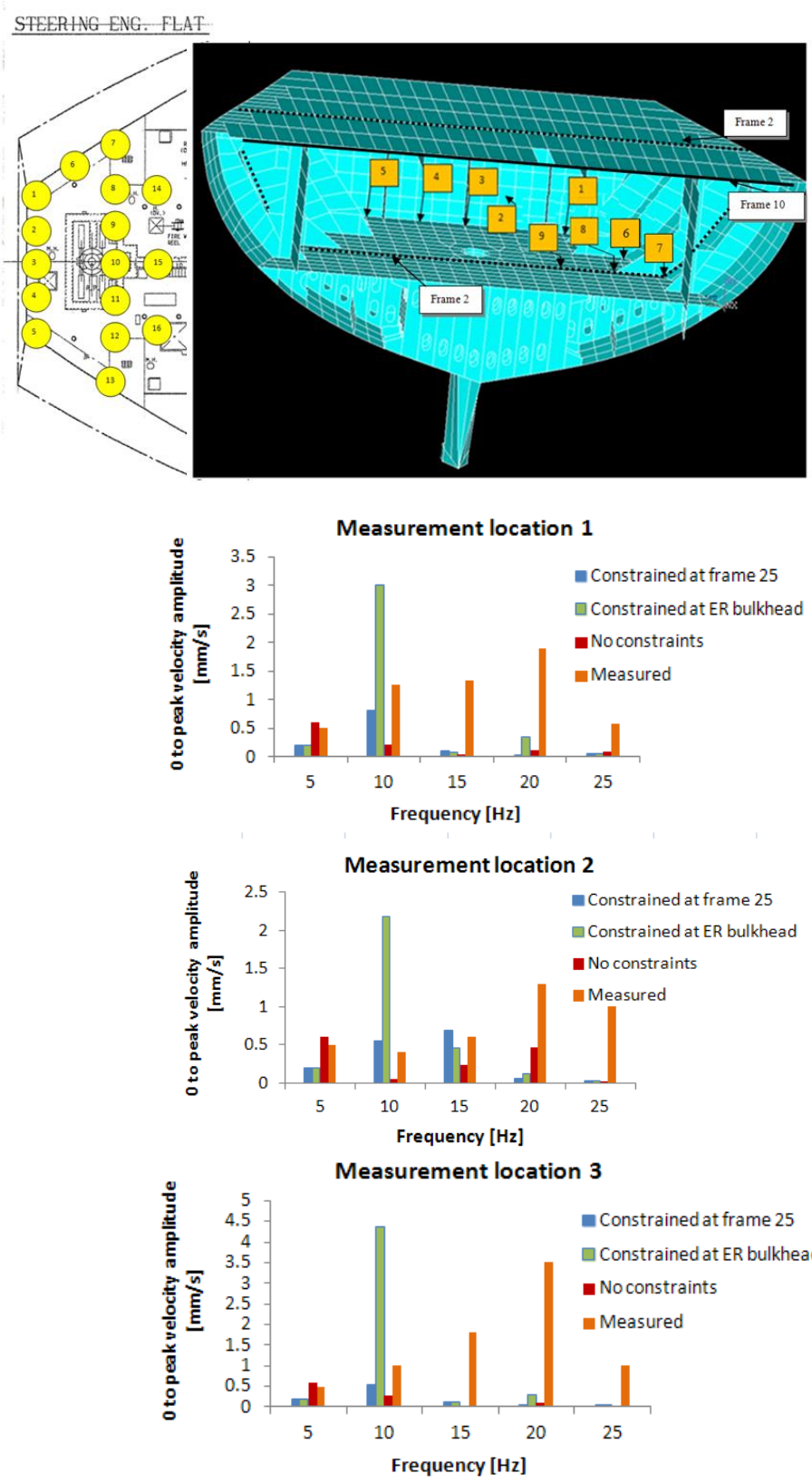

Figure 42 ***Comparison of simulation results at 75 rpm (full speed and power) with different boundary conditions and the measurement results at full speed and power (0 to peak average spectrum [mm/s])***

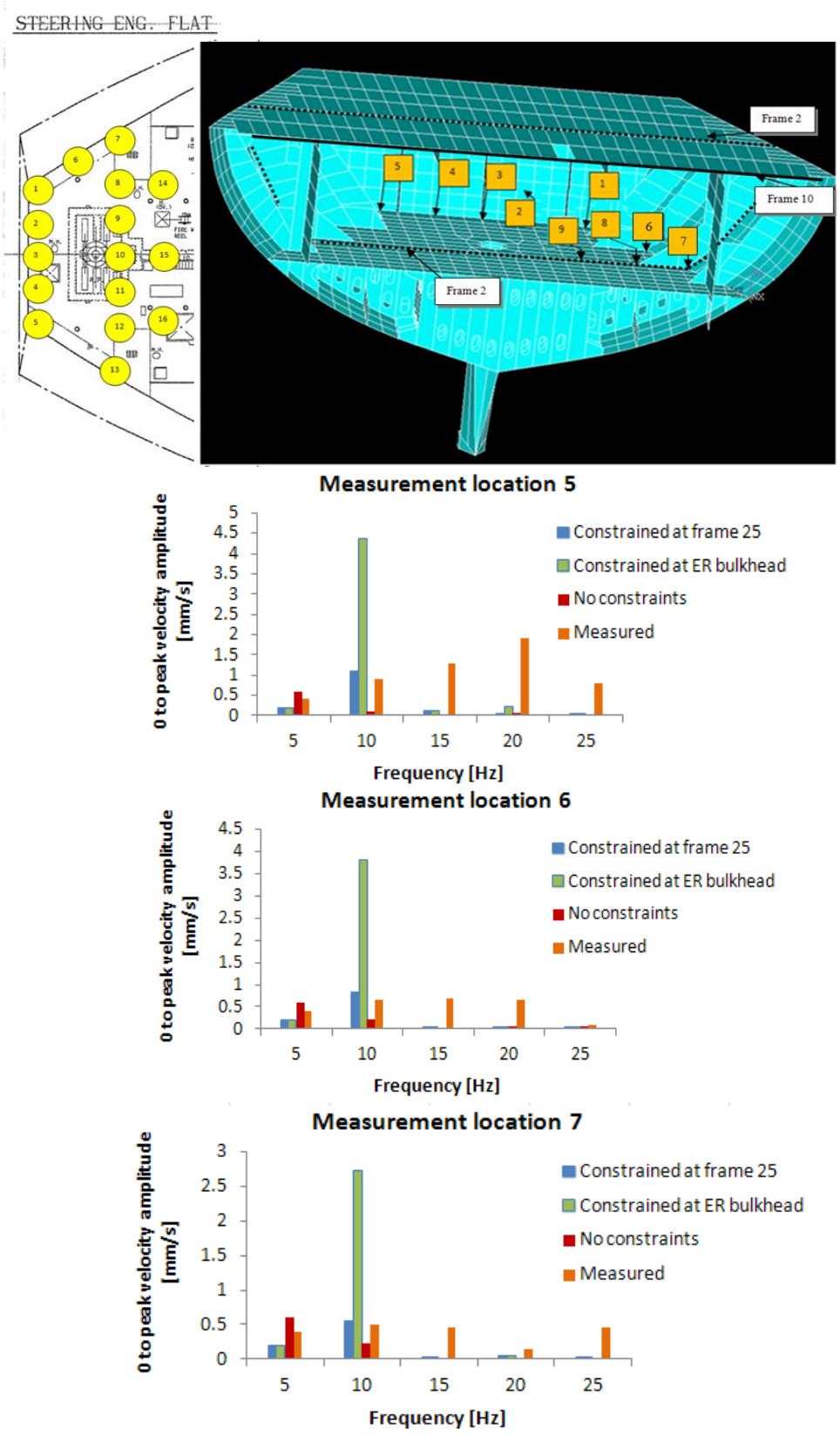

Figure 43 ***Comparison of simulation results at 75 rpm (full speed and power) with different boundary conditions and the measurement results at full speed and power (0 to peak average spectrum [mm/s])***

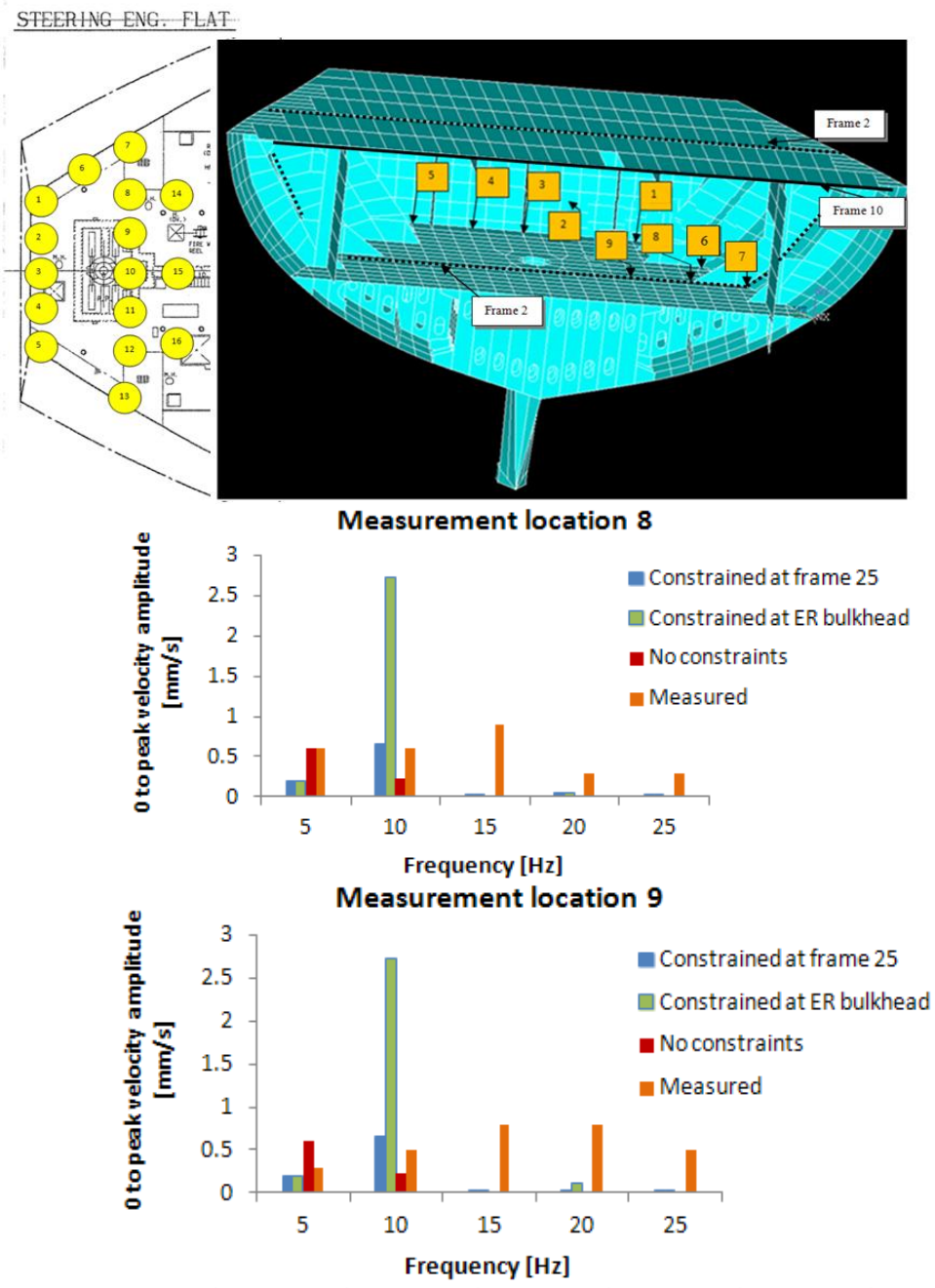

Figure 44 *Comparison of simulation results at 75 rpm (full speed and power) with different boundary conditions and the measurement results at full speed and power (0 to peak average spectrum [mm/s])*

7.5 Sensitivity of the Model

In Appendix VIII the simulation results of the response spectra at the measurement points are presented and compared with the measurement results. The general observation from the results However, in order to understand the outcome of the simulation results at the blade passing frequencies, and in order to explain any deviation between these outcomes and the measurement results, the frequency-response curve is a very useful tool. The most important aspect determining structural response amplitudes is the proximity of the excitation to the natural frequencies of the structure. Through the frequency-response curve simulation results a number of frequencies are identified with an increased sensitivity to excitation. Mode shapes at these sensitive frequencies have been obtained through Component Mode Synthesis Modelling and are presented in Appendix XI (for frame 25 constrained) and Appendix XII (for frame 21 constrained)

7.5.1 Effect of the Boundary Conditions, Added Mass and Damping

A number of frequencies have been selected for which the deflection shapes are presented in Appendix XI and Appendix XII (for the vessel constrained at frame 25 and 21 respectively). The choice of these frequencies is based on selecting peak response frequencies from the frequency range simulation results presented in Appendix VII.

Studying these deflection shapes is very important because they may explain why measurement results deviate from simulation results. Mode shapes are studied for the model with frame 25 constrained, as this is the model that is likely to be the most realistic. The frequencies selected for closer examination are:

- 8.8 Hz (dominant at both mooring deck and steering gear deck)
- 15.6 Hz (dominant at mooring deck)
- 18.1 Hz
- 27.3 Hz (dominant at mooring deck)

8.8 Hz

From the deflection shapes at 8.8 Hz shown in Appendix XI and Figure 45, it can be seen that the mode shape is dominated by a hull girder bending mode. The aft ship is behaving as a cantilevered beam clamped in at frame 25. Moving the constraints from frame 25 to 21 increases the bending stiffness of the section of the ship modelled, through which the response peak corresponding with this mode shape shifts from 8.8 Hz to 10 Hz (see also Appendix XII). Concerning the effect of damping and added mass the following is likely to be the case:

- In the model no effect of added mass due to the presence of water surrounding the hull has been taken into account. As the mode shape corresponding with 8.8 Hz peak response frequency is a global mode shape involving a heaving motion of the aft ship in the water, added mass is expected to play a role. The peak response is expected to be at a frequency under the 8.8 Hz as a result.
- Hydrodynamic damping from the water surrounding the hull has also not been taken into account into the model. For the same reason that added water mass is likely shift the peak occurring at 8.8 to a lower frequency, added hydrodynamic damping is expected to decrease the response amplitude compared to the response amplitude simulated at 8.8 Hz.

The shift of the peak response from 8.8 Hz to a lower frequency will result in simulation results at both the 1^{st} and 2^{nd} blade passing frequency to approach the measured response amplitudes even closer:

- With the original model the simulated response amplitudes at the 1^{st} blade passing frequency are all under predicted (considering fixed constraints at frame 25). The simulated response amplitude at the 1^{st} order blade passing frequency is however expected to increase if added hydrodynamic mass would be taken into account., as it will cause the resonance frequency previously at 8.8 to be at a lower frequency, closer to the 1^{st} blade passing frequency (1^{st} blade passing frequency = 5 Hz).

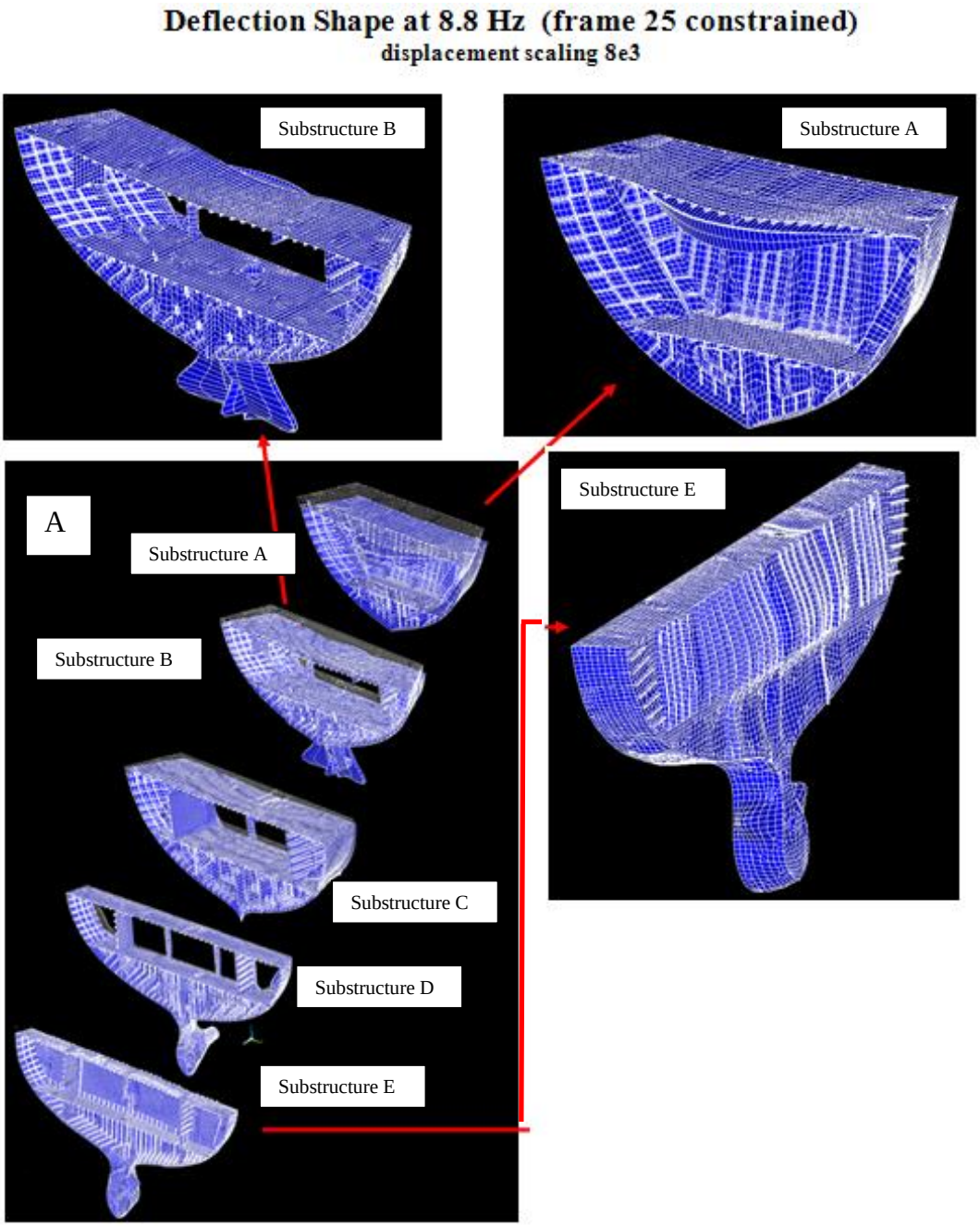

Figure 45 ***Mode shape at 8.8 Hz compiled from the component mode synthesis results (see section 7.2.2) In section A the un deformed shape has been plotted into the figure as a white see-through contour. This shows that, particularly for the aft section, rigid body modes play an important role, through which the ship sections perform a heaving motion in the water.***

- With the original model the simulated response amplitudes at the 2nd blade passing frequency are all over predicted (considering fixed constraints at frame 25). However, the simulated response amplitude at the 2nd blade passing frequency will be lower, if hydrodynamic added mass is taken into

account, as added mass will shift the resonance frequency previously at 8.8 Hz to a lower frequency, further away from the 2nd blade passing frequency (which is at 10Hz)

Although it has been mentioned that hydrodynamic damping is expected to decrease the amplitude amount the resonance frequency found at 8.8 Hz, the effect of the peak response moving to a lower frequency is expected to be much stronger than the effect of increased damping. In Appendix XIII can be seen that response simulation results for the first two blade passing orders coincide much better with measurement results after having shifted the peak response initially found at 8.8Hz, to 7.8 Hz.

15.6 Hz

From the deflection shapes at 15.6 Hz shown in Appendix XI and Figure 46 can be seen that the response at 15.6 Hz is related to a local natural frequency involving a first bending natural frequency of the aft part of the mooring deck. This is a more local mode shape which is further confirmed through the study of the mode shapes of the model constrained at frame 21 instead of frame 25 (see Appendix XII). These results show that changing the boundary conditions does not change the natural frequency and the corresponding mode shape. No hydrodynamic added mass has been taken into account. However, as this vibration mode concentrates on the mooring deck section, added mass is not expected to affect the natural frequency corresponding with this mode shape. Mass of winches and equipment however may slightly increase the natural frequency.

The simulated response however at the 3rd blade passing frequency is hugely under predicting the response at the 3rd blade passing frequency measured on board. In Appendix XIII simulation spectra are presented where the peak response, originally theoretically located at 15.8 Hz, has been shifted to 15 Hz, right on top of the 3rd blade passing frequency. Still, simulated response amplitudes for the 3rd blade passing frequency are much lower than the measured response amplitudes.

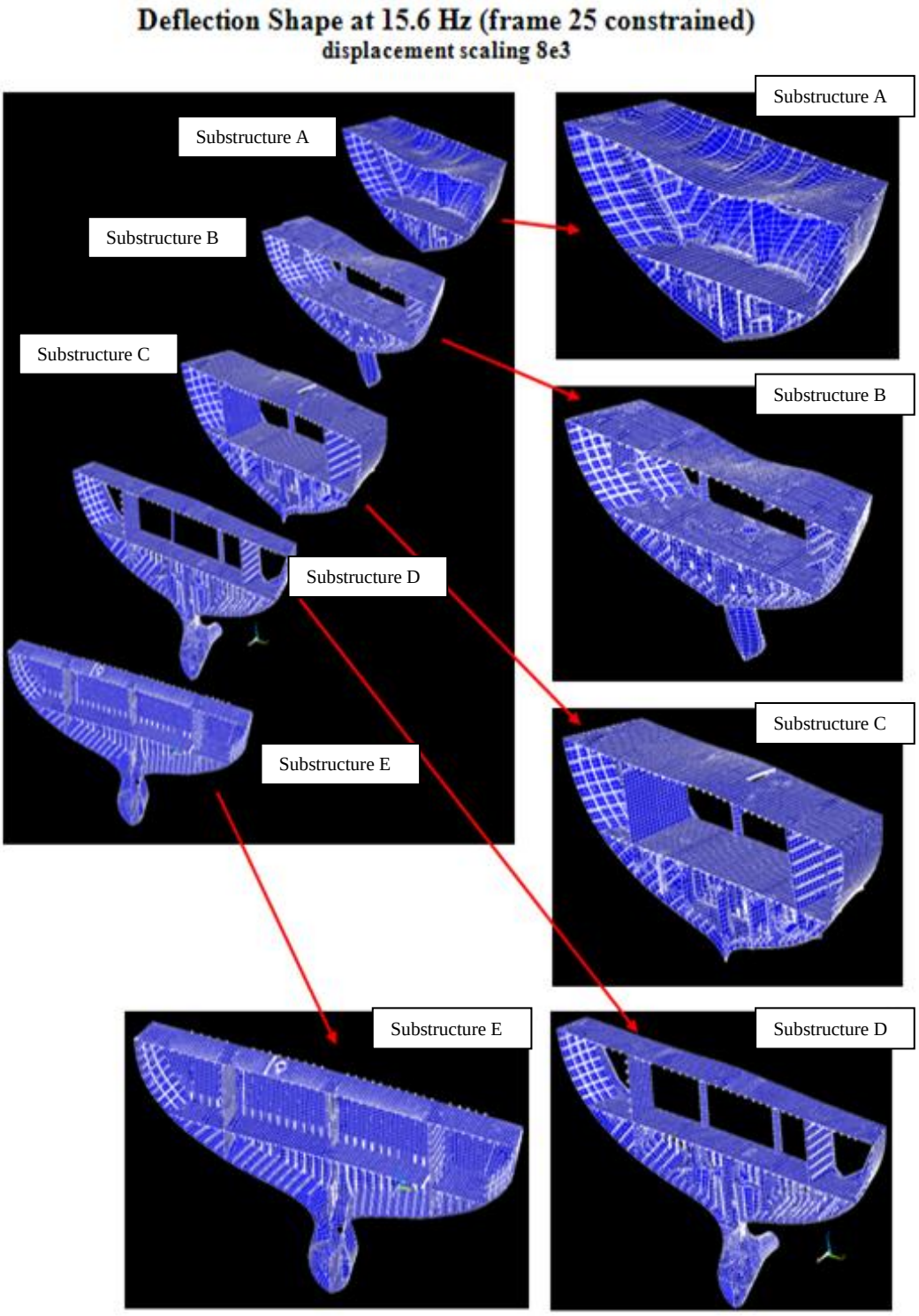

Figure 46 ***Mode shape at15.6 Hz compiled from the component mode synthesis results (see section 7.2.2)***

18.1 Hz

From the deflection shapes at 18.1 Hz shown in Figure 47 and Appendix XI can be seen that the response at 18.1 Hz is related to a more global mode shape where the mooring deck bending natural behaviour is coupled to elastic deformation of frame 21, the transom, and also, the steering gear deck double bottom (see Figure 48 and Figure 49). As this mode shape is in fact a coupling of deformations of every part of the structure, this frequency is found to be dominant in all simulation results of the model constrained at frame 25.

Constraining the model at frame 21 raises the peak response related to this mode shape from 18.1 Hz to 22 Hz, as can be seen from the simulation results in Appendix XII. This means that the stiffness of the model forward from frame 21 affects the natural frequency corresponding with 18.1 Hz, profoundly.

However, the structure forward from frame 21 (covering Substructures F, G and G in the component mode synthesis (CMS) model) has not been modelled at the same level of detail as the sections aft from frame 21. Some stiffening details had been omitted for modelling simplification purposes. From this analysis however, it appears that these stiffening details may shift the simulated peak response at 18.1 Hz towards 20 Hz. This means that the response amplitude simulated at 20 Hz (4^{th} blade passing frequency) will in fact be more dominant than initially simulated and will come closer to the measured response amplitude at the 4^{th} blade passing harmonic.

The more dominant role of the 18.1 mode shape in the response at the 4^{th} blade passing harmonic is further suggested through observing the relation between measured amplitudes measured at the edge of the steering gear deck, and measured towards the middle of the steering gear deck. Higher amplitudes have been measured towards the middle of the steering gear deck compared to the edge of the steering gear deck. This is in line with the simulated mode shape as demonstrated in Figure 49.

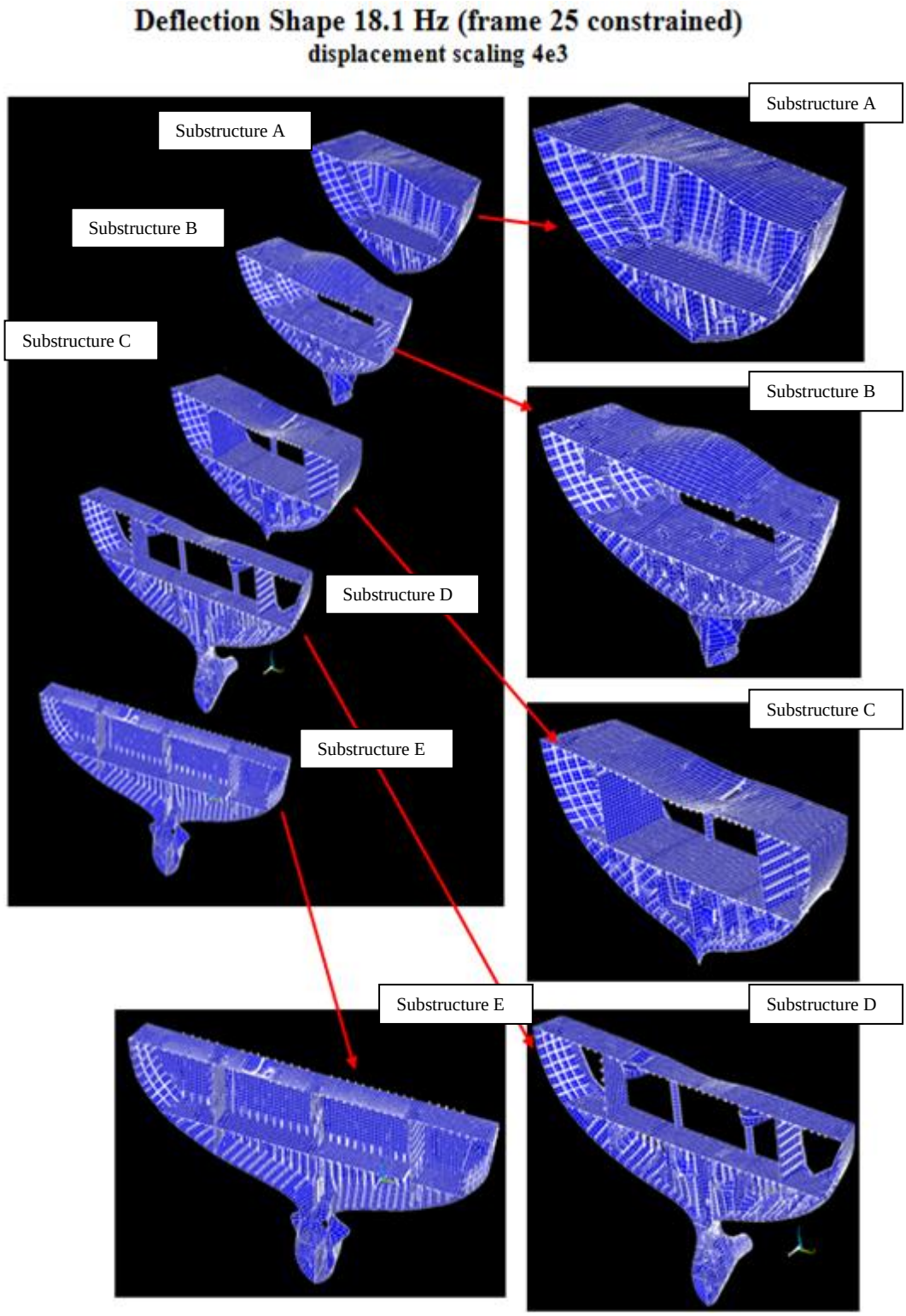

Figure 47 ***Mode shape at 18.1 Hz compiled from the component mode synthesis results (see section 7.2.2)***

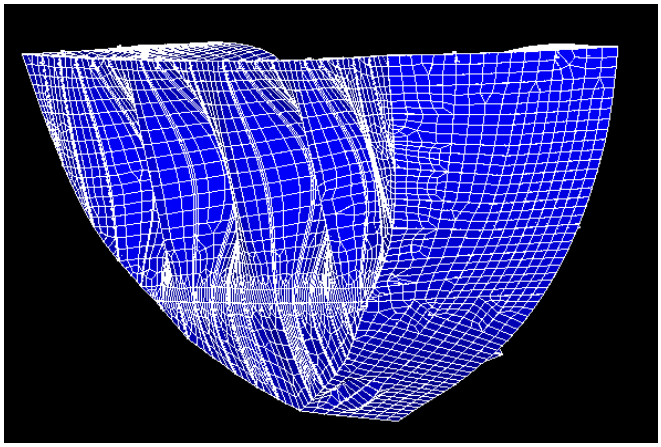

Figure 48 ***Periodic deformation at 18.1 Hz at the transom. Note that for presentation purposes the displacement field is presented at a phase shift of 180 degrees relative to the displacement field presented in Appendix XI***

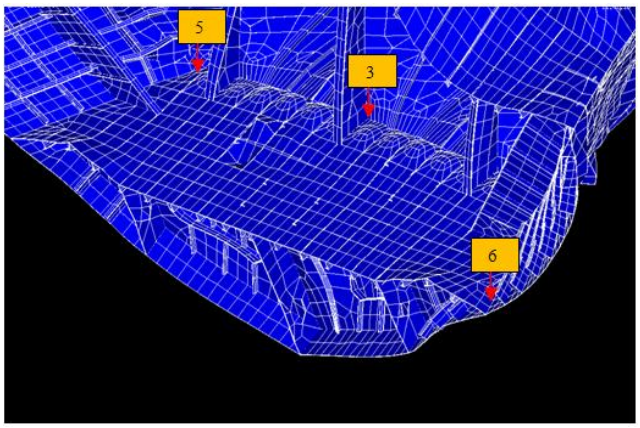

Figure 49 ***Through the deformation of the double bottom coupled to the deformation of the transom and mooring deck, 18.1 Hz is found to be dominant in the simulation results of the locations on the steering gear deck. For locations 8 and 9 (outside the area of the part of the model shown here) 18.1Hz becomes more dominant, as these locations are more in the middle of the deck, where the deflection is found to be higher than at the edges of the steering gear deck. Please note that the results presented in Figure 48 have been given a phase shift of 180 degrees relatively to the results presented in this figure. In this figure also a much higher amplification factor has been applied than in Figure 48.***

As discussed above for the 15.6 Hz peak, response amplitude results are presented in Appendix XIII where the resonance previously simulated at 18.1 Hz has been shifted to 20Hz, coinciding with the 4^{th} blade passing harmonic component. Although that causes the simulated response amplitudes at the 4^{th} order blade passing frequency to increase, the simulated response amplitudes are still considerably lower than the amplitude actually measured amplitudes for the location considered in this work.

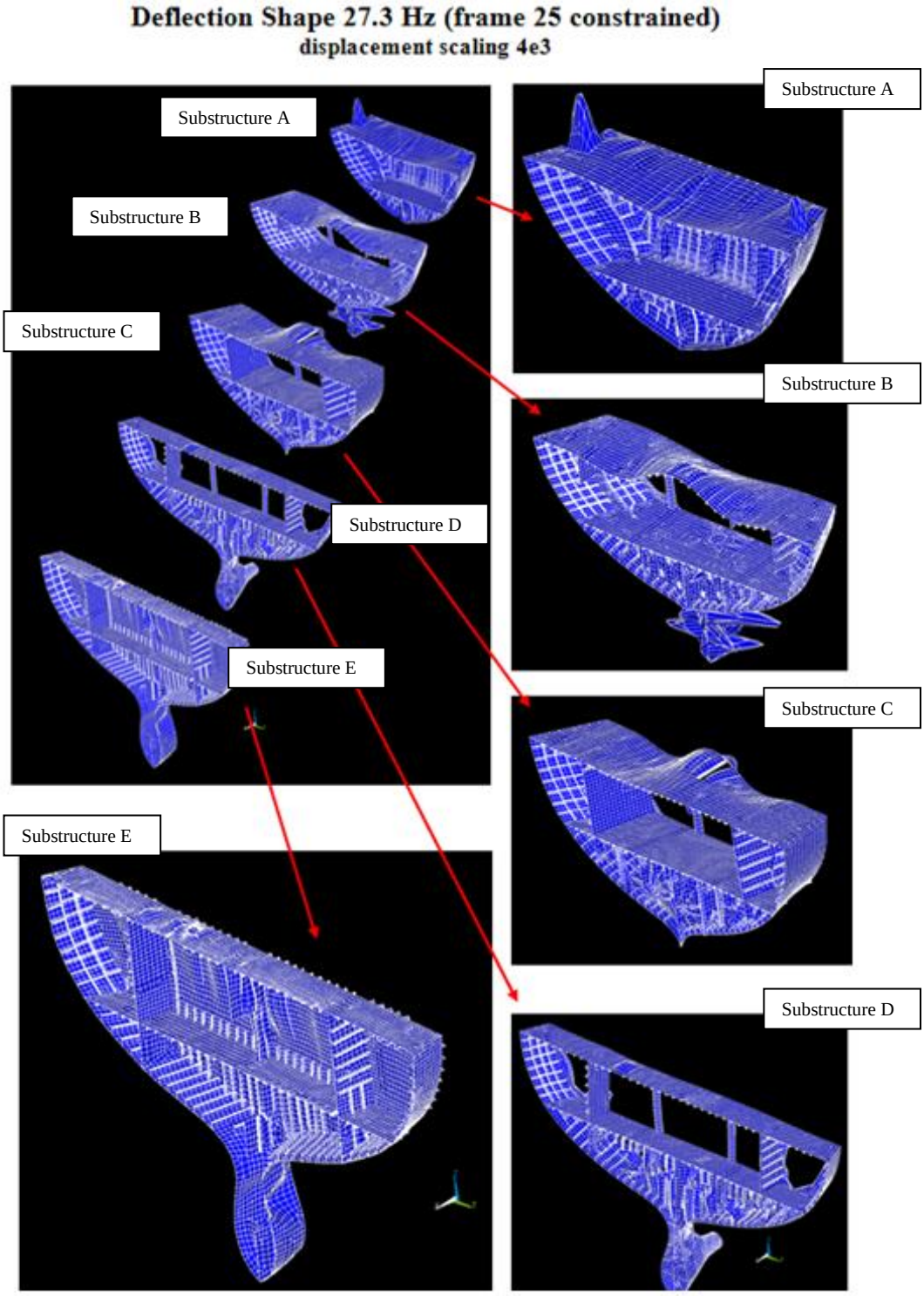

Figure 50 ***Mode shape at 27.3 Hz compiled from the component mode synthesis results (see section 7.2.2)***

27.3 Hz

In Appendix XI and Figure 50 can be seen that the simulated peak response at 27.3 Hz is related to a higher mode bending natural frequency of the aft deck. Boundary conditions have little effect on the natural frequency corresponding with this mode shape. This frequency was found to be dominant in the response calculation results carried out for the model constrained at frame 21 as well. The corresponding mode shape was found to be same as the mode shape found for the model with constraints at frame 25.

No mass of equipment mounted on the aft deck has been taken into account (winches and boulders). Added mass decreases the natural frequency. In Figure 51 the simulation results are compared with results obtained with masses added on the aft deck, which represent two winches each weighing 3 tons. As a result of the added mass, the frequency is seen dropping from 27.3 Hz to 26.3 Hz. Considering there are more items on the aft deck that add mass, but have not been modelled, it seems likely that this natural frequency moves even closer to towards 25 Hz, which is the frequency coinciding with the 5^{th} order blade passing frequency. As a result, simulation amplitudes at the 5^{th} blade passing frequency increases (25 Hz) getting closer to the amplitudes measured at 25 Hz. In Appendix XIII, simulation results are presented where the natural frequency at 27.3 Hz is assumed to have shifted to 25 Hz, corresponding exactly with the 5^{th} order blade passing frequency. As can be seen, simulated amplitudes are still lower than the measured amplitudes.

No hydrodynamic added mass has been taken into account. However, as this vibration mode concentrates on the mooring deck section, added hydrodynamic mass from the water surrounding the hull is not expected to affect the natural frequency corresponding with this mode shape.

simulation amplitudes at the 1^{st} and 2^{nd} blade passing frequencies will converge to the amplitudes measured at these frequency components. The effect can be seen in Appendix XIII where simulation results are shown which have been obtained after having shifted the peak response initially found at 8.8Hz, to 7.8 Hz, in order to correct for the effect of hydrodynamic added mass.

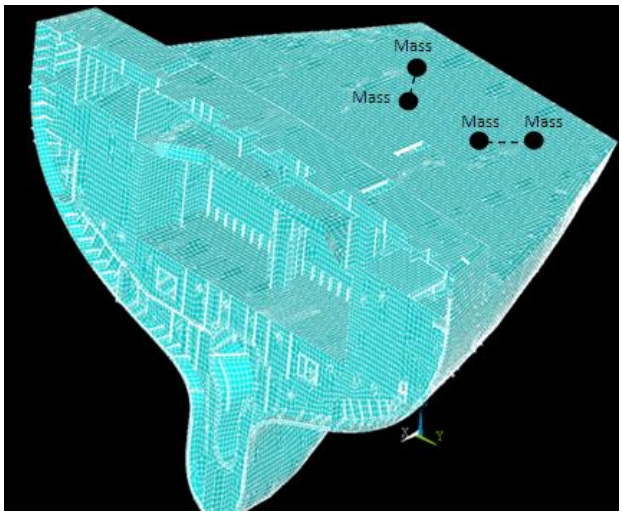

Aft ship model with masses representing the masses of two winches. Each winch is modelled through two masses each 1.5 tons

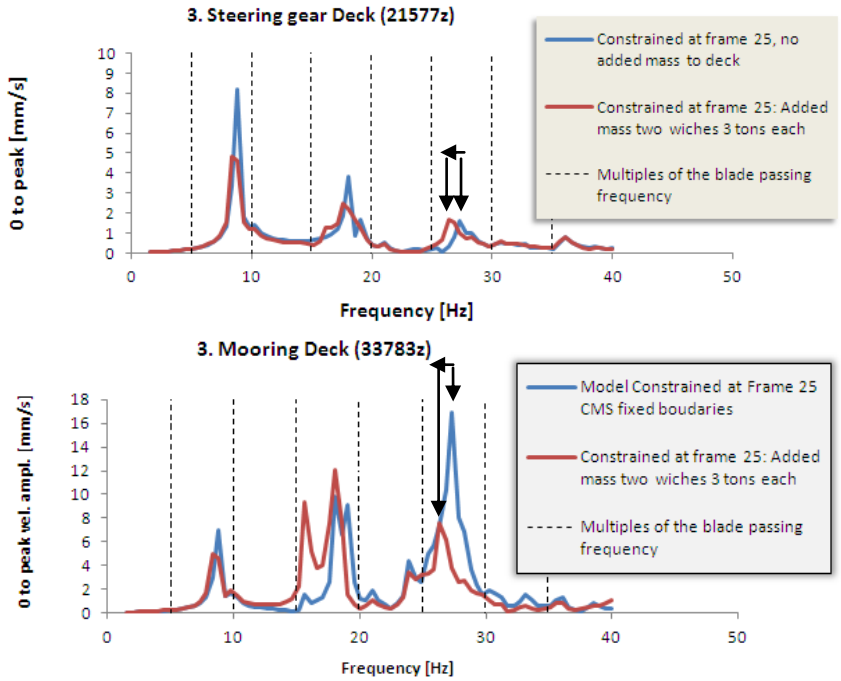

Figure 51, comparison simulation results without mass of aft deck winches modelled (blue line) and with aft deck winches modelled (red line). Simulations have both been performed with frame 25 constrained.

7.5.2 Excitation characteristic

In the section above (section 7.5.1) it has been established that the simulated response amplitudes at the first two blade passing harmonics are close to the measured amplitudes. Especially when considering that due to hydrodynamic added mass the simulated resonance frequency at 8.8 Hz will shift to a lower frequency,

Measured response amplitudes at order numbers higher than 2 are however a lot higher than the simulated response amplitudes. There is reason to believe that resonance plays an important role in that, but even when shifting natural frequencies right onto the 3rd, 4th and 5th order excitation frequencies, simulated response amplitudes are still a lot lower than the measured amplitudes (see Appendix XIII). On board machinery vibration measurements showed very low vibration levels at these frequencies (considerably lower than measured at the steering gear deck, compare Figure 12 with Figure 14). This further confirms that the explanation of the higher order vibration should be found in the hydrodynamic behaviour of the propeller, or the structural dynamic behaviour of the aft ship. Analysing response amplitudes at these higher order frequencies however, it is important to realise that there is a lot of uncertainty about amplitudes of excitation, particularly with aft ship geometries such as the geometry of the LNG carrier, for which this whole analysis has been carried out. Even though fluctuating hull pressure field simulations have been performed for only up to the 3rd order blade passing frequency, the 4th and 5th order play a very important role. It had been assumed that excitation at these orders is the same as the excitation calculated for the 3rd order. A realistic possibility is that the propeller excitation is in fact at these higher frequencies much higher that simulated. In addition, there was uncertainty about the exact geometry of the propeller which has been used as the input for the simulation of excitation.

Also through collapsing cavities higher order excitation amplitudes are likely to be amplified [3, 47]. Being in the steering gear deck with the ship sailing at full speed, violent cavitation noise and impulses could be heard/felt. Through the impulse like nature of the excitation it is likely that response amplitudes at natural frequencies are amplifies (see section 4.1.1.3).

7.5.3 Number and Type of Elements

As a rule of thumb it is recommended to choose the element size of the model in such a way that the expected wave length is no smaller than the length of six elements (considering the type of plate and beam elements applied in this model [22]) . In other words, it is assumed that six elements can accurately enough describe

one sinusoidal wave shape. From the simulated deflection shapes can be seen that the relevant wave lengths of the vibrations exceed by far the length of three elements. Bigger elements may therefore be applied which will reduce the size of the model. However, wave length in this case is not the only critical factor in element size choice. The geometry may also require a minimum number of elements (consider the size and distance between stiffening elements). As the structure consists of many stiffening elements, still a high number of elements will be required. The effect of using bigger elements will need to be verified and has not been done in this work. Also the necessity of using thick plate and beam elements need to be investigated.

7.6 The Contribution from Hull Girder Modes

As only a part of the ship structure has been modelled, no contributions from hull girder modes are correctly taken into account in the simulation results. Johannessen and Skaar have collected measurement date of hull girder natural frequencies of the first 5 modes and have plotted them in the graph shown in Figure 52 (see also section 4.2.1 'Hull Girder Approach'.). This graph is considered very useful for estimating the hull girder natural frequencies for the LNG carrier modelled in this work, as the hull geometry has a great resemblance with a typical hull geometry of bulk carriers.

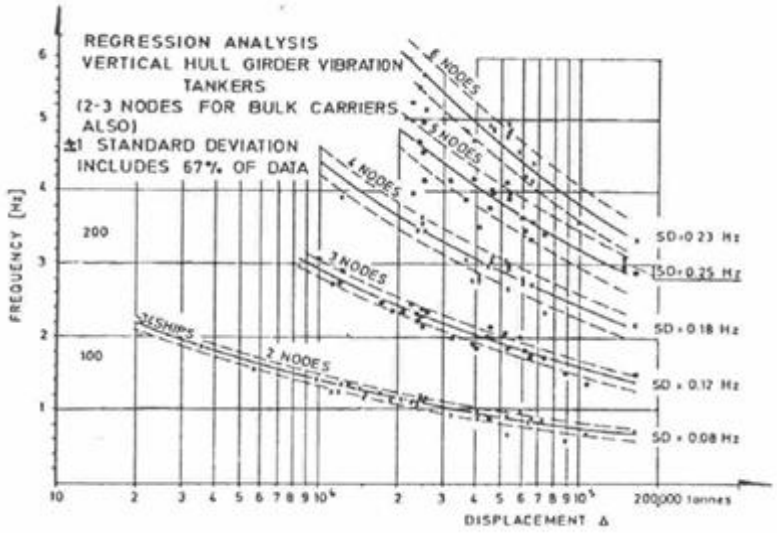

Figure 52 ***Empirical data originally presented by Johannessen and Skaar for vertical hull bending vibrations natural frequencies plotted against tonnes displacement.***

From the graph above the LNG carrier (84491 ton displacement) is estimated to have the following hull girder natural frequencies:

1st mode	0.8 Hz
2nd mode	1.5 Hz
3rd mode	2.5 Hz
4th mode	3.4 Hz
5th mode	3.8 Hz

Table 5 ***The estimated natural frequencies corresponding with the first 5 hull girder modes of the LNG carrier***

7.7 Correlation of Simulation Results

Following the study of the simulated response amplitudes plotted against frequency, the simulated impact of boundary conditions and the study of mode shapes corresponding with the simulated peak repose amplitudes the following changes have been made in order to make the simulation results correspond better with the measurement results. The model constrained at frame 25 has been used as a basis for the generating the correlated simulation results (see Figure 53 and Appendix XIII).

- 1st and 2nd blade passing frequency: Measurement results and study of the mode shape at the initially simulated peak response at 8.8 Hz (constrained at frame 25) suggest that hydrodynamic added mass (omitted in this mode) is very likely to shift the peak response to a lower frequency. Concerning the 1st and 2nd blade passing frequency response amplitude, the best correlation between simulated results and measured response amplitude was obtained by assuming a frequency shift of 1 Hz (to the left) of the entire response curve section between 0 and 11 Hz. (see results in Figure 53). Given that this model only covers a small part of the hull, and given the choice of the boundary conditions, the contributions from hull girder modes are not been taken into account in this model. Considering the relatively low sensitivity of the 8.8 Hz to the nature of the boundary conditions chosen close to the engine room bulkhead, it is considered not likely that this natural frequency is related to

one of the first 5 hull girder modes listed in Table 5 and will drop to the region where the hull girder natural frequencies were estimated, if the whole hull would have been modelled (i.e. 8.8 Hz is a local natural frequency, or is coupled to a hull girder mode higher than 5). Adding considering of the first 5 hull girder modes to the simulation results, the correlated simulated amplitudes of vibration at the 1st and 2nd order should probably be slightly higher than plotted in Figure 53.

- 3rd blade passing frequency: as simulated amplitudes at the 3rd blade passing frequency are much lower than the measured amplitudes, the peak response amplitude found at 15.6 Hz has been shifted to 15 Hz, so it coincides exactly with the 3rd blade passing frequency.
- 4th blade passing frequency: as simulated amplitudes at the 4th blade passing frequency are much lower than the measured amplitudes, the peak response found at 18.1 Hz has been shifted to 20 Hz, so it coincides with the 4th blade passing frequency. The increase of peak response frequency also corrects for the fact that past frame 21, not all stiffening elements have been modelled in order to simplify the model. Further justification of this decision can be taken from the observed impact of changing boundary conditions, on the peak response frequency for the mode shape in question.
- 5th blade passing frequency: as simulated amplitudes at the 5th blade passing frequency are much lower than the measured amplitudes, the peak response found at 27.3 Hz has been shifted to 25 Hz, so it coincides with the 5th blade passing frequency. A decrease of the natural frequency corresponding with the mode shape previously found at 27.3 Hz is likely, as added mass of deck equipment has not been taken into account, and is likely to have that impact.

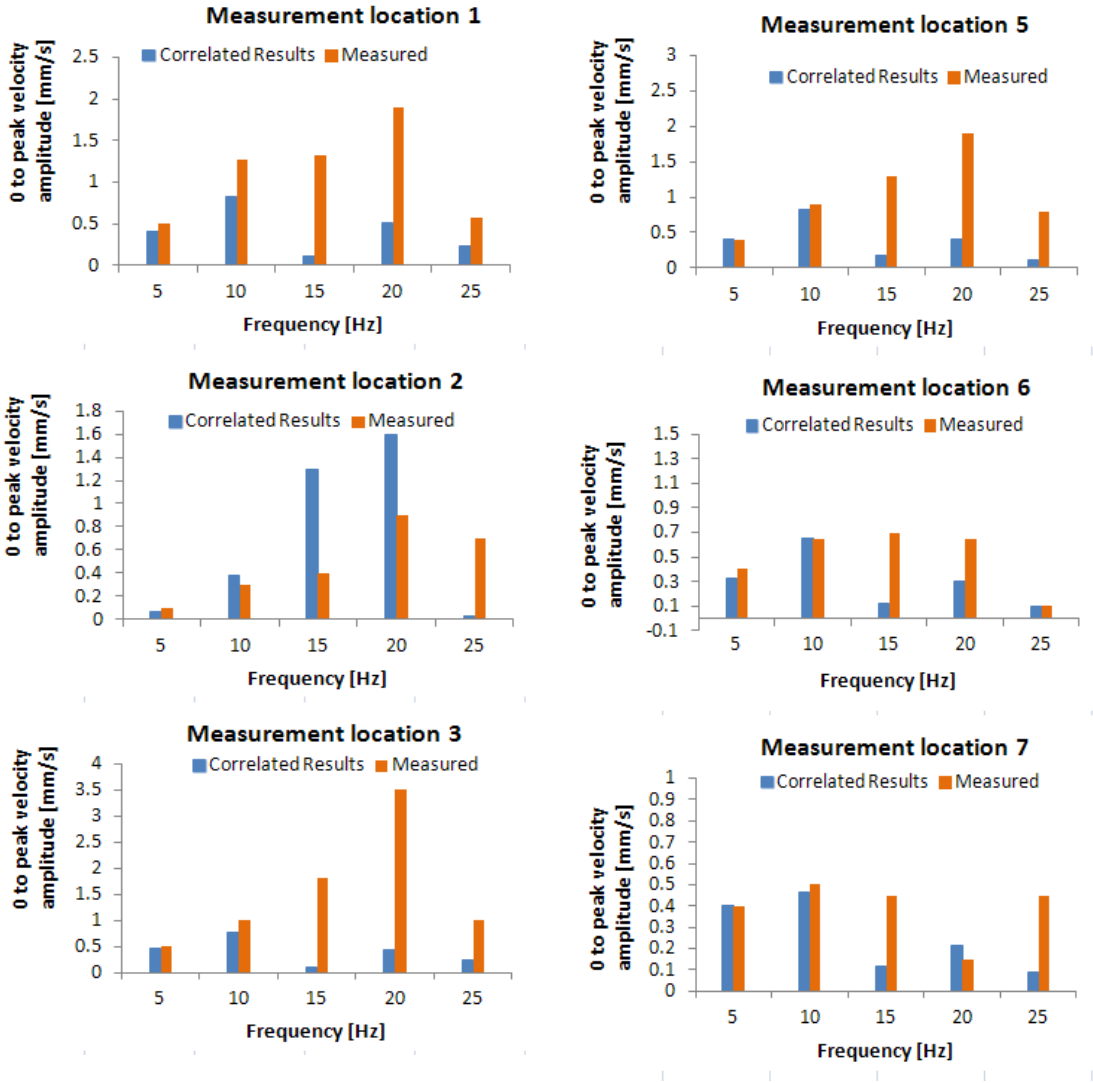

Figure 53 ***Correlated simulation results (blue colour) plotted together with the measured response amplitudes (orange)see also Appendix XIII***

7.8 Evaluation of FE and CMS Performance

With the simulation of the vibration structural behaviour, harmonic analysis results as presented in, Appendix VII and Appendix VIII have first been obtained through solving the full set of equations of motion in ANSYS using a so called sparse matrix solver. A sparse matrix solver solve a matrix based on the row reduction technique shown in Appendix VI [48].

Although nodal displacement results could be obtained from individual degrees of freedom (through which the results in section Appendix VII and Appendix VIII have

been obtained), no complete set of results (for all degrees of freedom at once) could the read at once due to the size of the result file. This meant that no visual presentation of deflection shapes could be obtained. Studying the displacement field, i.e. the way in which the structure periodically deforms, is very important to generate an understanding of the mechanisms behind vibrations propagation, as demonstrated in section 7.5.

In order to be able to study the mode shapes, component mode synthesis techniques have been used. Results are obtained through expansion of the mode shapes of the individual substructures. As the result output files for each substructure is much smaller than the out file of the entire structure, mode shapes can easily be generated. Through pasting together the mode shapes of all individual substructures, mode shapes of the total structure are obtained and can be studied (as presented in section 7.5.1.)

7.8.1 Accuracy of CMS results

In Appendix X results obtained through the CMS techniques are compared with the results obtained from the full set of equations of the full assembled structure. In Table 6 some of the properties of the substructures are presented. One of these properties is the number of mode shapes retained for generating the displacement field. Also the required CP time to calculate these mode shapes and natural frequencies is presented. This number of retained substructure normal modes has been determined through selecting all mode shapes with natural frequencies within the frequency range between 0 and $1.5 \times f_{max}$, (according to Rubin's principle) where f_{max} is the maximum frequency for which results are generated. As the frequency range of the solutions is chosen to be between 0 and 40 Hz, the mode shapes with natural frequencies between 0 and 60 Hz had been retained for both the free and fixed interface CMS models.

The evaluation of CMS modelling technique is based on frequencies at which peak responses are found according to the CMS modelling results. Sufficient accuracy of the simulation results is considered to have been obtained when the frequencies at which peak responses coincide with the frequencies at which peak responses have

been found according the full harmonic analysis results. This basically means that, considering frequency steps of 0.5 Hz are used (80 results for 80 frequencies over a 0 to 40 Hz frequency range), natural frequencies found through CMS, should be within a bandwidth between -0.25Hz and +0.25Hz from the natural frequencies found through the full harmonic analysis.

LNG vessel FE model	Number of nodes	Number of boundary nodes	Number of boundary degrees of freedom	Number of modes required*	Required CP time for calcuating eigenvectors	Required CP time for generation pass
PartHfixedcms	5819	348	2088	181	18.5	22.8
PartHfreecms				257	24.5	52.5
PartGfixedcms	6675	250	1500	373	29.8	40
PartGfreecms				419	39	100.8
PartFfixedcms	6675	250	1500	373	29.8	40
PartFfreecms				419	39	100.8
PartEfixedcms	10728	1198	7188	213	30	46.6
PartEfreecms				323	61	174
PartDfixedcms	11118	1140	6840	162	29.14	53.6
PartDfreecms				336	95	328
PartCfixedcms	14393	854	5124	195	38.11	68.13
PartCfreecms				335	75	225.7
PartBfixedcms	11705	633	3798	138	29.4	47.7
PartBfreecms				231	53	138.3
PartAfixedcms	7168	263	1578	91	18.8	25.4
PartAfreecms				154	24.6	53.3

Table 6 ***Table of properties of the substructures shown in Appendix IX . The number of retained mode shapes are also presented for each substructure together with the CP time required to calculate these mode shapes (eigenvectors). Fixed CMS is CMS based on fixed interface approach as applied with Craig-Bampton's method. Free CMS is CMS based on the free interface approach as applied with Rubin's Method***

In Appendix X can be seen that results obtained through free interface CMS were found to be almost identical to the results generated through the full harmonic analysis. Not only do the peak response frequencies coincide with the peak response frequencies found through the full harmonic analysis, also response amplitudes match the response amplitudes found through full harmonic analysis. The free interface CMS is based on Rubin's method with no residual interface flexibility modes taken into account.

Results obtained through fixed interface CMS deviate from the results obtained from the full assembled set of equations of motion.

7.8.2 Required CP Time for CMS Calculations

In Table 7 the registered required CP time for obtaining dynamic response results is presented for the full harmonic method, fixed interface and free interface CMS. In Figure 54 computation time required for each step are presented calculated according to Appendix VI, Appendix XVI and Appendix XXI.

Although CMS has solved the problem with handing large output files, Table 7 and Figure 54 show that CMS increases the required computation time by approximately 53%., compared to the time required for full harmonic analysis. It is easy to understand that calculating the mode shapes off course adds extra CP time onto the total CP time required to obtain the results. This effect has been taken into account into the calculation of the grand total CP time in Table 7. This effect becomes of course less noticeable when calculating the response for a higher number of frequencies, as the modal information only needs to be calculated once. However, Table 7 and Figure 54 also show that more CP time (+50%) is required for solving the CMS matrices, compared to solving the full set of equations of motion. This increase of CP time is a result of the fact that, although the total assembled CMS dynamic stiffness matrices are smaller than the matrices generated through the full solution, the CMS matrices are much denser and contain in fact a much higher number of non-zeros than the full dynamic stiffness matrix of the non-reduced full FE model (as also shown in Table 7.)

Total structure	Number of equations total assembled	Number of non zeros	Total CP in use pass	CP required for matrix formulation in use pass	Calculating Elemental and Nodal Solutions in use pass	Estimated CP for solving matrix in use pass
full solution	366973	1.49E+07	134	20	19	95
fixed interface CMS	15370	1.25E+08	180	18	na	162
free interface CMS	16118	1.28E+08	160	18	na	142

grandtotal cpu	Full solution	Fixed boundary CMS	Free boundary CMS
1 frequency step	115	524	1333
80 frequency steps	9170	14744	13973

*number of modes required is based on covering the frequency range from 0 to 1.5 times the maximum to be analysis frequency. In this case the frequency range is from 0 to 1.5 times 40 = 0 to 60 Hz

Table 7 ***Size of matrices and required computation times for different analysis techniques. Fixed interface CMS has been carried out according to Craig-Bampton, and free interface CMS has been carried out according to Rubin's method (both with a cut-out frequency of 1.5 f = 60 Hz)***

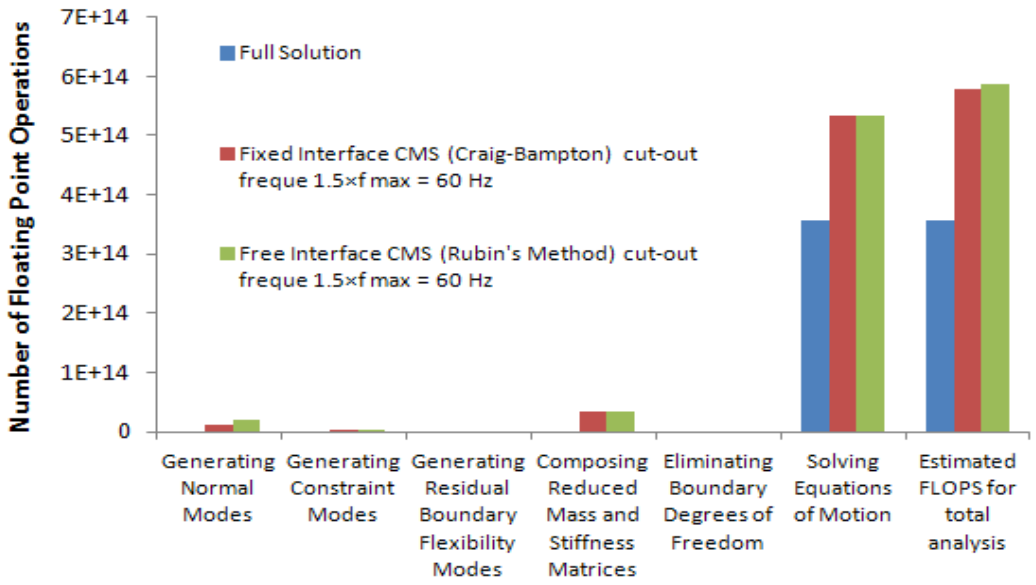

Figure 54 ***Required computation time for the different stages of the different analysis techniques performed on the LNG carrier model of section 7. Computation times have been calculated for the analysis of 80 frequency steps. Added to the graph is the estimated required number of floating point operations for obtaining results through the full harmonic analysis technique.***

7.9 Summary and Conclusion

In this section finite element modelling results of the aft ship of an LNG carrier have been studied and compared with measurement results taken on board. Fixed and free interface component mode synthesis has been applied and evaluated by comparing the results with the results obtained from the full finite element model.

7.9.1 Comparison with Measurement Results

Good coincidence has been found between the simulated response amplitudes and measured response amplitudes at the first two blade passing frequency components. Results in Appendix XIII show that after correction of the response curve for the effect of hydrodynamic added mass from the water surrounding the hull, simulation results will come even closer to the measured amplitudes (peak response at 8.8 Hz shifts to 7.8 Hz).

For blade passing frequencies above the 2nd order however, simulated response amplitudes were found to be a lot lower than the amplitudes measured on board.

7.9.2 Evaluation of Simulated Excitation Characteristics

At the 3rd, 4th and 5th order, dominant response amplitudes have been measured on the steering gear deck on board the LNG carrier sailing at full speed. Measured amplitudes at these orders are a lot higher than the simulated amplitudes. Although there is reason to believe that resonance plays an important role, Collapse of cavity volumes are assumed to play an even more important role, as violent cavitation has been experienced on board. These phenomena have not been taken into account through the vortex lattice method used for the simulation of the excitation characteristics of the propeller and are likely amplify the higher order excitation amplitudes [47]. There was also uncertainty about the geometry of the propeller used for the alternating pressure field simulation, as no digital geometry was available.

7.9.3 Choice of Boundary Conditions

Analysis has shown that choosing the right boundary conditions close to the engine room bulkhead is very important for simulating vibration levels on the steering gear deck and mooring deck. Particularly for the vibration amplitudes simulated at the 1st and 2nd mode questions arise about the relation between a peak response found at 8.8 Hz and a possible relation with any lower order hull girder modes. The contributions from these lower order hull girder modes are not included in the simulation results given that the model only covers a small part of the hull structure, and given the nature of the boundary conditions tested in this section. It is therefore recommended that simulation are carried out coupling the present model to a hull girder model (Deep Beam Elements) representing the rest of the vessel's hull from frame 25 forwards on.

The simulation results also suggest that more detail needs to be added to the model from frame 21 to 25. In order to simplify the model, not all stiffening details had been incorporated in this section, but appeared to play an important role for a particular natural frequency calculated at 18.1 Hz.

All considered, it can be concluded that frame 25 is a good choice of location for applying constraints, or from where the model is simplified forward on.

7.9.4 Element Size

Based on analysis of the wavelengths of the relevant mode shapes for this particular vessel, applying a coarser mesh is not expected to affect the results over the frequency range of interest.

7.9.5 Evaluation of Component Mode Synthesis (CMS) Techniques

Free and fixed boundary component mode synthesis techniques have been applied and were found very useful. Results obtained through free interface CMS coincided with the results obtained through the full FEM analysis. As the fixed interface CMS results deviated noticeably from the results obtained through the full finite element analysis, free interface CMS has been chosen as the most suitable method for modelling the vibrations of the aft ship of the LNG carrier.

Component mode synthesis was found very useful for obtaining information on the modes of vibrations. Through the reduced substructures the size of result files are hugely decreased and become very well manageable. As a results, no problems with obtaining a visual presentation of the mode shapes have been encountered, as was the case with the analysis of the results obtained through full harmonic analysis.

Although the total assembled matrices obtained through CMS are much smaller than the matrices obtained through the full harmonic analysis, these matrices were found to be a lot denser (contain much more non-zero entries). As a result, more CP time is required to solve the reduced matrix compared to the sparse full dynamic matrices. Particularly when obtaining the response for many frequency steps, this leads to a large increase of required computation time.

8 Methodology of an Alternative Approach to Classical CMS

As demonstrated in section 7 and as already discussed in the critical review (section 0), component mode synthesis offers various advantaged for modelling marine structures. However, through section 7 it has been demonstrated that component mode synthesis may increase the required computation time. This increase of computation time relatively to full finite element harmonic analysis is a result of the high number of interface degrees of freedom found in typical marine structures in combination with the fullness of the matrices that have to be solved in order to obtain the modal coordinates. In this section two alternative approaches to the Component mode synthesis method are suggested in order to reduce the size of the assembled CMS matrices: the Zoet method and the Rubin-Zoet method.

8	Methodology of an Alternative Approach to Classical CMS
8.1	Introduction
8.2	Interface stiffness and mass matrix
8.3	Proposed Reduction Technique
8.4	The Zoet Method with Boundary Residual Flexibility: a Reformulation of the Equations of Motion
8.5	Eliminating Residual Flexibility Modes from the Zoet Method
8.5.1	Compiling the Total Boundary Mobility Matrix
8.5.2	Eliminating Boundary Displacement Degrees of Freedom
8.5.3	Over Compensation of Residual Flexibility
8.6	The Rubin–Zoet Method
8.7	Comparing Required Number of Matrix Operations for the Different CMS Methods
8.7.1	Estimating Calculation Time: Floating Point Operations
8.7.2	Required Number of FLOPS for Zoet's Method
8.7.3	Required Number of FLOPS for the Rubin-Zoet Method
8.8	Discussion of Performance of the Proposed CMS Techniques
8.8.1	Formulating Matrices
8.8.2	The Zoet Method
8.8.3	The Zoet Method with Residual Flexibility Modes
8.8.4	Zoet Method versus Rubin-Zoet Method
8.8.5	Comparing CMS with Mode Superposition
8.9	Conclusions

Paragraph structure of chapter 8 'Methodology of an Alternative Approach to Classical CMS'

8.1 Introduction

As demonstrated in the case study above, CMS has proved to be beneficial for modelling the structural response of complex large parts of ship structures. CMS proved a solution for the problems with the presentation of the mode shapes experienced with the full harmonic analysis. Due to the size of the output file the mode shapes of the full solution could not be read and plotted as a 3d picture.

Not only did CMS modelling techniques make it possible to study mode shapes, CMS offers the advantage of synchronising the correlation of the model with the progress of the building process. The FE model will be subdivided in such a way that the CMS substructures coincide with the sections of the ship as it will be built. Every time a section is delivered, the modal information can be measured and used as an input of a part of the full model. Adjustments to the structure can still be implemented if the correlated model shows unfavourable response results.

CMS also offers the advantages of being able to reuse modal information for repeating substructures. Particularly mid ship sections and accommodation deck consist of repeating structural parts. Also symmetry of the ship's structure can be used to further reduce the required number of calculations of mode shapes.

However, Table 7, Figure 55 and Figure 56 show that in total, for both CMS methods (free and fixed), more calculation time is required, compared to the calculation time required for the full harmonic analysis. Table 7 shows the measured computation time for each sub-step following the full harmonic analysis, fixed and free interface CMS techniques. In Figure 55 and Figure 56 the required number of matrix operations are presented as calculated for each step according to Section 8.7 elaborates on how these values have been obtained) and serve as a good indication of the required amount of computation time.

It can be seen from these figures that, besides the extra calculation time for calculating normal modes, natural frequencies, constraint modes, and forming the reduced matrixes, most of the time is required for solving the reduced set of CMS equations of motion. Section 7.8 points out that, Although the number of equations used for CMS is a lot lower than the number of equations used for the full harmonic analysis, the compiled CMS matrices are much denser than the matrices compiled for the full harmonic analysis. As a result, the number of non-zeros in the CMS matrices is much higher, which leads to the observed (and calculated) higher required computation times. As can be seen when comparing Figure 55 and Figure 56, the effect of higher computation time becomes even stronger when calculating response for multiple frequencies. Calculating response for multiple frequencies is not only

very important for identifying the relevant critical frequencies of a structure, but also very important for identifying the frequencies where the lowest response is obtained, so that the excitation frequencies and response behaviour can be optimally tuned for the lowest noise and vibration levels.

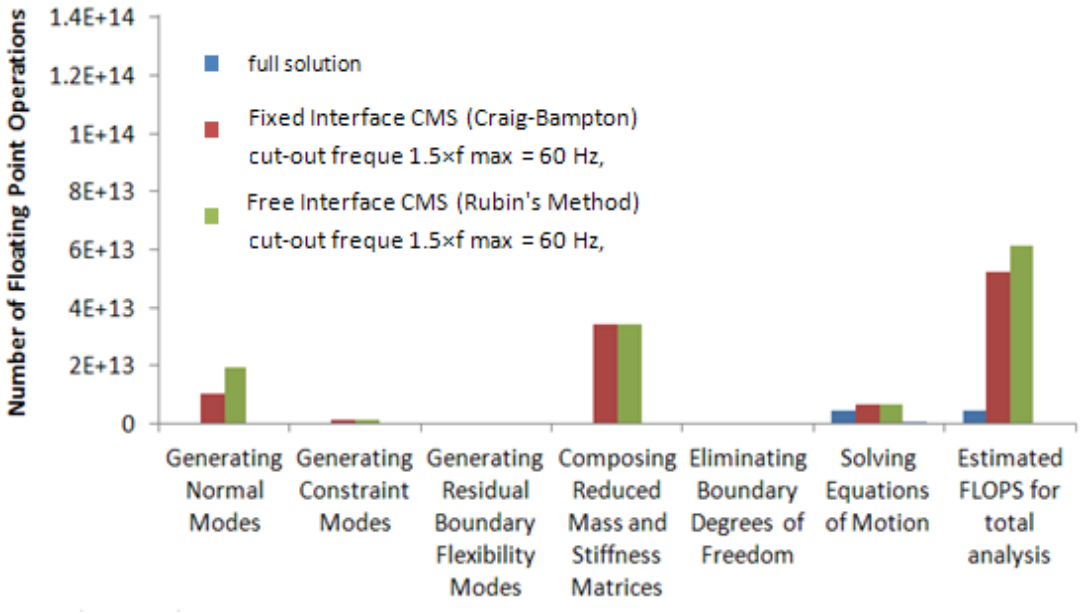

Figure 55 ***Required computation time for the different stages of the different analysis techniques performed on the LNG carrier model of section 7.Computation times have been calculated for the analysis of only one frequency step***

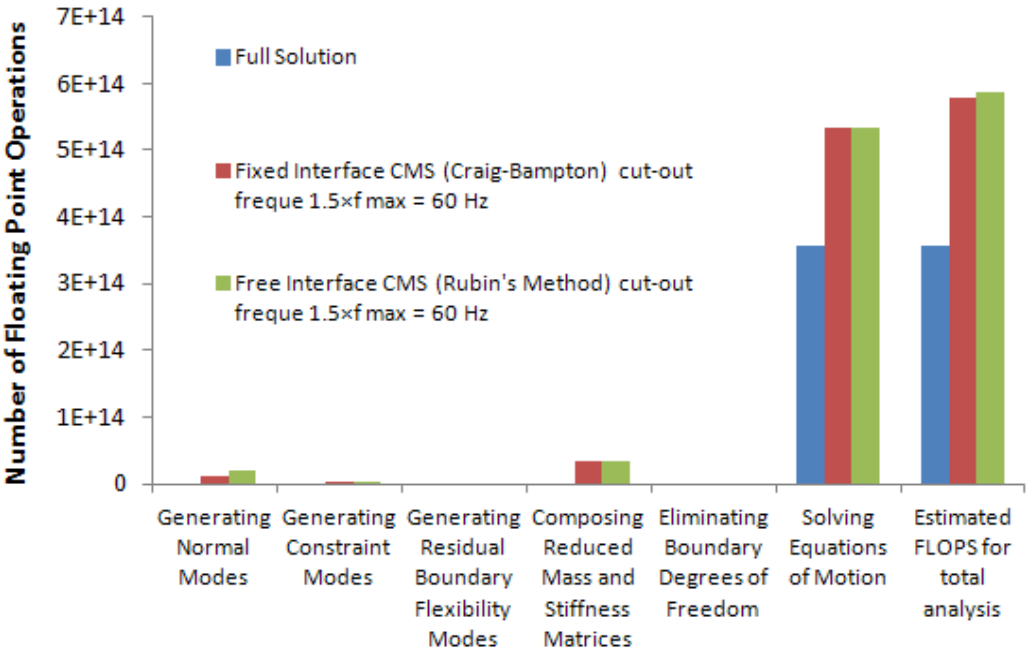

Figure 56 ***Required computation time for the different stages of the different analysis techniques performed on the LNG carrier model of section 7.Computation times have been calculated for the analysis of 80 frequency steps.***

As pointed out above, CMS offers the benefit of recycling modal information in case of repeating sub-structural elements and symmetry of the geometry. However, the higher required analysis time due to the need for multiple frequency calculations counteracts these benefits and result in a net increase of calculation time. The method in this section therefore focuses on reducing calculation times through reducing the size of the full CMS matrices

A very dominant factor in determining the size of the full assembled matrix is the number of connection nodes. For the description of a substructure according to the classical CMS methods the number of equations that are at least required is equal to the number of coupling degrees of freedom. In the case of the LNG model, this number is equal to the number of nodes shared with other substructures times the number of degrees of freedom of one node (which is 6, along x, y and z axis and rotation about x, y, and z axis). This is a result of the fact that the interaction between two substructures is described through setting up equilibrium and compatibility relations for each interface degree of freedom. Problems with high matrix densities

are typical for ship structures. Two substructures are coupled to each other through coupling lines on which many interface nodes are located. Compared to structures coupled to each other by a number of girders for instance (coupling points), ship structures will contain a much higher number of coupling points.

In this section two methods are suggested aiming at eliminating the interface degrees of freedom from the total set of equations of motion. The first method (the Zoet method) formulates the interaction between substructures solely through the modal coordinates rather than through the actual nodal displacements of the interface boundaries. The number of equations required becomes independent of the number of interface degrees of freedom and can be chosen equal to the number of mode shapes actually required for accurately enough describing the displacement field of the substructures. As can be seen in Table 6, the number of mode shapes required for describing the dynamic behaviour of the LNG carrier's sub-structure is a lot lower than the number of coupling degrees of freedom. Improving the results through incorporating the effect of residual flexibility is also presented and a reducing the number of equations of the full assembled matrix with residual compensation taken into account is presented.

Also a method is presented that is a hybrid of the classical Rubin method and the Zoet method and is referred to in this work as the Rubin-Zoet method.

The performance of the alternative methods are compared with the performance of the free interface CMS methods according to Rubin. The Rubin method is used as a benchmark as the best results have been obtained through this method according to the simulation results in section 7. The comparison is based on estimating the number of matrix operations (flops) required for each step for each different method.

8.2 Interface stiffness and mass matrix

The first step in exploring the possibilities of reducing the total equations of motion is formulating a description of substructures' interaction solely through the substructures' modal coordinates. This means, the number of equations required for solving the assembled structural dynamic behaviour is related only to the number of

mode shapes required and is independent from the number of interface degrees of freedom.

In Figure 57 two subsystems are shown, subsystem A (purple) and subsystem B (green). The red elements are the coupling elements forming an interface between subsystem A and subsystem B. Any dynamic deformation of the structures A and B results in deformation of the interface elements. Through the deformation of these interface elements reaction forces are generated on the interface nodes of substructure A and substructure B. These reaction forces are treated as excitation forces. The response of both substructures due to the interface reaction forces represents the effect of the interaction between the two separate structures. This interaction response is added to the dynamic response of the free uncoupled structures through which the coupled response is calculated.

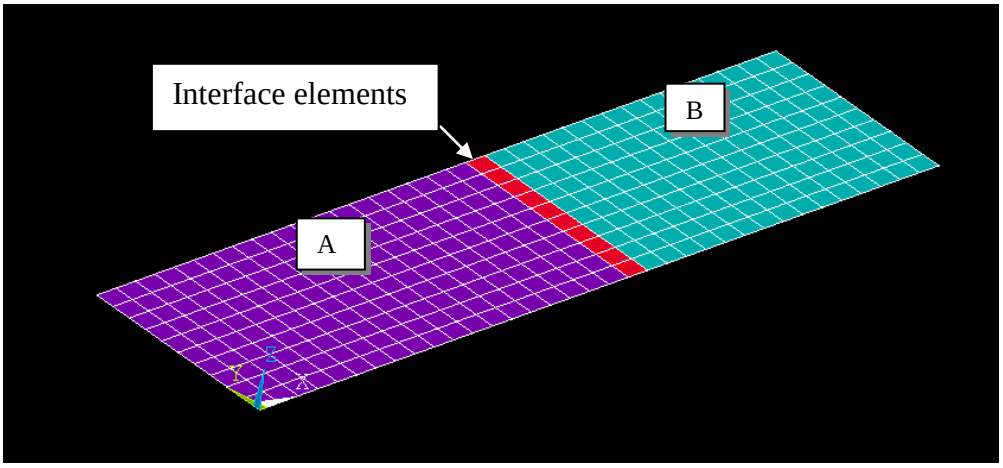

Figure 57 ***Example of two structures coupled to each other through interface elements***

This concept is demonstrated through the mass spring system shown in Figure 58 Considering the stiffness of the springs is $4e6\ N/m$ and each mass is 200 kg and has only one (horizontal) degree of freedom and an excitation force of 60 N is acting on mass 1, the total systems stiffness matrix is written as:

(8.1)

$$K = \begin{bmatrix} 4e6 & -2e6 & 0 & 0 \\ -2e6 & 4e6 & -2e6 & 0 \\ 0 & -2e6 & 4e6 & -2e6 \\ 0 & 0 & -2e6 & 4e6 \end{bmatrix}$$

(8.2)

The mass matrix is written as:

$$M = \begin{bmatrix} 200 & 0 & 0 & 0 \\ 0 & 200 & 0 & 0 \\ 0 & 0 & 200 & 0 \\ 0 & 0 & 0 & 200 \end{bmatrix}$$

The total un damped equation of motion becomes:

(8.3)

$$\begin{bmatrix} 4e6 & -2e6 & 0 & 0 \\ -2e6 & 4e6 & -2e6 & 0 \\ 0 & -2e6 & 4e6 & -2e6 \\ 0 & 0 & -2e6 & 4e6 \end{bmatrix} \begin{bmatrix} u_1 \\ u_2 \\ u_3 \\ u_4 \end{bmatrix} - \omega^2 \begin{bmatrix} 200 & 0 & 0 & 0 \\ 0 & 200 & 0 & 0 \\ 0 & 0 & 200 & 0 \\ 0 & 0 & 0 & 200 \end{bmatrix} \begin{bmatrix} u_1 \\ u_2 \\ u_3 \\ u_4 \end{bmatrix} = \begin{bmatrix} 60 \\ 0 \\ 0 \\ 0 \end{bmatrix}$$

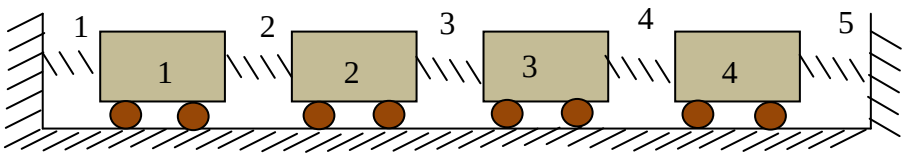

Figure 58 ***Mass spring system***

Consider the total system to be spit up in two parts so two separate subsystems A and B are generated:

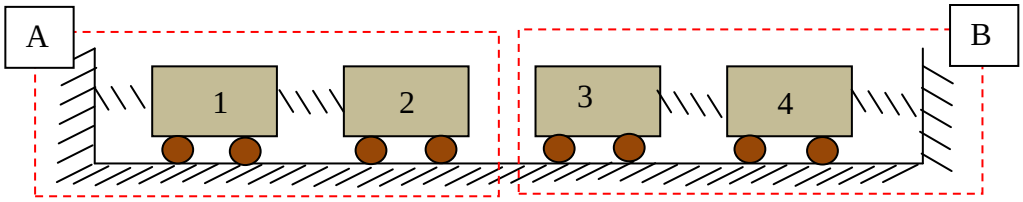

Figure 59 ***Mass spring system subdivided in two subsystems A and B***

The stiffness matrix of the uncoupled subsystems A and B is written as:

$$\begin{bmatrix} 4e6 & -2e6 & 0 & 0 \\ -2e6 & 2e6 & 0 & 0 \\ 0 & 0 & 2e6 & -2e6 \\ 0 & 0 & -2e6 & 4e6 \end{bmatrix} = \begin{bmatrix} K_A & 0 \\ 0 & K_B \end{bmatrix}$$

Where K_A and K_B are the individual uncoupled stiffness matrices of substructure A and B respectively

The stiffness matrix of the coupling element is K_{conn} =

$$\begin{bmatrix} 2e6 & -2e6 \\ -2e6 & 2e6 \end{bmatrix}$$

The internal forces induced in spring 3 by the dynamic interaction between the two subsystems is equal to the elements stiffness matrix times the displacement vector:

$$\begin{bmatrix} 0 & 0 & 0 & 0 \\ 0 & 2e6 & -2e6 & 0 \\ 0 & -2e6 & 2e6 & 0 \\ 0 & 0 & 0 & 0 \end{bmatrix} \begin{bmatrix} u_1 \\ u_2 \\ u_3 \\ u_4 \end{bmatrix} = \begin{bmatrix} 0 \\ f_{cA} \\ f_{cB} \\ 0 \end{bmatrix} = \begin{bmatrix} 0 & 0 & 0 \\ 0 & K_{conn} & 0 \\ 0 & 0 & 0 \end{bmatrix} \begin{bmatrix} u_A \\ u_B \end{bmatrix} \quad \textbf{(8.4)}$$

Where f_{cA} and f_{cB} are the interaction forces that are treated as excitation forces representing the effect of the two substructures coupled together and u_A and u_B are the displacement vectors of subsystem A and B respectively. The equation of motion according to above suggested concept is then written as:

$$\begin{bmatrix} K_A & 0 \\ 0 & K_B \end{bmatrix} \begin{bmatrix} u_A \\ u_B \end{bmatrix} - \omega^2 \begin{bmatrix} M_A & 0 \\ 0 & M_B \end{bmatrix} \begin{bmatrix} u_A \\ u_B \end{bmatrix} = \begin{bmatrix} f_A \\ f_B \end{bmatrix} - \begin{bmatrix} 0 & 0 & 0 \\ 0 & K_{conn} & 0 \\ 0 & 0 & 0 \end{bmatrix} \begin{bmatrix} u_A \\ u_B \end{bmatrix} \quad \textbf{(8.5)}$$

Where M_A and M_B are the uncoupled mass matrices of subsystem A and B respectively.

Applying this concept to the particular system shown in Figure 58 and Figure 59

$$\begin{bmatrix} 4e6 & -2e6 & 0 & 0 \\ -2e6 & 2e6 & 0 & 0 \\ 0 & 0 & 2e6 & -2e6 \\ 0 & 0 & -2e6 & 4e6 \end{bmatrix} \begin{bmatrix} u_1 \\ u_2 \\ u_3 \\ u_4 \end{bmatrix} - \omega^2 \begin{bmatrix} 200 & 0 & 0 & 0 \\ 0 & 200 & 0 & 0 \\ 0 & 0 & 200 & 0 \\ 0 & 0 & 0 & 200 \end{bmatrix} \begin{bmatrix} u_1 \\ u_2 \\ u_3 \\ u_4 \end{bmatrix} = \begin{bmatrix} 60 \\ 0 \\ 0 \\ 0 \end{bmatrix} - \begin{bmatrix} 0 \\ f_{cA} \\ f_{cB} \\ 0 \end{bmatrix}$$

(8.6)

Substituting (8.4) into (8.6) gives:

$$\begin{bmatrix} 4e6 & -2e6 & 0 & 0 \\ -2e6 & 2e6 & 0 & 0 \\ 0 & 0 & 2e6 & -2e6 \\ 0 & 0 & -2e6 & 4e6 \end{bmatrix} \begin{bmatrix} u_1 \\ u_2 \\ u_3 \\ u_4 \end{bmatrix} - \omega^2 \begin{bmatrix} 200 & 0 & 0 & 0 \\ 0 & 200 & 0 & 0 \\ 0 & 0 & 200 & 0 \\ 0 & 0 & 0 & 200 \end{bmatrix} \begin{bmatrix} u_1 \\ u_2 \\ u_3 \\ u_4 \end{bmatrix}$$

$$= \begin{bmatrix} 60 \\ 0 \\ 0 \\ 0 \end{bmatrix} - \begin{bmatrix} 0 & 0 & 0 & 0 \\ 0 & 2e6 & -2e6 & 0 \\ 0 & -2e6 & 2e6 & 0 \\ 0 & 0 & 0 & 0 \end{bmatrix} \begin{bmatrix} u_1 \\ u_2 \\ u_3 \\ u_4 \end{bmatrix}$$

(8.7)

Shifting the $\begin{bmatrix} 0 & 0 & 0 & 0 \\ 0 & 2e6 & -2e6 & 0 \\ 0 & -2e6 & 2e6 & 0 \\ 0 & 0 & 0 & 0 \end{bmatrix} \begin{bmatrix} u_1 \\ u_2 \\ u_3 \\ u_4 \end{bmatrix}$ matrix back to the left hand side

of (8.7) gives back the original full assembled equation of motion as the full stiffness matrix is obtained again:

$$\begin{bmatrix} 4e6 & -2e6 & 0 & 0 \\ -2e6 & 2e6 & 0 & 0 \\ 0 & 0 & 2e6 & -2e6 \\ 0 & 0 & -2e6 & 4e6 \end{bmatrix} + \begin{bmatrix} 0 & 0 & 0 & 0 \\ 0 & 2e6 & -2e6 & 0 \\ 0 & -2e6 & 2e6 & 0 \\ 0 & 0 & 0 & 0 \end{bmatrix} = \begin{bmatrix} 4e6 & -2e6 & 0 & 0 \\ -2e6 & 4e6 & -2e6 & 0 \\ 0 & -2e6 & 4e6 & -2e6 \\ 0 & 0 & -2e6 & 4e6 \end{bmatrix} \quad \textbf{(8.8)}$$

So

$$\begin{bmatrix} K_A & 0 \\ 0 & K_B \end{bmatrix} + \begin{bmatrix} 0 & 0 & 0 \\ 0 & K_{conn} & 0 \\ 0 & 0 & 0 \end{bmatrix} = K_{AB} \quad \textbf{(8.9)}$$

Where K_{ab} is the full stiffness matrix of subsystem A coupled to subsystem B.

8.3 Proposed Reduction Technique

Through the example in section 8.2 it has been demonstrated that the dynamic behaviour of two coupled substructures can be considered a superposition of the substructures' individual uncoupled response to the excitation forces and the substructures uncoupled response to the coupling forces generated in the coupling elements as a result of dynamic interaction between two adjacent substructures.

Through this principle the interaction between two individual subsystems is described through which a smaller reduction basis can be formulated compared to the classical CMS methods. An important aspect in obtaining this much smaller reduction basis is that a modal approach is adopted. Through the description of the coupling outlined above, no additional nodal displacement of the coupling points

need to be included in the reduction basis, as the coupling can be fully described through the modal coordinates that are also used to describe the internal displacement field of the substructures. The reduction basis used for this CMS method will therefore be a set of retained mode shapes for the substructures involved as will be demonstrated below for an un-damped mass spring system. For two individual uncoupled sub systems the following equations can be written:

$$(-\omega^2 M_A \phi_A + K_B \phi_A) a_A = f_A \quad \textbf{(8.10)}$$

$$(-\omega^2 M_B \phi_B + K_B \phi_B) a_B = f_B \quad \textbf{(8.11)}$$

Where:

ϕ_A and ϕ_B are the set of eigenvectors representing the retained (free interface) mode shapes for all degrees of freedom of subsystem A and B respectively.

M_A and M_B are the uncoupled free floating mass matrices of substructure A and B respectively and ω is the frequency of excitation in rad/sec.

K_A and K_B are the uncoupled free floating stiffness matrices of substructure A and B respectively

f_A and f_B are the excitation forces acting on substructure A and B respectively

a_A and a_B are the modal coordinates of the retained mode shapes of substructure A and B respectively

Composing the equation of motion of the coupled system is done according to equation (8.5). Expressed through a limited set of retained mode shapes and the corresponding modal coordinates:

$$-\omega^2 \begin{bmatrix} M_A & 0 \\ 0 & M_B \end{bmatrix} \begin{bmatrix} \phi_A & 0 \\ 0 & \phi_B \end{bmatrix} \begin{bmatrix} a_A \\ a_B \end{bmatrix} + \begin{bmatrix} K_A & 0 \\ 0 & K_B \end{bmatrix} \begin{bmatrix} \phi_A & 0 \\ 0 & \phi_B \end{bmatrix} \begin{bmatrix} a_A \\ a_B \end{bmatrix} = \quad \textbf{(8.12)}$$

$$\begin{bmatrix} f_A \\ f_B \end{bmatrix} - \begin{bmatrix} 0 & 0 & 0 \\ 0 & K_{conn} & 0 \\ 0 & 0 & 0 \end{bmatrix} \begin{bmatrix} \phi_A & 0 \\ 0 & \phi_B \end{bmatrix} \begin{bmatrix} a_A \\ a_B \end{bmatrix}$$

Where:

K_{conn} = the stiffness matrix of the coupling elements between substructure A and B

Reduction of the stiffness and mass matrix is obtained by pre multiplying with ϕ^T, as also applied with the mode superposition method, which gives:

$$-\omega^2 \begin{bmatrix} {\phi_A}^T & 0 \\ 0 & {\phi_B}^T \end{bmatrix} \begin{bmatrix} M_A & 0 \\ 0 & M_B \end{bmatrix} \begin{bmatrix} \phi_A & 0 \\ 0 & \phi_B \end{bmatrix} \begin{bmatrix} a_A \\ a_B \end{bmatrix} + \begin{bmatrix} {\phi_A}^T & 0 \\ 0 & {\phi_B}^T \end{bmatrix} \begin{bmatrix} K_A & 0 \\ 0 & K_B \end{bmatrix} \begin{bmatrix} \phi_A & 0 \\ 0 & \phi_B \end{bmatrix} \begin{bmatrix} a_A \\ a_B \end{bmatrix}$$
$$= \begin{bmatrix} {\phi_A}^T & 0 \\ 0 & {\phi_B}^T \end{bmatrix} \begin{bmatrix} f_A \\ f_B \end{bmatrix} - \begin{bmatrix} {\phi_A}^T & 0 \\ 0 & {\phi_B}^T \end{bmatrix} \begin{bmatrix} 0 & 0 & 0 \\ 0 & K_{conn} & 0 \\ 0 & 0 & 0 \end{bmatrix} \begin{bmatrix} \phi_A & 0 \\ 0 & \phi_B \end{bmatrix} \begin{bmatrix} a_A \\ a_B \end{bmatrix} \quad \textbf{(8.13)}$$

and moving $\begin{bmatrix} {\phi_A}^T & 0 \\ 0 & {\phi_B}^T \end{bmatrix} K_{conn} \begin{bmatrix} \phi_A & 0 \\ 0 & \phi_B \end{bmatrix} \begin{bmatrix} a_A \\ a_B \end{bmatrix}$ to the left side of the equation gives the reduced mass and stiffness matrices $\widetilde{M}$ and $\widetilde{K}$ of the total assembled system:

$$\bar{M} = \begin{bmatrix} {\phi_A}^T & 0 \\ 0 & {\phi_B}^T \end{bmatrix} \begin{bmatrix} M_A & 0 \\ 0 & M_B \end{bmatrix} \begin{bmatrix} \phi_A & 0 \\ 0 & \phi_B \end{bmatrix} \quad \textbf{(8.14)}$$

$$\bar{K} = \left\{ \begin{bmatrix} {\phi_A}^T & 0 \\ 0 & {\phi_B}^T \end{bmatrix} \begin{bmatrix} K_A & 0 \\ 0 & K_B \end{bmatrix} \begin{bmatrix} \phi_A & 0 \\ 0 & \phi_B \end{bmatrix} + \begin{bmatrix} {\phi_A}^T & 0 \\ 0 & {\phi_B}^T \end{bmatrix} \begin{bmatrix} 0 & 0 & 0 \\ 0 & K_{conn} & 0 \\ 0 & 0 & 0 \end{bmatrix} \begin{bmatrix} \phi_A & 0 \\ 0 & \phi_B \end{bmatrix} \right\} \quad \textbf{(8.15)}$$

As pointed out in section 8.2 equation (8.7) and (8.8) through equation

$\begin{bmatrix} K_A & 0 \\ 0 & K_B \end{bmatrix} + \begin{bmatrix} 0 & 0 & 0 \\ 0 & K_{conn} & 0 \\ 0 & 0 & 0 \end{bmatrix} = K_{AB}$ which is equal to the full matrix of the assembled substructures, (8.15) can also be written as :

$$\bar{K} = \begin{bmatrix} {\phi_A}^T & 0 \\ 0 & {\phi_B}^T \end{bmatrix} K_{AB} \begin{bmatrix} \phi_A & 0 \\ 0 & \phi_B \end{bmatrix} \quad \textbf{(8.16)}$$

If a consistent mass matrix is used and the coupling elements have a mass, the effect of the extra mass on the interface lines is also modelled as an external excitation force. The equation of motion becomes:

$$-\omega^2 \begin{bmatrix} M_A & 0 \\ 0 & M_B \end{bmatrix} \begin{bmatrix} \phi_A & 0 \\ 0 & \phi_B \end{bmatrix} \begin{bmatrix} a_A \\ a_B \end{bmatrix} + \begin{bmatrix} K_A & 0 \\ 0 & K_B \end{bmatrix} \begin{bmatrix} \phi_A & 0 \\ 0 & \phi_B \end{bmatrix} \begin{bmatrix} a_A \\ a_B \end{bmatrix}$$
$$= \begin{bmatrix} f_A \\ f_B \end{bmatrix} - K_{conn} \begin{bmatrix} \phi_A & 0 \\ 0 & \phi_B \end{bmatrix} \begin{bmatrix} a_A \\ a_B \end{bmatrix} + \omega^2 M_{conn} \begin{bmatrix} \phi_A & 0 \\ 0 & \phi_B \end{bmatrix} \begin{bmatrix} a_A \\ a_B \end{bmatrix} \quad \textbf{(8.17)}$$

The reduced mass matrix becomes:

$$\bar{M} = \left\{ \begin{bmatrix} \phi_A{}^T & 0 \\ 0 & \phi_B{}^T \end{bmatrix} \begin{bmatrix} M_A & 0 \\ 0 & M_B \end{bmatrix} \begin{bmatrix} \phi_A & 0 \\ 0 & \phi_B \end{bmatrix} + \begin{bmatrix} \phi_A{}^T & 0 \\ 0 & \phi_B{}^T \end{bmatrix} M_{conn} \begin{bmatrix} \phi_A & 0 \\ 0 & \phi_B \end{bmatrix} \right\} \quad \textbf{(8.18)}$$

In the same way as for the reduced stiffness matrix the reduced mass matrix can also be written as

$$\bar{M} = \begin{bmatrix} \phi_A{}^T & 0 \\ 0 & \phi_B{}^T \end{bmatrix} M_{AB} \begin{bmatrix} \phi_A & 0 \\ 0 & \phi_B \end{bmatrix} \quad \textbf{(8.19)}$$

Where M_{AB} which is the full matrix of the assembled substructures

8.4 The Zoet Method with Boundary Residual Flexibility

An alternative reduction technique is proposed in section 8.3 in order to eliminate the need to set up equations for each coupling degree of freedom. Coupling is only described through the response normal modal coordinates (rigid body and elastic modes) of the free interface substructures. This line of research has been chosen because the number of mode shapes required to describe the dynamic behaviour of a structure accurately enough, is for ship structures expected to be much lower than the number of coupling degrees of freedom, as was found the case for the CMS simulations for the LNG carrier presented in section 7 (see Table 3).

In this section a mathematical reformulation of the principles described in 8.3 is suggested. Through this formulation the reduced set of equations of motion is obtained by only using the interface degrees of freedom's mode shape vector values whereas the reduction basis presented in section 8.3 consist of the mode shapes with all the degrees of freedom of the substructures retained. Through this method, the formulation of the reduced equations of motion requires less matrix operations.

In addition, also the possibility of including interface (boundary) residual flexibility is included in this alternative formulation. The reason for adding residual boundary flexibility is because calculated alternating element stresses are very sensitive to errors in calculation of the displacement field. This means that a small deviation of calculated displacement may result in a much bigger deviation of the related element

stresses, and the related nodal stiffness forces. (also been described in [39]). Accurate calculation of reaction forces in nodes resulting from element deformation is very important for describing the interface forces between two substructures, resulting from dynamic interaction. Through including boundary (interface) residual flexibility a more accurate description of the boundary response is obtained.

In Appendix XVIII the process of generating the equations of motion and obtaining the dynamic response of two coupled structures is described in different steps. Step 1 in this analysis consists of obtaining the modes shapes. Appendix XVIII describes in step 1 how the boundary residual flexibility modes are calculated, together with an expression for the number of required real matrix operations (FLOPS) required for each step. The equations formulated in step 2 are derived from a reformulation of equation (8.20) (see equation (8.5)):

$$\begin{bmatrix} K_A & 0 \\ 0 & K_B \end{bmatrix} \begin{bmatrix} u_A \\ u_B \end{bmatrix} - \omega^2 \begin{bmatrix} M_A & 0 \\ 0 & M_B \end{bmatrix} \begin{bmatrix} u_A \\ u_B \end{bmatrix} = \begin{bmatrix} f_A \\ f_B \end{bmatrix} - \begin{bmatrix} 0 & 0 & 0 \\ 0 & K_{conn} & 0 \\ 0 & 0 & 0 \end{bmatrix} \begin{bmatrix} u_A \\ u_B \end{bmatrix} \quad \textbf{(8.20)}$$

The equations have been formulated in such a way that they very explicitly express the response of the assembled structure as a superposition of the individual uncoupled response (a_0 and u_{0res}) (excited by external forces f_A and f_B only) and the response of the individual substructures due to the interface forces (a_{BF} and $u_{bres,BF}$): These interface forces are indicated with forces f_{cA} and f_{cB} (connection or interface forces) and represent the effect of interaction between two adjacent substructures

Where

a_0 are the normal modal participation factors (modal coordinates) of a substructure representing the modal response of the individual uncoupled substructure that is only subjected by the external excitation force.

u_{0res} is the residual displacement vector representing the residual response of the individual uncoupled substructure that is only subjected by the external excitation force.

a_{BF} are the normal modal participation factors (modal coordinates) of a substructure representing the modal response of the individual uncoupled substructure subjected to the interface forces occurring due to interaction with another substructure.

$u_{bres,BF}$ is the residual displacement vector representing the residual response of a individual uncoupled substructure subjected only to the interface forces occurring due to interaction with another substructure.

The total response vector u of a coupled substructure is written as:

$$u = u_0 + u_{bBF} \tag{8.21}$$

Where u_0 is the displacement vector of a uncoupled substructure subjected by the external excitation force only and u_{bBF} is the response of a substructure to the interface forces resulting from interaction with adjacent sub structures.

$\alpha = \begin{bmatrix} a_A \\ a_B \\ u_{Ares} \\ u_{Bres} \end{bmatrix}$ = modal response vector of assembled substructure

$\alpha_{BF} = \begin{bmatrix} a_{A,BF} \\ a_{B,BF} \\ u_{Abres,BF} \\ u_{Bbres,BF} \end{bmatrix}$ = modal response vector due to interface forces resulting from interaction with adjacent sub-structures

$\alpha_0 = \begin{bmatrix} a_{0A} \\ a_{0B} \\ u_{0Ares} \\ u_{0Bres} \end{bmatrix}$ = modal response vector of the individual uncoupled sub structures due to excitation forces. Modal participation vector representing the dynamic behaviour of the total assembled structure writes as:

$$\alpha = \alpha_{BF} + \alpha_0 = \begin{bmatrix} a_A \\ a_B \\ u_{Ares} \\ u_{Bres} \end{bmatrix} = \begin{bmatrix} a_{A,BF} \\ a_{B,BF} \\ u_{Abres,BF} \\ u_{Bbres,BF} \end{bmatrix} + \begin{bmatrix} a_{0A} \\ a_{0B} \\ u_{0Ares} \\ u_{0Bres} \end{bmatrix} \tag{8.22}$$

Where:

- a_A and a_B are the complex rigid body and flexible modal coordinates of substructure A and B respectively representing the response of the assembled structure.
- u_{Ares} and u_{Bres} are the complex residual displacements of substructure A and B respectively representing the residual response of the assembled structure.
- a_{0A} and a_{0B} are the complex rigid body and flexible modal coordinates of substructure A and B representing the structural dynamic behaviour of the individual structures in uncoupled condition
- u_{0Ares} and u_{0Bres} are the complex residual interface node displacements of substructure A and B representing the structural dynamic behaviour of the individual structures in uncoupled condition
- $a_{A,BF}$ and $a_{B,BF}$ are the complex rigid body and flexible modal coordinates of substructure A and B respectively representing the response resulting from forces on the interfaces with adjacent substructures resulting from dynamic interaction..
- $u_{Abres,BF}$ and $u_{Bbres,BF}$ are the complex residual interface node displacements of substructure A and B respectively representing the residual (static) response resulting from forces on the interfaces with adjacent substructures resulting from dynamic interaction..

The important part of this formulation is the formulation of the interface forces. These interface forces are a function of the interface displacement and the stiffness and mass matrix of the connecting interface elements. Through the displacement of the interface nodes the coupling elements deformation is represented resulting in the reaction forces at the coupling nodes.

As explained above, the displacement field of the substructures is described by the modal coordinates of the individual uncoupled structures. Three types of modal coordinates are distinguished:

- flexible (free interface) modal coordinates
- rigid body modal coordinates (if applicable)

- residual compensation attachment modal coordinates (expressed through the nodal interface displacements u_b)

The interface displacement u_b is described as a superposition of normal, rigid and residual flexibility modes and is written as (see also equation (8.22)) :

$$u_b = \begin{bmatrix} \phi_{Abnormal} & 0 & I & 0 \\ 0 & \phi_{Bbnormal} & 0 & I \end{bmatrix} \begin{bmatrix} a_A \\ a_B \\ u_{Aresb} \\ u_{Bresb} \end{bmatrix} \quad \textbf{(8.23)}$$

Where:

- $\phi_{Abnormal}$ and $\phi_{Bbnormal}$= matrix containing the retained rigid body and elastic modes of substructure A and B respectively representing only the interface degrees of freedom between substructure A and B.
- u_{Aresb} and u_{Bresb} are the residual nodal displacements representing the residual response of the assembled structure representing only the interface degrees of freedom between substructure A and B.
- $\begin{bmatrix} \phi_{Abnormal} & 0 & I & 0 \\ 0 & \phi_{Bbnormal} & 0 & I \end{bmatrix} = R$ is the reduction matrix.
- a_A and a_B are the normal nodal coordinates representing the modal response of substructure A and B coupled together

Therefore (8.23) can be written as (see also equations (8.21)):

$$u_b = R\alpha \quad \textbf{(8.24)}$$

Where α is

$$\begin{bmatrix} a_A \\ a_B \\ u_{Aresb} \\ u_{Bresb} \end{bmatrix}$$

, representing the normal modal coordinates and the residual displacement coordinates of the interface degrees of freedom. For the boundary (interface) element forces we can write, according to equation (8.4):

$$\begin{bmatrix} f_{cA} \\ f_{cB} \end{bmatrix} = F_{conn} = -(K_{conn} + \omega C_{conn} i - \omega^2 M_{conn}) u_b \quad \textbf{(8.25)}$$

$$F_{conn} = -K_{dyn\,conn} u_b$$

Where

- K_{conn} and M_{conn} are the stiffness and mass matrix respectively of the connecting elements
- C_{conn} is the dampings factor of the connecting elements
- i is indication for the fact that ωC_{conn} is an imaginary component (90 degrees phase shift relatively to strain and inertia forces)
- ω is the excitation frequency [rad/s]
- $K_{dyn\,conn} = (K_{conn} + \omega C_{conn} i - \omega^2 M_{conn})$ = the dynamic interface elements stiffness matrix.
- F_{conn} is the vector representing all the forces from the connection element deformation (forces on both substructure A interface nodes f_{cA} and substructure B interface nodes f_{cB}.

Substituting equation (8.23) into equation (8.25) we get the expression for the connection node forces as a function of the modal coordinates representing the dynamic behaviour of the assembled structure:

$$F_{conn} = -K_{dyn\,conn} \begin{bmatrix} \phi_{Abnormal} & 0 & I & 0 \\ 0 & \phi_{Bbnormal} & 0 & I \end{bmatrix} \begin{bmatrix} a_A \\ a_B \\ u_{Aresb} \\ u_{Bresb} \end{bmatrix} \quad \textbf{(8.26)}$$

For the modal response coordinates resulting from the interface forces we can write, as a function of excitation force (see equation (8.22) and (6.27)):

$$a_{A,BF} = \frac{\phi_{Abnormal}{}^T f_{cA}}{(-\omega^2 + \varepsilon {\omega_{0A}}^2 \mathrm{i} + {\omega_{0A}}^2)} \quad \textbf{(8.27)}$$

$$a_{B,BF} = \frac{\phi_{Bbnormal}{}^T f_{cB}}{(-\omega^2 + \varepsilon {\omega_{0B}}^2 \mathrm{i} + {\omega_{0B}}^2)}$$

$$u_{Aresb} = G_{Aresb} f_{cA} \quad \textbf{(8.28)}$$

$u_{Bresb} = G_{Bresb} f_{cB}$

In a matrix notation the modal displacement due to interface node interaction forces α_{BF} is written as:

$$\alpha_{BF} = \begin{bmatrix} diag(-\omega^2 + \varepsilon {\omega_0}^2 \mathrm{i} + {\omega_0}^2)^{-1} & 0 \\ 0 & G_{resb} \end{bmatrix} \begin{bmatrix} \phi_{Abnormal} & 0 & I & 0 \\ 0 & \phi_{Bbnormal} & 0 & I \end{bmatrix}^T F_{conn} \quad \textbf{(8.29)}$$

Where:

- $diag(-\omega^2 + \varepsilon {\omega_0}^2 \mathrm{i} + {\omega_0}^2)^{-1} =$
  $\begin{bmatrix} diag(-\omega^2 + \varepsilon {\omega_{0A}}^2 \mathrm{i} + {\omega_{0A}}^2)^{-1} & 0 \\ 0 & diag(-\omega^2 + \varepsilon {\omega_{0B}}^2 \mathrm{i} + {\omega_{0B}}^2)^{-1} \end{bmatrix}$
- $G_{resb} = \begin{bmatrix} G_{Aresb} & 0 \\ 0 & G_{Bresb} \end{bmatrix}$
- G_{Aresb} and G_{Bresb}= the residual flexibility matrix for the interface degrees of freedom of substructure A and B respectively
- ω_{0A} and ω_{0B} are the natural frequencies of the retained elastic and rigid modes for substructure A and B respectively [rad/s]
- ω is the excitation frequency [rad/s]
- ε = damping expressed as a percentage of the strain energy (loss number)
- $\begin{bmatrix} \phi_{Abnormal} & 0 & I & 0 \\ 0 & \phi_{Bbnormal} & 0 & I \end{bmatrix}^T = R^T$ is the transposed reduction matrix used in this method.
- f_{cA} is the interface reaction forces at the interface degrees of freedom of substructure A
- f_{cB} is the interface reaction forces at the interface degrees of freedom of substructure B
- F_{conn} = total interface degrees of freedom reaction force vector $\begin{bmatrix} f_{cA} \\ f_{cB} \end{bmatrix}$

Substituting equation (8.26) into equation (8.27) and (8.28) gives the following expression is obtained:

$$\alpha_{BF} = \begin{bmatrix} diag(-\omega^2 + \varepsilon{\omega_0}^2\mathrm{i} + {\omega_0}^2)^{-1} & 0 \\ 0 & G_{resb} \end{bmatrix} [R]^T F_{conn} = \begin{bmatrix} \boldsymbol{a_{A,BF}} \\ \boldsymbol{a_{B,BF}} \\ \boldsymbol{u_{Aresb,BF}} \\ \boldsymbol{u_{Bresb,BF}} \end{bmatrix} \quad \textbf{(8.30)}$$

Considering expression (8.26) for the connection forces:

$$F_{conn} = -[K_{dyn\ conn}][R] \begin{bmatrix} a_A \\ a_B \\ u_{Aresb} \\ u_{Bresb} \end{bmatrix} = -[K_{dyn\ conn}][R]\alpha \quad \textbf{(8.31)}$$

Substituting (8.31) into (8.30) gives the expression for the contribution of the interface force response as a function of the assembled total response:

$$\boldsymbol{\alpha_{BF}} = -\begin{bmatrix} \boldsymbol{diag}(-\boldsymbol{\omega^2} + \boldsymbol{\varepsilon{\omega_0}^2\mathrm{i}} + \boldsymbol{{\omega_0}^2})^{-1} & \boldsymbol{0} \\ \boldsymbol{0} & \boldsymbol{G_{resb}} \end{bmatrix} [\boldsymbol{R}]^T [\boldsymbol{K_{dyn\ conn}}][\boldsymbol{R}] \begin{bmatrix} \boldsymbol{a_A} \\ \boldsymbol{a_B} \\ \boldsymbol{u_{Aresb}} \\ \boldsymbol{u_{Bresb}} \end{bmatrix} = \begin{bmatrix} \boldsymbol{a_{A,BF}} \\ \boldsymbol{a_{B,BF}} \\ \boldsymbol{u_{Aresb,BF}} \\ \boldsymbol{u_{Bresb,BF}} \end{bmatrix}$$

$$\alpha_{BF} = A\alpha = \begin{bmatrix} a_{A,BF} \\ a_{B,BF} \\ u_{Aresb,BF} \\ u_{Bresb,BF} \end{bmatrix}$$

$$A = -\begin{bmatrix} diag(-\omega^2 + \varepsilon{\omega_0}^2\mathrm{i} + {\omega_0}^2)^{-1} & 0 \\ 0 & G_{resb} \end{bmatrix} [R^T][K_{dyn\ conn}][R] \quad \textbf{(8.32)}$$

The total equation for solving $\boldsymbol{\alpha} = \begin{bmatrix} \boldsymbol{a_A} \\ \boldsymbol{a_B} \\ \boldsymbol{u_{Aresb}} \\ \boldsymbol{u_{Bresb}} \end{bmatrix}$ is written as:

$\alpha_0 + A\alpha = \alpha$ and therefore:

$[A - I]\alpha = -\alpha_0$ **(8.33)**

Substituting $\alpha = \begin{bmatrix} a_A \\ a_B \\ u_{Abres} \\ u_{Bbres} \end{bmatrix}$ into (8.23) gives the total deflection vector:

$$u = \begin{bmatrix} \phi_{Anormal} & 0 & \phi_A^c & 0 \\ 0 & \phi_{Bnormal} & 0 & \phi_B^c \end{bmatrix} \begin{bmatrix} a_A \\ a_B \\ u_{Aresb} \\ u_{Bresb} \end{bmatrix}$$

Where:

$\phi_{Anormal}$ and $\phi_{Bnormal}$ are matrices containing the retained normal modes representing all degrees of freedom of substructure A and B respectively.

ϕ_A^c and ϕ_B^c are the constraint modes of substructure A and B respectively (see equation (6.37) to (6.42)

$[A]$ is the boundary mobility matrix as this matrix expresses the sensitivity of the interface to the deformation of the interface elements (interface forces).

A reduction of matrix operations for composing the boundary mobility matrix is obtained through neglecting the inertia force term in the dynamic mass matrix of the interface elements. This term will be very small anyway, particularly at low frequencies. The dynamic interface stiffness will become $(K_{conn} + \omega C_{conn} i) = K_{dyn\ conn}$. If relative damping ε is used, as is the case in this work, the expression for the dynamic stiffness of the interface elements becomes independent of frequency and becomes $(K_{conn} + \varepsilon K_{conn} i)$

This means that step 2A to 2C in Appendix XVIII only need to be performed once, and not for every frequency step. As a consequence, in step 2C, the mobility matrix *A* does not need to be recalculated completely for each frequency step. As the response of boundary flexibility modes to a specific force is frequency independent, only the left upper $n_n \times n_n$ part of the $\begin{bmatrix} diag(-\omega^2 + \varepsilon {\omega_0}^2 \mathrm{i} + {\omega_0}^2)^{-1} & 0 \\ 0 & G_{resb} \end{bmatrix}$ matrix is frequency dependent. This means that only the first n_n rows of the mobility matrix need to be recalculated for each frequency step (where $n_n$is the number of normal modes retained for substructure *A* plus the number of normal modes retained for substructure *B*).

8.5 Eliminating Residual Flexibility Modes from the Zoet Method

As discussed in the critical review, one of the problems with component mode synthesis is the density of the reduced matrices representing the modal equation of motion. Ship sections are connected to each other through many lines which means

that the final element model of these sections as substructures, contain a high number of coupling nodes. As the classic CMS techniques are based on describing the interaction between two substructures through formulating compatibility and equilibrium relations for each coupling degree of freedom, a relatively high number of equations may still be required.

An alternative reduction technique is proposed in section 8.3 in order to eliminate the need to set up equations for each coupling degree of freedom. Coupling is only described through the response modal coordinates. This line of research has been chosen because the number of mode shapes required to describe the dynamic behaviour of a structure accurately enough, is for ship structures expected to be much lower than the number of coupling degrees of freedom, as was found the case for the CMS simulations for the LNG carrier presented in section 7 (see Table 3).

However, if including interface residual flexibility should be required, again the need arises to include all the degrees of freedom of all coupling nodes into the total set of equations of motion, as demonstrated in section. As an accurate description of the coupling forces is related to an accurate description of stain forces, the results of the total assembled dynamic behaviour calculations are very sensitive to errors in the description of the coupling node displacements (also been described in [39]). A description of the dynamic behaviour of two coupled substructures is given in section 8.4 that accommodates for interface residual flexibility to be taken into account.

However, by including boundary flexibility modes, a formulation of interaction between substructures has been obtained again that requires a number of equations that has to exceed the number of interface degrees of freedom.

In this section a technique is proposed for eliminating the boundary flexibility modes, and reducing the required number of equation back to the number of required normal mode shapes. The interaction between two substructures is again, as in section 8.3, described only through the modal coordinates of the normal modes. In the method suggested in this section, the effect of residual compensation has been incorporated into the description of interaction between modal coordinates i.e., into the boundary mobility matrix $[A]$.

8.5.1 Compiling the Total Boundary Mobility Matrix

The first step in obtaining reduction in the number of total assembled equation of motion is by formulating boundary mobility matrices $[A]$ for individual coupled pairs of substructures. Each coupled pair of substructures form a super element.

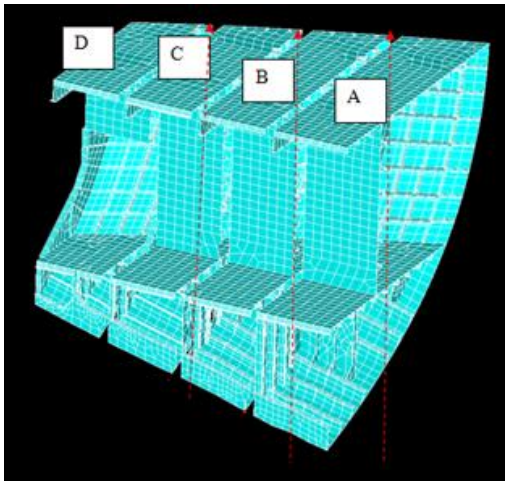

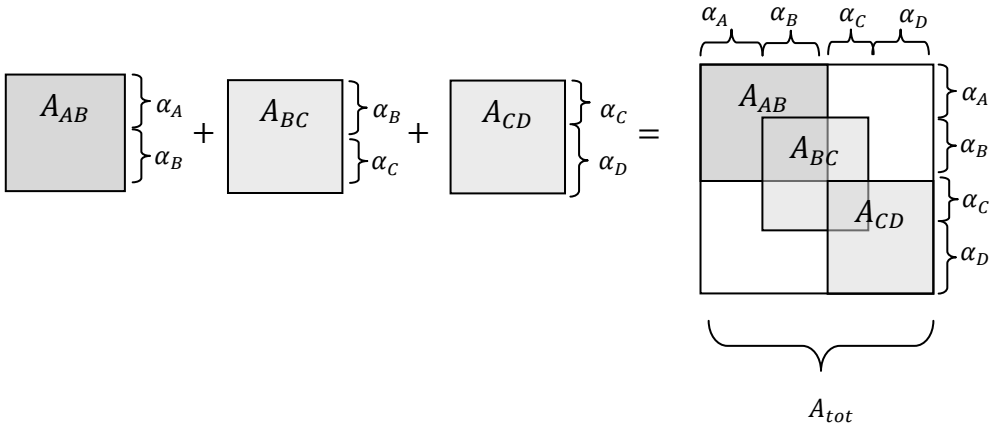

Where:

A_{AB} is the mobility matrix for substructure A and B coupled together

A_{BC} is the mobility matrix for substructure B and C coupled together

A_{CD} is the mobility matrix for substructure C and D coupled together

A_{tot} is the mobility matrix for all substructures added together

Figure 60 ***Demonstration of formulation of the total boundary mobility matrix***

The boundary mobility matrix, reflecting the behaviour of interface boundaries when all substructures are coupled, is obtained through adding all the boundary mobility matrices of all the pairs of substructures (super elements) into one matrix. Adding the super elements to from the total boundary mobility matrix is done in a similar way as done with the formulation of a total assembled stiffness or mass matrices through the stiffness matrices of individual elements with classical finite element modelling.

Figure 60 shows an example of a structure sub divided in four substructures A, B, C and D. The figure shows how boundary mobility matrices of pairs of substructures (i.e. interaction matrices between pairs of substructures) are used to form the total boundary mobility matrix reflecting the interaction between the substructures all coupled together.

The strategy of the approach is to eliminate the interface displacement degrees of freedom related to the residual flexibility modes of the boundary mobility matrices of the individual pairs of substructures (A_{AB} A_{BC} A_{CD}) by using a similar technique used with the static condensation according to Guyan (see equation (6.37) to (6.42)). With these reduced matrices the total assembled boundary mobility matrix A_{tot} is formulated as demonstrated in Figure 60. The total equation of motion is then formulated according to equation (8.33):

$$[A_{tot} - I]\alpha = -\alpha_0$$

Where α has become a vector representing only the modal coordinates of all the individual substructures.

8.5.2 Eliminating Interface Displacement Degrees of Freedom

Consider the boundary mobility matrix A_{AB} of two substructures, substructure A and substructure B. According to (8.33), the modal coordinates and interface displacements vector α is solved from the following equation:

$[A_{AB} - I]\alpha = -\alpha_0$

Where

$$\alpha = \begin{bmatrix} a_A \\ a_B \\ u_{Aresb} \\ u_{Bresb} \end{bmatrix} \text{ and } \alpha_0 = \begin{bmatrix} a_{0A} \\ a_{0B} \\ u_{0Aresb} \\ u_{0Bresb} \end{bmatrix}$$

$[A_{AB} - I]$, is divided in sections in such a way that the modal amplitudes are grouped and separated from the nodal interface node displacements which represent the residual compensation:

$$\begin{bmatrix} A_{aa} & \vdots & A_{au} \\ \cdots & \vdots & \cdots \\ A_{ua} & \vdots & A_{uu} \end{bmatrix} \begin{bmatrix} a_A \\ a_B \\ \cdots \\ u_{Aresb} \\ u_{Bresb} \end{bmatrix} = - \begin{bmatrix} a_{0A} \\ a_{0B} \\ \cdots \\ u_{0Aresb} \\ u_{0Bresb} \end{bmatrix} \quad \textbf{(8.34)}$$

A description of the equation of the interaction between two structures is now formulated based on only the modal coordinates, eliminating the degrees of freedom of equation (8.34) related to the residual interface displacement at the interface degrees of freedom. In Appendix XVIII the process used to achieve this is listed as a sequence of different steps (see step 4A to 4G).

Through the lower line in equation (8.34) the relation between the residual compensation deflections (u_{Aresb} and u_{Bresb}) and the normal modal coordinates of the normal modal coordinates (a_A and a_B containing both rigid body and elastic) is obtained:

$$[A_{ua}] \begin{bmatrix} a_A \\ a_B \end{bmatrix} + [A_{uu}] \begin{bmatrix} u_{Aresb} \\ u_{Bresb} \end{bmatrix} = - \begin{bmatrix} u_{0Aresb} \\ u_{0Bresb} \end{bmatrix}$$

$$\begin{bmatrix} u_{Aresb} \\ u_{Bresb} \end{bmatrix} = [A_{uu}]^{-1} \left\{ - \begin{bmatrix} u_{0Aresb} \\ u_{0Bresb} \end{bmatrix} - [A_{ua}] \begin{bmatrix} a_A \\ a_B \end{bmatrix} \right\} \quad \textbf{(8.35)}$$

$$\begin{bmatrix} u_{Aresb} \\ u_{Bresb} \end{bmatrix} = -[A_{uu}]^{-1} \begin{bmatrix} u_{0Aresb} \\ u_{0Bresb} \end{bmatrix} - [A_{uu}]^{-1} [A_{ua}] \begin{bmatrix} a_A \\ a_B \end{bmatrix}$$

The new matrix only containing the modal amplitudes as a variable is formulated by substituting (8.35) into the first line of (8.34):

$$[A_{aa}] \begin{bmatrix} a_A \\ a_B \end{bmatrix} + [A_{au}] \begin{bmatrix} u_{Aresb} \\ u_{Bresb} \end{bmatrix} = - \begin{bmatrix} a_{0A} \\ a_{0B} \end{bmatrix} \quad \textbf{(8.36)}$$

Substituting (8.35) into (8.36) gives:

$$[A_{aa}]\begin{bmatrix}a_A\\a_B\end{bmatrix} - [A_{au}]\left[[A_{uu}]^{-1}\begin{bmatrix}u_{0Ares}\\u_{0Bres}\end{bmatrix} + [A_{uu}]^{-1}[A_{ua}]\begin{bmatrix}a_A\\a_B\end{bmatrix}\right] = -\begin{bmatrix}a_{0A}\\a_{0B}\end{bmatrix}$$

$$[A_{aa}]\begin{bmatrix}a_A\\a_B\end{bmatrix} - [A_{au}][A_{uu}]^{-1}\begin{bmatrix}u_{0Ares}\\u_{0Bres}\end{bmatrix} - [A_{au}][A_{uu}]^{-1}[A_{ua}]\begin{bmatrix}a_A\\a_B\end{bmatrix} = -\begin{bmatrix}a_{0A}\\a_{0B}\end{bmatrix}$$

$$[A_{aa}]\begin{bmatrix}a_A\\a_B\end{bmatrix} - [A_{au}][A_{uu}]^{-1}[A_{ua}]\begin{bmatrix}a_A\\a_B\end{bmatrix} = -\begin{bmatrix}a_{0A}\\a_{0B}\end{bmatrix} + [A_{au}][A_{uu}]^{-1}\begin{bmatrix}u_{0Ares}\\u_{0Bres}\end{bmatrix} \quad \textbf{(8.37)}$$

The new matrix equation is written as:

$$\left[\tilde{A}_{AB} - I\right]\begin{bmatrix}a_A\\a_B\end{bmatrix} = \begin{bmatrix}\tilde{a}_{0A}\\\tilde{a}_{0B}\end{bmatrix} \quad \textbf{(8.38)}$$

$$\tilde{A}_{AB} - I = [A_{aa}] - [A_{au}][A_{uu}]^{-1}[A_{ua}] \quad \textbf{(8.39)}$$

Where:

$\tilde{A}_{AB}$ is the boundary **modal** mobility matrix expressing the response of the interface between two coupled structures as a function of modal coordinates of normal modes only.

$$\tilde{A}_{AB} = [A_{aa}] - [A_{au}][A_{uu}]^{-1}[A_{ua}] + I \quad \textbf{(8.40)}$$

$$\tilde{A}_{AB} = [A_{aa}] + [A_{res}] + I$$

Where:

A_{res} is the residual boundary modal mobility matrix, written as:

$$A_{res} = -[A_{au}][A_{uu}]^{-1}[A_{ua}] \quad \textbf{(8.41)}$$

Furthermore:

$$\begin{bmatrix}\tilde{a}_{0A}\\\tilde{a}_{0B}\end{bmatrix} = -\begin{bmatrix}a_{0A}\\a_{0B}\end{bmatrix} + [A_{au}][A_{uu}]^{-1}\begin{bmatrix}u_{0Aresb}\\u_{0Bresb}\end{bmatrix} \quad \textbf{(8.42)}$$

Considering the example of Figure 60, the same analysis is repeated to obtain $\tilde{A}_{BC}$, $\tilde{A}_{CD}$. $\tilde{A}_{tot}$ is then compiled with $\tilde{A}_{AB}$, $\tilde{A}_{BC}$, and $\tilde{A}_{CD}$, the number of rows and columns equal to the number of retained normal mode shapes of all individual structures together (see Figure 61).

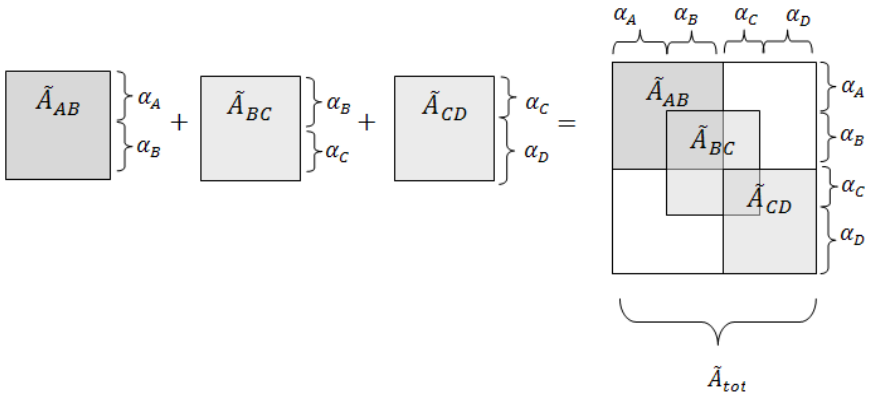

Figure 61 ***Composing the mobility matrix of the total substructure from the mobility matrices formulated from the individual pairs of substructures AB, BC and CD. The mobility matrices reflect the response of the substructure as a function of the normal modal coordinates only, but also include the effect of residual interface flexibility according to equation (8.35) to* (8.40). *See also Figure 60***

In Appendix XVIII the different steps are distinguished in the formulation of A_{res} and correction on $-\alpha_0$. As already discussed in section 8.4, the response of the residual boundary flexibility modes to the interface node loads is independent of the frequency of alternation of these loads. When neglecting the contribution of the interface inertia to the interface node loads, as also suggested in section 8.4, the degrees of freedom of the boundary mobility matrix that are related to the residual flexibility displacements are also frequency independent. This means that step 4A to 4C in Appendix XVIII only needs to be performed once as the resulting matrices remain the same for each frequency step.

8.5.3 Overcompensation of Residual Flexibility

In section 8.5.2 a method is proposed for eliminating the residual interface nodal deflection degrees of freedom from the set of dynamic equations obtained according to Zoet's method. This elimination is based on describing a relation between the residual compensation of the interface degrees of freedom and the normal modal

coordinates and bares resemblance with the formulation of a reduction basis developed by Guyan [49]. The residual compensation thus obtained can be expressed through the modal coordinates only and can be written as described in equation (8.38) to (8.40).

The equations of the total assembled structure involving *n* substructures is generated through adding the equations of the individual substructures, as demonstrated in Figure 61. A total structure consisting of *n* substructures is written as:

$$\left[\sum_{1}^{n-1}\left([\tilde{A}_{xy}]\right) - I\right]\begin{bmatrix}a_A\\a_B\end{bmatrix} = -\sum_{1}^{n-1}\begin{bmatrix}\tilde{a}_{0A}\\\tilde{a}_{0B}\end{bmatrix}$$

$\tilde{A}_{xy}$ is the boundary modal mobility matrix with residual compensation for substructure *x* coupled to substructure *y*.

As $\tilde{A}_{xy} = [A_{aa}] + [A_{res}] + I$ according to equation (8.40), this relation is also expressed as:

$$\left[\sum_{1}^{n-1}\left([[A_{aa}] + [A_{res}] + I]\right) - I\right]\begin{bmatrix}a_A\\a_B\end{bmatrix} = -\sum_{1}^{n-1}\begin{bmatrix}\tilde{a}_{0A}\\\tilde{a}_{0B}\end{bmatrix}$$

From this relation it can be seen that the approach developed above (section 8.5.2) will lead to an overcompensation of residual interface flexibility.

Prove of this is obtained as follows. According to this method, the total residual boundary mobility matrix becomes:

$$\sum_{1}^{n-1}[A_{res}]$$

According to equation (8.41) the thus obtained sum of residual boundary modal motilities of all substructures together is written as:

(8.43)

$$\sum_{1}^{n-1}[A_{res}] = \sum_{1}^{n-1} -[A_{au}][A_{uu}]^{-1}[A_{ua}]$$

The correct residual boundary modal mobility matrix for the full assembled matrix however can be deduced following exactly the same steps as in section 8.5.2, but this time considering the total assembled boundary mobility matrix with all degrees of freedom related to residual interface displacement retained:

$$-\left[\sum_{1}^{n-1} A_{au}\right]\left[\sum_{1}^{n-1} A_{uu}\right]^{-1}\left[\sum_{1}^{n-1} A_{ua}\right] \quad \textbf{(8.44)}$$

The error is generated through the difference in approach to the inverse of the A_{uu} matrix, as

$$\left[\sum_{1}^{n-1} A_{uu}\right]^{-1} \neq \sum_{1}^{n-1} [A_{uu}]^{-1}$$

In which case $[\sum_{1}^{n-1} A_{uu}]^{-1}$ generates a lower number than $\sum_{1}^{n-1} [A_{uu}]^{-1}$

Results obtained from (8.43) are therefore expected to be over compensated. The remedy for that is that more normal modes need to be applied.

8.6 The Rubin–Zoet Method

The method described in 8.5.2 can also be applied on the reduced dynamic stiffness matrix of the full assembled system matrix obtained through Rubin's Method. The skyline of the matrices formulating the reduced equations of motion of two coupled systems A and B according to Rubin looks as follows: (see section 6.5.2.2 for explanation of symbols)

$$A \times \begin{bmatrix} a \\ u_b \end{bmatrix} = \begin{bmatrix} \bar{F} \\ 0 \end{bmatrix}$$

For A representing two coupled systems *A* and *B* we write:

$$A = L^T \begin{bmatrix} {R_A}^T & 0 \\ 0 & {R_B}^T \end{bmatrix} \begin{bmatrix} K_A + C_A\omega - M_A & 0 \\ 0 & K_B + C_B\omega - M_B \end{bmatrix} \begin{bmatrix} R_A & 0 \\ 0 & R_B \end{bmatrix} L$$

In the same way as done in section 8.5.2, an expression for the reduced dynamic mass matrix is obtained:

$$[A_{aa} + A_{res}]\begin{bmatrix} a_A \\ a_B \end{bmatrix} = \begin{bmatrix} \bar{F}_A \\ \bar{F}_B \end{bmatrix} = \bar{F}$$

This expression is obtained in similar way as expressed in section 8.5.2. Consider lower line section of the matrix equation shown in Figure 62:

$$[A_{ua}]a + [A_{uu}]u_b = 0$$

$$u_b = [A_{uu}]^{-1}\{-[A_{ua}]a\} \qquad u_b = -[A_{uu}]^{-1}[A_{ua}]a \tag{8.45}$$

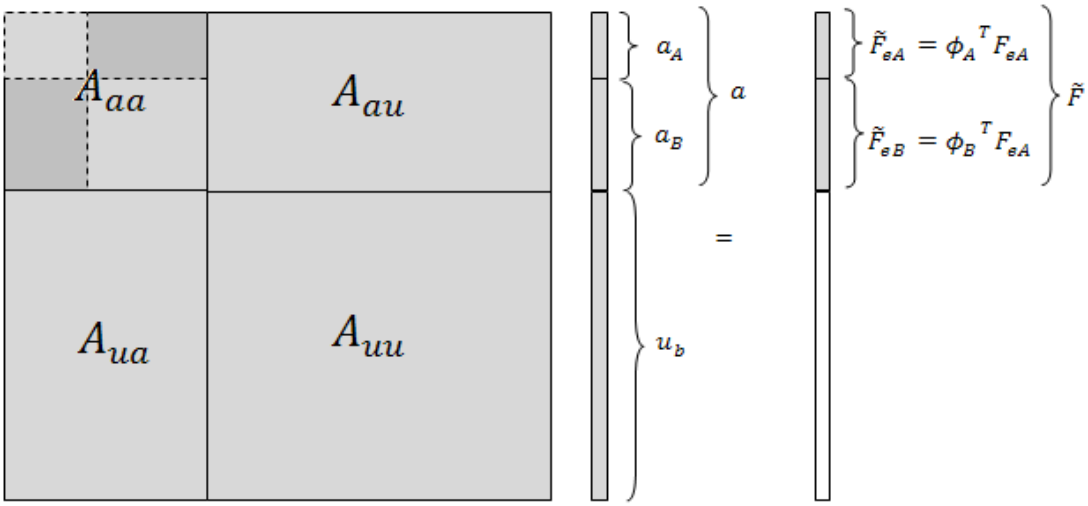

Figure 62 ***Skyline of matrices expressing the equations of motion for two coupled systems according to the Rubin's method***

The new matrix only containing the modal amplitudes as a variable is formulated by substituting (8.45) into the first line of the matrix equation shown in Figure 62:

$$[A_{aa}]a + [A_{au}]u_b = \bar{F} \tag{8.46}$$

$$[A_{aa}]a - [A_{au}][A_{uu}]^{-1}[A_{ua}]a = \bar{F}$$

The new reduced matrix (6.58) is written as:

$$[\tilde{A}]a = \bar{F} \tag{8.47}$$

Where $[\tilde{A}]$ is the reduced dynamic stiffness matrix

$$\tilde{A} = [A_{aa}] - [A_{au}][A_{uu}]^{-1}[A_{ua}] \tag{8.48}$$

$$-[A_{au}][A_{uu}]^{-1}[A_{ua}] = A_{res} \quad \textbf{(8.49)}$$

Where the A_{res} is the residual boundary stiffness matrix

$$[A_{aa} + A_{res}]a = \bar{F} \quad \textbf{(8.50)}$$

$\tilde{A}$ is a full matrix expressing the interaction between substructure A and B as a function of normal modal coordinates of substructure A and B only. The advantage of obtaining $\tilde{A}$ for the Rubin's method instead of for the Zoet method (section 8.4 and section 8.5) is that less matrix operations are required as the operations are performed on matrices containing all retained modal coordinates, but only halve the number of interface degrees of freedom than the Zoet method.

8.7 Comparing Required Calculation Time

In 8.2 to 8.6 new approaches to CMS modelling have been suggested. In this work, many advantages of using CMS methods for ships have been recognised. However, due to the high density of CMS matrices, more computation time is sometimes required for analysing a structure according to the classical CMS equations than for the analysis according to the full harmonic method. The new approaches to CMS in this work have therefore been suggested with the aim of reducing the total required computation times.

In this section the number of matrix operations required for obtaining calculation results for the LNG carrier analysed in section 7 is discussed. The number of matrix operations is a direct indication of the required computation time. The following methods are reviewed and compared for their required number of matrix operations:

- Mode Superposition
- Fixed Interface CMS
- Free Interface CMS
- Zoet method (with and without residual flexibility)
- Rubin-Zoet method (with and without residual flexibility)

8.7.1 Estimating Calculation Time: Floating Point Operations

In Appendix XV to Appendix XIX expression for the number of required floating point operations for each step for the different simulation methods are presented. In Appendix XX to Appendix XXIII the number of matrix operations is presented required, calculated when applying the analysis technique on the LNG carrier, for which simulation results have been presented in section 7 and Appendix VII to Appendix XIII.

Not for each step has the number of required matrix operations been obtained through direct calculation. The number of matrix operations required for solving the eigenvalue problem for obtaining mode shapes and natural frequencies has been obtained through measuring CP times the computer requires for generating the mode shapes and natural frequencies.

Appendix XIV gives an overview of some basic matrix operations and the equations used to estimate the corresponding required number of floating point operations. In Appendix XX to Appendix XXIII the number of real floating point operations (FLOPS) required for each step for the ana;ysis of the LNG carrier is presented, where each arithmetic operation (+,-,*,/) counts as one matrix operation ([48], see also Appendix XIV).

Similar to what has been done in section 7, the number of mode shapes and natural frequencies retained for all the different CMS analysis is based on selecting all mode shapes with corresponding natural frequencies within the frequency range between 0 and 1.5* f_{max} Hz, where f_{max} is the upper limit of the frequency range for which simulation results are generated. The calculated number of floating point operations is, again as in section 7, is based an analysis carried out for 80 frequency steps over a frequency range between 1 and 40 Hz.

In the presentation of the number of the performance of the different methods, the steps in the process are, similar to how ANSYS does it, grouped in two stages: the generation pass and the use pass. The generation pass is the stage in which the

reduced matrices are generated which form the super elements. These super elements are compiled into the total assembled matrix in the Use Pass. In the Use pass the equations are also solved.

8.7.2 Required Number of FLOPS for Zoet's Method

In this section the required number of FLOPS calculated for the Zoet method with and without residual flexibility is presented and compared with the required number of FLOPS for carrying out the same analysis according to the classical Rubin's method, mode superposition and according to the full harmonic analysis. With each method, the estimated required time for producing 80 sets of results for 80 frequencies equally divided between 1 and 40 Hz is presented.

The number of FLOPS for the classic free interface Rubin method (without residual interface flexibility) has been estimated according to Appendix XVI. For a more detailed presentation of calculated number of floating points see Appendix XVI and Appendix XXI.

The number of flops for the full harmonic analysis, and the number of FLOPS required for calculating the normal modes and natural frequencies have been estimated through the measured CP times when carrying out the analysis with ANSYS, as presented in Table 8 (see also section 7).

In Table 8 the properties of the subsystems are presented together with the measured CP time for calculating normal modes with ANSYS according to the Block Lanczos method. Also the measured CP time for the complete generation pass is registered in Table 8.

In Table 9 the calculated number of floating point operations for each sub step is presented applying the classical free interface CMS technique according to Rubin.

In Table 10 and Table 11 the calculated number of floating point operations for each sub step is presented applying Zoet's method without interface residual flexibility and with residual interface flexibility taken into account respectively.

In Figure 63 the number of floating point operations for each step for each method discussed in this sub-section is presented in a column graph.

LNG vessel FE model	Number of nodes	Number of boundary degrees of freedom	Method	Number of modes required*	Required CP for calcuating eigenvectors and eigenvalues	Required time generation pass
PartH	4991	2088	CMS fixed	181	18.5	22.8
			CMS free	257	24.5	52.5
PartG	5680	1536	CMS fixed	373	29.8	40
			CMS free	419	39	100.8
PartF	5680	1536	CMS fixed	373	29.8	40
			CMS free	419	39	100.8
PartE	8933	7188	CMS fixed	213	30	46.6
			CMS free	323	61	174
PartD	9833	6198	CMS fixed	162	29.14	53.6
			CMS free	336	95	328
PartC	11965	5124	CMS fixed	195	38.11	68.13
			CMS free	335	75	225.7
PartB	10044	3798	CMS fixed	138	29.4	47.7
			CMS free	231	53	138.3
PartA	6612	1578	CMS fixed	91	18.8	25.4
			CMS free	154	24.6	53.3

Table 8 ***Properties of substructure. Number of modes required is based on applying a cut-out frequency of 1.5 f max, which is in this case 60 Hz. CMS fixed refers to fixed interface CMS, CMS free refers to free interface CMS.***

Rubin's Method		
number of frequencies		80
Generation Pass		
Step number	Action	Estimated FLOPS
Calcuating natural frequencies and mode shapes		1.91E+13
1	Generating constraint modes	1.02E+12
2	Generating reduction basis	8.96E+11
3	Generating Reduced mass and stiffness	3.35E+13
Total Flops Generation Pass		5.45E+13
Use Pass		
Step number	Action	Estimated FLOPS
4	Compiling reduced dynamic stiffness	9.68E+08
5	Formulating compatibility and	6.84E+10
6	Solving the matrix equations	Sparse matrix approach
a.	Row reduction forward phase	5.32E+14
b.	Row reduction backward phase	6.24E+10
c.	Solving triangular matrix	4.16E+10
Total FLOPS Use Pass		5.32E+14
Grand total		5.87E+14

Table 9 ***Calculated number of floating point operations for Rubin's method (no residual compensation) analysis for 80 frequency steps***

Zoet's Method, No Residual Boundary Flexibility		
number of frequencies		80
Generation Pass		
Step number	Action	Estimated FLOPS
Calcuating natural frequencies and mode shapes		1.91E+13
1	Generating residual flexibility modes	n.a.
2	Formulating boundary mobility matrix	3.62E+10
4	Eliminating boundary degrees of	n.a.
Total Flops Generation Pass		1.91E+13
Use Pass		
Step number	Action	Estimated FLOPS
5	Composing Total Assembled System	6.32E+08
6	Solving the matrix equations	
a.	Row reduction forward phase	7.57E+11
b.	Row reduction backward phase	7.17E+08
c.	Solving triangular matrix	9.79E+08
Total FLOPS Use Pass		7.60E+11
Grand total		1.99E+13

Table 10 ***Calculated number of floating point operations for Zoet's method analysis for 80 frequency steps with no residual interface flexibility. Assumed cut-out frequency = 1.5 fmax = 60 Hz***

Zoet's Method With Residual Boundary Flexibility		
number of frequencies		80
Generation Pass		
Step number	Action	Estimated FLOPS
Calcuating natural frequencies and mode shapes		1.91E+13
1	Generating residual flexibility modes	1.97E+14
2	Formulating boundary mobility matrix	3.95E+12
4	Eliminating boundary degrees of	1.87E+13
Total Flops Generation Pass		2.39E+14
Use Pass		
Step number	Action	Estimated FLOPS
5	Composing Total Assembled System	6.32E+08
6	Solving the matrix equations	
a.	Row reduction forward phase	1.29E+12
b.	Row reduction backward phase	7.17E+08
c.	Solving triangular matrix	9.79E+08
Total FLOPS Use Pass		1.29E+12
Grand total		2.40E+14

Table 11 ***Calculated number of floating point operations for Zoet's method analysis for 80 frequency steps with residual interface flexibility taken into account. Assumed cut out frequency = 1.5 fmax = 60 Hz***

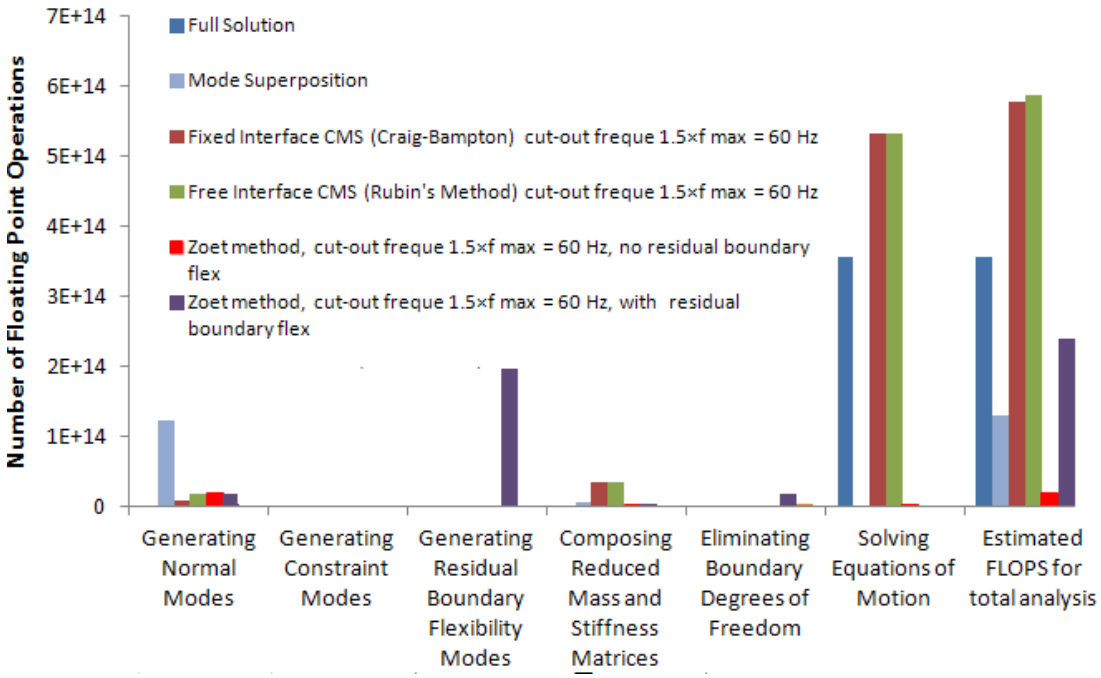

Figure 63 ***Comparing required FLOPS for Zoet's method (with and without interface residual flexibility) with the classical CMS methods (no residual compensation) analysis for 80 frequency steps between 0 and 40 Hz.***

8.7.3 Required Number of FLOPS for the Rubin-Zoet Method

In Table 12 the calculated number of floating point operations for each sub step is presented applying the CMS technique according to Rubin-Zoet, as described in section 8.6 (see also Appendix XIX and Appendix XXIII). In Figure 64 the computation times for the different stages of the different analysis techniques are presented in the form of a column graph.

Rubin-Zoet Method		
number of frequencies		80
Generation Pass		
Step number	Action	Estimated FLOPS
Calcuating natural frequencies and mode shapes		1.91E+13
1	Generating constraint modes	2.47E+12
2	Generating reduction basis	1.04E+12
3	Generating Reduced Mass, Stiffness	2.13E+13
4	Generating Reduced Equations of	2.88E+10
5	Forcing equilibrium and compatibility at the boundary degrees of freedom:	6.92E+10
6	Eliminating boundary degrees of	5.13E+12
Total Flops Generation Pass		4.92E+13
Use Pass		
Step number	Action	Estimated FLOPS
7	Formulating compatibility and	6.32E+08
8	Solving the matrix equations	
a.	Row reduction forward phase	7.57E+11
b.	Row reduction backward phase	7.17E+08
c.	Solving triangular matrix	5.30E+09
Total FLOPS Use Pass		7.64E+11
Grand total		4.99E+13

Table 12 ***Calculated number of floating point operations for the Rubin-Zoet method analysis for 80 frequency steps***

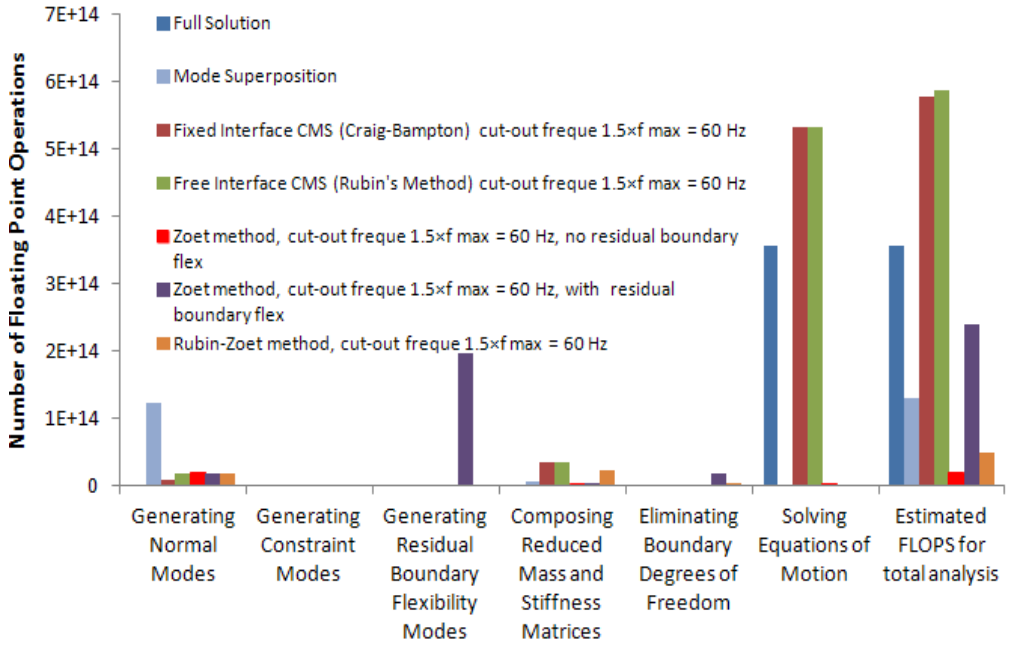

Figure 64 ***Calculated number of FLOPS for analysing 80 frequency steps for the LNG carrier's aft ship analysis. Rubin's method has been carried out without residual compensation.***

8.8 Discussion of Performance of the Proposed CMS Techniques

Two new CMS techniques have been presented in this section aiming at reducing computation time for obtaining structural harmonic simulation results of typical marine structures. These technique are Zoet's method and the Rubin Zoet method.

In section 8.7 and Appendix XX to Appendix XXIIII the calculated number of required matrix operations are presented required for getting calculation results for the LNG carrier, on which classical CMS and full harmonic analysis techniques have been tested (see section 7). Also the number of matrix operation required for the LNG carrier following the Zoet, Rubin Zoet and mode superposition method are presented. The required number of matrix operations is presented for producing 80 sets of results for 80 different frequencies equally divided over a range between 0 and 40 Hz.

Figure 64 and Figure 65 the computation times for the different stages of the different analysis techniques show that the highest reduction in computation time is achieved through applying Zoet's Method with no boundary residual compensation taken into account. Compared to Rubin's CMS method the total analysis time is reduced by 97%. Compared to the full harmonic method the computation time is reduced by 94% (see Table 13)

	Reduction Factor Computation TimeRelatively to Rubin's Method	Reduction Factor Computation Time Relatively to the Full Harmonic Analysis
Full Solution	-39.31%	0.00%
Mode Superposition	-77.66%	-63.20%
Fixed Interface CMS (Craig-Bampton) cut-out freque 1.5×f max = 60 Hz	-1.48%	62.32%
Free Interface CMS (Rubin's Method) cut-out freque 1.5×f max = 60 Hz	0.00%	64.77%
Zoet method, cut-out freque 1.5×f max = 60 Hz, no residual boundary flex	-96.61%	-94.41%
Zoet method, cut-out freque 1.5×f max = 60 Hz, with residual boundary flex	-59.04%	-32.52%
Rubin-Zoet method, cut-out freque 1.5×f max = 60 Hz	-91.49%	-85.98%

Table 13 ***Difference in percentage between calculation time required and the calculation time required for the classic Rubin's method and full harmonic analysis. Comparison is made for the calculation of 80 sets of results for 80 different frequencies equally divided over a range between 0 and 40 Hz. (Rubin's method carried out without residual compensation)***

8.8.1 Formulating Matrices

As can be seen from Figure 64 and Figure 65 the total computation time required for generating the results according to the classic CMS method is dominated by the required time to solve the matrices. This is, as discussed in previous sections, due to the high number of interface degrees of freedom for which the compatibility relations are all individually described according to the classic Craig-Bampton and Rubin's method. This leads to relatively large and, even more importantly, dense matrices for which a high number of matrix operations is required for solving.

Different matrix compilation techniques have been presented in this work which are based on adding extra steps in the formulation of the matrices (the so called generation pass) through which the number of the dynamic equations that need to be solved in the end, is reduced. Evaluation of the required computation time for each CMS method is in fact a comparison between the extra calculation time required in the generation pass for the reduction of calculation time in the use pass, and the reduction of calculation time gained in the uses pass for solving the equation of motion.

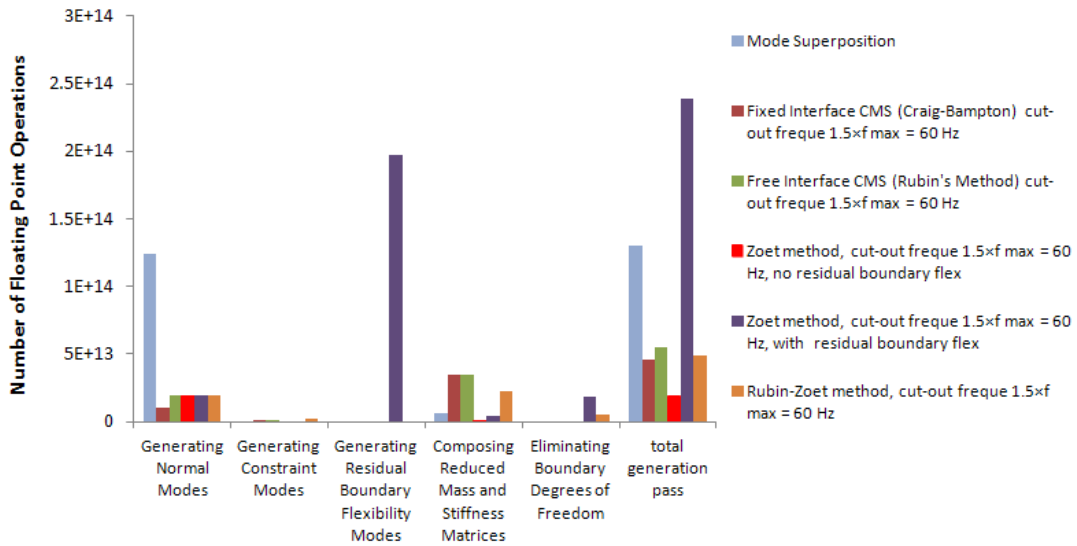

Figure 65 ***Comparison computation time required for the generation pass for different methods The required number of matrix operations is presented for producing 80 sets of results for 80 different frequencies equally divided over a range between 0 and 40 Hz.***

8.8.2 The Zoet Method without Residual Boundary Modes

With the Zoet technique, the reduction of the total assembled matrix representing the CMS equations of motion is based on formulating compatibility and equilibrium relations through the modal coordinates of the retained normal modes of the coupled substructures.

As described above, the compatibility relations between two substructures for the classical CMS method is done for each interface degree of freedom separately. As the number of interface degrees of freedom is much higher than the number of retained normal modes (see Table 8), the formulation of the compatibility relations requires much more time for the classic CMS method, as can be very distinctly seen in Figure 65. So, not only the total amount of calculation time for solving the equations of motion is reduced in the use pass (which was the aim of the development of the alternative approach) also the total amount of computation time in the generation pass for the formulation of the dynamic relation between the substructures has been decreased.

8.8.3 The Zoet Method with Boundary Residual Flexibility Modes

If residual boundary flexibility has to be taken into account, a situation has arisen that the description of dynamic interaction between two structures is again, like the classical CMS methods, based on involving all the interface physical degrees of freedom. In order reduce the set of equations again, two extra steps are required in the use pass, compared to the classic CMS method:

- The formulation of residual flexibility modes
- The elimination of interface degrees of freedom according to the method described in 8.5.2.

These two extra steps largely increase the calculation time in the generation pass, compared to the classical CMS method, as can be seen from *Figure 65*. It largely decreases the computation time in the use pass, due to a reduction of the number of steps required for solving the set of equations of motion. Particularly when many sets

of solutions need to be generated, the increase of computation time in the generation pass is paid off in the use pass.

All considered, computation time using Zoet's method with interface residual flexibility relatively to the Rubin's CMS method is estimated to decrease by 59%. Compared to the full harmonic method the computation time is reduced by a factor 32% (see Table 13).

8.8.4 Zoet Method versus Rubin-Zoet Method

From the CMS simulation results presented in section 7, it can be concluded that the compatibility relations and equilibrium requirements at the interface nodes are sufficiently described according to the Rubin method. From a theoretical point of view, it is expected that the equilibrium and compatibility relations are better described through the relation formulated by Rubin, compared to the relations formulated by the Zoet method without boundary residual flexibility taken into account. This is because the reduction basis applied for the Rubin method also contains, apart from the retained number of normal modes, static constraint modes, through which already a part of the omitted flexible modes is represented.

If residual boundary flexibility would be required for the Zoet method, it can be seen from Figure 64 and Figure 65 that the Rubin-Zoet method would be a much more efficient method, resulting in 92% reduction in calculation time compared to the Rubin's method, and 86% reduction in computation time compared to the full harmonic finite element method approach (see Table 13). The following reasons are listed for that:

- Rubin Zoet method does not require the calculation of boundary residual flexibility modes, but uses interface or boundary constraint modes instead. Especially when individual uncoupled substructures are not fully constrained, the calculation of residual boundary flexibility modes takes much more time, as steps 1B to 1F (see Appendix XXII) need to be added for applying pseudo constraints and eliminating rigid body degrees of freedom.

- With fully constrained uncoupled substructures, calculating residual flexibility modes requires roughly the same number of matrix operations as generating constraint modes. This is demonstrated in Figure 66 where the estimated number of matrix operations for the use pass are presented, applying the Zoet method, with residual boundary flexibility modes, with constrained substructures. However, reducing the number of equations by eliminating the flexibility modes the method described in described section 8.5.2. requires more time for the Zoet method, even when the rigid body degrees of freedom of the individual substructures are constrained. This is because the Zoet method has roughly double the number of interface degrees of freedom that need to be eliminated. This higher number of interface nodes is a consequence of working with interface elements instead of interface nodes.

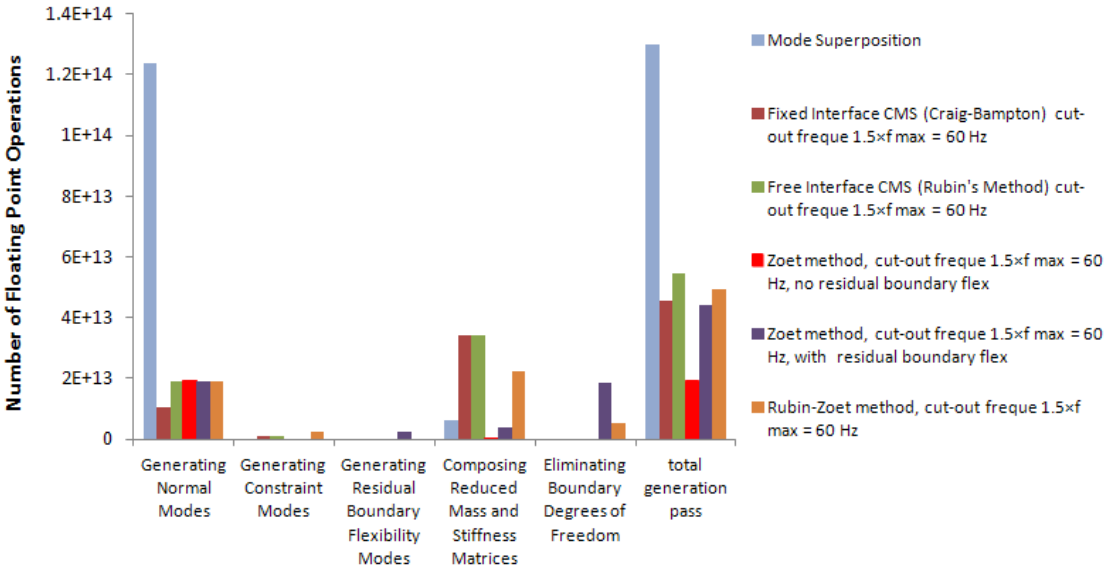

Figure 66 ***Comparison computation time required for the generation pass for different methods, with rigid body degrees of freedom constrained for the uncoupled sub structures. The required number of matrix operations is presented for producing 80 sets of results for 80 different frequencies equally divided over a range between 0 and 40 Hz.***

8.8.5 Comparing CMS with Mode Superposition

In Figure 65 an advantage of CMS can be seen relatively to the technique of applying modal reduction to the full structure. Results have not been produced through mode superposition, but it is assumed that retaining a number of mode shapes based on a cut out frequency of $1.5 \times f_{max}$ will give results at least just as accurate as the results obtained through Rubin's method. For measuring calculation time, all mode shapes based on this selection criterion have been calculated, through which the total calculation time required for mode superposition has been estimated.

Looking closer at Figure 64, it can be seen that much more CP time is required for generating modes shapes and natural frequencies of the entire structures, than the CP time required for calculating the mode shapes and natural frequencies of all the individual substructures put together. This particularly has an impact on the required CP time on for generating a smaller number of output sets (see Figure 67 A).

From Figure 67 A, it can be seen that producing one output set at around 40 Hz, through classical mode superposition, requires in fact much more computation time than the full methods, and the classical CMS methods.

However, as the calculation time required for solving the modal equations of motion is a lot lower, Figure 67 B shows that with an increasing number of output sets, the classical mode superposition technique becomes more beneficial in reduction computation time relatively to the full harmonic analysis and the classical CMS methods. This is because the calculation of modes shapes and natural frequencies only has to be done once, no matter how many output sets between 0 and 40 Hz are required.

Although the mode superposition method beats the classical methods in reducing computation time in the case of calculating 80 output sets, mode superposition technique does not solve problem encountered in the post processing phase when deformed shapes need to be plotted. The amount of output information still remains the same as for the full solution, as the number of degrees of freedom that need to be stored and plotted is still the same as well.

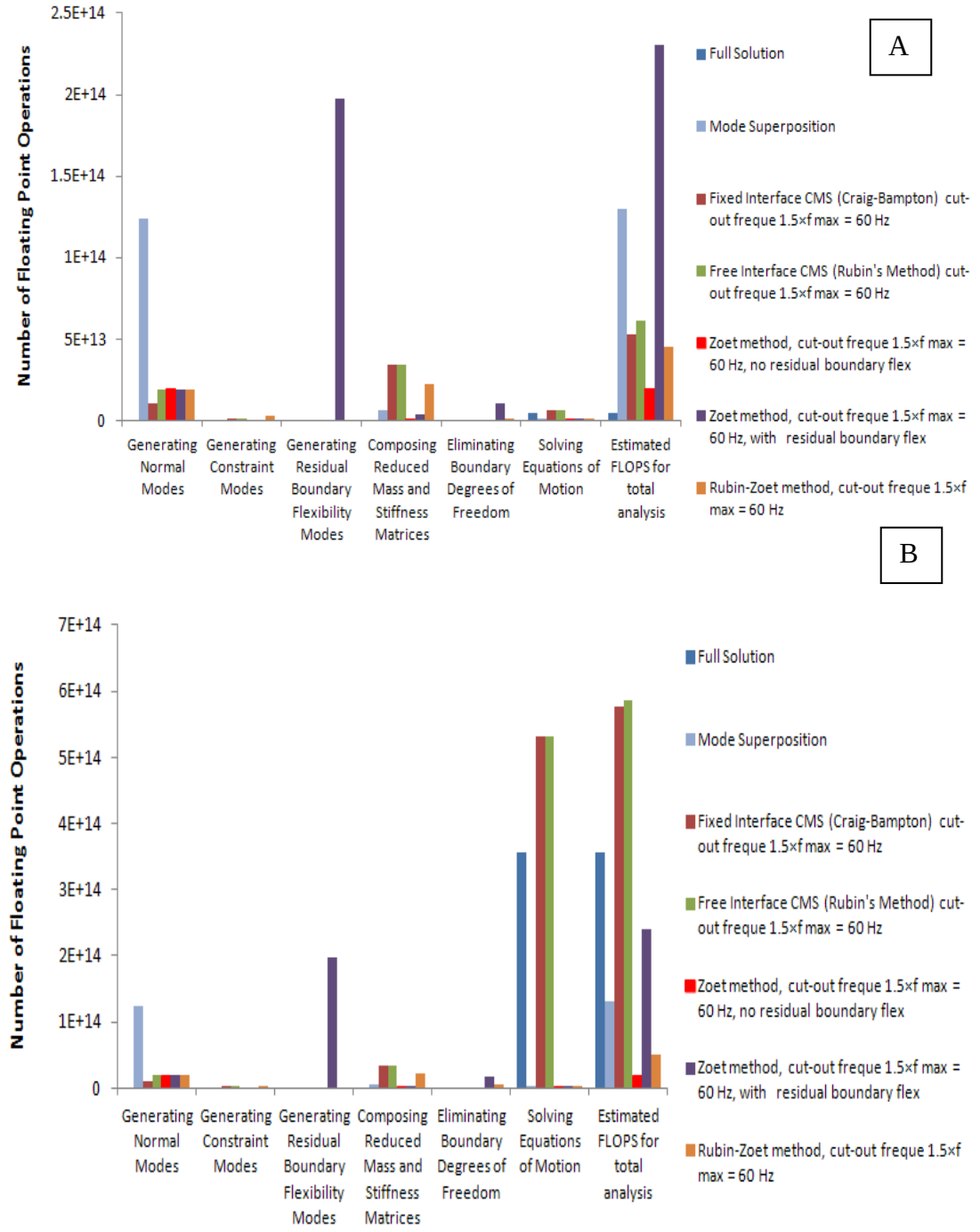

Figure 67 ***A: comparison calculation time required for generating one outset at around 40 Hz. B: comparison calculation time required for generating 80 output sets at frequencies equally distributed between 1 and 40 Hz. (Rubin's method carried out without residual compensation)***

8.9 Conclusions

Two new CMS reduction techniques have been proposed based on eliminating interface residual flexibility modes from the total CMS matrix. The two methods are the Zoet method (with and without residual flexibility) and the Rubin- Zoet method. These two methods, together with the classical fixed CMS method (Craig-Bampton) and free interface CMS (Rubin's method without boundary residual flexibility modes) have been reviewed in this section based on required computation time. The best computation time efficiency has been calculated for the Zoet method with no boundary residual flexibility modes taken into account.

However, if interface flexibility has to be taken into account for the sake of the accuracy of the results, the Rubin Zoet method is expected to be a better choice, based on computation time economics.

More computation time is needed for the Zoet method with residual interface flexibility for the following reasons:

- Formulation of compatibility at the interface lines is primarily based on formulating equilibrium of modal forces occurring in the interface **elements**. The number of residual boundary flexibility modes that need to be eliminated for the reduction of the total CMS dynamic stiffness matrix is equal to the total number of degrees of freedom of all nodes of all interface elements. Compatibility according to the Rubin's method is formulated for interface **lines**. The number of residual boundary flexibility modes that need to be eliminated is equal to the total number of degrees of freedom of all nodes on a line, which is roughly half of the number of degrees of freedom compared to the number that need to be eliminated for the Zoet method.
- When rigid body degrees of freedom of the uncoupled substructures are **not** fully constrained, required computation time for the Zoet method is further increased, compared to the Rubin-Zoet method. The reason for that is that the Zoet method relies on residual flexibility modes for compensating the effect of omitted normal modes whereas the Rubin Zoet method relies on constraint

modes for the description of the compensation for omitted normal modes. As the residual flexibility modes for substructures with unconstrained rigid body degrees of freedom require computation time expensive rigid body dof elimination procedures are required, procedures that are not necessary for the calculation of constraint modes.

Because the elimination of the residual flexibility degrees of freedom for the Zoet and Rubin-Zoet method is carried out according to the same procedure, the accuracy of the results is initially assumed to be the same, as the effect of overcompensation of interface flexibility, (as a penalty to the reduction technique), is assumed to be the same as well. However, the difference between the two techniques lays in the description of the interface compatibility and equilibrium relations. It cannot be estimated at this stage if there is a beneficial effect of either of the formulations on the effect of overcompensation of residual interface flexibility.

9 Case Study: Evaluating Zoet's Method

In section 8 two new approaches to CMS have been presented: Zoet's method (with and without boundary residual flexibility modes) and a method where compatibility and equilibrium of interfaces between substructures are described according to Rubin's method, and reduction of the total assembled CMS matrices is obtained in the same way as for the Zoet method (Rubin-Zoet method). These new approaches to CMS have been suggested with the aim of reducing the total required computation times compared to the classic Rubin's CMS method. Calculation results of the number of matrix operations for each analysis technique presented in section 8.7 and section 8.8 show that the biggest reduction in computation time can be achieved by applying Zoet's method without residual interface flexibility compensation taken into account.

9	Case Study: Evaluating Zoet's Method
9.1	Properties of the Test Model
9.1.1	Size types of Elements, and Properties of the Substructures
9.1.2	Excitation Characteristic
9.1.3	Damping and Added Mass
9.1.4	Boundary Conditions
9.2	Software Used
9.3	Evaluation of the Zoet Method
9.3.1	Relevance of Residual Boundary Flexibility Modes
9.3.2	Results for Individual Pairs of Substructures
9.3.3	Results with Multiple Coupled Structures
9.3.4	Evaluation of Required Computation Time
9.3.5	Estimated Consequences of Overcompensation on the Calculation Time for the LNG Carrier
9.4	Residual Boundary Flexibility and Overcompensation: a Discussion
9.4.1	The Effect of the Need for Residual Boundary Flexibility Modes
9.4.2	Over Compensation of Residual Flexibility
9.5	Conclusion
9.5.1	Evaluation Rubin-Zoet Method
9.5.2	Evaluation Zoet Method with Residual Compensation
9.5.3	Evaluation Rubin Method with Interface Modes
9.5.4	Evaluation Mode Superposition Method
9.5.5	Using CMS for Time-Domain Analysis

Paragraph structure of chapter 9 'Case Study: Evaluating Zoet's Method'

In this section a special test case model is presented together with simulation results obtained through the Zoet method without residual interface flexibility compensation and with residual boundary flexibility compensation taken into account. The aim of the model is to investigate the need for residual interface flexibility compensation for

the Zoet method, to investigate the effect of overcompensation of residual flexibility, when residual flexibility modes have to be included for the Zoet method.

9.1 Properties of the Test Model

Figure 68 shows the structure used for this case study. As the size of the entire LNG model analysed in section 7 made it unpractical for testing the newly proposed methods, only a part of the LNG structure has been used. The structure is divided in four substructures (see Figure 69 and Table 14). Dynamic simulations have been carried out for the following configurations:

- Substructure A and B coupled (see Appendix XXVI and Appendix XXVII)
- Substructure B and C coupled (see Appendix XXVI and Appendix XXVII)
- Substructure C and D coupled (see Appendix XXVI and Appendix XXVII)
- Substructure A, B and C coupled (see Appendix XXIX)
- Substructure A, B, C and D coupled (see Appendix XXVIII)

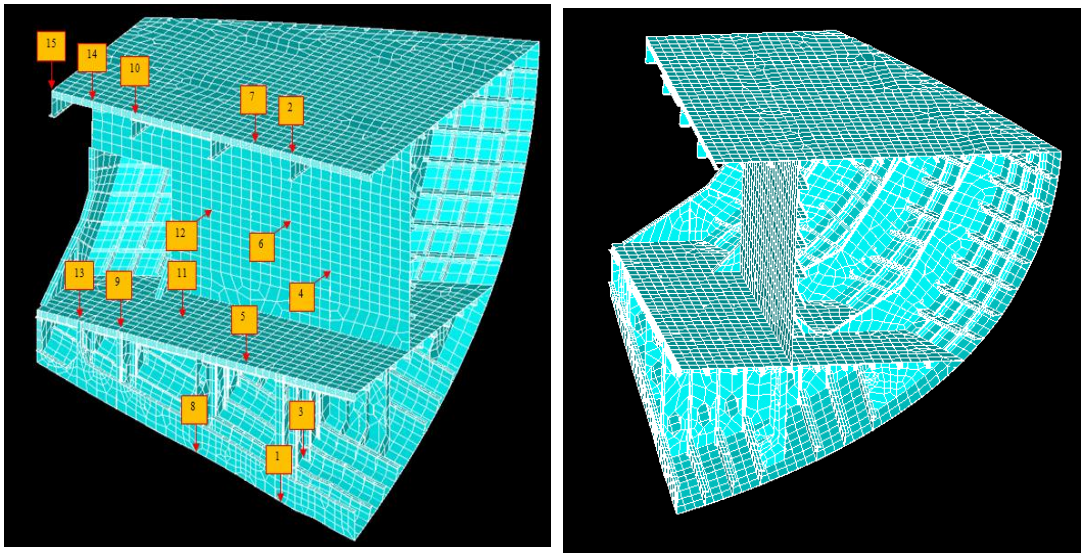

Figure 68 ***Structure used for testing Zoet's method. Measurement location are indicated through the yellow numbers***

For all configurations results are compared applying the following simulation techniques:

- The full harmonic analysis

- Free and fixed interface CMS
- Zoet's method with and without residual flexibility.

9.1.1 Size types of Elements, and Properties of the Substructures

As described in 7.2, two types of elements have been used, shell181 elements for modelling hull and deck plating and BEAM188 elements for modelling stiffeners and girders.

The shell181 is a four node thick plate element as described in Appendix IV.

The BEAM188 element has been selected as it represents a thick beam element where the effect of the rotary inertia and shear deformation has been taken into account as described in Appendix III.

The total coupled model consists of:

- 6924 nodes
- 7641 elements

Evaluation of the results in carried out through for a selected number of nodes shown in Figure 68. These number of nodes have been selected following the study of the mode shapes at the frequencies where the highest response was found according to the full harmonic analysis of the full structure (sub A, B, C and D coupled, see Appendix XXVIII).

Sub structural division is according to Figure 69 and Table 14 lists the properties of the substructures A to D.

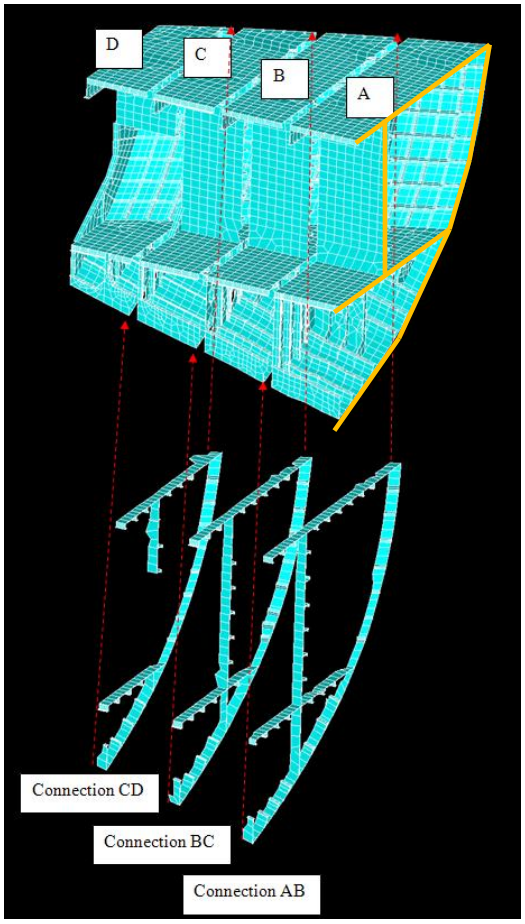

Figure 69 ***Structure used for evaluation of Zoet's method. The model is constrained on the yellow lines on the right hand side of substructure A.***

9.1.2 Excitation Characteristic

An arbitrary number of nodes at the lower section of the entire model has been selected to be subjected to a nodal load in vertical direction of 127 N. This will result in roughly 3.8 kPa alternating hull pressure, which roughly coincides with the amplitude of pressure fluctuation calculated for the 1st blade passing frequency (see section 7.5.2). 80 simulation results are produced applying this alternating pressure distribution for 80 different frequencies equally distributed over a frequency range between 1 and 40 Hz.

	Method	Number of nodes	Number of boundary nodes		Number of boundary degrees of freedomnodes	Number of modes required retained	Required CP for calcuating eigenvectors and eigenvalues	Required CP generation pass
Part A	PartAfixedcms	1903	Bounary A-B	140	840	25	9.3	11.8
	PartAfreecms		Bounary A-B	140	840	31	11	14.8
Part B	PartBfixedcms	1695	Boundary B-A	140	840	21	9.5	11.8
			Boundary B-C	120	720			
	PartBfreecms		Boundary B-A	140	840	75	11	16.5
			Boundary B-C	120	720			
Part C	PartCfixedcms	1342	Boundary C-B	120	720	16	9.1	9.4
			Boundary C-D	96	576			
	PartCfreecms		Boundary C-B	120	720	59	9.5	13.42
			Boundary C-D	96	576			
part D	PartDfixedcms	1160	Boundary D-C	96	576	15	8.84	9.1
	PartDfreecms		Boundary D-C	96	576	41	8.7	10.7
	PartD Zoet		Boundary D-C	95	570	105	10	13.8

Total structure	Number of equations total assembled matrix	Number of non zeros	Total measured CP in use pass	measured CP required for matrix formulation in use pass	Calculating Elemental and Nodal Solutions in Use Pass	measured CP for solving matrix in use pass for 80 frequency steps
full solution	33564	1318574	14.5	8.7	2.2	288
fixed boundary cms	2213	3707241	7.6	4	na	288
free boundary cms	2342	4092804	7.6	4	na	288

Table 14 ***Properties of the models used for the different methods. Free interface CMS has been carried according to the Rubin's method (without residual compensation) and the fixed interface CMS has been carried out according to the Craig-Bampton method.***

9.1.3 Damping and Added Mass

A loss number of 2% has been applied, a typical value used for representing the structural damping of steel structures. No hydrodynamic damping or added mass has been applied.

9.1.4 Boundary Conditions

The model is constrained at the nodes on the far right end side on the yellow lines shown in Figure 69. This means that, when applying free CMS, the substructures B to D are free floating and all rigid boundary modes need to be retained.

9.2 Software Used

Free and fixed interface CMS has been tested using ANSYS. The fixed interface CMS results obtained through ANSYS have been calculated according to the Craig-Bampton method. The free interface CMS results have been obtained through ANSYS13 according to the Rubin's method. No residual compensation has been applied in the free interface CMS technique used through ANSYS. However, contribution from omitted normal modes is for a great part compensated at the interface nodes with the classic Rubin's method through the inclusion of constraint modes into the reduction basis.

The Zoet method has been tested using a combination between ANSYS, MATLAB and excel. Stiffness and mass matrices, mode shapes, natural frequencies modal coordinates a_0 have obtained through ANSYS and have been written away in text files (using Harwell-Boeing format for the matrices) or have been exported to excel. Input data for further calculations in MATLAB are read from the text files and excel files and the results are calculated according to the method described in section 8.

Also performance applying the different methods is compared through estimating the number of matrix operations required for the different steps of the analysis.

9.3 Evaluation of the Zoet Method

Evaluation of the new modelling techniques is based on studying a set of 80 output sets representing simulation results for 80 different frequencies over a range between 0 and 40 Hz. For each substructure simulation results for 4 locations are evaluated. These locations are selected based study of simulation results performed through the full harmonic analysis (see Figure 68 and Appendix XXIV). The results obtained through the full harmonic analysis are the benchmark for this study.

Evaluation of the modelling results will be based on the computation time required for obtaining results that are 'accurate enough'. Sufficient accuracy of the simulation results is considered to have been obtained when the frequencies at which peak responses are found, coincide with the frequencies on which peak responses have

been found according the full harmonic analysis results. This basically means that, considering frequency steps of 0.5 Hz are used (80 frequencies over a 40 Hz frequency range), natural frequencies found through any of the evaluated method, should be within a bandwidth between -0.25Hz and +0.25Hz from the natural frequencies found through the full harmonic analysis.

9.3.1 Relevance of Residual Boundary Flexibility Modes

A comparison has been made between results obtained through Zoet's method without taking interface residual flexibility into account and with the interface residual flexibility taken into account. As explained in section 8, CMS technique proposed has been developed in such a way that it is not necessary to include the displacement of each interface degree of freedom in the set of equations, in order to be able to describe the interaction between the substructures. This way the size of the matrix that needs to be solved does not depend on the number of coupling degrees of freedom, but may be defined by the number of mode required for accurately enough describing the dynamic displacement of the substructures.

In Appendix XXVII simulation results from different models are presented taking a great number of modes into account applying a cut-out frequency of 120 Hz, equal to three times the maximum frequency that is analysed producing results over a frequency range between 1 and 40 Hz taking steps of approximately 0.5 Hz.

As can be seen in Appendix XXVII and Figure 70, taking into account residual interface flexibility (residual compensation) at the interface nodes is very important for getting accurate enough results. The results according to Zoet's method plotted in these graphs have been obtained by expanding only the normal mode shapes for either the analysis with residual interface flexibility taken into account or the analysis with no residual interface flexibility taken into account.

Taking residual interface flexibility into account gives results for the Zoet method, which are comparable with the results obtained through the classic Rubin's method.

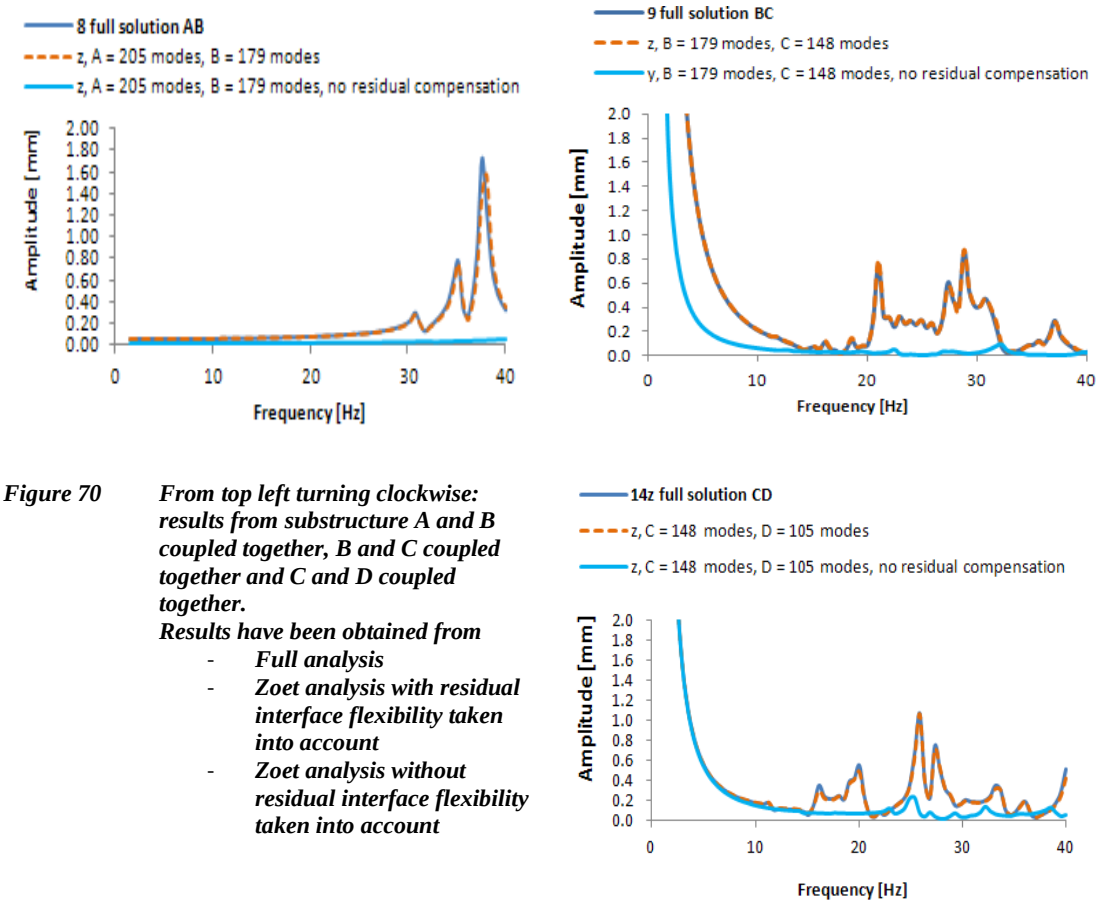

Figure 70 ***From top left turning clockwise: results from substructure A and B coupled together, B and C coupled together and C and D coupled together.***
Results have been obtained from

- ***Full analysis***
- ***Zoet analysis with residual interface flexibility taken into account***
- ***Zoet analysis without residual interface flexibility taken into account***

9.3.2 Results for Individual Pairs of Substructures

Simulation results according to Zoet's method **with** residual interface flexibility compensation have been produced for each pair of substructures and are presented in Appendix XXVI (see also Figure 71). The simulation results are presented either for the y direction or the z direction for the location number shown in the legend. The subscript 'c' to the direction letter y or z, means that the results have been obtained (in y or z direction) not by just expanding the normal modes, but also expanding the contribution from the boundary residual flexibility modes. Simulation results have been produced retaining different number of modes:

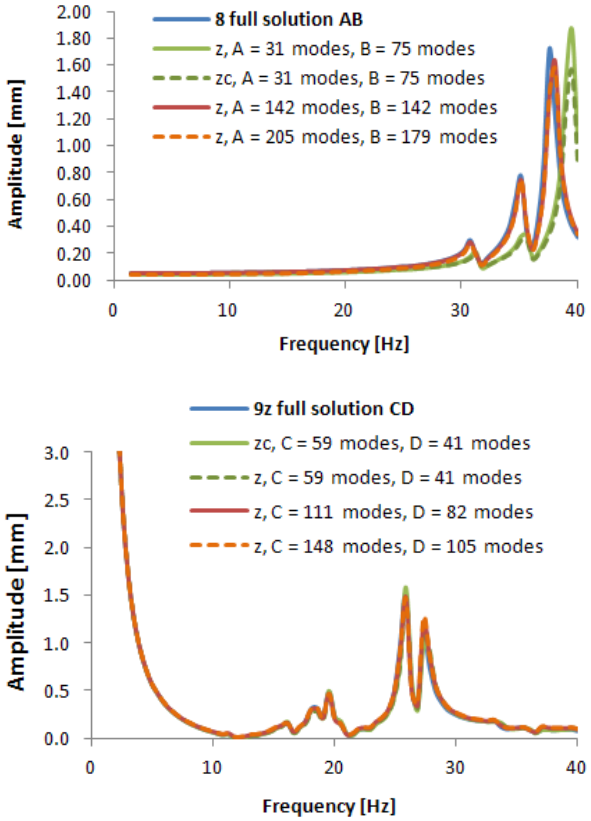

Figure 71 ***Some results from the simulation of substructure AB and substructure CD. The subscription 'c' indicates that the results have been obtained by expanding the residual contribution from the residual flexibility modes in addition to the expansion of the normal modes. See Appendix XXVI for more results)***

Substructure A;

retaining 31 modes: cut-out frequency = 60 Hz ($1.5\times f_{max}$)

retaining 142 modes: cut-out frequency = 120 Hz ($3\times f_{max}$)

retaining 205 modes: cut-out frequency = 145 Hz ($3.5\times f_{max}$)

Substructure B;

retaining 79 modes: cut-out frequency = 60 Hz ($1.5\times f_{max}$)

retaining 142 modes: cut-out frequency = 80 Hz ($2\times f_{max}$)

retaining 179 modes: cut-out frequency = 120 Hz ($3\times f_{max}$)

Substructure C;

retaining 59 modes: cut-out frequency = 60 Hz ($1.5\times f_{max}$)

retaining 111 modes: cut-out frequency = 80 Hz ($2\times f_{max}$)

retaining 148 modes: cut-out frequency = 120 Hz ($3\times f_{max}$)

Substructure D;

retaining 41 modes: cut-out frequency = 60 Hz (1.5×f_{max})

retaining 82 modes: cut-out frequency = 80 Hz (2×f_{max})

retaining 105 modes: cut-out frequency = 120 Hz (3×f_{max})

As can also been seen in Figure 71 and Appendix XXVI, good results are generally obtained for each number of modes taken into account.

The exception is the model pairing substructure A with substructure B. As also can be seen from Figure 70, residual static modes play an important role in the response of the structure. This is mainly related to the response of substructure A depending largely the contributions of higher mode numbers, as demonstrated in Figure 72. In Figure 72 the calculation results for the response of just substructure A (not coupled to other substructures) are presented.

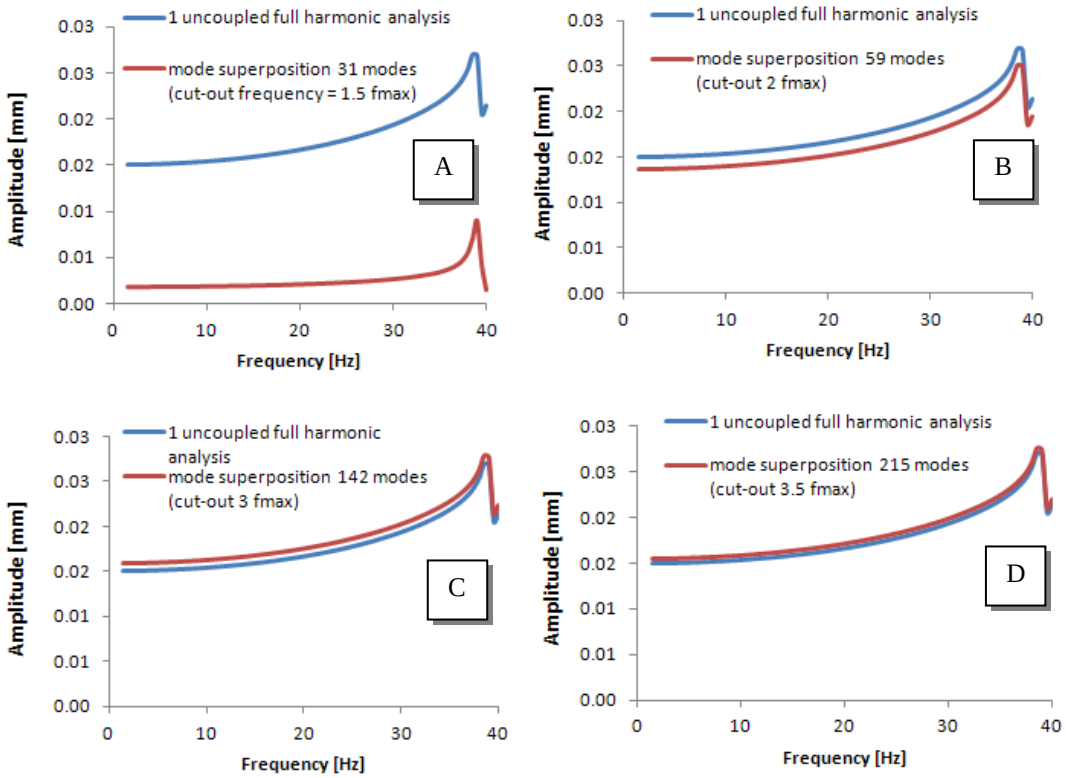

Figure 72 ***Calculated response at location 1 in z direction on substructure A. Response is obtained through mode superposition (red curve) and full harmonic analysis (blue curve). Mode superposition results are obtained applying a cut-out frequency of 60 Hz (1.5×f_{max}), 80 Hz (2×f_{max}), 120 Hz (3×f_{max}) and 140 Hz (3.5×f_{max}) in graph A, B, C and D respectively***

As can be seen from in Figure 72, accurately describing the vibration amplitudes at location 1 (at one of the interface nodes between substructure A and B), requires the superposition of far more modal contributions than the number of modes obtained through applying a cut-out frequency of $1.5\times f_{max}$. Even when applying a cut-out frequency of $3.5\times f_{max}$ still differences in calculated response amplitudes can be seen between the results obtained through full harmonic analysis and the response obtained through mode superposition.

In Figure 73 can be seen that the response of the uncoupled substructures B to D can be accurately enough described through mode superposition applying a cut-out frequency of $1.5\times f_{max}$. This is why a higher number of normal modes has been retained for substructure A than for substructure B to D.

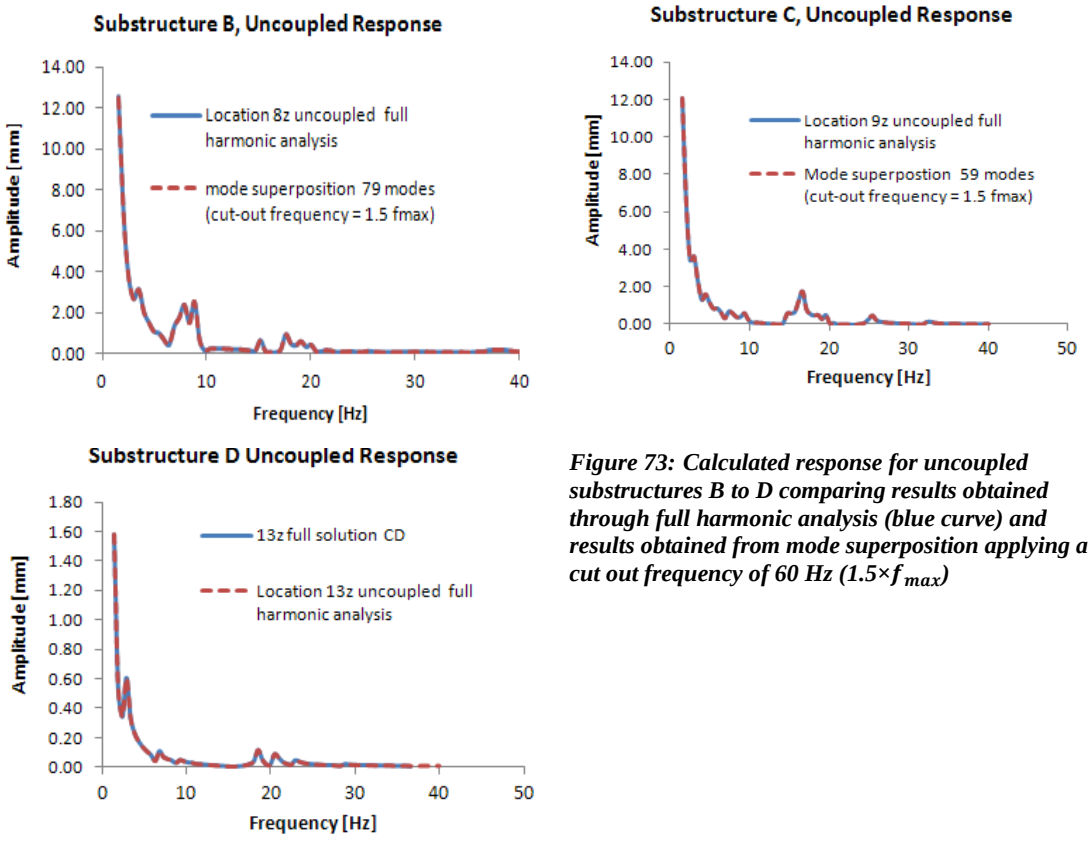

Figure 73: Calculated response for uncoupled substructures B to D comparing results obtained through full harmonic analysis (blue curve) and results obtained from mode superposition applying a cut out frequency of 60 Hz ($1.5\times f_{max}$)

9.3.3 Results with Multiple Coupled Structures

In Appendix XXIV results obtained from free interface (Rubin method with no residual compensation) and fixed interface (Craig Bampton) CMS are plotted together with results obtained from the full harmonic analysis (obtained through analysis with ANSYS). These graphs show that free interface CMS is very accurate whereas the results produced through the fixed interface CMS deviate from the full analysis results. The number of mode shapes retained for the free and fixed interface CMS is based on selecting all modes with natural frequencies within the range between 0 and 1.5×f_{max}, which in this case is between 0 and 60 Hz, considering our maximum analysed frequency is 40 Hz.

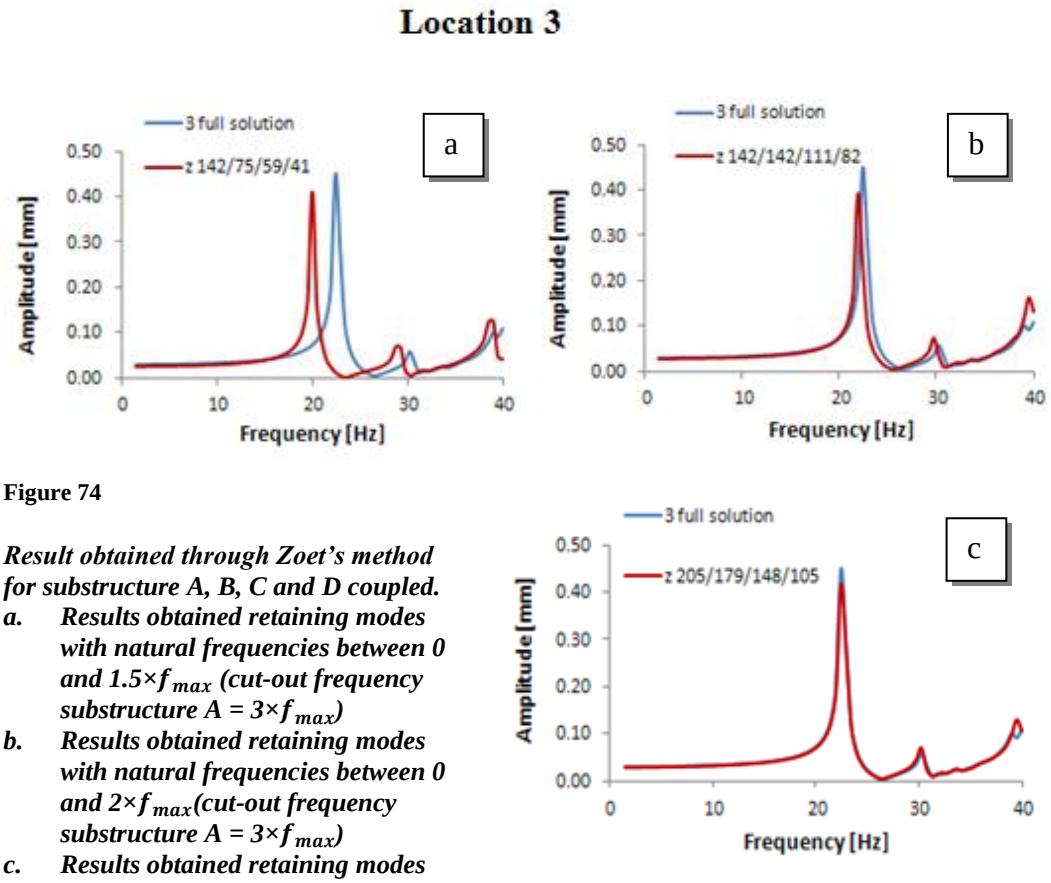

Figure 74

Result obtained through Zoet's method for substructure A, B, C and D coupled.

a. Results obtained retaining modes with natural frequencies between 0 and 1.5×f_{max} (cut-out frequency substructure A = 3×f_{max})

b. Results obtained retaining modes with natural frequencies between 0 and 2×f_{max}(cut-out frequency substructure A = 3×f_{max})

c. Results obtained retaining modes with natural frequencies between 0 and 3×f_{max}(cut-out frequency substructure A = 3.5×f_{max})

In Appendix XXVIII results are presented from the simulation run through the Zoet's method compared with simulation results obtained through free interface CMS. The comparison with the free interface CMS (Rubin's method with no residual compensation) has been made as the results from the free interface CMS coincide with the full analysis results.

In the results obtained through Zoet's Method, the effect of over-compensation of the residual flexibility can clearly be seen (see also Figure 74), as described section 8.5.3. The results in a too flexible behaviour of the structure's interface boundaries, which results in peak responses (natural frequencies) to be located at lower frequencies than the peak response frequencies found through the full harmonic analysis and the classic Rubin's free interface CMS analysis. As a result, the number of retained normal modes needed to be increased. The upper limit of the frequency range over which the modes have been selected had to be increased from $1.5\times f_{max}$ to $3\times f_{max}$ which meant that a range of 0 to 120 Hz needed to be adopted instead of a range between 0 and 60 Hz, as was found to be sufficient for the classic Rubin's method (with no residual compensation). By increasing the number of retained elastic modes, the contribution from the boundary flexibility modes decreases. As it is through the elimination of the contribution from these boundary flexibility modes that boundaries flexibility is over compensated, this overcompensation effect is decreased as well.

In Appendix XXIX simulation results have been presented of the mode containing only substructure A, B and C coupled together. In Appendix XXIX and Figure 75 can be seen that the effect of overcompensation has become less strong. Adopting a cut-out frequency of $2\times f_{max}$ already give accurate enough results.

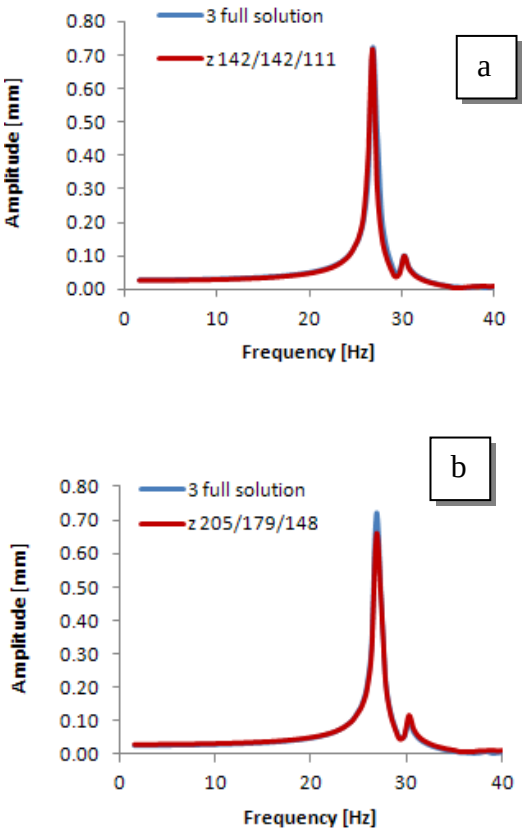

Figure 75

Result obtained for location 3 (see Figure 68 and Appendix XXIX) through Zoet's method for substructure A, B and C coupled.

- ***a. Results obtained retaining modes with natural frequencies between 0 and $2\times f_{max}$ (cut-out frequency substructure A = $3\times f_{max}$)***
- ***b. Results obtained retaining modes with natural frequencies between 0 and $3\times f_{max}$(cut-out frequency substructure A = $3.5\times f_{max}$)***

9.3.4 Evaluation of Required Computation Time

To evaluate the effectiveness of the Zoet method in reducing computation time, the required number of floating point operations for a number simulation methods have been calculated, as described in Appendix XV to Appendix XIX (see Figure 76). These numbers have been combined with measured CP times required for obtaining modal information (see Table 15). The number of FLOPS have been calculated taking into consideration that the response at 80 frequency steps has been calculated over a frequency range between 1 and 40 Hz.

The number of FLOPS has been calculated for the following methods:

- Modal reduction on the full model. The number of retained normal modes is based on applying a cut-out frequency of $1.5\times f_{max}$ = 60 Hz (where f_{max} is

the upper limit of the analysed frequency range = 40 Hz).Hz), following the instruction in Appendix XV.

- Free interface CMS according to the Rubin method without residual compensation (calculated with ANSYS). The number of retained normal modes for the individual substructures is based on applying a cut-out frequency of 1.5×f_{max} = 60 Hz (where f_{max} is the upper limit of the analysed frequency range = 40 Hz). The steps listed in Appendix XVI are followed.
- Free interface CMS according to the Rubin method with interface reduction using interface modes, according to Appendix XVII . The number of retained normal modes for the individual substructures is based on applying a cut-out frequency of 1.5×f_{max} = 60 Hz (where f_{max} is the upper limit of the analysed frequency range = 40 Hz). Selection of number of interface modes is based on applying a cut-out frequency of ×3.5f_{max}according to Tran [41]. Appendix XXX shows how the number of FLOPS are obtained for the PHD test model (see also Appendix XXXI)
- Zoet Method with residual compensation according to Appendix XVIII. A higher number of mode shapes needs to be selected in order to reduce the effect of residual interface flexibility overcompensation. The number of retained normal modes for the individual substructures is based on applying a cut-out frequency of 3×f_{max} = 120 Hz (where f_{max} is the upper limit of the analysed frequency range = 40 Hz).. (see also Appendix XXXI)
- Rubin-Zoet method according to Appendix XIX. The same number of mode shapes has been selected as for the Zoet method (see also Appendix XXXI)

	Method	Number of nodes	Number of boundary nodes		Number of boundary degrees of freedomnodes	Number of modes required retained	Required CP for calcuating eigenvectors and eigenvalues	Required CP generation pass
Part A	PartAfixedcms	1903	Bounary A-B	140	840	25	9.3	11.8
	PartAfreecms		Bounary A-B	140	840	31	11	14.8
	PartA Zoet and Rubin-Zoet method		Bounary A-B	140	840	205	16.3	18.9
Part B	PartBfixedcms	1695	Boundary B-A	140	840	21	9.5	11.8
			Boundary B-C	120	720			
	PartBfreecms		Boundary B-A	140	840	75	11	16.5
			Boundary B-C	120	720			
	PartB Zoet and Rubin-Zoet method		Boundary B-A	141	846	179	13.3	18.3
			Boundary B-C	120	720			
Part C	PartCfixedcms	1342	Boundary C-B	120	720	16	9.1	9.4
			Boundary C-D	96	576			
	PartCfreecms		Boundary C-B	120	720	59	9.5	13.42
			Boundary C-D	96	576			
	PartC Zoet and Rubin-Zoet method		Boundary C-B	124	744	148	12	17.6
			Boundary C-D	96	576			
part D	PartDfixedcms	1160	Boundary D-C	96	576	15	8.84	9.1
	PartDfreecms		Boundary D-C	96	576	41	8.7	10.7
	PartD Zoet and Rubin-Zoet method		Boundary D-C	95	570	105	10	13.8

Table 15 ***PHD test case model: Comparing size and density of matrices generated through the different methods. Free interface CMS has been carried according to the Rubin's method and the fixed interface CMS has been carried out according to the Craig-Bampton method.***

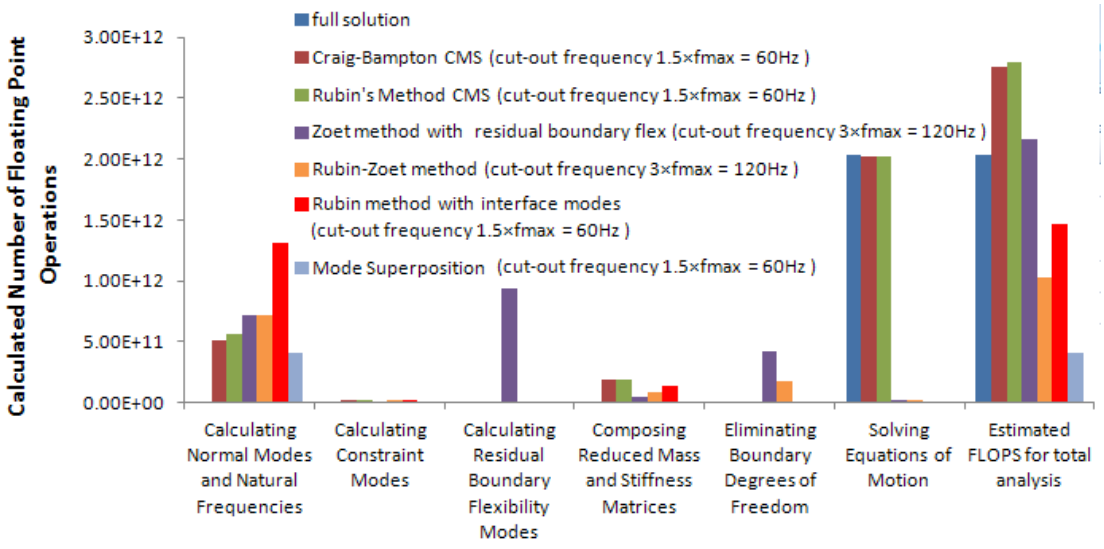

Figure 76 ***PHD test case model: Calculated number of FLOPS for analysing 80 frequency steps. Free interface CMS has been carried according to the Rubin's method (without residual compensation). The fixed interface CMS method has been carried out according to the classic Craig-Bampton method.***

	Computation Time Difference with Rubin's Method	Computation Time Difference with Full Harmonic Analysis	Computation Time Difference with Rubin's Method with Interface Modes
full solution	-27.5%	0.0%	37.9%
Mode Superposition	-85.4%	-79.8%	-72.2%
Craig-Bampton CMS (cut-out frequency 1.5×fmax = 60Hz)	-1.7%	35.6%	87.1%
Rubin's Method CMS (cut-out frequency 1.5×fmax = 60Hz)	0.0%	38.0%	90.4%
Rubin method with interface modes	-47.5%	-27.5%	0.0%
Zoet method with residual boundary flex (cut-out frequency 3×fmax = 120Hz)	-22.9%	6.4%	46.8%
Rubin-Zoet method (cut-out frequency 3×fmax = 120Hz)	-63.3%	-49.4%	-30.2%

Table 16 ***PHD test case model: Differences in total computation time between simulation techniques expressed in percentages restively to: Classical Rubin's method (no residual compensation), full harmonic analysis, Rubin's method with interface reduction. Comparison has been made based on producing 80output sets for 80 frequencies equally distributed between 1 and 40 Hz.***

In Table 16 and Figure 76 can be seen that analysis times are reduced by 23% and by 63% relatively to the classic Rubin's CMS method when applying the Zoet Method or Rubin-Zoet method respectively. With the Rubin-Zoet method also a reduction of calculation time is achieved relatively to the already existing interface reduction method according to the IRS method (see section 6.5.3.)

9.3.5 Consequences of Overcompensation on LNG Carrier

In section 8.7 the required computation times for analysing the LNG carrier's structure's dynamic response through the newly developed CMS methods are compared with the computation times required for analysis of the structure through classic CMS approaches and the full harmonic analysis. With the calculation of the time required for the analysis according to the CMS methods, the choice of the number of normal modes retained in the reduction basis was based on selecting all mode shapes with natural frequencies between 0 and number of $1.5\times f_{max}$ (f_{max} is the upper limit of the analysed frequency range = 40 Hz, which results in a cut-out frequency of 60 Hz).

In Figure 77 A the estimated required calculation time for each step for different simulation technique is presented through bar graphs, based on applying the above mentioned cut out frequency of 60 Hz. However, from the analysis results of the case study's structure it has been concluded that a higher number of normal modes is

required for the Zoet and Rubin-Zoet method. Simulation results on the PHD test structure suggest that the cut-out frequency for the Zoet and Rubin-Zoet method has been increased to $3\times f_{max}$ in order to minimise the effect of overcompensation of residual interface flexibility, which was to be expected from the matrix compilation method (as described in section 8.5.3). By increasing the number of retained elastic modes, the contribution from the boundary flexibility modes decreases. As it is through the elimination of the contribution from these boundary flexibility modes that boundaries flexibility is over compensated, this overcompensation effect is decreased as well. Figure 77 B compares the calculation times required for the Zoet and Rubin-Zoet method applying the increased cut-out frequency of $3\times f_{max}$ =120 Hz with the classical methods for which the calculation times are still based on applying a a cut-out frequency of $1.5\times f_{max}$ = 60 Hz.

No comparison is made with the reduction that could have been obtained by reducing the interface degrees of freedom by applying interface modes. ANSYS did not offer the option of interface reduction through interface modes, and the substructures of the LNG carrier were too big to calculate the interface modes with the MATLAB code (see also Appendix XXXII for more extended presentation of results).

As can be seen from Figure 77, despite of the increase of calculation time for the Zoet and Rubin-Zoet method due to the need for increasing the number of normal modes, huge reductions of calculation times are still achieve, both relatively to the time required for the full harmonic analysis and the time required for the classical CMS (reduction of 67% and 80% respectively)

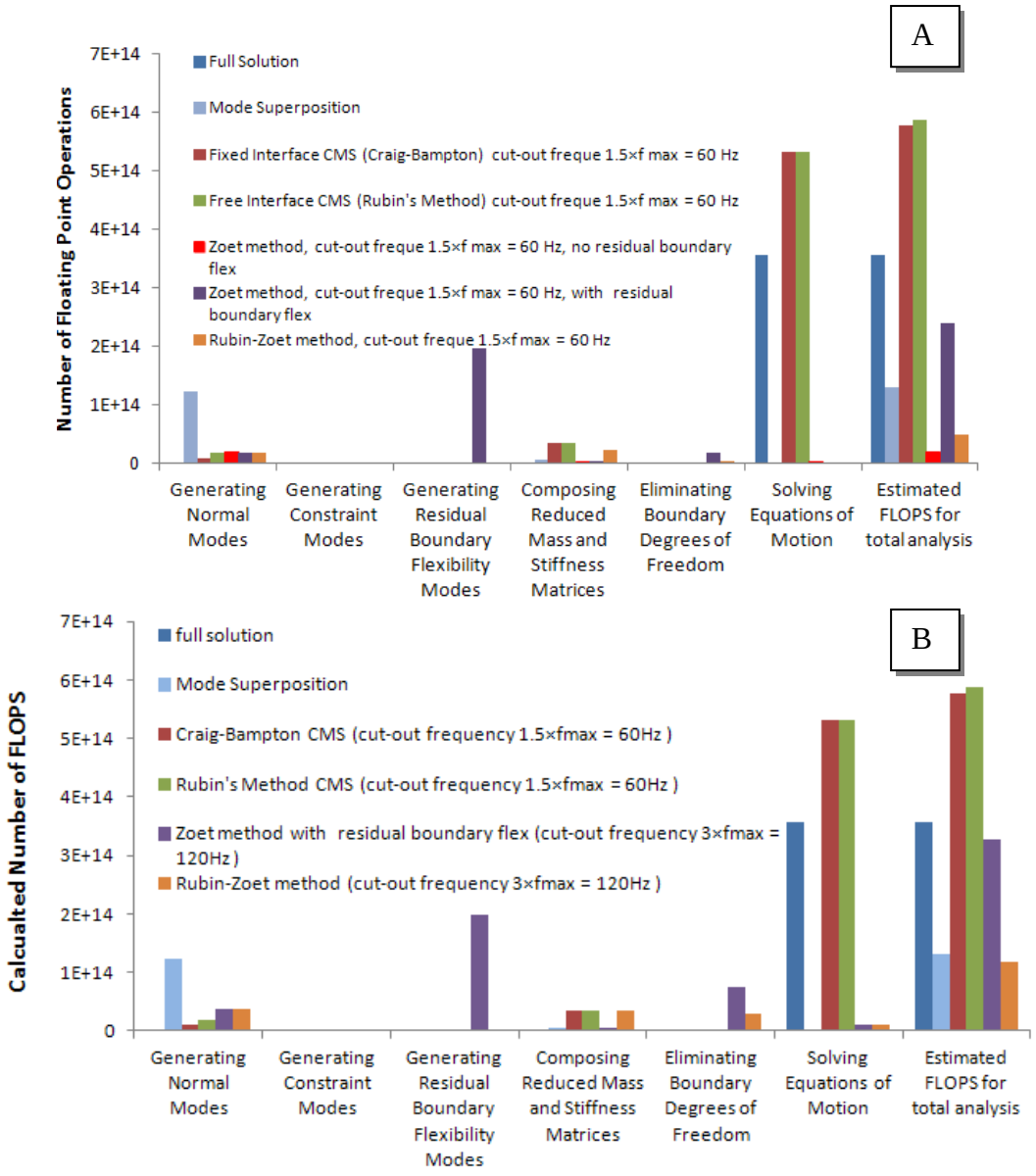

Figure 77 ***Comparing the reduction in simulation time for the different methods applied for the structural dynamic analysis for 80 frequency steps for the LNG carrier. Graph A compares simulation times applying a cut-out frequency of $1.5\times f_{max}$= 60 Hz for all methods. In graph B the cut-out frequency for the Rubin and Rubin Zoet method has been increased to $3\times f_{max}$, = 120 Hz.***

	Cut out frequency 1.5 fmax = 60 Hz		Cut out frequency 3 fmax = 120 Hz	
	Reduction Factor Computation TimeRelatively to Rubin's Method	Reduction Factor Computation Time Relatively to the Full Harmonic Analysis	Reduction Factor Computation TimeRelatively to Rubin's Method	Reduction Factor Computation Time Relatively to the Full Harmonic Analysis
Full Solution	-39.3%	0.0%	-39.3%	0.0%
Mode Superposition	-77.7%	-63.2%	-77.7%	-63.2%
Craig-Bampton CMS	-1.5%	62.3%	-1.5%	62.3%
Rubin's Method CMS	0.0%	64.8%	0.0%	64.8%
Zoet Method	-59.0%	-32.5%	-44.4%	-8.4%
Rubin Zoet method	-91.5%	-86.0%	-80.1%	-67.1%

Table 17 ***Differences in total computation time between simulation techniques expressed in percentages restively to: Classical Rubin's method (no residual compensation), full harmonic analysis. Comparison has been made based on producing 80output sets for 80 frequencies equally distributed between 1 and 40 Hz.***

9.4 Residual Interface Flexibility and Overcompensation: a Discussion

In this section the Zoet method with and without residual interface flexibility compensation has been tested by using the method on a part of the structure of the LNG carrier. This test structure has been subdivided in four substructures and the Zoet method has been tested using different numbers of normal mode shapes that were retained in the reduction basis.

It has been concluded from the simulation results, that including residual interface flexibility compensation in the Zoet method is crucial for the simulation results. This has consequences for the effectiveness of the Zoet method, and puts the Rubin-Zoet method in front, even compared to the applying the existing interface reduction technique according to the IRS method (see section 6.5.3).

The need for residual boundary flexibility modes means that the interface degree of freedom elimination technique presented in paragraph 8.5.2. had to be applied, in order to achieve reduction of computation time. However, the related final matrix compilation procedure results in overcompensation of the residual flexibility, which made it necessary in increase the number of normal modes in the reduction basis.

In the following section a discussion takes place about the consequences of the need to include residual interface flexibility (as mentioned above) and the consequences of interface flexibility overcompensation, and how its impact may be reduced.

9.4.1 The Effect of the Need for Residual Boundary Flexibility Modes

In Figure 78 the required computation time for the different modelling techniques is presented through a bar graph. Simulation results of sets of two coupled structures (as presented in Appendix XXVI) clearly showed that including the residual boundary flexibility modes for the Zoet Method is crucial for the accuracy of the outcome of the simulation results. This is why the required computation time for the Zoet method without residual interface flexibility compensation has not been included in Figure 78.

As can be seen from Figure 78, the Rubin Zoet method requires much less computation time than the Zoet method, now that residual flexibility modes are required. The higher amount of computation time for the Zoet method comes from the fact that the static contribution from the compensation of the omitted modes relies on the introduction of boundary flexibility modes whereas the Zoet-Rubin method relies on constraint modes for the compensation of the omitted modes.

Unfortunately, the number of matrix operation required for generating flexibility modes is much higher than the number of operation required for generating constraint modes. This is because the calculation of flexibility modes requires inverting the full stiffness matrix of a substructure whereas the calculation of the constraint modes requires inverting the stiffness matrix with the interface degrees of freedom eliminated.

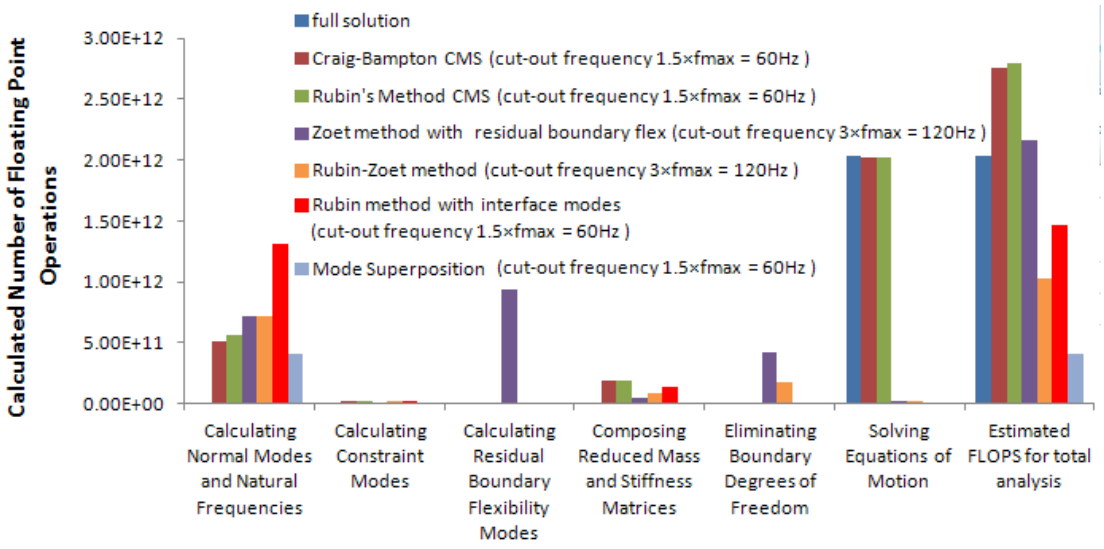

Figure 78 ***Comparing computation time for different simulation techniques for the calculation of the harmonic dynamic behaviour of the PHD test structure. Comparison has been made based on producing 80output sets for 80 frequencies equally distributed between 1 and 40 Hz. Rubin's method has been carried out without residual compensation.***

However, as the substructures B to D are not constrained, the residual boundary flexibility modes have to be calculated for the Zoet method using pseudo constraints according to section 8.4 and Appendix V. This makes the calculation of the residual boundary flexibility modes even more expensive than the calculation of the constraint modes. This is why the Zoet method requires much more calculation time than the Rubin-Zoet method. Figure 78 demonstrates that this effect has a huge impact on computation time for the PHD test model.

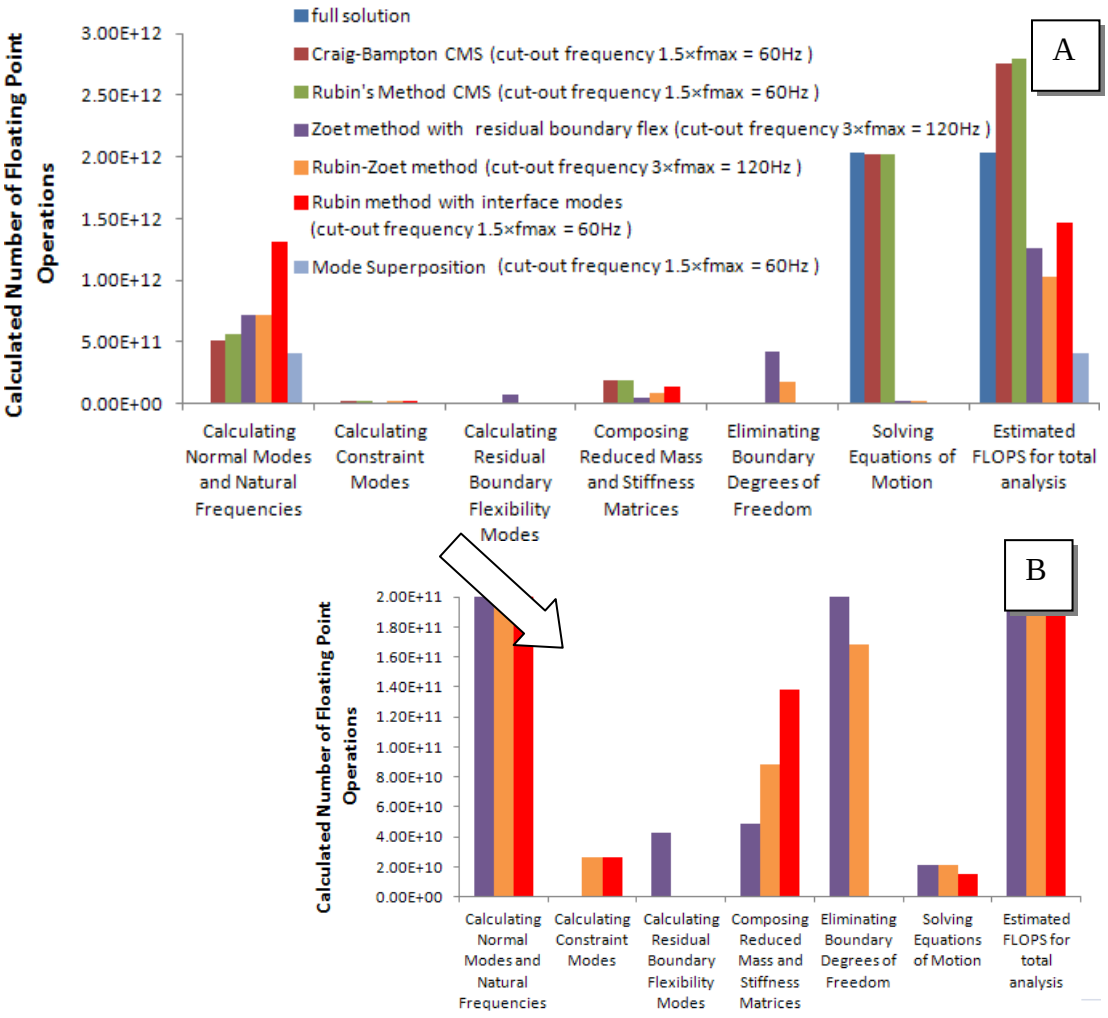

Figure 79 ***Comparing required computation times considering the rigid body modes of substructure B to D fixed.. This is to demonstrate that calculating boundary flexibility modes is more expensive than calculating constraint modes even without the added cost of eliminating the effect of rigid body modes in case substructures are not constrained. B is a zoomed in version of graph A.***

In Figure 79 is demonstrated what the required calculation time for the test case model would be if all rigid body degrees of freedom of the uncoupled substructures would have been constrained. Calculating boundary flexibility modes cost roughly twice as much computation time than the generation of constraint modes in this case, which is a result of having to invert bigger matrices for generating boundary flexibility modes compared to the computation of constraint modes.

9.4.2 Overcompensation of Residual Flexibility

In Figure 78 the required computation time for the different modelling techniques is presented through a bar graph. Simulation results of sets of two coupled structures (as presented in Appendix XXVI) clearly showed that including the residual boundary flexibility modes for the Zoet Method is crucial for the accuracy of the outcome of the simulation results.

However, in order achieve reduction in computation time relatively to the classical CMS methods, the interface degree of freedom elimination technique according to 8.5 had to be applied. Through this technique of assembling the total reduced stiffness and mass matrices, overcompensation of the residual interface flexibility takes place when coupling more than two substructures together (as explained in section 8.5.3). This effect can be clearly seen in the simulation results of the PHD test case model. As a consequence of the overcompensation, resonance peaks in the response curves obtained through the Zoet method occur at lower frequencies compared to the results obtained through classical CMS and full harmonic analysis (see Figure 74, and Appendix XXVIII). In order to reduce this effect, the cut-out frequency used for selecting the number of normal modes for each substructure had to be increased from 1.5 $f_{max} = 60\ Hz$ to 3 $f_{max} = 120Hz$. By increasing the number of retained elastic modes, the contribution from the boundary flexibility modes decreases. As it is through the elimination of the contribution from these boundary flexibility modes that boundaries flexibility is over compensated, this overcompensation effect is decreased as well.

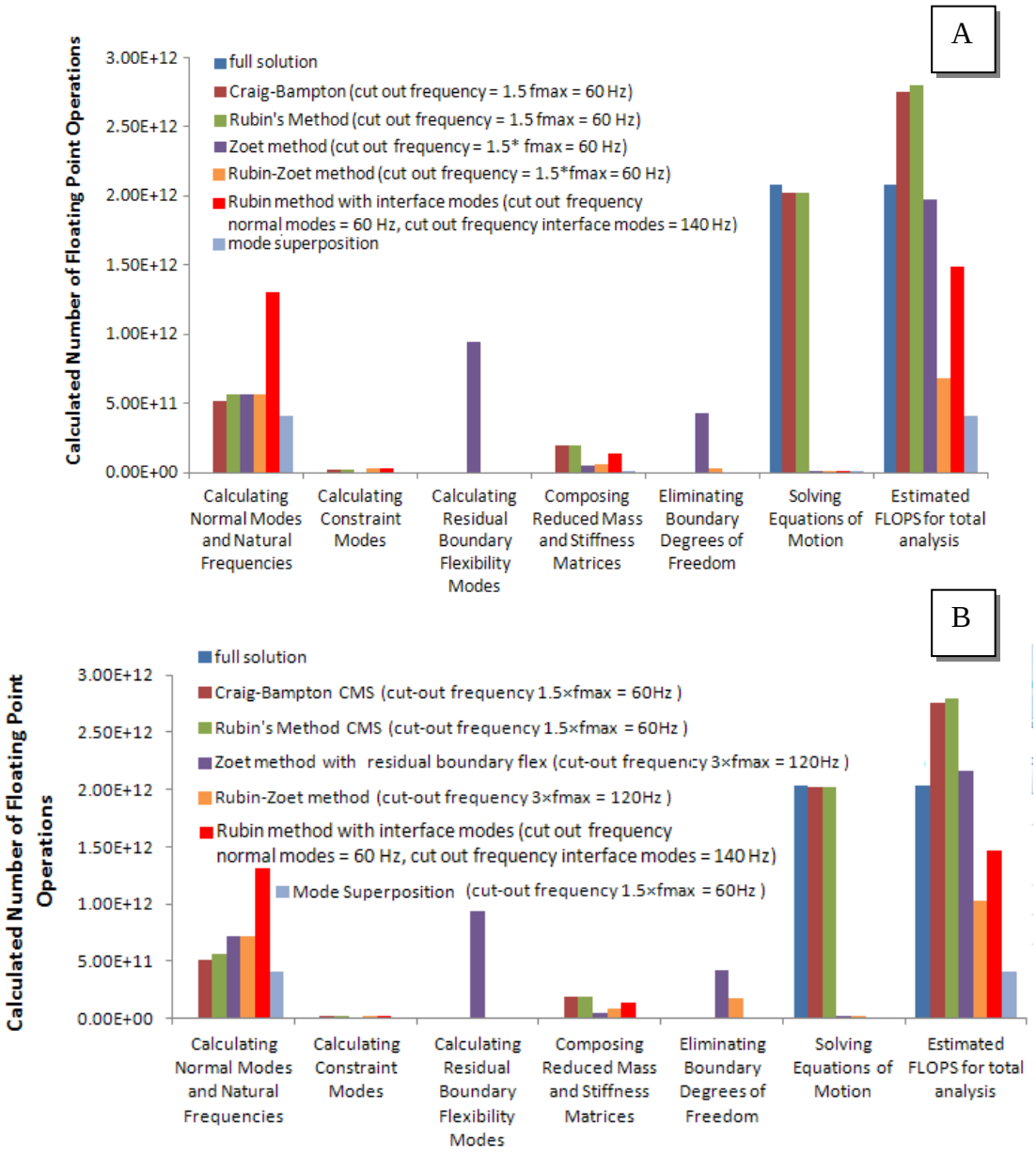

Figure 80 ***Effect of increasing the cut-out frequency for the test case model. Graph A represents the calculation times applying cut-out frequencies of*** $1.5 * f_{max} = 60Hz$ ***for all methods. In graph B the cut-out frequency has been increased to*** $3 * f_{max} = 120\ Hz$ ***for the Zoet and Rubin Zoet method, required for the accuracy of the results. Required calculation results are presented for producing results for 80 frequency steps.***

In section 9 (case study) it has also been demonstrated that the effect of residual flexibility overcompensation seems to become stronger with an increasing number of coupled substructures. When coupling three substructures together, a cut-out frequency of 2 f_{max} gave very accurate dynamic response calculation results. Adding an extra substructure required an increase of the cut-out frequency to 3 f_{max}.

Rubin's Method and the Effect of Overcompensation of Residual Flexibility

Although the Rubin-Zoet method has not been tested, it is assumed that the same increase of cut-out frequency is required for the Rubin-Zoet method, as overcompensation of residual flexibility is assumed to take place in the same manner.

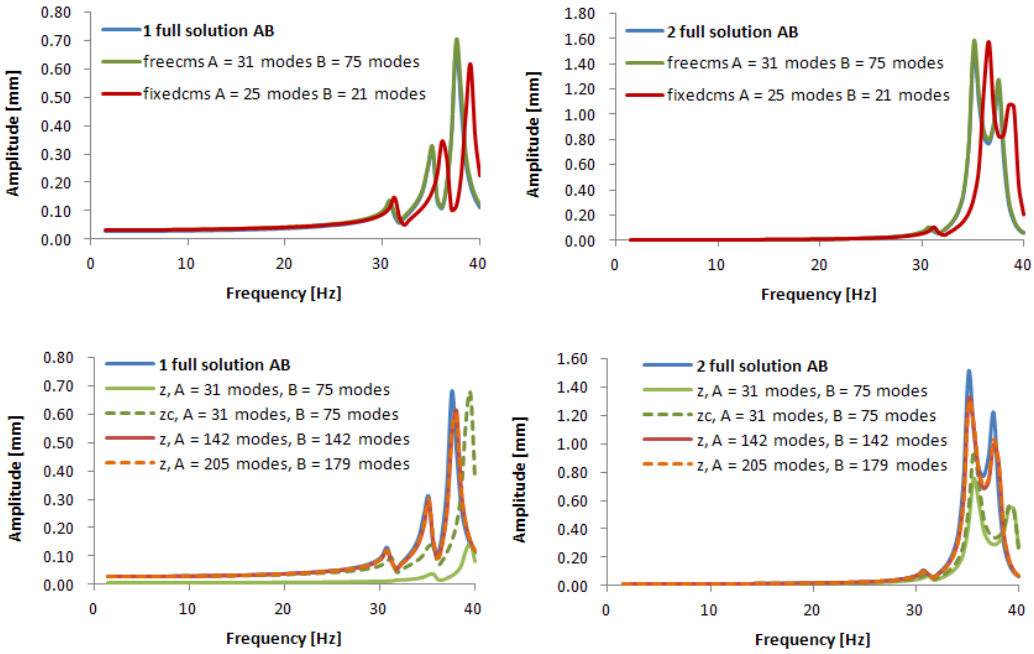

Figure 81 ***Simulation results using different simulation techniques for two coupled sub structures A and B as described in Appendix XXV***

However, it still remains to be investigated if the effect of overcompensation is equally strong using the Zoet technique as for the Rubin- Zoet technique. In Figure 81 the simulation results are presented considering only two coupled substructures: substructure A and Substructure B. The simulation results show that for this particular configuration more mode shapes needed to be expanded using the Zoet

Method, compared to the Rubin Method in order to get roughly the same degree accuracy.

Important to note for these two sets of substructures, is that static compensation plays an important role. Many important global mode shapes of the substructures are above the cut-out frequency of 60 Hz, as substructure A is constrained. The better quality of results of the classic Rubin's technique whilst retaining a much lower number of normal modes suggest that through a better description of compatibility and equilibrium relations, the static contribution is much better described through the Rubin's method. This may also mean that through the reduced number of equations, obtained through the interface degree of freedom elimination technique suggested in this work, the Rubin Zoet reduced set of equations may give a better formulation of modal interaction between substructures as well.

The Effect of Choice of Substructures on Overcompensation of Residual flexibility

Also the choice of distribution of substructures may have an effect on the accuracy of the results and the effect of overcompensation. Considering the results presented in Figure 81, static compensation plays an important role in the outcome of the simulation results, simulating dynamic interaction between substructure A and B of the PHD test model presented in section 9.1. and Appendix XXV. Reason for that is that the constraints at substructure A, this substructure has become a very stiff substructure. Important natural frequencies with global dynamic mode shapes are, as a consequence, way above the classically applied cut-out frequency of $1.5\ f_{max} = 60\text{Hz}$. This means that the dynamic behaviour of substructure A cannot be accurately enough described through classic mode superposition, applying a cut-out frequency of $1.5\ f_{max} = 60\text{Hz}$, and a disproportionate higher number of mode shapes needs to be applied as a results. This results in a mathematical description of the sub-structural interaction that depends largely on the presence of the residual flexibility modes. It is very well possible, but have not been tested in this work, that substructures and their boundary conditions should be chosen in such a way, that natural frequencies involving global deformation mode shapes should be as low as possible, preferably with in the frequency range between 0 and $1.5\ f_{max}$. This way,

the mathematical description of the modal dynamic interaction becomes less dependent on the residual modal compensation. As a consequence, the effect of overcompensation of the residual flexibility is expected to be less as well, so that the cut-out frequency can be lower than the here applied 3 f_{max}.

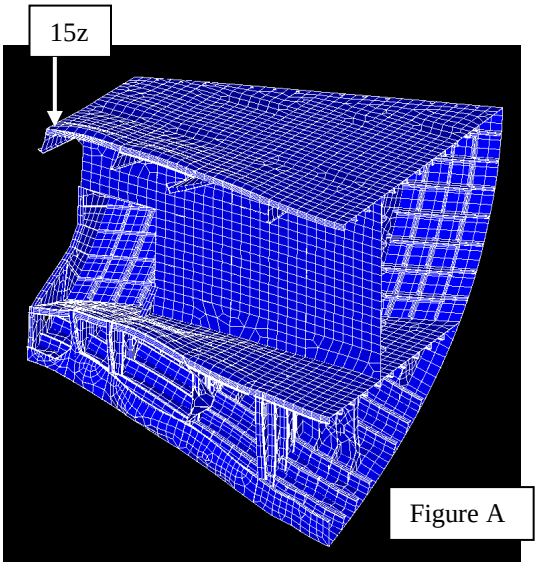

Mode shape at 22.5 Hz according to full harmonic results (see Appendix XXIV)

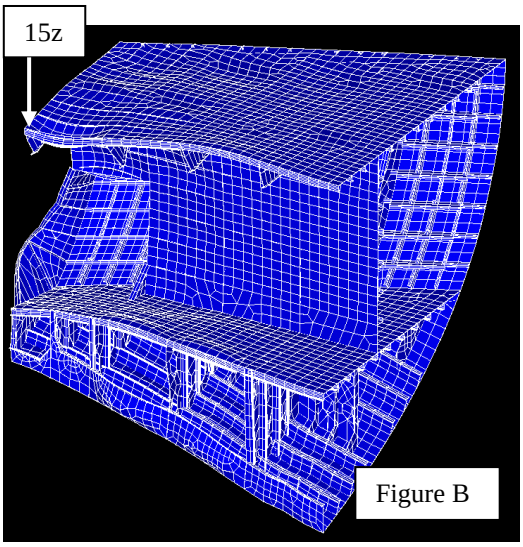

Mode shape at 30.25 Hz according to full harmonic results (see Appendix XXIV)

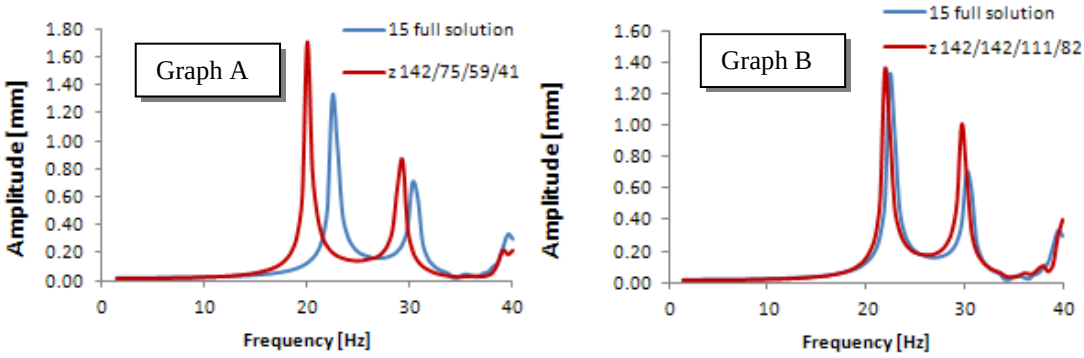

Figure 82 ***As can be seen from the graphs, the effect of overcompensation is less prominent at the resonance peak associated with the mode shape shown in figure B. Graph A shows the results obtained from the Zoet method with residual interface flexibility, applying a cut-out frequency of $1.5f_{max}$ for selecting normal modes of substructure B to D ($3f_{max}$ for substructure A) and together with the results obtained from the full harmonic analysis. Graph B shows the results obtained from the Zoet method with residual interface flexibility, applying a cut-out frequency of $2f_{max}$ for selecting normal modes of substructure B to D, ($3f_{max}$ for substructure A) together with the results obtained from the full harmonic analysis.***

This effect can be further demonstrated with Figure 82. In Figure 82 the deformed shape corresponding with two different frequencies of resonance calculated through the full method of the full PHD model, are presented. Also the graph of the

simulation results obtained through the Zoet method are presented for location 15, plotted together with the results obtained through the full harmonic analysis.

As can be seen from Figure 82, the biggest effect of overcompensation can be seen close to the peak frequency of 22.5 Hz. The effect of overcompensation becomes smaller for the resonance occurring close to 30.25 Hz. This can be seen very clearly from graph A in Figure 82, plotting the results from the Zoet method with residual flexibility applying a cut-out frequency of 2 f_{max} together with the results obtained through the full harmonic analysis. A likely reason for the decreasing effect of overcompensation of residual flexibility is that the related mode shape at 30.25 Hz is less dependent on the description of residual flexibility than the mode shape at 22.5 Hz. This is because the mode shape at 30.25 Hz seems to be the result of a coupling between more localised (elastic) modes, of which most of them have their natural frequencies lower than the cut-out frequency.

9.5 Conclusion

In this section different CMS techniques, the Zoet method with and without residual interface flexibility compensation has been tested and evaluated based on accuracy (compared to full harmonic analysis results) and required computation time. The substructure on which the methods have been tested is subdivided in four substructures and the modelling methods have been evaluated based on required computation time for generating 80 sets of results for 80 frequencies equally distributed between 1 and 40 Hz. It has been established that the boundary conditions have not been described accurately enough through the Zoet method. Boundary flexibility modes had to be incorporated to arrive at the same level of accuracy as the classical CMS methods. Considering the need for incorporating interface flexibility compensation, the computation time for the Zoet method increases drastically, especially when rigid body degrees of freedom of uncoupled substructures are not fully constrained.

From a computation time point of view, the Rubin Zoet method was found to be the most time efficient CMS technique. Figure 83 shows graphs comparing computation

times required for all methods, in order to get similar accuracies, i.e. that the results coincide well enough with the results obtained from the full harmonic analysis.

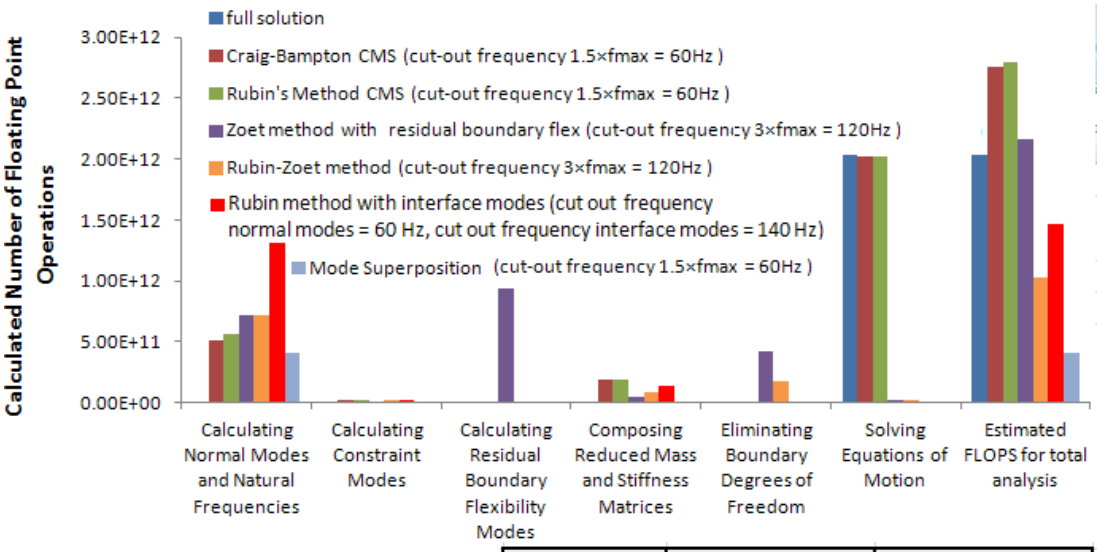

	Computation Time Difference with Rubin's Method	Computation Time Difference with Full Harmonic Analysis	Computation Time Difference with Rubin's Method with Interface Modes
full solution	-27.5%	0.0%	37.9%
Mode Superposition	-85.4%	-79.8%	-72.2%
Craig-Bampton CMS (cut-out frequency 1.5×fmax = 60Hz)	-1.7%	35.6%	87.1%
Rubin's Method CMS (cut-out frequency 1.5×fmax = 60Hz)	0.0%	38.0%	90.4%
Rubin method with interface modes	-47.5%	-27.5%	0.0%
Zoet method with residual boundary flex (cut-out frequency 3×fmax = 120Hz)	-22.9%	6.4%	46.8%
Rubin-Zoet method (cut-out frequency 3×fmax = 120Hz)	-63.3%	-49.4%	-30.2%

Figure 83 ***PHD Test case model: Differences in total computation time between simulation techniques expressed in percentages restively to: Classical Rubin's method (no residual compensation), full harmonic analysis and Rubin's method with interface reduction. Analysis times are based on producing 80 result sets for 80 frequencies evenly distributed between 1 and 40 Hz.***

9.5.1 Evaluation Rubin-Zoet Method

Considering the need for including residual boundary flexibility modes for the Zoet method, the Rubin-Zoet method approach was found to be the most time economic approach, based on the calculated number of floating point operations required for each step in the analysis. Although the Rubin-Zoet method has not been tested, it is assumed that the effect of overcompensation of residual flexibility (as described in section 8.5.3) is the same as found for the Zoet method, as both methods use the same procedure for the reduction of the final CMS matrices (as described in 8.5.2).

Estimated calculation times are therefore also based on the need to increase the number of retained normal modes (by increasing the cut-out frequency from 1.5 f_{max} to 3 f_{max}) in order to reduce the effect of overcompensation of interface flexibility. By increasing the number of retained elastic modes, the contribution from the boundary flexibility modes decreases. As it is through the elimination of the contribution from these boundary flexibility modes that boundaries flexibility is over compensated, this overcompensation effect is decreased as well.

Compared to the classic CMS methods, an increase of computation time in the generation pass is required in order to reduce the CMS matrices and achieve reduction of computation time required for solving these CMS matrices (see Figure 83):

- Applying the interface degree of freedom elimination technique suggested in section 8.5 has to be applied as an extra step to the classic CMS generation pass and adds extra calculation time (see Figure 83):
- A higher number of retained normal modes had to be applied compared to classical CMS, in order to reduce the effect of overcompensation of residual flexibility. This increases the computation time required for calculating mode shapes and natural frequencies, as again can be seen in Figure 83

Figure 83 also clearly demonstrates that the decrease of computation time achieved through the reduction of the CMS matrices is much larger than the increase of computation time required in the generation pass described above.

Although it has been assumed that the impact of overcompensation of interface flexibility of the Rubin-Zoet method is the same as for the Zoet method, the question remains how this impact is affected by the differences in describing interface compatibility and equilibrium between the Zoet and Rubin-Zoet method.

9.5.2 Evaluation Zoet Method with Residual Compensation

The Zoet Method with Residual flexibility modes requires more computation time than the Rubin-Zoet method because:

- The calculation of residual interface flexibility requires much more computation time than the computation of constraint modes, through which the classical Rubin's method described residual compensation. This is particularly because the rigid body modes of three of the four individual uncoupled substructures are un-constrained. Expensive rigid body degrees of freedom elimination techniques are required for the calculation of the residual boundary flexibility modes.

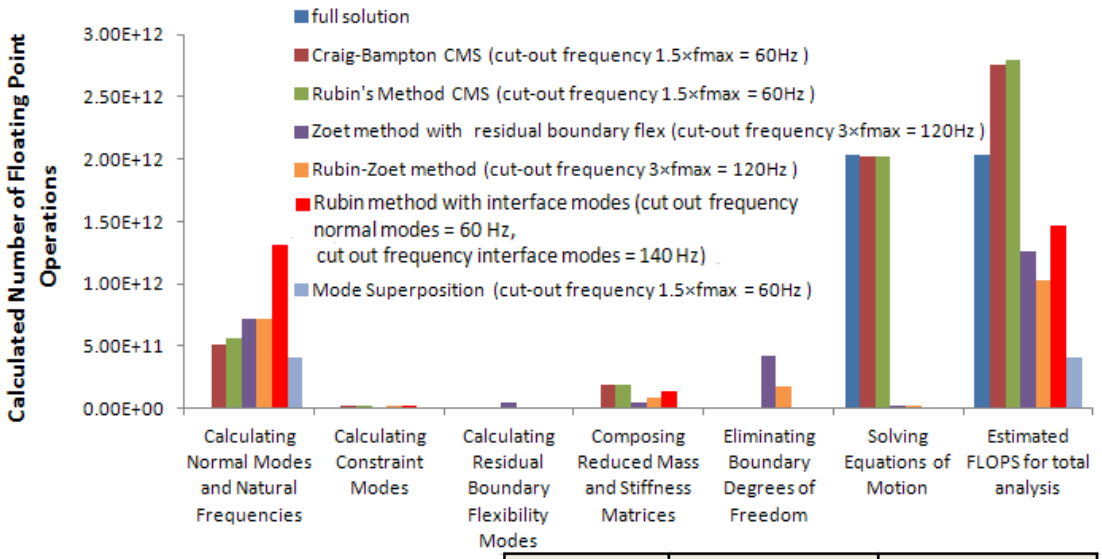

	Computation Time Difference with Rubin's Method	Computation Time Difference with Full Harmonic Analysis	Computation Time Difference with Rubin's Method with Interface Modes
full solution	-27.5%	0.0%	37.9%
Mode Superposition	-85.4%	-79.8%	-72.2%
Craig-Bampton CMS (cut-out frequency 1.5×fmax = 60Hz)	-1.7%	35.6%	87.1%
Rubin's Method CMS (cut-out frequency 1.5×fmax = 60Hz)	0.0%	38.0%	90.4%
Rubin method with interface modes	-47.5%	-27.5%	0.0%
Zoet method with residual boundary flex (cut-out frequency 3×fmax = 120Hz)	-55.0%	-37.9%	-14.3%
Rubin-Zoet method (cut-out frequency 3×fmax = 120Hz)	-63.3%	-49.4%	-30.2%

Figure 84 ***PHD Test case model assuming rigid body degrees of freedom of the uncoupled structures restrained: Differences in total computation time between simulation techniques expressed in percentages restively to: Classical Rubin's method (no residual compensation), full harmonic analysis and Rubin's method with interface reduction. Analysis times are based on producing 80 result sets for 80 frequencies evenly distributed between 1 and 40 Hz.***

- The application of the matrix reduction technique (eliminating interface degrees of freedom) requires more calculation time as roughly double the number of interface degrees of freedom is retained for the Zoet method, as a consequence of defining compatibility and equilibrium through interface elements instead of interface nodes.

Reduction of computation times similar to the Rubin-Zoet method may be achieved when rigid degrees of freedom of the individual uncoupled substructures are constrained, as shown in Figure 84. This will make the Zoet method 14% faster than the boundary interface reduction method following the IRS method.

9.5.3 Evaluation Rubin Method with Interface Modes

Although the method has not been tested, calculation times that would have been required for the Rubin's method applying interface reduction through introducing interface modes have also been estimated based on a cut-out frequency of 1.5 f_{max}. Interface modes with their corresponding natural frequencies have been calculated. The number of retained interface modes has been based on applying a cut-out frequency of 3.5 f_{max} following the findings of Tran [41]

Although this reduction technique considerably reduces the size of the total assembled set of equations of motion, the Rubin-Zoet method has been found superior in reducing calculation time for the following reason:

- Generating the reduced stiffness and mass matrix according to the IRS method (see section 6.5.3) results in an increase of required calculation time in the generation pass, compared to the Rubin-Zoet method.
- The Rubin's method with interface modes requires extra calculation time in the generation time for the calculating of interface modes and natural frequencies. The increase of calculation time has been estimated to supersede the calculation time of the normal modes for the Rubin-Zoet method, even though the Rubin-Zoet method is assumed to require an increased cut-out frequency of 3 f_{max}, instead of 1.5 f_{max}

9.5.4 Evaluation Mode Superposition Method

Figure 83 the computation time required for obtaining modal coordinates through performing classical modal reduction on the full model is presented. As can be seen, mode superposition brings the highest efficiency in computation time. However, disadvantages relatively to CMS techniques are:

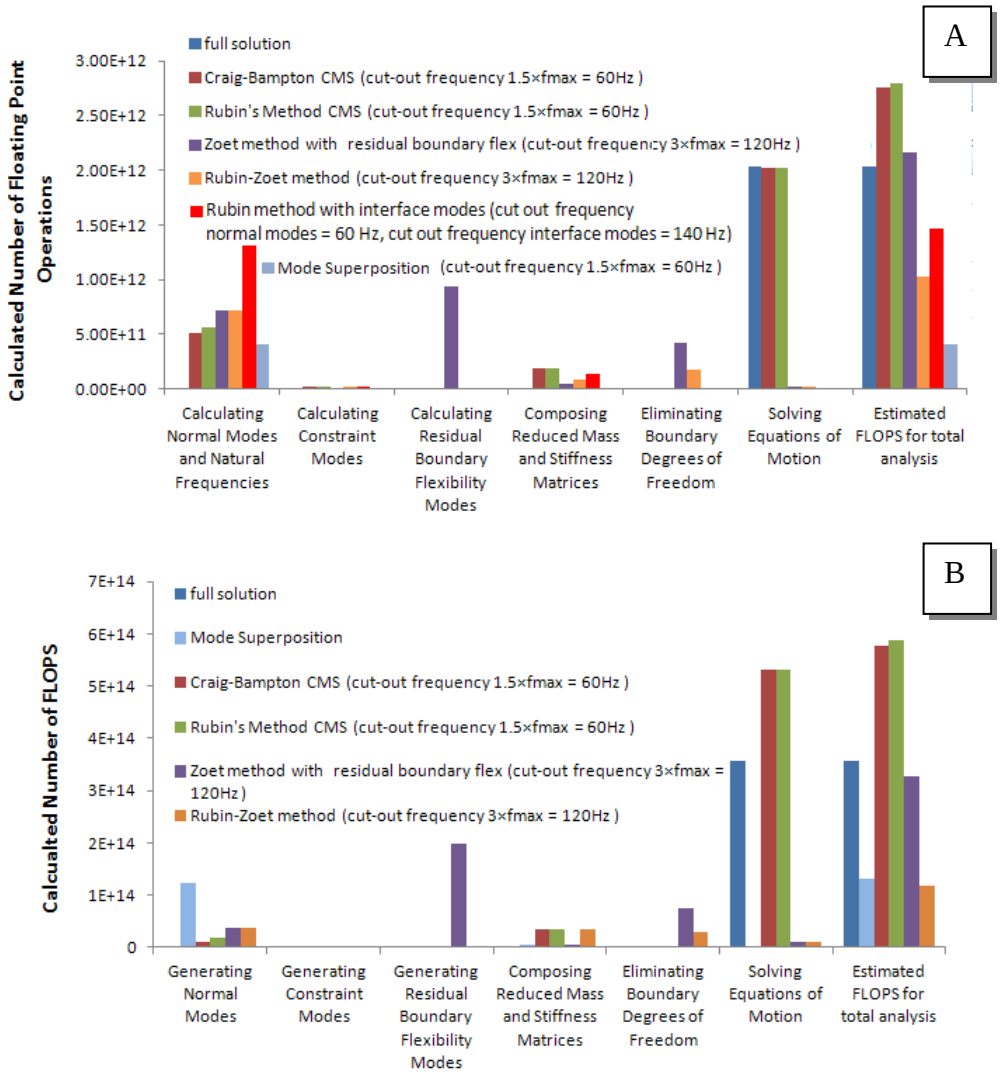

Figure 85 ***Number of floating point operations required for the different techniques considering the analysis of the PHD test case model (graph A) and the analysis of the LNG structure (graph B). Calculation times presented are based on running the free interface models retaining a sufficient number of normal modes so that equal levels of accuracy is obtained comparing output results with the results obtained through the full harmonic analysis.***

- Problems with plotting mode shapes as experienced with the full harmonic annalysis remain, as memory requirements stay the same as the size of the output files don't change.
- A disproportionately higher increase of computation time may be required for calculating the natural frequencies and mode shapes for the total structure compared to the total time required for calculating of the mode shapes and natural frequencies of all uncoupled substructures. This effect is demonstrated in Figure 85 and becomes stronger with:
    - Increase of model size (as can be seen comparing the required computation time for the LNG model and the PHD test model in Figure 85)
    - Increases with the number of substructures applied.

9.5.5 Using CMS for Time-Domain Analysis

Reducing time required to solve CMS matrices is also very beneficial for reducing analysis times required to run a time domain, transient analysis. This type of analysis could be useful to carry out for the aft ship of the LNG carrier as violent cavitation (cavity implosion) was found to generate an impulsive irregular excitation characteristic which could have been the reason for the dominant presence of the higher order blade passing frequency components in the vibration measurement results. Figure 86 shows the estimated number of floating point operations (computation time) required for carrying out a time domain analysis running over 2 seconds and requiring 2400 time steps (see Figure 86 for more details on the assumed conditions of the simulation).

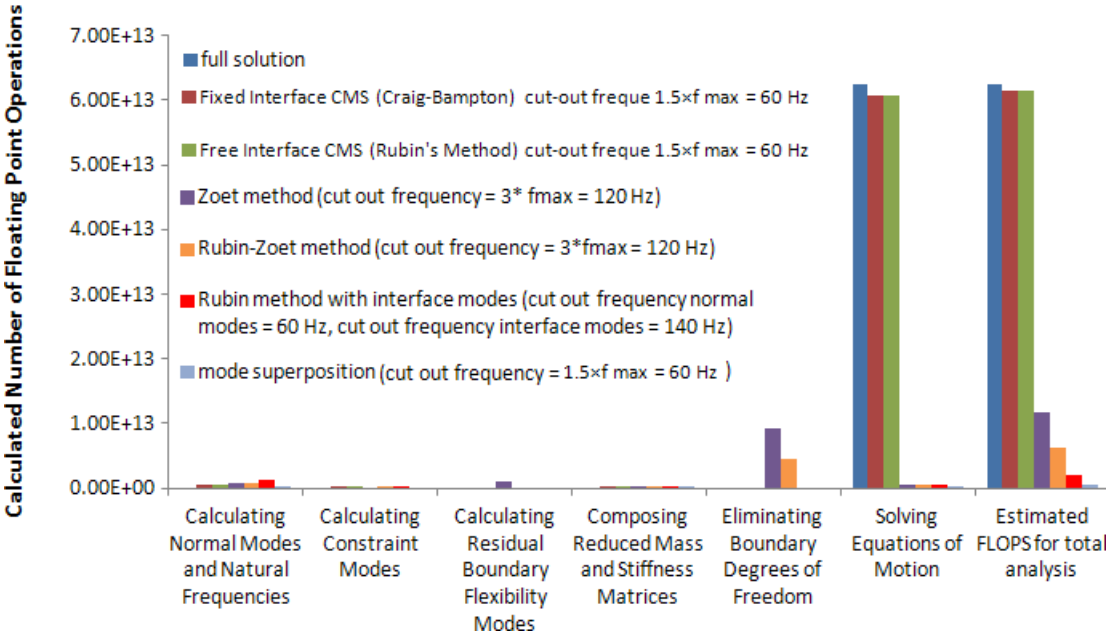

Figure 86 ***Simulation time for time domain analysis calculating the dynamic response over 2 seconds in 2400 time steps (PHD test model). Number of time steps is based on subdividing the highest frequency of interest into 20 steps. This highest frequency of interest is assumed to be*** $1.5 * f_{max}$ ***according to Rubin's criteria.*** f_{max} ***is 40 Hz, as most of the vibration energy is concentrated over the first 5 blade passing frequency orders. Calculation times presented are based on running the free interface models retaining a sufficient number of normal modes so that equal levels of accuracy is obtained comparing output results with the results obtained through the full harmonic analysis.***

As can be seen from Figure 86, reduced CMS methods are very effective in reducing computation time for time domain analysis. However, as the interface reduction technique according to the Zoet and Rubin Zoet needs to be carried out for each time step, the computation time required in the generation stage increases with the number of integration steps. This means that the interface reduction technique according to IRS method (using interface modes) becomes more effective with an increasing number of time steps, as the interface reduction only needs to be carried out once, which means that the calculation time in the generation pass is independent of the number of time steps or frequencies for which simulation results need to be produced.

10 Discussion

This chapter begins with a recap of the thesis, giving a summary of the background and motivation and aims of the work and the steps taken in order to contribute to the aim. In the section 10.2 “Contributions and Achievements” a summary is given of what has been achieved in this work and how these achievements contribute to the aims described section 2 and paragraph 10.1.

In section 10.3 “Shortcomings and Limitations of the Zoet and Rubin-Zoet Methods” short comings of the developed reduction methods are identified. This leads to paragraph 10.4 “Future Work” where future work is suggested

10	Discussion
10.1	Recap of the thesis
10.1.1	Aim of This Work
10.1.2	Critical Review and Selection of Modelling Techniques
10.1.3	Modelling of the Structural Response of an LNG Carrier
10.1.4	Problems Encountered with the Full Harmonic Analysis
10.1.5	Advantages of a Sub-Structural Approach
10.1.6	Identified Problems with Classical Sub-Structural Approaches
10.1.7	Development of the Zoet Method
10.1.8	Zoet Method with Residual Boundary Flexibility
10.1.9	The Rubin-Zoet Method
10.2	Contributions and Achievements
10.3	Shortcomings and Limitations of the Zoet and Rubin-Zoet Methods
10.3.1	Increase of Required Cut-Out Frequency
10.3.2	Analysing a Lower Number of Frequencies
10.3.3	Analysing over a Smaller Frequency Range
10.3.4	Using Zoet and Rubin-Zoet for Time-Domain Analysis
10.4	Future Work

Paragraph structure of chapter 10 ‘Discussion’

10.1 Recap of the thesis

In the marine industry there is a lot of pressure on structural designers to design marine structures that have to be capable of withstanding high alternating loads. These alternating loads result in high vibration levels and high alternating stresses through which crew performance and passenger comfort is affected and lifetime of structures and machinery is reduced.

The pressure for understanding the characteristics of irregular forces and corresponding structural response mechanism is even increasing. In view of recent research done for the FP7 EU project SILENV, addressing impact of noise and vibrations on humans and underwater life, more stringent noise and vibration requirements are expected in the near future. In addition, given the global economic environment and raising fuel prices, equipment and structures are dynamically further pushed to the limits.

Using (the right) theoretical deterministic structural response evaluation modelling techniques is more important than ever. New radical design concepts are developed in the marine industry, and relying on tradition or statistical modelling techniques becomes impossible.

10.1.1 Aim of This Work

This work is focussing on the problems with classical structural modelling techniques related to:

- Labour intensity of the process of generating structural models
- Problems with (large) computation times required for obtaining structural dynamic response calculation results
- Problems with handing large result files

10.1.2 Critical Review and Selection of Modelling Techniques

The first step in finding solution to the modelling problems experienced in the industry is a critical review of some state of the art modelling techniques used.

For selecting the most suitable modelling technique, also noise and vibration measurement results have been studied which have been taken on board three different types of vessels for the EU research project SILENV.

From the studies of the measurement results and literature review, propeller and engine vibration excitation spectra were found to have most of the energy concentrated in very distinct tonal harmonics rapidly decreasing in amplitude with increasing order number. Combined with the complex nature of ship structures, and

the related low modal density, Finite Element based modelling techniques have been found the most suitable modelling technique for modelling the structural vibratory response of marine structures.

10.1.3 Modelling of the Structural Response of a LNG Carrier

After selecting finite element based modelling techniques as the most suitable technique for modelling ship structural response to propeller and engine excitation, some of these techniques have been tested in this work. A finite element model has been built of a LNG carrier on board which the author has carried out vibration measurement. As the vessel is equipped with (very low vibration) steam turbines, only the propeller excitation has been taken into account. The alternating hull pressure field induced by the propeller calculated by SSPA has been used.

In order to study the response behaviour of the structure, simulations have not only been carried out for the blade passing harmonic frequencies of interest, but for a range of 80 frequencies equally distributed over a range between 0 to 40 Hz. 40 Hz has been chosen as the maximum limit, as through the measurement results all vibration energy was found to be concentrated between 0 and 35 Hz. Plotting amplitude levels against frequency shows where the relevant resonance peaks are. As the proximity of resonance frequencies to excitation frequency is the most important factor in the sensitivity of the model, simulation results for such a number of frequencies is very useful to understand the vibratory response of the model and to be able to understand any discrepancies between the modelling results and the measurement results.

Good correlation between the measurement results and simulation results was found for the response at the first two blade passing frequencies. Simulated response to higher order blade passing frequencies however were found to be much lower than measured. The unsteady nature of some of the vibration measurement results and the noise experienced at the aft ship during the measurement campaign strongly suggest that violent cavitation took place at the aft ship. Predicted amplitudes of excitation at orders higher than 2 become less reliable, as the amplifying effect of cavity implosion is not taken into account with the simulation of the excitation. His problem

is typical for the type of vessel at hand as the shape of the aft ship induces a highly irregular distribution of wake at the propeller.

10.1.4 Problems Encountered with the Full Harmonic Analysis

With the generation of results for the LNG carrier through the classical full harmonic analysis, problems have been experienced due to the size of the output files. As a result, no mode shapes could be studied, which is crucial for fully understanding the mechanisms of the simulated structural dynamic behaviour.

Component Mode Synthesis modelling (CMS) techniques brought the solution to the problem. Component mode synthesis is a sub-structural modelling technique based on subdividing the total to be analysed structure into a number of sub structures. Of these substructures so called super elements are generated containing modal information of these individual uncoupled substructures. Two groups of CMS methods are distinguished: a method based on describing the sub-structural dynamic properties with all interface nodes fully constrained (fixed interface CMS) and with all interface nodes free (free interface CMS). The CMS methods tested on the LNG carrier are the free interface CMS method according to Rubin (with no residual interface flexibility taken into account) and the fixed interface method according to Craig-Bampton.

The accuracy of these methods have been evaluated through comparison of the simulation results with the results obtained through the classic full harmonic finite element analysis. As the most important aspect of structural response is the proximity of natural frequencies to the excitation frequencies, a CMS method was assumed to be accurate enough if calculated peak response frequencies coincide with the peak response frequencies found through the full harmonic analysis. As a frequency step of 0.5Hz has been applied, this means that the calculated CMS peak response frequency should be between -0.25 Hz and +0.25 Hz from the peak response frequencies calculated through the full harmonic finite element method.

Based on retaining a number of normal modes applying a cut out frequency of 1.5 f_{max}, free interface CMS based on Rubin's method has been identified as the

most suitable CMS modelling technique for modelling ship vibrations. Not only did the peak response frequencies obtained from the Rubin's method modelling technique coincide with the peak response frequencies obtained from the full harmonic finite element analysis, calculated amplitudes also coincided very well with the amplitudes obtained from the full harmonic analysis.

10.1.5 Advantages of a Sub-Structural Approach

Free interface Component Mode Synthesis (CMS) was found to give the most accurate results, using the full harmonic analysis results as reference. Not only does the free CMS method give the best results, this technique also has other great advantages. As a free interface approach is adopted, the modal properties can be much easier correlated through modal information obtained through measurements performed on substructures that already have been built. This means that the structural properties of the complete structural model are already correlated to measurement results, whilst the actual structure has not been completely built yet.

Another very important advantage of a sub structural approach is that marine structures typically consist of many repeating structural elements (frame sections, decks etc.) for which calculated natural frequencies and mode shapes can be reused. Also CMS can be used for reduction using the symmetry of models. This not only reduces calculation times, but also reduces the effort that has to be put in creating the model (describing the geometry).

10.1.6 Identified Problems with Classical Sub-Structural Approaches

However, carrying out the simulations through the classical CMS techniques using ANSYS, the total required commutation time had increased by roughly 53%, compared to the time needed for the classical harmonic analysis (see Figure 87).

An inventory of the different steps in the analysis following Rubin's free interface CMS method (as used by ANSYS) has been made. For each step expressions have been formulated for the number of floating point operations required (FLOPS). Using the number of floating point operations as an indication of the amount of computation time, the conclusion has been drawn that the computation time required

for solving the reduced set of equations of motion was the most dominant aspect in the total analysis time required for getting dynamic response results through CMS.

The way of formulating compatibility and equilibrium on interfaces between substructures was found to be an important aspect resulting in the higher calculation times. Classical CMS formulates the interaction between substructures for each interface degree of freedom separately. This means that with a high number of coupling nodes, as was the case with the LNG structure, relatively large matrices are formed according to the classical CMS method. Although these matrices are still a lot smaller than the full matrix formed according to the classical full harmonic analysis, the high density of the CMS matrices resulted in the increase of time needed for solving the matrix equations of motion (50% increase for the LNG carrier)

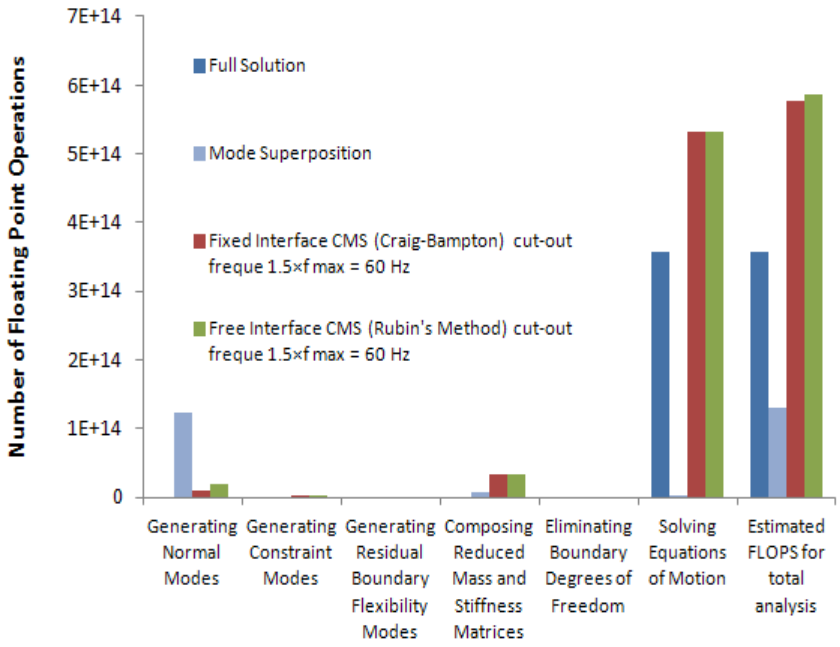

Figure 87 ***Comparing calculation time required for calculating the structural response at 80 frequencies evenly distributed from 1 to 40 Hz for the LNG carrier. Free interface method is carried out according the Rubin's method and the fixed interface method is carried out according to the Craig-Bampton method. A cut out frequency of 60 Hz ($1.5\ f_{max}$) has been applied for selecting the normal modes.***

10.1.7 Development of the Zoet Method

As the density of the reduced matrices could not be reduced, this work focussed on decreasing the size of the matrices by introducing an alternative way of formulating compatibility and equilibrium relations on the interfaces between substructures. The description of compatibility and equilibrium was described through modal coordinates instead of physical interface displacement coordinates, which created an independency of the number of connecting nodes between substructures. This is the method referred to in this work as the Zoet method.

10.1.8 Zoet Method with Residual Interface Flexibility

Simulation results using this method however demonstrated that including residual boundary flexibility modes was crucial for an accurately enough definition of the equilibrium relations. Introducing boundary flexibility modes however meant that the size of the CMS matrix was again, as with the classical method, dictated by the number of coupling nodes between substructures.

The next step in the development was the introduction of a interface residual flexibility mode elimination technique through which a description of sub structural interaction was formulated based on the modal coordinates of the retained substructure normal modes alone. This CMS technique is referred to in this work as the Zoet method with residual interface compensation.

However, with the development of the theory, it had already been recognised that the method of compiling the total assembled CMS matrix, should result in an overcompensation of residual flexibility. This has been confirmed by modelling results running different analysis techniques on a test structure that has been subdivided into four substructures. Increasing the number of retained normal modes based on a cut-out frequency of 3 f_{max} (instead of the classically applied 1.5 f_{max}) the effect of overcompensation was reduced and good coincidence with the full harmonic analysis results was achieved. By increasing the number of retained elastic modes, the contribution from the boundary flexibility modes decreases. As it is through the elimination of the contribution from these boundary flexibility modes

that boundaries flexibility is over compensated, this overcompensation effect is decreased as well.

Although reduction of calculation time has been achieved with the Zoet method with residual interface flexibility, relatively to the classical CMS methods, the Zoet method is not the most effective method when there are substructures involved that have unconstrained rigid body degrees of freedom in uncoupled condition. For the calculation of the residual flexibility modes, these rigid body degrees of freedom need to be eliminated, which is a costly computation event.

10.1.9 The Rubin-Zoet Method

As rigid body degrees of freedom occurred with three of the four substructures of the test structure, and occur with many typical ship substructures, a third CMS method is suggested.

This method is based on applying the same matrix reduction technique as used for the Zoet method (with residual interface flexibility), but is applied on the interface compatibility and equilibrium formulations according to the classic Rubin's technique. This technique is referred to in this work as the Rubin- Zoet technique. A huge advantage of this technique is that the omitted normal modes are compensated through constraint modes, instead of residual flexibility modes, as was the case with the Zoet method. This means that no expensive rigid body degrees of freedom elimination techniques are required in case of unconstrained rigid body degrees of freedom for individual substructures.

Considering the same total CMS matrix compilation technique is used as for the Zoet technique, overcompensation of residual flexibility is however likely to occur in the same manner, and an increase of cut-out frequency for selecting the number of retained normal modes is required.

Also assuming a cut-out frequency of for 3 f_{max} for selecting normal modes for the Rubin-Zoet method was found the most time economic CMS method of all CMS methods described.

Using constraint modes instead of residual flexibility modes means that in case of the PHD test structure, a reduction of computation time by 50% may be achieved applying the Rubin-Zoet method instead of the Zoet method. Better economy may also be achieved with the Rubin-Zoet method compared to the already existing interface reduction method using interface modes according to the IRS method (see section 6.5.3). In the case of the PHD test structure, required computation time decreases by 31% applying the Rubin-Zoet method instead of the Rubin method using the interface reduction technique according to the IRS method (see Figure 88).

10.2 Contributions and Achievements

Due to the increased pressure on the marine industry on reducing noise and vibration levels, structural response modelling techniques are increasingly used as a tool for evaluating design concepts on their impact on noise and vibrations. From literature review, critical review of the principles of most used modelling techniques, and from studies of measurement result, finite element modelling technique has been selected as the most appropriate modelling technique for simulating structural response for marine structures. However, many problems with the application of the finite element technique for the simulation the response of marine structures are experienced. The following problems are encountered:

- Due to the typically complex geometry of marine structures, building a finite element model (describing the geometry and generating the mesh) is often labour intensive.
- Uncertainty in material properties, added (hydrodynamic) mass and damping, excitation characteristic and inaccuracies in the described geometry.
- Due to the complex geometry and scale of the structure, problems occur with the size of the generated dynamic matrices (number of degrees of freedom) and result in problems with:
    - Required computer memory
    - Problems with handling output files (plotting mode shapes, obtaining results)
    - Required computation time

These problems have also been experienced with the modelling of the structural response of the aft ship of an LNG carrier presented in this thesis.

Considering the nature of ship structures, a sub-structural approach as adopted with component mode synthesis techniques has been further investigated. Two new approaches to component mode synthesis methods have been suggested, in order to overcome problems with computation time encountered with the application of the classical component mode synthesis techniques. The following has been achieved through these new methods:

10.2.1 Decreasing Effort Required for Building the Model

A sub-structural approach to marine structures may be very efficient in reducing required effort that has to be put in building the model, making use of the fact that a marine structure can be subdivided in many repeating similar substructures. Time required to model large part of a ship structure and required computer storage memory can be decreased as only one repeating substructure needs to be modelled. In addition, symmetry can also be used to reduce the model size.

10.2.2 Building More Accurate Models

Uncertainty about material properties and accuracy of the described geometry can be partly eliminated using sub structural modelling techniques. By choosing the substructures in such a way that they coincide with the sections as they are built in reality, modal properties can be correlated to modal measurements results taken on the actual sections, once they have been built.

10.2.3 Reducing Required Computer Memory

A sub-structural approach to marine structures may be very efficient in reducing required computer memory, making use of the fact a marine structure can be subdivided in many repeating similar substructures. Modal information needs to be obtained only once for such a substructure, through which the final matrix can be compiled and the total assembled sub structural behaviour can be solved.

As results are produced per substructure, output files are much smaller. In this work, problems have been experienced with presenting modeshapes obtained through full harmonic finite element analysis. These problems were related to the size of the output files and have been successfully circumnavigated by applying classical component mode synthesis.

10.2.4 Reducing Required Computation Time

Although the size of stiffness and mass matrices is reduced considerable through the CMS reduction technique, the high number of coupling degrees of freedom between substructures, as typically seen for ship structures, largely increases the density of the final CMS matrices. Although, as pointed out above, these matrices are still considerably smaller than the matrices that need to be solved for the full harmonic analysis, the high density of these matrices has resulted an increase of computation time, even exceeding the computation time required for the full harmonic analysis.

In order to reduce the computation time required for solving the CMS matrices, two new CMS matrix reduction techniques have been proposed:

- The Zoet Methods (with and with residual boundary flexibility modes)
- The Rubin-Zoet method

Tests have been run on a smaller scale structure with the application of the Zoet Method. As a penalty to the applied interface reduction, an increase of the number of retained normal modes was required in order to achieve the same accuracy as the classic Rubin method. No tests have been carried out with the Rubin-Zoet method, but as the same interface reduction technique has been used, the same increase of the required number of retained normal modes as for the Zoet method is assumed, in order to get the same accuracy.

Based on above, comparison of required computation times for different modelling techniques has been done as presented in Figure 88 and Table 18. In these figures and table also a comparison is done applying an existing interface reduction

technique according to the IRS method, which is based on using interface modes (see section 6.5.3).

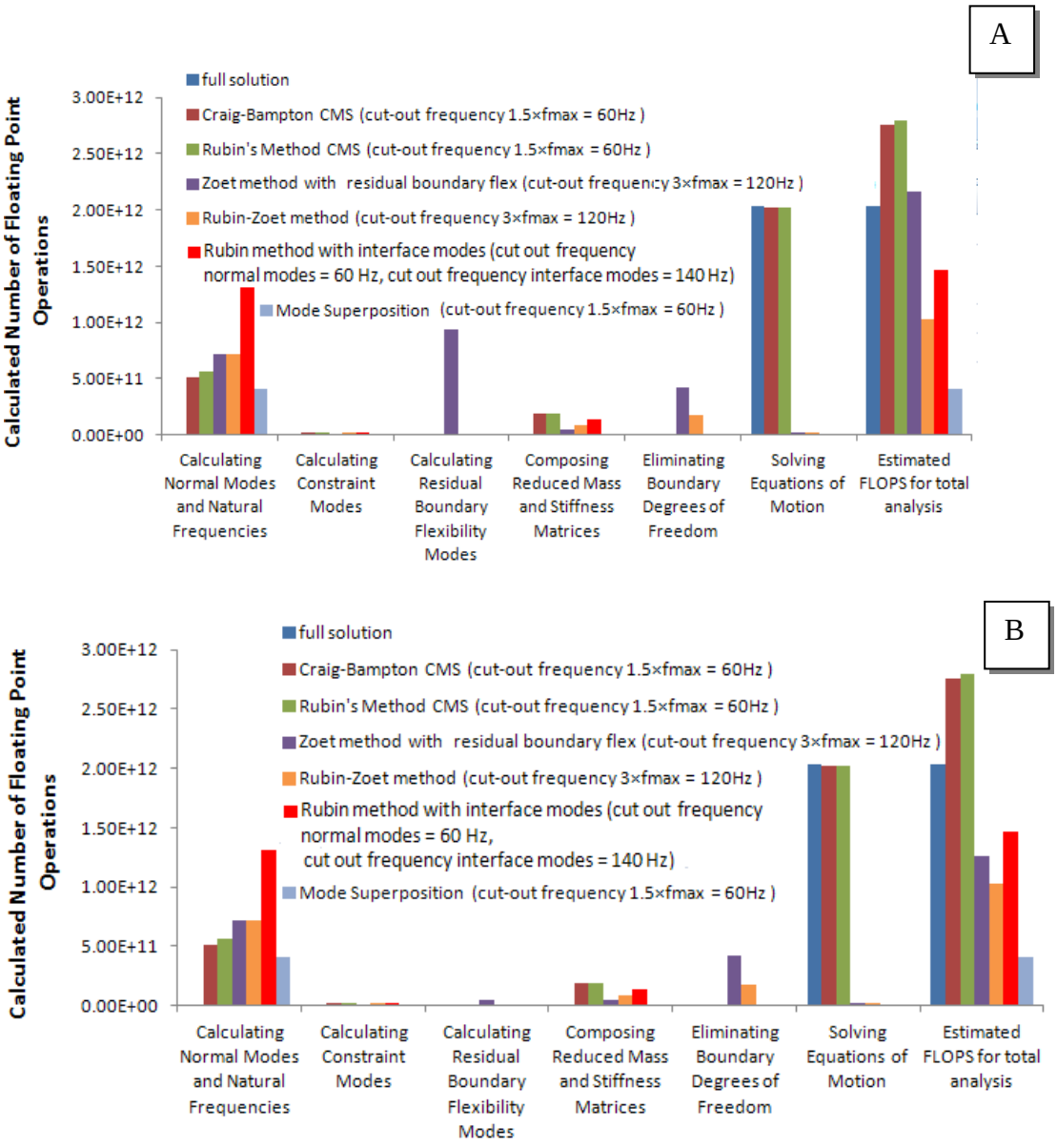

Figure 88 ***PHD test case model: Graph A: Comparing computation time for different simulation techniques for the calculation of the harmonic dynamic behaviour of the PHD test structure. Graph B shows the computation time required if rigid body modes of the individual uncoupled substructures would have been fully constrained***

In Figure 88 calculation times are plotted in bar graphs for each step for the different analysis types. As can be seen in graph B, the Zoet method brings a considerable reduction of computation time compared to the existing CMS methods, as long as all rigid body modes of the individual substructures are fully constrained (total computation time reduced by 55%, see Table 18B).

A

	Computation Time Difference with Rubin's Method	Computation Time Difference with Full Harmonic Analysis	Computation Time Difference with Rubin's Method with Interface Modes
full solution	-27.5%	0.0%	37.9%
Mode Superposition	-85.4%	-79.8%	-72.2%
Craig-Bampton CMS (cut-out frequency 1.5×fmax = 60Hz)	-1.7%	35.6%	87.1%
Rubin's Method CMS (cut-out frequency 1.5×fmax = 60Hz)	0.0%	38.0%	90.4%
Rubin method with interface modes	-47.5%	-27.5%	0.0%
Zoet method with residual boundary flex (cut-out frequency 3×fmax = 120Hz)	-22.9%	6.4%	46.8%
Rubin-Zoet method (cut-out frequency 3×fmax = 120Hz)	-63.3%	-49.4%	-30.2%

B

	Computation Time Difference with Rubin's Method	Computation Time Difference with Full Harmonic Analysis	Computation Time Difference with Rubin's Method with Interface Modes
full solution	-27.5%	0.0%	37.9%
Mode Superposition	-85.4%	-79.8%	-72.2%
Craig-Bampton CMS (cut-out frequency 1.5×fmax = 60Hz)	-1.7%	35.6%	87.1%
Rubin's Method CMS (cut-out frequency 1.5×fmax = 60Hz)	0.0%	38.0%	90.4%
Rubin method with interface modes	-47.5%	-27.5%	0.0%
Zoet method with residual boundary flex (cut-out frequency 3×fmax = 120Hz)	-55.0%	-37.9%	-14.3%
Rubin-Zoet method (cut-out frequency 3×fmax = 120Hz)	-63.3%	-49.4%	-30.2%

Table 18 ***PHD test case model: Differences in total computation time between simulation techniques expressed in percentages restively to: Classical Rubin's method, full harmonic analysis, Rubin's method with interface reduction. Table A gives the results for the case that substructure B to D have unconstrained rigid body degrees of freedom. In table B the results are presented considering all substructure's rigid body degrees of freedom in uncoupled condition fully constrained.***

Comparison of computation time is also made in the graphs with computation time required for an interface reduction technique according to the IRS method, a technique also designed to reduce the size of CMS matrices (see section 6.5.3). It can be seen in Figure 88B that the Zoet method also reduces the analysis time relatively to this existing reduction technique (reduction of 14%, see Table 18B).

However, in most cases, substructures rigid body degrees of freedom are not fully constrained. This results in a sharp increase of calculation time required for the Zoet method. A approach, although it has not been tested in this work, according to the Rubin-Zoet method would be far more beneficial. As can be seen from Figure 88B and Table 18B, the Rubin-Zoet method reduces computation time by 63.3% compared to the classic CMS technique, and by 31 % compared with the Rubin's method, applying interface reduction according to the IRS method.

In Figure 88 and Table 18 can be seen that mode superposition based on modal reduction of the full dynamic matrices is the most time efficient method of all (see 'mode superposition' in Figure 88 and Table 18). However, the following remarks can be made in favour of the Zoet and Rubin-Zoet methods:

- Obtaining results through modal reduction of the full model does not solve the problems encountered in this work with obtaining full sets of results and plotting deformed shapes from these full sets of results. These problems were related to the size of the result files, which is not reduced through the application of modal reduction technique of the full model.
- One important advantage of a sub-structural approach is reduction of computation time that could be achieved when a structure consist of repeating similar sub structures. The number of times that steps in the generation pass need to be repeated can be reduced, as the CMS matrix of only one set of two interacting repeating substructures need to be generated and reduced. These matrices are reused when the total CMS matrix is generated. The computation time reducing effect of this has not been considered in these tests.

10.3 Shortcomings and Limitations of the Zoet and Rubin-Zoet Methods

An important shortcoming of both the Zoet method and the Rubin Zoet method is that the interface residual flexibility elimination technique, in combination with the total CMS matrix compilation technique, results in an over-compensation of residual flexibility. In order to reduce the effect of this over-compensation, an increase of the number of retained normal modes per substructure is needed. This reduces the efficiency of the proposed CMS techniques with increasing number of substructures, and the IRS method interface reduction technique (using interface modes) may become more effective in reducing computation time (see section 6.5.3).

The effectiveness of the Zoet and Rubin –Zoet method is not only limited through the number of substructures used, but also through:

- The number of simulation results required
- The frequency range over which simulation results need to be produced

10.3.1 Increase of Required Cut-Out Frequency

Testing the Zoet method on a test case model, it was found that with the application on a two-substructure model, retaining a number of normal modes based on a cut-out frequency of 1.5 f_{max} was found to be sufficient. This coincides with the required number of retained normal modes for the classic CMS method.

Coupling three substructure together however showed that the number of retained normal modes per substructure had to be increased, and had to be based on applying a the cut-out frequency of 2 f_{max}, in order to get the same level of accuracy as obtained with the classical CMS method.

Coupling 4 substructures together showed that the number of retained normal modes had to be increased again, based on applying a the cut-out frequency of 3 f_{max}, in order to get the same level of accuracy as obtained with the classical CMS method.

The increased effect of overcompensation with an increasing number of substructures is potentially a weak point considering the aim of developing the

reduced CMS method. An important aspect of reducing the calculation time envisaged in this work is the ability to reuse calculated dynamic matrices of (many) repeating sub structural elements, a typical marine structure can be subdivided in. As this required computation time for solving the final high density CMS matrices was by far the most dominant factor determining the total time required for CMS analysis, the first step to effectively reusing repeating substructures was to reduce the size of the final CMS matrices. This has been achieved very effectively through the proposed reduction techniques (Zoet and Rubin Zoet).

However, the penalty that has to be paid for that is an increase of time required in the generation of the reduced CMS matrices.

Due to the effect of overcompensation of residual flexibility, the amount of time required for the generation pass may disproportionately increase with the number of substructures, as the number of required normal modes per substructure needs to be increased as well. The number of required normal modes also increases the size of the total assembled CMS matrix.

Theoretically that means that there is a maximum number of substructures at which the Zoet and Rubin Zoet can still be beneficial compared to the Rubin's method using the IRS method for reducing the interface degrees of freedom.

10.3.2 Analysing a Lower Number of Frequencies

Important to note is that the benefit of the newly introduced technique relatively to the classical full harmonic analysis only starts above a certain number of frequencies for which output results are generated. This is because reduction of time required for solving the final reduced CMS matrices needs to outweigh the extra computation time that is invested in the generation pass. This extra computation time required in order to reduce computation time is due to the need to calculate the following:

- Normal modes and natural frequencies
- Constraint modes or residual flexibility modes
- Reducing the stiffness and mass matrices
- Formulating compatibility relations

- Calculating residual modal flexibility (eliminating residual interface flexibility degrees of freedom)

This is however not just a weak point for the Zoet or Rubin-Zoet method, but this is an even more dominant phenomenon compromising the economy of the already existing interface reduction technique according to the IRS method (see section 6.5.3), as a bigger investment in computation time is required in the generation pass due to the need for calculating the interface modes. In the case of the test structure used for the case study in this work, Figure 89A shows that when choosing less than 35 frequency steps over a range from 1 to 40 Hz, classic harmonic analysis starts to become more economical than the newly introduced Rubin-Zoet method (taking into account an increased number of retained normal modes for matching the accuracy of the results with the classical Rubin Method).

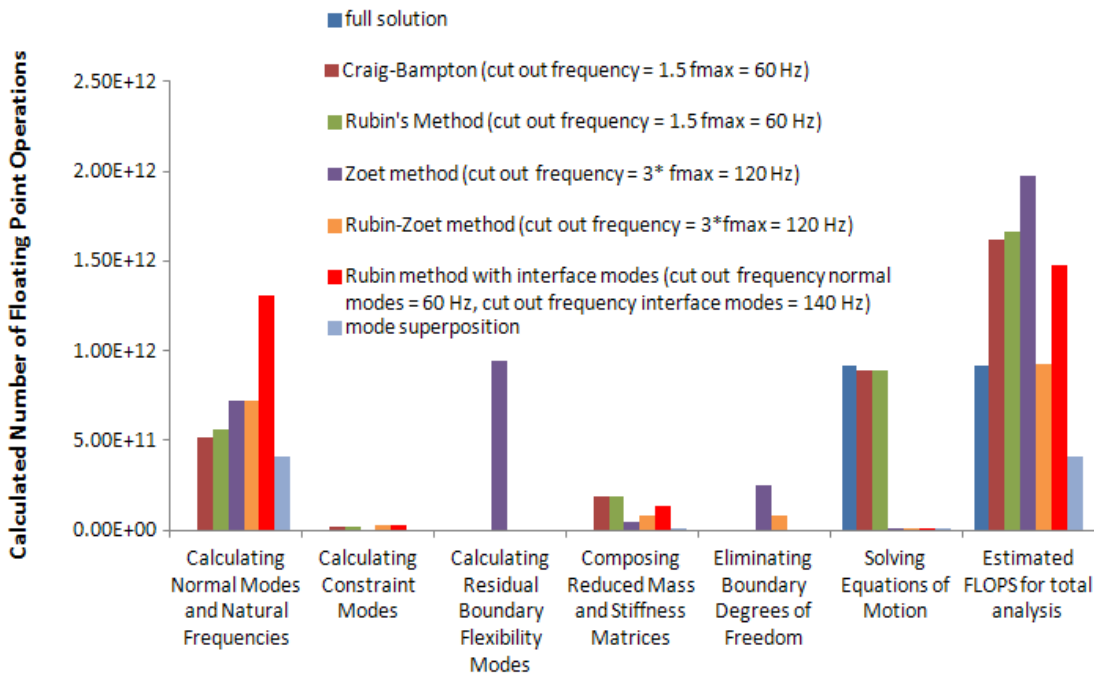

Figure 89 ***Computation times required for the calculation of 35 frequency steps***

10.3.3 Analysing over a Smaller Frequency Range

Considering the effect of overcompensation of residual interface flexibility contribution, the Zoet and Rubin Zoet method do not only become less beneficial in

reducing analysis time with a decreasing **number** of analysed frequencies, but also with a **decrease of maximum frequency** analysed (frequency range of analysis). Increase of the cut-out frequency was required in order to compensate the effect of overcompensation of the residual interface flexibility effect. Applying the tradition cut-out frequency of 1.5 f_{max}, according to Rubin's criteria (as effectively applied on the traditional CMS methods) the effect of overcompensation manifested itself as a shift of peak frequencies over the **entire frequency range** from 1 to 40 Hz to the left, as can be seen from Figure 90. The effect was found to be even stronger at the lower peak frequencies.

Considering carrying out an analysis decreasing the maximum frequency of interest from 40 Hz to 25 Hz, the number of retained normal modes however can unfortunately not be reduced. This means that the computation time required in the generation pass does not decrease either.

This means that the interface reduction technique according to the IRS method could become more competitive, as a reduction of the maximum simulation frequency (f_{max}) should allow a decrease of the number of retained normal modes and interface modes, following Rubins criteria for the section of the retained normal modes (1.5 f_{max}) and applying a cut-out frequency of 3.5 f_{max} for the section of the number of retained interface modes according to Tran's findings.

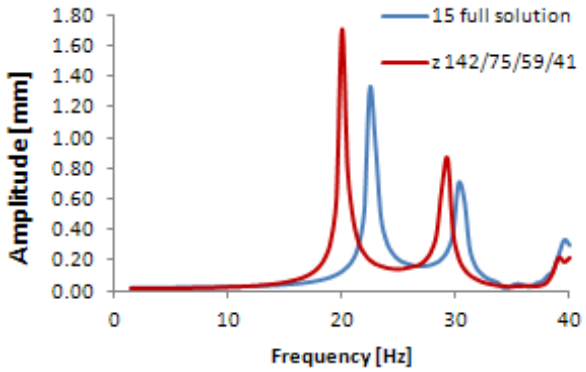

Figure 90 ***Effect of overcompensation on location 15. Applying a cut-out frequency of 1.5 f max, overcompensation of residual interface flexibility applying the Zoet method (red line) shifts the peak response frequencies to the left.***

10.3.4 Using Zoet and Rubin-Zoet for Time-Domain Analysis

Reducing time required to solve CMS matrices is also very beneficial for running a time domain, transient analysis. This type of analysis could be useful to carry out for the aft ship of the LNG carrier as violent cavitation (cavity implosion) was found to generate an impulsive irregular excitation characteristic which could have been the reason for the dominant presence of the higher order blade passing frequency components in the vibration measurement results. Figure 91 shows the estimated number of floating point operations (computation time) required for carrying out a time domain analysis running over 2 seconds and requiring 2400 time steps (see Figure 91 for more details on the assumed conditions of the simulation).

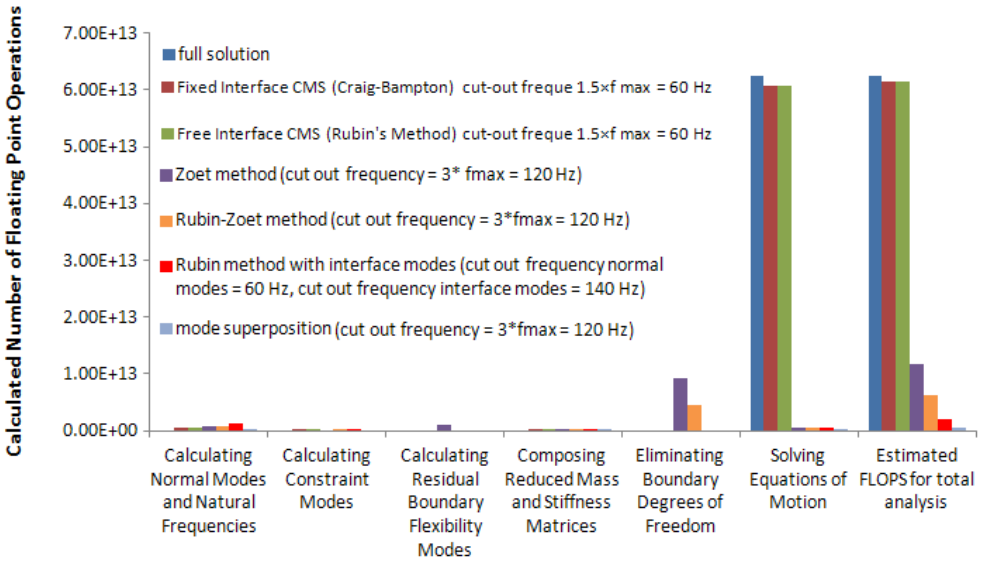

Figure 91 ***Simulation time for time domain analysis calculating the dynamic response over 2 seconds in 2400 time steps. Number of time steps is based on subdividing the highest frequency of interest into 20 steps. This highest frequency of interest is assumed to be*** $1.5 * f_{max}$ ***according to Rubin's criteria.*** f_{max} ***is 40 Hz, as most of the vibration energy is concentrated over the first 5 blade passing frequency orders.***

As can be seen from Figure 91, reduced CMS methods are very effective in reducing computation time for time domain analysis. However, as the interface reduction technique according to the Zoet and Rubin Zoet needs to be carried out for each time step, the computation time required in the generation stage increases with the number of integration steps. This means that the interface reduction technique according to the IRS method (using interface modes) becomes more effective with an increasing number of time steps, as the interface reduction only needs to be carried out once,

which means that the calculation time in the generation pass is independent of the number of time steps or frequencies for which simulation results need to be produced.

10.4 Future Work

With the identification of shortcomings and limitations of the proposed modelling technique it has been established that the Zoet and, mainly the Rubin-Zoet method could be the most effective methods within a certain bandwidth of minimum number of simulation results and maximum number of simulation results required.

Considering the frequency range of interest identified for the LNG carrier and the modal density of the generated structure representing the aft ship of this LNG carrier, running 80 simulations for frequencies equally distributed between 0 and 40 Hz the simulation results produced were found to be of a sufficiently high resolution. This resolution of results is necessary in order to identify relevant peak response frequencies. It is the proximity of these peak (resonance) frequencies to the excitation frequencies that determines for the greatest part the structural response amplitude and therefore the vibration and alternating stress levels occurring. As the proximity of these resonance peaks also determine the sensitivity of the modelling results to the modelling assumptions (added mass, boundary conditions) being able to plot amplitudes against frequency of excitation at a sufficiently high number of steps (resolution) is crucial and form a very effective tool for designing ships keeping vibration levels at a minimum.

Considering the importance of such simulation results, the Zoet and Rubin Zoet method have been developed with the main aim of reducing the calculation time using a sub structural approach, through which the method becomes competitive with existing CMS methods and CMS matrix reduction techniques (according to the IRS method). With the given frequency range of interest and the number of results required (frequency steps), the Zoet, and mainly the Rubin-Zoet method were found to be competitive with existing sub structural approaches to vibratory response modelling.

However, only tests with the Zoet method have been carried out. It had been established that the effect of overcompensation of residual interface flexibility, a side effect of the residual interface flexibility DOF elimination technique, increases with the number of substructures used. It has also been established that the overcompensation of residual interface flexibility limits the time reducing capabilities of the modelling technique in relation to the selected frequency range of interest.

Also, no actual calculation results have been produced applying the Rubin Method using interface modes. Although a cut out frequency of 3.5 f_{max} has been applied for selecting the retained interface modes (based on test carried out by Tran [41]), it is not sure if this cut out frequency would be sufficiently high for ship structures.

All considered, the following future activities are suggested:

- Carry out test simulations with the Rubin-Zoet method in order to establish the effect of overcompensation of residual interface flexibility in comparison with the Zoet method
- Investigate the effect of boundary conditions and modal density of substructures on the effects of interface residual over-compensation.
- Develop an algorithm for counter compensating the over over-compensation of residual flexibility. This could certainly easily be done for a series of repeating identical coupled substructures.
- Evaluate the accuracy of the Rubin method with interface reduction according to the IRS method (see section 6.5.3).

11 Final Concluding Remarks

Due to increasing pressure on the marine industry to reduce noise and vibration levels, the aim of this work was to contribute to an understanding of the mechanism behind structural vibrations typically occurring on board ships, and to contribute to the development of a practical design tool helping the marine structural designer design the structure so that vibration levels on the ship will be kept to a minimum.

For that purpose, the author has carried out vibration and noise measurements on board various ships, which were used for evaluating the nature of excitation sources and correlation of simulation results obtained from a finite element model of a part of the aft ship of an LNG carrier. Results obtained through the full harmonic analysis showed good correlation with the measurement results from the field.

Because problems occurred with the post processing of results obtained through full harmonic analysis, component mode synthesis (CMS) sub-structural modelling techniques had to be used in order to be able to study mode shapes.

Apart from providing a solution to the problems experienced with the post processing, two other important advantages of using a sub-structural approach for typical marine structures have been recognised:

- Decreasing the amount of effort required for building the model: Marine structures can be subdivided in many repeating identical substructures. Only one of these substructures have to be modelled, through which the process of building the model is simplified. This also reduces the required computer memory for storing the model.
- Decreasing computation time required in the generation pass: Time required in the generation pass (the set up of the final matrices that need to be solved) can be reduced as calculating modal information and applying the reduction techniques for repeating identical substructures only need to be done once. The calculated information is then reused with the compilation of the total CMS matrix.

- More accurate models: Sub dividing a model in substructures means that a model can already be correlated to modal measurement results obtained from the field once a part of the marine structure is already finished.

Although the CMS techniques used on the model of the aft ship of the LNG carrier does offer these advantages, it has been established that classical CMS increases the total required computation time compared to the computation required for full analysis. This increase of computation time related to the number of nodes coupling the substructures together, through which relatively large and dense CMS matrices are formed that require a higher amount of computation time to solve.

Recognising the practical potential of sub structural modelling for ships, new interface reduction techniques have been developed: the Zoet method, and the Rubin Zoet method. An important aspect of the evaluation of the methods was the estimation of the required number of floating point operations for each method. Included in that comparison was also the Rubin's method using an already existing interface reduction technique according to The IRS method.

Based on simulation results obtained using the full harmonic analysis method, free and fixed CMS method, together with the inventory of required computation time, the Rubin-Zoet method was found to be the most time economical sub structural analysis method. Estimation of computation time required for analysing a test structure suggest that through the Zoet-Rubin method a decrease of total computation time by 49.4% can be achieved relative to the full harmonic finite element analysis, 63.3% relative to the classic Rubin's methods, and 30% relative to the Rubin's method using the already existing interface reduction technique according to the IRS method (see section 6.5.3).

However, an important short coming of the Zoet and Rubin Zoet interface reduction technique is that with an increasing number of substructures, an increasing number of normal modes per substructure needs to be retained. This application of higher cut-out frequencies is needed in order to reduce the increasing effect of residual interface flexibility over-compensation, which is a consequence of the interface reduction technique applied. This may not be a great problem with the application of a high

number of identical coupled substructures, as modal information only has to be carried out for one structure, but when considering many different substructures, the need to increase the number of retained normal modes may considerably increase computation time in the generation pass, and other CMS technique may become more economical.

Considering the promising results obtained for the Zoet method, and the reduction in computation time that may be obtained through the Rubin-Zoet method, recommendations for future work focuses on finding a solution for the above described problems occurring with over-compensation of residual interface flexibility. Future research approaches suggested are:

- Carry out test simulations with the Rubin-Zoet method in order to establish the effect of overcompensation of residual interface flexibility in comparison with the Zoet method
- Investigate the effect of boundary conditions and modal density of substructures on the effects of interface residual over-compensation.
- Develop an algorithm for counter compensating the over over-compensation of residual flexibility. This could certainly easily be done for a series of repeating identical coupled substructures.
- Evaluate the accuracy of the Rubin method with interface reduction according to The IRS method.

1. van Wijngaarden, E. *Recent developments in predicting propeller-induced hull pressure pulses*. in *Proc. of the 1st int. ship noise & vibration conf*. 2005.
2. Vorus, W.S., *Principles of Naval Architecture*, E.V. Lewis, Editor 1988, The Society of Naval Architects and Marine Engineers: Jersey City, NJ. p. 255-316.
3. van Wijngaarden, E., J. Bosschers, and G. Kuiper. *Aspects of the cavitating propeller tip vortex as a source of inboard noise and vibration*. in *FEDSM2005-77271, ASME Fluids Engineering Division Summer Meeting and Exhibition*. 2005.
4. Boorsma, A. and S. Whitworth. *Understanding the Details of Cavitation*. in *Second International Symposium on Marine Propulsors (smp "11), Hamburg, Germany*. 2011.
5. Kinns, R. and C. Bloor, *Hull vibration excitation due to monopole and dipole propeller sources.* Journal of sound and vibration, 2004. **270**(4): p. 951-980.
6. Collier, R.D., *Ship and platform noise, propeller noise.* Handbook of Acoustics, 1998: p. 407-415.
7. Carlton, J., *Marine propellers and propulsion*. 2012: Butterworth-Heinemann.
8. Chen, J.-H. and Y.-S. Shih, *Basic design of a series propeller with vibration consideration by genetic algorithm.* Journal of Marine Science and Technology, 2007. **12**(3): p. 119-129.
9. Kuiper, G., *New Developments Around Sheet and Tip Vortex Cavitation on Ships Propellers.* http://resolver. caltech. edu/cav2001: lecture. 007, 2001.
10. Köhler, E., E. Schopf, and U. Mohr, *Crankshaft Assembly Design, Mechanics and Loading.* Handbook of Diesel Engines, 2010: p. 221-290.
11. Woud, P.I.K., *Maritieme Wertuigkunde III*, 1996, Delft University of Technology: Delft.
12. Rao, S.S., *Mechanical Vibrations*, ed. L. Fischer. 2004, Upper Saddle River, New Jersey: Pearson Education.
13. Miedema, S. and Z. Lu. *The dynamic behavior of a diesel engine*. in *Proceedings of the WEDA XXII technical conference and 34th Texas A&M dredging seminar, Denver, Colorado, USA*. 2002.
14. Shipping, A.B.o., *Guidance Notes on Ship Vibrations*. 2006, Houston: American Bureau of Shipping.
15. Woud, H.K., *Maritieme Werktuigkunde IV*. Vol. IV. 1999, Delft: Delft University of Technology.
16. J.H. Stainsby, K.B., D.P. Griffiths, *Main Engine Balance Weight Failure Investigation*, 2011, Lloyd's Register EMEA.
17. P.Zoet, G.T., C.Bell, S.Allan, *Failure of Crankshaft Balance Weights of the Main Engine of a Car Ferry*, in *MARNAV*, A.I. O.Turan, R.E.Kurt, Editor 2012, University of Strathclyde: Glasgow, Scotland. p. 163-175.
18. P. Zoet, J.H., J. Sundberg, E. Haimov, *Sub-Task 4.2.2, Deliverable 4.7: Comparison Performance Versus Requirements*, in *SILENV EU collaborative Project 234182 'Ships oriented Innovative soLutions to rEduce Noise and Vibrations'*, R. Dambra, Editor 2012, EU.

19. Yang, T.-j., et al., *Adaptive vibration isolation system for diesel engine.* Journal of Marine Science and Application, 2004. **3**(2): p. 30-35.
20. P.Zoet, J.H., J.Sundberg, E.Haimov, *Designing Ships for Low Vibrations: A Case Study*, in *MARNAV 2012*, A.I. O.Turan, R.E.Kurt, Editor 2012, University of Strathclyde: Glasgow. p. 63-75.
21. Senjanović, I., S. Tomašević, and N. Vladimir, *An advanced theory of thin-walled girders with application to ship vibrations.* Marine Structures, 2009. **22**(3): p. 387-437.
22. Petyt, M., *Introduction to Finite Element Vibration Analysis*. 1990, Cambridge: Cambridge University Press.
23. Newland, D.E., *Mechanlical Vibration Analaysis and Computation*. 1989: Longman Singapore Publishers.
24. Lee, U., J. Kim, and A.Y. Leung, *The spectral element method in structural dynamics.* Shock and Vibration Digest, 2000. **32**(6): p. 451-465.
25. Cabos, C. and H.G. Matthies. *The Energy Finite Element Method NoiseFEM*. in *IUTAM Symposium on the Vibration Analysis of Structures with Uncertainties*. 2011. Springer.
26. Rubin, S., *Improved component-mode representation for structural dynamic analysis.* AIAA journal, 1975. **13**(8): p. 995-1006.
27. Ajith, V. and S. Gopalakrishnan, *Wave propagation in stiffened structures using spectrally formulated finite element.* European Journal of Mechanics-A/Solids, 2013.
28. Lee, U., *Spectral element method in structural dynamics*. 2009: John Wiley & Sons.
29. Norton, M.P. and D.G. Karczub, *Fundamentals of noise and vibration analysis for engineers*. 2003: Cambridge university press.
30. Fahy, F.J., *Statistical energy analysis: a critical overview.* Philosophical Transactions of the Royal Society of London. Series A: Physical and Engineering Sciences, 1994. **346**(1681): p. 431-447.
31. Lyon, R.H., R.G. DeJong, and M. Heckl, *Theory and application of statistical energy analysis.* The Journal of the Acoustical Society of America, 1995. **98**(6): p. 3021-3021.
32. Hynna, P., P. Klinge, and J. Vuoksinen, *Prediction of structure-borne sound transmission in large welded ship structures using statistical energy analysis.* Journal of sound and vibration, 1995. **180**(4): p. 583-607.
33. Zoet, P., *Evaluation of FEM and SEA for simulating ship noise and vibration*, in *1st International Synmposium on Naval Architecture and Maritime*, A.D.A.a. H.Yilmaz, Editor 2011, Yildiz Technical University: Istanbul. p. 665-679.
34. Craig, R.R., *Coupling of substructures for dynamic analysis.* AIAA journal, 1968. **6**: p. 1313-1319.
35. MacNeal, R.H., *A hybrid method of component mode synthesis.* Computers & Structures, 1971. **1**(4): p. 581-601.
36. Rixen, D.J., *A dual Craig–Bampton method for dynamic substructuring.* Journal of Computational and applied mathematics, 2004. **168**(1): p. 383-391.

37. Van Der Valk, P., *Model reduction and interface modeling in dynamic substructuring*, 2010, Master's thesis Delft University of Technology Delft, the Netherlands.
38. Liu, W., *Structural dynamic analysis and testing of coupled structures*, 2000, PhD thesis, Imperial College of Science, Technology and Medicine, University of London.
39. Secora, C.K., *Residual flexibility methods for decoupled analysis of integrated structural systems.* ETD http://hdl. handle. net/1911/17243, 1998.
40. Junge, M., et al., *Interface-reduction for the Craig–Bampton and Rubin method applied to FE–BE coupling with a large fluid–structure interface.* International journal for numerical methods in engineering, 2009. **77**(12): p. 1731-1752.
41. Tran, D.-M., *Component mode synthesis methods using interface modes. Application to structures with cyclic symmetry.* Computers & Structures, 2001. **79**(2): p. 209-222.
42. Flanigan, C.C. *Model reduction using Guyan, IRS, and dynamic methods*. in *PROCEEDINGS-SPIE THE INTERNATIONAL SOCIETY FOR OPTICAL ENGINEERING*. 1998. SPIE INTERNATIONAL SOCIETY FOR OPTICAL.
43. Bourquin, F., *Component mode synthesis and eigenvalues of second order operators: discretization and algorithm.* Modélisation mathématique et analyse numérique, 1992. **26**(3): p. 385-423.
44. Craig Jr, R.R. and C.-j. Chang, *On the use of attachment modes in substructure coupling for dynamic analysis.* transformation, 1977. **10**(4): p. 3.
45. Gere, M., Timoshenko, S.P., *Mechanics of Materials*. 1998: Stanley Thornes Ltd.
46. Sanchez-Caja, A., *Unsteady Analysis of Pressure Pulses in a CLT Propeller Using a Lifting Surface Vortex-Lattice Method*, in *MARNAV 2012*, A.I. O.Turan, R.E.Kurt, Editor 2012, University of Strathclyde: Glasgow. p. 197-202.
47. Boorsma, A. and E.P. Carden, *Use of Operational Modal Analysis in Solving Ship Vibration Issues*, in *Modal Analysis Topics, Volume 3*. 2011, Springer. p. 281-288.
48. Lay, D.C., *Linear Algebra and its Applications*. 2nd ed, ed. L. Rosatone. 1997, Reading: Addison Wesley.
49. Guyan, R.J., *Reduction of stiffness and mass matrices.* AIAA journal, 1965. **3**(2): p. 380-380.
50. Hunger, R., *Floating point operations in matrix-vector calculus*. 2005: Munich University of Technology, Inst. for Circuit Theory and Signal Processing.
51. Kan, j.v., *Numerieke Wiskunde voor Technici*. 3rd ed. 1996, Delft: Delftse Universitaire Pers. 128.

Appendix I *Equipment Used for Noise and Vibration Measurements*

The B&K 2250 hand held meter/analyser is used as shown in figure 2. Important features used are the high resolution spectra that can be produced, the signal capturing facilities (which makes post processing possible) and the logging option. The meter is used both as a vibration meter and a noise meter.

Hand held meter:

Make and type	:	B&K 2250
Serial number	:	2644991 (see appendix I for calibration certificate)

Microphone

Make and type	:	B&K 4189
Serial number	:	2638752 (see appendix I for calibration certificate)
Frequency range	:	0-20kHz

Accelerometer

Make and type	:	B&K 4366
Serial number	:	0635619
Frequency range:	;	0.2 Hz to 8 kHz

Analysis software

Type	:	BZ 7230 FFT by B&K combined with Microsoft excel

Frequency analysis based on the Fast Fourier Transform [FFT] algorithm is the tool of choice for measurement and diagnostics of machinery noise and vibration. The frequency 'profile' of a machine is its fingerprint, revealing its sources of noise and vibration and their paths to the measurement position.

The 2250 with the BZ 7230 FFT software has many narrow band features :-

- Real time operation [no loss of data] up to 20 kHz.
- 100 up to 6400 lines giving a resolution down to 16 mHz
- Linear and exponential averaging
- Signal capture and recording
- Engineering units, SI metric and UK imperial units
- Acceleration, velocity, displacement .....

Plus Max hold, spectrum overlay, zoom, tachometer function, trigger, transient and continuous signals, RMS, PWR, PSD, ESD, Peak, P-P ..... etc., software also included for analysis, reporting and downloading to a PC.

Figure 1: Specification B&K 2250 with BZ 7230 software as advertised on www.gracey.com, internet site for hiring noise and vibration measuring equipment.

CERTIFICATE OF CALIBRATION

ISSUED BY	Gracey & Associates	BSI CERTIFICATE	FS 25913
DATE OF ISSUE	24 May 2010	CERTIFICATE NUMBER	2010-0511
DATE OF CALIBRATION	19 May 2010		
CALIBRATION INTERVAL	12 months		PAGE 1 OF 2

Gracey & Associates
High Street, Chelveston
NN9 6AS
Tel: 01933 624212
Fax: 01933 624608
www.gracey.com

TEST ENGINEER
Jamie Bishop

APPROVING SIGNATORY
Greg Rice

Manufacturer	Bruel & Kjaer UK Limited	Customer	
Model	B&K 4189	Gracey & Associates	
Serial Number	2638752		
Description	Microphone - 1/2" free-field - 0 VDC		

Standards
BS EN 61672 Class 1

Conditions

Atmospheric Pressure	102.2 kPa
Temperature	22.8 ℃
Relative Humidity	40.8 %

Calibration Data

Sensitivity	-25.00 dB

Laboratory Equipment Used

Equipment	S/N	Last Cal	Equipment	S/N	Last Cal
HP 34401	3146A16728	09-Jul-09	Druck DPI 141	479	22-Jul-09
B&K 4134	1675305	27-Apr-09	Stanford DS360	33213	15-Jul-09
Norsonic 1253	20848	24-Apr-09			

Notes

We certify that the above product was duly tested and found to be within the specification at the points measured (except where indicated). Measurements are traceable to UKAS reference sources from the UK National Physical Laboratory. Where no national or international standards exist, traceability is to standards maintained by the manufacturer. Our Quality Management System has been assessed to comply with BS EN ISO 9001:2008 - BSI Certificate number FS 25913. Tests were carried out in environmental conditions controlled to the extent appropriate to the instrument's specification. All relevant test certificates are available for inspection.
The uncertainties are for a confidence probability of not less than 95%.
This certificate is issued in accordance with the conditions of accreditation granted by the British Standards Institution which has assessed the measurement capability of the laboratory and its traceability to recognised national standards and to the units of measurement realised at the corresponding national standards laboratory. Copyright of this certificate is owned by Gracey & Associates and may not be reproduced other than in full except with their prior written approval.

Gracey & Associates is the trading name of W T Gracey Ltd. Registered in Chelveston England No 1176412
BSI approved for the hire and calibration of noise and vibration instruments. Established 1972

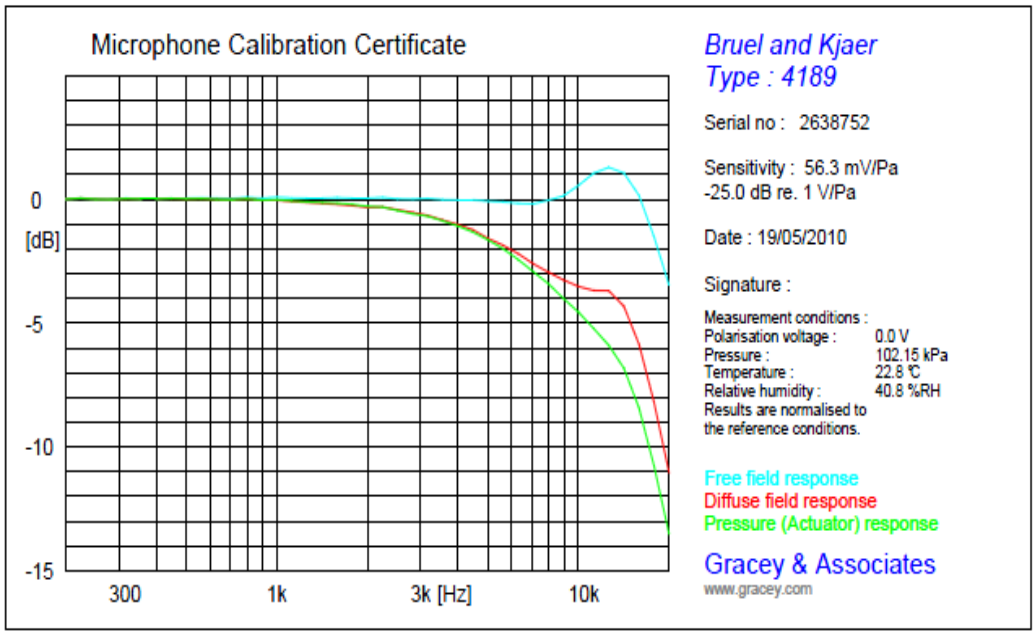

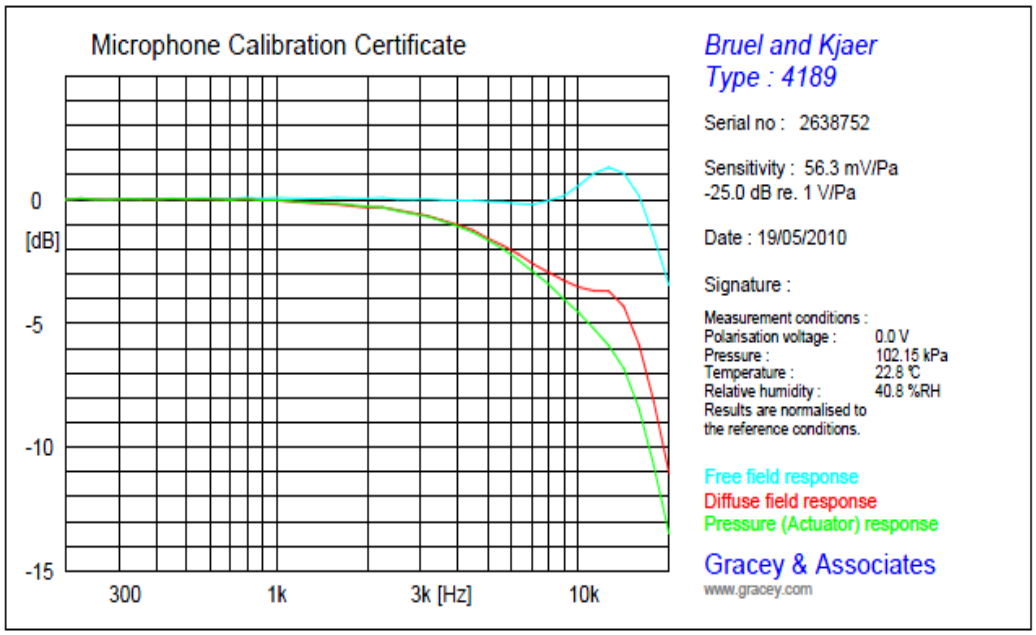

Comment : 20100511

Manufacturers' Specifications
Bruel & Kjaer 4366 - Accelerometer

Piezoelectric Charge Accelerometer

Charge sensitivity : 5 pC/ms^{-2} or 50 pC/g ± 2 % **
Voltage sensitivity : 4 mV/ms^{-2} or 40 mV/g ± 2 % **

Mounted resonance : 16 kHz
Frequency range - 5 % : 0.2 Hz to 5000 Hz
Frequency range - 10 % : 0.1 Hz to 8000 Hz

Capacitance - typical : 1100 pF excluding cable

Max transverse sensitivity : < 2 %
Piezoelectric material : PZ23
Construction : Delta shear

Typical temperature transient sensitivity : 0.02 ms^{-2}/°
Typical magnetic sensitivity (50 Hz to 0.03T) : 1 ms^{-2}/tesla
Typical acoustic sensitivity (154 dB SPL) : 0.001 ms^{-2}
Minimum leakage resistance at 20 °C : 20 GΩ
Ambient temperature range : -74 to 250 °C

Maximum operational shock (Peak) : ± 20 kms^{-2};
Maximum continuous sinusoidal acceleration (Peak) : 20 kms^{-2}
Maximum acceleration (Peak) with mounting magnet : 50 kms^{-2}

Electrical Connector : 10-32 UNF, side entry
Recommended cable : AO 0038

Mechanical
Mounting thread : 10-32 UNF, 3.2 mm deep
Mounting torque : 1 Nm, max = 2 Nm, min = 0.5 Nm
Dimensions - body : 16 mm diameter
Dimensions - overall height : 19 mm
Dimension - across base flats : 16 mm - spanner size

CERTIFICATE OF CALIBRATION

ISSUED BY	Gracey & Associates	BSI CERTIFICATE	FS 25913
DATE OF ISSUE	18 December 2009	CERTIFICATE NUMBER	2009-1217
DATE OF CALIBRATION	18 December 2009		
CALIBRATION INTERVAL	12 months		PAGE 1 of 2

Gracey & Associates
High Street, Chelveston
NN9 6AS
Tel: 01933 624212
Fax: 01933 624608
www.gracey.com

TEST ENGINEER
Greg Rice

APPROVING SIGNATORY
Greg Rice

Standards

Manufacturer	Bruel & Kjaer UK Limited
Model	B&K 4366
Serial Number	0635619
Description	Accelerometer set

Customer
Gracey & Associates

Calibration Data

Voltage Sensitivity	3.750 mV/ms^{-2}
Frequency	159.15 Hz

Conditions

Atmospheric Pressure	100.9 kPa
Temperature	20.8 ℃
Relative Humidity	35.4 %

Adjustments or Comments

Notes

We certify that the above product was duly tested and found to be within the specification at the points measured (except where indicated). Measurements are traceable to UKAS reference sources from the UK National Physical Laboratory. Where no national or international standards exist, traceability is to standards maintained by the manufacturer. Our Quality Management System has been assessed to comply with BS EN ISO 9001:2008 - BSI Certificate number FS 25913. Tests were carried out in environmental conditions controlled to the extent appropriate to the instrument's specification. All relevant test certificates are available for inspection.

The uncertainties are for a confidence probability of not less than 95%.

This certificate is issued in accordance with the conditions of accreditation granted by the British Standards Institution which has assessed the measurement capability of the laboratory and its traceability to recognised national standards and to the units of measurement realised at the corresponding national standards laboratory. Copyright of this certificate is owned by Gracey & Associates and may not be reproduced other than in full except with their prior written approval.

Appendix II *Full Girder Approach*

In this section the wave approach is demonstrated for a beam that is not constrained at the free edges and no damping occurs. These boundary conditions have been chosen as it is a commonly accepted approach for the boundary conditions of a ship hull bending properties represented by an Euler beam.

Because of the finite nature of the beam and the boundary conditions, there are distinct frequencies where the beam has a very high response resulting in a situation that little effort is needed to generate high vibration levels. Because of the finite nature of the beam and the presence of the boundary conditions, different waves occur in the beam travelling is different directions. At certain frequencies waves travelling from the excitation source to the boundaries (incident waves) interact with the waves reflected back from the boundaries in such a way a very distinct fixed spatial distribution of amplitude over the length of the beam occurs (standing wave). At what frequencies that occurs depends on the relation between the speed of propagation of the wave, and the frequency of alteration of the vertical displacement of the particles. Very importantly, it also depends on what phase shift the incident wave undergoes when it bounces back at the boundaries and travels back towards the excitation source. With the modelling of the ship's hull as a beam it is very practical to adopt a modal approach to vibrations, which is obtained from the wave equations and the formulation of the boundary conditions as will be demonstrated in this section. Starting from the general solution as described above:

$$\hat{v}_{(x)} = A_1 cos(kx) + A_2 sin(kx) + A_3 cosh(kx) + A_4 sinh(kx)$$

Considering the ends of the beam to be unconstrained, no bending moment and shear forces will occur at $x = 0$ and $x = L$. The boundary conditions are mathematically described as follows:

No shear forces implies:

$$D = \frac{\partial}{\partial x}\left(EI\frac{\partial^2 v_{(t,x)}}{\partial^2 x}\right) = EI\frac{\partial^3 v_{(t,x)}}{\partial^3 x} = 0$$

$\boldsymbol{x = 0}$ $\quad \frac{\partial^3 \hat{v}_{(0)}}{\partial^3 x} = 0$ $\qquad$ $\boldsymbol{x = L}$ $\quad \frac{\partial^3 \hat{v}_{(L)}}{\partial^3 x} = 0$ **(11.1)**

$$\frac{\partial^3 \hat{v}_{(x)}}{\partial^3 x} = k^3 A_1 sin(kx) - k^3 A_2 cos(kx) + a^3 A_3 sinh(ax) + k^3 A_4 cosh(kx)$$

$\boldsymbol{x = 0}$ $\quad \frac{\partial^3 \hat{v}_{(0)}}{\partial^3 x} = -k^3 A_2 + k^3 A_4 = 0$

Therefore: $A_2 = A_4$ **(11.2)**

$\boldsymbol{x = L}$ $\quad \frac{\partial^3 \hat{v}_{(L)}}{\partial^3 x} = k^3 A_1 sin(kL) - k^3 A_2 cos(kL) + k^3 A_3 sinh(kL) + k^3 A_4 cosh(kL)$ **(11.3)**

No bending moments implies:

$$M = EI\frac{\partial^2 v_{(t,x)}}{\partial^2 x} = 0$$

$\boldsymbol{x = 0}$ $\quad \frac{\partial^2 \hat{v}_{(0)}}{\partial^2 x} = 0$ $\qquad$ $\boldsymbol{x = L}$ $\quad \frac{\partial^2 \hat{v}_{(L)}}{\partial^2 x} = 0$ **(11.4)**

$$\frac{\partial^2 \hat{v}_{(x)}}{\partial^2 x} = -k^2 A_1 cos(kx) - k^2 A_2 sin(kx) + k^2 A_3 cosh(kx) + k^2 A_4 sinh(kx)$$

$\boldsymbol{x = 0}$ $\quad \frac{\partial^2 \hat{v}_{(x)}}{\partial^2 x} = -k^2 A_1 + k^2 A_3 = 0$

Therefore: $A_1 = A_3$ **(11.5)**

$\boldsymbol{x = L}$ $\quad \frac{\partial^2 \hat{v}_{(L)}}{\partial^2 x} = -k^2 A_1 cos(kL) - k^2 A_2 sin(kL) + k^2 A_3 cosh(kL) + k^2 A_4 sinh(kL)$ **(11.6)**

Substituting equation (11.2) and (11.5) into (11.3) and (11.6) gives:

$$\frac{\partial^2 \hat{v}_{(L)}}{\partial^2 x} = -k^2 A_1 cos(kL) - k^2 A_2 sin(kL) + a^2 A_1 cosh(kL) + k^2 A_2 sinh(kL) = 0 \quad \textbf{(11.7)}$$

$$\frac{\partial^3 \hat{v}_{(L)}}{\partial^3 x} = k^3 A_1 sin(kL) - k^3 A_2 cos(kL) + k^3 A_1 sinh(kL) + k^3 A_2 cosh(kL) = 0$$

In matrix notation the two equations (11.7) become:

$$\begin{bmatrix} \left(k^2 cosh(kL) - k^2 cos(kL)\right) & \left(k^2 sinh(kL) - k^2 sin(kL)\right) \\ \left(k^3 sin(kL) + k^3 sinh(kL)\right) & \left(k^3 cosh(kL) - k^3 cos(kL)\right) \end{bmatrix} \begin{bmatrix} A_1 \\ A_2 \end{bmatrix} = 0 \quad \textbf{(11.8)}$$

In order to get the non trivial solution the determinant for matrix (11.8) should be equal to zero:

$$det \begin{bmatrix} \left(cosh(kL) - cos(kL)\right) & \left(sinh(kL) - sin(kL)\right) \\ \left(sin(kL) + sinh(kL)\right) & \left(cosh(kL) - cos(kL)\right) \end{bmatrix} = 0 \quad \textbf{(11.9)}$$

$$det = \left(cosh(kL) - cos(kL)\right)\left(cosh(kL) - cos(kL)\right) - \left(sinh(kL) - sin(kL)\right)\left(sin(kL) + sinh(kL)\right) = 0$$

Rewriting (11.9) the frequency equation becomes:

$$cos(kL)cosh(kL) = 1 \quad \textbf{(11.10)}$$

This is only true when $kL = (n + \frac{1}{2})\pi$ for $n = \{1,2,3 \ldots \infty\}$, where n is the mode number, from which the natural frequencies ω_n can be calculated according to

$$k = \frac{(n + \frac{1}{2})\pi}{L} = \sqrt[4]{\left({\omega_n}^2 \frac{\rho A}{EI}\right)} \quad \textbf{(11.11)}$$

From the matrix equation (11.8) we can establish a description of the mode shape corresponding with frequency *n*. The relation taken from equation (11.8) between A_1 and A_2 is:

$$A_1 = A_2 \frac{\left(sin(kL) - sinh(kL)\right)}{\left(cosh(kL) - cos(kL)\right)} = A_2 a \quad \textbf{(11.12)}$$

Substituting equation (11.12) into the general solution (6.11) gives:

$$\hat{v}_{(x,t)} = A_2\left[a\left(cos(kx) + cosh(kx)\right) + sin(kx) + sinh(kx)\right]\cos(\omega t) \quad \textbf{(11.13)}$$

Substitution of (11.11) into (11.13) gives:

$$\hat{v}_{n(x)} =$$

$$A_n\left[a_n\left(cos\left(\frac{(n+\frac{1}{2})\pi}{L}x\right)+cosh\left(\frac{(n+\frac{1}{2})\pi}{L}x\right)\right)+sin\left(\frac{(n+\frac{1}{2})\pi}{L}x\right)+sinh\left(\frac{(n+\frac{1}{2})\pi}{L}x\right)\right]$$

where **(11.14)**

$$\boldsymbol{a_n = \frac{\left(sin\left((n+\frac{1}{2})\pi\right)-sinh\left((n+\frac{1}{2})\pi\right)\right)}{\left(cosh\left((n+\frac{1}{2})\pi\right)-cos\left((n+\frac{1}{2})\pi\right)\right)}}$$

The total response according to the mode superposition technique is equal to

$$\hat{v}_{(x)} =$$

$$\sum_{n=1}^{n=\infty} A_n\left[a_n\left(cos\left(\frac{(n+\frac{1}{2})\pi}{L}x\right)+cosh\left(\frac{(n+\frac{1}{2})\pi}{L}x\right)\right)+sin\left(\frac{(n+\frac{1}{2})\pi}{L}x\right)+sinh\left(\frac{(n+\frac{1}{2})\pi}{L}x\right)\right]$$

.

Appendix III *Formulation of the Beam Element*

The equation of motion of a beam elements is determined through the following steps:

- Obtaining the energy expression for all degrees of freedom:
- Formulating the displacement function is formulated and substituted into the energy expression
- Substituting the energy expression in substituted into the Lagrange Equation through which the mass matrix and stiffness matrix are obtained.

Energy Expression

The energy expressions are separately obtained for the axial deformation (deformation in normal direction along the x axis of the beam), torsional deformation about the x axis and bending deformations. The strain expression is based on Hooke's law which is the classical relation between stress (ultimately representing force) and strain (representing deformation) [22, 45]

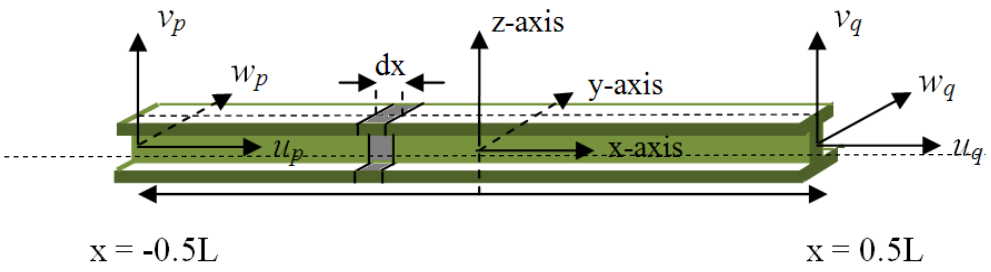

Figure 92 **Axis and orientation on a two node beam element (node p and node q). Displacement in x, y and z direction are indicated with u, w and v respectively. Rotations about the x, y and z axis are indicated through θ_x, θ_y and θ_z respectively.**

The kinetic energy expression is based on Newton's law through which initially a relation between the continuous acceleration distribution over the element is given and the resulting inertia forces.

Beam Axial Deformation

It is assumed that axial deformation (*du*) results in axial stresses only. According to Hooke's law (see Figure 92):

$$\sigma_x = E\varepsilon_x \quad \textbf{(11.15)}$$

$$F_x = A\sigma_x = AE\varepsilon_x \quad \textbf{(11.16)}$$

The strain energy of a beam element with an infinitively small length dx:

$$dU_x = \frac{1}{2}A\sigma_x\varepsilon_x dx \quad \textbf{(11.17)}$$

Where:

ε_x = strain in x direction = $\frac{\partial u}{\partial x}$

σ_x is stress in x direction (normal stress) [Pa]

E = elasticity modulus [Pa]

dU_x = virtual stain energy

Integrating over the beam length gives the axial strain energy relation

$$U_x = \frac{1}{2}\int_{-0.5L}^{0.5L} EA{\varepsilon_x}^2 dx \quad \textbf{(11.18)}$$

Substituting ε_x = strain in x direction = $\frac{\partial u}{\partial x}$ into equation (11.18)

$$U = \frac{1}{2}\int_{-0.5L}^{0.5L} EA\left(\frac{\partial u}{\partial x}\right)^2 dx \quad \textbf{(11.19)}$$

The kinetic energy of a infinitively small length dx:

$$T_x = \frac{1}{2}\rho A\dot{u}^2 \quad \textbf{(11.20)}$$

Integrating over the beam length gives the axial kinetic energy relation:

$$T = \frac{1}{2}\int_{-0.5L}^{0.5L} \rho A\dot{u}^2\, dx \quad \textbf{(11.21)}$$

Beam Torsional Deformation

Torsional deformation of a beam about the x axis is expresses through an angular deformation θ_x. Considering Figure 92, this angular deformation results mainly in shear stresses τ_{xy} and τ_{xz} all occurring in the zy plane. When the shear centre of the cross-section coincides with the axis about which the couple is acting, warping is

assumed not to be restrained. As a result the torsional couple about the x-axis is assumed not to result in a normal stress σ_x

However, when beam elements are attached to other elements outside their centre of rotation, the presence of these other elements attached to the beam element restrain warping through which normal stresses do occur due to torsional couples. This is particularly the case with beams representing stiffeners on a plate field. Plate elements should be modelled in many cases on top of the beam element with the implication that the nodes of the beam should be placed outside the centre of rotation of the beam element.

The effect of warping being restrained (warping distortion) is expressed through a warping function $\psi(y,z)$. Without restrain of warping $\psi(y,z) = 0$.

$$\epsilon_y = \epsilon_z = \gamma_{yz} = 0 \quad \textbf{(11.22)}$$

$$\varepsilon_x = \frac{\partial^2 \theta_x}{\partial x^2}\psi(y,z) \quad \textbf{(11.23)}$$

$$\gamma_{xy} = \frac{\partial \theta_x}{\partial x}\left(\frac{\partial \psi(y,z)}{\partial y} - z\right) \quad \textbf{(11.24)}$$

$$\gamma_{xz} = \frac{\partial \theta_x}{\partial x}\left(\frac{\partial \psi(y,z)}{\partial z} + y\right) \quad \textbf{(11.25)}$$

Where

τ_{xy} is the shear stress [Pa]

γ_{xy} is shear strain

ψ is the warping function

The relevant relations between strain (deformation) and stress are according to Hooke's law in shear:

$$\tau_{xy} = G\gamma_{xy} \quad \tau_{xz} = G\gamma_{xz} \quad \sigma_x = E\varepsilon_x \quad \textbf{(11.26)}$$

Where G is shear modulus according to Hooke's law in shear:

$$G = \frac{E}{2(1-\nu)}$$

And ν is the Poisson ratio which is considered to be around 0.3 for steel

Work done by τ_{xy}=

$$dW = \frac{1}{2}\tau_{xy}\gamma_{xy}dAdx \quad \textbf{(11.27)}$$

Work done by τ_{xz}=

$$dW = \frac{1}{2}\tau_{xz}\gamma_{xz}dAdx \quad \textbf{(11.28)}$$

Work done by σ_x=

$$dU_x = \frac{1}{2}\sigma_x\varepsilon_x dAdx \quad \textbf{(11.29)}$$

Integrating over the length of the elements gives:

$$U = \frac{1}{2}\int_{-0.5L}^{0.5L}\int_A \left(\tau_{xy}\gamma_{xy} + \tau_{xz}\gamma_{xz} + \sigma_x\varepsilon_x\right) dAdx \quad \textbf{(11.30)}$$

Substituting equation (11.23), (11.24) and (11.25) into (11.30) gives:

$$U = \frac{1}{2}\int_{-0.5L}^{0.5L} GJ\left(\frac{\partial\theta_x}{\partial x}\right)^2 dx + \frac{1}{2}\int_{-0.5L}^{0.5L} E\int_A \left(\frac{\partial^2\theta_x}{\partial x^2}\psi\right)^2 dA \quad \textbf{(11.31)}$$

Where:

$$J = \int_A \left(\left(\frac{\partial\psi}{\partial y} - z\right)^2 + \left(\frac{\partial\psi}{\partial z} + y\right)^2\right) dA \quad \textbf{(11.32)}$$

The kinetic energy expression for torsional deformation of the beam about the x axis is:

$$T = \frac{1}{2}\int_{-0.5L}^{0.5L} \rho I_x \dot{\theta}_x{}^2 \quad \textbf{(11.33)}$$

Where:

ρ = specific mass of the material
I_x is the second moment of area about the y axis

Beam Bending Deformation

The relation between beam bending strain and stresses is expressed through the relation:

$$u(x,z) = -z\frac{\partial v}{\partial x} \qquad \varepsilon_x = -z\frac{\partial^2 v}{\partial x^2} \tag{11.34}$$

For wavelengths greater than ten times the cross sectional dimensions of the element the slender beam approach can be applied:

$$\gamma_{xz} = \frac{\partial u}{\partial z} + \frac{\partial v}{\partial x} = 0 \tag{11.35}$$

For deep beams:

$$\gamma_{xz} = \frac{\partial u}{\partial z} + \frac{\partial v}{\partial x} = -\theta_y + \frac{\partial v}{\partial x} \tag{11.36}$$

For the slender beam the strain energy stored in the element is assumed to be only related to ε_x and is therefore expressed as:

$$U_x = \frac{1}{2}\int_V \sigma_x \varepsilon_x dV = \frac{1}{2}\int_V E{\varepsilon_x}^2 dV \tag{11.37}$$

Substituting equation (11.34) into equation (11.37) gives the strain energy equation for the slender beam:

$$U = \frac{1}{2}\int_{-0.5L}^{0.5L} EI_y \left(\frac{\partial^2 v}{\partial x^2}\right)^2 dx \tag{11.38}$$

For deep beams extra strain energy is generated from the fact that deformation of the cross section area takes place (the cross-sectional area is not perpendicular to the deflexion line). γ_{xz} follows the relation of equation (11.36). The shear stress is expressed as:

$$\tau_{xz} = \kappa G \gamma_{xz} \tag{11.39}$$

$$dU = \frac{1}{2}\kappa G \gamma_{xz}\gamma_{xz} dx dy dz$$

Where κ are general values that can be found in the literature for different types of cross-sections. Substituting equation (11.36) into (11.39) gives the expression of the strain energy as a result of shear stresses with the bending of a deep beam:

$$\frac{1}{2}\int_{-0.5L}^{0.5L} \kappa AG\left(\frac{\partial v}{\partial x}-\theta_y\right)^2 dx \tag{11.40}$$

Total strain energy for the deep beam:

$$U=\frac{1}{2}\int_{-0.5L}^{0.5L} EI_y\left(\frac{\partial^2 v}{\partial x^2}\right)^2 dx+\frac{1}{2}\int_{-0.5L}^{0.5L} \kappa AG\left(\frac{\partial v}{\partial x}-\theta_y\right)^2 dx \tag{11.41}$$

For the kinetic energy equation we can write for a slender beam:

$$T=\frac{1}{2}\int_{-0.5L}^{0.5L} \rho A\dot{v}^2\, dx \tag{11.42}$$

For a deep beam the kinetic energy from the rotary inertia effect of the cross sectional area cannot be neglected anymore and is taken into account:

$$\frac{1}{2}\int_{-0.5L}^{0.5L} \rho I_y \dot{\theta}_y{}^2\, dx \tag{11.43}$$

The total kinetic energy equation for a deep beam is:

$$T=\frac{1}{2}\int_{-0.5L}^{0.5L} \rho A\dot{v}^2\, dx+\frac{1}{2}\int_{-0.5L}^{0.5L} \rho I_y \dot{\theta}_y{}^2\, dx \tag{11.44}$$

Where:

ρ = specific mass of the material
I_y is the second moment of area about the y axis

Displacement Functions

The second step is obtaining the displacement functions. The displacement function is an expression of the element's deformation between the nodes as a function of the displacements at the nodes themselves. These displacements are expressed through a polynomial in the form.

$$v(\xi) = a_1 + a_2\xi + a_3\xi^2 + \cdots a_n\xi^{(n-1)} \quad \textbf{(11.45)}$$

The displacement function is in fact a description of the displacement as a sum of *n* number of assumed mode shapes (modal approach). In principle, the more constants the polynomial consists of, the more precise the deformation shape of the element is likely to be described. However, the maximum number of polynomial constants that can be taken into account depends on the number of degrees of freedom the element has. In this section the displacement functions of the beam and the plate element are presented:

The displacement function of a beam is based on the beam as shown in Figure 92

$\xi = \frac{x}{0.5l}$ = a non dimensional coordinate

a_n = the polynomial constant

In case of a two node beam, considering the deflection in vertical direction (*v* according to Figure 92 the total number of degrees of freedom is 4. Rotation about the y-axis and translation along the z-axis of node p (2 degrees of freedom) and rotation about the y-axis and translation along the z-axis of node q (2 degrees of freedom) makes four degrees of freedom in total. Through the four degrees of freedom four polynomial constants can be expressed as a function of the above mentioned 4 displacement degrees of freedom:

For a slender beam :

$$v(\xi) = a_1 + a_2\xi + a_3\xi^2 + a_3\xi^3 \quad \textbf{(11.46)}$$

$$\frac{dv}{d\xi} = 0.5L\frac{dv}{dx} = 0.5L\theta_y = [a_1 + a_2\xi + a_3\xi^2 + a_3\xi^3]' = a_2 + 2a_3\xi + 3a_4\xi^2 \quad \textbf{(11.47)}$$

For a deep beam the rotation θ_y is expressed through a separate polynomial:

$$\theta_y(\xi) = b_1 + b_2\xi + b_3\xi^2 \quad \textbf{(11.48)}$$

Through the static equilibrium requirements a relation between coefficients b_n and a_n is formulated through which the coefficients b_n are illuminated. The static equilibrium requires the following relation (see also equation (11.37) and (11.39).

Static equilibrium requirements dictate:

$$EI_y\left(\frac{\partial^2\theta_y}{\partial x^2}\right) + \kappa AG\left(\frac{\partial v}{\partial x} - \theta_y\right) = 0 \quad \textbf{(11.49)}$$

$$\kappa AG\left(\frac{\partial^2 v}{\partial x^2} - \frac{\partial\theta_y}{\partial x}\right) = 0 \quad \textbf{(11.50)}$$

Through which b_n is expressed in a_n

$$b_1 = \frac{1}{0.5L}a_2 + \frac{6\beta}{0.5L}a_4 \qquad b_2 = \frac{2}{0.5L}a_3 \qquad b_3 = \frac{2}{0.5L}a_4 \qquad \beta = \frac{EI_z}{kAG(0.5L)^2} \quad \textbf{(11.51)}$$

In order to find the factors of the polynomial expression a_n the displacements and rotations are evaluated at $x = -\frac{1}{2}L\ (v_p, \theta_{y_p})$ and $x = \frac{1}{2}L\ (v_q\ , \theta_{y_q})$

For a deep beam we can write:

$$\begin{aligned}
x = -\frac{1}{2}L \qquad & \xi = -1 \qquad & v_p &= a_1 + a_2(-1) + a_3(-1)^2 + a_3(-1)^3 \\
& \xi = -1 \qquad & \theta_{y_p} &= b_1 + b_2(-1) + b_3(-1)^2 \\
x = \frac{1}{2}L \qquad & \xi = 1 \qquad & v_q &= a_1 + a_2(1) + a_3(1)^2 + a_3(1)^3 \\
& \xi = 1 \qquad & \theta_{y_p} &= b_1 + b_2(1) + b_3(1)^2
\end{aligned} \quad \textbf{(11.52)}$$

Substituting the relations between b_n and a_n according to equation (11.51) into equations (11.52) gives in matrix notation:

$$\begin{bmatrix} 1 & -1 & 1 & -1 \\ 0 & 1 & -2 & 6\beta+3 \\ 1 & 1 & 1 & 1 \\ 0 & 1 & 2 & 6\beta+3 \end{bmatrix} \begin{bmatrix} a_1 \\ a_2 \\ a_3 \\ a_4 \end{bmatrix} = \begin{bmatrix} v_p \\ \frac{1}{2}L\theta_{y_p} \\ v_q \\ \frac{1}{2}L\theta_{y_p} \end{bmatrix}$$

$$[A]\{a\} = \{\bar{v}_e\} \quad \textbf{(11.53)}$$

Through the relations in equation (11.53) the vector $\{a\}$, which is the vector of polynomial constants, is expressed as a function of the elements nodal displacement vector$\{v_e\}$:

$$\{a\} = [A]^{-1}\{\bar{v}_e\} \quad \textbf{(11.54)}$$

Through the formulation of the polynomial constants as a function of the nodal displacement vector, a description is obtained of any displacement along the x-axis of the beam as a function of the nodal displacements. Through substitution of these relations into the energy equation, the energy expressions can be written as a function of the nodal displacements as well.

$$v(\xi) = [\xi][A]^{-1}\{\bar{v}_e\} \quad \textbf{(11.55)}$$

Where

$[\xi] = [1 \quad \xi \quad \xi^2 \quad \xi^3]$

$[\xi][A]^{-1}$ is merged into a matrix $N(\xi)$

$$v(\xi) = N(\xi)\{\bar{v}_e\} \quad \textbf{(11.56)}$$

$v(\xi)$ is a scalar and describes the vertical deflection of the beam as a function of ξ and as a function of the rotational and vertical displacements at the beam's ends.

$$N(\xi) = \frac{1}{4(1+3\beta)}[N_1(\xi) \quad N_1(\xi) \quad N_1(\xi) \quad N_1(\xi)]\{\bar{v}_e\} \quad \textbf{(11.57)}$$

$$v(\xi) = \left[N_1(\xi) \quad \left(\frac{1}{2}L\right)N_1(\xi) \quad N_1(\xi) \quad \left(\frac{1}{2}L\right)N_1(\xi)\right]\{v_e\}$$

Where $\{v_e\} = \begin{bmatrix} v_p \\ \theta_{y_p} \\ v_q \\ \theta_{y_p} \end{bmatrix}$

$$N_1(\xi) = \frac{1}{4(1+3\beta)}(2+6\beta-3(1+2\beta)\xi+\xi^3)$$

$$N_2(\xi) = \frac{1}{4(1+3\beta)}(1+3\beta-\xi-(1+3\beta)\xi^2+\xi^3)$$

$$N_3(\xi) = \frac{1}{4(1+3\beta)}(2+6\beta+3(1+2\beta)\xi-\xi^3)$$

$$N_4(\xi) = \frac{1}{4(1+3\beta)}(1+3\beta-\xi+(1+3\beta)\xi^2+\xi^3)$$

$$N_v = \left[N_1(\xi) \quad \left(\frac{1}{2}L\right)N_1(\xi) \quad N_1(\xi) \quad \left(\frac{1}{2}L\right)N_1(\xi)\right] \tag{11.58}$$

The expression for the angle of rotation $\theta(\xi)_y$ becomes:

$$\theta_y(\xi) = \frac{\partial N(\xi)}{\partial \xi}\{\overline{v_e}\} \tag{11.59}$$

$$\theta_y(\xi) = \left[\left(\frac{1}{\frac{1}{2}L}\right)\frac{\partial N_1(\xi)}{\partial \xi} \quad \frac{\partial N_1(\xi)}{\partial \xi} \quad \left(\frac{1}{\frac{1}{2}L}\right)\frac{\partial N_1(\xi)}{\partial \xi} \quad \frac{\partial N_1(\xi)}{\partial \xi}\right]\{v_e\}$$

$$N_5(\xi) = \frac{\partial N_1(\xi)}{\partial \xi}$$

$$N_6(\xi) = \frac{\partial N_2(\xi)}{\partial \xi}$$

$$N_7(\xi) = \frac{\partial N_3(\xi)}{\partial \xi}$$

$$N_8(\xi) = \frac{\partial N_4(\xi)}{\partial \xi}$$

$$N_\theta = \left[\left(\frac{1}{\frac{1}{2}L}\right)\frac{\partial N_1(\xi)}{\partial \xi} \quad \frac{\partial N_1(\xi)}{\partial \xi} \quad \left(\frac{1}{\frac{1}{2}L}\right)\frac{\partial N_1(\xi)}{\partial \xi} \quad \frac{\partial N_1(\xi)}{\partial \xi}\right] \tag{11.60}$$

Substituting the displacement function into the energy expression

Through the strain and kinetic energy equations and the displacement functions the equation of motion can be obtained through substitution into the Lagrange equation. This chapter demonstrates how the equation of motion i.e. the mass matrix and stiffness matrix are obtained for a deep beam from the above mentioned functions.

Through substitution of the displacement functions (11.57) and (11.59) into the kinetic energy equation (11.44) and substituting the kinetic energy function into the Lagrange equation we get:

$$T = \frac{1}{2}\int_{-0.5L}^{0.5L} \rho A \dot{v}^2 \, dx + \frac{1}{2}\int_{-0.5L}^{0.5L} \rho I_y \dot{\theta}_y{}^2 \, dx$$

$$T = \frac{1}{2}\dot{v}_e{}^T \rho A \int_{-1}^{1} N_v{}^T N_v \, d\xi \, \dot{v}_e + \frac{1}{2}\dot{v}_e{}^T \rho I_y \int_{-1}^{1} N_\theta{}^T N_\theta \, d\xi \, \dot{v}_e$$

Lagrange equation:

$$\frac{d}{dt}\left(\frac{\partial T}{\partial \dot{z}}\right) + \frac{\partial U}{\partial z} + \frac{\partial D}{\partial \dot{z}} = f$$

$$\frac{d}{dt}\left(\frac{\partial T}{\partial \dot{z}}\right) = M\ddot{v}_e$$

Kinetic energy equation:

$$T = \frac{1}{2}\int_{-0.5L}^{0.5L} \rho A \dot{v}^2 \, dx + \frac{1}{2}\int_{-0.5L}^{0.5L} \rho I_y \dot{\theta}_y{}^2 \, dx$$

Substitution of the displacement function into the kinetic energy relation and the kinetic energy relation into the Lagrange equation:

$$M\ddot{v}_e = \rho A \int_{-1}^{1} N_v{}^T N_v \, d\xi \, \ddot{v}_e + \rho I_y \int_{-1}^{1} N_\theta{}^T N_\theta \, d\xi \, \ddot{v}_e$$

$$M = \rho A \int_{-1}^{1} N_v{}^T N_v \, d\xi + \rho I_y \int_{-1}^{1} N_\theta{}^T N_\theta \, d\xi \qquad \textbf{(11.61)}$$

Substituting the displacement function into the strain energy equation for deep beams gives:

$$U = \frac{1}{2}\int_{-0.5L}^{0.5L} EI_y \left(\frac{\partial^2 v}{\partial x^2}\right)^2 dx + \frac{1}{2}\int_{-0.5L}^{0.5L} \kappa AG \left(\frac{\partial v}{\partial x} - \theta_y\right)^2 dx$$

$$U = \frac{1}{2} v_e EI_y \int_{-1}^{1} {N''_v}^T N''_v \, d\xi v_e + \frac{1}{2} v_e \kappa AG \int_{-1}^{1} ({N'_v}^T N'_v - 2{N'_v}^T N_\theta + {N_\theta}^T N_\theta) d\xi v_e$$

Substituting the strain energy equation into the $\frac{\partial U}{\partial z}$ term of the Lagrange equation gives the stiffness matrix:

$$\frac{\partial U}{\partial z} = K v_e = EI_y \int_{-1}^{1} {N''_v}^T N''_v \, d\xi v_e + \kappa AG \int_{-1}^{1} ({N'_v}^T N'_v - 2{N'_v}^T N_\theta + {N_\theta}^T N_\theta) d\xi v_e$$

$$K = EI_y \int_{-1}^{1} {N''_v}^T N''_v \, d\xi + \kappa AG \int_{-1}^{1} ({N'_v}^T N'_v - 2{N'_v}^T N_\theta + {N_\theta}^T N_\theta) d\xi \quad \textbf{(11.62)}$$

Appendix IV *Formulation of the Plate Element*

Energy Expressions for Plates

A plate element is considered to be storing two types of energy

- Energy as a result of in-plane loads
- Energy as a result of bending loads normal to the plate middle surface.

For the bending strain and inertia energies, a distinction is made between the formulation of the energy expressions for thin plates and thick plates. For the thick plates the strain energy as a result of the deformation of the cross-sectional area are taken into account through an extra term, in same way as has been done for the beam element. This extra strain energy is a result of the angle of deformation of the cross-sectional area normal to the cross-section $\frac{\partial u}{\partial z}$ or $\frac{\partial w}{\partial z}$ is not equal to the angular deformation of rotation about the y-axis or x-axis respectively $\left(\frac{\partial v}{\partial x} \text{ or } \frac{\partial v}{\partial y}\right)$. For the thick plate an extra energy term is also added for the kinetic energy where the rotary inertia about the x and y axis is assumed to have an appreciable contribution to the total kinetic energy expression of the element.

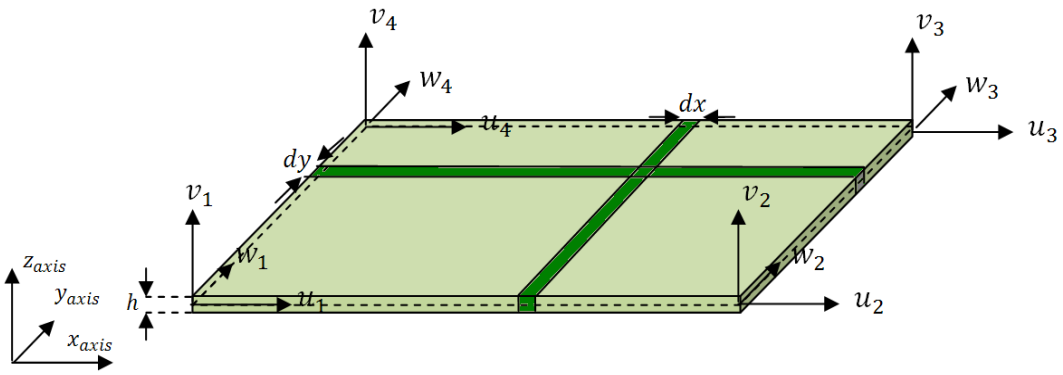

Figure 93 **Axis and orientation on a four node plate element (node 1, 2, 3 and 4). Displacement in x, y and z direction are indicated with u, w and v respectively. Rotations about the x, y and z axis are indicated through θ_x, θ_y and θ_z respectively.**

Plate In-Plane Deformation:

In this section the energy expression for the in plane stresses is formulated. These are stresses that are a result of forces acting parallel to the middle plane of the plate and are uniformly distributed over through the thickness. There are no forces acting in

the z direction and the only stresses occurring are in x and y direction. The strain energy equation is written as:

$$U = \frac{1}{2}\int_V (\sigma_x \varepsilon_x + \sigma_y \varepsilon_y + \tau_{xy}\gamma_{xy}) dV \quad \textbf{(11.63)}$$

In matrix form this can be expressed as :

$$U = \frac{1}{2}\int_V [\sigma]^T [\varepsilon] dV \quad \textbf{(11.64)}$$

Where:

$[\sigma] = \begin{bmatrix} \sigma_x \\ \sigma_y \\ \tau_{xy} \end{bmatrix}$ = stress matrix

$[\varepsilon] = \begin{bmatrix} \varepsilon_x \\ \varepsilon_y \\ \gamma_{xy} \end{bmatrix} = \begin{bmatrix} \varepsilon_x \\ \varepsilon_y \\ \frac{\partial u}{\partial y} + \frac{\partial w}{\partial x} \end{bmatrix}$ = strain matrix

The relation between strain and stress is expressed through the matrix *D* so that we can write:

$$\sigma = [D][\varepsilon] \quad \textbf{(11.65)}$$

Where:

$$[D] = \begin{bmatrix} \frac{E}{(1-\nu^2)} & \frac{E\nu}{(1-\nu^2)} & 0 \\ \frac{E\nu}{(1-\nu^2)} & \frac{E}{(1-\nu^2)} & 0 \\ 0 & 0 & \frac{E}{2(1+\nu)} \end{bmatrix}$$

and therefore the strain energy can be written as:

$$\boldsymbol{U = \frac{1}{2}\int_V [\varepsilon]^T [D][\varepsilon]\, dV}$$

Ultimately we can write for the in plane strain energy:

$$U = \frac{1}{2}\int_A h[\varepsilon]^T [D][\varepsilon]\, dA \quad \textbf{(11.66)}$$

Where h is the thickness (height) of the plate. For the plane kinetic energy we can write:

$$T = \frac{1}{2}\int_A \rho h(\dot{u}^2 + \dot{w}^2)dA \quad \textbf{(11.67)}$$

Plate Bending Deformation:

The relation between plate bending strain and stresses is expressed through the relation:

$$u(x,z) = -z\frac{\partial v}{\partial x} \qquad \varepsilon_x = -z\frac{\partial^2 v}{\partial x^2} \quad \textbf{(11.68)}$$

$$u(y,z) = -z\frac{\partial v}{\partial y} \qquad \varepsilon_y = -z\frac{\partial^2 v}{\partial y^2}$$

$$\gamma_{xy} = \frac{\partial u}{\partial y} + \frac{\partial w}{\partial x} = -z2\frac{\partial^2 v}{\partial x \partial y}$$

For thin plates is written:

$$\gamma_{xz} = \frac{\partial u}{\partial z} + \frac{\partial v}{\partial x} = 0 \quad \textbf{(11.69)}$$

$$\gamma_{yz} = \frac{\partial u}{\partial z} + \frac{\partial w}{\partial y} = 0$$

For thick plates:

$$\gamma_{xz} = \frac{\partial u}{\partial z} + \frac{\partial v}{\partial x} = \theta_y + \frac{\partial v}{\partial x} \quad \textbf{(11.70)}$$

$$\gamma_{yz} = \frac{\partial u}{\partial z} + \frac{\partial w}{\partial x} = -\theta_x + \frac{\partial v}{\partial y}$$

The bending strain energy expression is written as: **(11.71)**

$$U = \frac{1}{2}\int_V (\sigma_x \varepsilon_x + \sigma_y \varepsilon_y + \tau_{xy}\gamma_{xy})dV$$

$$\sigma = [D][\varepsilon] \quad \textbf{(11.72)}$$

$$U = \frac{1}{2}\int_V [\varepsilon]^T [D][\varepsilon]\, dV$$

where for an orthotropic plate with material properties in all direction the same can be written:

$$[D] = \begin{bmatrix} \frac{E}{(1-\nu^2)} & \frac{E\nu}{(1-\nu^2)} & 0 \\ \frac{E\nu}{(1-\nu^2)} & \frac{E}{(1-\nu^2)} & 0 \\ 0 & 0 & \frac{E}{2(1+\nu)} \end{bmatrix}$$

$$\text{and } [\varepsilon] = \begin{bmatrix} \varepsilon_x \\ \varepsilon_y \\ \gamma_{xy} \end{bmatrix} \quad \textbf{(11.73)}$$

Substituting equation (11.68) into (11.73) gives:

$$\varepsilon = -z\chi = -z \begin{bmatrix} \frac{\partial^2 v}{\partial x^2} \\ \frac{\partial^2 v}{\partial y^2} \\ -z2\frac{\partial^2 v}{\partial x \partial y} \end{bmatrix} \quad \textbf{(11.74)}$$

Substituting equation (11.74) into (11.72) and integrating over z (the thickness of the plate) gives the strain energy equation for a slender bending plate:

$$U = \frac{1}{2}\int_A \frac{h^3}{12}[\chi]^T[D][\chi]dA \quad \textbf{(11.75)}$$

For a thick plates extra shear stresses occur due to the deformation of the normals. This extra shear deformation results in extra strain energy being stored in the plate element in x and y direction:

$$\gamma_{xz} = \frac{\partial u}{\partial z} + \frac{\partial v}{\partial x} \neq 0 \quad \textbf{(11.76)}$$

$$\gamma_{yz} = \frac{\partial u}{\partial z} + \frac{\partial v}{\partial y} \neq 0$$

$$\gamma_{xz} = \theta_y + \frac{\partial v}{\partial x} \neq 0$$

$$\gamma_{yz} = -\theta_x + \frac{\partial v}{\partial y} \neq 0$$

$$[\gamma] = \begin{bmatrix} \theta_y + \dfrac{\partial v}{\partial x} \\ -\theta_x + \dfrac{\partial v}{\partial y} \end{bmatrix}$$

Resulting extra strain energy due to thickness effect:

$$\frac{1}{2}\int_V [\tau]^T [\gamma] dV$$

Where:

$$[\tau] = \begin{bmatrix} \tau_{xz} \\ \tau_{yz} \end{bmatrix} = \kappa [D^s][\gamma]$$

and

$$[D^s] = \begin{bmatrix} G & 0 \\ 0 & G \end{bmatrix} = \frac{E}{2(1+\nu)} \begin{bmatrix} 1 & 0 \\ 0 & 1 \end{bmatrix}$$

Where G is the shear modulus according to Hooke's law in shear:

$$G = \frac{E}{2(1-\nu)}$$

And ν is the Poisson ratio which is considered to be around 0.33 for steel

The total strain energy equation for a thick plate is:

$$U = \frac{1}{2}\int_A \frac{h^3}{12} [\chi]^T [D][\chi] dA + \frac{1}{2}\int_A \kappa h [\gamma]^T [D^s][\gamma] dA \quad \textbf{(11.77)}$$

Bending inertia forces for a plate are expressed through the following relations:

$$T = \frac{1}{2}\int_A \rho h \dot{v}^2 \, dA \quad \textbf{(11.78)}$$

For the thick plate also the inertia effect of the rotation of the cross-sectional areas are taken into account. The total kinetic energy becomes:

$$T = \frac{1}{2}\int_A \rho \left(h\dot{v}^2 + \frac{h^3}{12}\dot{\theta}_x{}^2 + \frac{h^3}{12}\dot{\theta}_y{}^2 \right) dA \quad \textbf{(11.79)}$$

Displacement Function

The displacement function of a plate is obtained in similar manor. Considering a four node square $l \times l$ plate element in figure Figure 93 the displacement function can be represented by a polynomial with twelve terms as there are 12 degrees of freedom (3 degrees of freedom for each node (rotation about y and x axis and vertical translation v) for each of the four nodes).The displacement function becomes:

$$v(\xi,\eta) = a_1 + a_2\xi + a_3\eta + a_4\xi^2 + a_5\eta\xi + a_6\eta^2 + a_7\xi^3 + a_8\xi^2\eta + a_9\xi\eta^2 + a_{10}\eta^3 + a_{11}\xi^3\eta + a_{12}\xi\eta^3$$

Where:

$\xi = \frac{x}{0.5l}$ = a non dimensional coordinate

$\eta = \frac{y}{0.5l}$ = a non dimensional coordinate

a_n = the polynomial constant

For a thin plate the relation between the rotation about the x or y axis is obtained through differentiating the displacement function to y and x respectively

For a thick plate an extra set of displacement equations is formulated for the rotation about x and y axis:

$$\theta(\xi,\eta) = b_1 + b_2\xi + b_3\eta + b_4\xi^2 + b_5\eta\xi + b_6\eta^2 + b_7\xi^2\eta + b_8\xi\eta^2$$

Relations between a_n and b_n coefficients are formulated in a similar way as for the beam element through the relations but are not further elaborated on in this work

Through the strain and kinetic energy equations and the displacement functions the equation of motion can be obtained through substitution into the Lagrange equation. As this is done in a similar way as for the beam element, this is not further discussed here.

Appendix V *Residual Compensation for Free Floating Structures*

In order to include the contribution from residual flexibility to the response of a structure applying mode superposition, the stiffness matrix needs to be inverted so that the flexibility matrix is obtained. Inverting the stiffness matrix of a structure that is not fully constrained is however impossible, as the stiffness matrix will be singular. Obtaining the flexibility matrix is still possible through elimination of the rigid body degrees of freedom. This is done through applying so called pseudo constraint to the structure at arbitrary nodes, so that no rigid body motions are prevented. A flexibility matrix G_c is calculated for the substructure by inverting the stiffness matrix with the pseudo constraints applied [37, 39]

In the next step the obtained flexibility matrix with the pseudo constraints involved is corrected for the presence of these pseudo constraints through a projection matrix *P*. This projection matrix is based on the formulation of a corrected excitation force that is compensated for the reaction forces occurring in the pseudo constraints, resulting from restraining the rigid body modes. These reaction forces F_r are equal to the rigid body inertia forces and are expressed through:

$$F_r = M\phi_r\ddot{a}_r \quad \textbf{(11.80)}$$

Where

M = the mass marix

ϕ_r = the matrix of rigid body modes

$\ddot{a}_r$ = the acceleration rigid body modal coordinate

The corrected or so called equilibrated excitation force F_{eq} becomes:

$$F_{eq} = F - M\phi_r\ddot{a}_r \quad \textbf{(11.81)}$$

Where F is the original excitation force.

An expression for the rigid modal acceleration coordinates $\ddot{a}_r$ is required. This is obtained through projecting the full stiffness, mass and damping matrix and external force matrix onto the subspace spanned by the rigid body modes and setting up the equation of motion (${\phi_r}^T$, being the transposed matrix of rigid body modes):

$$\phi_r{}^T M\phi_r\ddot{a}_r + \phi_r{}^T M\phi_e\ddot{a}_r + \phi_r{}^T C\phi_e\dot{a}_e + \phi_r{}^T K\phi_e a_e = \phi_r{}^T F \quad \textbf{(11.82)}$$

As the rigid body modes ϕ_r, like the elastic modes ϕ_e are orthogonal to the damping, mass and stiffness matrix, $\phi_r{}^T M\phi_e$ and $\phi_r{}^T C\phi_e$ and $\phi_r{}^T K\phi_e$ become zero.

The equation of motion is rewritten as

$$\phi_r{}^T M\phi_r\ddot{a}_r = \phi_r{}^T F$$

Consider the mode shapes to be normalised to the mass matrix, $\phi_r{}^T M\phi_r$ becomes an identity matrix I

$$I\ddot{a}_r = \phi_r{}^T F \quad \textbf{(11.83)}$$

$$\ddot{a}_r = \phi_r{}^T F$$

Substituting (11.83) into (11.81) gives:

$$F_{eq} = F - M\phi_r\phi_r{}^T F \quad \textbf{(11.84)}$$

The projection matrix P is formulated:

$$F_{eq} = F - M\phi_r\phi_r{}^T F = \left(1 - M\phi_r\phi_r{}^T\right)F = PF \quad \textbf{(11.85)}$$

$$P = \left(1 - M\phi_r\phi_r{}^T\right) \quad \textbf{(11.86)}$$

The corrected flexibility matrix is obtained through the following relations :

$$u_{static} = G_c F_{eq} = G_c PF \quad \textbf{(11.87)}$$

Although rigid body motion has been eliminated, contribution of rigid body motion to the elastic modes may still be present. In order to eliminate the interaction between rigid body modes and elastic modes the u_{static} representation in equation (11.87) is orthogonolised with the rigid body modes. This means that:

$$\phi_r{}^T M u_{orthogonal\,static} = 0 \quad \textbf{(11.88)}$$

$$u_{orthogonal\,static} = u_{static} + \phi_r a_r{}' \quad \textbf{(11.89)}$$

Where $a_r{}'$ is a correction vector, such that ${\phi_r}^T M u_{orthogonal\ static} = 0$. Substituting equation (11.89) into equation (11.88) gives an expression for $a_r{}'$

$$a_r{}' = -{\phi_r}^T M u_{static} \quad \textbf{(11.90)}$$

Substituting (11.88) into (11.89) gives the following expression:

$$u_{orthogonal\ static} = u_{static} - \phi_r {\phi_r}^T M u_{static} \quad \textbf{(11.91)}$$

Substituting (11.87) into (11.91) gives:

$$u_{orthogonal\ static} = (1 - \phi_r {\phi_r}^T M) u_{static} F = P^T G_c P F \quad \textbf{(11.92)}$$

The newly corrected flexibility matrix G_E is calculated following equation (11.92):

$$G_E = P^T G_c P \quad \textbf{(11.93)}$$

For calculating residual elasticity for an unconstrained free floating structure the following equations can be formulated following equation (6.32):

$$u = \phi a + G_E F - \phi_e \Lambda^{-1} {\phi_e}^T F \quad \textbf{(11.94)}$$

Where ϕ is the matrix containing all retained mode shapes including rigid body modes. ϕ_e is the matrix containing all the retained elastic mode shapes, i.e. all retained mode shapes excluding the rigid body modes.

$$G_{res} = G_E - \phi_e \Lambda^{-1} {\phi_e}^T \quad \textbf{(11.95)}$$

.

Appendix VI *Sparse Matrix Solver: Row Reduction Technique*

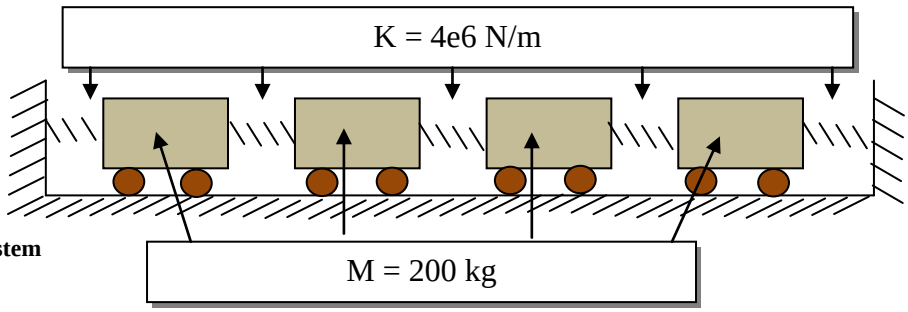

Mass spring system

Consider the following stiffness matrix K, mass matrix M and the excitation load vector F:

$$K = \begin{bmatrix} 4e6 & -2e6 & 0 & 0 \\ -2e6 & 4e6 & -2e6 & 0 \\ 0 & -2e6 & 4e6 & -2e6 \\ 0 & 0 & -2e6 & 4e6 \end{bmatrix}$$

$$M = \begin{bmatrix} 200 & 0 & 0 & 0 \\ 0 & 200 & 0 & 0 \\ 0 & 0 & 200 & 0 \\ 0 & 0 & 0 & 200 \end{bmatrix}$$

$$F = \begin{bmatrix} 60 \\ 0 \\ 0 \\ 0 \end{bmatrix}$$

Consider the excitation frequency to be 10 Hz:

$\omega = 62.8\ [\frac{rad}{s}]$ = (10Hz)

Undamped dynamic stiffness matrix :

$$[K - \omega^2 M] = \begin{bmatrix} 4e6 - 200 * 62.8^2 & -2e6 & 0 & 0 \\ -2e6 & 4e6 - 200 * 62.8^2 & -2e6 & 0 \\ 0 & -2e6 & 4e6 - 200 * 62.8^2 & -2e6 \\ 0 & 0 & -2e6 & 4e6 - 200 * 62.8^2 \end{bmatrix}$$

$$[K - \omega^2 M] = [F] = \begin{bmatrix} 3.210e6 & -2e6 & 0 & 0 \\ -2e6 & 3.210e6 & -2e6 & 0 \\ 0 & -2e6 & 3.210e6 & -2e6 \\ 0 & 0 & -2e6 & 3.210e6 \end{bmatrix} \begin{bmatrix} \hat{u}_1 \\ \hat{u}_2 \\ \hat{u}_3 \\ \hat{u}_4 \end{bmatrix} = \begin{bmatrix} 60 \\ 0 \\ 0 \\ 0 \end{bmatrix}$$

Forward phase: generating zeros on the lower triangle below the main diagonal:

Starting with matrix: $\begin{bmatrix} 3.210e6 & -2e6 & 0 & 0 \\ -2e6 & 3.210e6 & -2e6 & 0 \\ 0 & -2e6 & 3.210e6 & -2e6 \\ 0 & 0 & -2e6 & 3.210e6 \end{bmatrix} \begin{bmatrix} \hat{u}_1 \\ \hat{u}_2 \\ \hat{u}_3 \\ \hat{u}_4 \end{bmatrix} = \begin{bmatrix} 60 \\ 0 \\ 0 \\ 0 \end{bmatrix}$

Step 1 $row2 = -\left(\frac{r_{11}}{r_{21}}\right) row2 + row1$

$$\begin{bmatrix} 3.210e6 & -2e6 & 0 & 0 \\ 0 & 3.15e6 & -3.21e6 & 0 \\ 0 & -2e6 & 3.210e6 & -2e6 \\ 0 & 0 & -2e6 & 3.210e6 \end{bmatrix} \begin{bmatrix} \hat{u}_1 \\ \hat{u}_2 \\ \hat{u}_3 \\ \hat{u}_4 \end{bmatrix} = \begin{bmatrix} 60 \\ 60 \\ 0 \\ 0 \end{bmatrix}$$

Step 2 $row3 = -\left(\frac{r_{22}}{r_{32}}\right) row3 + row2$

$$\begin{bmatrix} 3.210e6 & -2e6 & 0 & 0 \\ 0 & 3.15e6 & -3.21e6 & 0 \\ 0 & 0 & 1.85e6 & -3.15e6 \\ 0 & 0 & -2e6 & 3.210e6 \end{bmatrix} \begin{bmatrix} \hat{u}_1 \\ \hat{u}_2 \\ \hat{u}_3 \\ \hat{u}_4 \end{bmatrix} = \begin{bmatrix} 60 \\ 60 \\ 60 \\ 0 \end{bmatrix}$$

Step 3 $row4 = -\left(\frac{r_{33}}{r_{43}}\right) row4 + row3$

$$\begin{bmatrix} 3.210e6 & -2e6 & 0 & 0 \\ 0 & 3.15e6 & -3.21e6 & 0 \\ 0 & 0 & 1.85e6 & -3.15e6 \\ 0 & 0 & 0 & -1.81e5 \end{bmatrix} \begin{bmatrix} \hat{u}_1 \\ \hat{u}_2 \\ \hat{u}_3 \\ \hat{u}_4 \end{bmatrix} = \begin{bmatrix} 60 \\ 60 \\ 60 \\ 60 \end{bmatrix}$$

Backward phase: generating ones on the main diagonal and zeros above the pivots

Starting with matrix $\begin{bmatrix} 3.210e6 & -2e6 & 0 & 0 \\ 0 & 3.15e6 & -3.21e6 & 0 \\ 0 & 0 & 1.85e6 & -3.15e6 \\ 0 & 0 & 0 & -1.81e5 \end{bmatrix} \begin{bmatrix} \hat{u}_1 \\ \hat{u}_2 \\ \hat{u}_3 \\ \hat{u}_4 \end{bmatrix} = \begin{bmatrix} 60 \\ 60 \\ 60 \\ 60 \end{bmatrix}$

Step 1: generating ones on the main diagonal

$$row4 = row4\left(\frac{1}{r_{44}}\right)$$

$$row3 = row3\left(\frac{1}{r_{33}}\right)$$

$$row2 = row2\left(\frac{1}{r_{22}}\right)$$

$$row1 = row1\left(\frac{1}{r_{11}}\right)$$

$$\begin{bmatrix} 1 & -0.623 & 0 & 0 \\ 0 & 1 & -1.018 & 0 \\ 0 & 0 & 1 & -1.703 \\ 0 & 0 & 0 & 1 \end{bmatrix} \begin{bmatrix} \hat{u}_1 \\ \hat{u}_2 \\ \hat{u}_3 \\ \hat{u}_4 \end{bmatrix} = \begin{bmatrix} 1.87e-5 \\ 1.9e-5 \\ 3.24e-5 \\ -0.33e-4 \end{bmatrix}$$

Step 2, generating zeros above pivots:

$$row3 = row3 - \left(\frac{r_{34}}{r_{44}}\right) row4$$

$$\begin{bmatrix} 1 & -0.623 & 0 & 0 \\ 0 & 1 & -1.018 & 0 \\ 0 & 0 & 1 & 0 \\ 0 & 0 & 0 & 1 \end{bmatrix} \begin{bmatrix} \hat{u}_1 \\ \hat{u}_2 \\ \hat{u}_3 \\ \hat{u}_4 \end{bmatrix} = \begin{bmatrix} 1.87e-5 \\ 1.9e-5 \\ -0.53e-4 \\ -0.33e-4 \end{bmatrix}$$

$$row2 = row2 - \left(\frac{r_{23}}{r_{33}}\right) row3$$

$$\begin{bmatrix} 1 & -0.623 & 0 & 0 \\ 0 & 1 & -1.018 & 0 \\ 0 & 0 & 1 & 0 \\ 0 & 0 & 0 & 1 \end{bmatrix} \begin{bmatrix} \hat{u}_1 \\ \hat{u}_2 \\ \hat{u}_3 \\ \hat{u}_4 \end{bmatrix} = \begin{bmatrix} 1.87e-5 \\ -0.52e-4 \\ -0.53e-4 \\ -0.33e-4 \end{bmatrix}$$

$$row1 = row1 - \left(\frac{r_{12}}{r_{22}}\right) row2$$

$$\begin{bmatrix} 1 & 0 & 0 & 0 \\ 0 & 1 & 0 & 0 \\ 0 & 0 & 1 & 0 \\ 0 & 0 & 0 & 1 \end{bmatrix} \begin{bmatrix} \hat{u}_1 \\ \hat{u}_2 \\ \hat{u}_3 \\ \hat{u}_4 \end{bmatrix} = \begin{bmatrix} -0.31e-4 \\ -0.52e-4 \\ -0.53e-4 \\ -0.33e-4 \end{bmatrix}$$

The response therefore is

$$\begin{bmatrix} \hat{u}_1 \\ \hat{u}_2 \\ \hat{u}_3 \\ \hat{u}_4 \end{bmatrix} = \begin{bmatrix} -0.31e-4 \\ -0.52e-4 \\ -0.53e-4 \\ -0.33e-4 \end{bmatrix}$$

Part 1		
Step		Number of real matrix operations
A	Calculating $\left(\frac{M_{((a+b),1)}}{M_{(1,1)}}\right)$ Multiplying row 1 with $\left(\frac{M_{((a+b),1)}}{M_{(1,1)}}\right)$	10 + (a+b+ e) *6
B	Row(a+b) – row 1 (pivot position $M_{((a+b),1)}$ becomes 0	(a+b +e)*2
	Total number of operations =	8×(a+b+e)+10
C	Repeating step A and B for row (a+b-1) to row 2 Colum 1 becomes zero except for $M_{(1,1)}$	(a+b-1) × (8×(a+b +e)+10)
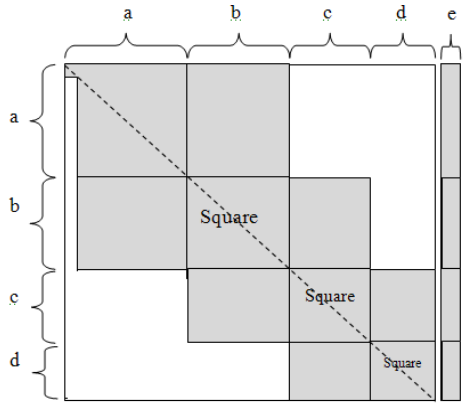		
D	Calculating $\left(\frac{M_{((a+b),2)}}{M_{(2,2)}}\right)$ Multiplying row 2 with $\left(\frac{M_{((a+b),2)}}{M_{(2,2)}}\right)$	10+ (a+b +e-1)*6
E	Row (a+b) – row 2 (pivot position $M_{((a+b),2)}$ becomes 0	(a+b +e-1)*2
	Total number of operations =	8×(a+b +e-1)+10
F	Repeating step D and E for row (a+b-1) to row 3 Colum 2 becomes zero except for $M_{(1,2)}$ and $M_{(2,2)}$	(a+b-2) ×(8×(a+b +e-1)+10)
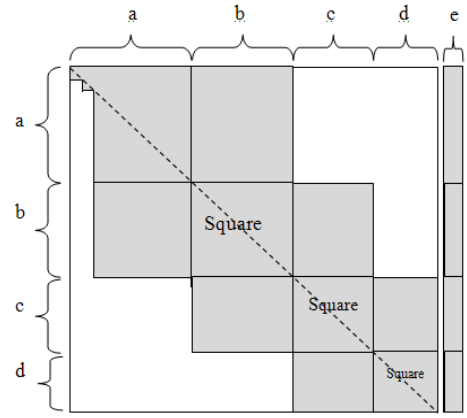		
An expression for the total number of matrix operations n_1 required for part 1 (generating zeros under the main diagonal for column 1 to a) can be written as follows:		

$$n_1 = \sum_{k=0}^{k=a-1} (8 \times (a + b + c + d + e - k) + 10)(a + b - 1 - k)$$

This results in a matrix with a skyline as shown in the figure below:

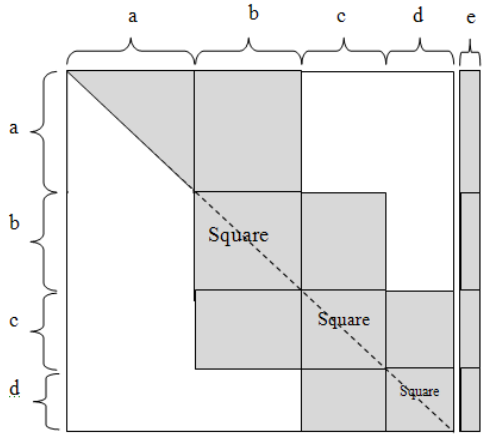

Part 2

In a similar way for part 2:

$$n_2 = \sum_{k=0}^{k=b-1} (8 \times (b + c + e - k) + 10)(b + c - 1 - k)$$

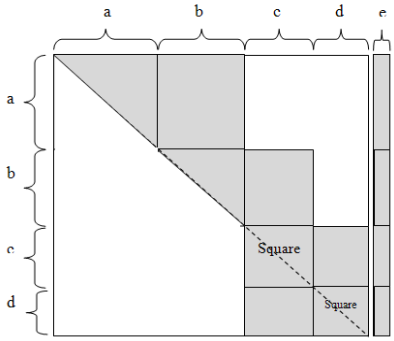

Part 3
And for part 3: $$n_3 = \sum_{k=0}^{k=c+d-1} (8 \times (c+d+e-k)+10)(c+d-1-k)$$ 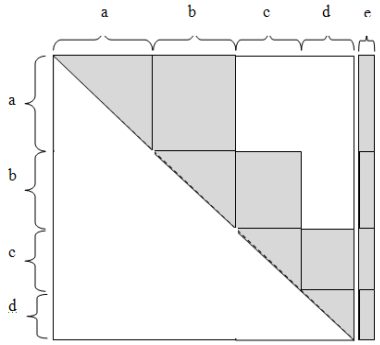

The Backward phase is the next step in the row reduction procedure where ones are generated on the main diagonal (so the matrix becomes a unit upper triangular matrix). The number of operations required for the backward phase can be expressed as follows (see also Appendix XIV)

For row 1 to a:		
		Number of real operations
Row 1	Calculating $\frac{1}{M_{1,1}}$ Multiplying the non zeros in row 1 by $\frac{1}{M_{1,1}}$	10 + 6*(a+b)
Row 2	Calculating $\frac{1}{M_{2,2}}$ Multiplying the non zeros in row 2 by $\frac{1}{M_{2,2}}$	10 + 6*(a+b-1)
Row k	Calculating $\frac{1}{M_{k,k}}$ Multiplying the non zeros in row a by $\frac{1}{M_{k,k}}$	10 + 6*(a+b-k)
Total number of operations:		
$$\sum_{k=0}^{k=a-1} (6 * (a+b-k)+10)$$		

For row a+1 to row (a+b+c):		
		Number of real operations
Row a+1	Calculating $\frac{1}{M_{a+1,a+1}}$ Multiplying the non zeros in row (a+1) by $\frac{1}{M_{a+1,a+1}}$	10 + 6*(b+c)
Row a+2	Calculating $\frac{1}{M_{a+2,a+2}}$ Multiplying the non zeros in row (a+2) by $\frac{1}{M_{a+2,a+2}}$	10 + 6*(b+c-1)
Row (a+b+k)	Calculating $\frac{1}{M_{(a+b+k),(a+b+k)}}$ Multiplying the non zeros in row (a+k) by $\frac{1}{M_{(a+b+k),(a+b+k)}}$	10+ 6*(b+c-k)
Total number of operations:		
$\sum_{k=0}^{k=b-1} (6 * (b + c - k) + 10)$		

For row (a+b+1) to row (a+b+c+d):		
		Number of operations
Row a+b+1	Calculating $\frac{1}{M_{\mathrm{a+b+1,a+b+1}}}$ Multiplying the non zeros in row a+b+1 by $\frac{1}{M_{\mathrm{a+b+1,a+b+1}}}$	10+ 6*(c+d+1)
Row a+b+c+d	Calculating $\frac{1}{M_{\mathrm{(a+b+c+d),(a+b+c+d)}}}$ Multiplying the non zeros in row a+b+c+d by $\frac{1}{M_{\mathrm{(a+b+c+d),(a+b+c+d)}}}$	10+ 6*(c+d+1-c-d+1)
Total number of operations:		
$\sum_{k=0}^{k=c+d-1} (6 * (c + d + 1 - k) + 10)$		

Solving a real unit triangular matrices requires about n^2 operations, where n is the number of rows or columns of the matrix [48]. Solving an imaginary triangular matrix requires twice the number of operation ($2n^2$)

Appendix VII *Results FEM for Different Boundary Conditions*

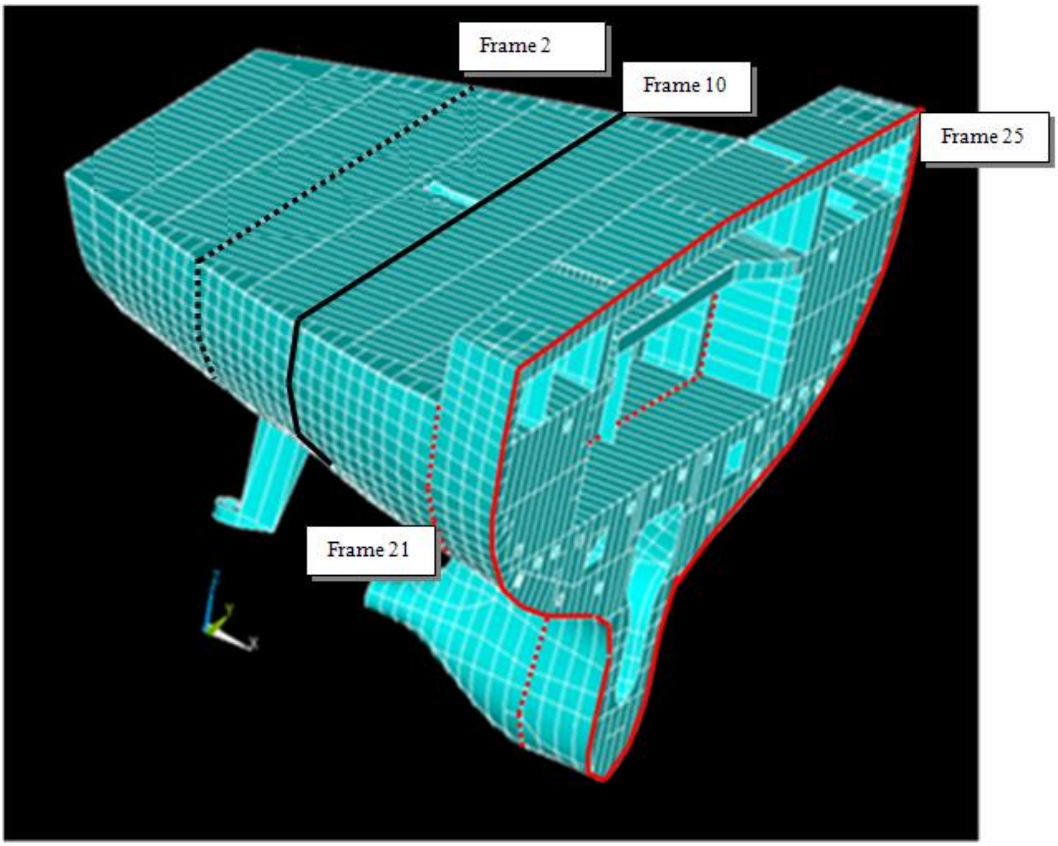

Frame 25

Frame 21

Frame 10

Frame 2

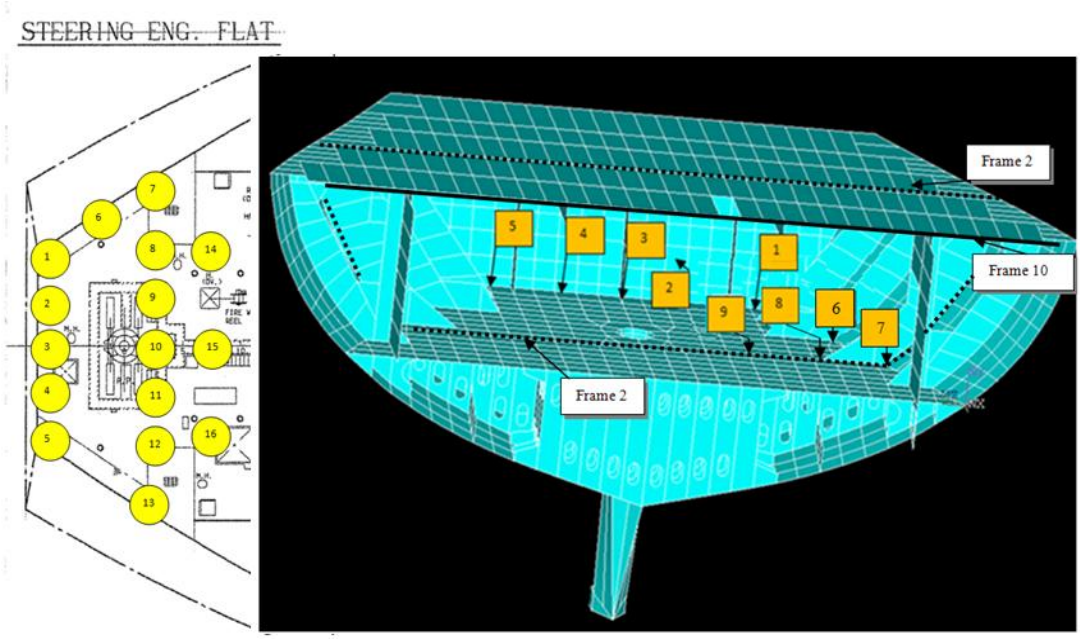

Simulation results positions on steering gear deck

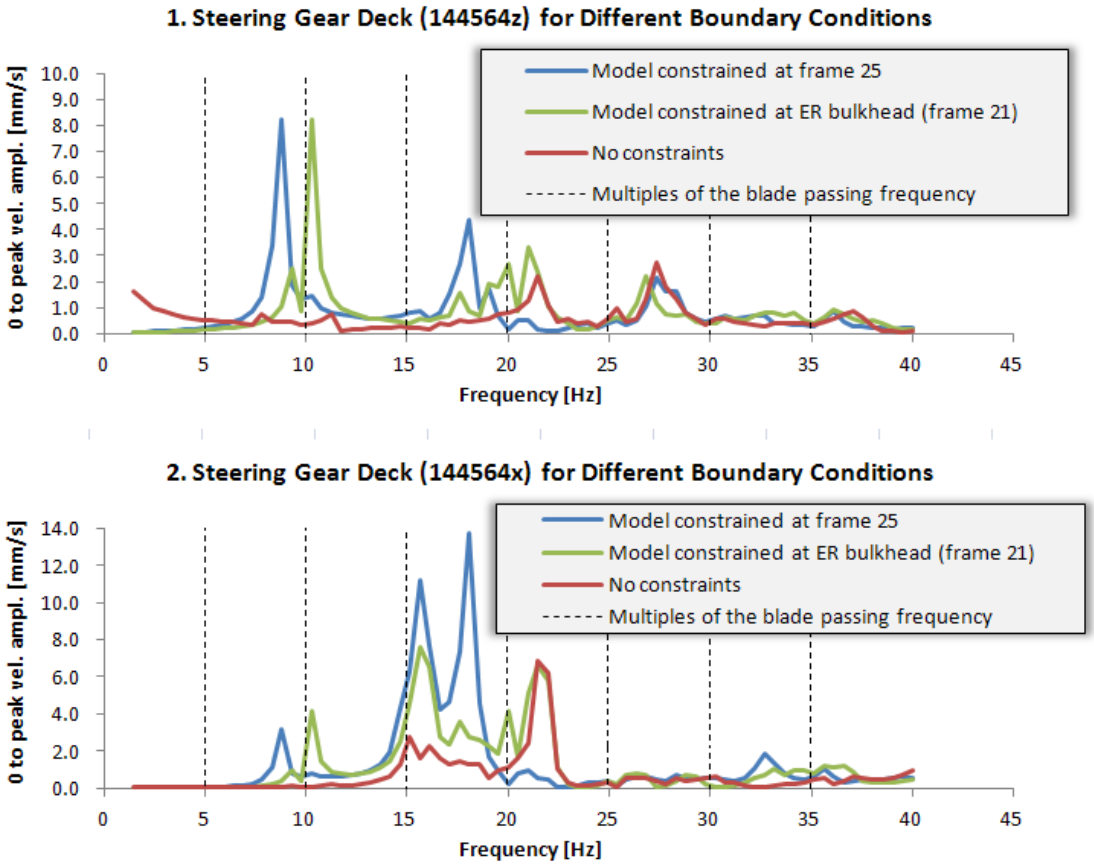

Simulation results 0 to peak vibration velocity amplitudes at different boundary conditions

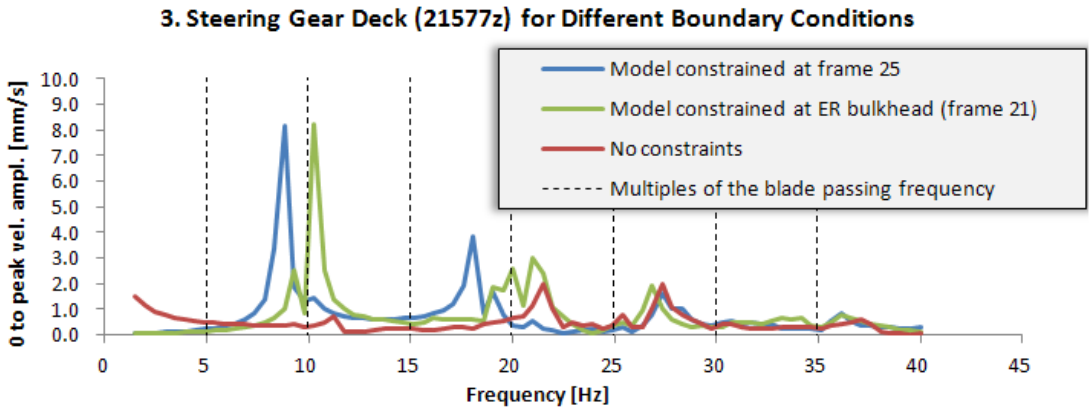

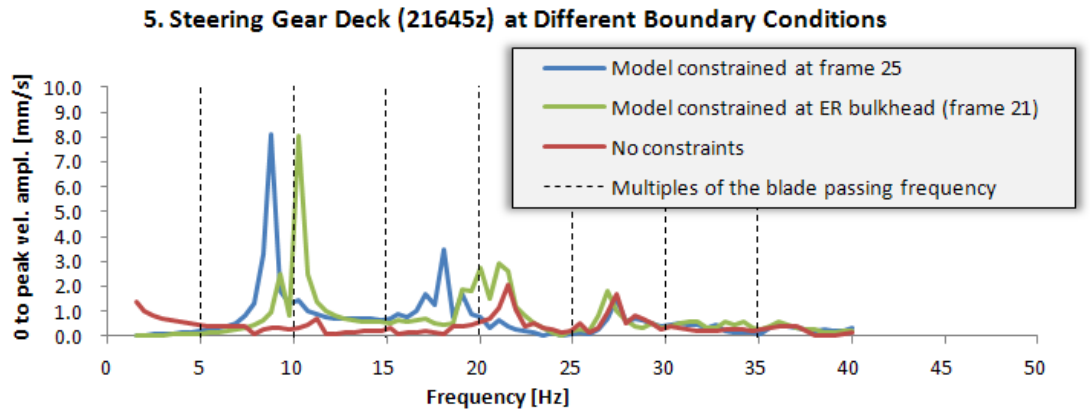

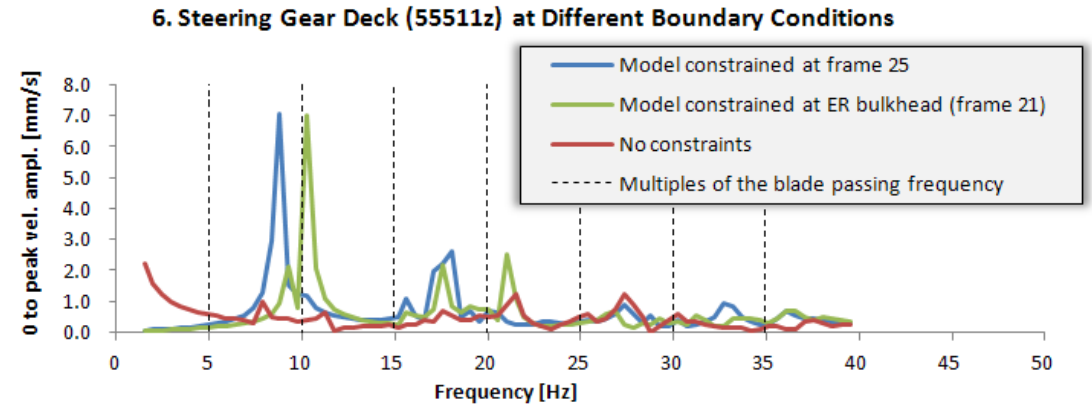

Simulation results 0 to peak vibration velocity amplitudes at different boundary conditions

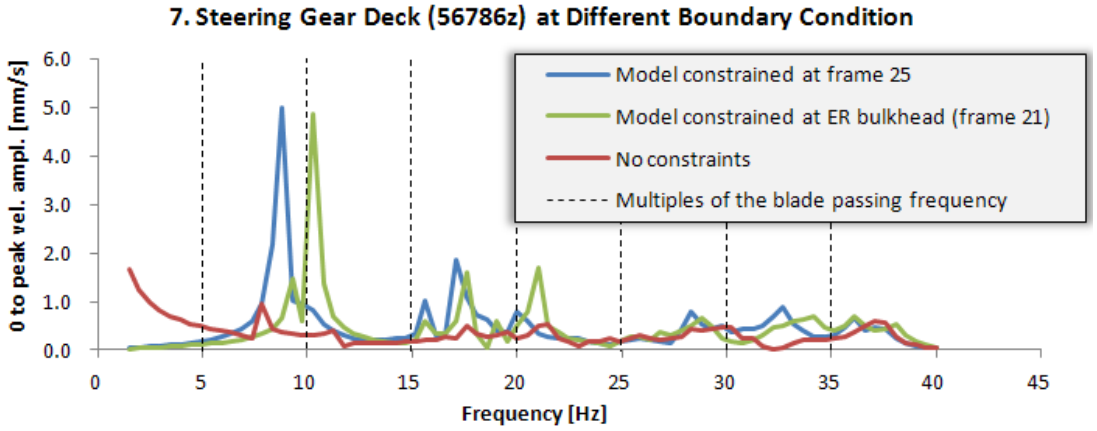

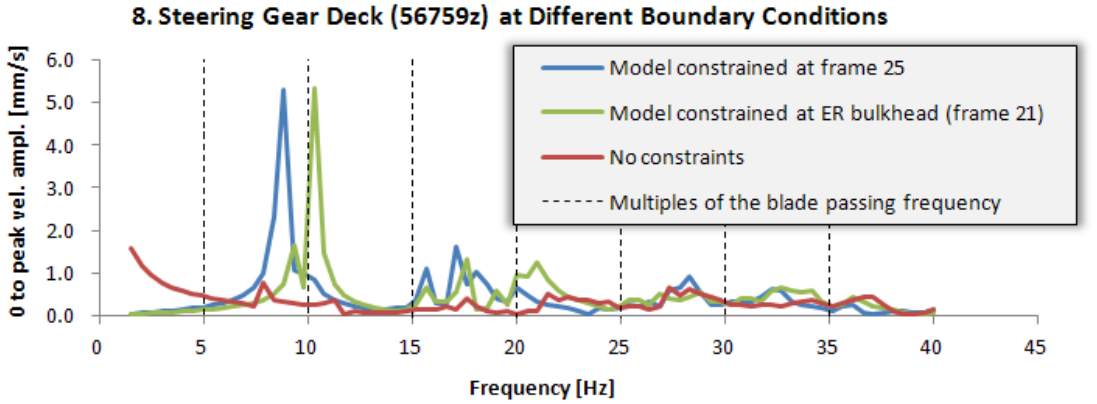

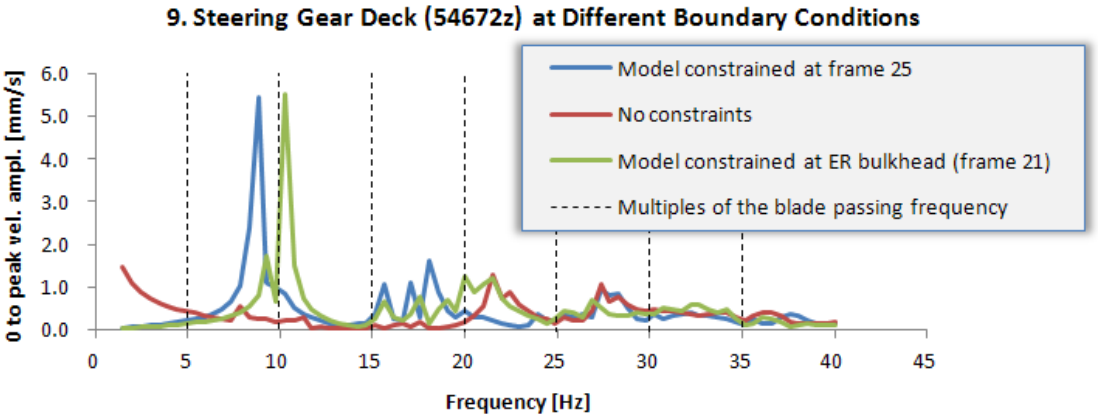

Simulation results 0 to peak vibration velocity amplitudes at different boundary conditions

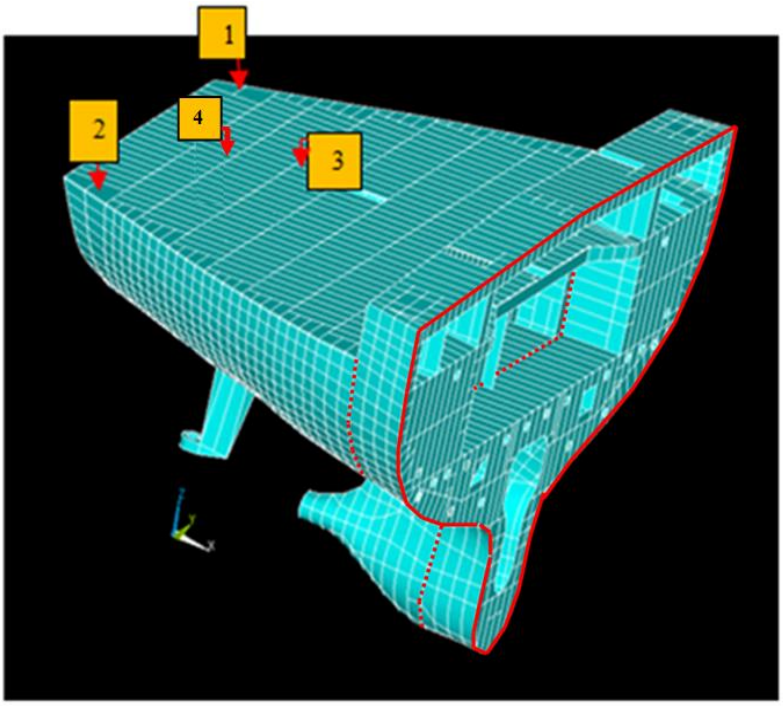

Simulation results position on mooring deck

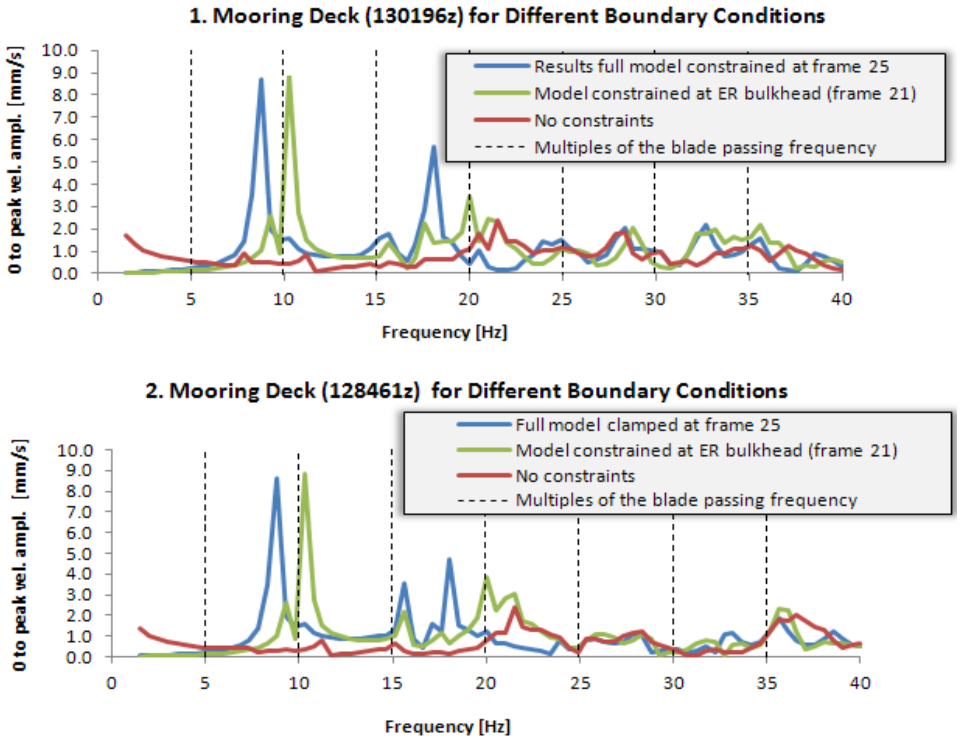

Simulation results 0 to peak vibration velocity amplitudes at different boundary conditions

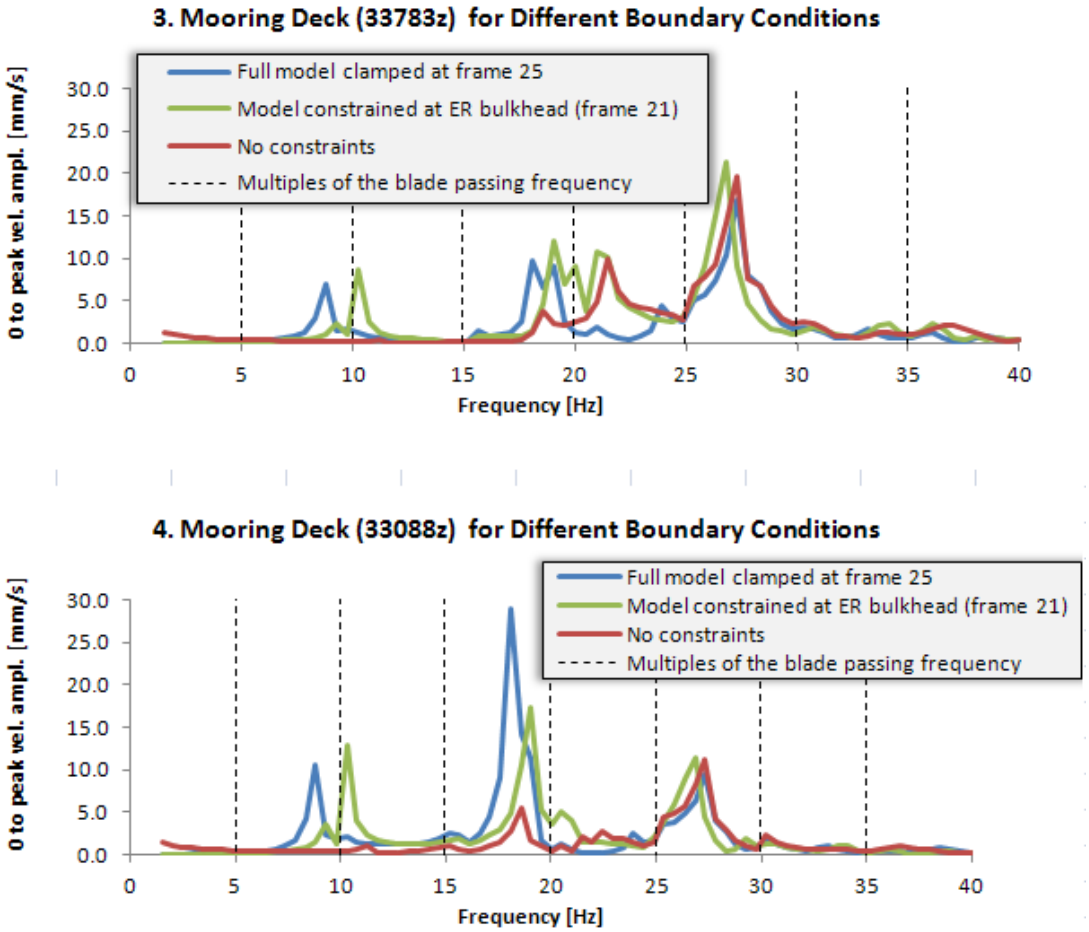

Simulation results 0 to peak vibration velocity amplitudes at different boundary conditions

Appendix VIII *Comparing Simulation Results with Measurement Results*

Location 1

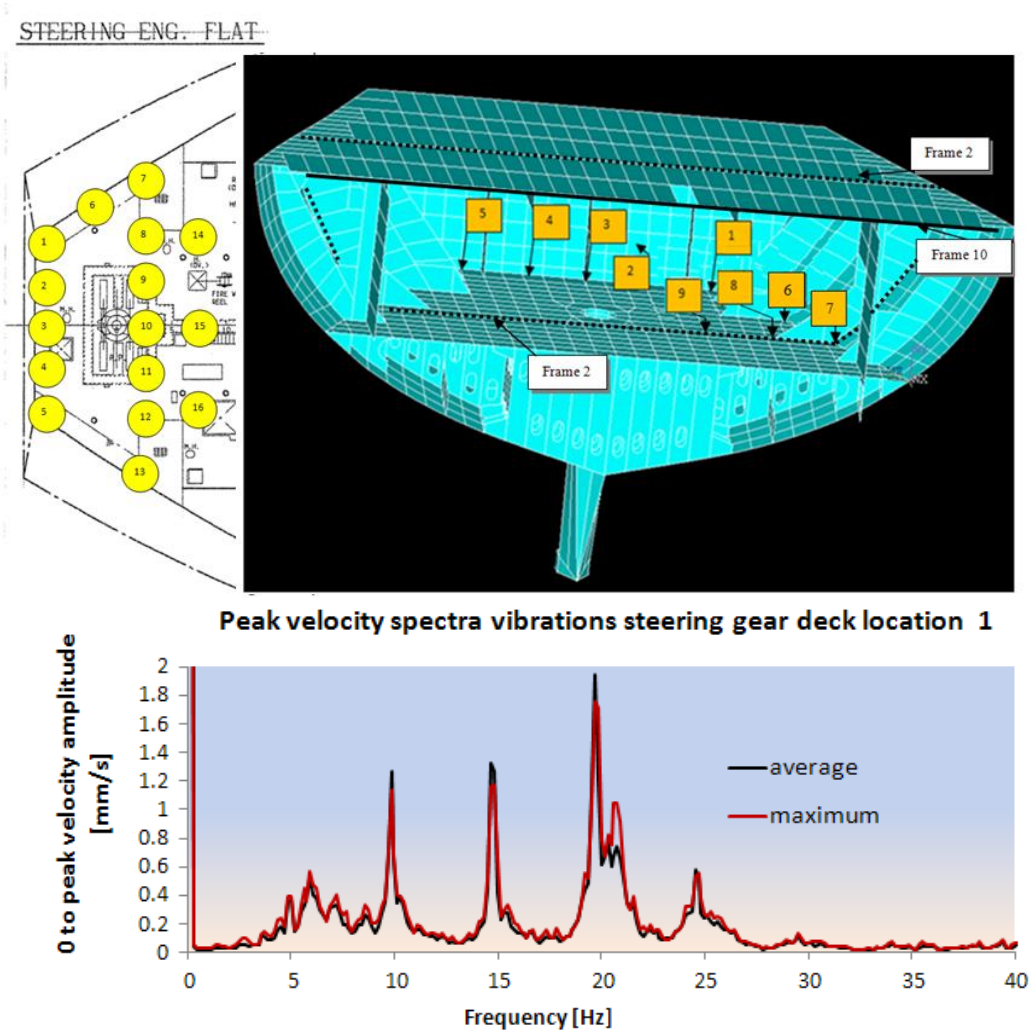

FFT velocity spectrum from measurements taken location 1 (vertical) with ship sailing at 19 knots (propeller speed 75 rpm). Levels are presented as 0 to peak velocity amplitudes [mm/s]

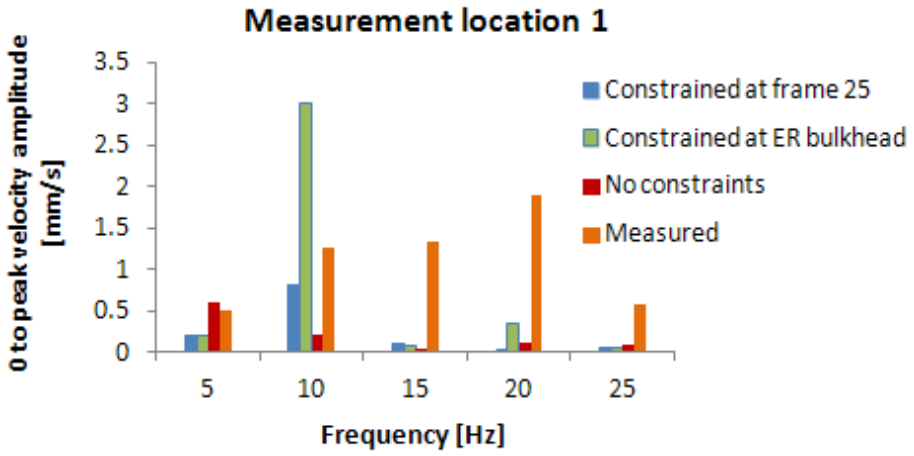

Comparison of simulation results with different boundary conditions and the measurement results**(average spectrum)**

Location 2 hull plating

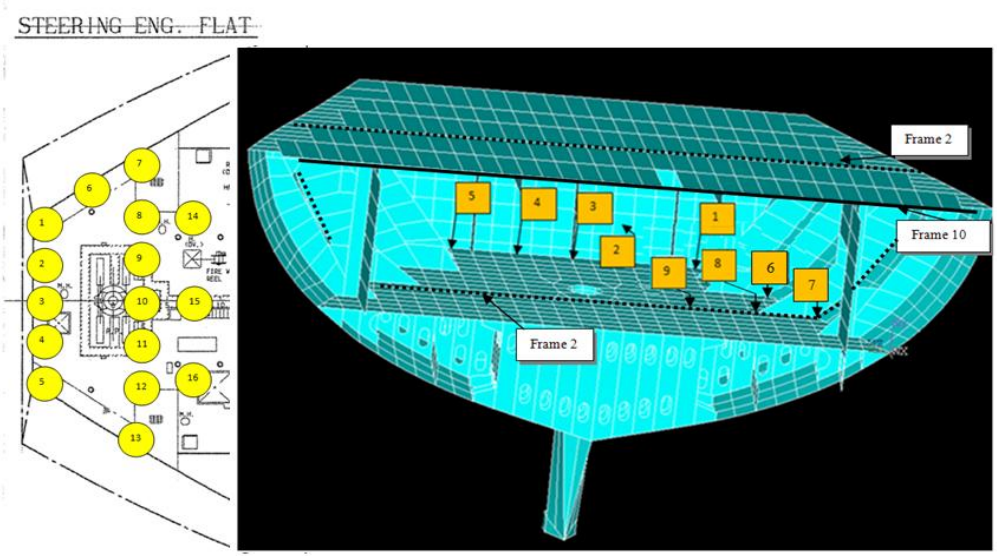

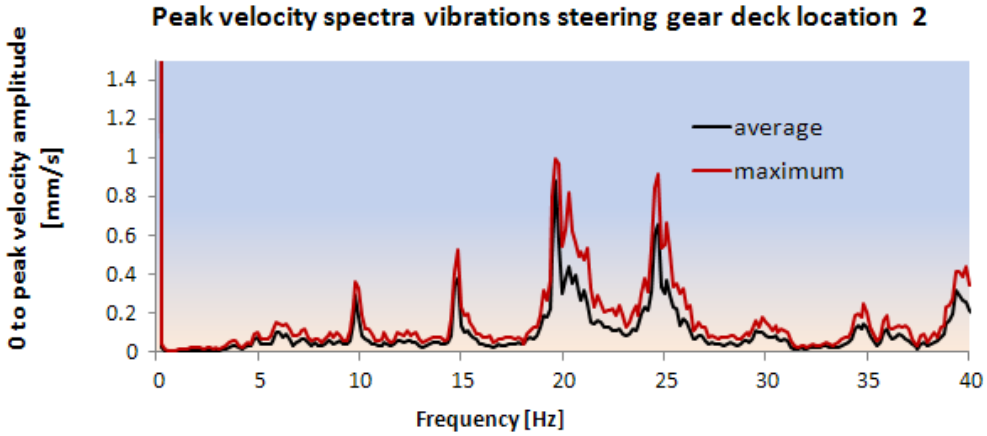

FFT velocity spectrum from measurements taken location 2 (longitudinal) with ship sailing at 19 knots (propeller speed 75 rpm). Levels are presented as 0 to peak velocity amplitudes [mm/s]

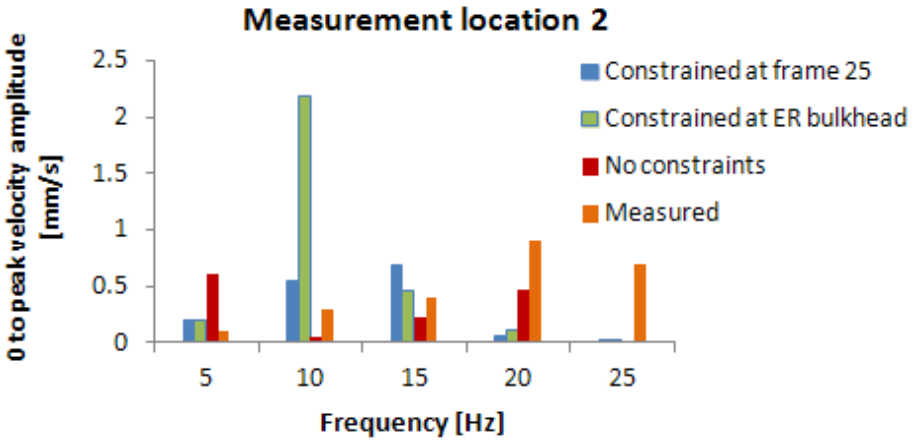

Comparison of simulation results with different boundary conditions and the measurement results(average spectrum)

Location 3

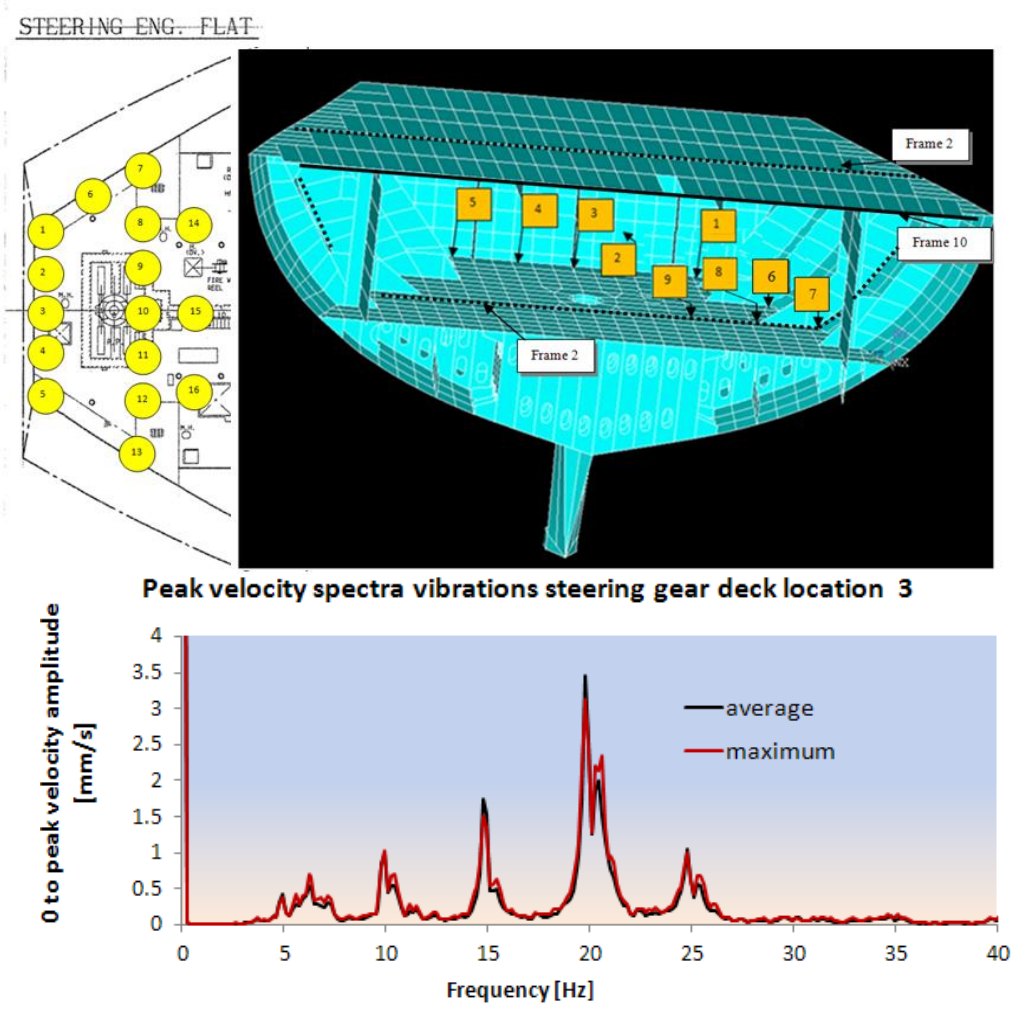

FFT velocity spectrum from measurements taken location 3 (vertical) with ship sailing at 19 knots (propeller speed 75 rpm). Levels are presented as 0 to peak velocity amplitudes [mm/s]

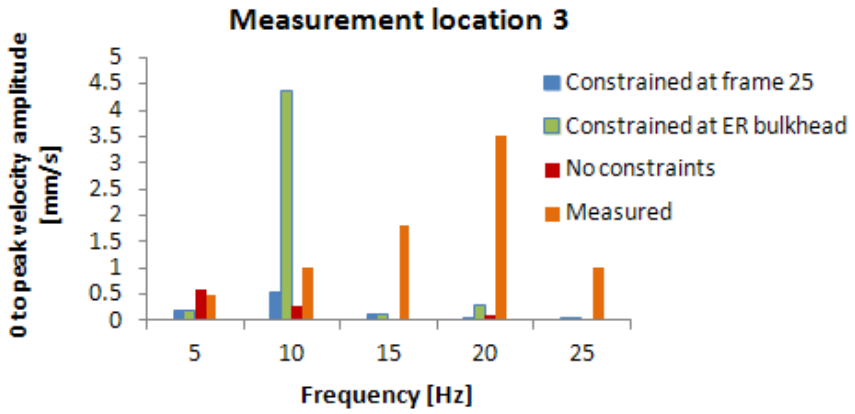

Comparison of simulation results with different boundary conditions and the measurement results(average spectrum)

Location 5

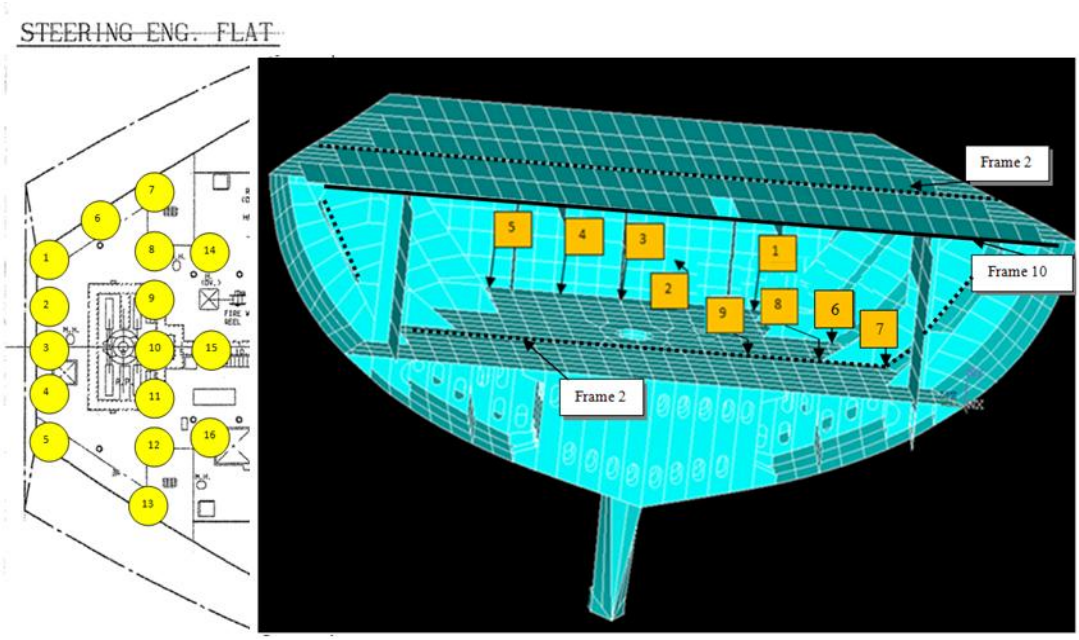

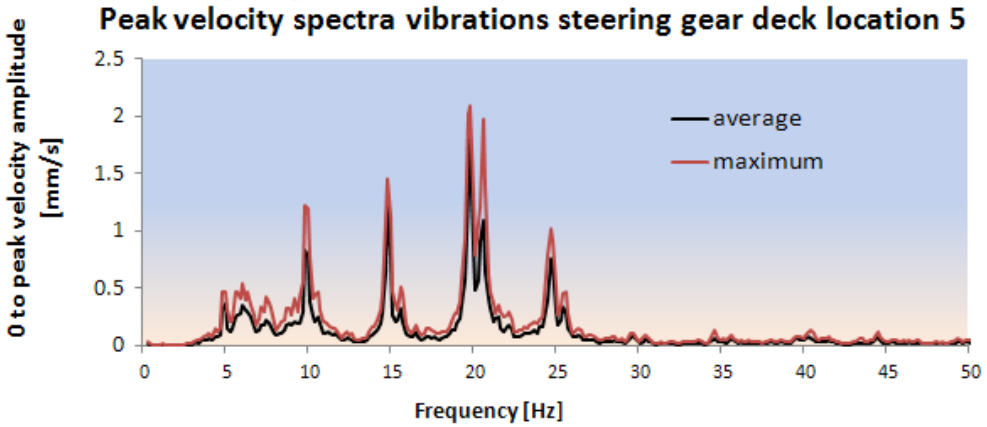

FFT velocity spectrum from measurements taken location 5 (vertical) with ship sailing at 19 knots (propeller speed 75 rpm). Levels are presented as 0 to peak velocity amplitudes [mm/s]

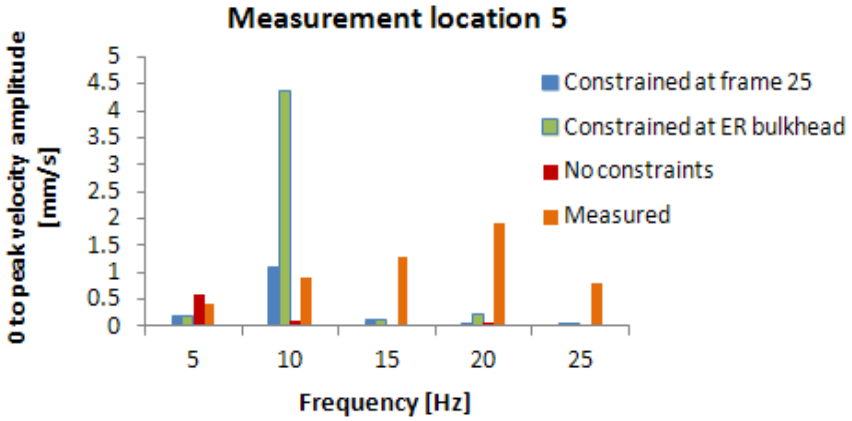

Comparison of simulation results with different boundary conditions and the measurement results(average spectrum)

Location 6

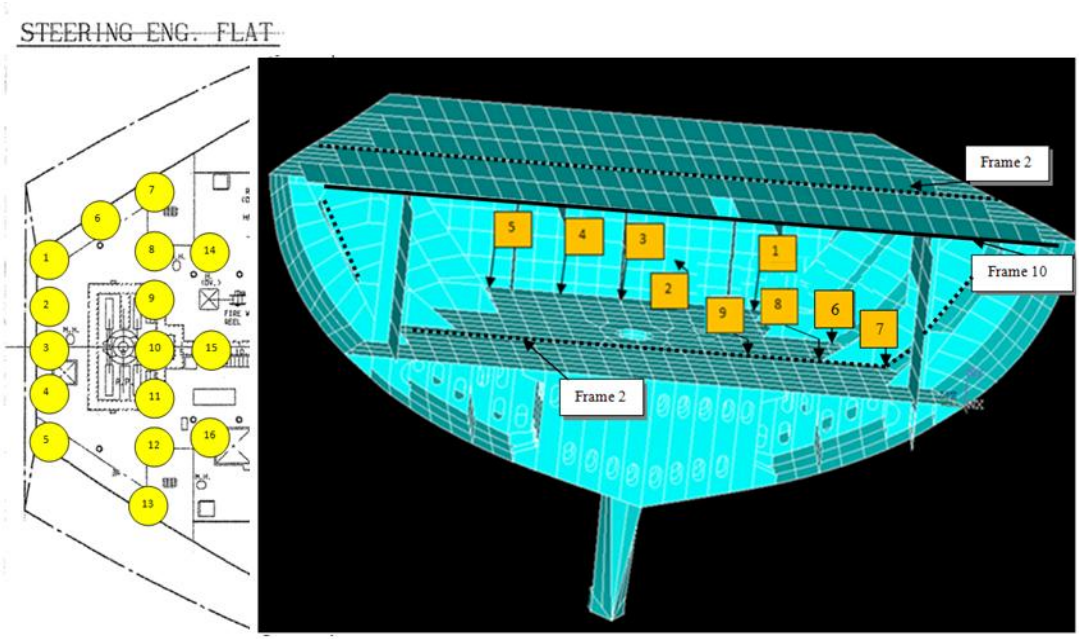

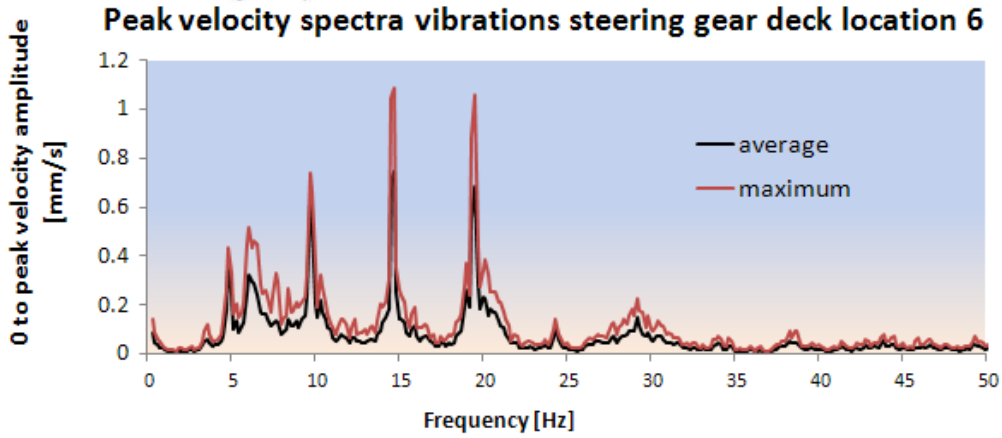

FFT velocity spectrum from measurements taken location 6 (vertical) with ship sailing at 19 knots (propeller speed 75 rpm). Levels are presented as 0 to peak velocity amplitudes [mm/s]

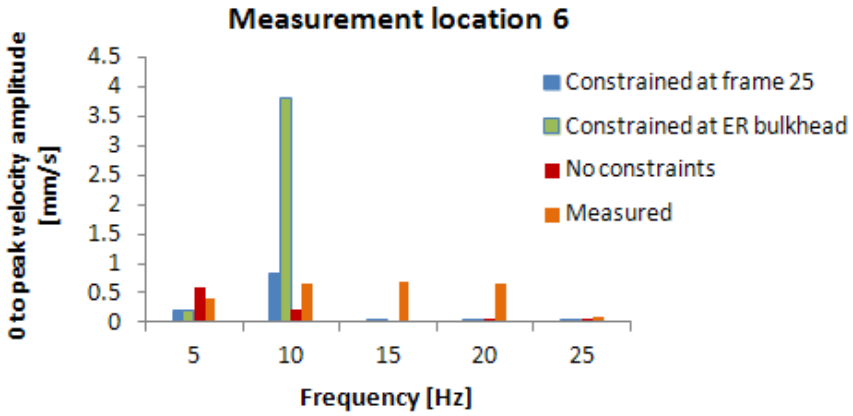

Comparison of simulation results with different boundary conditions and the measurement results (average spectrum)

Location 7

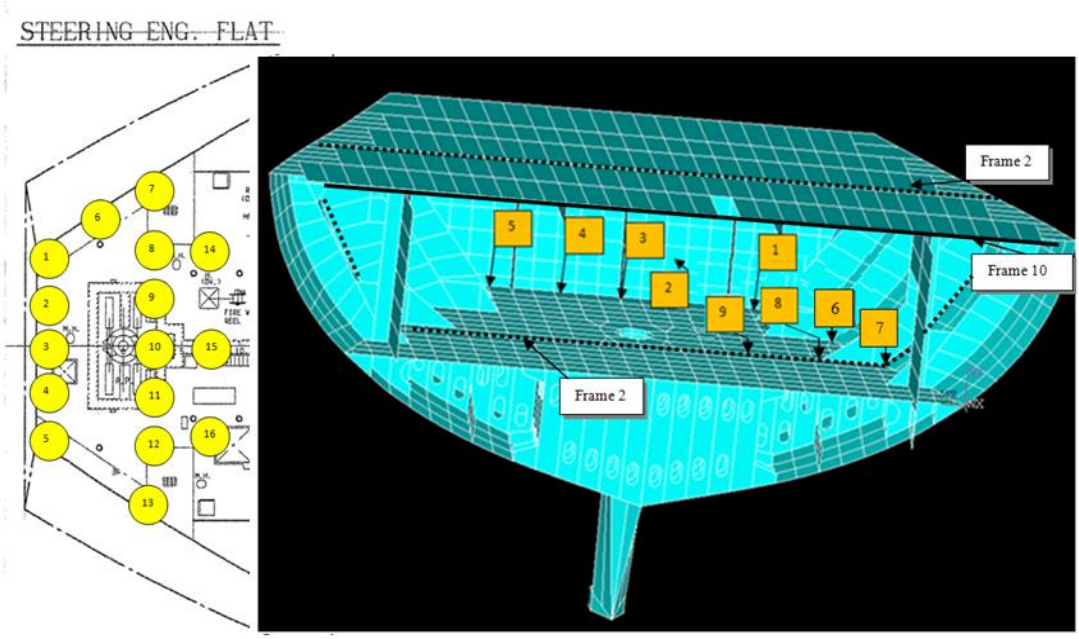

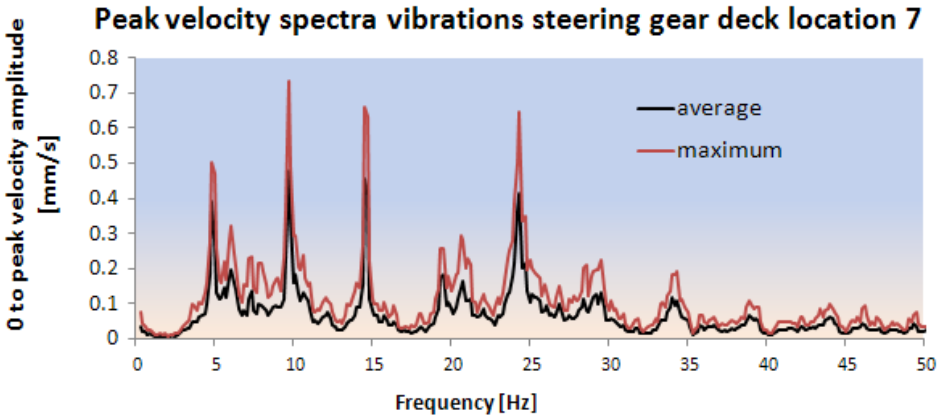

FFT velocity spectrum from measurements taken location 7 (vertical) with ship sailing at 19 knots (propeller speed 75 rpm). Levels are presented as 0 to peak velocity amplitudes [mm/s]

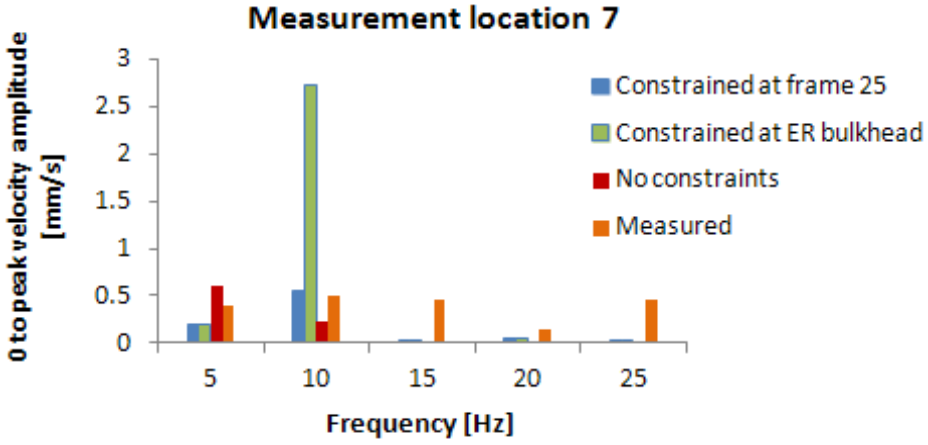

Comparison of simulation results with different boundary conditions and the measurement results (average spectrum)

Location 8

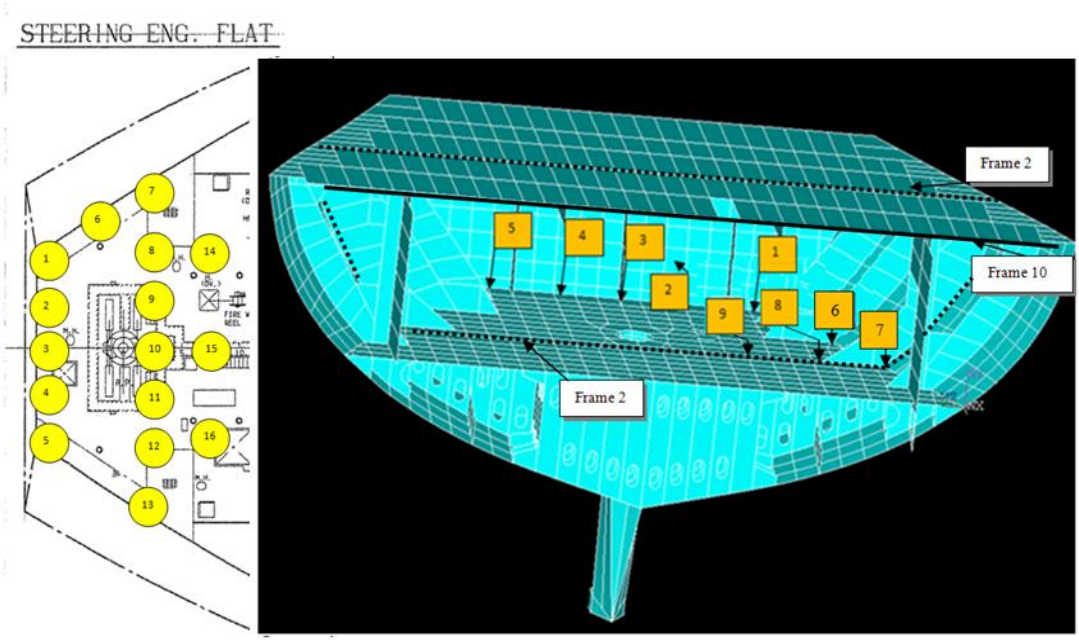

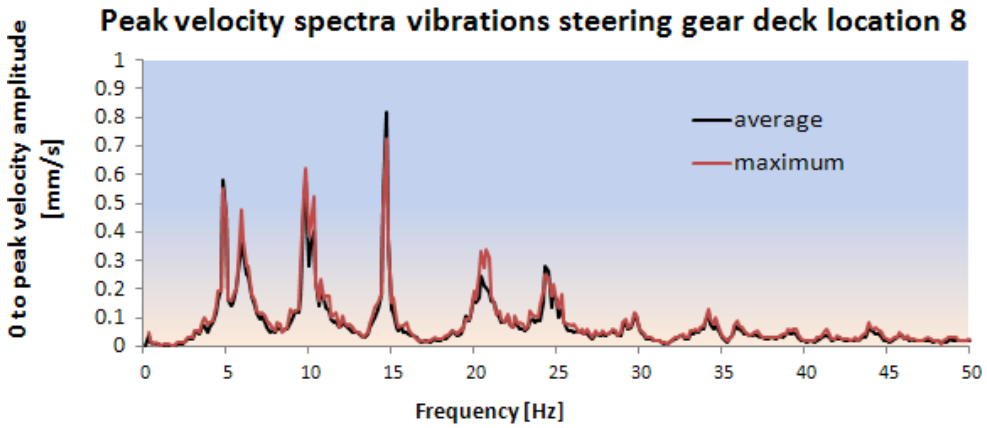

FFT velocity spectrum from measurements taken location 8 (vertical) with ship sailing at 19 knots (propeller speed 75 rpm). Levels are presented as 0 to peak velocity amplitudes [mm/s]

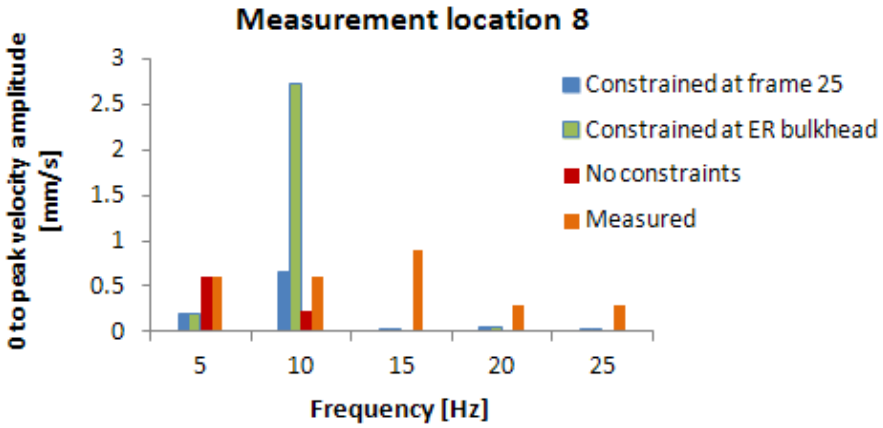

Comparison of simulation results with different boundary conditions and the measurement results(average spectrum)

Location 9

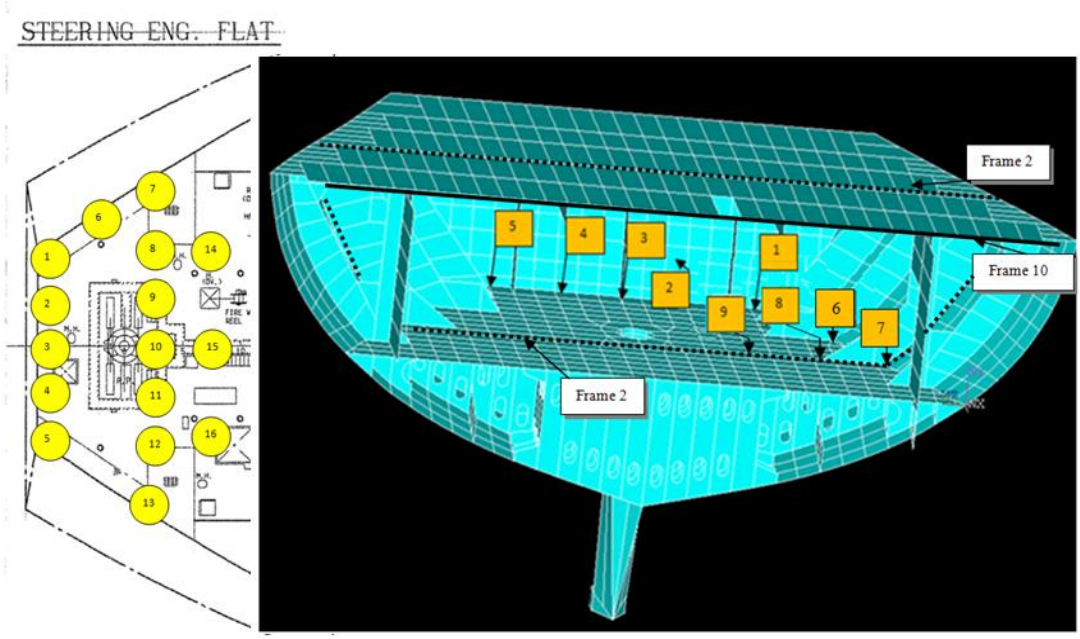

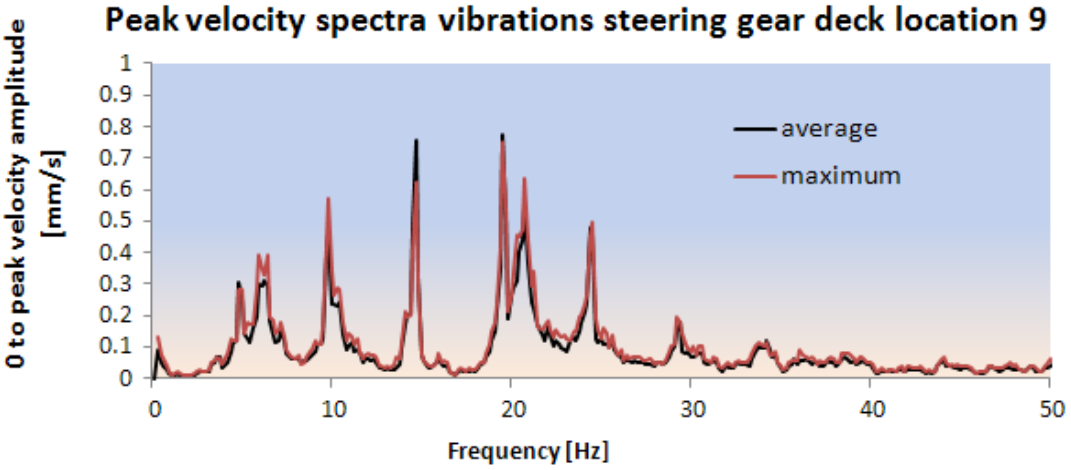

FFT velocity spectrum from measurements taken location 9 (vertical) with ship sailing at 19 knots (propeller speed 75 rpm). Levels are presented as 0 to peak velocity amplitudes [mm/s]

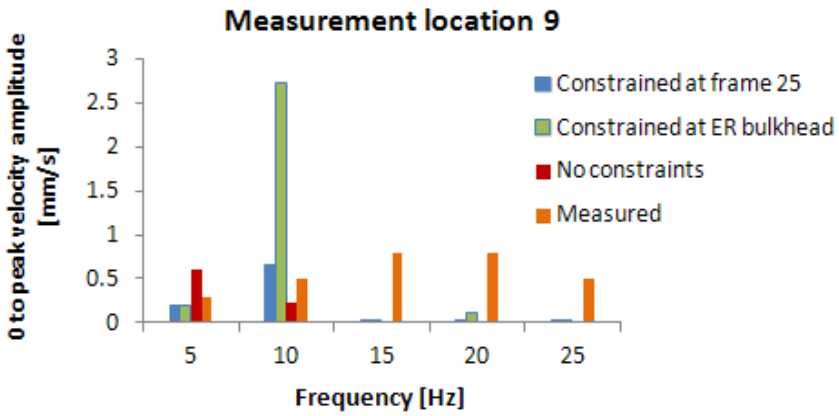

Comparison of simulation results with different boundary conditions and the measurement results(average spectrum)

Appendix IX *Substructures*
LNG carrier CMS

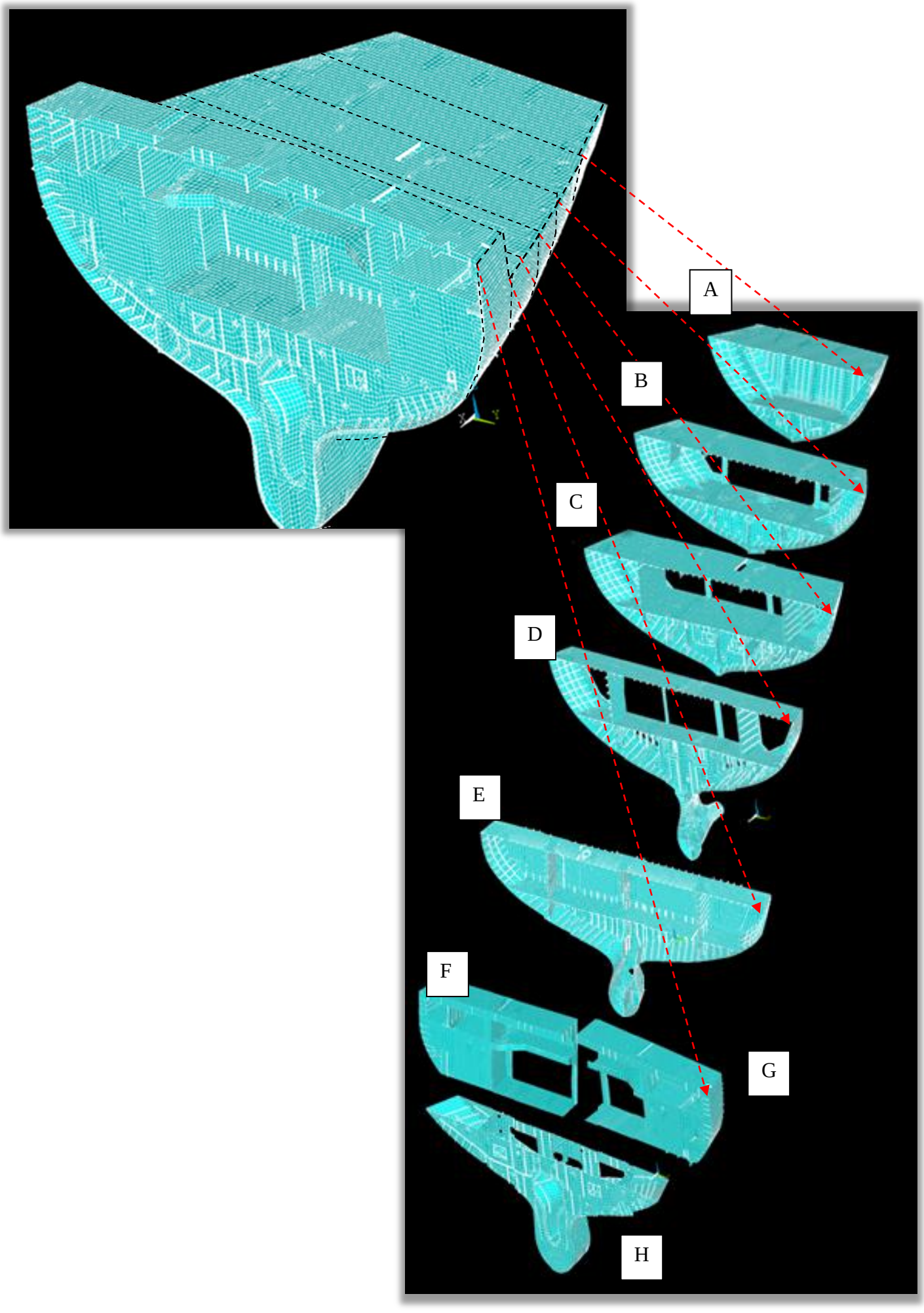
A
B
C
D
E
F
G
H

Substructure A

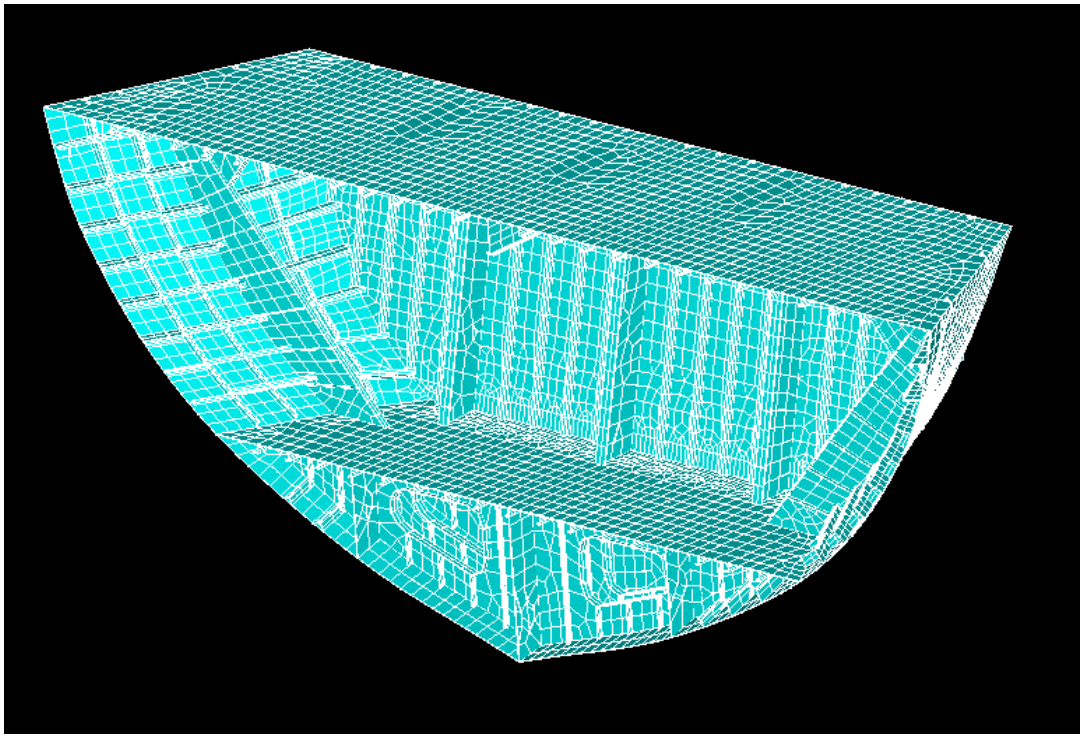

Number of nodes	7168
Number of master nodes (interface nodes)	263
Number of modes fixed interface CMS between 0 and 60 Hz*	91
Number of modes free interface CMS between 0 and 60 Hz*	154

*CMS analysis has been carried out in order to analyse the response over a frequency range from 1 to 40 Hz. The number of modes taken into consideration with the analysis is the number of modes that is within frequency range between 0 and 1.5 times the maximum frequency (which is 1.5 times 40 Hz = 60 Hz)

Substructure B

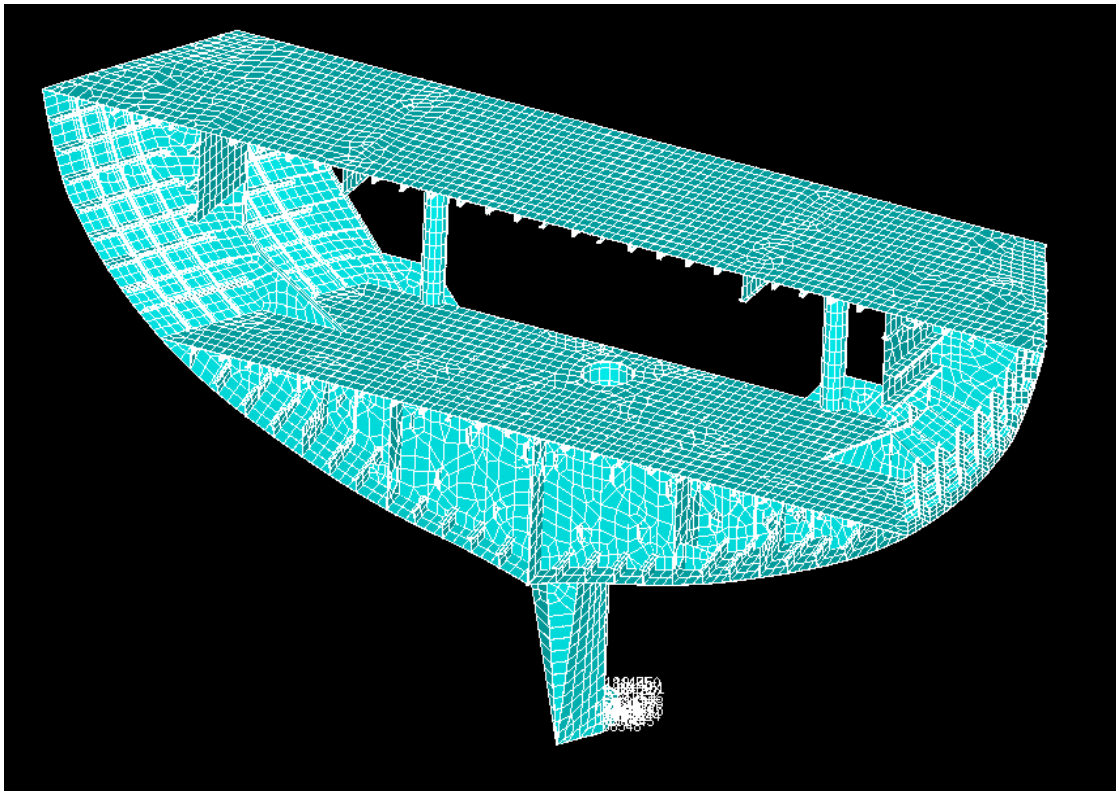

Number of nodes	11705
Number of master nodes (interface nodes)	633
Number of modes fixed interface CMS between 0 and 60 Hz*	138
Number of modes free interface CMS between 0 and 60 Hz*	231

*CMS analysis has been carried out in order to analyse the response over a frequency range from 1 to 40 Hz. The number of modes taken into consideration with the analysis is the number of modes that is within frequency range between 0 and 1.5 times the maximum frequency (which is 1.5 times 40 Hz = 60 Hz)

Substructure C

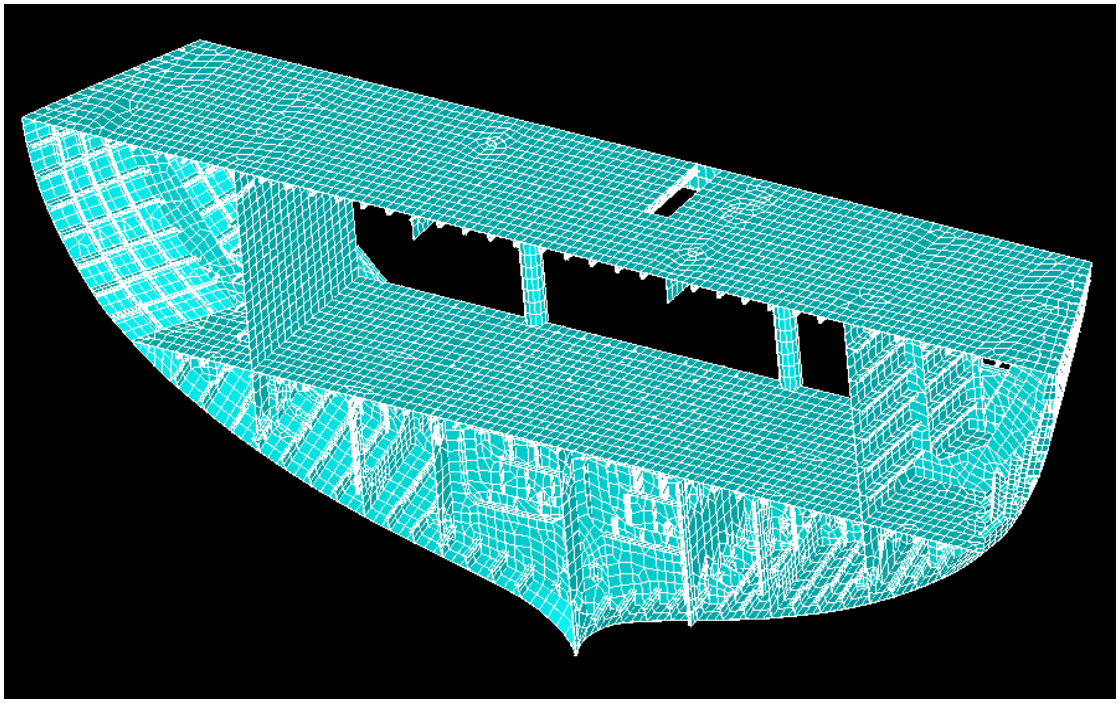

Number of nodes	14393
Number of master nodes (interface nodes)	854
Number of modes fixed interface CMS between 0 and 60 Hz*	195
Number of modes free interface CMS between 0 and 60 Hz*	335

*CMS analysis has been carried out in order to analyse the response over a frequency range from 1 to 40 Hz. The number of modes taken into consideration with the analysis is the number of modes that is within frequency range between 0 and 1.5 times the maximum frequency (which is 1.5 times 40 Hz = 60 Hz)

Substructure D

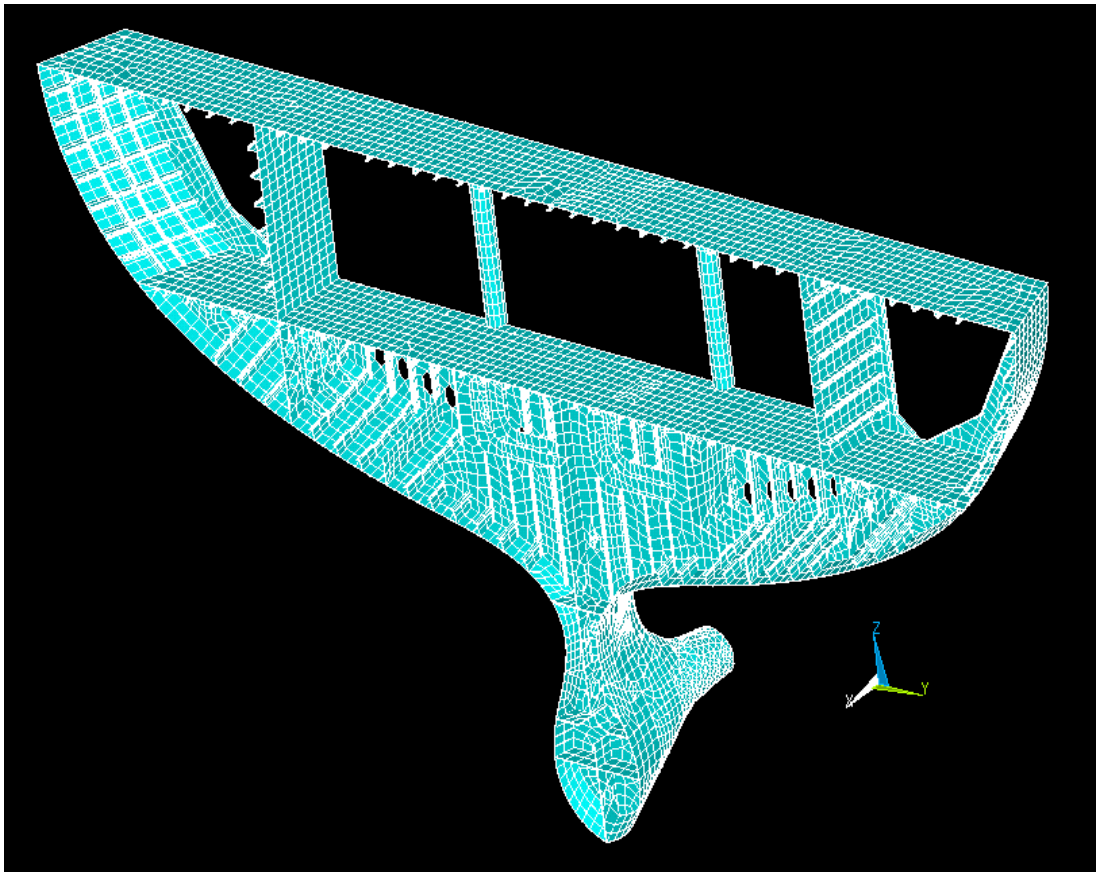

Number of nodes	11118
Number of master nodes (interface nodes)	1033
Number of modes fixed interface CMS between 0 and 60 Hz*	162
Number of modes free interface CMS between 0 and 60 Hz*	336

*CMS analysis has been carried out in order to analyse the response over a frequency range from 1 to 40 Hz. The number of modes taken into consideration with the analysis is the number of modes that is within frequency range between 0 and 1.5 times the maximum frequency (which is 1.5 times 40 Hz = 60 Hz)

Substructure E

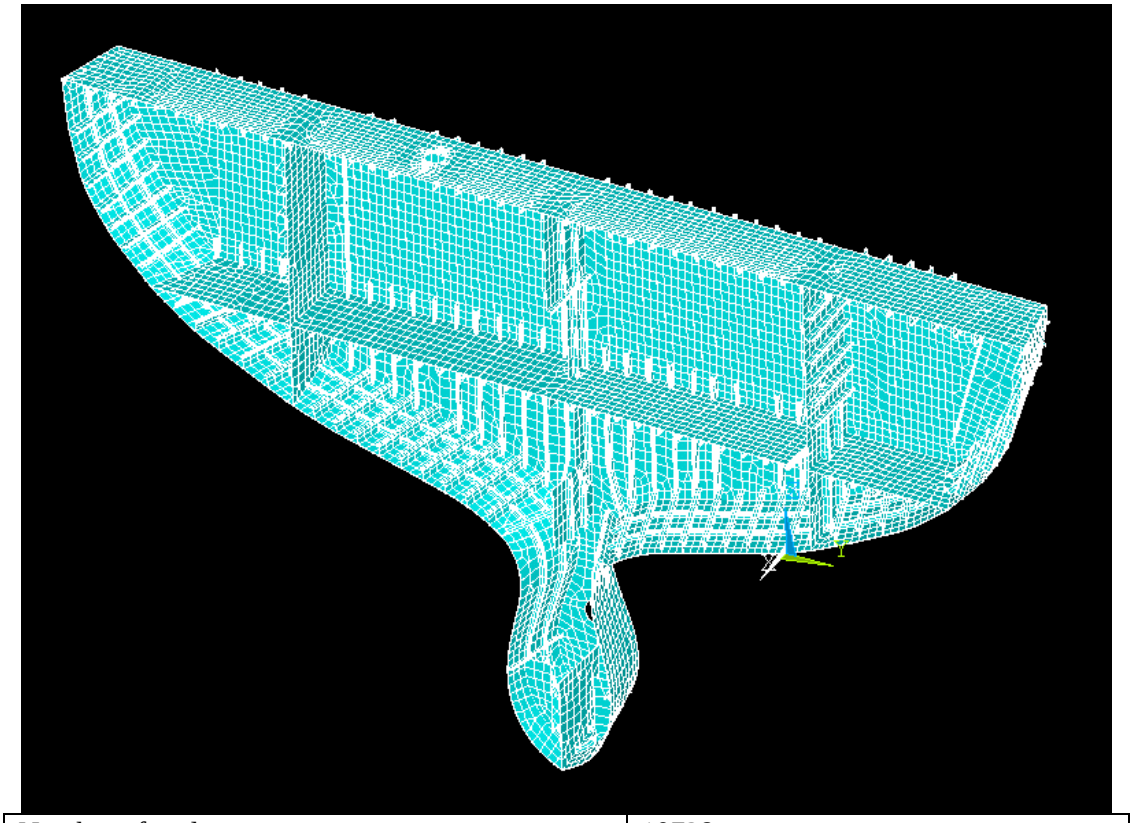

Number of nodes	10728
Number of master nodes (interface nodes)	1198
Number of modes fixed interface CMS between 0 and 60 Hz*	213
Number of modes free interface CMS between 0 and 60 Hz*	323

*CMS analysis has been carried out in order to analyse the response over a frequency range from 1 to 40 Hz. The number of modes taken into consideration with the analysis is the number of modes that is within frequency range between 0 and 1.5 times the maximum frequency (which is 1.5 times 40 Hz = 60 Hz)

Substructure F and G

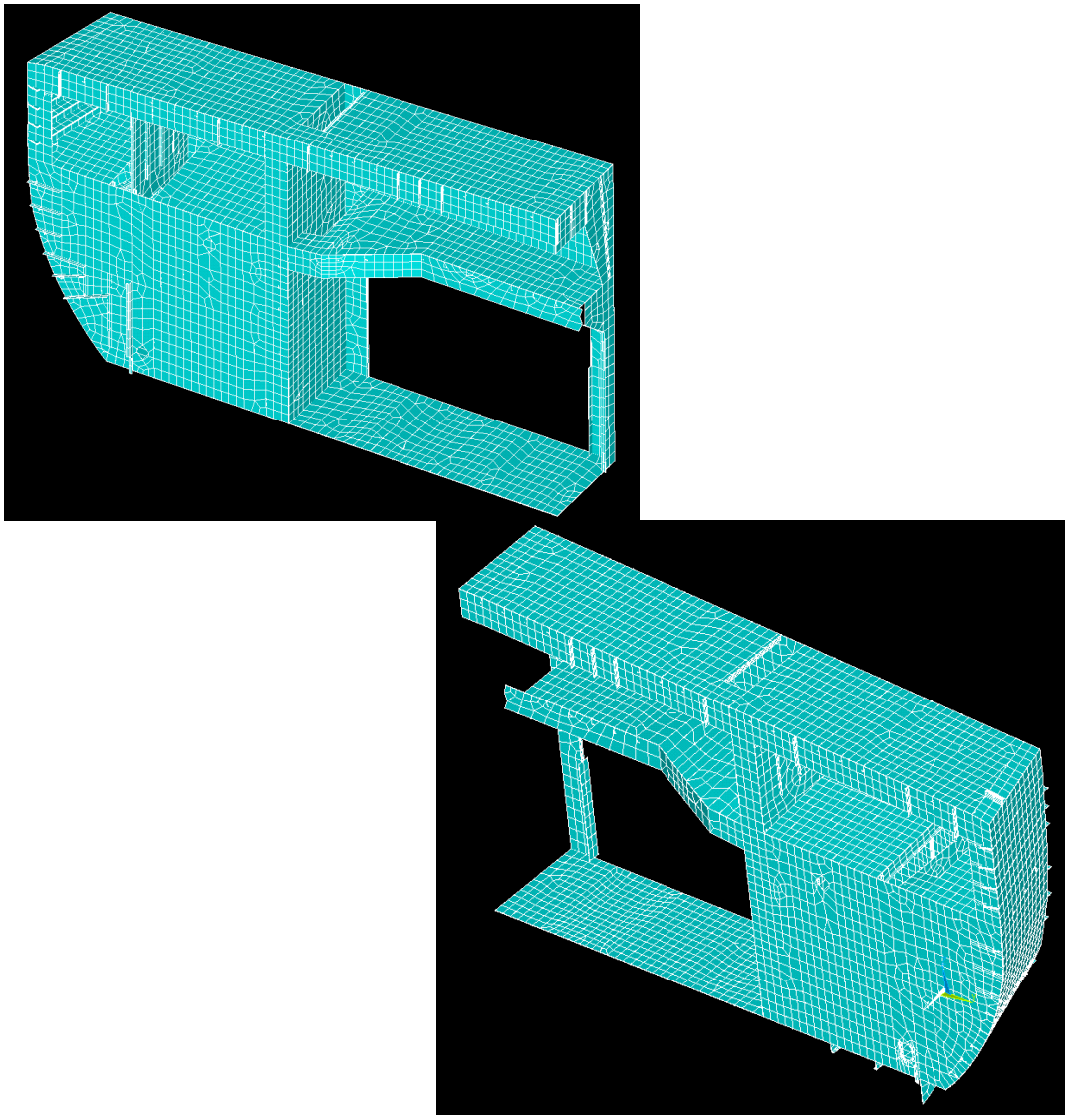

Number of nodes	F = G= 6675
Number of master nodes (interface nodes)	F = G = 256
Number of modes fixed interface CMS between 0 and 60 Hz*	F = G = 373
Number of modes free interface CMS between 0 and 60 Hz*	F = G = 419

*CMS analysis has been carried out in order to analyse the response over a frequency range from 1 to 40 Hz. The number of modes taken into consideration with the analysis is the number of modes that is within frequency range between 0 and 1.5 times the maximum frequency (which is 1.5 times 40 Hz = 60 Hz)

Substructure H

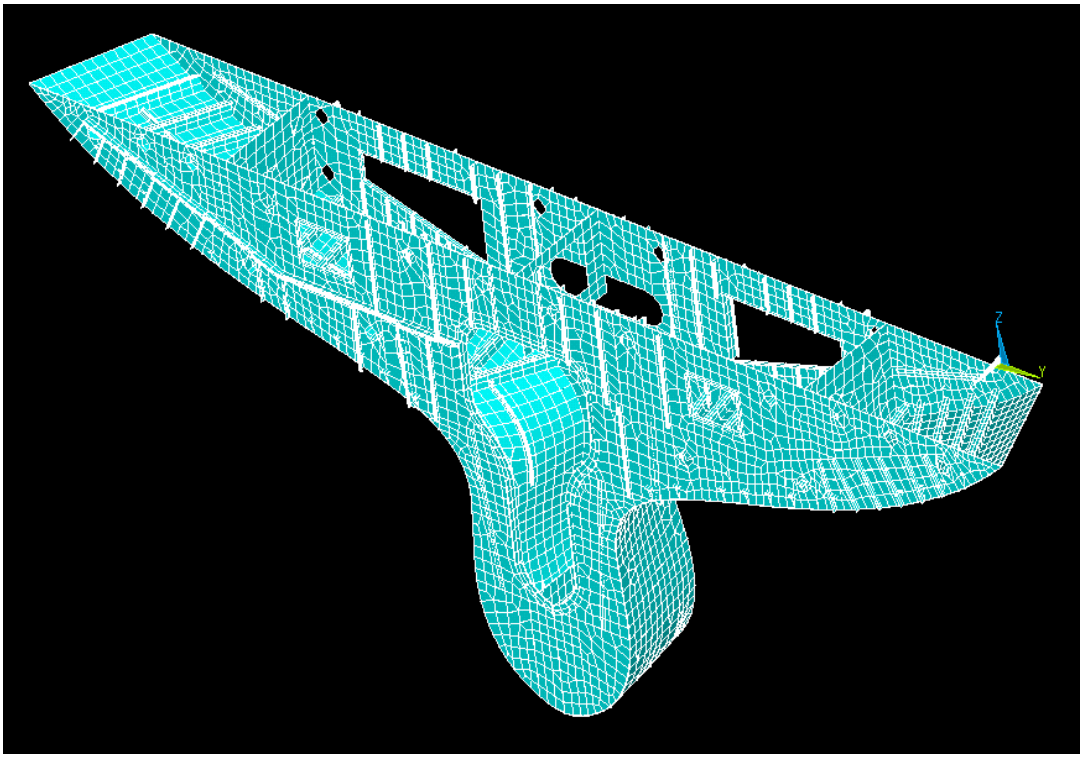

Number of nodes	5819
Number of master nodes (interface nodes)	348
Number of modes fixed interface CMS between 0 and 60 Hz*	181
Number of modes free interface CMS between 0 and 60 Hz*	257

*CMS analysis has been carried out in order to analyse the response over a frequency range from 1 to 40 Hz. The number of modes taken into consideration with the analysis is the number of modes that is within frequency range between 0 and 1.5 times the maximum frequency (which is 1.5 times 40 Hz = 60 Hz)

Appendix X *Results Full FEM, Fixed Interface CMS and Free Interface CMS*

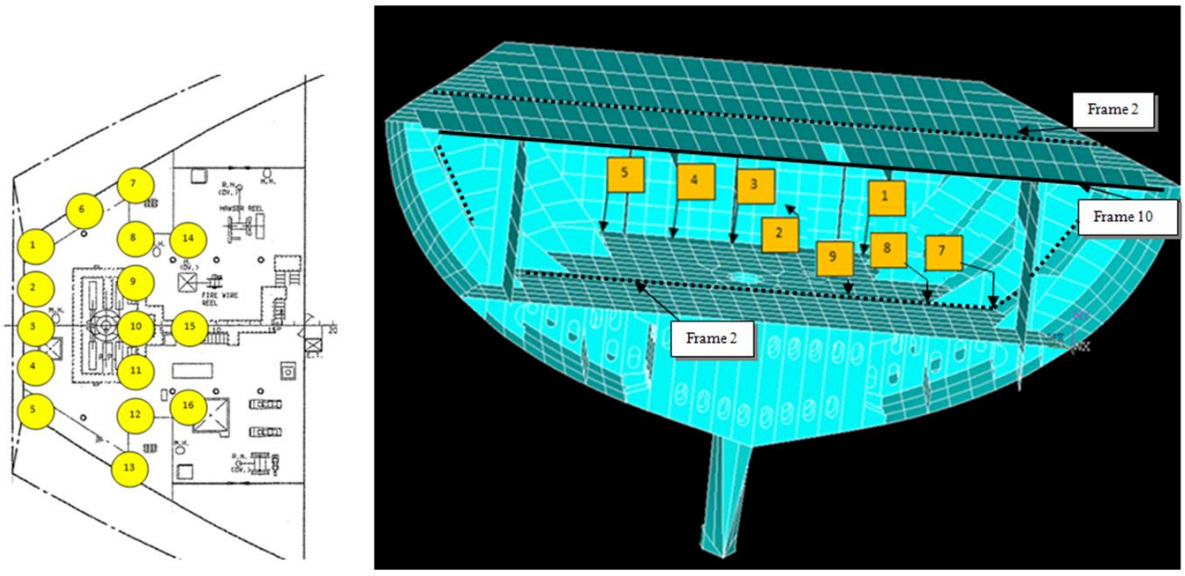

Simulation results positions on steering gear deck

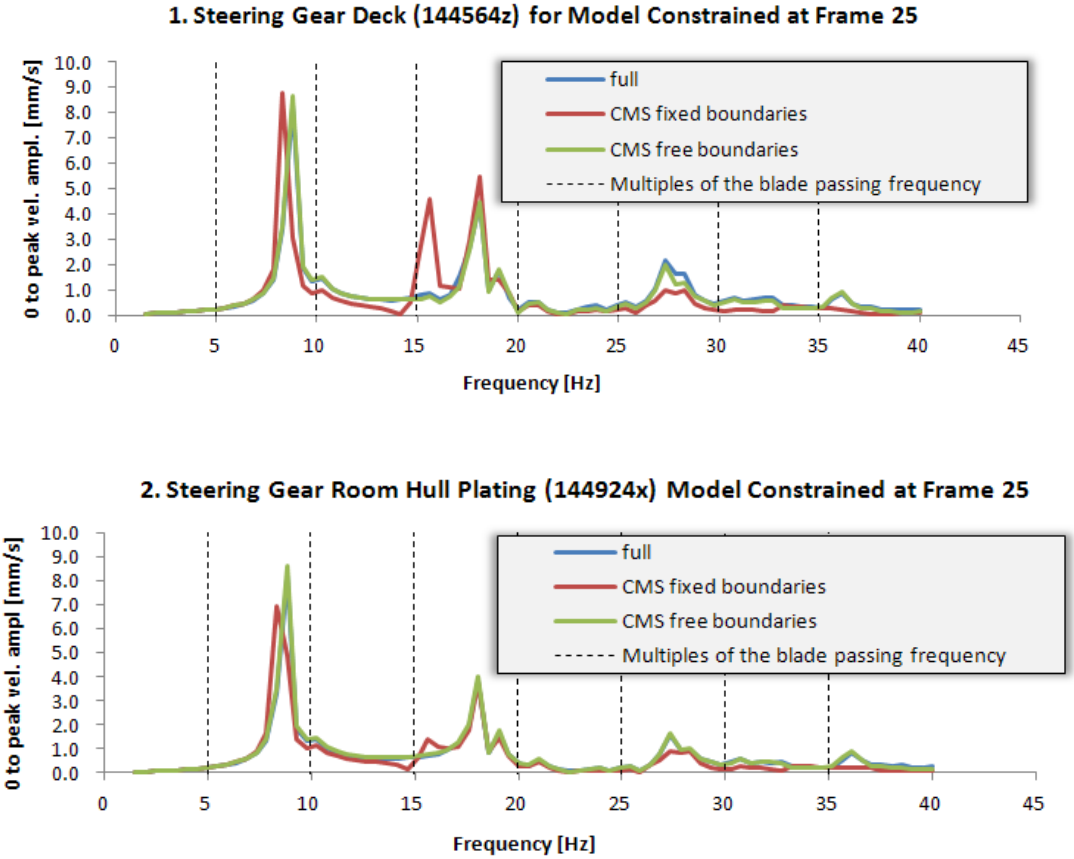

Simulation results 0 to peak vibration velocity amplitudes on the steering gear deck

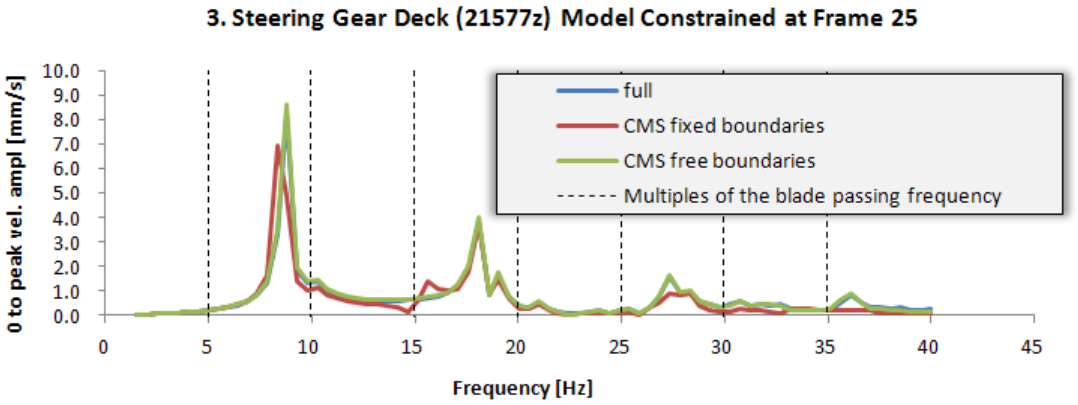

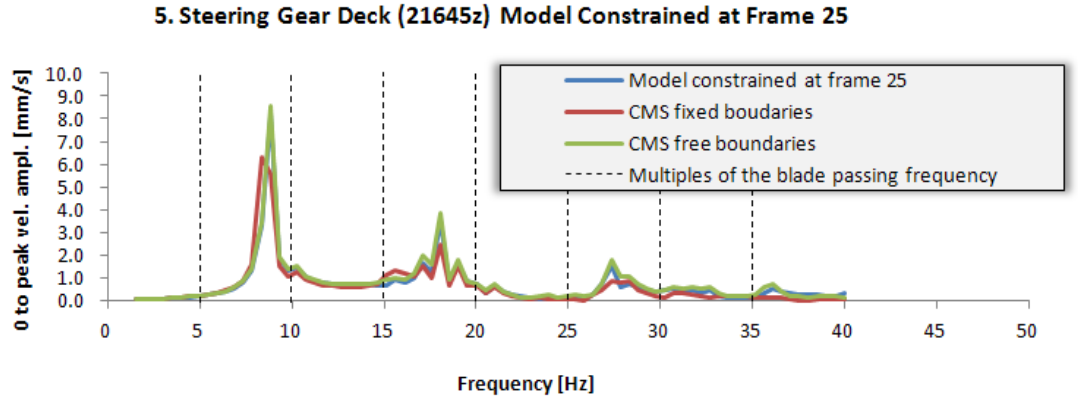

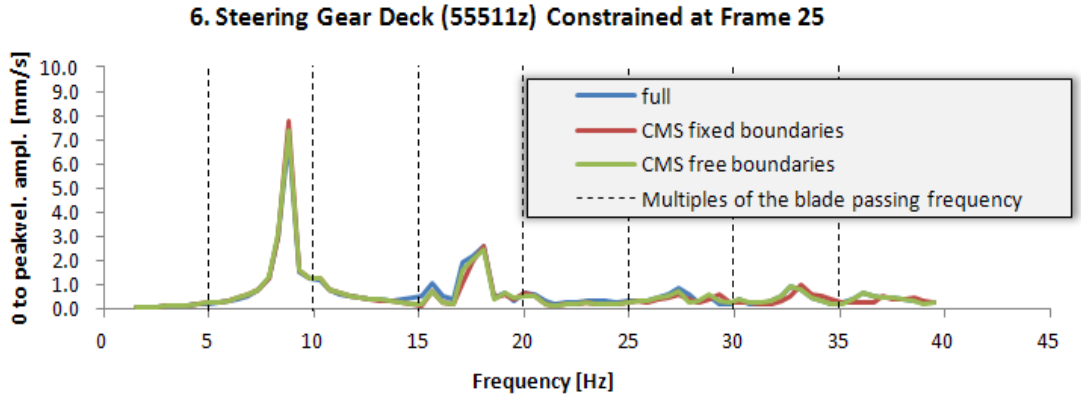

Simulation results 0 to peak vibration velocity amplitudes on the steering gear deck

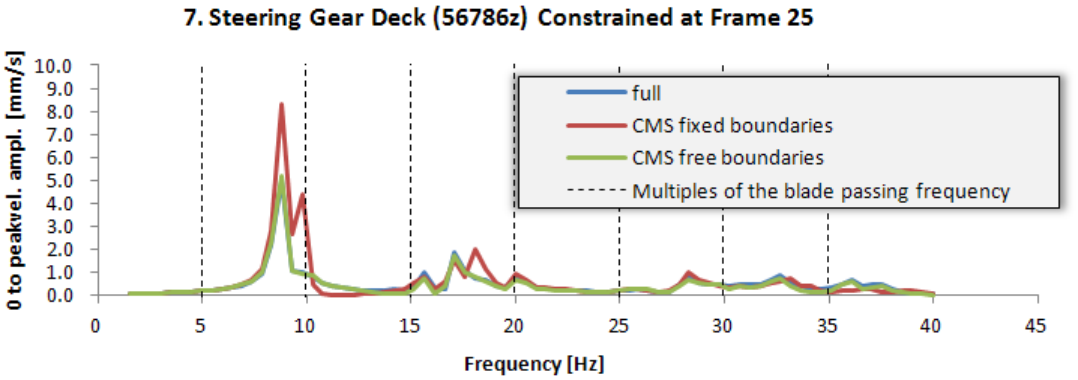

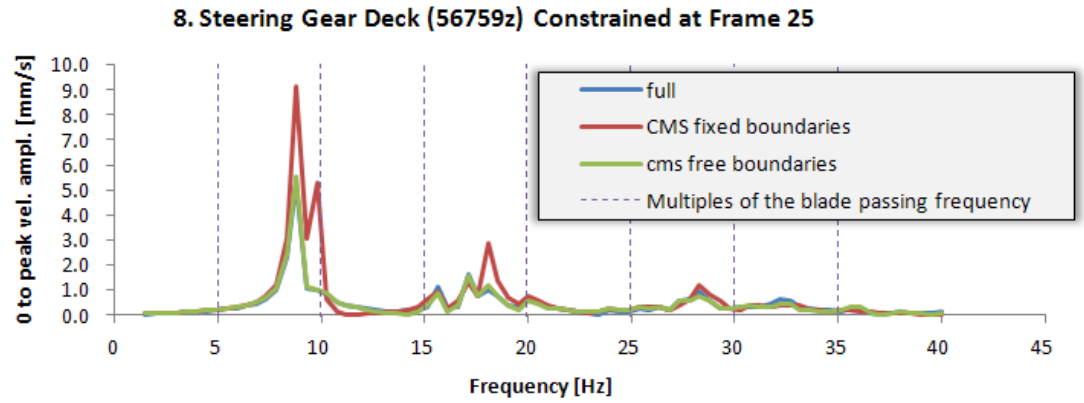

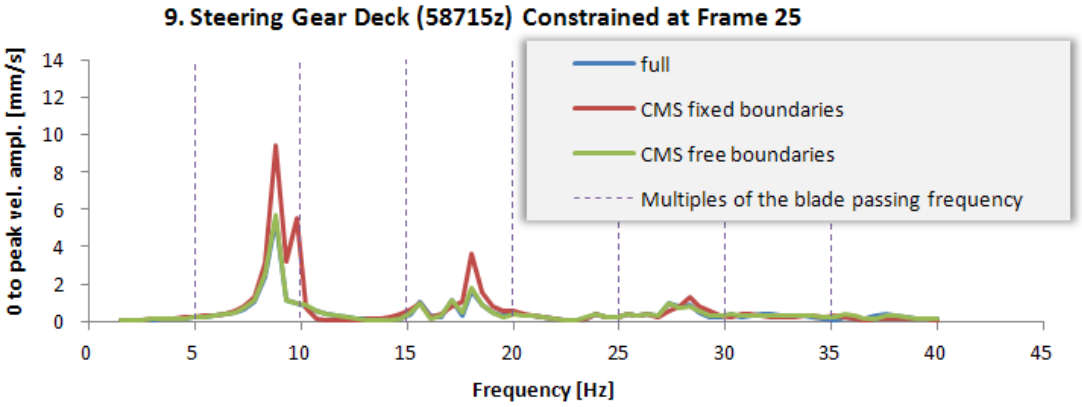

Simulation results 0 to peak vibration velocity amplitudes on the steering gear deck

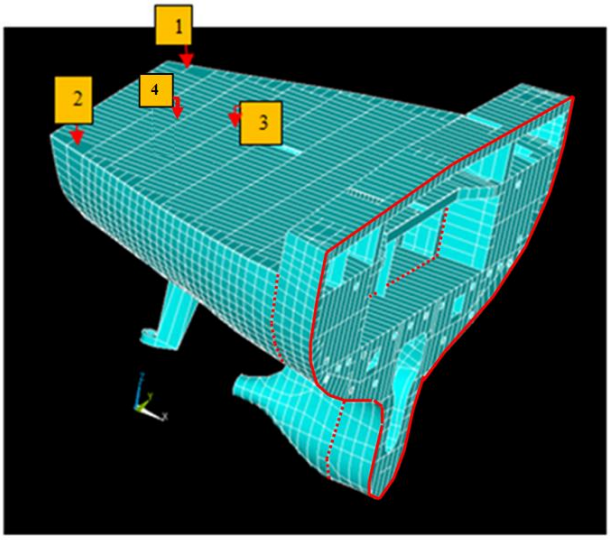

simulation results positions on mooring deck

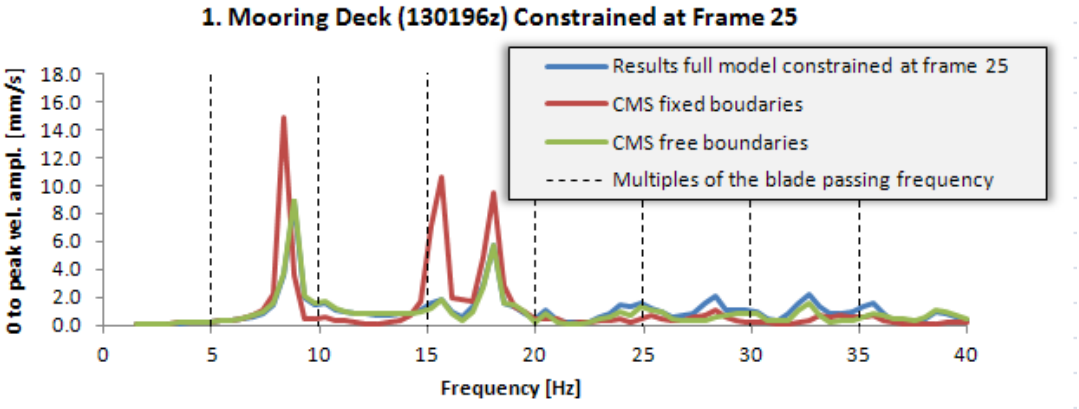

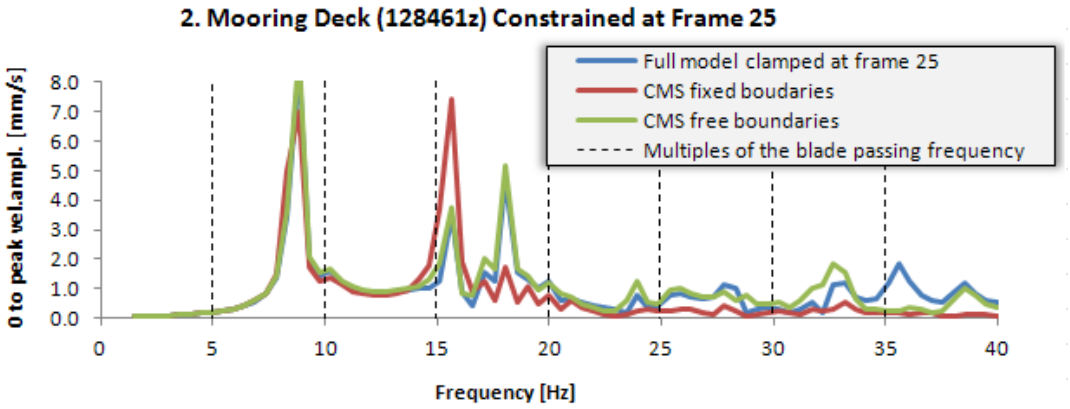

Simulation results 0 to peak vibration velocity amplitudes on the mooring deck

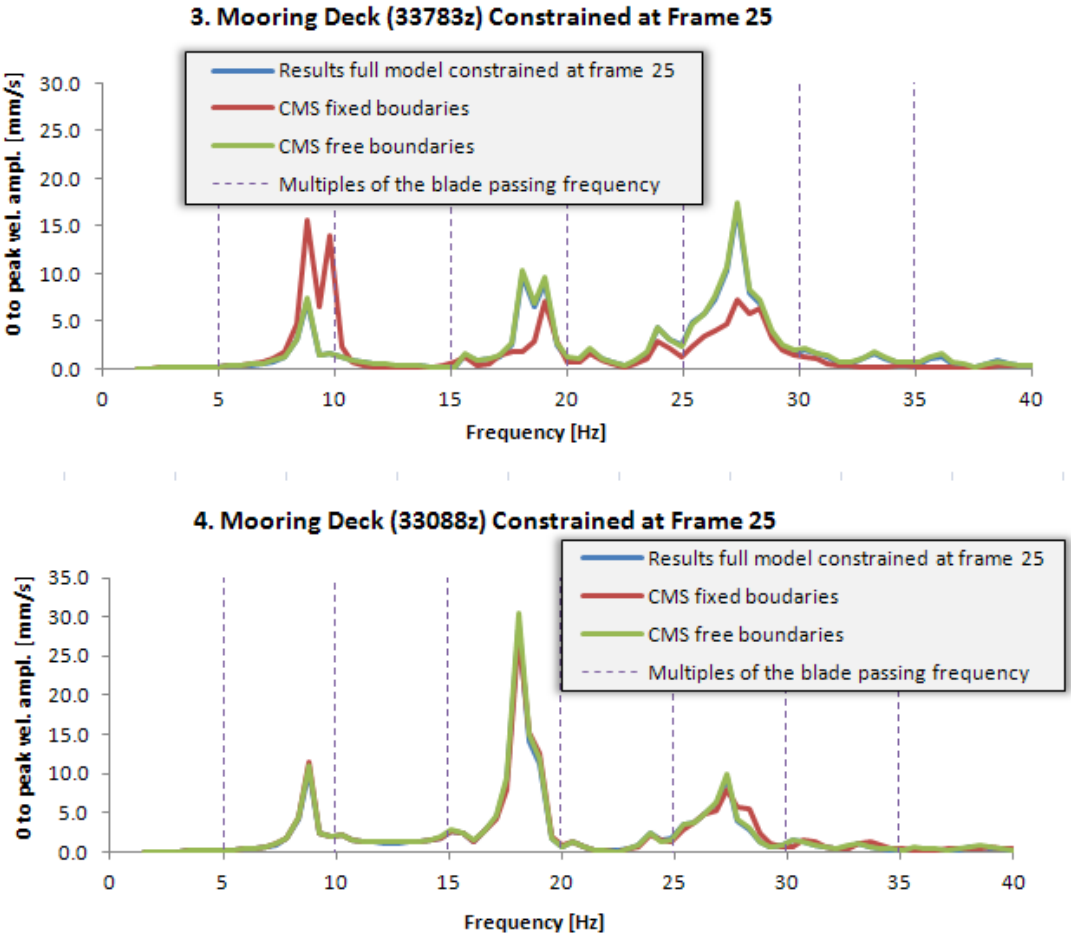

Simulation results 0 to peak vibration velocity amplitudes on the mooring deck

Appendix XI *Simulated Deflection Shapes for Model Constrained at Frame 25*

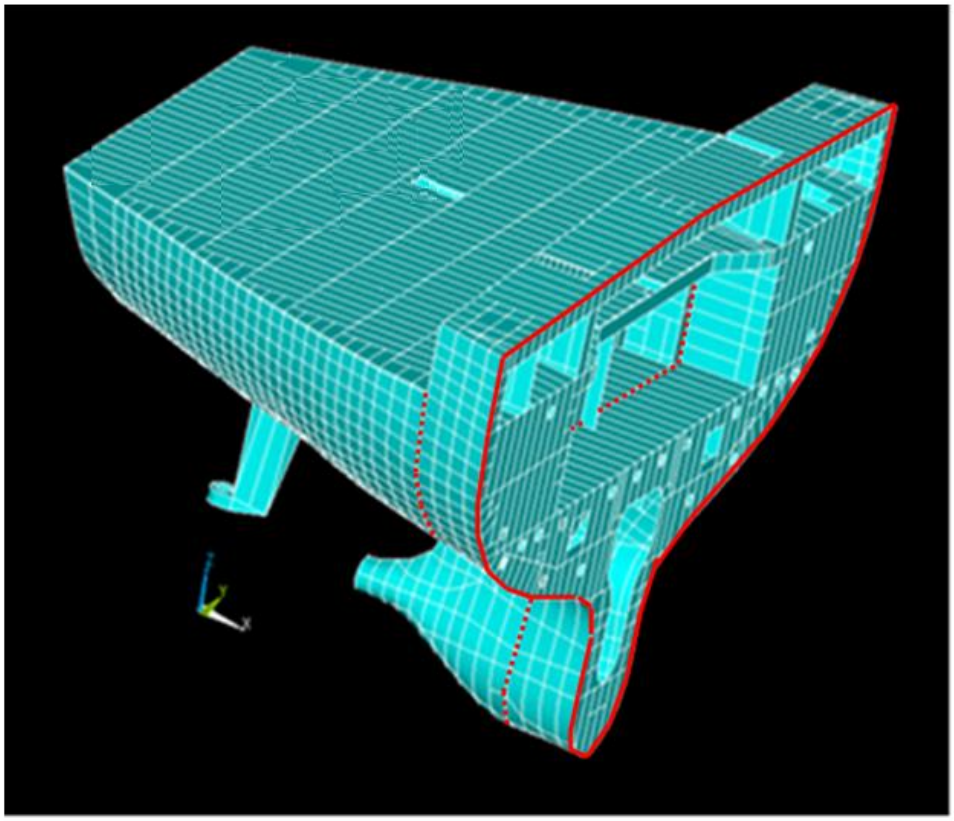

Frame 25

Frame 21

Deflection Shape at 8.8 Hz (frame 25 constrained)

displacement scaling 8e3

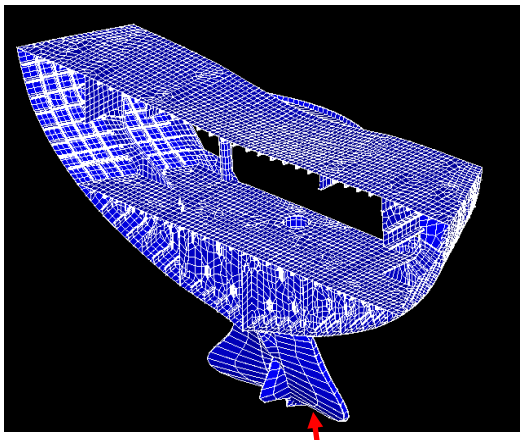

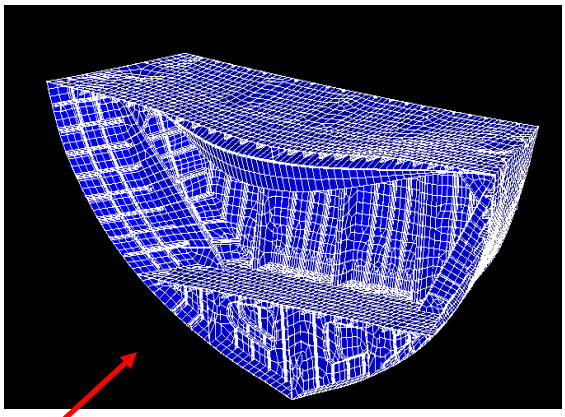

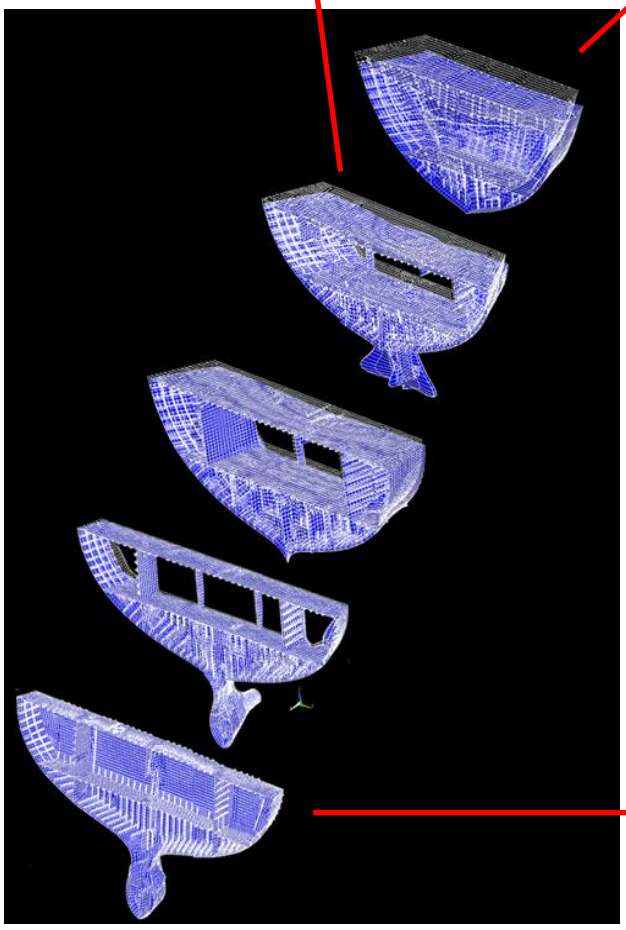

Substructures added together. Pictures shows the deformed shape plotted together with the un-deformed shape which clearly shows the presence of the effect of a first bending global mode shape of the aft ship. The deformed shape of sections A and B are shown enlarged at the top of the figure. Through these two pictures also the presence of a bending mode at the aft part of the aft deck can be identified. The deformed shapes of sections C to H do not show any local elastic deformation apart from section E. That is why they have not been shown in more detail here. Vibration levels at these sections at 8.8 Hz are largely due to the global first bending mode-shape of the aft ship, which is shown through the summary picture immediately left to this text.

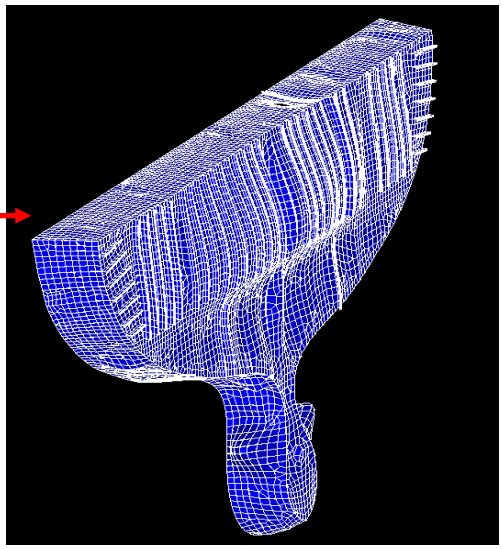

Flexibility at section E has a great impact on the natural frequency corresponding with the mode shape illustrated above.

Deflection Shape at 15.6 Hz (frame 25 constrained)
displacement scaling 8e3

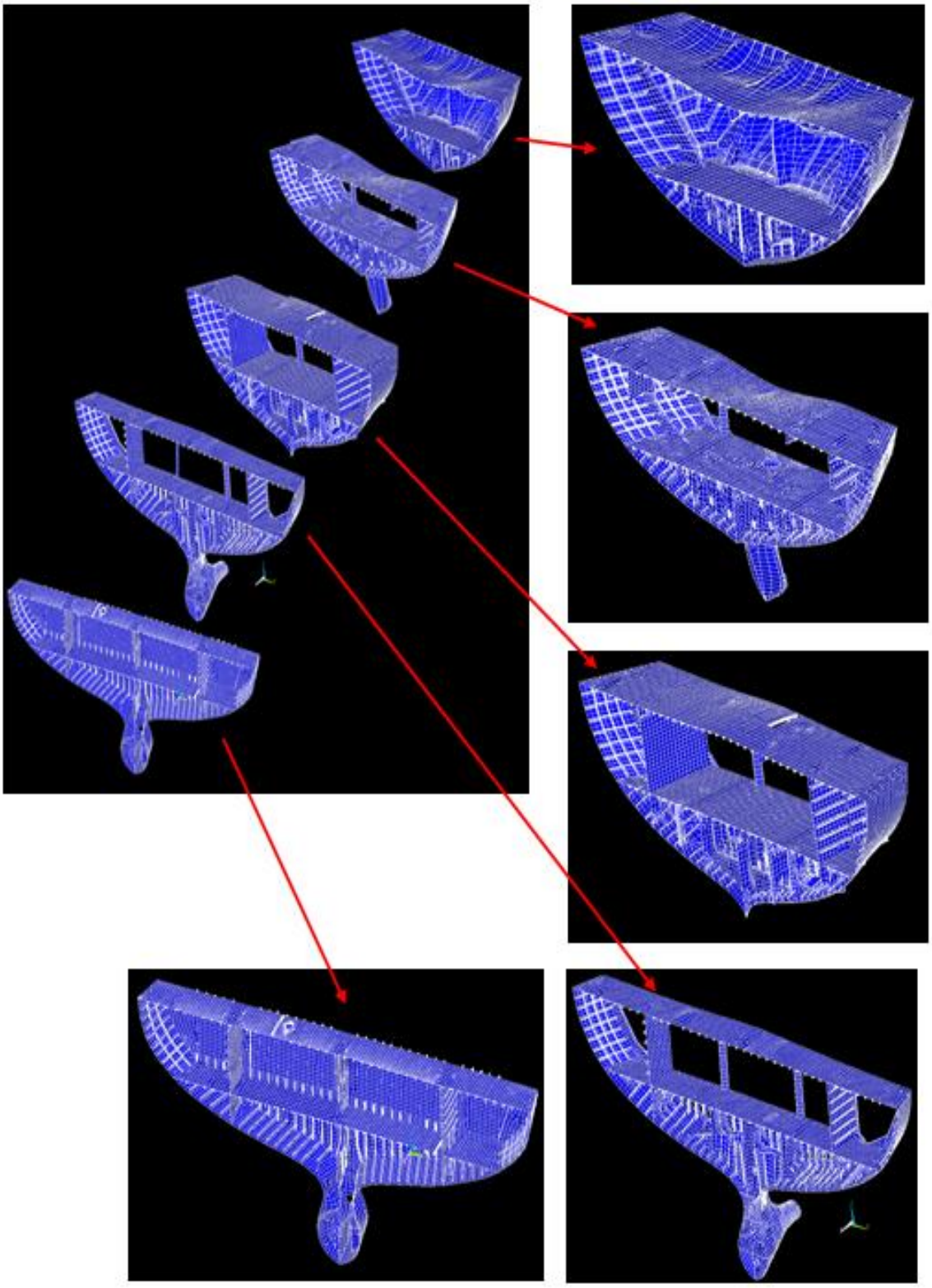

Deflection Shape 18.1 Hz (frame 25 constrained)
displacement scaling 4e3

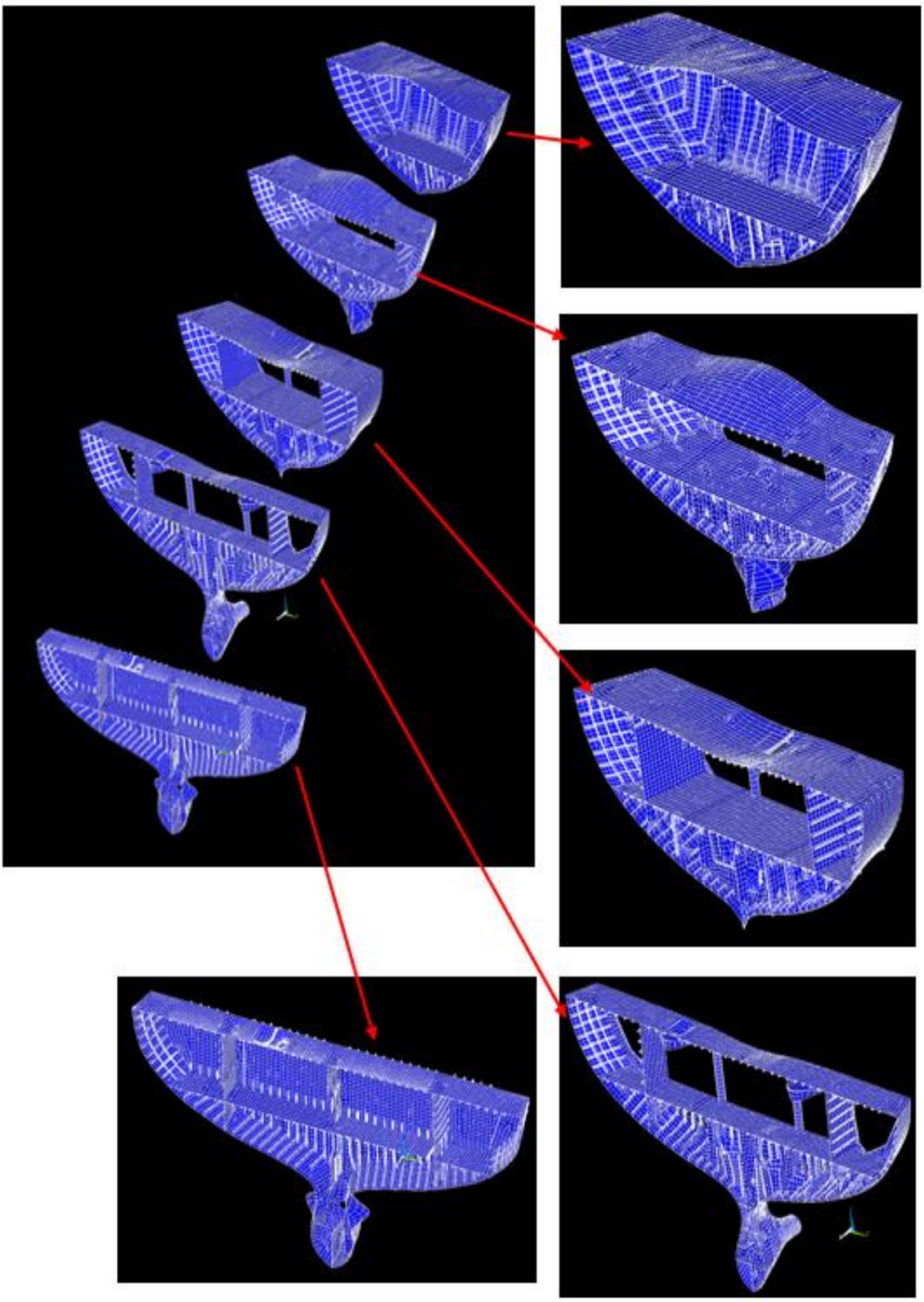

Deflection Shape 27.3 Hz (frame 25 constrained)
displacement scaling 4e3

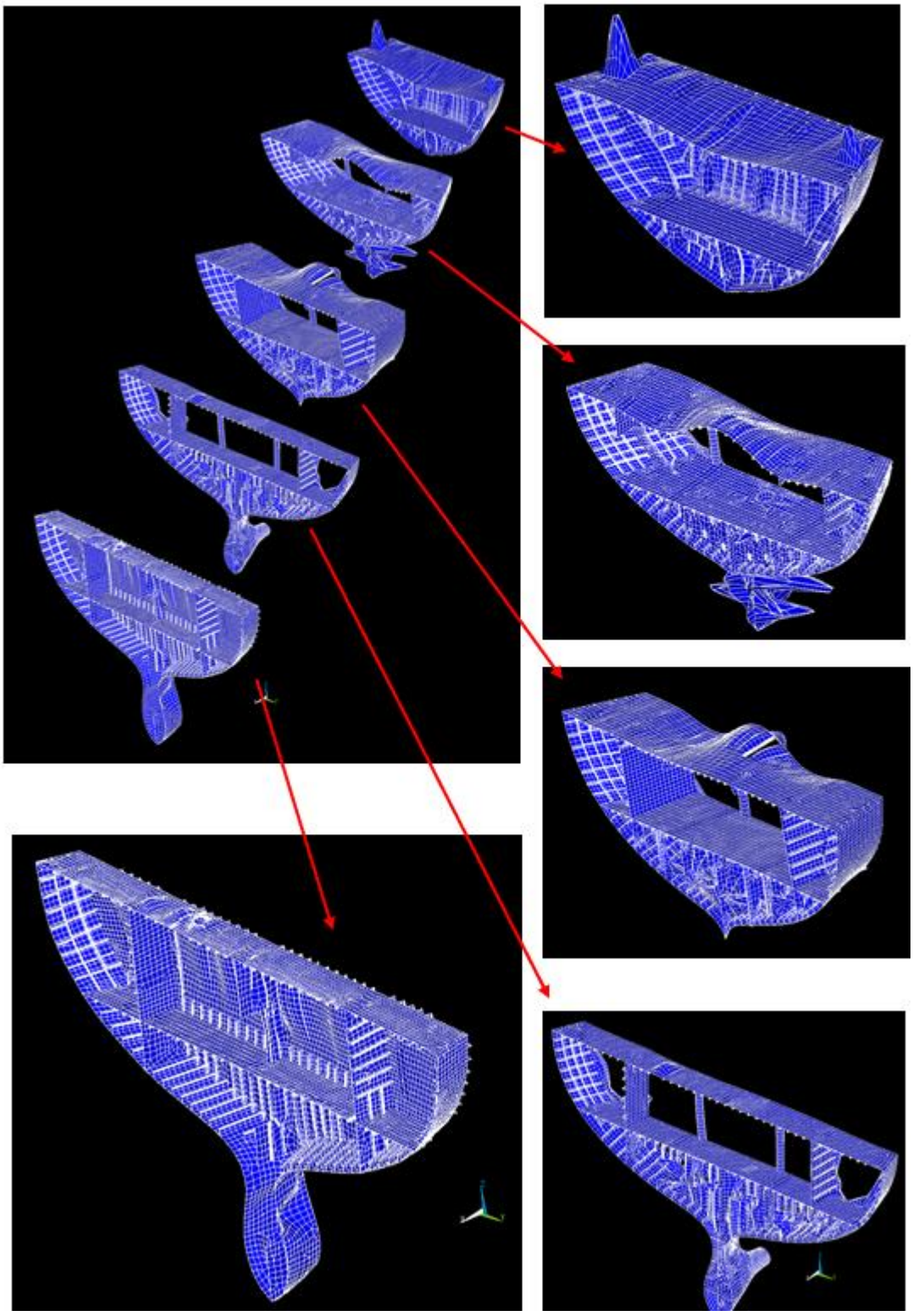

Appendix XII *Simulated Deflection Shapes for Model Constrained at Frame 21*

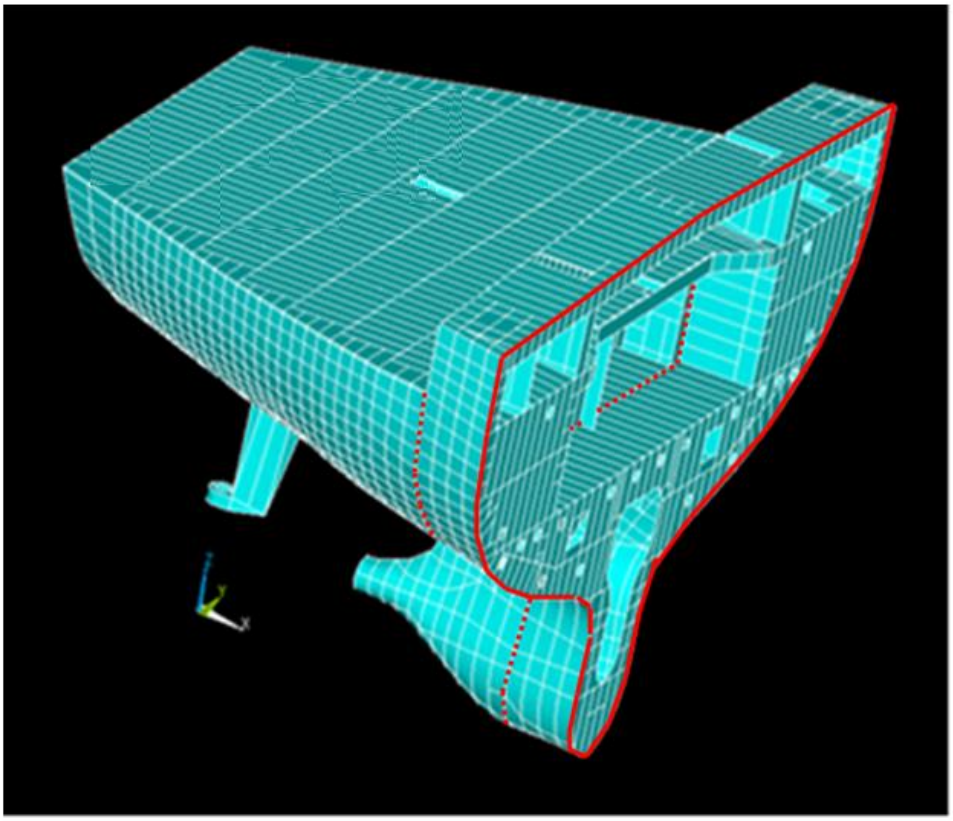

Frame 25

Frame 21

Deflection Shape at 10 Hz (engine room bulk head (frame 21) constrained)

displacement scaling 8e3

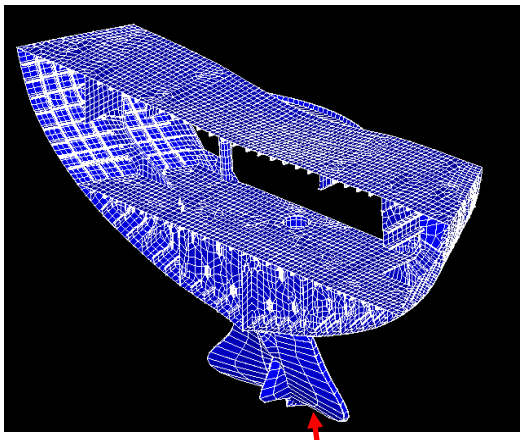

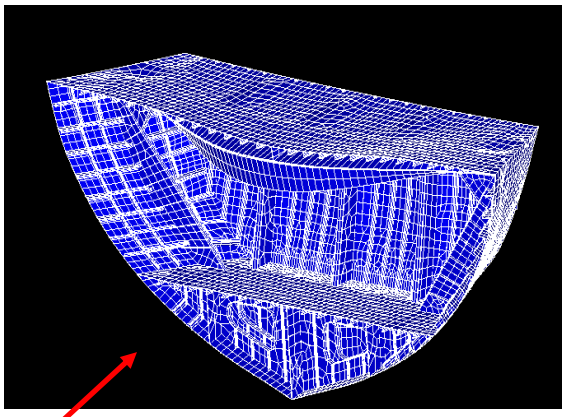

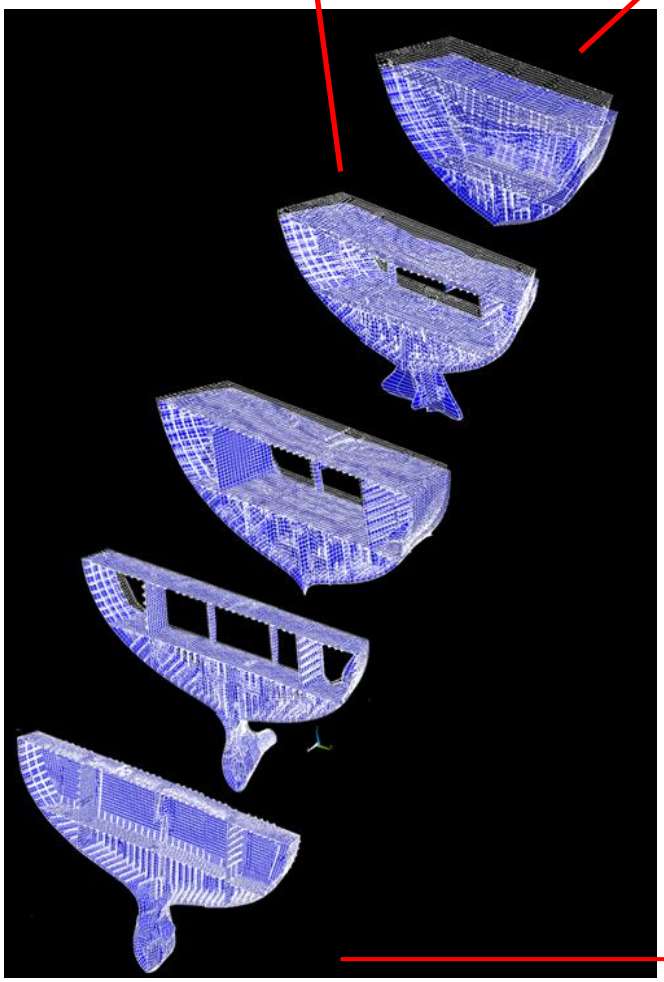

Substructures added together. Pictures shows the deformed shape plotted together with the un-deformed shape which clearly shows the presence of the effect of a first bending global mode shape of the aft ship. The deformed shape of sections A and B are shown enlarged at the top of the figure. Through these two pictures also the presence of a bending mode at the aft part of the aft deck can be identified. The deformed shapes of sections C to H do not show any local elastic deformation apart from section E. That is why they have not been shown in more detail here. Vibration levels at these sections at 8.9 Hz are largely due to the global first bending mode-shape of the aft ship, which is shown through the summary picture immediately left to this text.

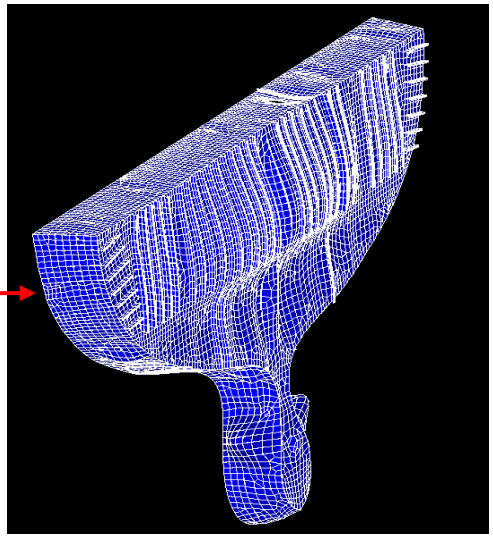

At section E the flexibility of the bulk head plays an important role This explains why constraining frame 21 instead of frame 25 affects the resonance frequency corresponding with this mode-shape.

Deflection Shape at 15.6 Hz (engine room bulk head (frame 21) constrained)

displacement scaling 8e3

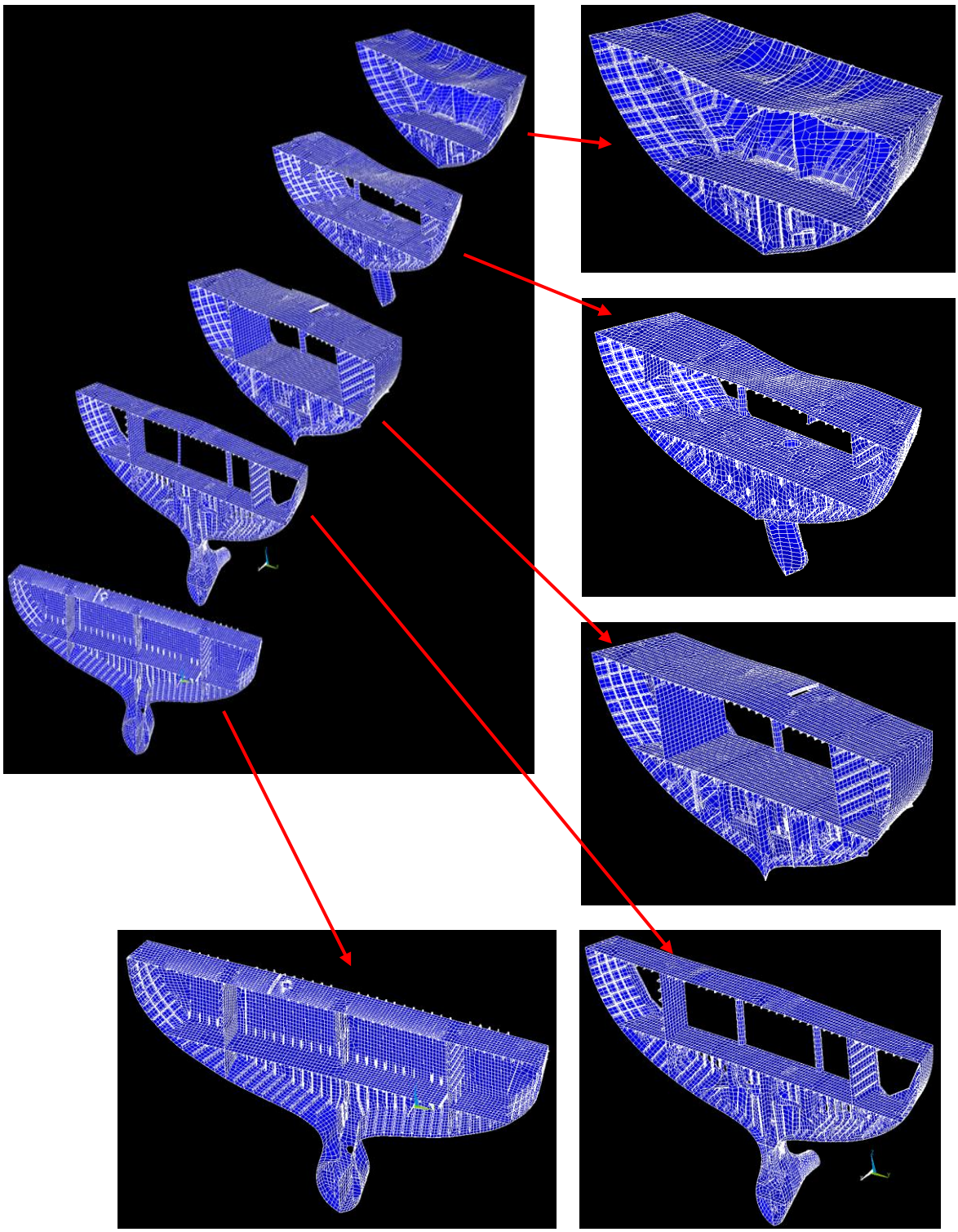

Deflection Shape at 19 Hz (engine room bulk head (frame 21) constrained.
displacement scaling 4e3

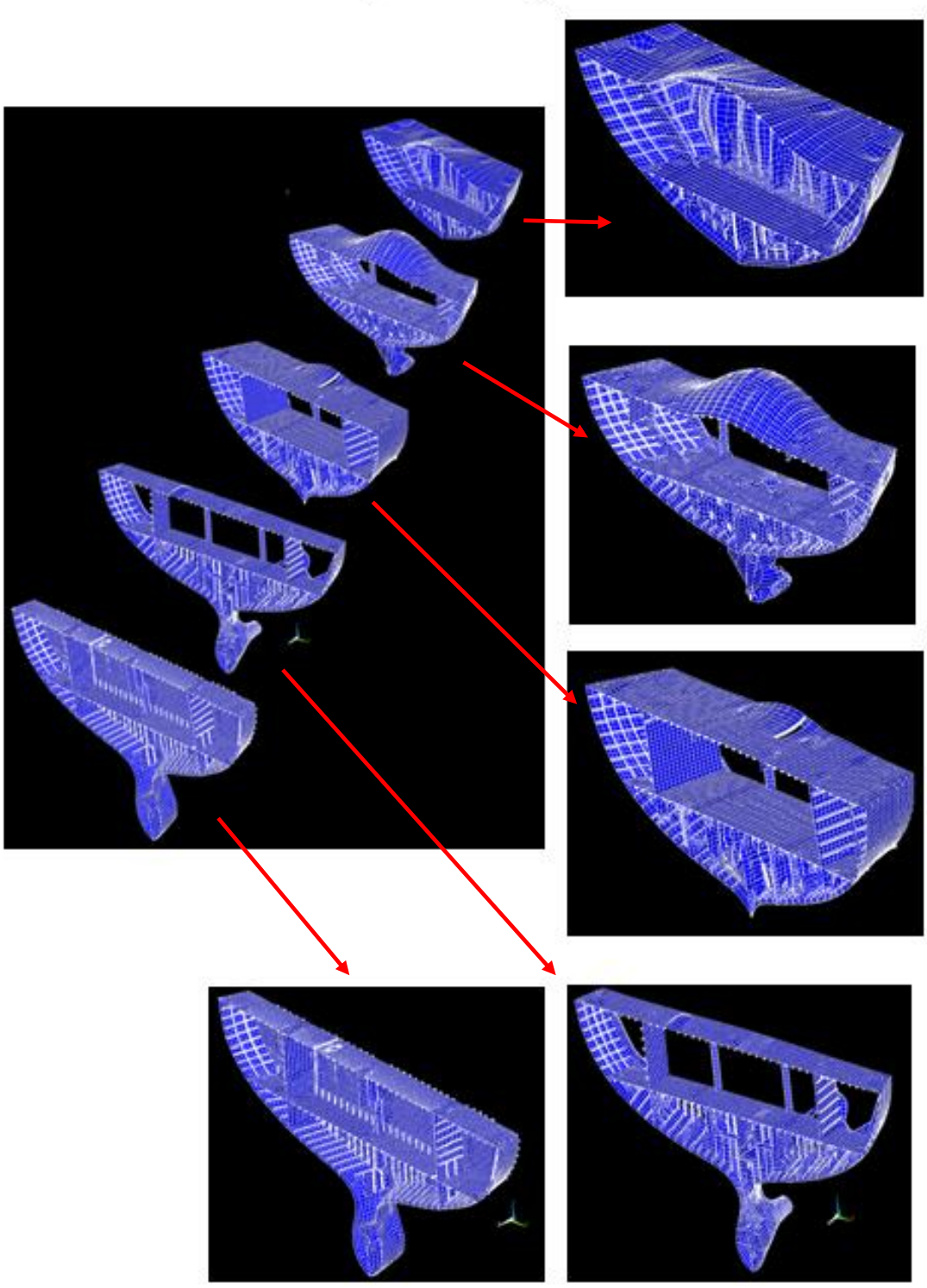

Deflection Shape at 22 Hz (engine room bulk head (frame 21) constrained.
displacement scaling 4e3

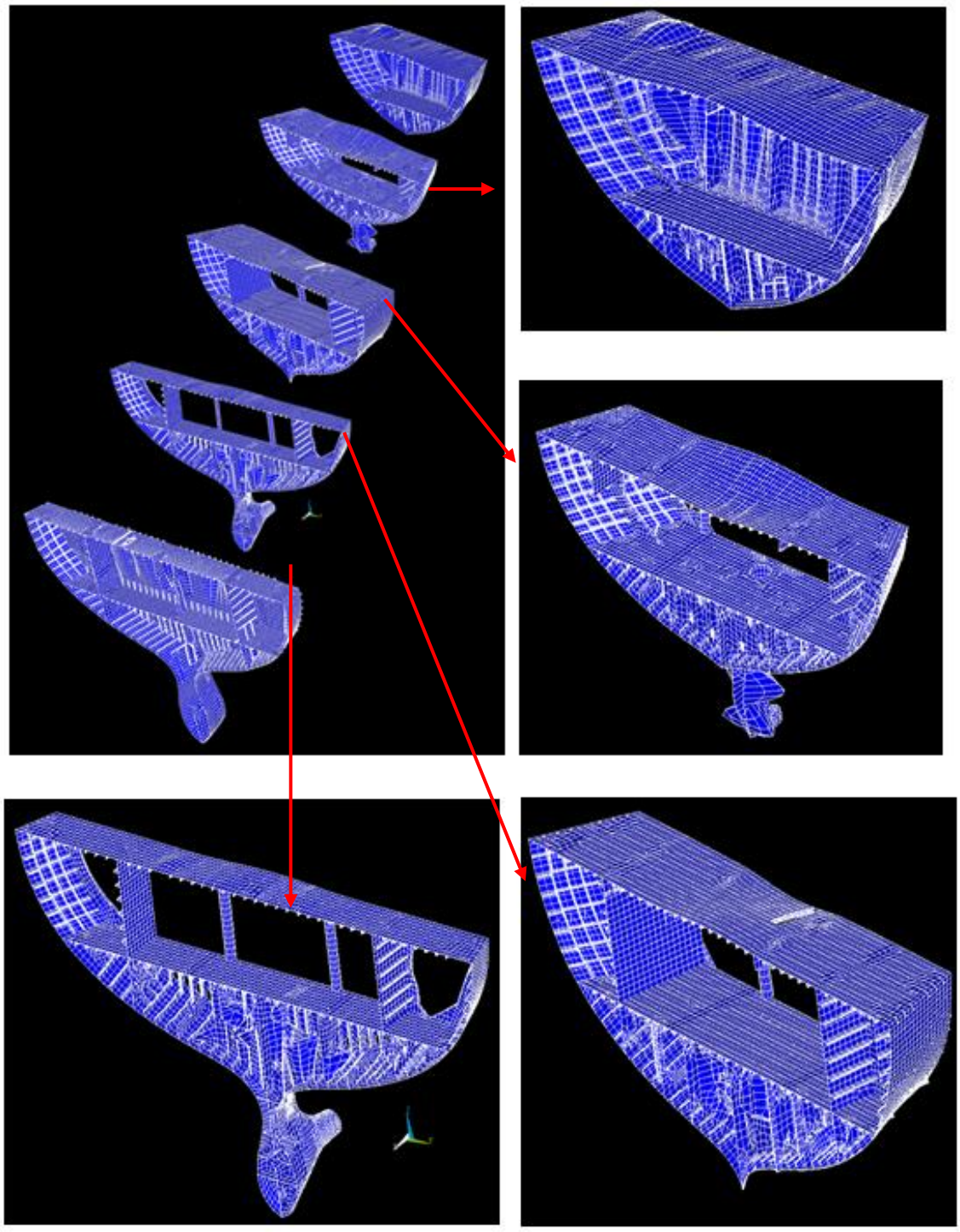

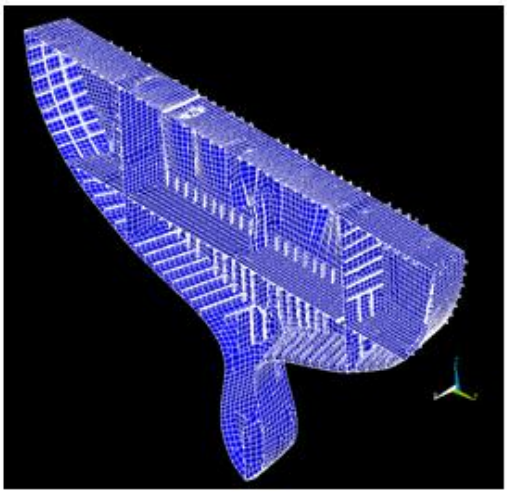

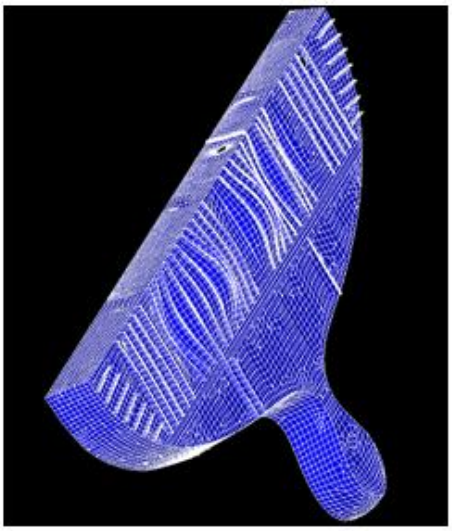

Appendix XIII *Comparing Correlated Simulated Spectra With Measurement Results*

Correlated modelling results are plotted together with the measurement results. The amplitudes of the first two blade passing frequencies (at 5 and 10 Hz) have been obtained from the simulation results produced for the model constrained at frame 25. The adjustment done for the response at the first two blade passing frequencies shifting the 8.8 Hz natural frequency to 7.8 Hz, as a correction for the absence of absence of hydrodynamic added mass in the original model. For orders higher than 2, peak response frequencies the closest to the orders in question have been shifted in such a way that the peak response frequencies coincide with the blade passing order.

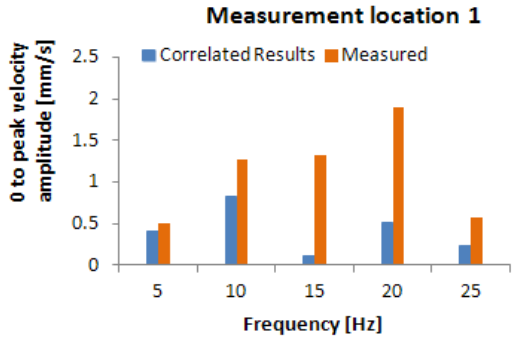

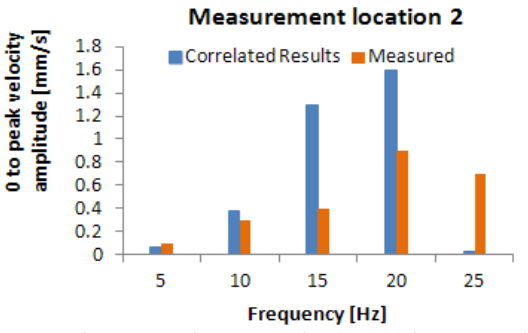

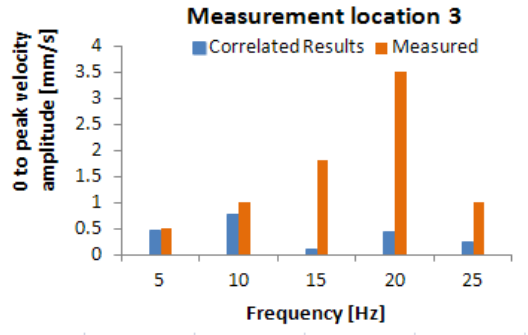

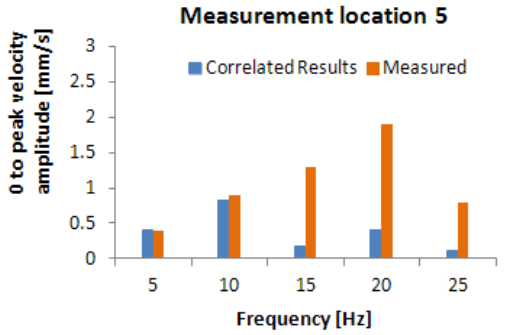

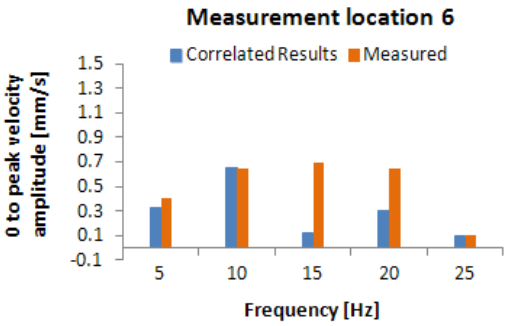

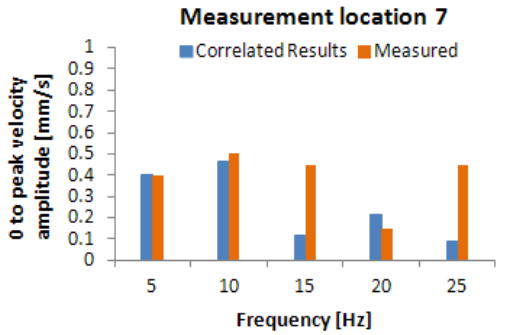

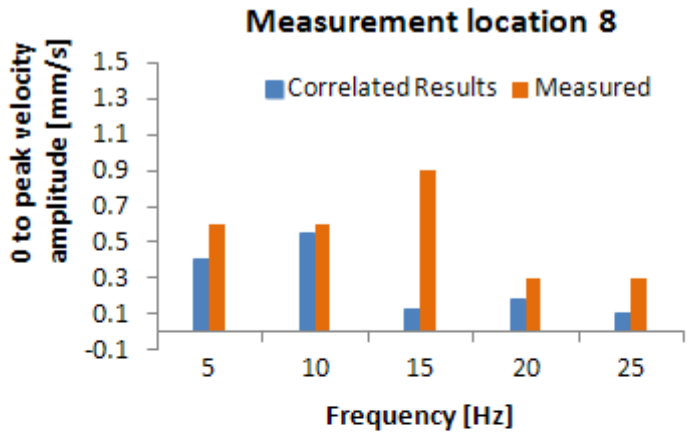
Measurement location 8
0 to peak velocity amplitude [mm/s]
Correlated Results
Measured
1.5
1.3
1.1
0.9
0.7
0.5
0.3
0.1
-0.1
5
10
15
20
25
Frequency [Hz]

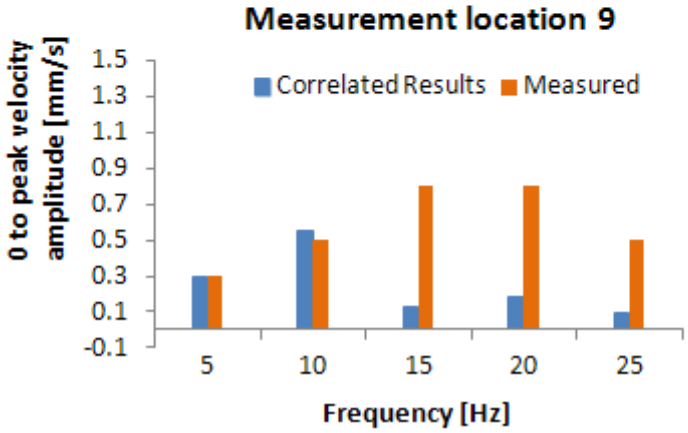
Measurement location 9
0 to peak velocity amplitude [mm/s]
Correlated Results
Measured
1.5
1.3
1.1
0.9
0.7
0.5
0.3
0.1
-0.1
5
10
15
20
25
Frequency [Hz]

Appendix XIV *Matrix-Vector Calculus and Number of Required Floating Point Operations*

An Important part of the evaluation of the different CMS techniques proposed in this work is the estimation of the number of floating point operations required for each step. Hereby a list is given of the required number of complex and real floating point operations for matrix multiplication, adding and subtracting. A real floating point operation (FLOP) is a +, -, /, or × operation on two real numbers. A complex floating point operation is a +, -, /, or × operation on two real two complex numbers [48, 50, 51]:

One complex multiplication consists of 4 real multiplication and two real summations. This means that 1 complex multiplication (1 complex floating point) is equal to 6 real multiplications.

One complex summation consists of 2 real summations.

One complex division consist of 10 real operations considering:

$$\frac{a+bi}{c+di} = \frac{(a+bi)(c-di)}{c^2+d^2} = \frac{(ac+bd)}{(c^2+d^2)} + \left(\frac{(-ad+bc)}{(c^2+d^2)}\right)i$$

Which involves a complex multiplication $(a+bi)(c-di)$ (= 6 real flops)

plus 2 real multiplications (c^2+d^2) plus 2 real divisions $\frac{(ac+bd)}{(c^2+d^2)}$ and $\frac{(-ad+bc)}{(c^2+d^2)}$

In this work the real floating point operations are calculated as a great number of operations (mainly in the generation pass) do not require calculation with complex numbers (such as reduction of mass and stiffness matrices). In addition also the fact that a multiplication of two complex numbers is more expensive than adding two complex numbers is reflected.

		Approximate Number of Complex FLOPS	Approximate Number of Real FLOPS
Multiplying two full matrices: $A^{N\times M} * C^{M\times L}$	$A^{N\times M}$ is a full $N \times M$ matrix $C^{M\times L}$ is a full $M \times L$ matrix	2*N*M*L (N*M*L complex multiplications plus N*M*L complex summations)	8*N*M*L (6*N*M*L real multiplications plus 2*N*M*L real summations)
Multiplying a full matrices with a sparse band matrix: $A^{N\times M} * C^{M\times L}$	$A^{N\times M}$ is a full $N \times M$ matrix $C^{M\times L}$ is a sparse $M \times L$ matrix with an average bandwidth of W	2*N*M*W (N*M*W complex multiplications plus N*M*W complex summations)	8*N*M*W (6*N*M*W real multiplications plus 2*N*M*W real summations)
Multiplying a sparse band matrix with a full matrix: $A^{N\times M} * C^{M\times L}$	$A^{N\times M}$ is a sparse $N \times M$ matrix with an average bandwidth of W $C^{M\times L}$ is a full $M \times L$ matrix	2*W*M*L (W*M*L complex multiplications plus W*M*L complex summations)	8*W*M*L (6*W*M*L real multiplications plus 2*W*M*L real summations)
Multiplying a matrix with a vector: $A^{N\times M} * f$	$A^{N\times M}$ is a $N \times M$ matrix and f is a $M \times 1$ vector	2*N*M (N*M complex multiplications plus N*M complex summations)	8* N*M (6*N*M real multiplications plus 2*N*M real summations)

Multiplying a full matrices with a diagonal band matrix with bandwidth W=1: $A^{N\times M} * C^{M\times L}$	$A^{N\times M}$ is a full $N \times M$ matrix $C^{M\times L}$ is a sparse $M \times L$ matrix with a bandwidth of 1	N*M (N*M*W complex multiplications plus no complex summations)	6*N*M (6*N*M*W real multiplications plus 0 real summations)
Inverse of a sparse matrix through LU factorisation $A^{N\times N}$	$A^{N\times N}$ is a sparse $N \times N$ matrix with an average bandwidth of W	$\frac{4}{3}(N(2k+1) - k(k+1))\,N$ Where $k = \frac{(W-1)}{2}$	$\frac{4}{3} * 8 * (N(2k+1) - k(k+1))\,N$ Where $k = \frac{(W-1)}{2}$
Inverse of a full matrix $A^{N\times N}$	$A^{N\times N}$ is a full square $N \times N$ matrix	$2N^3$	$16N^3$

Solving a $N \times N$ triangular matrix with ones on the main dagonal		N*N Approx 0.5* N*N complex multiplications and 0.5*N*N complex summations	4*N*N Approx 6*0.5* N*N real multiplications and 2*0.5*N*N real summations

		Approximate Number of Real FLOPS
Multiplying one full complex matrices with a full real matrix: $A^{N\times M} * C^{M\times L}$	$A^{N\times M}$ is a full $N \times M$ complex matrix $C^{M\times L}$ is a full $M \times L$ real matrix	4*N*M*L (2*N*M*L real multiplications plus 2*N*M*L real summations)
Multiplying a complex sparse band matrix with a real full matrix: $A^{N\times M} * C^{M\times L}$	$A^{N\times M}$ is a complex sparse $N \times M$ matrix with an average bandwidth of W $C^{M\times L}$ is a full real $M \times L$ matrix	4*W*M*L (2*W*M*L real multiplications plus 2*W*M*L real summations)

Appendix XV *Steps and Estimated Number of Matrix Operation Mode Superposition*

Step 1: Calculating Reduced Matrices

$$\Phi^T f = \Phi^T M \Phi + \Phi^T (K - \varepsilon K i)\Phi$$

Where Φ is the reduction basis consisting of a number of vectors representing the retained mode shapes

K = the stiffness matrix of the total structure

M is the mass matrix of the total structure

ε is the loss number representing the damping as a fixed percentage of the spring potential energy

See section 6.4.2

Step	Description of action	Estimated number of real FLOPS
1A	Calculating $\Phi^T f$ Multiplying a real full $n \times n_n$ matrix with a full complex $n \times 1$ matrix	$4 * n * n_n$
1B	$\Phi^T M$ Multiplying a real $n_n \times n$ matrix with a real sparse $n \times n$ matrix with bandwidth $n_{bandwidth}$	$2 * n * n_n * n_{bandwidth}$
1C	$\Phi^T M \Phi$ Multiplying a full real $n_n \times n$ matrix with a full real $n \times n_n$ matrix	$2 * n * n_n * n_n$
1D	$\Phi^T (K - \varepsilon K i)$ Multiplying a real $n_n \times n$ matrix with a complex $n \times n$ matrix	$4 * n * n_n * n_{bandwidth}$
1E	$\Phi^T (K - \varepsilon K i)\Phi$ Multiplying a complex $n_n \times n$ matrix with a real $n \times n_n$ matrix	$4 * n * n_n * n_n$

n = the number of degrees of freedom of the total structure
n_n = the number of mode shapes required
$n_{bandwidth}$ is the average bandwidth of the sparse diagonal symmetric stiffness and mass matrix

Appendix XVI *Steps and Estimated Number of Matrix Operation Classic Rubin's Method*

Step 1: Calculating constraint modes		
Constraint modes = $\phi^{ci} = -[k^{II}]^{-1}[k^{IB}]$ (according to equation (6.40))		
Step	**Description of action**	**Estimated number of FLOPS**
1A	Calculating $-[k^{II}]^{-1}$ Inverting a $n_i \times n_i$ matrix through LU decomposition	$\frac{4}{3}(n_i(2k+1) - k(k+1))\, n_i$ Where $k = \frac{(n_{bandwidth}-1)}{2}$
1B	Calculating $-[k^{II}]^{-1}[k^{IB}]$ Multiplying a full $n_i \times n_i$ matrix with a sparse $n_i \times n_{boundary}$ matrix	$2 * n_i * n_{boundary} * n_{bandwidth}$
n_i = the number of internal (slave) degrees of freedom of a substructure $n_{boundary}$ = the total number of interface degrees of freedom of the substructure. $n_{bandwidth}$ is the average bandwidth of the sparse diagonal symmetric matrix k^{II}		

Step 2: Generating reduction basis		
Reduction basis $R = \begin{bmatrix} 0 & I \\ [\phi_i] - [\phi^{ci}][\phi_b] & [\phi^{ci}] \end{bmatrix}$ (according to equation (6.67))		
Step	Description of action	Estimated number of FLOPS
2A	Calculating $a = [\phi^{ci}][\phi_b]$ Multiplying a full $n_i \times n_{boundary}$ matrix with a full $n_{boundary} \times n_n$ matrix	$2 * n_i * n_{boundary} * n_n$
2B	Calculating $\phi_{ni} - \phi_c\phi_{nb} = \phi_{ni} - a$ Where a is obtained from step 2A Subtracting a full $n_i \times n_n$ matrix from a full $n_i \times n_n$ matrix	$n_i * n_n$
n_i = the number of internal (slave) degrees of freedom of a substructure $n_{boundary}$ = the total number of interface degrees of freedom of the substructure. n_n = the number of retained normal modes		

Step 3: Reducing Stiffness and Mass Matrices

Calculating the reduced stiffness and mass matrix according to $\bar{K}_A = R^T K_A R$ and $\bar{M}_A = R^T M_A R$ according to section 6.5.2.2

Step 3A	Calculating $a = K_A R$ and $M_A R$ Multiplying a sparse $n \times n$ matrix with a sparse $n \times n_a$ matrix. This action needs to be performed twice: once for the mass matrix and once for the stiffness matrix.	Estimated number of FLOPS: $2 * 2 * n_a * n * n_{bandwidth}$

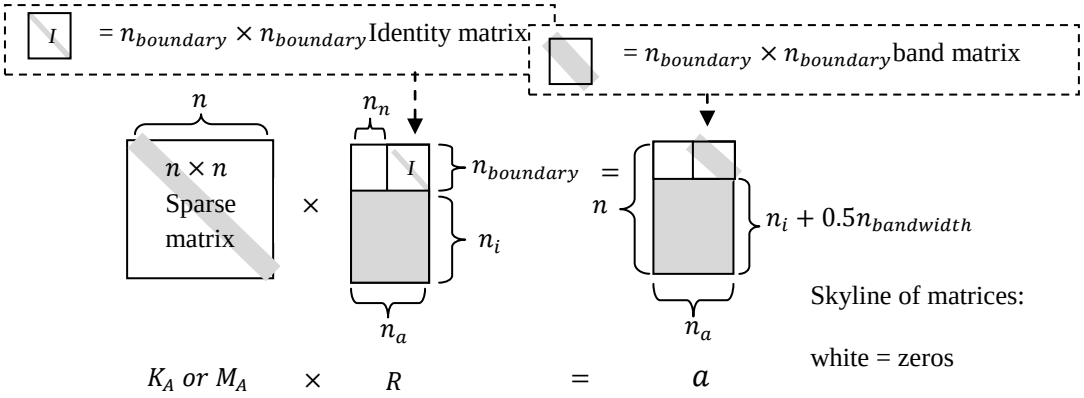

Step 3B	Calculating $\bar{K}_A$ or $\bar{M}_A = R^T K_A R$ or $R^T M_A R = R^T a$ Where a is obtained from step 3A Multiplying a sparse $n_a \times n$ matrix with a full $n \times n_a$ matrix. This action needs to be performed twice: once for the mass matrix and once for the stiffness matrix	Estimated number of FLOPs: $2 * 2 * n_i * n_a * n_n$ + $2 * 2 * (n_i + 1) * n_a * n_{boundary}$

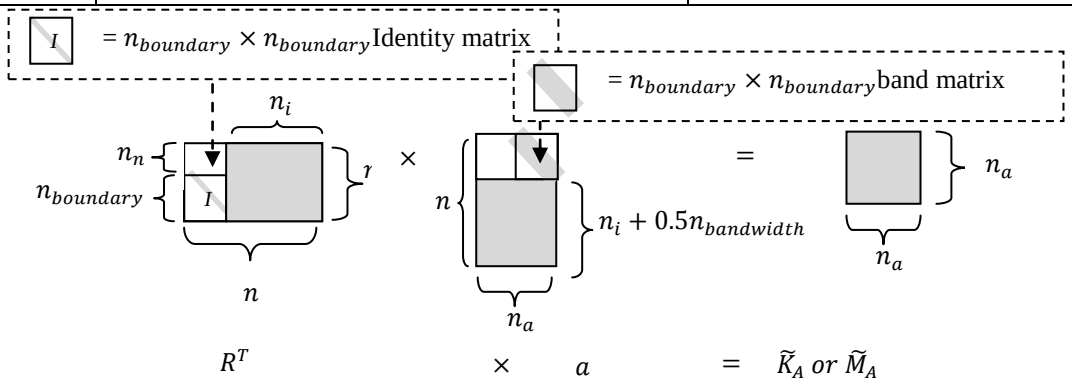

n is the number of degrees of freedom of a substructure
n_a is the number of retained normal modes plus the number of constraint modes (interface degrees of freedom)
$n_{boundary}$ = the total number of interface degrees of freedom of the substructure.
n_n = the number of retained normal modes
$n_{bandwidth}$ is the average bandwidth of the sparse diagonal symmetric matrix $K_A$or M_A
n_i = the number of internal (slave) degrees of freedom of a substructure.

Step 3C	Reducing external load vector: $R^T \begin{bmatrix} F_{bA} \\ F_{eA} \end{bmatrix}$ Multiplying a real sparse $n_a \times n$ matrix with a full complex $n \times 1$ vector	Estimated number of FLOPS: $4 * n_i * n_n$ + $4 * (n_i + 1) * n_{boundary}$

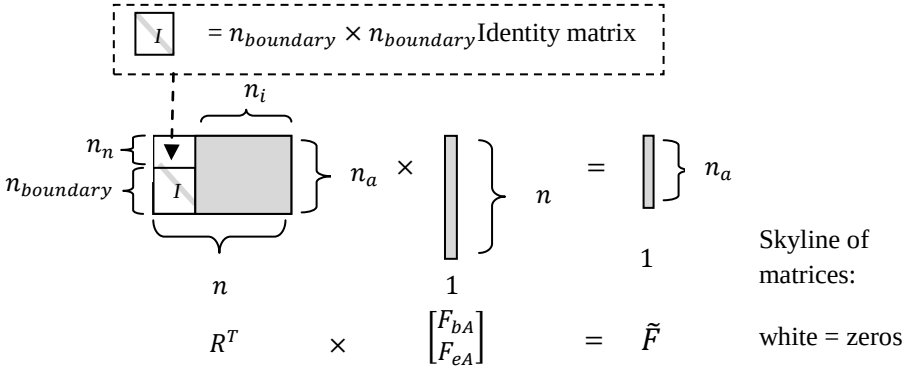

n is the number of degrees of freedom of a substructure
n_a is the number of retained normal modes plus the number of constraint modes (interface degrees of freedom)
$n_{boundary}$ = the total number of interface degrees of freedom of the substructure.
n_n = the number of retained normal modes
n_i = the number of internal (slave) degrees of freedom of a substructure
$n_{bandwidth}$ is the average bandwidth of the sparse diagonal symmetric matrix $K_A$or M_A

Step 4: Generating reduced equations of motion
(see equations (6.54) to (6.56) section 6.5.1.3)

Calculating

$[\bar{K} - \varepsilon\bar{K} - \omega^2\bar{M}]$Where $\bar{K}$ and $\bar{M}$ are the reduced stiffness and mass matrix of the total assembled structure. The total reduced dynamic stiffness matrix $[\bar{K} - \varepsilon\bar{K} - \omega^2\bar{M}]$ is calculated from the reduced dynamic stiffness matrices of the individual substructures obtained in step 3.

$$[\bar{K} - \varepsilon\bar{K}] = \begin{bmatrix} \bar{K}_A - \varepsilon\bar{K}_N & 0 & 0 & 0 \\ 0 & \bar{K}_B - \varepsilon\bar{K}_N & 0 & 0 \\ 0 & 0 & \ddots & 0 \\ 0 & 0 & 0 & \bar{K}_N - \varepsilon\bar{K}_N \end{bmatrix}$$

$$[\bar{M}] = \begin{bmatrix} \bar{M}_A & 0 & 0 & 0 \\ 0 & \bar{M}_B & 0 & 0 \\ 0 & 0 & \ddots & 0 \\ 0 & 0 & 0 & \bar{M}_N \end{bmatrix}$$

Step	Description of action	Estimated number of FLOPS
4A	Calculating $k_N = \bar{K}_N - \varepsilon\bar{K}_N$ for all N substructures the total structure consists of: Calculating $\varepsilon\bar{K}_N$ = multiplying an imaginary $(n_{Nboundary} + n_{Nn}) \times (n_{Nboundary} + n_{Nn})$ matrix with the loss number ε	$\sum_{N=A}^{N=N} (n_{Nboundary} + n_{Nn}) * (n_{Nboundary} + n_{Nn})$
	$k_N = \bar{K}_N - \varepsilon\bar{K}_N$ = Adding real $(n_{Nboundary} + n_{Nn}) \times (n_{Nboundary} + n_{Nn})$ matrices to complex $(n_{Nboundary} + n_{Nn}) \times (n_{Nboundary} + n_{Nn})$ matrices.	$2\sum_{N=A}^{N=N} (n_{Nboundary} + n_{Nn}) * (n_{Nboundary} + n_{Nn})$
	$3 * \sum_{N=A}^{N=N} (n_{Nboundary} + n_{Nn}) * (n_{Nboundary} + n_{Nn})$	

n_{Nn} = the number of normal modes of substructure N
$n_{Nboundary}$ = number of master (connecting) degrees of freedom of substructure N
f = number of frequencies analysed
N = Number of substructures involved

Step	Description of action	Estimated number of FLOPS
4B	Compiling $[\overline{K} - \varepsilon\overline{K}] = \begin{bmatrix} k_A & 0 & 0 & 0 \\ 0 & k_B & 0 & 0 \\ 0 & 0 & \ddots & 0 \\ 0 & 0 & 0 & k_n \end{bmatrix}$ Where k_N are the matrices obtained from step 4A Adding complex $(n_{Nboundary} + n_{Nn}) \times (n_{Nboundary} + n_{Nn})$ matrices to complex $(n_{Nboundary} + n_{Nn}) \times (n_{Nboundary} + n_{Nn})$ matrices.	$2 * \sum_{N=A}^{N=N} (n_{Nboundary} + n_{Nn}) * (n_{Nboundary} + n_{Nn})$
	$[\overline{M}] = \begin{bmatrix} \overline{M}_A & 0 & 0 & 0 \\ 0 & \overline{M}_B & 0 & 0 \\ 0 & 0 & \ddots & 0 \\ 0 & 0 & 0 & \overline{M}_N \end{bmatrix}$ Adding real $(n_{Nboundary} + n_{Nn}) \times (n_{Nboundary} + n_{Nn})$ matrices to real $(n_{Nboundary} + n_{Nn}) \times (n_{Nboundary} + n_{Nn})$ matrices.	$\sum_{N=A}^{N=N} (n_{Nboundary} + n_{Nn}) * (n_{Nboundary} + n_{Nn})$
	$3 * \sum_{N=A}^{N=N} (n_{Nboundary} + n_{Nn}) * (n_{Nboundary} + n_{Nn})$	

n_{Nn} = the number of normal modes of substructure N
$n_{Nboundary}$ = number of master (connecting) degrees of freedom of substructure N
f = number of frequencies analysed
N = Number of substructures involved

Step 5. Forcing equilibrium and compatibility at the interface degrees of freedom:

$$[L]^T[\overline{K} - \varepsilon\overline{K}][L]$$

$[L]^T[\overline{M}][L]$ (see equations (6.53) to (6.56))

5A	$ak = [\overline{K} - \varepsilon\overline{K}][L]$ $\quad am = [\overline{M}][L]$	Number of FLOPS
	Calculating ak : Multiplying a complex full $(n_{BNtotal} + 2 * n_{b\,total}) \times (n_{BNtotal} + 2 * n_{b\,total})$ matrix with a real sparse $(n_{BNtotal} + 2 * n_{b\,total}) \times (n_{BNtotal} + n_{b\,total})$ matrix with bandwidth of 1	$4 * n_B * (n_{Ntotal} + n_{b\,total})$
	Calculating am: Multiplying a real full $(n_{BNtotal} +$ *2*nb total×nBNtotal+2*nb total* matrix with a real sparse $(n_{BNtotal} + 2 * n_{b\,total}) \times (n_{BNtotal} +$ *nb total* matrix with bandwidth of 1	$2 * n_B * (n_{Ntotal} + n_{b\,total})$
5B	Calculating $bk = [L]^T[ak]$ and $bm = [L]^T[am]$	Number of FLOPS
	Multiplying a sparse real $(n_{BNtotal} + n_{b\,total}) \times (n_{BNtotal} + 2 * n_{b\,total})$ matrix with bandwidth 1, with a complex full $(n_{BNtotal} + 2 * n_{b\,total}) \times (n_{BNtotal} + n_{b\,total})$ matrix	$4 * n_B * (n_{Ntotal} + n_{b\,total})$
	Multiplying a sparse real $(n_{BNtotal} + n_{b\,total}) \times (n_{BNtotal} + 2 * n_{b\,total})$ matrix with bandwidth 1, with a real full $(n_{BNtotal} + 2 * n_{b\,total}) \times (n_{BNtotal} + n_{b\,total})$ matrix	$2 * n_B * (n_{Ntotal} + n_{b\,total})$
5C	Compiling $B = [[L]^T[\overline{K} - \varepsilon\overline{K}][L] - [L]^T[\overline{M}][L]\omega^2]$	Number of FLOPS
	$c = [L]^T[\overline{M}][L]\omega^2$ = Multiplying a real $(n_{b\,total} + n_{Ntotal}) \times (n_{b\,total} + n_{Ntotal})$ with ω^2	$f * (n_{b\,total} + n_{Ntotal})(n_{b\,total} + n_{Ntotal})$
	$[[L]^T[\overline{K} - \varepsilon\overline{K}][L] - [L]^T[\overline{M}][L]\omega^2] = bk + c$ Adding complex $(n_{b\,total} + n_{Ntotal}) \times (n_{b\,total} + n_{Ntotal})$ matrices to real $(n_{b\,total} + n_{Ntotal}) \times (n_{b\,total} + n_{Ntotal})$ matrices.	$2 * f * (n_{b\,total} + n_{Ntotal})(n_{b\,total} + n_{Ntotal})$

$$L^T R^T[F]$$

= eliminating redundant interface degrees of freedom and stating that the external force at the retained interface degrees of freedom are zero, so that an equilibrium of forces is obtained

n_B = the number of rows or columns of the total assembled *B* matrix. $(n_{BNtotal} + 2 * n_{b\,total})$

$n_{b\,total}$ = the total number of master (connecting) degrees of freedom (interface node degrees of freedom) of the total assembled structure.

n_{Ntotal} is the total number of normal modes taken into account for all individual substructures added together.

Appendix XVII *Steps and Estimated Number of Matrix Operations Rubin's Method using Interface Modes*

Step 1: Calculating constraint modes		
Constraint modes = $\phi^{ci} = -[k^{II}]^{-1}[k^{IB}]$ (according to equation (6.40)) See also section 6.5.3		
Step	**Description of action**	**Estimated number of FLOPS**
1A	Calculating $-[k^{II}]^{-1}$ Inverting a $n_i \times n_i$ matrix through LU decomposition	$\frac{4}{3}(n_i(2k+1) - k(k+1))\, n_i$ Where $k = \frac{(n_{bandwidth}-1)}{2}$
1B	Calculating $-[k^{II}]^{-1}[k^{IB}]$ Multiplying a full $n_i \times n_i$ matrix with a sparse $n_i \times n_{boundary}$ matrix	$2 * n_i * n_{boundary} * n_{bandwidth}$
n_i = the number of internal (slave) degrees of freedom of a substructure $n_{boundary}$ = the total number of interface degrees of freedom of the substructure. $n_{bandwidth}$ is the average bandwidth of the sparse diagonal symmetric matrix k^{II}		

$$K_L \emptyset_{interface} = M_L \emptyset_{interface} \omega^2$$

Step 2: Reducing the Interface degrees of freedom		
Generating reduced stiffness and mass matricesK_L and M_L $K_L = T^T K_A T$ and $M_L = T^T M_A T$ $R_G = \begin{bmatrix} I \\ \phi_A^{ci} \end{bmatrix}$ and ${R_G}^T = \begin{bmatrix} I & \phi_A^{ciT} \end{bmatrix}$ See equation (6.73)		
Step	**Description of action**	**Estimated number of FLOPS**
2A	Calculating $a_K = K_A R_G$ and $a_M = M_A R_G$ Multiplying a sparse $n_i \times n_i$ matrix with a full $n_i \times n_b$ matrix. This is done twice: once for the reduction of the stiffness matrix and once for the reduction of the mass matrix	$2 * n_i * n_b * n_{bandwidth}$ + $2 * n_i * n_b * n_{bandwidth}$
2B	Calculating $K_L = {R_G}^T a_K$ and $M_L = {R_G}^T a_M$ Multiplying a full $n_b \times n_i$ matrix with a full $n_i \times n_b$ matrix. This is done twice: once for the reduction of the stiffness matrix and once for the reduction of the mass matrix	$2 * n_i * n_b * n_b$ + $2 * n_i * n_b * n_b$
n_i = the number of internal (slave) degrees of freedom of a substructure n_b = the total number of interface degrees of freedom of the substructure. $n_{bandwidth}$ is the average bandwidth of the sparse diagonal symmetric matrix k^{II}		

Step 3: Generating reduction basis		
Reduction basis $R_{IRS} = \begin{bmatrix} 0 & [\phi_{interface\ b}] \\ [\phi_i] - [\phi^{ci}][\phi_b] & [\phi_{interface\ i}] \end{bmatrix}$ (according to equation (6.77))		
Step	Description of action	Estimated number of FLOPS
3A	Calculating $a = [\phi^{ci}][\phi_b]$ Multiplying a full $n_i \times n_b$ matrix with a full $n_b \times n_n$ matrix	$2 * n_i * n_b * n_n$
3B	Calculating $[\phi_i] - [\phi^{ci}][\phi_b] = \phi_i - a$ Where a is obtained from step 3A Subtracting a full $n_i \times n_n$ matrix from a full $n_i \times n_n$ matrix	$n_i * n_n$
n_i = the number of internal (slave) degrees of freedom of a substructure n_b = the total number of physical interface degrees of freedom of the substructure. n_n = the number of retained normal modes n_L = the number of retained interface modes (cut-off frequency 3.5 times maximum frequency)		

Step 4: Reducing Stiffness and Mass Matrices

Calculating the reduced stiffness and mass matrix according to $\bar{K}_A = {R_{IRS}}^T K_A R_{IRS}$ and $\bar{M}_A = {R_{IRS}}^T M_A R_{IRS}$ according to section 6.5.3.1

Step 4A	Calculating $a = K_A R_{IRS}$ and $M_A R_{IRS}$ Multiplying a sparse $n \times n$ matrix with a sparse $n \times n_a$ matrix. This action needs to be performed twice: once for the mass matrix and once for the stiffness matrix.	Estimated number of FLOPS: $2 * 2 * n_a * n * n_{bandwidth}$

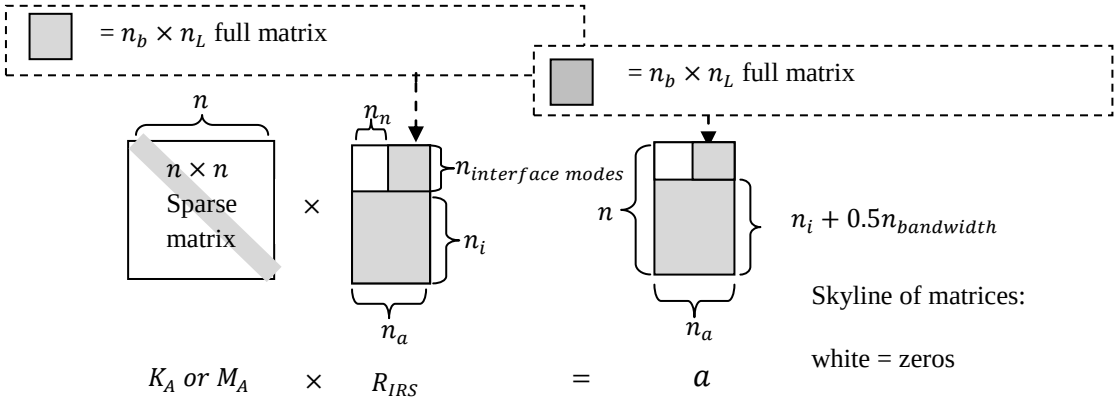

Step 4B	Calculating $\bar{K}_A$ or $\bar{M}_A = {R_{IRS}}^T K_A R$ or ${R_{IRS}}^T M_A R = {R_{IRS}}^T a$ Where a is obtained from step 4A Multiplying a sparse real $n_a \times n$ matrix with a sparse real $n \times n_a$ matrix. This action needs to be performed twice: once for the mass matrix and once for the stiffness matrix	Estimated number of FLOPs: $2 * 2 * n_i * n_a * n_n$ + $2 * 2 * n * n_a * n_L$

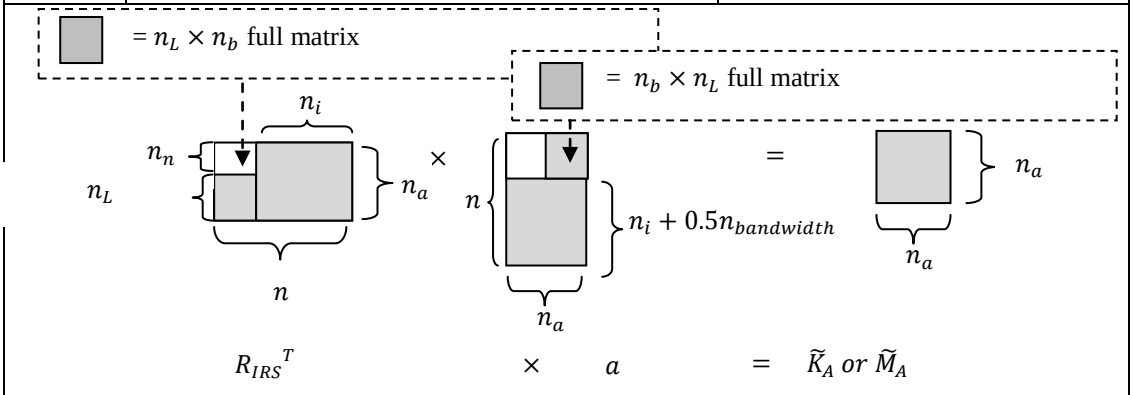

n is the total number of degrees of freedom of a substructure
n_a is the number of retained normal modes plus the number of interface modes
n_L = number of retained interface modes (cut-off frequency 3.5 times maximum frequency)
n_n = the number of retained normal modes
n_b = the total number of physical interface degrees of freedom of the substructure.
$n_{bandwidth}$ is the average bandwidth of the sparse diagonal symmetric matrix $K_A$or M_A
n_L = number of retained interface modes (cut-off frequency 3.5 times maximum frequency)
n_i = the number of internal (slave) degrees of freedom of a substructure.

Step 4C	Reducing external load vector: $R_{IRS}{}^{T}\begin{bmatrix}F_{bA}\\F_{eA}\end{bmatrix}$ Multiplying a sparse $n_a \times n$ matrix with a full $n \times 1$ vector	Estimated number of FLOPS: $2 * n_i * n_n$ + $2 * n * n_L$

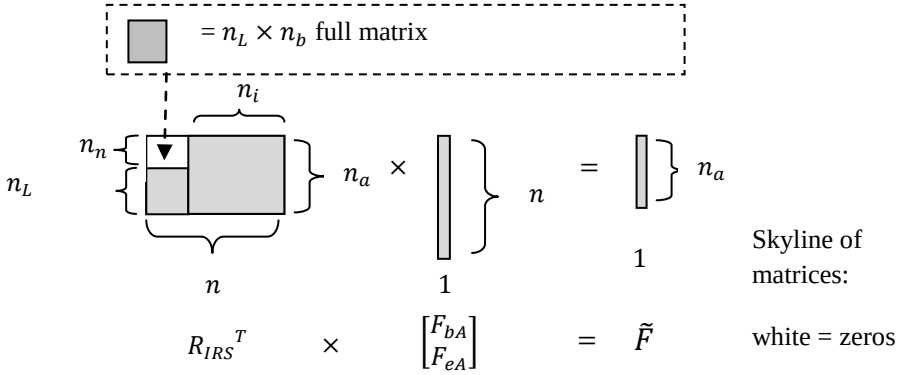

n is the total number of degrees of freedom of a substructure
n_a is the number of retained normal modes plus the number of interface modes
n_L = number of retained interface modes (cut-off frequency 3.5 times maximum frequency)
n_n = the number of retained normal modes
n_b = the total number of physical interface degrees of freedom of the substructure.
$n_{bandwidth}$ is the average bandwidth of the sparse diagonal symmetric matrix $K_A$or M_A
n_L = number of retained interface modes (cut-off frequency 3.5 times maximum frequency)
n_i = the number of internal (slave) degrees of freedom of a substructure.

Step 5: Generating reduced equations of motion

Calculating

$[\bar{K} - \varepsilon\bar{K} - \omega^2\tilde{M}]$ Where $\bar{K}$ and $\tilde{M}$ are the reduced stiffness and mass matrix of the total assembled structure. The total reduced dynamic stiffness matrix $[\bar{K} - \varepsilon\bar{K} - \omega^2\bar{M}]$ is calculated from the reduced dynamic stiffness matrices of the individual substructures obtained in step 3.

$$[\bar{K} - \varepsilon\bar{K}] = \begin{bmatrix} \bar{K}_A - \varepsilon\bar{K}_N & 0 & 0 & 0 \\ 0 & \bar{K}_B - \varepsilon\bar{K}_N & 0 & 0 \\ 0 & 0 & \ddots & 0 \\ 0 & 0 & 0 & \bar{K}_N - \varepsilon\bar{K}_N \end{bmatrix}$$

$$[\bar{M}] = \begin{bmatrix} \bar{M}_A & 0 & 0 & 0 \\ 0 & \bar{M}_B & 0 & 0 \\ 0 & 0 & \ddots & 0 \\ 0 & 0 & 0 & \bar{M}_N \end{bmatrix}$$

Step	Description of action	Estimated number of FLOPS
5A	Calculating $k_N = \bar{K}_N - \varepsilon\bar{K}_N$ for all N substructures the total structure consists of:	
	Calculating $\varepsilon\bar{K}_N$ = multiplying an imaginary $(n_{LN} + n_{Nn}) \times (n_{LN} + n_{Nn})$ matrix with the loss number ε	$\sum_{N=A}^{N=N} (n_{LN} + n_{Nn}) * (n_{LN} + n_{Nn})$
	$k_N = \bar{K}_N - \varepsilon\bar{K}_N$ = Adding complex $(n_{LN} + n_{Nn}) \times (n_{LN} + n_{Nn})$ matrices to $(n_{LN} + n_{Nn}) \times (n_{LN} + n_{Nn})$ matrices.	$2 * \sum_{N=A}^{N=N} (n_{LN} + n_{Nn}) * (n_{LN} + n_{Nn})$

$$3 * \sum_{N=A}^{N=N} (n_{LN} + n_{Nn}) * (n_{LN} + n_{Nn})$$

n_{Nn} = the number of retained normal modes of substructure N
n_{LN} = number of retained interface modes for substructure N
f = number of frequencies analysed
N = Number of substructures involved

Step	Description of action	Estimated number of FLOPS
5B	Compiling $[\overline{K} - \varepsilon\overline{K}] = \begin{bmatrix} k_A & 0 & 0 & 0 \\ 0 & k_B & 0 & 0 \\ 0 & 0 & \ddots & 0 \\ 0 & 0 & 0 & k_n \end{bmatrix}$ Where k_N are the matrices obtained from step 5A Adding complex $(n_{LN} + n_{Nn}) \times (n_{LN} + n_{Nn})$ matrices to $(n_{LN} + n_{Nn}) \times (n_{LN} + n_{Nn})$ matrices.	$2 * \sum_{N=A}^{N=N} (n_{LN} + n_{Nn}) * (n_{LN} + n_{Nn})$
	$[\overline{M}] = \begin{bmatrix} \overline{M}_A & 0 & 0 & 0 \\ 0 & \overline{M}_B & 0 & 0 \\ 0 & 0 & \ddots & 0 \\ 0 & 0 & 0 & \overline{M}_N \end{bmatrix}$ Adding real $(n_{LN} + n_{Nn}) \times (n_{LN} + n_{Nn})$ matrices to real $(n_{LN} + n_{Nn}) \times (n_{LN} + n_{Nn})$ matrices.	$\sum_{N=A}^{N=N} (n_{LN} + n_{Nn}) * (n_{LN} + n_{Nn})$
$3 * \sum_{N=A}^{N=N} (n_{LN} + n_{Nn}) * (n_{LN} + n_{Nn})$		
n_{Nn} = the number of retained normal modes of substructure N n_{LN} = number of retained interface modes for substructure N f = number of frequencies analysed N = Number of substructures involved		

Step 6. Forcing equilibrium and compatibility at the interface degrees of freedom:

Formulating L according to equation (6.82):

$$L = \left[\underset{I}{-\left[\emptyset_{Lkept}{}^{T}\emptyset_{Lkept}\right]^{-1}\left\{\left[\emptyset_{Lkept}{}^{T}\right][0 \quad -\emptyset_{Lred} \quad 0]\right\}} \right]$$

Where $\emptyset_{Lkept}$ are the retained interface modes for all substructures involved that have not been made redundant

Where $\emptyset_{Lred}$ are the retained interface modes made redundant through the formulation of the compatibility relations

Step	Action	Estimated number of FLOPS
6A	Calculating $a = \emptyset_{Lkept}{}^{T}\emptyset_{Lkept}$ Multiplying a full $n_{Lkept} \times n_b$ with a full $n_b \times n_{Lkept}$ matrix	$2 * n_b{*}n_{Lkept} * n_{Lkept}$
6B	Calculating $b = [\emptyset_{Lret}{}^{T}][0 \quad -\emptyset_{Lred} \quad 0]$ Multiplying a full $n_{Lret} \times n_b$ matrix with a sparse $n_b \times (n_{Lkept} + n_{Lred})$ matrix	$2 * n_b{*}n_{Lkept} * n_{Lred}$
6C	Calculating $\left[\emptyset_{Lret}{}^{T}\emptyset_{Lret}\right]^{-1} = a^{-1}$ Inverting a full $n_{Lkept} \times n_{Lkept}$ matrix	$\frac{4}{3}{n_{Lkept}}^{3}$
6D	Calculating $-\left[\emptyset_{Lret}{}^{T}\emptyset_{Lret}\right]^{-1}\left\{\left[\emptyset_{Lret}{}^{T}\right][0 \quad -\emptyset_{Lred} \quad 0]\right\} = a^{-1}b$ Multiplying a full $n_{Lkept} \times n_{Lkept}$ matrix with a sparse $n_{Lkept} \times (n_{Lkept} + n_{Lred})$ matrix	$2 * n_{Lkept}{*}n_{Lkept} * n_{Lred}$

n_b is the number of physical interface degrees of freedom

n_{Lred}= total number of retained interface modes made redundant for all substructures put together

n_{Lkept} = total number of retained interface modes not made redundant for all substructures put together

Step 7. Forcing equilibrium and compatibility at the interface degrees of freedom for the reduced mass and stiffness matrices:

$$[L]^T[\overline{K} - \varepsilon\overline{K}][L]$$

$$[L]^T[\overline{M}][L]$$

Step	Action	Estimated number of FLOPS
7A	$ak = [\overline{K} - \varepsilon\overline{K}][L]$ and $am = [\overline{M}][L]$ ak : Multiplying a complex sparse $(n_L + n_{Ntotal}) \times (n_L + n_{Ntotal})$ matrix with a real sparse $(n_{Ntotal} + n_L) \times (n_{Ntotal} + n_{Lret})$ matrix am : Multiplying a real sparse $(n_L + n_{Ntotal}) \times (n_L + n_{Ntotal})$ matrix with a real sparse $(n_{Ntotal} + n_L) \times (n_{Ntotal} + n_{Lret})$ matrix	$4 * \left((n_{Lkept} + n_{Ntotal})^2 + (n_{Lkept} + n_{Ntotal}) * n_{Lred} * n_{Lred}\right)$ + $2 * \left((n_{Lkept} + n_{Ntotal})^2 + (n_{Lkept} + n_{Ntotal}) * n_{Lred} * n_{Lred}\right)$
7B	Calculating $bk = [L]^T[ak]$ and $bm = LTam$ Multiplying a real sparse $(n_{Ntotal} + n_{Lret}) \times (n_{Ntotal} + n_L)$ matrix with a full complex $(n_L + n_{Ntotal}) \times (n_{Ntotal} + n_{Lret})$ matrix Multiplying a real sparse $(n_{Ntotal} + n_{Lret}) \times (n_{Ntotal} + n_L)$ matrix with a full real $(n_L + n_{Ntotal}) \times (n_{Ntotal} + n_{Lret})$ matrix	$4 * \left((n_{Lkept} + n_{Ntotal})^2 + (n_{Lkept} + n_{Ntotal})^2 * n_{Lred}\right)$ + $2 * \left((n_{Lkept} + n_{Ntotal})^2 + (n_{Lkept} + n_{Ntotal})^2 * n_{Lred}\right)$

n_b is the number of physical interface degrees of freedom
n_{Lred}= total number of retained interface modes made redundant for all substructures put together
n_{Lkept} = total number of retained interface modes not made redundant for all substructures put together
n_{Ntotal}= total number of retained normal modes (flexibility and elastic modes) of all substructures together

Step	Action	Estimated number of FLOPS
7C	Compiling $B = [[L]^T[\bar{K} - \varepsilon\bar{K}][L] - [L]^T[\bar{M}][L]\omega^2]$	
	$c = [L]^T[\bar{M}][L]\omega^2$ Multiplying a real sparse $(n_{Ntotal} +$ *nLkept×nNtotal+nLkept* with $\omega 2$	$f * (n_{Lkept} + n_{Ntotal})(n_{Lkept} + n_{Ntotal})$
	$[[L]^T[\bar{K} - \varepsilon\bar{K}][L] - [L]^T[\bar{M}][L]\omega^2] = bk + c$ Adding complex $(n_{Ntotal} + n_{Lkept}) \times (n_{Ntotal} + n_{Lkept})$ matrices to a real $(n_{Ntotal} + n_{Lkept}) \times (n_{Ntotal} + n_{Lkept})$ matrices.	$2 * f * (n_{Lkept} + n_{Ntotal})(n_{Lkept} + n_{Ntotal})$
$L^T R^T [F]$ = eliminating redundant interface degrees of freedom and stating that the external force at the retained interface degrees of freedom are zero, so that an equilibrium of forces is obtained		
n_{Lkept} total number of retained interface modes not made redundant through the compatibility relations n_{Ntotal} = the total number of retained normal modes of all substructures.		

Appendix XVIII *Steps and Estimated Number of Matrix Operations Zoet's Method*

Step 1: Calculating $G_{res} = K^{-1} - \phi_e \Lambda^{-1} \phi_e^{\ T}$ according to equation (6.59) (see section 6.4.3 and 6.5.2.2) for each individual substructure

K^{-1}= the inverse of a substructure's full stiffness matrix

Where ϕ_e represents the set of retained elastic modes

Λ^{-1} is the inverse diagonal matrix containing the natural frequencies corresponding with the retained elastic modes

Step		Number of Flops Required
1A	Calculating $a = K^{-1}$ Inverting a $(n-c) \times (n-c)$ matrix Where K is the stiffness matrix with the degrees of freedom eliminated where constraints are applied.	$\frac{4}{3}((n-c)(2k+1) - k(k+1))\,(n-c)$ Where $k = \frac{(n_{bandwidth}-1)}{2}$
1G	Calculating $b = \Lambda^{-1} \phi_e^{\ T}$ Multiplying a diagonal sparse $n_e \times n_e$ matrix with a full $n_e \times n_{boundary}$ matrix	$n_e * n_b$
1H	Calculating $c = \phi_e \Lambda^{-1} \phi_e^{\ T} = \phi_e b$ Where b has been obtained from step 1B Multiplying a full $n_{boundary} \times n_e$ matrix with a full $n_e \times n_{boundary}$ matrix	$2 * n_e * {n_{boundary}}^2$
1I	Calculating $K^{-1} - \phi_e \Lambda^{-1} \phi_e^{\ T} = a - c$ Where a has been obtained from step 1A and c has been obtained from step 1C Subtracting a full $n_{boundary} \times n_{boundary}$ from a full $n_{boundary} \times n_{boundary}$ matrix	${n_{boundary}}^2$

n is the total number of degrees of freedom of an individual substructure
c is the number of constraints on the individual substructure
$n_{boundary}$ is the number of interface degrees of freedom of the individual substructure
n_e is the number of retained elastic modes of the individual substructure
$n_{bandwidth}$ is the average bandwidth of the sparse diagonal symmetric matrix k^{II} of the individual substructure

In Case of Unconstrained Structure (see Appendix V)

$G_{res} = G_{E\ attacnment} - \phi_e \Lambda^{-1} {\phi_e}^T$ (Step 1G-1I)

$G_E = P^T G_c P$ (Step 1E and 1F)

$P = \left(I - M\phi_r {\phi_r}^T\right)$ (Step 1B to 1D)

$G_c = K^{-1}$ (Step 1A)

Step	Description of action	Estimated number of FLOPS
1A	Calculating $a = G_c = K^{-1}$ Inverting a sparse $(n-c) \times (n-c)$ matrix Where K is the stiffness matrix with the degrees of freedom eliminated where pseudo constraints are applied.	$\frac{4}{3} * ((n-6)(2k+1) - k(k+1))\ (n-6)$ Where $k = \frac{(n_{bandwidth}-1)}{2}$
1B	Calculating $b = \left(\phi_r {\phi_r}^T\right)$ Multiplying a full $n_c \times k$ with a full $k \times n_c$ matrix	$2 * {n_c}^2 k$
1C	Calculating $c = \left(M\phi_r {\phi_r}^T\right) = Mb$ Where b has been obtained in Step 1A Multiplying a sparse $n_c \times n_c$ matrix with a full $n_c \times n_c$ matrix	$2 * {n_c}^2 n_{bandwidth}$
1D	Calculating $P = \left(I - M\phi_r {\phi_r}^T\right) = I - c$ Where c has been obtained from step 1C	n_c

n is the total number of degrees of freedom of an individual substructure
c is the number of pseudo constraints on an individual substructure
n_c is the total number of degrees of freedom of the G_c matrix
k is the number of rigid body modes (= 6)
$n_{bandwidth}$ is the average bandwidth of the Sparse matrix *M or*

Calculating $G_{E\ attachment} = P^T G_c P$ for one substructure

Where $G_{E\ attacnment}$ is the section of G_E representing the degrees of freedom of the interface nodes.

Step	Description of action	Estimated number of FLOPS
1E	Calculating $e = G_c P = aP$ Where a has been obtained from step 1A Multiplying a full $n_c \times n_c$ with a full $n_c \times n_b$ matrix	$2 * {n_c}^2 * n_b$
1F	Calculating $f = \boldsymbol{G_{E\ attachment}} = P^T G_c P = P^T e$ Where e has been obtained from step 1E Multiplying a full $n_b \times n_c$ with a full $n_c \times n_b$ matrix	$2 * n_c * {n_b}^2$

Calculating Residual Attachment Modes: $\boldsymbol{G_{res} = G_{E\ attacnment} - \phi_e \Lambda^{-1} {\phi_e}^T}$

Step	Description of action	Estimated number of FLOPS
1G	Calculating g = $\Lambda^{-1} {\phi_e}^T$ Multiplying a diagonal sparse $n_e \times n_e$ matrix with a full $n_e \times n_b$ matrix	$n_e * n_b$
1H	Calculating $h = \phi_e \Lambda^{-1} {\phi_e}^T = \phi_e g$ Where g has been obtained in step 1G Multiplying a full $n_b \times n_e$ matrix with a full $n_e \times n_b$ matrix	$2 * n_e * {n_b}^2$
1I	Calculating $G_{E\ attacnment} - \phi_e \Lambda^{-1} {\phi_e}^T = G_{E\ attacnment} - h$ Where h has been obtained from step 1H Subtracting a full $n_b \times n_b$ from a full $n_b \times n_b$ matrix	${n_b}^2$

n_c is the total number of degrees of freedom of the G_c matrix
n_b is the number of interface degrees of freedom
n_e is the number of retained elastic modes

Step 2: Formulating interface mobility $[A]$ matrix for a pair of coupled substructures (substructure A and B) (see section 8.4, equation (8.32))

$$A = -\begin{bmatrix} diag(-\omega^2 + \varepsilon{\omega_0}^2\mathrm{i} + {\omega_0}^2)^{-1} & 0 \\ 0 & G_{resb} \end{bmatrix}[R^T]\left[K_{dyn\ conn}\right][R] = \text{Step 2C}$$

$$[R^T]\left[K_{dyn\ conn}\right][R] = \text{Step 2A and 2B}$$

Note that the matrix $R = \begin{bmatrix} \phi_{Abnormal} & 0 & I & 0 \\ 0 & \phi_{Bbnormal} & 0 & I \end{bmatrix}$

Step 2A	Calculating $a = \left[K_{dyn\ conn}\right][R]$ Multiplying a complex sparse $n_{boundary} \times n_{boundary}$ matrix with a sparse complex $n_{boundary} \times n_a$ matrix	Estimated number of FLOPS: $8 * n_{Aboundary} * n_{bandwidth} * n_{An}$ + $8 * n_{Bboundary} * n_{bandwidth} * n_{Bn}$ + $2 * n_{boundary} * n_{bandwidth}$

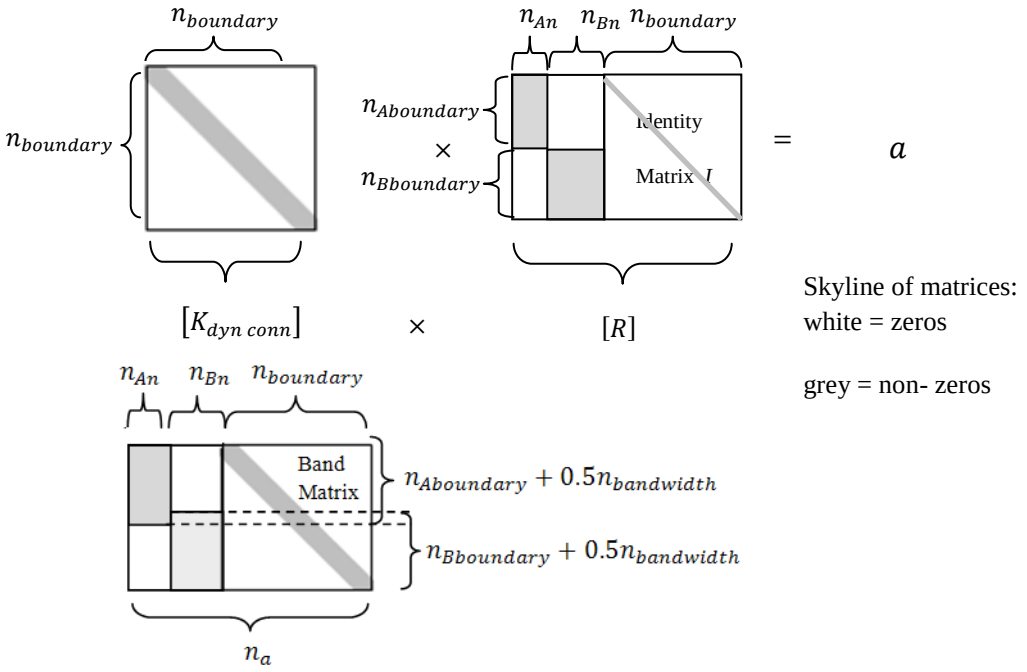

Skyline of matrices:
white = zeros

grey = non- zeros

$n_{boundary}$ is the total number of degrees of freedom of all interface element nodes.
n_a is the total number of retained normal modes and residual flexibility modes of subsystem A and B together
$n_{Aboundary}$ = the number of interface degrees of freedom of substructure A
$n_{Bboundary}$ = the number of interface degrees of freedom of substructure B
n_{An} = the number of retained normal modes of substructure A
n_{Bn} = the number of retained normal modes of substructure B
$n_{bandwidth}$ is the average bandwidth of the Sparse matrix $K_{dyn\ conn}$
f = the number of frequencies analysed. If $\left[K_{dyn\ conn}\right]$ is considered to consist of stiffness and damping only and interface inertia forces are neglected, f is 1 as there is no frequency dependency

Step 2B	Calculating $b = [R^T][K_{dyn\ conn}][R] = R^T a$ a is the result from step 2A Multiplying a complex sparse $n_a \times n_{boundary}$ matrix with a full complex $n_{boundary} \times n_a$ matrix	Estimated number of FLOPS: $8 * n_{Aboundary} * {n_{An}}^2 +$ $8 * (0.5 * n_{bandwidth}) * n_{Bboundary} n_{An} +$ $8 * n_{bandwidth} * n_{Aboundary} n_{An} +$ + $8 * (0.5 * n_{bandwidth}) * n_{Aboundary} n_{Bn} +$ $8 * n_{Bboundary} * {n_{Bn}}^2 +$ $8 * n_{bandwidth} * n_{Bboundary} n_{Bn} +$ + $2 * n_{boundary} * n_{bandwidth}$

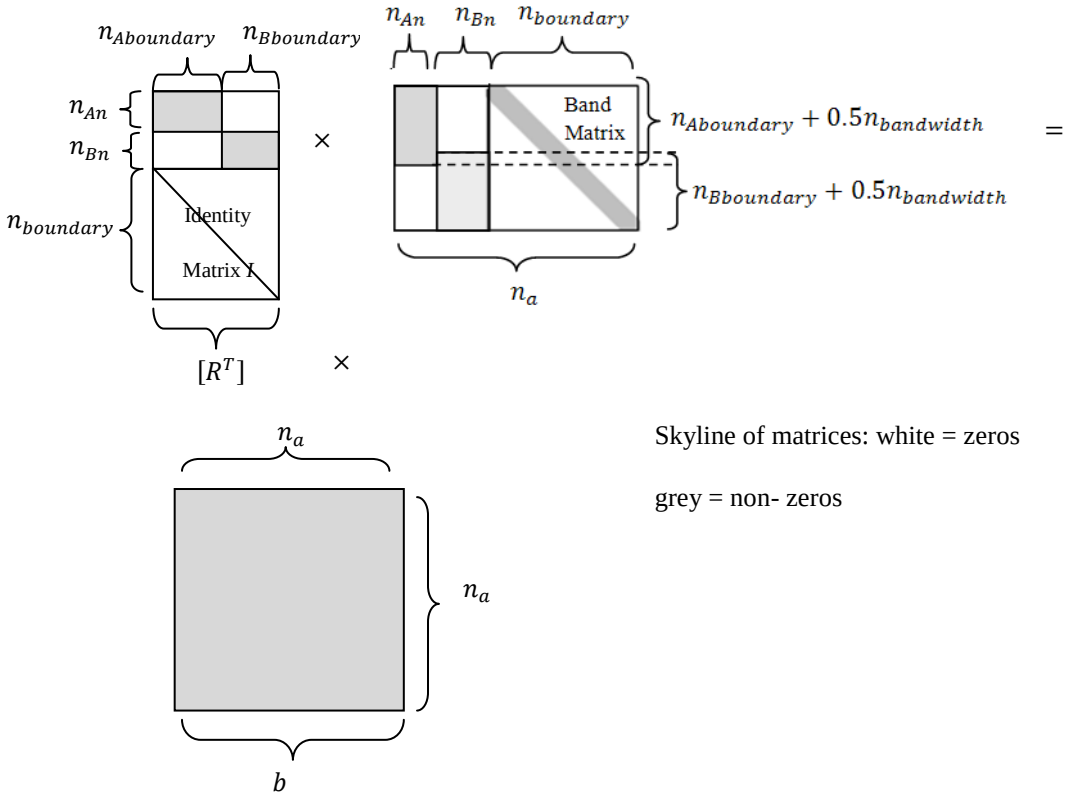

Skyline of matrices: white = zeros

grey = non- zeros

$n_{boundary}$ is the total number of degrees of freedom of all interface element nodes.
n_a is the total number of retained normal modes and residual flexibility modes of subsystem A and B together
n_N is the total number of retained normal modes of subsystem A and B together
$n_{Aboundary}$ = the number of interface degrees of freedom of substructure A
$n_{Bboundary}$ = the number of interface degrees of freedom of substructure B
n_{An} = the number of retained normal modes of substructure A
n_{Bn} = the number of retained normal modes of substructure B
$n_{bandwidth}$ is the average bandwidth of the Sparse matrix $K_{dyn\ conn}$
f = the number of frequencies analysed. If $[K_{dyn\ conn}]$ is considered to consist of stiffness and damping only and interface inertia forces are neglected, f is 1 as there is no frequency dependency

2C	Calculating $$A = -\begin{bmatrix} diag(-\omega^2 + \varepsilon{\omega_0}^2\mathrm{i} + {\omega_0}^2)^{-1} & 0 \\ 0 & G_{resb} \end{bmatrix} b$$ b is the result from step 2B (see equation (8.32)) Multiplying a sparse complex $n_a \times n_a$ matrix with a full complex $n_a \times n_a$ matrix	Estimated number of FLOPS $$2 * f * n_a + 8 * {n_{Aboundary}}^3 + 8 * {n_{Bboundary}}^3$$

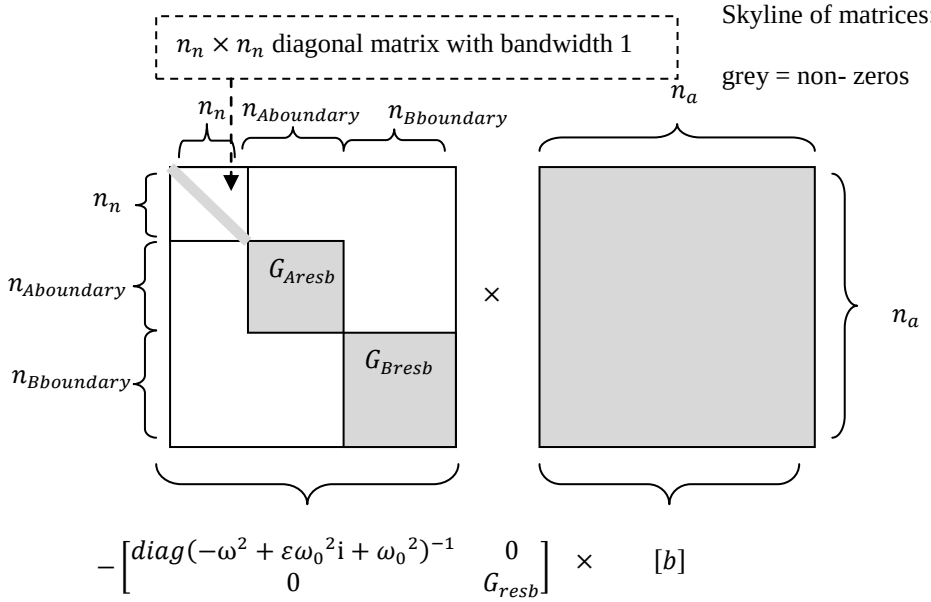

2D	Calculating $[A - I]$ Subtracting a complex $n_a \times n_a$ identity matrix from a full $n_a \times n_a$ matrix	Estimated number of FLOPS: $2 * f * n_a$

$n_{boundary}$ is the total number of degrees of freedom of all interface element nodes.
n_a is the total number of retained normal modes and residual flexibility modes of subsystem A and B together
$n_{Aboundary}$ = the number of interface degrees of freedom of substructure A
$n_{Bboundary}$ = the number of interface degrees of freedom of substructure B
n_{An} = the number of retained normal modes of substructure A
n_{Bn} = the number of retained normal modes of substructure B
n_n= the total number of normal modes for substructure A and B together
f = number of frequencies analysed

Step 3: Calculating α_0

Calculating α_0, modal coordinates representing the response of the uncoupled substructures due external alternating loads acting on the substructures. Only the modal coordinates belonging to the normal modes are calculated and no residual compensation has been taken into account for the uncoupled dynamic behaviour. Therefore (see equation (6.27)):

$$\alpha_0 = [diag(-\omega^2 + \varepsilon {\omega_0}^2 \mathrm{i} + {\omega_0}^2)^{-1}][R^T] f_e$$

Where *R* is the matrix containing the retained eigenvectors representing only the retained normal mode shapes.

Step	Description of action	Estimated number of FLOPS
3A	$a = [R^T] f_e$ Multiplying a full complex $n_n \times n$ matrix with a complex $n \times 1$ vector	$f * 8 * n_f * n_n$
3B	$\alpha_0 = [diag(-\omega^2 + \varepsilon {\omega_0}^2 \mathrm{i} + {\omega_0}^2)^{-1}][R^T] F_e$ $\alpha_0 = [diag(-\omega^2 + \varepsilon {\omega_0}^2 \mathrm{i} + {\omega_0}^2)^{-1}] a$ Where a is the matrix obtained from step 3A Multiplying a complex diagonal $n_n \times n_n$ matrix with a complex sparse $n_n \times 1$ vector	$f * 6 * n_n$

n is the total number of degrees of freedom of the substructure
n_n is the number of retained normal modes
n_f is the number of degrees of freedom subjected to external loads

Step 4: Eliminating Interface Degrees of Freedom

See equation (8.35) to (8.39) in section 8.5

$$\left[\tilde{A}\right] = [A_{aa}] + [A_{au}][A_{uu}]^{-1}[A_{ua}] \quad \text{(step 4F)}$$

And

$$\begin{bmatrix}\tilde{a}_{0A}\\ \tilde{a}_{0B}\end{bmatrix} = -\begin{bmatrix}a_{0A}\\ a_{0B}\end{bmatrix} + [A_{au}][A_{uu}]^{-1}\begin{bmatrix}u_{0Ares}\\ u_{0Bres}\end{bmatrix} \quad \text{(step 4G)}$$

Step	Description of action	Estimated number of FLOPS
4A	Calculating $a = [A_{uu}]^{-1}$ Inverting a full complex $n_{boundary} \times n_{boundary}$ through LU factorisation	$\frac{4}{3} * 8 * {n_{boundary}}^3$
4B	Calculating $b = [A_{uu}]^{-1}[A_{ua}] = a * [A_{ua}]$ Where a is the matrix obtained from step 4A Multiplying a full $n_{boundary} \times n_{boundary}$ matrix with a full $n_{boundary} \times n_n$ matrix	$8 * n_n * {n_{boundary}}^2$
4C	Calculating $c = [A_{uu}]^{-1}\begin{bmatrix}u_{0Ares}\\ u_{0Bres}\end{bmatrix} = a\begin{bmatrix}u_{0Ares}\\ u_{0Bres}\end{bmatrix}$ Where a is the matrix obtained from step 4A Multiplying a full complex $n_{boundary} \times n_{boundary}$ with a complex $n_{boundary} \times 1$ vector	$8 * {n_{boundary}}^2$
4D	$d = [A_{au}][A_{uu}]^{-1}[A_{ua}] = [A_{au}]b$ Where b is the matrix obtained from step 4B Multiplying a full complex $n_n \times n_{boundary}$ with a full $n_{boundary} \times n_n$ complex matrix	$f * 8 * n_{boundary} * {n_n}^2$
4E	$e = [A_{au}][A_{uu}]^{-1}\begin{bmatrix}u_{0Ares}\\ u_{0Bres}\end{bmatrix} = [A_{au}]c$ Where c is the matrix obtained from step 4C Multiplying a full complex $n_n \times n_{boundary}$ matrix with a complex $n_{boundary} \times 1$ vector	$f * 8 * n_{boundary} * n_n$

$n_{boundary}$ is the total number of degrees of freedom of all interface element nodes.
n_n= the total number of normal modes for substructure A and B together
f = number of frequencies analysed

Step	Description of action	Estimated number of FLOPS
4F	Calculating $\tilde{A} = [A_{aa}] + [A_{au}][A_{uu}]^{-1}[A_{ua}] = [A_{aa}] + d$ Where c is the matrix obtained from step 4C Adding a full $n_n \times n_n$ matrix to a full $n_n \times n_n$ matrix	$f * 2 * n_n * n_n$
4G	Calculating $\begin{bmatrix}\tilde{a}_{0A}\\ \tilde{a}_{0B}\end{bmatrix} = -\begin{bmatrix}a_{0A}\\ a_{0B}\end{bmatrix} + [A_{au}][A_{uu}]^{-1}\begin{bmatrix}u_{0Ares}\\ u_{0Bres}\end{bmatrix} = -\begin{bmatrix}a_{0A}\\ a_{0B}\end{bmatrix} + e$ Where e is the matrix obtained from step 4E Adding a n_n vector to an n_n vector	$f * 2 * n_n$
$n_{boundary}$ is the total number of degrees of freedom of all interface element nodes. n_n= the total number of normal modes for substructure A and B together f = number of frequencies analysed		

Step 5: Compiling total matrix:

Adding Pairs of coupled substructures where $\tilde{A}_{AB}$is the boundary mobility matrix through which the interaction between substructure A and B is expressed, and $\tilde{A}_{BC}$ is the boundary mobility matrix through which the interaction between substructure B and C is expressed. $\tilde{A}_{ABC}$ the boundary mobility matrix through which the assembled dynamic behaviour of substructure A, B and C coupled together can be calculated.

5A	$\tilde{A}_{ABc} = \tilde{A}_{AB} + \tilde{A}_{BC}$	$2 * f * n_{BCn} * n_{BCn} + 2 * f * n_{CDn} * n_{CDn} \ldots\ldots + 2 * f * n_{YZn} * n_{YZn}$
$n_{boundary}$ is the total number of degrees of freedom of all interface element nodes. n_n= the total number of normal modes for substructure A and B together f = number of frequencies analysed n_{BCn} = the number of retained normal modes of substructure B and C together n_{CDn} = the number of retained normal modes of substructure C and D together n_{YZn} = the number of retained normal modes of substructure Y and Z together		

Appendix XIX *Steps and Estimated Number of Matrix Operations Rubin-Zoet Method*

Step 1: Calculating constraint modes		
Constraint modes = $\phi^{ci} = -[k^{II}]^{-1}[k^{IB}]$ (according to equation (6.40))		
Step	**Description of action**	**Estimated number of FLOPS**
1A	Calculating $-[k^{II}]^{-1}$ Inverting a $n_i \times n_i$ matrix through LU decomposition	$\frac{4}{3}(n_i(2k+1) - k(k+1))\, n_i$ Where $k = \frac{(n_{bandwidth}-1)}{2}$
1B	Calculating $-[k^{II}]^{-1}[k^{IB}]$ Multiplying a full $n_i \times n_i$ matrix with a sparse $n_i \times n_{boundary}$ matrix	$2 * n_i * n_{boundary} * n_{bandwidth}$
n_i = the number of internal (slave) degrees of freedom of a substructure $n_{boundary}$ = the total number of interface degrees of freedom of the substructure. $n_{bandwidth}$ is the average bandwidth of the sparse diagonal symmetric matrix k^{II}		

Step 2: Generating reduction basis		
Reduction basis $R = \begin{bmatrix} 0 & I \\ [\phi_{ni} - \phi^{ci}\phi_{nb}] & \phi^{ci} \end{bmatrix}$ (according to equation (6.67))		
Step	Description of action	Estimated number of FLOPS
2A	Calculating $a = \phi^{ci}\phi_{nb}$ Multiplying a full $n_i \times n_{boundary}$ matrix with a full $n_{boundary} \times n_n$ matrix	$2 * n_i * n_{boundary} * n_n$
2B	Calculating $\phi_{ni} - \phi^{ci}\phi_{nb} = \phi_{ni} - a$ Where a is obtained from step 2A Subtracting a full $n_i \times n_n$ matrix from a full $n_i \times n_n$ matrix	$n_i * n_n$
n_i = the number of internal (slave) degrees of freedom of a substructure $n_{boundary}$ = the total number of interface degrees of freedom of the substructure. n_n = the number of retained normal modes		

Step 3: Generating Reduced Mass, Stiffness and External Load Matrices

Calculating the reduced stiffness and mass matrix according to $\bar{K}_A = R^T K_A R$ and $\bar{M}_A = R^T M_A R$ according to section 6.5.2.2

Step 3A	Calculating $a = K_A R$ and $M_A R$ Multiplying a sparse $n \times n$ matrix with a sparse $n \times n_a$ matrix. This action needs to be performed twice: once for the mass matrix and once for the stiffness matrix.	Estimated number of FLOPS: $2 * 2 * n_a * n * n_{bandwidth}$

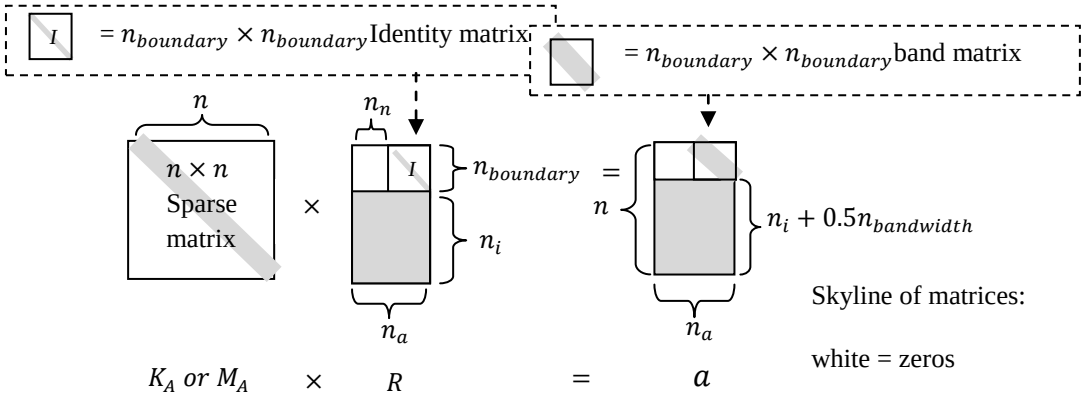

Step 3B	Calculating $\bar{K}_A$ or $\bar{M}_A = R^T K_A R$ or $R^T M_A R = R^T a$ Where a is obtained from step 3A Multiplying a sparse $n_a \times n$ matrix with a full $n \times n_a$ matrix. This action needs to be performed twice: once for the mass matrix and once for the stiffness matrix	Estimated number of FLOPs: $2 * 2 * n_i * n_a * n_n$ + $2 * 2 * (n_i + 1) * n_a * n_{boundary}$

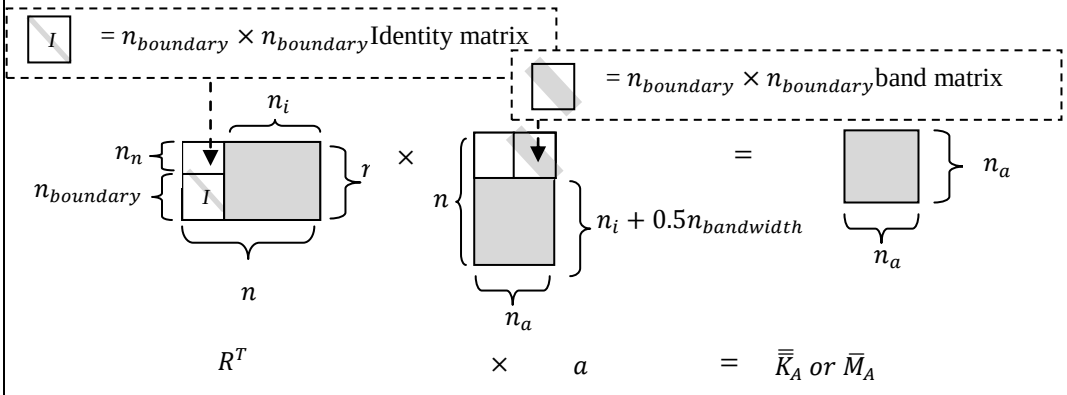

n is the number of degrees of freedom of a substructure
n_a is the number of retained normal modes plus the number of constraint modes (interface degrees of freedom)
$n_{boundary}$ = the total number of interface degrees of freedom of the substructure.
n_n = the number of retained normal modes
$n_{bandwidth}$ is the average bandwidth of the sparse diagonal symmetric matrix $K_A$or M_A
n_i = the number of internal (slave) degrees of freedom of a substructure.

Step 3C	Reducing external load vector: $R^T \begin{bmatrix} F_{bA} \\ F_{eA} \end{bmatrix}$ Multiplying a sparse $n_a \times n$ matrix with a full $n \times 1$ vector	Estimated number of FLOPS: $2 * n_i * n_n$ + $2 * (n_i + 1) * n_{boundary}$

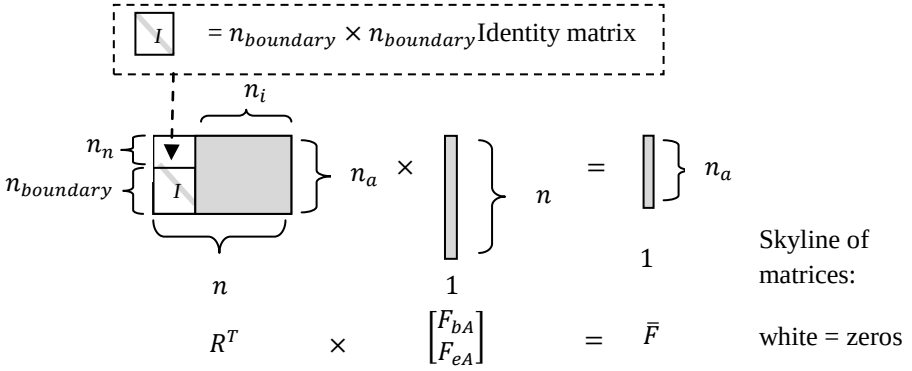

n is the number of degrees of freedom of a substructure
n_a is the number of retained normal modes plus the number of constraint modes (interface degrees of freedom)
$n_{boundary}$ = the total number of interface degrees of freedom of the substructure.
n_n = the number of retained normal modes
n_i = the number of internal (slave) degrees of freedom of a substructure
$n_{bandwidth}$ is the average bandwidth of the sparse diagonal symmetric matrix $K_A$or M_A

Step 4: Generating Reduced Equations of Motion of Coupled Sets of Substructures
(see equations (6.54) to (6.56) section 6.5.1.3)

Calculating $\bar{K}_{AB}$ and $\omega^2\bar{M}_{AB}$

$$\bar{K}_{AB} = \begin{bmatrix} \bar{K}_A & 0 \\ 0 & \bar{K}_B \end{bmatrix} \text{ and } \omega^2\bar{M}_{AB} = \begin{bmatrix} -\omega^2\bar{M}_A & 0 \\ 0 & \omega^2\bar{M}_B \end{bmatrix}$$

Where $\bar{K}$ and $\bar{M}$ are the reduced stiffness and mass matrix of the total assembled structure obtained in step 3. Subscript A and B refers to the fact that the stiffness or mass matrix belongs to substructure A or B

Step	Description of action	Estimated number of FLOPS
4A	Calculating $\omega^2\bar{M}_A$ and $\omega^2\bar{M}_B$ Multiplying $(n_{boundary} + n_{An}) \times (n_{boundary} + n_{An})$ and a $(n_{boundary} + n_{Bn}) \times (n_{boundary} + n_{Bn})$ matrix with a scalar ω^2 (excitation frequency squared)	$f * (n_{boundary} + n_{An}) * (n_{boundary} + n_{An}) + f * (n_{boundary} + n_{Bn}) * (n_{boundary} + n_{Bn})$
4B	Adding $\omega^2\bar{M}_A$ to $\omega^2\bar{M}_B$: Adding two real sparse $(n_{boundary} + n_{An}) \times (n_{boundary} + n_{An})$ matrices.	$f * (n_{boundary} + n_{An}) * (n_{boundary} + n_{An}) + f * (n_{boundary} + n_{Bn}) * (n_{boundary} + n_{Bn})$
4C	Adding $\bar{K}_A$ to $\bar{K}_B$: Adding two real sparse $(n_{boundary} + n_{An}) \times (n_{boundary} + n_{An})$ matrices	$(n_{boundary} + n_{An}) * (n_{boundary} + n_{An}) + (n_{boundary} + n_{Bn}) * (n_{boundary} + n_{Bn})$

n_{An} and n_{Bn}= the number of normal modes of substructure *A* and of substructure *B* respectively
$n_{boundary}$ = number of master (connecting) degrees of freedom between substructure A and B
f = number of frequencies analysed
N = Number of substructures involved

Step 5. Forcing equilibrium and compatibility at the interface degrees of freedom for each pair of coupled substructures:

Calculating
$[L]^T[\overline{K}_{AB} - \overline{K}_{AB}\varepsilon - \omega^2\overline{M}_{AB}][L]$

5A	Calculating $\overline{K}_{AB} - \overline{K}_{AB}\varepsilon - \omega^2\overline{M}_{AB}$	Number of Flops
	$\overline{K}_{AB}\varepsilon$: Multiplying a complex sparse matrix $(2 * n_{boundary} + n_{Ntotal}) \times (2 * n_{boundary} + n_{Ntotal})$ with a scalar ε	$2 * \left(n_{Aboundary} + n_{An}\right)^2 + 2 * \left(n_{Bboundary} + n_{Bn}\right)^2$
	$\omega^2\overline{M}_{AB}$:Multiplying a real sparse matrix $(2 * n_{boundary} + n_{Ntotal}) \times (2 * n_{boundary} + n_{Ntotal})$ with a scalar ω^2	$f * \left(n_{Aboundary} + n_{An}\right)^2 + f * \left(n_{Bboundary} + n_{Bn}\right)^2$
	Calculating $\overline{K}_{AB} - \overline{K}_{AB}\varepsilon - \omega^2\overline{M}_{AB}$	$f * 2 * \left(n_{Aboundary} + n_{An}\right)^2 + f * 2 * \left(n_{Bboundary} + n_{Bn}\right)^2$
Total	$(2 + 3f) * \left(n_{Nboundary} + n_{An}\right)^2 + (2 + 3f) * \left(n_{Nboundary} + n_{Bn}\right)^2$	
5B	Calculating $[\overline{K}_{AB} - \overline{K}_{AB}\varepsilon - \omega^2\overline{M}_{AB}][L]$ Multiplying a sparse complex $n_B \times n_B$ matrix with a real sparse $n_B \times \left(n_{Ntotal} + n_{boundary}\right)$ matrix with bandwidth of 1 Calculating $[L]^T[\overline{K}_{AB} - \overline{K}_{AB}\varepsilon - \omega 2MABL$ Multiplying a real sparse $\left(n_{Ntotal} + n_{boundary}\right) \times n_B$ matrix with a complex sparse $n_B \times \left(n_{Ntotal} + n_{boundary}\right)$ matrix with bandwidth of 1	$4 * f * \left(\left(n_{Aboundary} + n_{An}\right)^2 + \left(n_{Bboundary} + n_{Bn}\right)^2\right)$ + $4 * f * \left(n_{Ntotal} + n_{boundary}\right)^2$

$L^T R^T[F]$

= eliminating redundant interface degrees of freedom and stating that the external force at the retained interface degrees of freedom are zero, so that an equilibrium of forces is obtained

$n_{Aboundary}$ number of interface degrees of freedom of substructure A
$n_{boundary}$ = the total number of master (connecting) degrees of freedom (interface node degrees of freedom) between two adjacent substructures (*A* and *B* in this case)
$n_{An} and\ n_{An}$ are number of retained normal (elastic plus rigid body modes) for substructure A and B respectively
n_{Ntotal} is the total number of normal modes taken into account for all individual substructures A and B added together.
f = number of frequencies analysed
$n_B = (2 * n_{boundary} + n_{Ntotal})$

Step 6: Eliminating the Interface Degrees of Freedom
According to 'The Rubin–Zoet Method' section 8.6

$$[\tilde{A}] = [A_{aa}] + [A_{au}][A_{uu}]^{-1}[A_{ua}] \qquad \text{(step 4F)}$$

And

$$\begin{bmatrix}\tilde{a}_{0A}\\ \tilde{a}_{0B}\end{bmatrix} = -\begin{bmatrix}a_{0A}\\ a_{0B}\end{bmatrix} + [A_{au}][A_{uu}]^{-1}\begin{bmatrix}u_{0Ares}\\ u_{0Bres}\end{bmatrix} \qquad \text{(step 4G)}$$

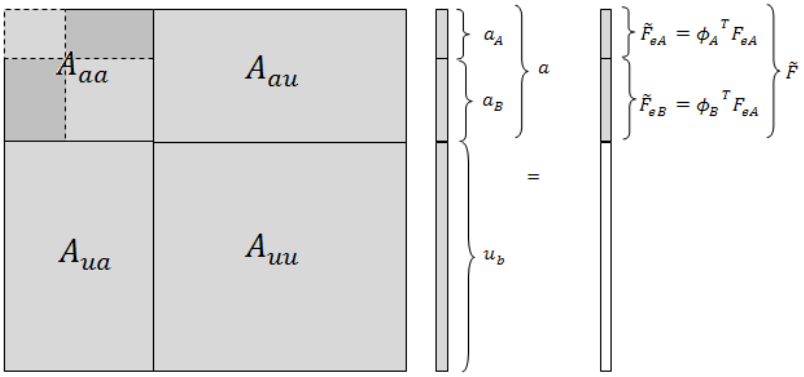

Step	Description of action	Estimated number of FLOPS
6A	Calculating $a = [A_{uu}]^{-1}$ Inverting a full complex $n_{boundary} \times n_{boundary}$ matrix through LU factorisation	$\frac{4}{3} * 8 * n_{boundary}{}^3$
6B	Calculating $b = [A_{uu}]^{-1}[A_{ua}] = a * [A_{ua}]$ Where a is the matrix obtained from step 6A Multiplying a full complex $n_{boundary} \times n_{boundary}$ matrix with a full complex $n_{boundary} \times n_n$ matrix	$n_n * 8 * n_{boundary}{}^2$
6D	$d = [A_{au}][A_{uu}]^{-1}[A_{ua}] = [A_{au}]b$ Where b is the matrix obtained from step 6B Multiplying a full complex $n_n \times n_{boundary}$ with a full complex $n_{boundary} \times n_n$ matrix	$f * 8 * n_{boundary} * n_n{}^2$

$n_{boundary}$ number of interface degrees of freedom
n_n= the total number of normal modes for substructure A and B together
n_{An} and n_{Bn}= the number of normal modes of substructure *A* and of substructure *B* respectively
f = number of frequencies analysed

6F	Calculating $\tilde{A} = [A_{aa}] + [A_{au}][A_{uu}]^{-1}[A_{ua}] = [A_{aa}] + d$ Where c is the matrix obtained from step 4C Adding a full complex $n_n \times n_n$ matrix to a full complex $n_n \times n_n$ matrix	$f * 2 * n_n * n_n$
$n_{boundary}$ number of interface degrees of freedom n_n= the total number of normal modes for substructure A and B together f = number of frequencies analysed		

Step 7: Compiling total matrix:

Adding Pairs of coupled substructures where $\tilde{A}_{AB}$is the boundary stiffness matrix through which the interaction between substructure A and B is expressed, and $\tilde{A}_{BC}$ is the boundary stiffness matrix through which the interaction between substructure B and C is expressed. $\tilde{A}_{ABC}$ the boundary stiffness matrix through which the assembled dynamic behaviour of substructure A, B and C coupled together can be calculated.

7	$\tilde{A}_{ABc} = \tilde{A}_{AB} + \tilde{A}_{BC} \ldots + \tilde{A}_{YZ}$	$f * 2 * n_{BCn} * n_{BCn} + f * 2 * n_{CDn} * n_{CDn} \ldots\ldots + f * 2 * n_{YZn} * n_{YZn}$
$n_{boundary}$ number of interface degrees of freedom n_n= the total number of normal modes for substructure A and B together f = number of frequencies analysed n_{BCn} = the number of retained normal modes of substructure B and C together n_{CDn} = the number of retained normal modes of substructure C and D together n_{YZn} = the number of retained normal modes of substructure Y and Z together		

Appendix XX *Calculation of the Number of FLOPS for Mode Superposition Method on the LNG carrier*

Calculation of required floating point operations is based on retaining mode shapes of the full model with natural frequencies that are within a range between 0 and 1.5* f_{max} Hz, where f_{max} is the upper limit of the frequency range for which simulation results are generated. In this case f_{max} is 40 Hz, which means that the cut-out frequency is 1.5*40=60 Hz. 1668 mode shapes where found to have natural frequencies within that range and are retained. The number of floating point operations has been calculated for 80 frequency steps in the range between 1 and 40 Hz.

Following the steps from Appendix XV:

Mode Superposition: Calcuating the Reduced Stiffness and Mass Matrices			Number of FLOPS
Step 1A	n	366973	2.45E+09
	nn	1668	
	n bandwidth	40	
Step 1B	n	366973	4.90E+10
	nn	1668	
	n bandwidth	40	
Step 1C	n	366973	2.04E+12
	nn	1668	
	n bandwidth	40	
Step 1D	n	366973	9.79E+10
	nn	1668	
	n bandwidth	40	
Step 1E	n	366973	4.08E+12
	nn	1668	
	n bandwidth	40	
Total number of FLOPS			6.28E+12

Summary of required number of floating point operations:

Total structure	Number of equations total assembled matrix	Number of non zeros	calculating Normal Modes and Natural Frequencies		Constraint/Residual Attachment Modes and Reducing Matrices		Total Computation Time Generation Pass	
			CPU	FLOPS	CPU	FLOPS	CPU	FLOPS
full solution	366973	1.49E+07	n.a.	n.a.	n.a.	n.a.	n.a.	n.a.
Mode superposition, f cut-out = 1.5 fmax = 60Hz	1668	2782224	2665	1.24E+14	135	6.28E+12	2.80E+03	1.30E+14

Total structure	Generating Full Assembled Matrix		Solving Full Assembled Matrices		Total Computation Time Use Pass		Total Computation Time Generation plus Use Pass	
	CPU	FLOPS	CPU	FLOPS	CPU	FLOPS	CPU	FLOPS
full solution	20	7.71E+10	7600.0	3.56E+14	7620.0	3.56E+14	7620.0	3.56E+14
Mode superposition, f cut-out = 1.5 fmax = 60Hz	n.a.	n.a.	21	9.92E+11	21	9.92E+11	2821.3	1.31E+14

Brown numbers have been calculated through an estimated relation between measured computation time and number of calculated floating point operation. CPU= CP time

Appendix XXI *Calculation of the Number of FLOPS for Rubin's Method Applied on the LNG Carrier*

In this appendix the calculated number of FLOPS for each sub step is presented applying the free interface CMS method according to Rubin (see section 6.5.2.2). The CMS model of the LNG carrier described in Appendix IX is used. In Appendix XVI the steps required for Rubin's Method are explained.

LNG vessel FE model	Number of nodes	Number of boundary degrees of freedom	Method	Number of modes required*	Required CP for calcuating eigenvectors and eigenvalues	Required time generation pass
PartH	4991	2088	CMS fixed	181	18.5	22.8
			CMS free	257	24.5	52.5
PartG	5680	1536	CMS fixed	373	29.8	40
			CMS free	419	39	100.8
PartF	5680	1536	CMS fixed	373	29.8	40
			CMS free	419	39	100.8
PartE	8933	7188	CMS fixed	213	30	46.6
			CMS free	323	61	174
PartD	9833	6198	CMS fixed	162	29.14	53.6
			CMS free	336	95	328
PartC	11965	5124	CMS fixed	195	38.11	68.13
			CMS free	335	75	225.7
PartB	10044	3798	CMS fixed	138	29.4	47.7
			CMS free	231	53	138.3
PartA	6612	1578	CMS fixed	91	18.8	25.4
			CMS free	154	24.6	53.3

Fixed and free CMS is CMS based on the fixed interface approach (Craig-Bampton) and the free interface approach (Rubin's method without residual compensation) respectively.

For all methods a cut-out frequency of 1.5* f_{max} Hz (=60 Hz) has been applied for the selection of the number of normal modes.

The number of floating point operations has been calculated producing 80 output sets for frequencies evenly distributed range between 1 and 40 Hz.

Step 1: Generating constraint modes			Step 1A	Step 1B
PartH	ni	27858	4.14E+10	4.65E+09
	n boundary	2088		
PartG	ni	32544	5.65E+10	4.00E+09
	n boundary	1536		
PartF	ni	32544	5.65E+10	4.00E+09
	n boundary	1536		
PartE	ni	46410	1.15E+11	2.67E+10
	n boundary	7188		
PartD	ni	52800	1.49E+11	2.62E+10
	n boundary	6198		
PartC	ni	66666	2.37E+11	2.73E+10
	n boundary	5124		
PartB	ni	56467	1.70E+11	1.72E+10
	n boundary	3798		
PartA	ni	38097	7.74E+10	4.81E+09
	n boundary	1578		
Total number of FLOPS for each step			9.02E+11	1.15E+11
Grand total for calcuating all required constraint modes (Step 1)				1.02E+12

Calculated required number of FLOPS for each sub step of step 1 (see Appendix XVI for explanation of sub steps and symbols). The number of floating point operations has been calculated producing 80 output sets for frequencies evenly distributed range between 1 and 40 Hz.

Step 2: Generating the reduction basis			Step 2A	Step 2B
PartH	ni	27858	2.99E+10	7.16E+06
	n boundary	2088		
	nn	257		
PartG	ni	32544	4.19E+10	1.36E+07
	n boundary	1536		
	nn	419		
PartF	ni	32544	4.19E+10	1.36E+07
	n boundary	1536		
	nn	419		
PartE	ni	46410	2.16E+11	1.50E+07
	n boundary	7188		
	nn	323		
PartD	ni	52800	2.20E+11	1.77E+07
	n boundary	6198		
	nn	336		
PartC	ni	66666	2.29E+11	2.23E+07
	n boundary	5124		
	nn	335		
PartB	ni	56467	9.91E+10	1.30E+07
	n boundary	3798		
	nn	231		
PartA	ni	38097	1.85E+10	5.87E+06
	n boundary	1578		
	nn	154		
Total number of FLOPS for each step			8.96E+11	1.08E+08
Grand total for calculating step 2				8.96E+11

Calculated required number of FLOPS for each sub step of step 2 (see Appendix XVI for explanation of sub steps and symbols). The number of floating point operations has been calculated producing 80 output sets for frequencies evenly distributed range between 1 and 40 Hz.

			Step 3			Step 4	
Step 3: Generating reduced mass and stiffness			Step 3A	Step 3B	Step 3C	Step 4A	Step 4B
PartH	n	29946	1.29E+10	6.13E+11	1.31E+08	1.65E+07	1.65E+07
	nn	257					
	nbandwidth	46					
	na	2345					
	n boundary	2088					
	ni	27858					
PartG	n	34080	1.23E+10	4.98E+11	1.27E+08	1.15E+07	1.15E+07
	nn	419					
	nbandwidth	46					
	na	1955					
	n boundary	1536					
	ni	32544					
PartF	n	34080	1.23E+10	4.98E+11	1.27E+08	1.15E+07	1.15E+07
	nn	419					
	nbandwidth	46					
	na	1955					
	n boundary	1536					
	ni	32544					
PartE	n	53598	7.41E+10	1.05E+13	6.97E+08	1.69E+08	1.69E+08
	nn	323					
	nbandwidth	46					
	na	7511					
	n boundary	7188					
	ni	46410					
PartD	n	58998	7.09E+10	9.02E+12	6.90E+08	1.28E+08	1.28E+08
	nn	336					
	nbandwidth	46					
	na	6534					
	n boundary	6198					
	ni	52800					
PartC	n	71790	7.21E+10	7.95E+12	7.28E+08	8.94E+07	8.94E+07
	nn	335					
	nbandwidth	46					
	na	5459					
	n boundary	5124					
	ni	66666					
PartB	n	60265	4.47E+10	3.67E+12	4.55E+08	4.87E+07	4.87E+07
	nn	231					
	nbandwidth	46					
	na	4029					
	n boundary	3798					
	ni	56467					
PartA	n	39675	1.26E+10	4.57E+11	1.32E+08	9.00E+06	9.00E+06
	nn	154					
	nbandwidth	46					
	na	1732					
	n boundary	1578					
	ni	38097					
Total number of FLOPS for each step			3.12E+11	3.32E+13	3.09E+09	4.84E+08	4.84E+08
Grand total for generating reduced matrices					3.35E+13	9.68E+08	

Forcing compatibility and equilibrium relations			Step 5A	Step 5B	Step 5C
	nB	31520	3.05E+09	3.05E+09	6.23E+10
	n Ntotal+n b	16118			
Grand total FLOPS for forcing compatibility and equilib			6.84E+10		

Calculated required number of FLOPS for each step 3 to step 5

Total structure	Number of equations total assembled matrix	Number of non zeros	calculating Normal Modes and Natural Frequencies		Constraint/Residual Attachment Modes and Reducing Matrices		Total Computation Time Generation Pass	
			CP Time	FLOPS	CP Time	FLOPS	CP Time	FLOPS
full solution	366973	1.49E+07	n.a.	n.a.	n.a.	n.a.	n.a.	n.a.
Mode superposition, f cut-out = 1.5 fmax = 60Hz	1668	2782224	2665	1.24E+14	135	6.28E+12	2.80E+03	1.30E+14
fixed interface CMS (Craig-Bampton), f cut-out = 1.5 fmax = 60Hz	15370	1.25E+08	223.55	1.04E+13	121	5.60E+12	344.2	1.60E+13
free interface CMS (Rubin's Method), f cut-out = 1.5 fmax = 60Hz	16118	1.34E+08	411.1	1.91E+13	762	3.54E+13	1173.4	5.45E+13

Generation pass: Table of CP times and numbers of floating point operation. *Black numbers have been directly measured (CP time) or calculated (FLOPS). Brown numbers have been calculated through an estimated relation between measured computation time and number of calculated floating point operation.*

Total structure	Generating Full Assembled Matrix		Solving Full Assembled Matrices		Total Computation Time Use Pass	
	CP Time	FLOPS	CP Time	FLOPS	CP Time	FLOPS
full solution	20	7.71E+10	7600.0	3.56E+14	7620.0	3.56E+14
Mode superposition, f cut-out = 1.5 fmax = 60Hz	n.a.	n.a.	21	9.92E+11	21	9.92E+11
fixed interface CMS (Craig-Bampton), f cut-out = 1.5 fmax = 60Hz	18	6.94E+10	12960.0	5.32E+14	13322.2	5.32E+14
free interface CMS (Rubin's Method), f cut-out = 1.5 fmax = 60Hz	18	6.94E+10	11360.0	5.32E+14	12551.4	5.32E+14

Use pass: Table of CP times and numbers of floating point operation. *Black numbers have been directly measured (CP time) or calculated (FLOPS). Brown numbers have been calculated through an estimated relation between measured computation time and number of calculated floating point operation.*

Total structure	Total Computation Time Generation plus Use Pass	
	CP Time	FLOPS
full solution	7620.0	3.56E+14
Mode superposition, f cut-out = 1.5 fmax = 60Hz	2821.3	1.31E+14
fixed interface CMS (Craig-Bampton), f cut-out = 1.5 fmax = 60Hz	13666.5	5.48E+14
free interface CMS (Rubin's Method), f cut-out = 1.5 fmax = 60Hz	13724.8	5.87E+14

Total number CP and FLOPS for total analysis. *Black numbers have been directly measured (CP time) or calculated (FLOPS). Brown numbers have been calculated through an estimated relation between measured computation time and number of calculated floating point operation.*

variable	number of rows	Number of Columns																			
		1578	2220	2904	3936	780	660	1122	138	180	126	154	231	335	336	323	419	419	257
Ub AB	1578	2.49E+06	3.50E+06									2.43E+05	3.65E+05						
Ub BC	2220	3.50E+06	4.93E+06	6.45E+06								3.42E+05	5.13E+05	7.44E+05					
Ub CD	2904		6.45E+06	8.43E+06	1.14E+07								6.71E+05	9.73E+05	9.76E+05				
Ub DE	3936			1.14E+07	1.55E+07	3.07E+06	2.60E+06	4.42E+06						1.32E+06	1.32E+06	1.27E+06			
Ub EF	780				3.07E+06	6.08E+05	5.15E+05	8.75E+05	1.08E+05	1.40E+05	9.83E+04				2.62E+05	2.52E+05	3.27E+05	3.27E+05	2.00E+05
Ub EG	660				2.60E+06	5.15E+05	4.36E+05	7.41E+05	9.11E+04	1.19E+05	8.32E+04				2.22E+05	2.13E+05	2.77E+05	2.77E+05	1.70E+05
Ub EH	1122				4.42E+06	8.75E+05	7.41E+05	1.26E+06	1.55E+05	2.02E+05	1.41E+05				3.77E+05	3.62E+05	4.70E+05	4.70E+05	2.88E+05
Ub FG	138				5.43E+05	1.08E+05	9.11E+04	1.55E+05	1.90E+04	2.48E+04	1.74E+04				4.64E+04	4.46E+04	5.78E+04	5.78E+04	3.55E+04
Ub FH	180				7.08E+05	1.40E+05	1.19E+05	2.02E+05	2.48E+04	3.24E+04	2.27E+04				6.05E+04	5.81E+04	7.54E+04	7.54E+04	4.63E+04
Ub GH	126				4.96E+05	9.83E+04	8.32E+04	1.41E+05	1.74E+04	2.27E+04	1.59E+04				4.23E+04	4.07E+04	5.28E+04	5.28E+04	3.24E+04
aA	154	2.43E+05	3.42E+05									2.37E+04							
aB	231	3.65E+05	5.13E+05	6.71E+05									5.34E+04						
aC	335		7.44E+05	9.73E+05	1.32E+06	2.62E+05	2.22E+05	3.77E+05	4.64E+04	6.05E+04	4.23E+04			1.12E+05					
aD	336			9.76E+05	1.32E+06	2.52E+05	2.13E+05	3.62E+05	4.46E+04	5.81E+04	4.07E+04				1.13E+05				
aE	323				1.27E+06	2.52E+05	2.13E+05	3.62E+05	4.46E+04	5.81E+04	4.07E+04					1.04E+05			
aF	419					3.27E+05	2.77E+05	4.70E+05	5.78E+04	7.54E+04	5.28E+04						1.76E+05		
aG	419					3.27E+05	2.77E+05	4.70E+05	5.78E+04	7.54E+04	5.28E+04							1.76E+05	
aH	257					2.00E+05	1.70E+05	2.88E+05	3.55E+04	4.63E+04	3.24E+04								6.60E+04

Skyline of matrix representing the dynamic stiffness of the total assembled structure composed according to Rubin's Method as applied in ANSYS. Coloured cells are full matrix sections. The numbers in the coloured cells show the number of non zeros in these sections.

Rubin's Method		
number of frequencies		80
Generation Pass		
Step number	Action	Estimated FLOPS
Calcuating natural frequencies and mode shapes		1.91E+13
1	Generating constraint modes	1.02E+12
2	Generating reduction basis	8.96E+11
3	Generating Reduced mass and stiffness	3.35E+13
Total Flops Generation Pass		5.45E+13

Use Pass		
Step number	Action	Estimated FLOPS
4	Compiling reduced dynamic stiffness	9.68E+08
5	Formulating compatibility and	6.84E+10
6	Solving the matrix equations	Sparse matrix approach
a.	Row reduction forward phase	5.32E+14
b.	Row reduction backward phase	6.24E+10
c.	Solving triangular matrix	4.16E+10
Total FLOPS Use Pass		5.32E+14

Grand total	5.87E+14

All modeshapes have been selected with the natural frequencies within the range between 0 and 1.5×fmax
The fmax is the highest frequency in the frequency range for which results have been obtained (= 40 Hz in this case)
Fmax in this case = 40 Hz, modeshapes have been selected over a frequency range between 0 and 60 Hz

Summary of required number of FLOPS for each step for the Rubin Method. The number of floating point operations has been calculated producing 80 output sets for frequencies evenly distributed range between 1 and 40 Hz.

Appendix XXII *Required Number of Flops for Application of the Zoet Method on the CMS Model of the LNG Carrier*

In this appendix the calculated number of FLOPS for each sub step is presented applying the Zoet method according to section 8 for the CMS model of the LNG carrier described in Appendix IX.

LNG vessel FE model	Number of nodes	Number of boundary nodes		Number of boundary degrees of freedom	Method	Number of modes required*	Required CP for calcuating eigenvectors and eigenvalues	Required time generation pass
PartH	4991	Boundary H-E	298	2088	CMS fixed	181	18.5	22.8
		Boundary H-G	86		CMS free	257	24.5	52.5
		Boundary H-F	86		Zoet (frequency range to 1.5×f max)	257	24.5	52.5
PartG	5680	Boundary G-H	86	1536	CMS fixed	373	29.8	40
		Boundary G-F	57		CMS free	419	39	100.8
		Boundary G-E	205		Zoet (frequency range to 1.5×f max)	419	39	100.8
PartF	5680	Boundary F-G	57	1536	CMS fixed	373	29.8	40
		Boundary F-H	86		CMS free	419	39	100.8
		Boundary F-E	205		Zoet (frequency range to 1.5×f max)	419	39	100.8
PartE	8933	Boundary E-H	298	7188	CMS fixed	213	30	46.6
		Boundary E-G	205		CMS free	323	61	174
		Boundary E-F	205		Zoet (frequency range to 1.5×f max)	323	61	174
PartD	9833	Boundary D-E	656	6198	CMS fixed	162	29.14	53.6
		Boundary D-C	484		CMS free	336	95	328
					Zoet (frequency range to 1.5×f max)	336	95	328
PartC	11965	Boundary C-D	484	5124	CMS fixed	195	38.11	68.13
		Boundary C-B	370		CMS free	335	75	225.7
					Zoet (frequency range to 1.5×f max)	335	75	225.7
PartB	10044	Boundary B-C	370	3798	CMS fixed	138	29.4	47.7
		Boundary B-A	263		CMS free	231	53	138.3
					Zoet (frequency range to 1.5×f max)	231	53	138.3
PartA	6612	Boundary A-B	263	1578	CMS fixed	91	18.8	25.4
					CMS free	154	24.6	53.3
					Zoet (frequency range to 1.5×f max)	154	24.6	53.3

Fixed and free CMS is CMS based on the fixed interface approach (Craig-Bampton) and the free interface approach (Rubin's method without residual compensation) respectively.

For all methods a cut-out frequency of 1.5* f_{max} Hz (=60 Hz) has been applied for the selection of the number of normal modes.

The number of floating point operations has been calculated producing 80 output sets for frequencies evenly distributed range between 1 and 40 Hz.

Step 2: Formulating the boundary mobility matrix				Step 2A	Step 2B	Step 2C	Step 2D
Part H-F		nAboundary	516	1.20E+08	1.16E+09	7.31E+07	1.08E+05
		nBboundary	516				
		nboundary	1032				
		nAn	257				
		nBn	419				
		na	1708				
		nn	676				
Part H-G		nAboundary	516	1.20E+08	1.16E+09	7.31E+07	1.08E+05
		nBboundary	516				
		nboundary	1032				
		nAn	257				
		nBn	419				
		na	1708				
		nn	676				
Part H-E		nAboundary	1788	3.55E+08	2.94E+09	5.38E+07	9.28E+04
		nBboundary	1788				
		nboundary	3576				
		nAn	257				
		nBn	323				
		na	4156				
		nn	580				
Part G-F		nAboundary	342	9.74E+07	1.10E+09	1.12E+08	1.34E+05
		nBboundary	342				
		nboundary	684				
		nAn	419				
		nBn	419				
		na	1522				
		nn	838				
Part G-E		nAboundary	1230	3.08E+08	3.23E+09	8.81E+07	1.19E+05
		nBboundary	1230				
		nboundary	2460				
		nAn	419				
		nBn	323				
		na	3202				
		nn	742				

Part I of Step 2 for Zoet method with no residual interface flexibility taken into account. The interface in this case is again the interface between two structures. The number of floating point operations has been calculated producing 80 output sets for frequencies evenly distributed range between 1 and 40 Hz.

Step 2: Formulating the boundary mobility matrix				Step 2A	Step 2B	Step 2C	Step 2D
Part F-E		nAboundary	1230	3.08E+08	3.23E+09	8.81E+07	1.19E+05
		nBboundary	1230				
		nboundary	2460				
		nAn	419				
		nBn	323				
		na	3202				
		nn	742				
Part E-D		nAboundary	3936	8.83E+08	8.13E+09	6.95E+07	1.05E+05
		nBboundary	3936				
		nboundary	7872				
		nAn	323				
		nBn	336				
		na	8531				
		nn	659				
Part D-C		nAboundary	2904	6.62E+08	6.20E+09	7.20E+07	1.07E+05
		nBboundary	2904				
		nboundary	5808				
		nAn	336				
		nBn	335				
		na	6479				
		nn	671				
Part C-B		nAboundary	2220	4.23E+08	3.60E+09	5.13E+07	9.06E+04
		nBboundary	2220				
		nboundary	4440				
		nAn	335				
		nBn	231				
		na	5006				
		nn	566				
Part B-A		nAboundary	1578	2.04E+08	1.29E+09	2.37E+07	6.16E+04
		nBboundary	1578				
		nboundary	3156				
		nAn	231				
		nBn	154				
		na	3541				
		nn	385				
Total FLOPS for substeps				3.48E+09	3.20E+10	7.05E+08	1.05E+06
Grand total FLOPS for step 2							3.62E+10

Part II of Step 2 for Zoet method with no residual boundary flexibility taken into account. The boundary in this case is the interface between two structures. The number of floating point operations has been calculated producing 80 output sets for frequencies evenly distributed range between 1 and 40 Hz.

Step 1: Generating residual compensation modes			Step 1A	Step 1B	Step 1C	Step 1D	Step 1E	Step 1F
PartH	nc	29946	1.09E+11					
	k	6						
	n boundary	2088						
	nbandwidth	40						
PartG	nc	34074	1.41E+11	1.39E+10	92882998080	34074	3.56671E+12	1.60781E+11
	k	6						
		1536						
	nbandwidth	40						
PartF	nc	34074	1.41E+11	1.39E+10	92882998080	34074	3.56671E+12	1.60781E+11
	k	6						
		1536						
	nbandwidth	40						
PartE	nc	53592	3.48E+11	3.45E+10	2.29768E+11	53592	4.12893E+13	5.53791E+12
	k	6						
		7188						
	nbandwidth	40						
PartD	nc	58992	4.22E+11	4.18E+10	2.78404E+11	58992	4.31388E+13	4.53238E+12
	k	6						
		6198						
	nbandwidth	40						
PartC	nc	71784	6.25E+11	6.18E+10	4.12235E+11	71784	5.28074E+13	3.76943E+12
	k	6						
		5124						
	nbandwidth	40						
PartB	nc	60258	4.41E+11	4.36E+10	2.90482E+11	60258	2.75813E+13	1.73842E+12
	k	6						
		3798						
	nbandwidth	40						
PartA	nc	39669	1.91E+11	1.89E+10	1.2589E+11	39669	4.96637E+12	1.97558E+11
	k	6						
		1578						
	nbandwidth	40						
Total number of FLOPS for each step			2.42E+12	2.28E+11	1.52E+12	3.52E+05	1.77E+14	1.61E+13
Grand total for calcuating all required constraint			1.97E+14					

Part I of Step 1 in case residual boundary flexibility is taken into account. The boundary in this case is the interface between two structures. The number of floating point operations has been calculated producing 80 output sets for frequencies evenly distributed range between 1 and 40 Hz.

Step 1: Generating residual compensation modes				Step 1G	Step 1H	Step 1I
Part H-F	Boundary H-F	ne	257	1.33E+05	1.37E+08	2.66E+05
		nboundary	516			
	Boundary F-H	ne	419	2.16E+05	2.23E+08	2.66E+05
		nboundary	516			
Part H-G	Boundary H-G	ne	257	1.33E+05	1.37E+08	2.66E+05
		nboundary	516			
	Boundary G-H	ne	419	2.16E+05	2.23E+08	2.66E+05
		nboundary	516			
Part H-E	Boundary H-E	ne	257	4.60E+05	1.64E+09	3.20E+06
		nboundary	1788			
	Boundary E-H	ne	323	5.78E+05	2.07E+09	3.20E+06
		nboundary	1788			
Part G-F	Boundary G-F	ne	419	1.43E+05	9.80E+07	1.17E+05
		nboundary	342			
	Boundary F-G	ne	419	1.43E+05	9.80E+07	1.17E+05
		nboundary	342			
Part G-E	Boundary G-E	ne	419	5.15E+05	1.27E+09	1.51E+06
		nboundary	1230			
	Boundary E-G	ne	323	3.97E+05	9.77E+08	1.51E+06
		nboundary	1230			
Part F-E	Boundary F-E	ne	419	5.15E+05	1.27E+09	1.51E+06
		nboundary	1230			
		ne	323	3.97E+05	9.77E+08	1.51E+06
		nboundary	1230			
Part E-D	Boundary E-D	ne	323	1.27E+06	1.00E+10	1.55E+07
		nboundary	3936			
	Boundary D-E	ne	336	1.32E+06	1.04E+10	1.55E+07
		nboundary	3936			
Part D-C	Boundary D-C	ne	336	9.76E+05	5.67E+09	8.43E+06
		nboundary	2904			
	Boundary C-D	ne	335	9.73E+05	5.65E+09	8.43E+06
		nboundary	2904			
Part C-B	Boundary C-B	ne	335	7.44E+05	3.30E+09	4.93E+06
		nboundary	2220			
		ne	231	5.13E+05	2.28E+09	4.93E+06
		nboundary	2220			
Part B-A	Boundary B-A	ne	231	3.65E+05	1.15E+09	2.49E+06
		nboundary	1578			
		ne	154	2.43E+05	7.67E+08	2.49E+06
		nboundary	1578			
				1.03E+07	4.83E+10	7.64E+07
						4.84E+10

Part II of Step 1 in case residual boundary flexibility is taken into account. The number of floating point operations has been calculated producing 80 output sets for frequencies evenly distributed range between 1 and 40 Hz.

Step 2: Formulating the boundary mobility matrix				Step 2A	Step 2B	Step 2C	Step 2D
Part H-F		nAboundary	516	1.27E+08	1.17E+09	7.46E+09	2.73E+05
		nBboundary	516				
		nboundary	1032				
		nAn	257				
		nBn	419				
		na	1708				
		nn	676				
Part H-G		nAboundary	516	1.27E+08	1.17E+09	7.46E+09	2.73E+05
		nBboundary	516				
		nboundary	1032				
		nAn	257				
		nBn	419				
		na	1708				
		nn	676				
Part H-E		nAboundary	1788	4.32E+08	2.96E+09	2.13E+11	6.65E+05
		nBboundary	1788				
		nboundary	3576				
		nAn	257				
		nBn	323				
		na	4156				
		nn	580				
Part G-F		nAboundary	342	1.00E+08	1.10E+09	3.05E+09	2.44E+05
		nBboundary	342				
		nboundary	684				
		nAn	419				
		nBn	419				
		na	1522				
		nn	838				
Part G-E		nAboundary	1230	3.44E+08	3.20E+09	7.79E+10	5.12E+05
		nBboundary	1230				
		nboundary	2460				
		nAn	419				
		nBn	323				
		na	3202				
		nn	742				

Part I of Step 2 for Zoet method with residual boundary flexibility taken into account. The number of floating point operations has been calculated producing 80 output sets for frequencies evenly distributed range between 1 and 40 Hz.

Step 2: Formulating the boundary mobility matrix				Step 2A	Step 2B	Step 2C	Step 2D
Part F-E		nAboundary	1230	3.44E+08	3.20E+09	7.79E+10	5.12E+05
		nBboundary	1230				
		nboundary	2460				
		nAn	419				
		nBn	323				
		na	3202				
		nn	742				
Part E-D		nAboundary	3936	1.25E+09	8.21E+09	2.12E+12	1.36E+06
		nBboundary	3936				
		nboundary	7872				
		nAn	323				
		nBn	336				
		na	8531				
		nn	659				
Part D-C		nAboundary	2904	8.65E+08	6.23E+09	8.75E+11	1.04E+06
		nBboundary	2904				
		nboundary	5808				
		nAn	336				
		nBn	335				
		na	6479				
		nn	671				
Part C-B		nAboundary	2220	5.41E+08	3.58E+09	3.95E+11	8.01E+05
		nBboundary	2220				
		nboundary	4440				
		nAn	335				
		nBn	231				
		na	5006				
		nn	566				
Part B-A		nAboundary	1578	2.64E+08	1.28E+09	1.41E+11	5.67E+05
		nBboundary	1578				
		nboundary	3156				
		nAn	231				
		nBn	154				
		na	3541				
		nn	385				
Total substep				4.40E+09	3.21E+10	3.91E+12	6.25E+06
Grand total step 2							3.95E+12

Part II of Step 2 for Zoet method with residual boundary flexibility taken into account. The number of floating point operations has been calculated producing 80 output sets for frequencies evenly distributed range between 1 and 40 Hz.

Step 4: Eliminating Boundary Degrees of Freedom			Step 4A	Step 4B	Step 4C	Step 4D	Step 4E	Step 4F	Step 4G	Step 5 Composing Total
Part H-F	n boundary	1032	1.17E+10	5.76E+09	8.52E+06	3.02E+11	4.46E+08	7.31E+07	1.08E+05	
	nn	676								
Part H-G	n boundary	1032	1.17E+10	5.76E+09	8.52E+06	3.02E+11	4.46E+08	7.31E+07	1.08E+05	7.31E+07
	nn	676								
Part H-E	n boundary	3576	4.88E+11	5.93E+10	1.02E+08	7.70E+11	1.33E+09	5.38E+07	9.28E+04	5.38E+07
	nn	580								
Part G-F	n boundary	684	3.41E+09	3.14E+09	3.74E+06	3.07E+11	3.67E+08	1.12E+08	1.34E+05	1.12E+08
	nn	838								
Part G-E	n boundary	2460	1.59E+11	3.59E+10	4.84E+07	8.67E+11	1.17E+09	8.81E+07	1.19E+05	8.81E+07
	nn	742								
Part F-E	n boundary	2460	1.59E+11	3.59E+10	4.84E+07	8.67E+11	1.17E+09	8.81E+07	1.19E+05	8.81E+07
	nn	742								
Part E-D	n boundary	7872	5.20E+12	3.27E+11	4.96E+08	2.19E+12	3.32E+09	6.95E+07	1.05E+05	6.95E+07
	nn	659								
Part D-C	n boundary	5808	2.09E+12	1.81E+11	2.70E+08	1.67E+12	2.49E+09	7.20E+07	1.07E+05	7.20E+07
	nn	671								
Part C-B	n boundary	4440	9.34E+11	8.93E+10	1.58E+08	9.10E+11	1.61E+09	5.13E+07	9.06E+04	5.13E+07
	nn	566								
Part B-A	n boundary	3156	3.35E+11	3.07E+10	7.97E+07	2.99E+11	7.78E+08	2.37E+07	6.16E+04	2.37E+07
	nn	385								
	Total FLOPS for sub steps		9.39E+12	7.74E+11	1.22E+09	8.49E+12	1.31E+10	7.05E+08	1.05E+06	6.32E+08
	Grand Total FLOPS for Step 4 and 5									1.87E+13

Eliminating interface degrees of freedom from the super elements. (see section 8.5.2). The boundary is in this case the interface between two substructures. The number of floating point operations has been calculated producing 80 output sets for frequencies evenly distributed range between 1 and 40 Hz.

Total structure	Number of equations total assembled matrix	Number of non zeros	calculating Normal Modes and Natural Frequencies		Constraint/Residual Attachment Modes and Reducing Matrices		Total Computation Time Generation Pass	
			CP Time	FLOPS	CP Time	FLOPS	CP Time	FLOPS
full solution	366973	1.49E+07	n.a.	n.a.	n.a.	n.a.	n.a.	n.a.
Mode superposition, f cut-out = 1.5 fmax = 60Hz	1668	2782224	2665	1.24E+14	135	6.28E+12	2.80E+03	1.30E+14
fixed interface CMS (Craig-Bampton), f cut-out = 1.5 fmax = 60Hz	15370	1.25E+08	223.55	1.04E+13	121	5.60E+12	344.2	1.60E+13
free interface CMS (Rubin's Method), f cut-out = 1.5 fmax = 60Hz	16118	1.34E+08	411.1	1.91E+13	762	3.54E+13	1173.4	5.45E+13
Zoet method cut-out frequency 1.5×f max =60 Hz	2474	2.98E+06	411.1	1.91E+13	1	3.62E+10	411.9	1.91E+13
Zoet method cut-out frequency 1.5×f max =60 Hz, **with** residual boundary flex	2474	2.98E+06	411.1	1.91E+13	4.73E+03	2.20E+14	5145.8	2.39E+14

Generation pass: Table of CP times and numbers of floating point operation. *Black numbers have been directly measured (CP time) or calculated (FLOPS). Brown numbers have been calculated through an estimated relation between measured computation time and number of calculated floating point operation.*

Total structure	Generating Full Assembled Matrix		Solving Full Assembled Matrices		Total Computation Time Use Pass	
	CP Time	FLOPS	CP Time	FLOPS	CP Time	FLOPS
full solution	20	7.71E+10	7600.0	3.56E+14	7620.0	3.56E+14
Mode superposition, f cut-out = 1.5 fmax = 60Hz	n.a.	n.a.	21	9.92E+11	21	9.92E+11
fixed interface CMS (Craig-Bampton), f cut-out = 1.5 fmax = 60Hz	18	6.94E+10	12960.0	5.32E+14	13322.2	5.32E+14
free interface CMS (Rubin's Method), f cut-out = 1.5 fmax = 60Hz	18	6.94E+10	11360.0	5.32E+14	12551.4	5.32E+14
Zoet method cut-out frequency 1.5×f max =60 Hz	0.16	6.32E+08	16.2	7.59E+11	428.2	7.60E+11
Zoet method cut-out frequency 1.5×f max =60 Hz, **with** residual boundary flex	0.16	6.32E+08	27.5	1.29E+12	5173.5	1.29E+12

Use pass: Table of estimated CP time (CPU) and numbers of floating point operation. *Black numbers have been directly measured (CP time) or calculated (FLOPS). Brown numbers have been calculated through an estimated relation between measured computation time and number of calculated floating point operation.*

Total structure	Total Computation Time Generation plus Use Pass	
	CP Time	FLOPS
full solution	7620.0	3.56E+14
Mode superposition, f cut-out = 1.5 fmax = 60Hz	2821.3	1.31E+14
fixed interface CMS (Craig-Bampton), f cut-out = 1.5 fmax = 60Hz	13666.5	5.48E+14
free interface CMS (Rubin's Method), f cut-out = 1.5 fmax = 60Hz	13724.8	5.87E+14
Zoet method cut-out frequency 1.5×f max =60 Hz	840.1	1.99E+13
Zoet method cut-out frequency 1.5×f max =60 Hz, **with** residual boundary flex	10319.4	2.40E+14

Total number CP time and FLOPS for total analysis *Black numbers have been directly measured (CP time) or calculated (FLOPS). Brown numbers have been calculated through an estimated relation between measured computation time and number of calculated floating point operation.*

	aH	aG	aF	aE	aD	aC	aB	aA	
	Number of Columns								
Number of rows	257	419	419	323	336	335	231	154	
257	66049	107683	107683	83011					aH
419	107683	175561	175561	135337					aG
419	107683	175561	175561	135337					aF
323	83011	135337	135337	104329	108528				aE
336				108528	112896	112560			aD
335					112560	112225	77385		aC
231						77385	53361	35574	aB
154							35574	23716	aA

Skyline of the total assembled matrix. The skyline of the total assembled matrices for both Zoet's method with residual interface flexibility taken into account and Zoet's method without residual interface flexibility taken into account looks similar. Numbers in the cells are the number of non zeros in the particular section of the matrix. The grey section are all full matrix sections.

Zoet's Method, No Residual Boundary Flexibility

number of frequencies	80

Generation Pass		
Step number	Action	Estimated FLOPS
Calcuating natural frequencies and mode shapes		1.91E+13
1	Generating residual flexibility modes	n.a.
2	Formulating boundary mobility matrix	3.62E+10
4	Eliminating boundary degrees of	n.a.
Total Flops Generation Pass		1.91E+13

Use Pass		
Step number	Action	Estimated FLOPS
5	Composing Total Assembled System	6.32E+08
6	Solving the matrix equations	
a.	Row reduction forward phase	7.57E+11
b.	Row reduction backward phase	7.17E+08
c.	Solving triangular matrix	9.79E+08
Total FLOPS Use Pass		7.60E+11

Grand total	1.99E+13

All modeshapes have been selected with the natural frequencies within the range between 0 and 1.5×fmax
The fmax is the highest frequency in the frequency range for which results have been obtained (= 40 Hz in this case)
Fmax in this case = 40 Hz, modeshapes have been selected over a frequency range between 0 and 60 Hz

Summary of required number of FLOPS for each step for the Zoet method with no residual interface flexibility taken into account. The number of floating point operations has been calculated producing 80 output sets for frequencies evenly distributed range between 1 and 40 Hz.

Zoet's Method With Residual Boundary Flexibility		
number of frequencies		80
Generation Pass		
Step number	Action	Estimated FLOPS
Calcuating natural frequencies and mode shapes		1.91E+13
1	Generating residual flexibility modes	1.97E+14
2	Formulating boundary mobility matrix	3.95E+12
4	Eliminating boundary degrees of	1.87E+13
Total Flops Generation Pass		2.39E+14
Use Pass		
Step number	Action	Estimated FLOPS
5	Composing Total Assembled System	6.32E+08
6	Solving the matrix equations	
a.	Row reduction forward phase	1.29E+12
b.	Row reduction backward phase	7.17E+08
c.	Solving triangular matrix	9.79E+08
Total FLOPS Use Pass		1.29E+12
Grand total		2.40E+14

All modeshapes have been selected with the natural frequencies within the range between 0 and 1.5×fmax
The fmax is the highest frequency in the frequency range for which results have been obtained (= 40 Hz in this case)
Fmax in this case = 40 Hz, modeshapes have been selected over a frequency range between 0 and 60 Hz

Summary of required number of FLOPS for each step for the Zoet method **with** residual interface flexibility taken into account. The number of floating point operations has been calculated producing 80 output sets for frequencies evenly distributed range between 1 and 40 Hz.

.

Appendix XXIII *Required Number of Flops for Application of the Rubin-Zoet Method on the CMS Model of the LNG Carrier*

In this appendix the calculated number of FLOPS for each sub step is presented applying the Rubin-Zoet method according to section 8.6 for the CMS model of the LNG carrier described in Appendix IX.

In Appendix XIX a description of the sub steps and symbols used is given.

LNG vessel FE model	Number of nodes	Number of boundary nodes		Number of boundary degrees of freedom	Method	Number of modes required*	Required CP for calcuating eigenvectors and eigenvalues	Required time generation pass
PartH	4991	Boundary H-E	298	2088	CMS fixed	181	18.5	22.8
		Boundary H-G	86		CMS free	257	24.5	52.5
		Boundary H-F	86		Rubin-Zoet (frequency range to 1.5×f max)	257	24.5	52.5
PartG	5680	Boundary G-H	86	1536	CMS fixed	373	29.8	40
		Boundary G-F	57		CMS free	419	39	100.8
		Boundary G-E	205		Rubin-Zoet (frequency range to 1.5×f max)	419	39	100.8
PartF	5680	Boundary F-G	57	1536	CMS fixed	373	29.8	40
		Boundary F-H	86		CMS free	419	39	100.8
		Boundary F-E	205		Rubin-Zoet (frequency range to 1.5×f max)	419	39	100.8
PartE	8933	Boundary E-H	298	7188	CMS fixed	213	30	46.6
		Boundary E-G	205		CMS free	323	61	174
		Boundary E-F	205		Rubin-Zoet (frequency range to 1.5×f max)	323	61	174
PartD	9833	Boundary D-E	656	6198	CMS fixed	162	29.14	53.6
		Boundary D-C	484		CMS free	336	95	328
					Rubin-Zoet (frequency range to 1.5×f max)	336	95	328
PartC	11965	Boundary C-D	484	5124	CMS fixed	195	38.11	68.13
		Boundary C-B	370		CMS free	335	75	225.7
					Zoet (frequency range to 1.5×f max)	335	75	225.7
PartB	10044	Boundary B-C	370	3798	CMS fixed	138	29.4	47.7
		Boundary B-A	263		CMS free	231	53	138.3
					Zoet (frequency range to 1.5×f max)	231	53	138.3
PartA	6612	Boundary A-B	263	1578	CMS fixed	91	18.8	25.4
					CMS free	154	24.6	53.3
					Rubin-Zoet (frequency range to 1.5×f max)	154	24.6	53.3

Fixed and free CMS is CMS based on the fixed interface approach (Craig-Bampton) and the free interface approach (Rubin's method without residual compensation) respectively.

For all methods a cut-out frequency of 1.5* f_{max} Hz (=60 Hz) has been applied for the selection of the number of normal modes.

The number of floating point operations has been calculated for applying the Rubin-Zoet method for 80 frequency steps in the range between 1 and 40 Hz.

Step 1: Generating constraint modes				Step 1A	Step 1B
PartH	Boundary H-E	ni	27858	4.14E+10	1.15E+09
		n boundary	516		
	Boundary H-G	ni	29946	4.78E+10	1.24E+09
		n boundary	516		
	Boundary H-F	ni	29946	4.78E+10	4.28E+09
		n boundary	1788		
Part G	Boundary G-H	ni	33564	6.01E+10	1.39E+09
		n boundary	516		
	Boundary G-F	ni	33738	6.07E+10	9.23E+08
		n boundary	342		
	Boundary G-E	ni	32850	5.75E+10	3.23E+09
		n boundary	1230		
Part F	Boundary F-G	ni	33738	6.07E+10	9.23E+08
		n boundary	342		
	Boundary F-H	ni	33564	6.01E+10	1.39E+09
		n boundary	516		
	Boundary F-E	ni	32850	5.75E+10	3.23E+09
		n boundary	1230		
part E	Boundary E-H	ni	51810	1.43E+11	7.41E+09
		n boundary	1788		
	Boundary E-G	ni	52368	1.46E+11	5.15E+09
		n boundary	1230		
	Boundary E-F	ni	52368	1.46E+11	5.15E+09
		n boundary	1230		
	Boundary E-D	ni	49662	1.32E+11	1.56E+10
		n boundary	3936		
PartD	Boundary D-E	ni	55062	1.62E+11	1.73E+10
		n boundary	3936		
	Boundary D-C	ni	56094	1.68E+11	1.30E+10
		n boundary	2904		
PartC	Boundary C-D	ni	68886	2.53E+11	1.60E+10
		n boundary	2904		
	Boundary C-B	ni	69570	2.58E+11	1.24E+10
		n boundary	2220		
PartB	Boundary B-C	ni	58044	1.80E+11	1.03E+10
		n boundary	2220		
	Boundary B-A	ni	58686	1.84E+11	7.41E+09
		n boundary	1578		
PartA	Coupling B-A	ni	38097	7.74E+10	4.81E+09
		n boundary	1578		
Total number of FLOPS for each step				2.34E+12	1.32E+11
Grand total for calcuating all required constraint modes (Step 1)					2.47E+12

Number of FLOPS required for step 1 for analysing the LNG carrier in Appendix IX, according to the Rubin-Zoet method, applying a cut-out frequency of 60 Hz analysing 80 frequency steps between 1 and 40 Hz.

Step 2: Generating the reduction basis				Step 2A	Step 2B
PartH	0	ni	27858	7.39E+09	7.16E+06
		n boundary	516		
		nn	257		
	0	ni	29946	7.94E+09	7.70E+06
		n boundary	516		
		nn	257		
	0	ni	29946	2.75E+10	7.70E+06
		n boundary	1788		
		nn	257		
Part G	Boundary G-H	ni	33564	1.45E+10	1.41E+07
		n boundary	516		
		nn	419		
	Boundary G-F	ni	33738	9.67E+09	1.41E+07
		n boundary	342		
		nn	419		
	Boundary G-E	ni	32850	3.39E+10	1.38E+07
		n boundary	1230		
		nn	419		
Part F	Boundary F-G	ni	33738	9.67E+09	1.41E+07
		n boundary	342		
		nn	419		
	Boundary F-H	ni	33564	1.45E+10	1.41E+07
		n boundary	516		
		nn	419		
	Boundary F-E	ni	32850	3.39E+10	1.38E+07
		n boundary	1230		
		nn	419		
Part E	Boundary E-H	ni	51810	5.98E+10	1.67E+07
		n boundary	1788		
		nn	323		
	Boundary E-G	ni	52368	4.16E+10	1.69E+07
		n boundary	1230		
		nn	323		
0	Boundary E-F	ni	52368	4.16E+10	1.69E+07
		n boundary	1230		
		nn	323		
	Boundary E-D	ni	49662	1.26E+11	1.60E+07
		n boundary	3936		
		nn	323		
PartD	Boundary D-E	ni	55062	1.46E+11	1.85E+07
		n boundary	3936		
		nn	336		
	Boundary D-C	ni	56094	1.09E+11	1.88E+07
		n boundary	2904		
		nn	336		

Number of FLOPS required for Part I of Step 2 for analysing the LNG carrier in Appendix IX, according to the Rubin-Zoet method, applying a cut-out frequency of 60 Hz analysing 80 frequency steps between 1 and 40 Hz.

Step 2: Generating the reduction basis				Step 2A	Step 2B
PartC	Boundary C-D	ni	68886	1.34E+11	2.31E+07
		n boundary	2904		
		nn	335		
	Boundary C-B	ni	69570	1.03E+11	2.33E+07
		n boundary	2220		
		nn	335		
PartB	Boundary B-C	ni	58044	5.95E+10	1.34E+07
		n boundary	2220		
		nn	231		
	Boundary B-A	ni	58686	4.28E+10	1.36E+07
		n boundary	1578		
		nn	231		
PartA	Coupling B-A	ni	38100	1.85E+10	5.87E+06
		n boundary	1578		
		nn	154		
Total number of FLOPS for each step				1.04E+12	2.90E+08
Grand total for calculating step 2					1.04E+12

Number of FLOPS required for Part II of Step 2 for analysing the LNG carrier in Appendix IX, according to the Rubin-Zoet method, applying a cut-out frequency of 60 Hz analysing 80 frequency steps between 1 and 40 Hz.

	Step 3: Generating reduced mass and stiffness matrices		Step 3A	Step 3B	Step 3C
PartH	n	28374	3.51E+09	6.66E+10	4.31E+07
	na	773			
	n bandwidth	40			
	n	30462	3.77E+09	7.16E+10	4.63E+07
	na	773			
	n bandwidth	40			
	n	31734	1.04E+10	5.01E+11	1.22E+08
	na	2045			
	n bandwidth	40			
Part G	n	34080	5.10E+09	1.17E+11	6.28E+07
	na	935			
	n bandwidth	40			
	n	34080	4.15E+09	7.82E+10	5.13E+07
	na	761			
	n bandwidth	40			
	n	34080	8.99E+09	3.57E+11	1.08E+08
	na	1649			
	n bandwidth	40			
Part F	n	34080	4.15E+09	7.82E+10	5.13E+07
	na	761			
	n bandwidth	40			
	n	34080	5.10E+09	1.17E+11	6.28E+07
	na	935			
	n bandwidth	40			
	n	34080	8.99E+09	3.57E+11	1.08E+08
	na	1649			
	n bandwidth	40			
Part E	n	53598	1.81E+10	9.24E+11	2.19E+08
	na	2111			
	n bandwidth	40			
	n	53598	1.33E+10	5.05E+11	1.63E+08
	na	1553			
	n bandwidth	40			
0	n	53598	1.33E+10	5.05E+11	1.63E+08
	na	1553			
	n bandwidth	40			
	n	53598	3.65E+10	3.60E+12	4.23E+08
	na	4259			
	n bandwidth	40			
PartD	n	58998	4.03E+10	4.02E+12	4.70E+08
	na	4272			
	n bandwidth	40			
	n	58998	3.06E+10	2.36E+12	3.63E+08
	na	3240			
	n bandwidth	40			

Number of FLOPS required for Part I of Step 3 for analysing the LNG carrier in Appendix IX, according to the Rubin-Zoet method, applying a cut-out frequency of 60 Hz analysing 80 frequency steps between 1 and 40 Hz.

	Step 3: Generating reduced mass and stiffness matrices		Step 3A	Step 3B	Step 3C
PartC	n	71790	3.72E+10	2.89E+12	4.46E+08
	na	3239			
	n bandwidth	40			
	n	71790	2.93E+10	1.82E+12	3.56E+08
	na	2555			
	n bandwidth	40			
PartB	n	60264	2.36E+10	1.39E+12	2.85E+08
	na	2451			
	n bandwidth	40			
	n	60264	1.74E+10	7.68E+11	2.12E+08
	na	1809			
	n bandwidth	40			
PartA	n	39678	1.10E+10	4.57E+11	1.32E+08
	na	1732			
	n bandwidth	40			
	Total number of FLOPS for each step		3.25E+11	2.10E+13	3.89E+09
	Grand total for calculating step 3				2.13E+13

Number of FLOPS required for Part II of Step 3 for analysing the LNG carrier in Appendix IX, according to the Rubin-Zoet method, applying a cut-out frequency of 60 Hz analysing 80 frequency steps between 1 and 40 Hz.

Formulating the boundary mobility matrix			Step 4A	Step 4B	Step 4C	Step 5A	Step 5B
Part H-F	nAboundary	528	1.21E+08	2.42E+08	1.43E+08	3.66E+08	9.48E+08
	nBboundary	528					
	nboundary	1056					
	nAn	257					
	nBn	419					
	na	1732					
	nn	676					
Part H-G	nAboundary	528	1.21E+08	2.42E+08	1.43E+08	3.66E+08	9.48E+08
	nBboundary	528					
	nboundary	1056					
	nAn	257					
	nBn	419					
	na	1732					
	nn	676					
Part H-E	nAboundary	1122	3.19E+08	6.38E+08	3.34E+08	9.65E+08	2.20E+09
	nBboundary	1122					
	nboundary	2244					
	nAn	257					
	nBn	323					
	na	2824					
	nn	580					
Part G-F	nAboundary	498	1.35E+08	2.69E+08	1.35E+08	4.07E+08	1.11E+09
	nBboundary	498					
	nboundary	996					
	nAn	419					
	nBn	419					
	na	1834					
	nn	838					
Part G-E	nAboundary	780	2.12E+08	4.25E+08	1.95E+08	6.42E+08	1.59E+09
	nBboundary	780					
	nboundary	1560					
	nAn	419					
	nBn	323					
	na	2302					
	nn	742					
Part F-E	nAboundary	780	2.12E+08	4.25E+08	1.95E+08	6.42E+08	1.59E+09
	nBboundary	780					
	nboundary	1560					
	nAn	419					
	nBn	323					
	na	2302					
	nn	742					

Number of FLOPS required for Part I of Step 4 and 5 for analysing the LNG carrier in Appendix IX, according to the Rubin-Zoet method, applying a cut-out frequency of 60 Hz analysing 80 frequency steps between 1 and 40 Hz.

Formulating the boundary mobility matrix			Step 4A	Step 4B	Step 4C	Step 5A	Step 5B
Part E-D	nAboundary	3936	2.91E+09	5.82E+09	2.92E+09	8.81E+09	1.84E+10
	nBboundary	3936					
	nboundary	7872					
	nAn	323					
	nBn	336					
	na	8531					
	nn	659					
Part D-C	nAboundary	2904	1.68E+09	3.36E+09	1.68E+09	5.08E+09	1.08E+10
	nBboundary	2904					
	nboundary	5808					
	nAn	336					
	nBn	335					
	na	6479					
	nn	671					
Part C-B	nAboundary	2220	1.00E+09	2.01E+09	9.61E+08	3.03E+09	6.50E+09
	nBboundary	2220					
	nboundary	4440					
	nAn	335					
	nBn	231					
	na	5006					
	nn	566					
Part B-A	nAboundary	1578	5.02E+08	1.00E+09	4.80E+08	1.52E+09	3.24E+09
	nBboundary	1578					
	nboundary	3156					
	nAn	231					
	nBn	154					
	na	3541					
	nn	385					
Total Number of FLOPS for each substep			7.22E+09	1.44E+10	7.18E+09	2.18E+10	4.73E+10
Grand Total Number of FLOPS for step 4 and 5						9.80E+10	

Number of FLOPS required for Part II of Step 4 and 5 for analysing the LNG carrier in Appendix IX, according to the Rubin-Zoet method, applying a cut-out frequency of 60 Hz analysing 80 frequency steps between 1 and 40 Hz.

Step 4: Calcuating reduced boundary mobility matrix			Step 6A	Step 6B	Step 6D	Step 6F	Step 7 Composing Total Matrix
Part H-F	n boundary	528	1.57E+09	1.51E+09	1.54E+11	7.31E+07	
	nn	676					
Part H-G	n boundary	528	1.57E+09	1.51E+09	1.54E+11	7.31E+07	7.31E+07
	nn	676					
Part H-E	n boundary	1122	1.51E+10	5.84E+09	2.42E+11	5.38E+07	5.38E+07
	nn	580					
Part G-F	n boundary	498	1.32E+09	1.66E+09	2.24E+11	1.12E+08	1.12E+08
	nn	838					
Part G-E	n boundary	780	5.06E+09	3.61E+09	2.75E+11	8.81E+07	8.81E+07
	nn	742					
Part F-E	n boundary	780	5.06E+09	3.61E+09	2.75E+11	8.81E+07	8.81E+07
	nn	742					
Part E-D	n boundary	3936	6.50E+11	8.17E+10	1.09E+12	6.95E+07	6.95E+07
	nn	659					
Part D-C	n boundary	2904	2.61E+11	4.53E+10	8.37E+11	7.20E+07	7.20E+07
	nn	671					
Part C-B	n boundary	2220	1.17E+11	2.23E+10	4.55E+11	5.13E+07	5.13E+07
	nn	566					
Part B-A	n boundary	1578	4.19E+10	7.67E+09	1.50E+11	2.37E+07	2.37E+07
	nn	385					
Number of FLOPS for each sub step			1.10E+12	1.75E+11	3.86E+12	7.05E+08	6.32E+08
Grand total of FLOPS for step 6 and 7							5.14E+12

Number of FLOPS required for Step 6 and 7 for analysing the LNG carrier in Appendix IX, according to the Rubin-Zoet method, applying a cut-out frequency of 60 Hz analysing 80 frequency steps between 1 and 40 Hz.

Total structure	Number of equations total assembled matrix	Number of non zeros	calculating Normal Modes and Natural Frequencies		Constraint/Residual Attachment Modes and Reducing Matrices		Total Computation Time Generation Pass	
			CPTime	FLOPS	CPTime	FLOPS	CPTime	FLOPS
full solution	366973	1.49E+07	n.a.	n.a.	n.a.	n.a.	n.a.	n.a.
Mode superposition, f cut-out = 1.5 fmax = 60Hz	1668	2782224	2665	1.24E+14	135	6.28E+12	2.80E+03	1.30E+14
fixed interface CMS (Craig-Bampton), f cut-out = 1.5 fmax = 60Hz	15370	1.25E+08	223.55	1.04E+13	121	5.60E+12	344.2	1.60E+13
free interface CMS (Rubin's Method), f cut-out = 1.5 fmax = 60Hz	16118	1.34E+08	411.1	1.91E+13	762	3.54E+13	1173.4	5.45E+13
Rubin-Zoet method cut-out frequency 1.5×f max = 60 Hz	2474	2.98E+06	411.1	1.91E+13	647	3.01E+13	1058.5	4.92E+13

Generation pass: Table of CP times and numbers of floating point operation. *Black numbers have been directly measured (CP time) or calculated (FLOPS). Brown numbers have been calculated through an estimated relation between measured computation time and number of calculated floating point operation.*

Total structure	Generating Full Assembled Matrix		Solving Full Assembled Matrices		Total Computation Time Use Pass	
	CPTime	FLOPS	CPTime	FLOPS	CPTime	FLOPS
full solution	20	7.71E+10	7600.0	3.56E+14	7620.0	3.56E+14
Mode superposition, f cut-out = 1.5 fmax = 60Hz	n.a.	n.a.	21	9.92E+11	21	9.92E+11
fixed interface CMS (Craig-Bampton), f cut-out = 1.5 fmax = 60Hz	18	6.94E+10	12960.0	5.32E+14	13322.2	5.32E+14
free interface CMS (Rubin's Method), f cut-out = 1.5 fmax = 60Hz	18	6.94E+10	11360.0	5.32E+14	12551.4	5.32E+14
Rubin-Zoet method cut-out frequency 1.5×f max = 60 Hz	0.16	6.32E+08	16.3	7.63E+11	1075.0	7.64E+11

Use pass: Table of CP times and numbers of floating point operation. *Black numbers have been directly measured (CP time) or calculated (FLOPS). Brown numbers have been calculated through an estimated relation between measured computation time and number of calculated floating point operation.*

Total structure	Total Computation Time Generation plus Use Pass	
	CPTime	FLOPS
full solution	7620.0	3.56E+14
Mode superposition, f cut-out = 1.5 fmax = 60Hz	2821.3	1.31E+14
fixed interface CMS (Craig-Bampton), f cut-out = 1.5 fmax = 60Hz	13666.5	5.48E+14
free interface CMS (Rubin's Method), f cut-out = 1.5 fmax = 60Hz	13724.8	5.87E+14
Rubin-Zoet method cut-out frequency 1.5×f max = 60 Hz	2133.5	4.99E+13

Total number CP time and FLOPS for total analysis. *Black numbers have been directly measured (CP time) or calculated (FLOPS). Brown numbers have been calculated through an estimated relation between measured computation time and number of calculated floating point operation.*

	aH	aG	aF	aE	aD	aC	aB	aA	
	Number of Columns								
Number of rows	257	419	419	323	336	335	231	154	
257	66049	107683	107683	83011					aH
419	107683	175561	175561	135337					aG
419	107683	175561	175561	135337					aF
323	83011	135337	135337	104329	108528				aE
336				108528	112896	112560			aD
335					112560	112225	77385		aC
231						77385	53361	35574	aB
154							35574	23716	aA

Skyline of the total assembled dynamic stiffness matrix obtained through the Rubin-Zoet method.

Rubin-Zoet Method

number of frequencies	80

Generation Pass

Step number	Action	Estimated FLOPS
Calcuating natural frequencies and mode shapes		1.91E+13
1	Generating constraint modes	2.47E+12
2	Generating reduction basis	1.04E+12
3	Generating Reduced Mass, Stiffness	2.13E+13
4	Generating Reduced Equations of	2.88E+10
5	Forcing equilibrium and compatibility at the boundary degrees of freedom:	6.92E+10
6	Eliminating boundary degrees of	5.13E+12
Total Flops Generation Pass		4.92E+13

Use Pass

Step number	Action	Estimated FLOPS
7	Formulating compatibility and	6.32E+08
8	Solving the matrix equations	
a.	Row reduction forward phase	7.57E+11
b.	Row reduction backward phase	7.17E+08
c.	Solving triangular matrix	5.30E+09
Total FLOPS Use Pass		7.64E+11

Grand total	4.99E+13

All modeshapes have been selected with the natural frequencies within the range between 0 and 1.5×fmax
The fmax is the highest frequency in the frequency range for which results have been obtained (= 40 Hz in this case)
Fmax in this case = 40 Hz, modeshapes have been selected over a frequency range between 0 and 60 Hz

Summary of required number of FLOPS for each step for the Rubin-Zoet method. The required number of FLOPS for solving the matrix equation (step 6) is calculated according to Appendix VI.

	Reduction Factor Computation TimeRelatively to Rubin's Method	Reduction Factor Computation Time Relatively to the Full Harmonic Analysis
Full Solution	-39.31%	0.00%
Mode Superposition	-77.66%	-63.20%
Fixed Interface CMS (Craig-Bampton) cut-out freque 1.5×f max = 60 Hz	-1.48%	62.32%
Free Interface CMS (Rubin's Method) cut-out freque 1.5×f max = 60 Hz	0.00%	64.77%
Zoet method, cut-out freque 1.5×f max = 60 Hz, no residual boundary flex	-96.61%	-94.41%
Zoet method, cut-out freque 1.5×f max = 60 Hz, with residual boundary flex	-59.04%	-32.52%
Rubin-Zoet method, cut-out freque 1.5×f max = 60 Hz	-91.49%	-85.98%

Difference in percentage in computation time relatively to Rubin's free interface (interface) method or relatively to the full harmonic method. As can be seen, the Rubin's method free interface method requires 65 % more calculation time compared to the full method. The Zoet method reduces the calculation time by 96% relative to Rubin's method.

Appendix XXIV *CMS Results of the Case Study Model According to ANSYS*

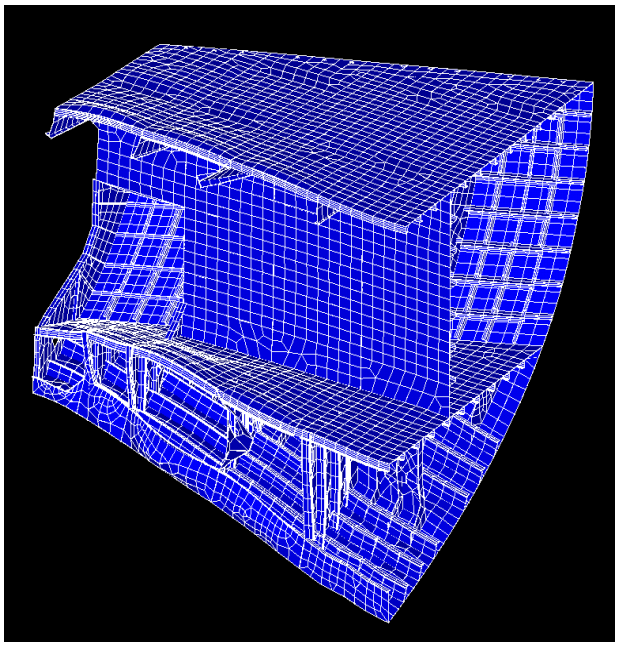

22.45 Hz

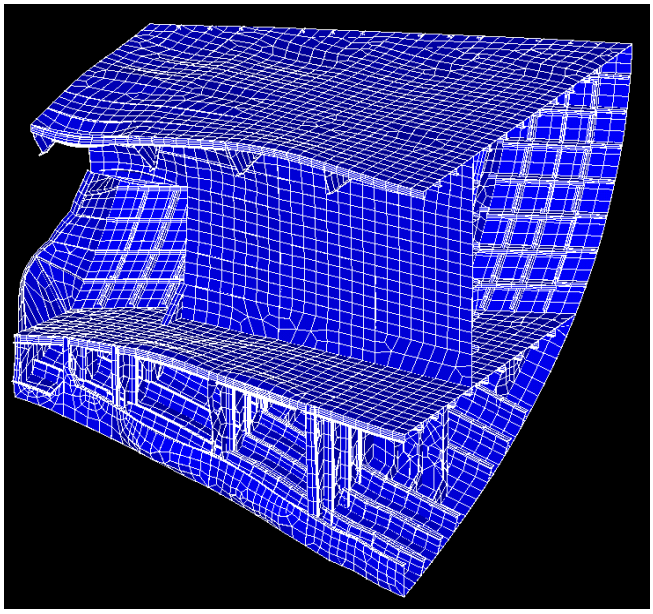

30.25 Hz

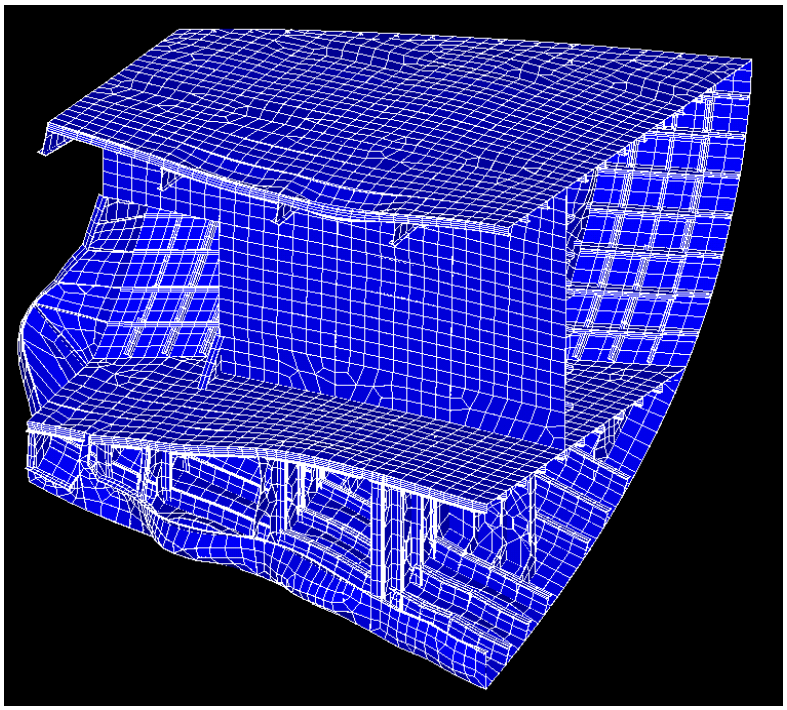

35.13 Hz

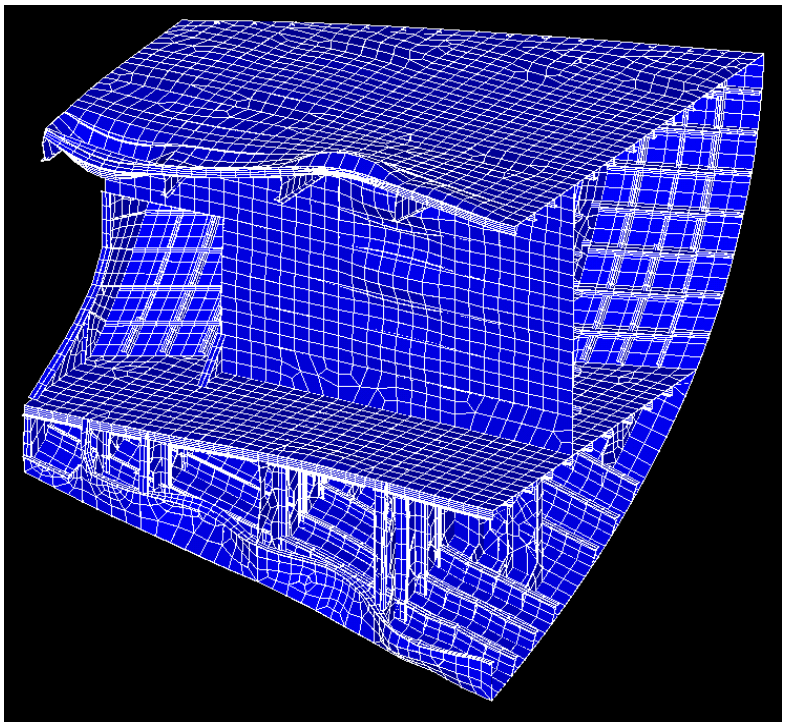

39.5 Hz

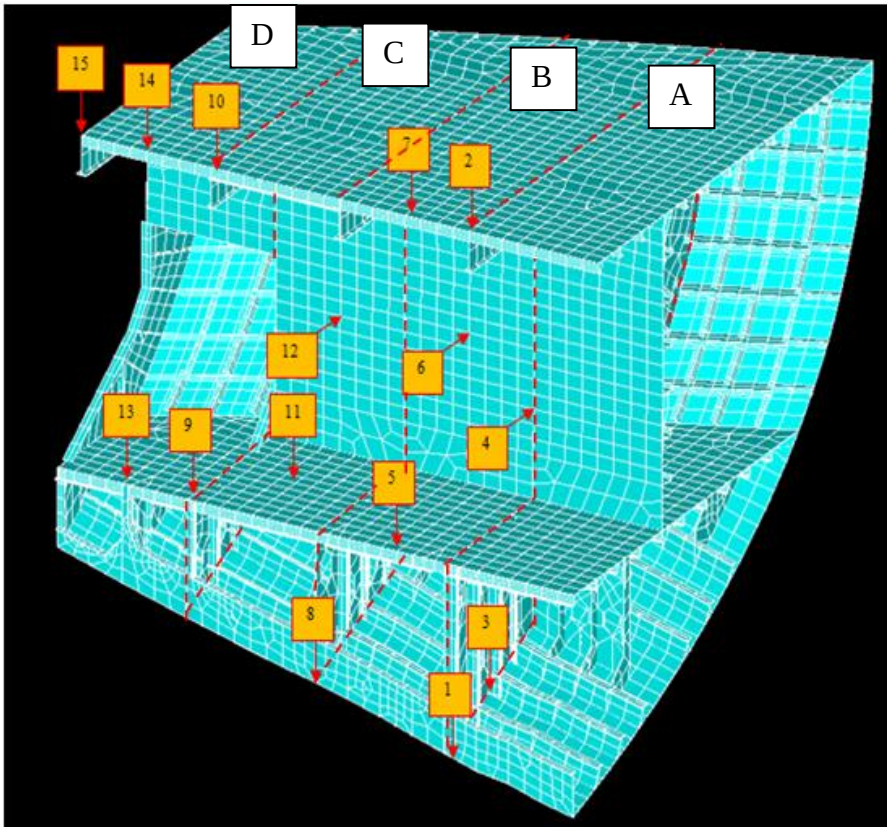

Test model flexible boundary CMS	Number of nodes	Number of modes required	Number of boundary nodes	Number of boundary degrees of freedomnodes	Required CP for calcuating eigenvectors and eigenvalues	Required CP generation pass
PartAfixedcms	1903	25	140	840	9.3	11.8
PartAfreecms		31	140	840	11	14.8
PartBfixedcms	1695	21	140 and 120	1560	9.5	11.8
PartBfreecms		75	140 and 120	1566	11	16.5
PartCfixedcms	1342	16	120 and 96	1296	9.1	9.4
PartCfreecms		59	120 and 96	1320	9.5	13.42
PartDfixedcms	1160	15	95	570	8.84	9.1
PartDfreecms		41	95	570	8.7	10.7

Test model subdivided into four substructures (A, B, C and D). Dotted line show the interface boundaries of the substructures. Model is clamped at the nodes on the far right side of substructure A.

Fixed CMS = fixed interface CMS according to Craig-Bampton

Free CMS is free interface CMS according to Rubin's method (without residual compensation)

For selecting the number of retained normal modes, a cut-out frequency has been applied of 1.5 fmax = 60 Hz for both methods

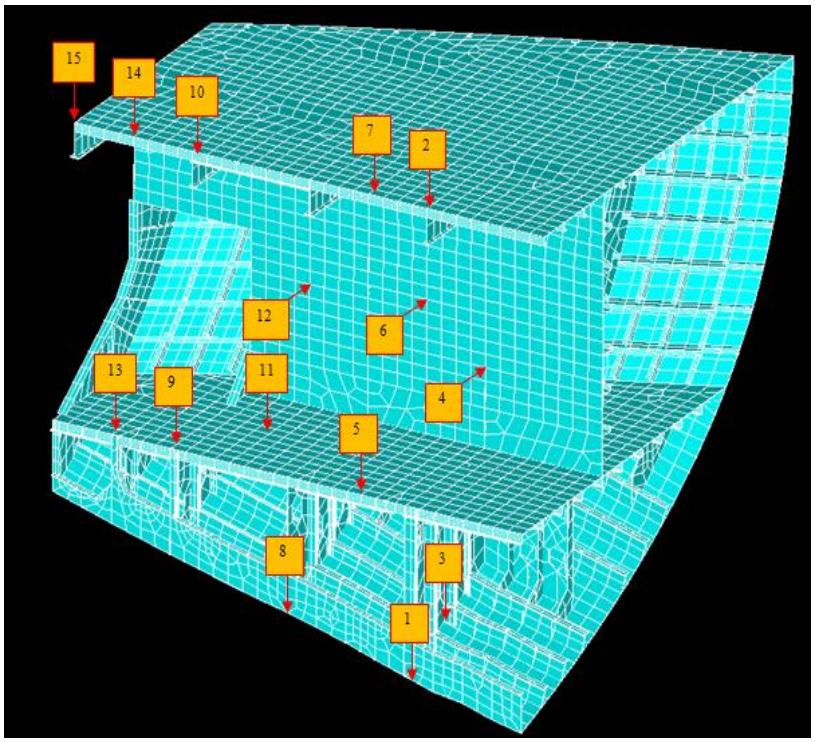

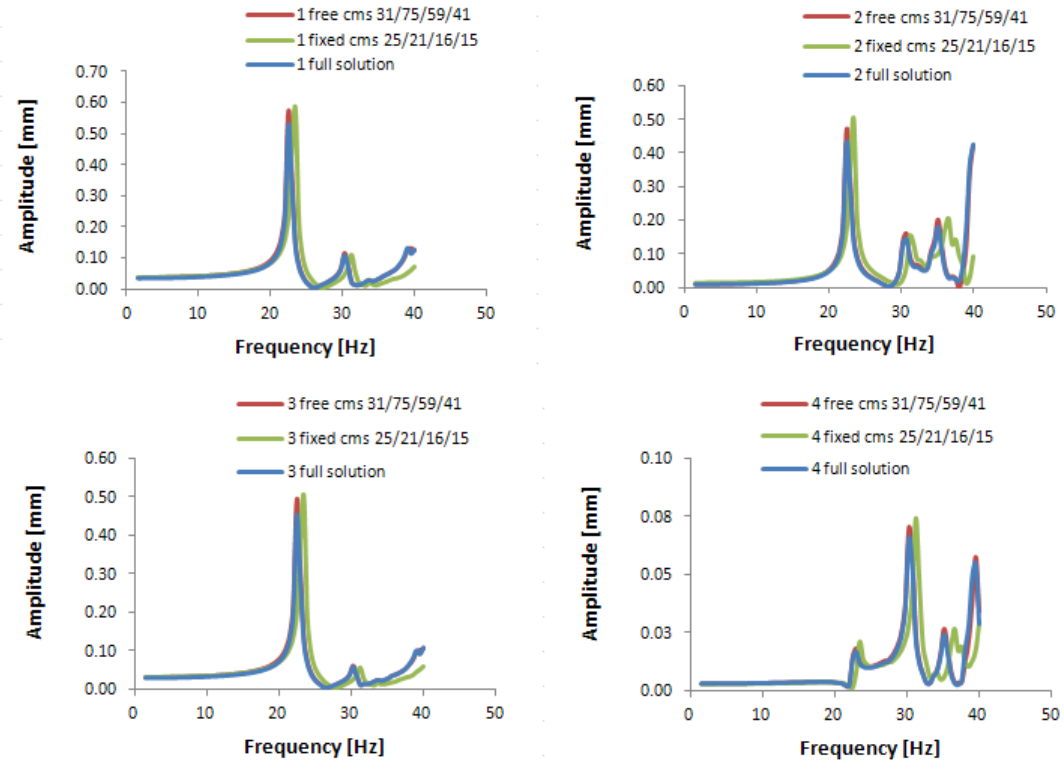

Full simulation results and simulation results for free (Rubin's method without residual compensation)and fixed (Craig Bampton) interface CMS applying a cut-out frequency of 1.5 fmax = 60Hz.
Number of modes taken for substructure A,B,C and D:
31, 75, 59 and 41 respectively for free interface Rubin's method (31/75/59/41)
25, 21, 16 and 15 respectively for fixed interface Craig-Bampton's method (25/21/16/15)

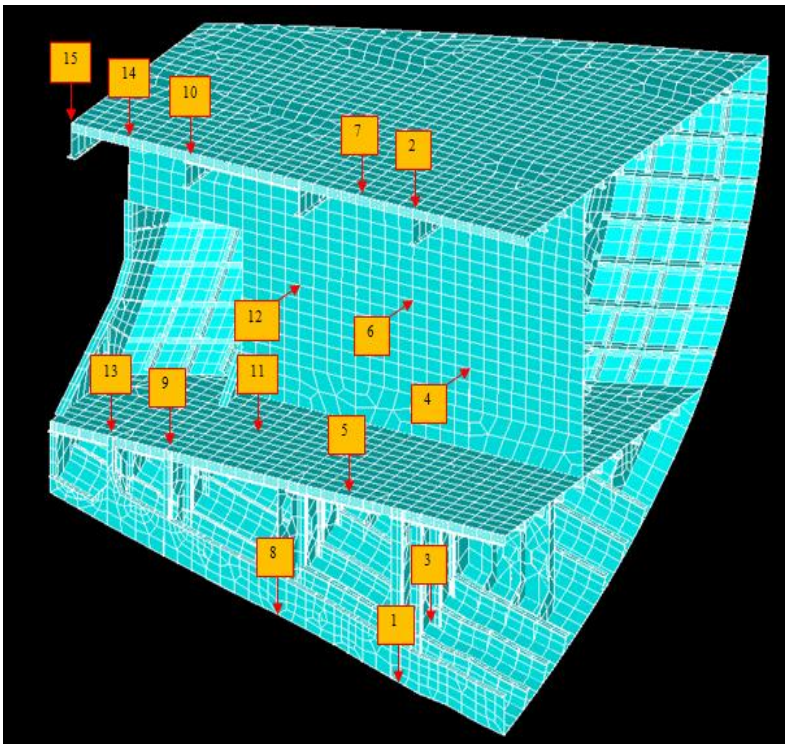

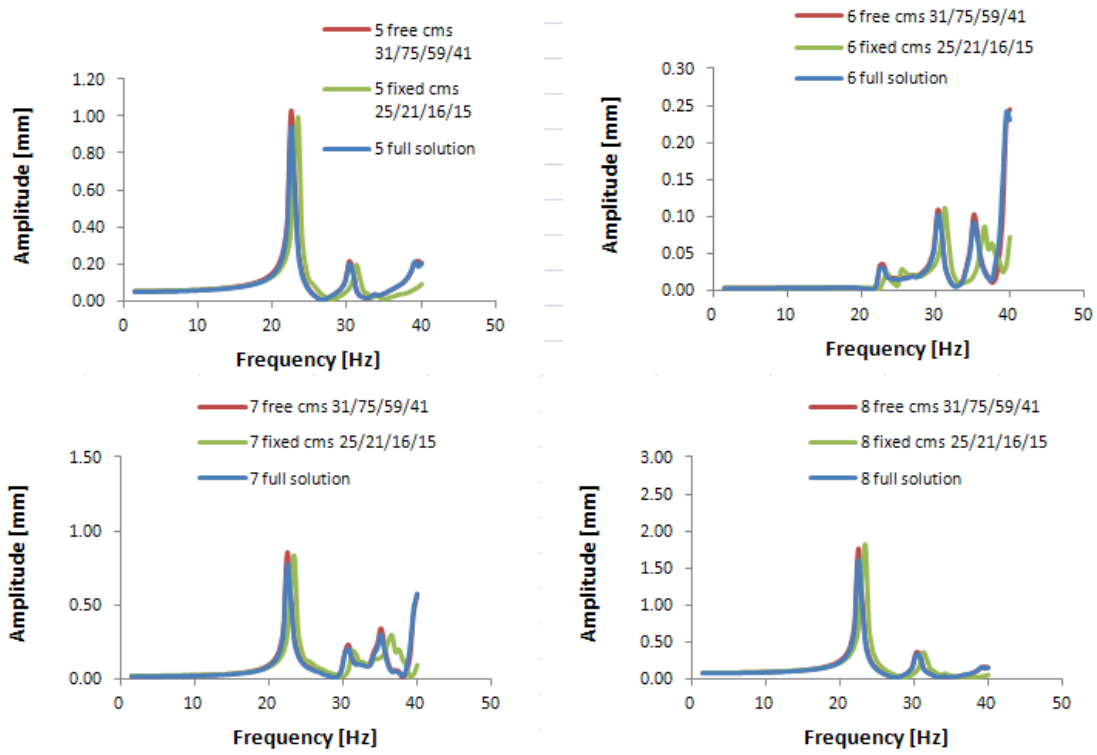

Full simulation results and simulation results for free (Rubin's method without residual compensation)and fixed (Craig Bampton) interface CMS applying a cut-out frequency of 1.5 fmax = 60Hz.
Number of modes taken for substructure A,B,C and D:
31, 75, 59 and 41 respectively for free interface Rubin's method (31/75/59/41)
25, 21, 16 and 15 respectively for fixed interface Craig-Bampton's method (25/21/16/15)

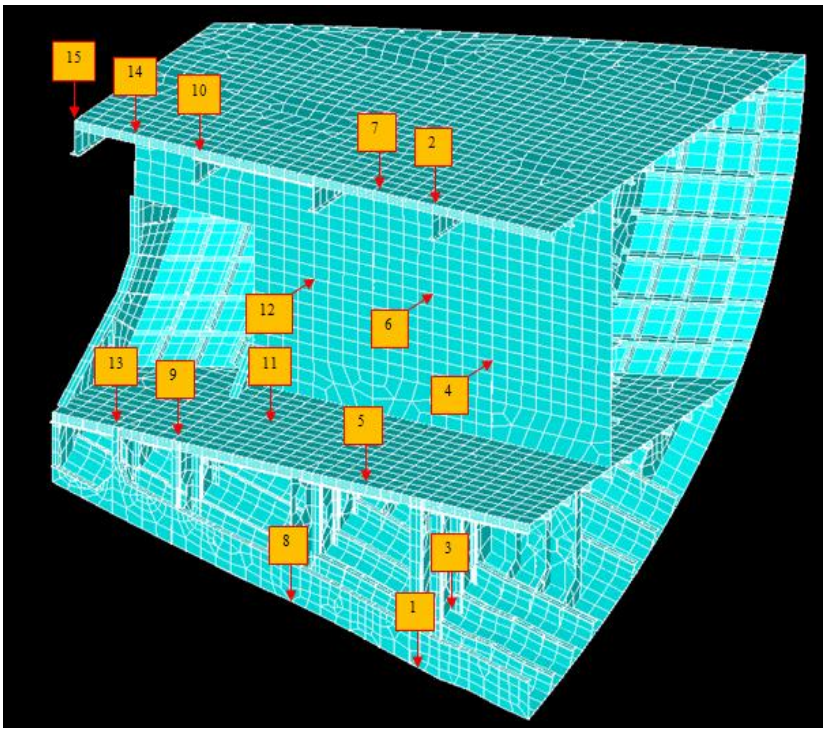

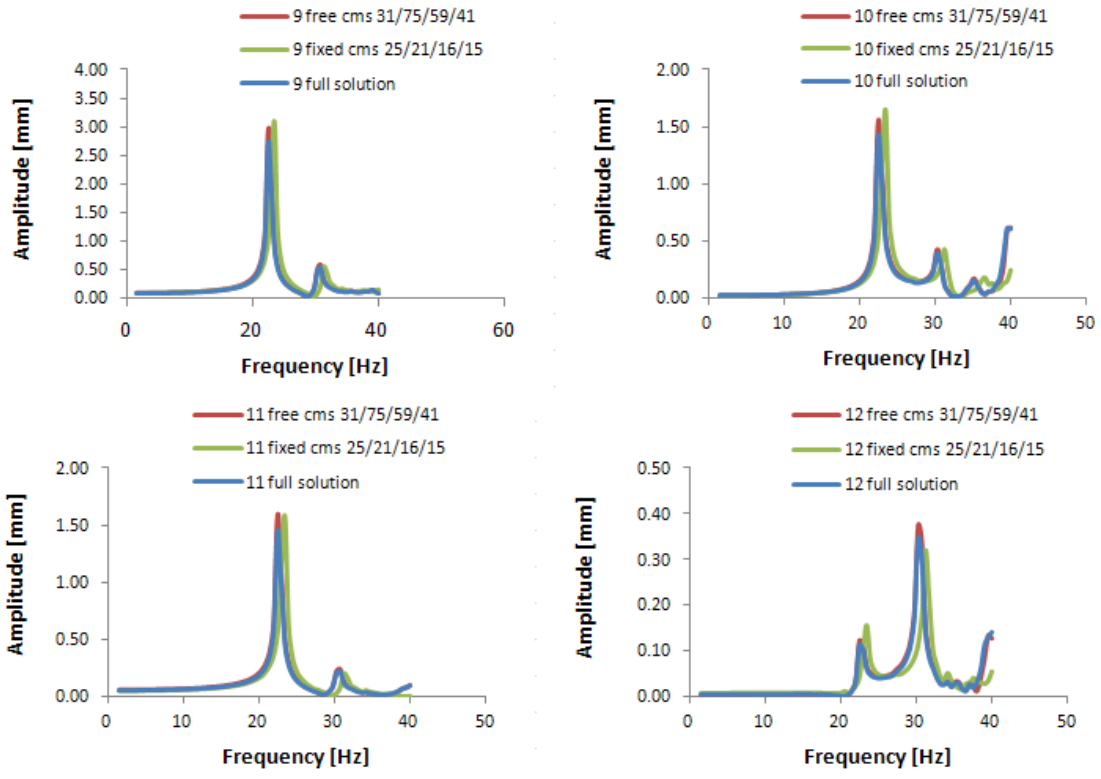

Full simulation results and simulation results for free (Rubin's method without residual compensation)and fixed (Craig Bampton) interface CMS applying a cut-out frequency of 1.5 fmax = 60Hz.
Number of modes taken for substructure A,B,C and D:
31, 75, 59 and 41 respectively for free interface Rubin's method (31/75/59/41)
25, 21, 16 and 15 respectively for fixed interface Craig-Bampton's method (25/21/16/15)

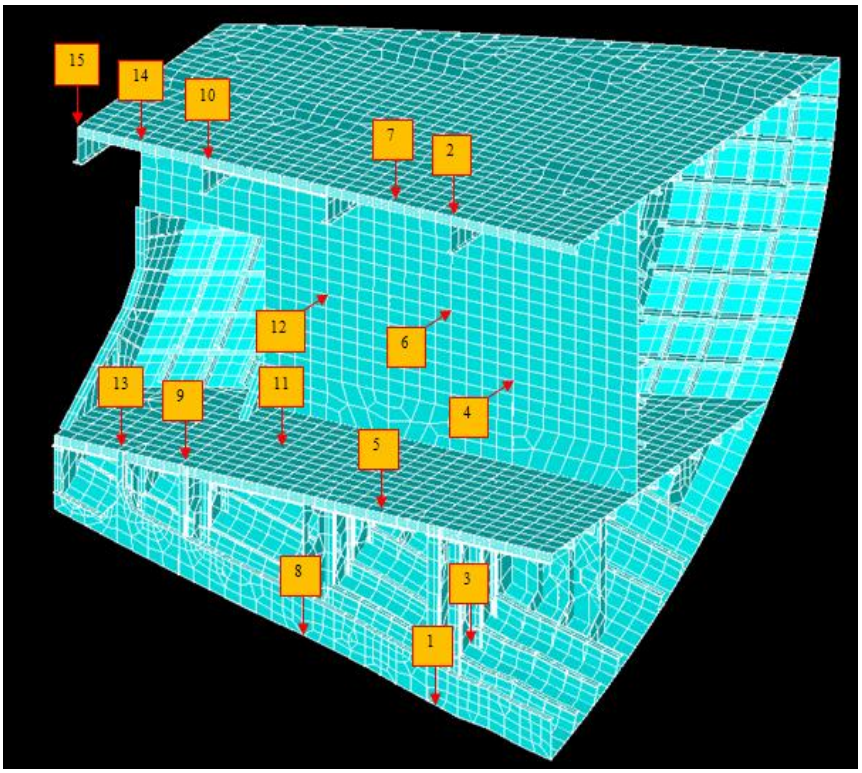

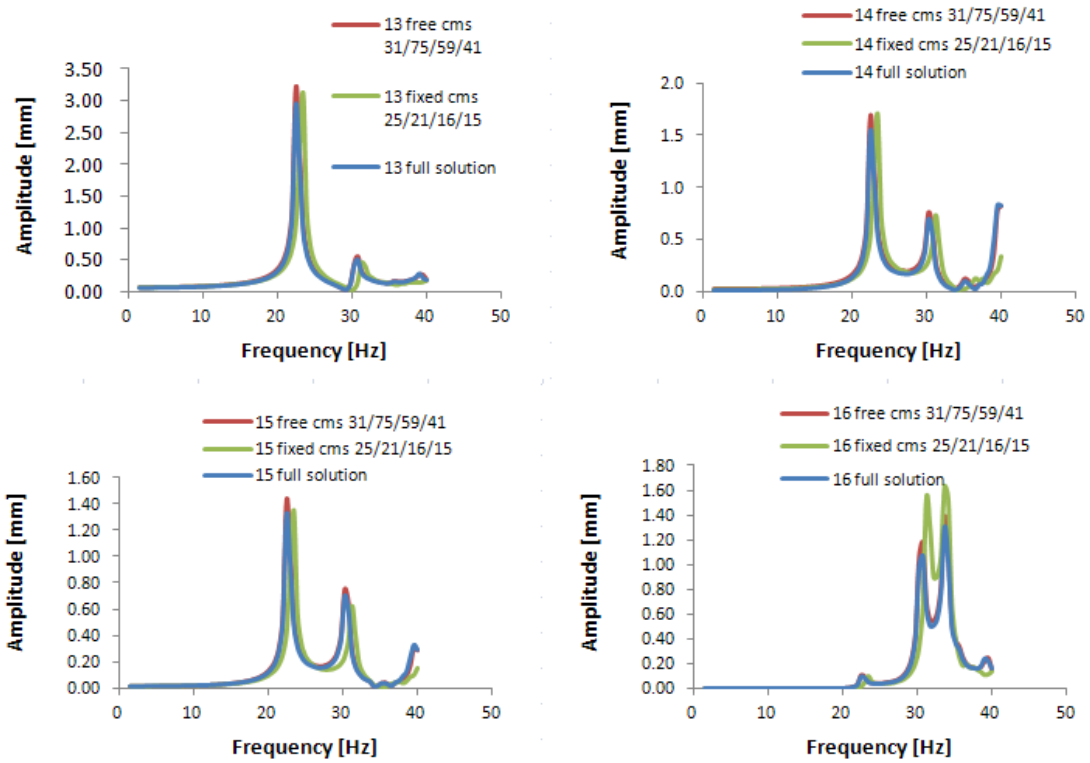

Full simulation results and simulation results for free (Rubin's method without residual compensation)and fixed (Craig Bampton) interface CMS applying a cut-out frequency of 1.5 fmax = 60Hz.
Number of modes taken for substructure A,B,C and D:
31, 75, 59 and 41 respectively for free interface Rubin's method (31/75/59/41)
25, 21, 16 and 15 respectively for fixed interface Craig-Bampton's method (25/21/16/15)

Appendix XXV *Test Case Substructure Division for the Zoet Method*

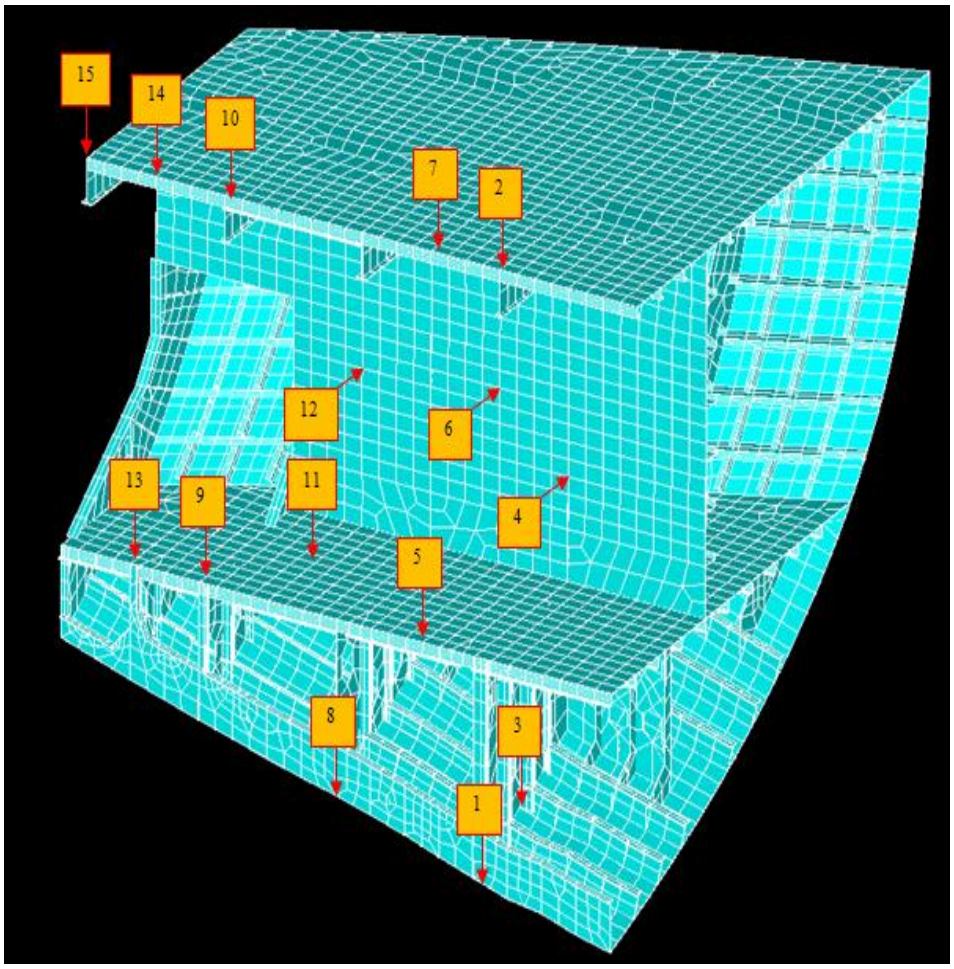
15
14
10
7
2
12
6
13
9
11
4
5
8
3
1

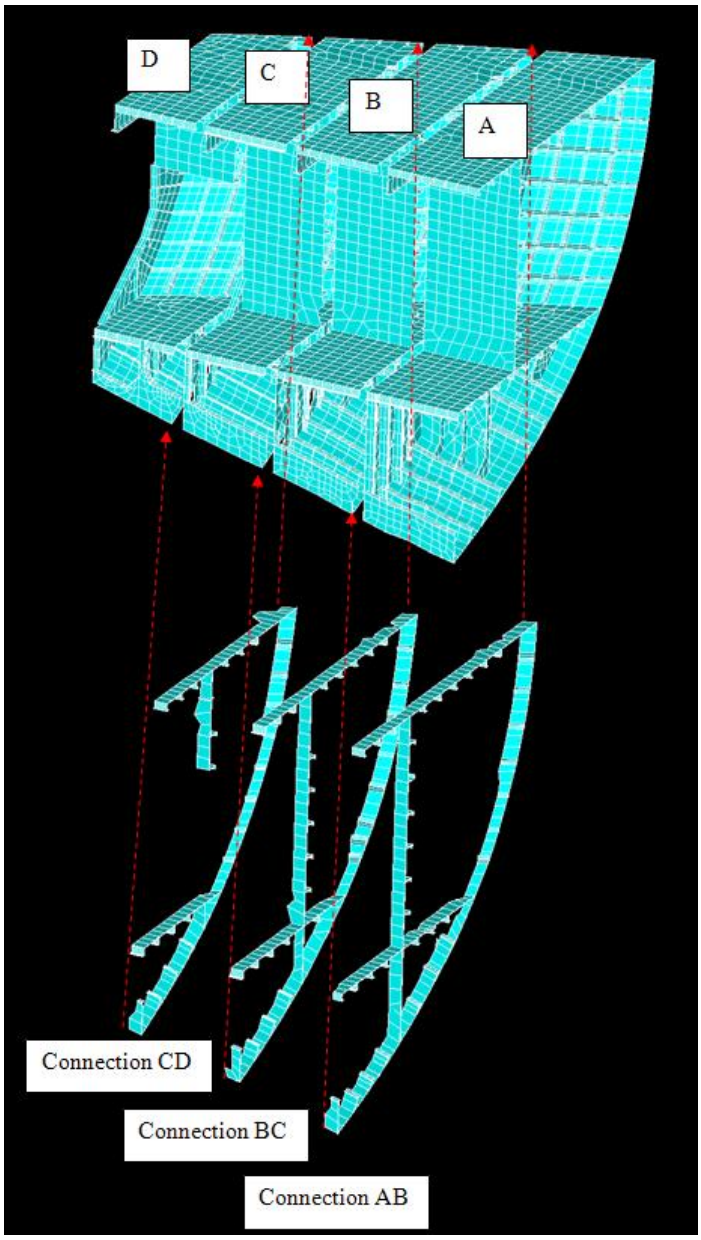

Test model flexible boundary CMS	Number of nodes	Number of modes required	Number of boundary nodes	Number of boundary degrees of freedomnodes	Required CP for calcuating eigenvectors and eigenvalues	Required time generation pass
PartAfreecms	1903	31	140	840	10.2	14.8
PartA Zoet	1903	205	140	840	16.3	18.9
PartBfreecms	1695	75	140 and 120	1560	11	16.5
PartB Zoet	1555	179	141 and 120	1566	13.3	18.3
PartCfreecms	1342	59	120 and 96	1296	9.5	13.4
PartC Zoet	1222	148	124 and 96	1320	12	17.6
PartDfreecms	1160	41	95	570	8.7	10.7
PartD Zoet	1064	105	95	570	10	13.8

Free CMS is free interface CMS according to Rubin's method (without residual compensation)
For selecting the number of retained normal modes, a cut-out frequency has been applied of 1.5 fmax = 60 Hz for Rubin's method, and 3 fmax = 120 Hz for Zoet's method (see section 9.3)

Appendix XXVI *Test Case Results Zoet Method Individual pair of Substructures*

Results Substructure A and B

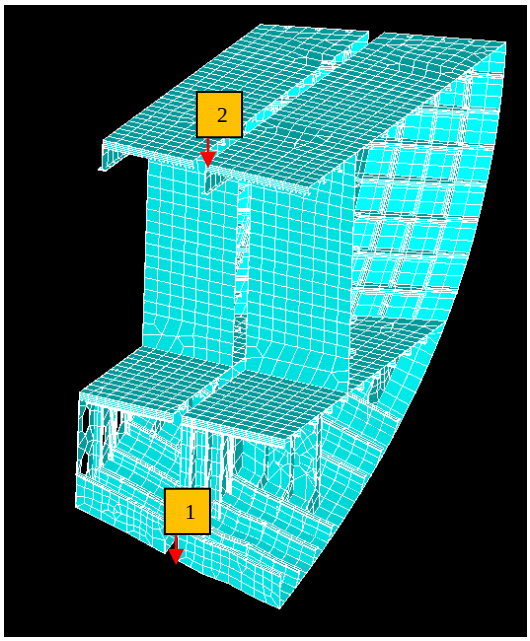

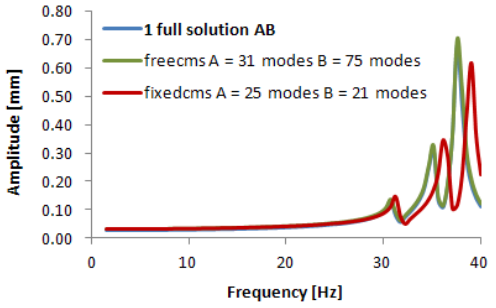

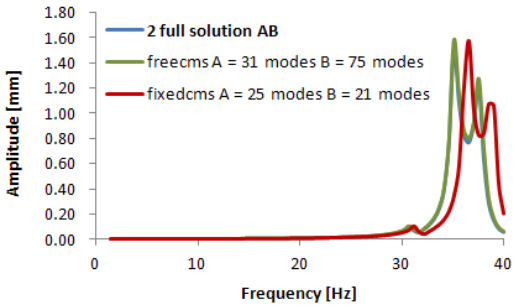

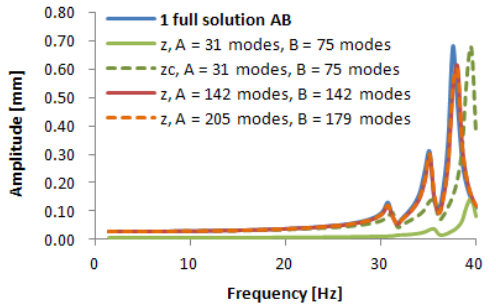

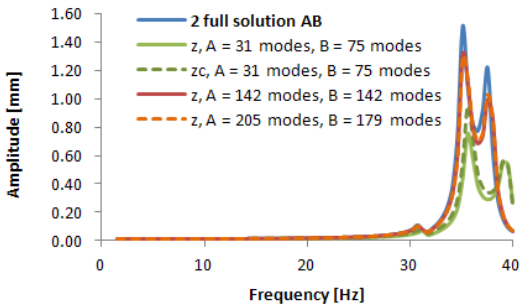

y and z are simulation results obtained in z and y direction respectively by only expanding the normal modes

yc and zc are the simulation results obtained through expanding both normal and static modes in y and z direction respectively

Results Substructure A and B

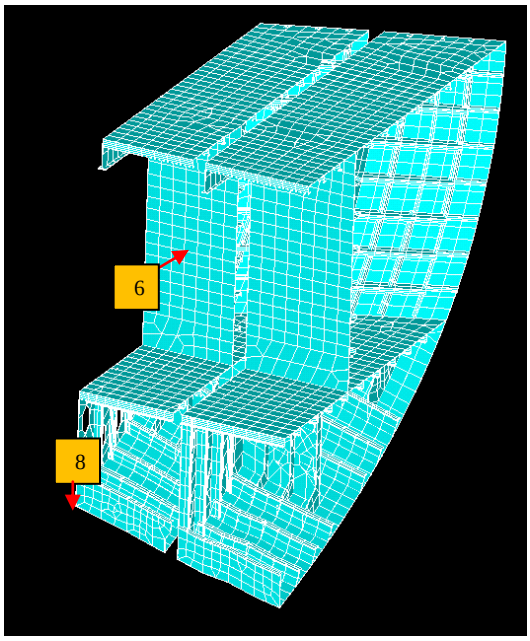

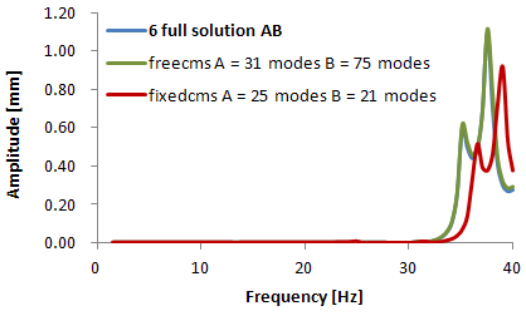

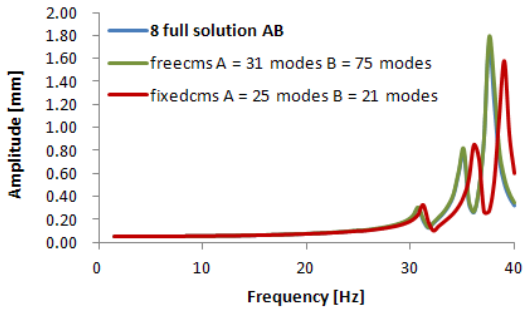

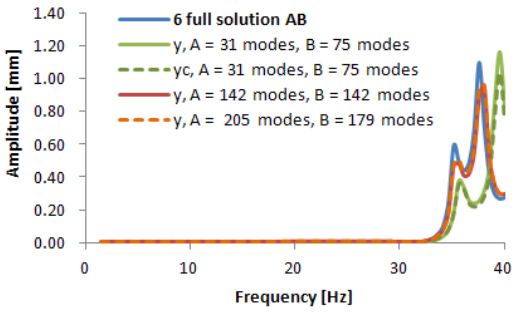

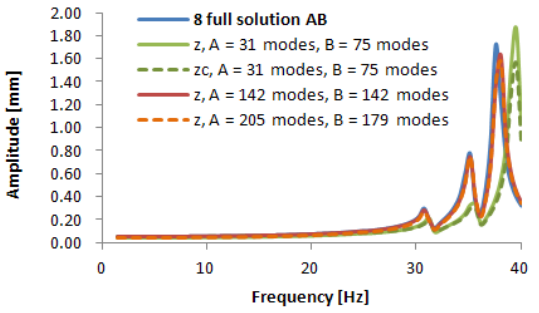

y and z are simulation results obtained in z and y direction respectively by only expanding the normal modes

yc and zc are the simulation results obtained through expanding both normal and static modes in y and z direction respectively

Results Substructure B and C

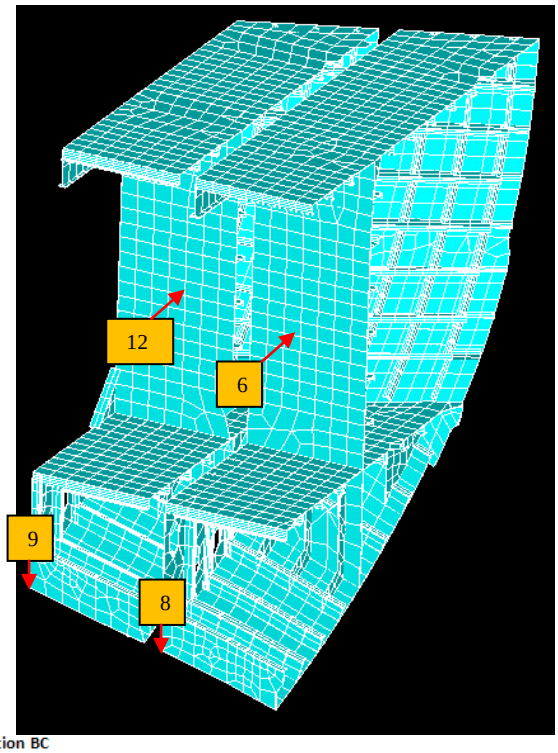

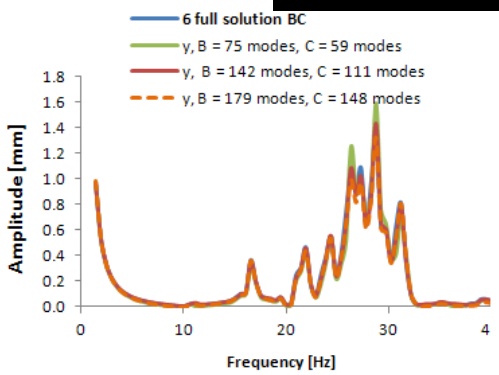

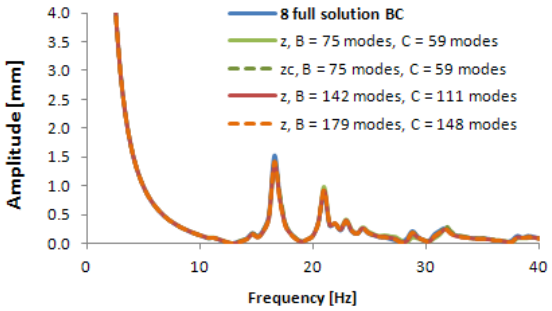

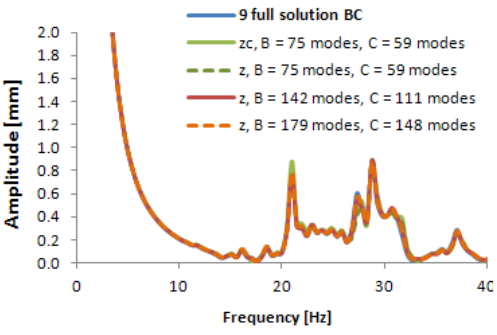

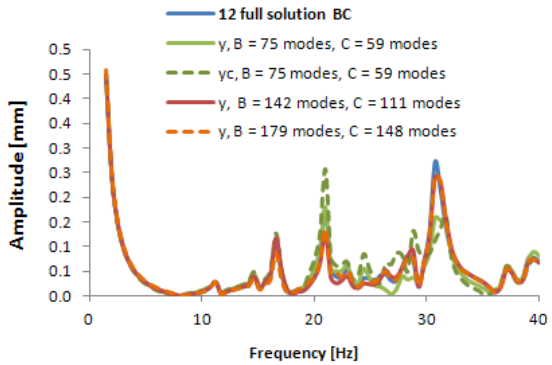

y and z are simulation results obtained in z and y direction respectively by only expanding the normal modes

yc and zc are the simulation results obtained through expanding both normal and static modes in y and z direction respectively

Results Substructure C and D

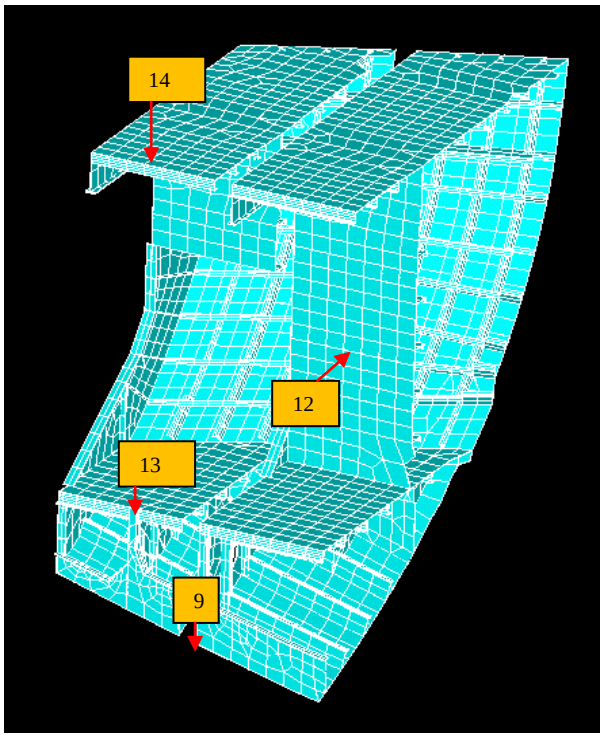

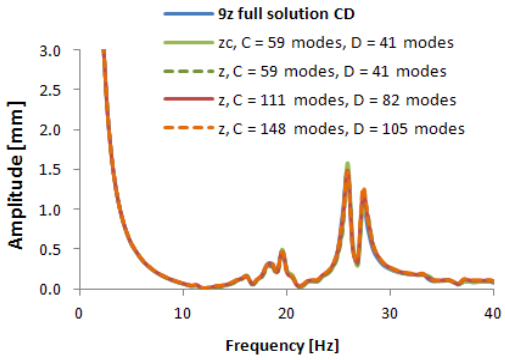

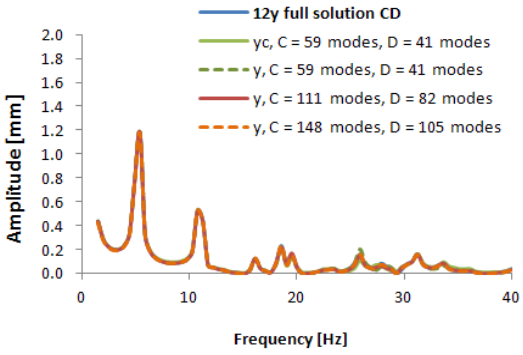

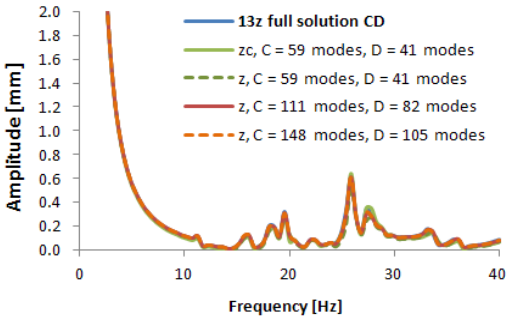

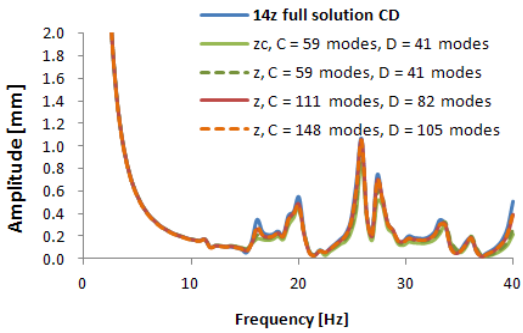

y and z are simulation results obtained in z and y direction respectively by only expanding the normal modes

yc and zc are the simulation results obtained through expanding both normal and static modes in y and z direction respectively

Appendix XXVII *Evaluation of the Effect of Residual Interface Flexibility on the Results of Zoet's method*

Results Substructure A and B

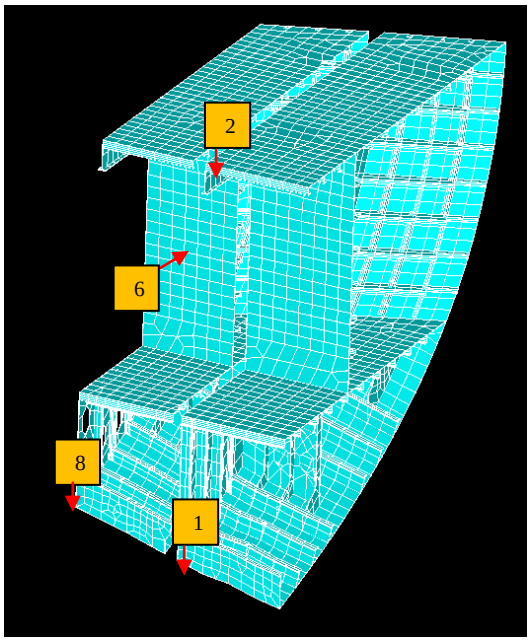

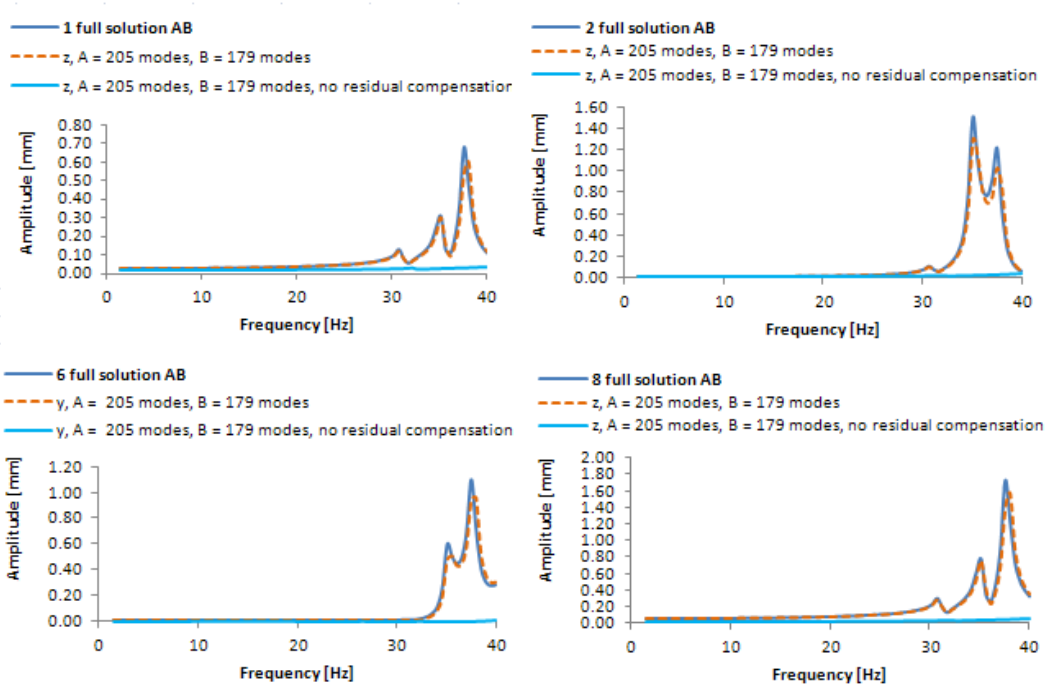

y and z are simulation results obtained in z and y direction respectively by only expanding the normal modes

yc and zc are the simulation results obtained through expanding both normal and static modes in y and z direction respectively

Results Substructure B and C

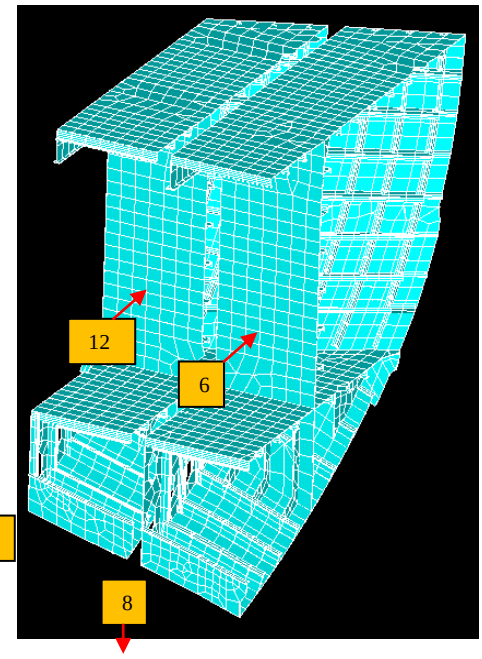

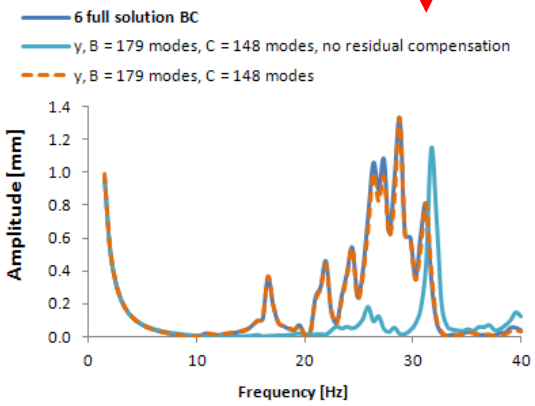

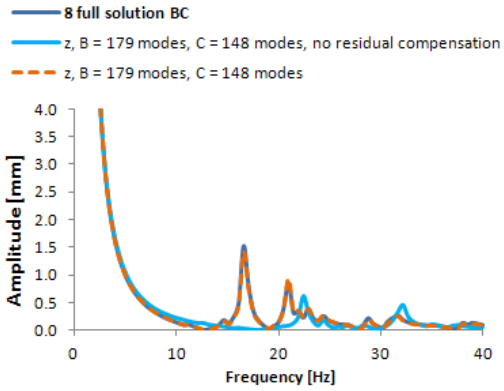

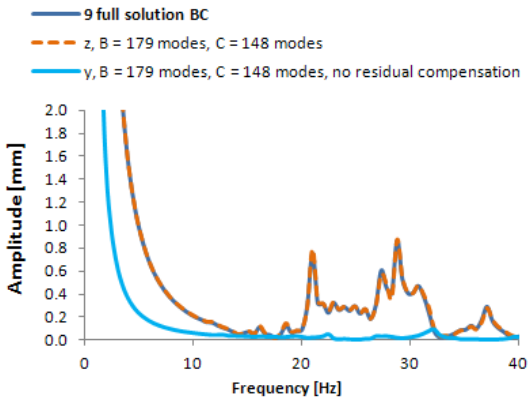

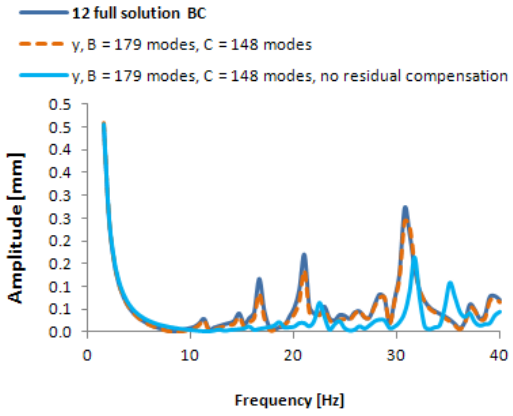

y and z are simulation results obtained in z and y direction respectively by only expanding the normal modes

yc and zc are the simulation results obtained through expanding both normal and static modes in y and z direction respectively

Results Substructure C and D

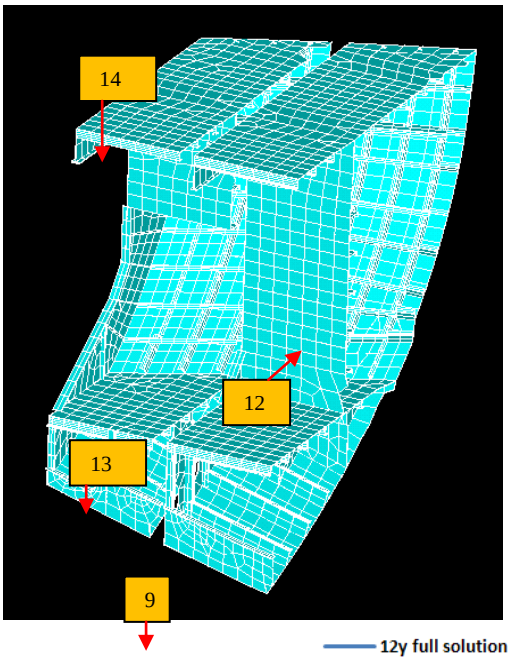

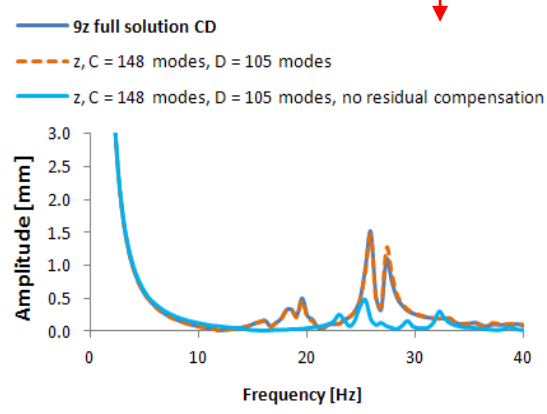

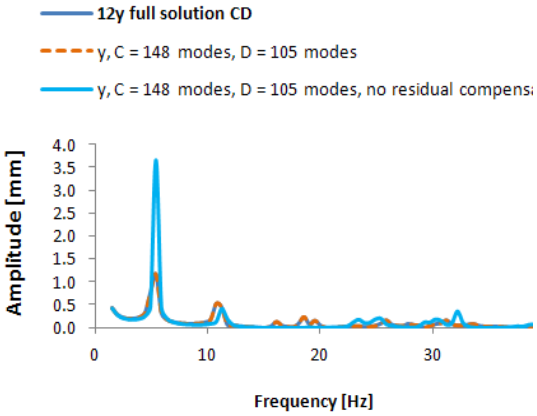

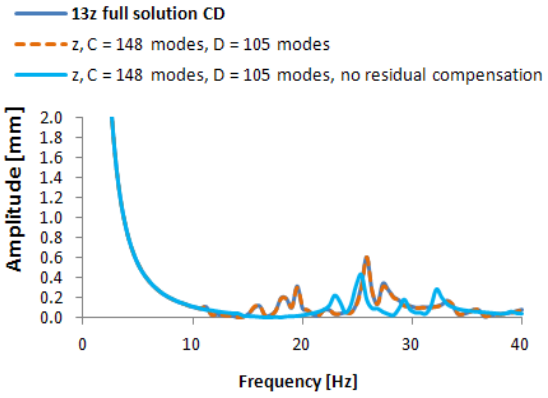

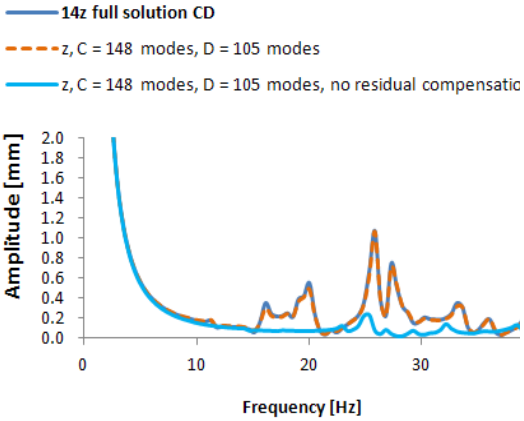

y and z are simulation results obtained in z and y direction respectively by only expanding the normal modes

yc and zc are the simulation results obtained through expanding both normal and static modes in y and z direction respectively

Appendix XXVIII *Test Case Results Zoet Method Total Dynamic Behaviour A, B, C and D Coupled*

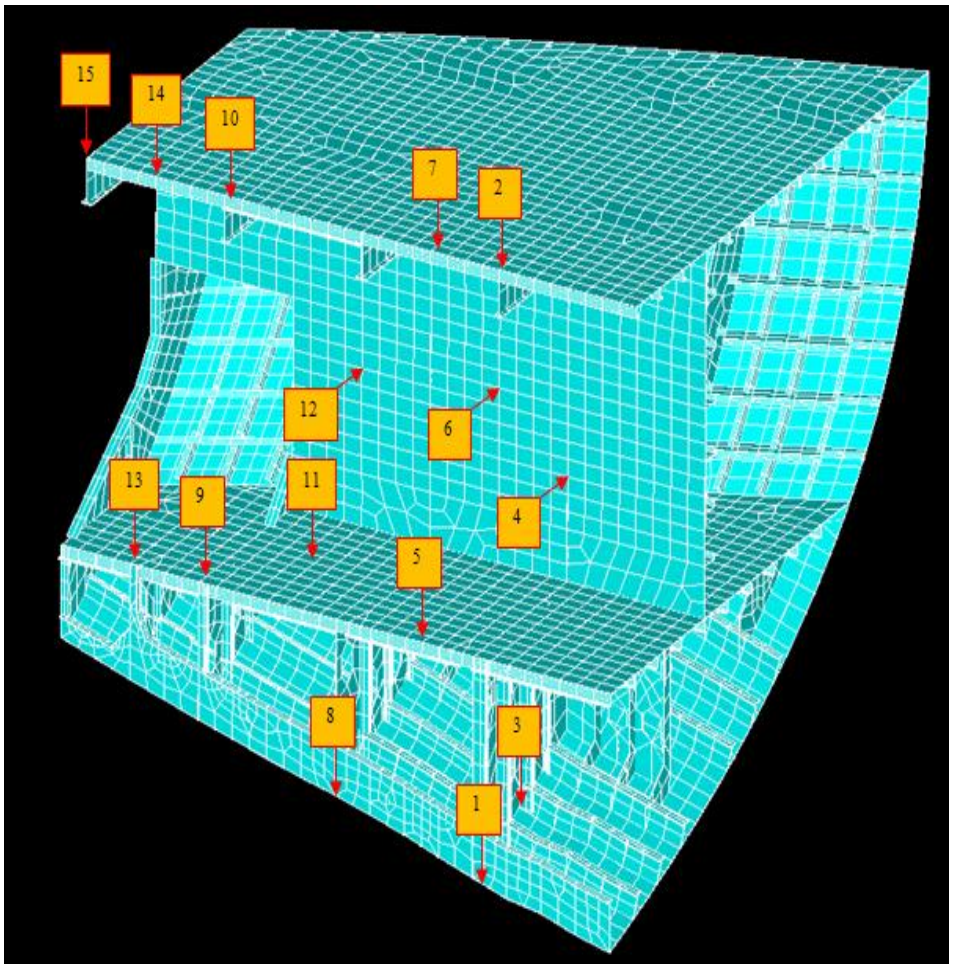

Location 1 **Location 2**

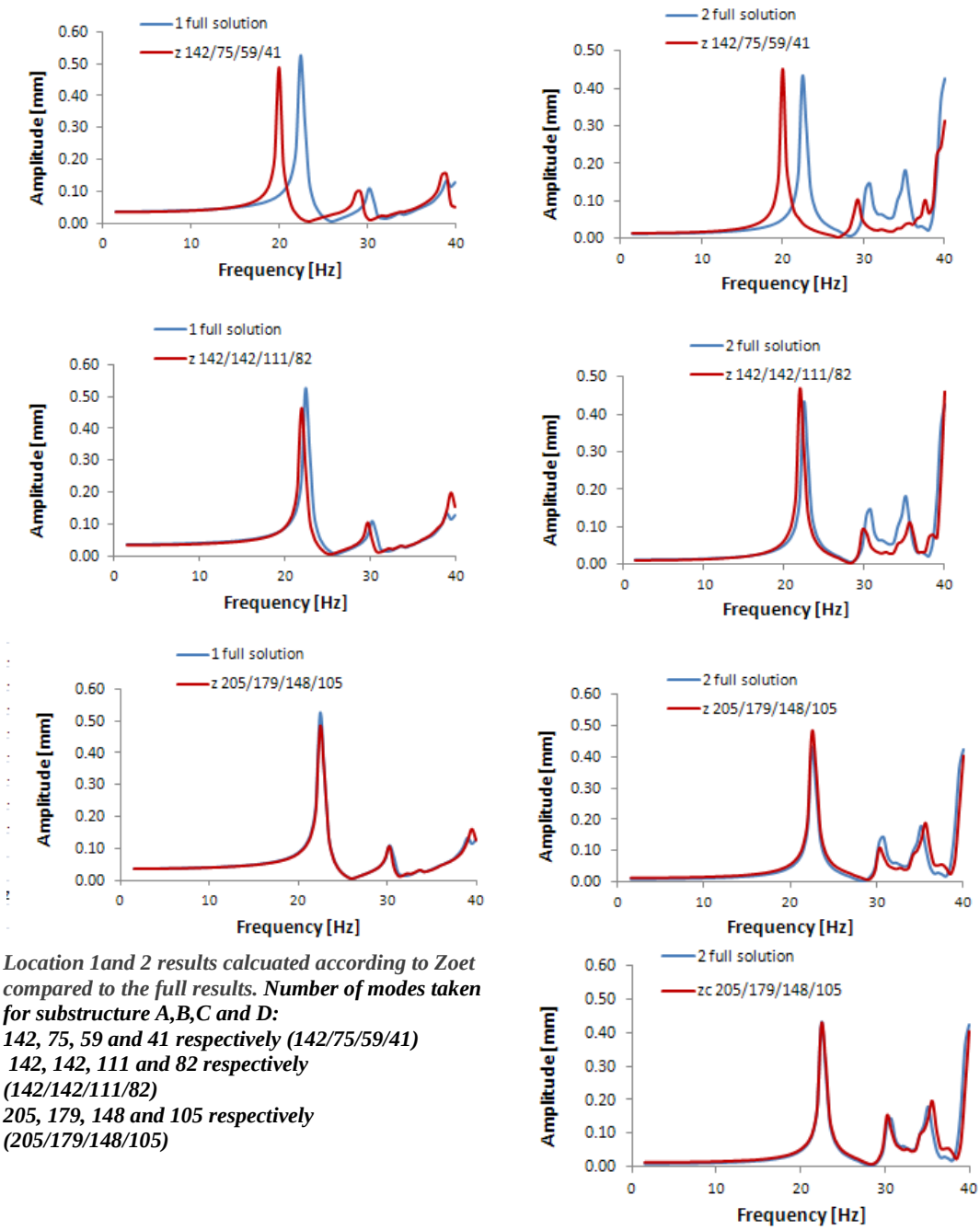

Location 1and 2 results calcuated according to Zoet compared to the full results. ***Number of modes taken for substructure A,B,C and D:***
142, 75, 59 and 41 respectively (142/75/59/41)
142, 142, 111 and 82 respectively (142/142/111/82)
205, 179, 148 and 105 respectively (205/179/148/105)

y and z are simulation results obtained in z and y direction respectively by only expanding the normal modes

yc and zc are the simulation results obtained through expanding both normal and static modes in y and z direction respectively

Location 3 **Location 4**

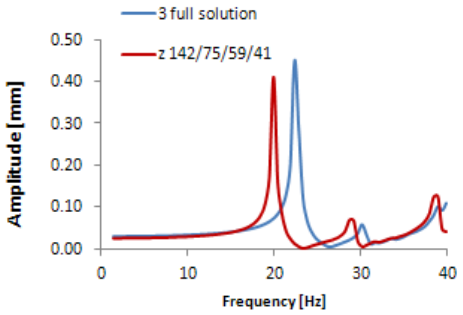

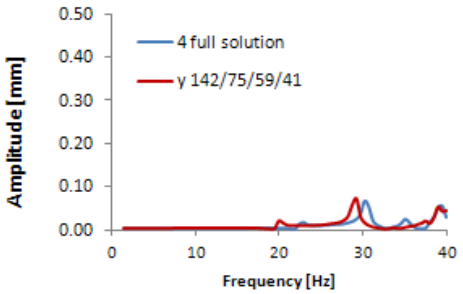

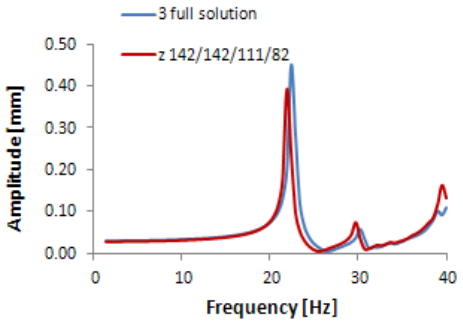

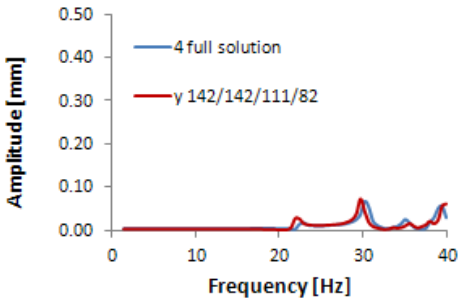

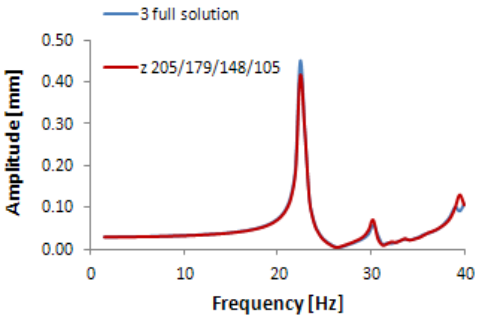

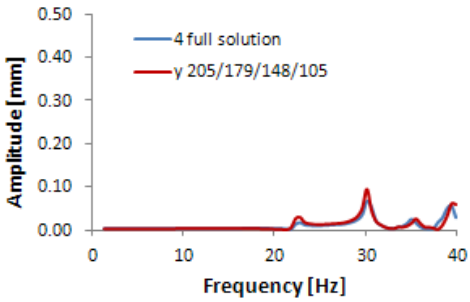

Location 3and 4 results calcuated according to Zoet compared to the full results. ***Number of modes taken for substructure A,B,C and D:***
142, 75, 59 and 41 respectively (142/75/59/41)
142, 142, 111 and 82 respectively (142/142/111/82)
205, 179, 148 and 105 respectively (205/179/148/105)

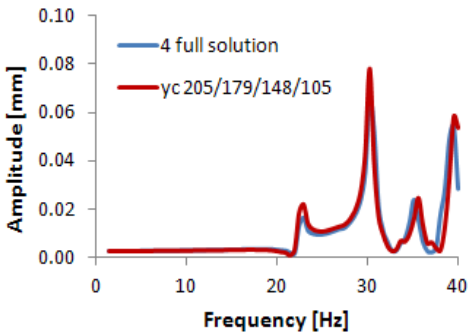

y and z are simulation results obtained in z and y direction respectively by only expanding the normal modes

yc and zc are the simulation results obtained through expanding both normal and static modes in y and z direction respectively

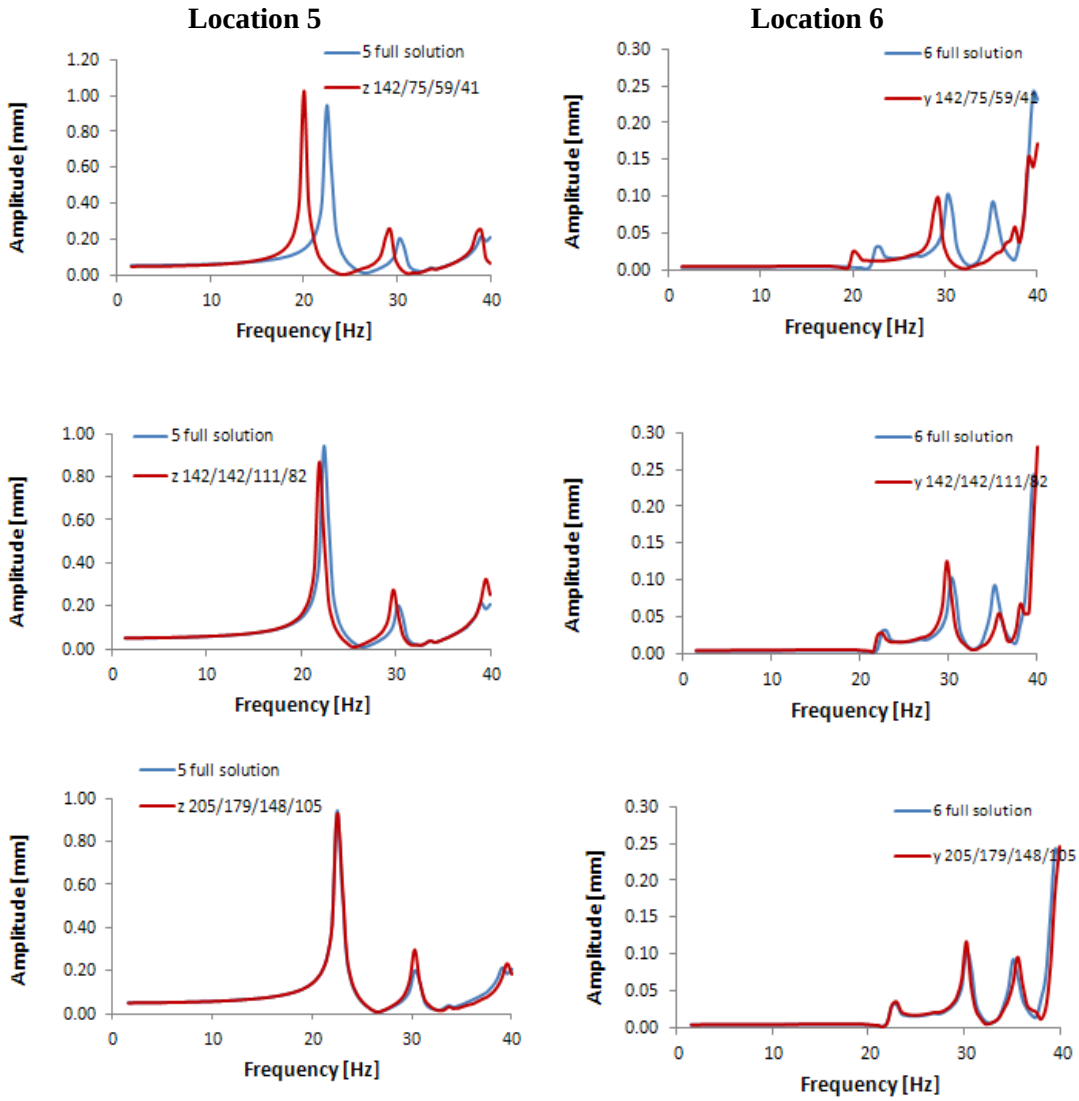

Location 5and 6 results calcuated according to Zoet compared to the full results. ***Number of modes taken for substructure A,B,C and D:***

142, 75, 59 and 41 respectively (142/75/59/41)
142, 142, 111 and 82 respectively (142/142/111/82)
205, 179, 148 and 105 respectively (205/179/148/105)

y and z are simulation results obtained in z and y direction respectively by only expanding the normal modes

yc and zc are the simulation results obtained through expanding both normal and static modes in y and z direction respectively

Location 7	Location 8

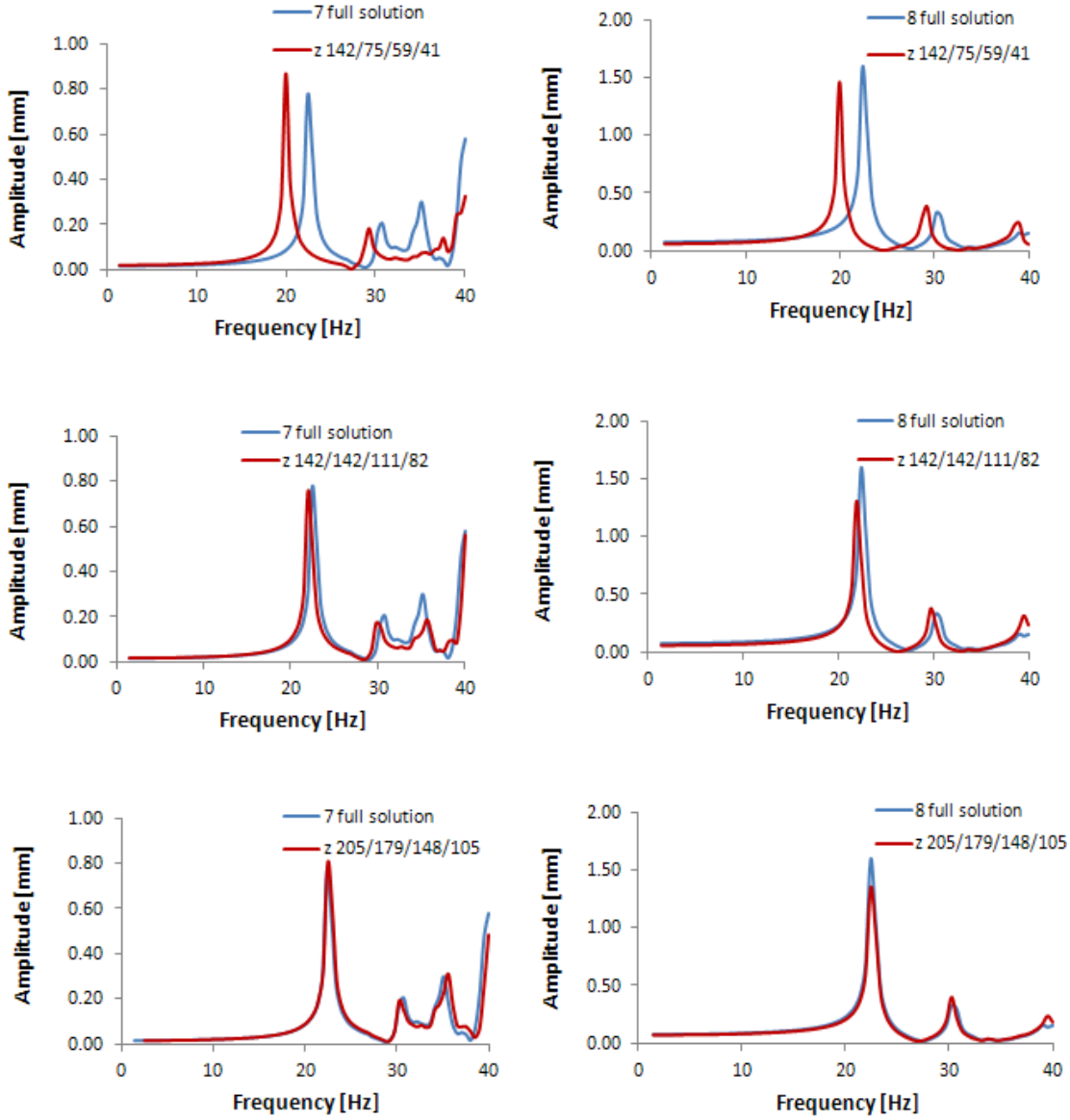

Location 7and 8 results calcuated according to Zoet compared to the full results. ***Number of modes taken for substructure A,B,C and D:***

142, 75, 59 and 41 respectively (142/75/59/41)
142, 142, 111 and 82 respectively (142/142/111/82)
205, 179, 148 and 105 respectively (205/179/148/105)

y and z are simulation results obtained in z and y direction respectively by only expanding the normal modes

yc and zc are the simulation results obtained through expanding both normal and static modes in y and z direction respectively

Location 9	Location 10

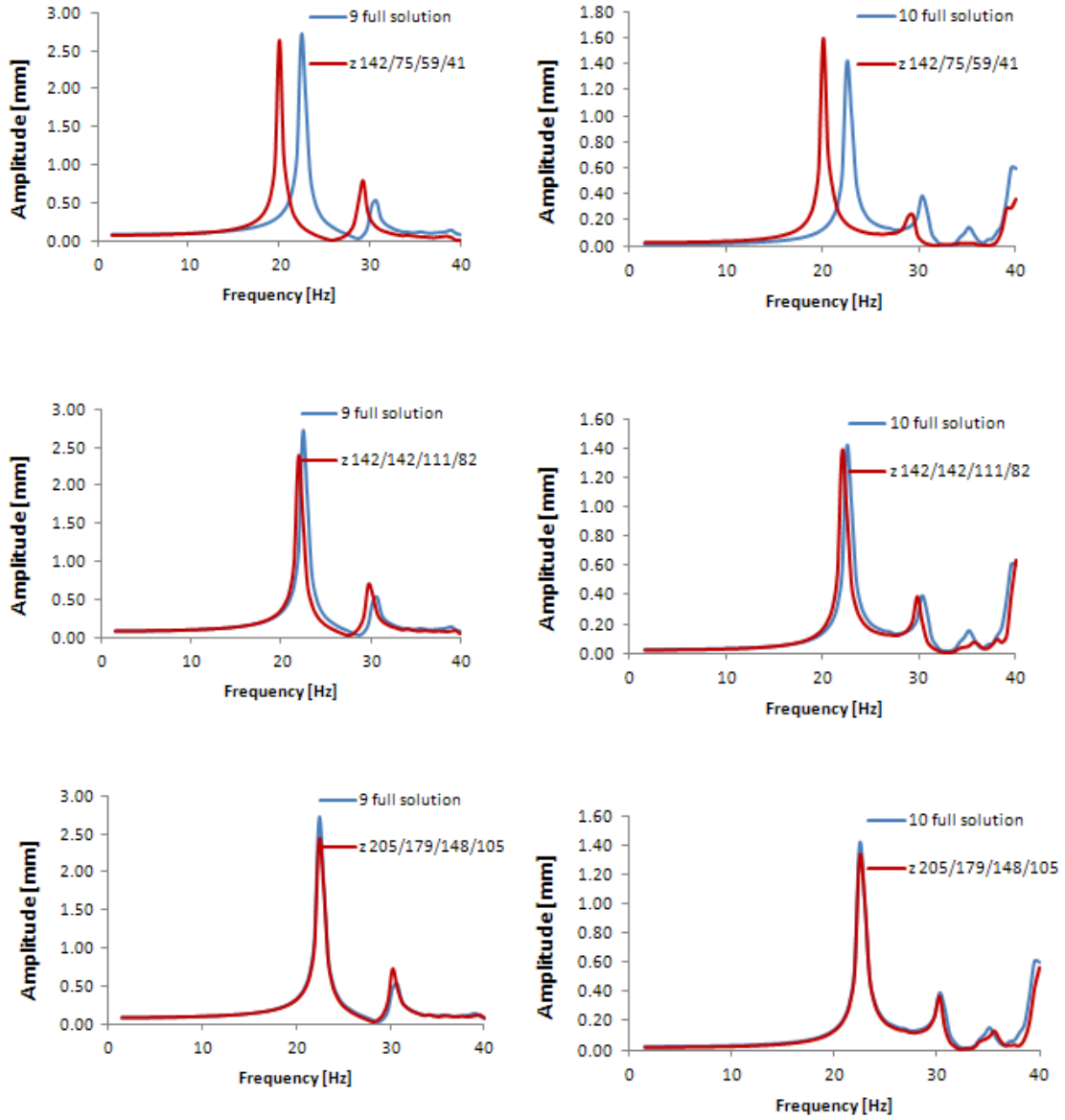

Location 9and10 results calcuated according to Zoet compared to the full results. ***Number of modes taken for substructure A,B,C and D:***

142, 75, 59 and 41 respectively (142/75/59/41)
142, 142, 111 and 82 respectively (142/142/111/82)
205, 179, 148 and 105 respectively (205/179/148/105)

y and z are simulation results obtained in z and y direction respectively by only expanding the normal modes

yc and zc are the simulation results obtained through expanding both normal and static modes in y and z direction respectively

Location 11	Location 12

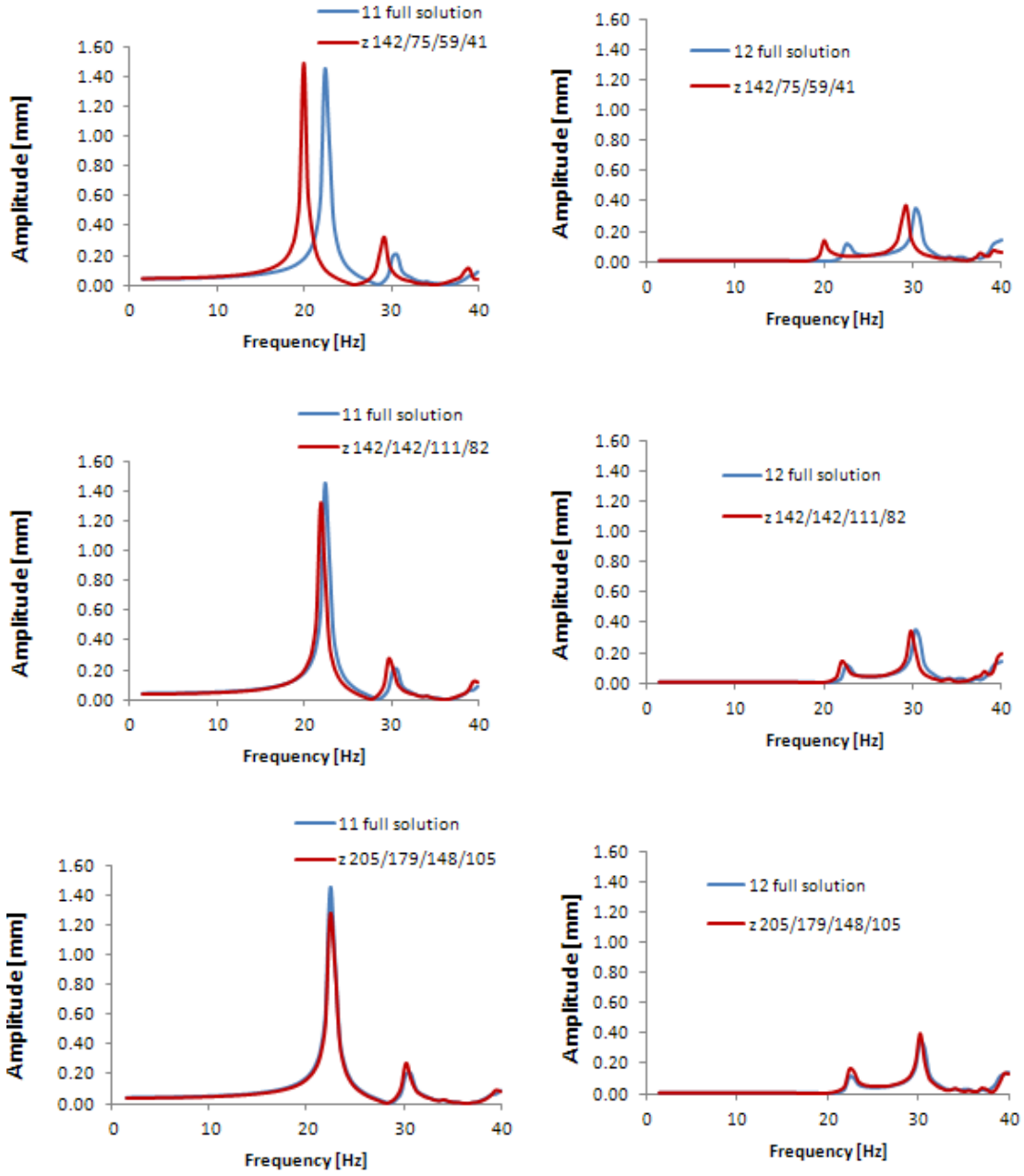

Location 11and12 results calcuated according to Zoet compared to the full results. ***Number of modes taken for substructure A,B,C and D:***

142, 75, 59 and 41 respectively (142/75/59/41)
142, 142, 111 and 82 respectively (142/142/111/82)
205, 179, 148 and 105 respectively (205/179/148/105)

y and z are simulation results obtained in z and y direction respectively by only expanding the normal modes

yc and zc are the simulation results obtained through expanding both normal and static modes in y and z direction respectively

Location 13	Location 14
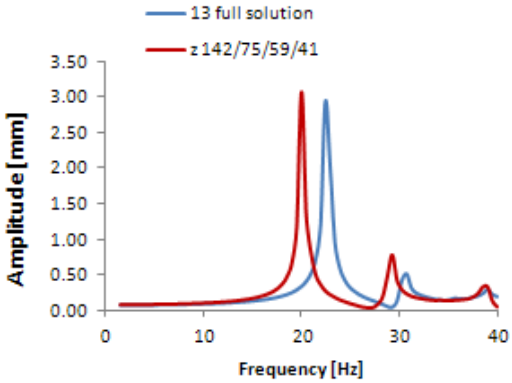	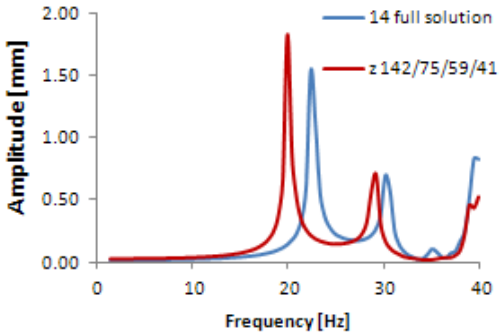
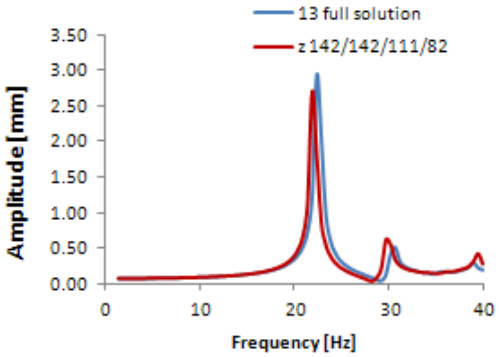	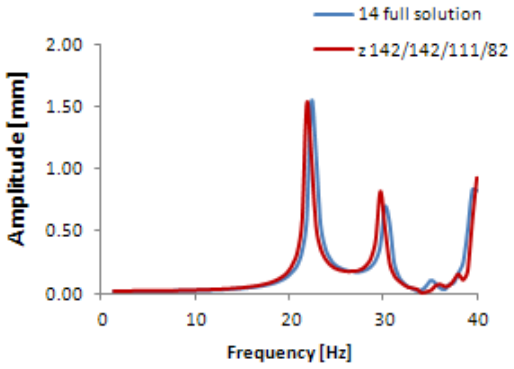
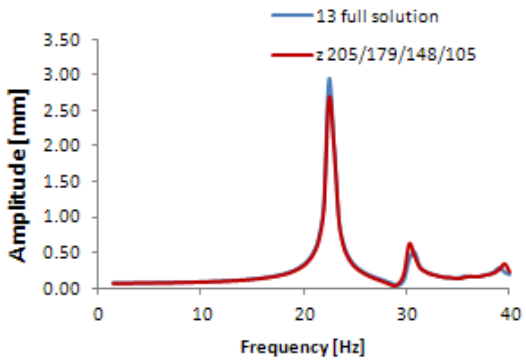	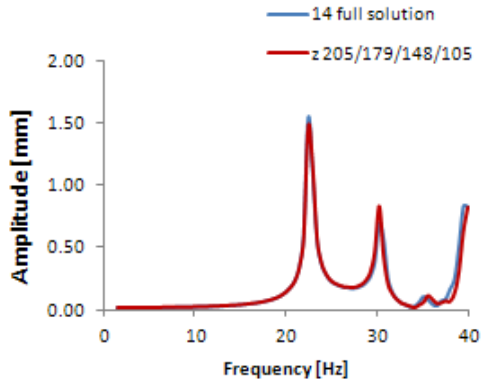

Location 13and14 results calcuated according to Zoet compared to the full results. Number of modes taken for substructure A,B,C and D:

142, 75, 59 and 41 respectively (142/75/59/41)
142, 142, 111 and 82 respectively (142/142/111/82)
205, 179, 148 and 105 respectively (205/179/148/105)

y and z are simulation results obtained in z and y direction respectively by only expanding the normal modes

yc and zc are the simulation results obtained through expanding both normal and static modes in y and z direction respectively

Location 15

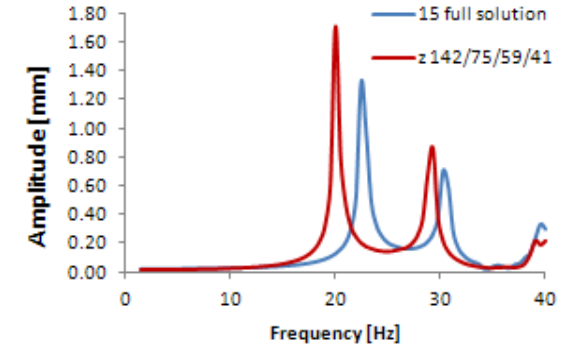

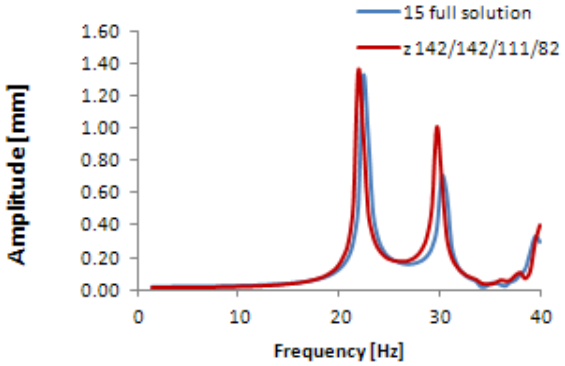

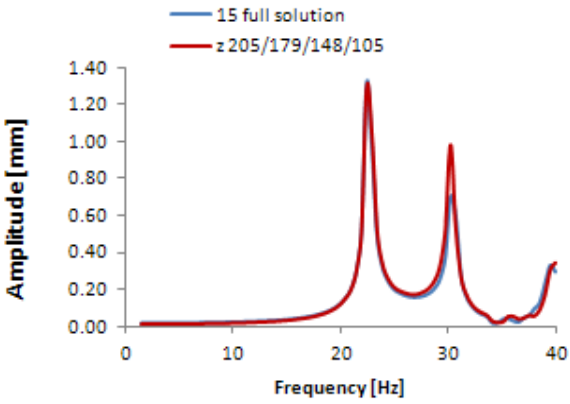

Location 15 results calcuated according to Zoet compared to the full results. ***Number of modes taken for substructure A,B,C and D:***

142, 75, 59 and 41 respectively (142/75/59/41)
142, 142, 111 and 82 respectively (142/142/111/82)
205, 179, 148 and 105 respectively (205/179/148/105)

y and z are simulation results obtained in z and y direction respectively by only expanding the normal modes

yc and zc are the simulation results obtained through expanding both normal and static modes in y and z direction respectively

Appendix XXIX *Reduced Test Case Results Zoet Method, Substructures A, B and C Coupled*

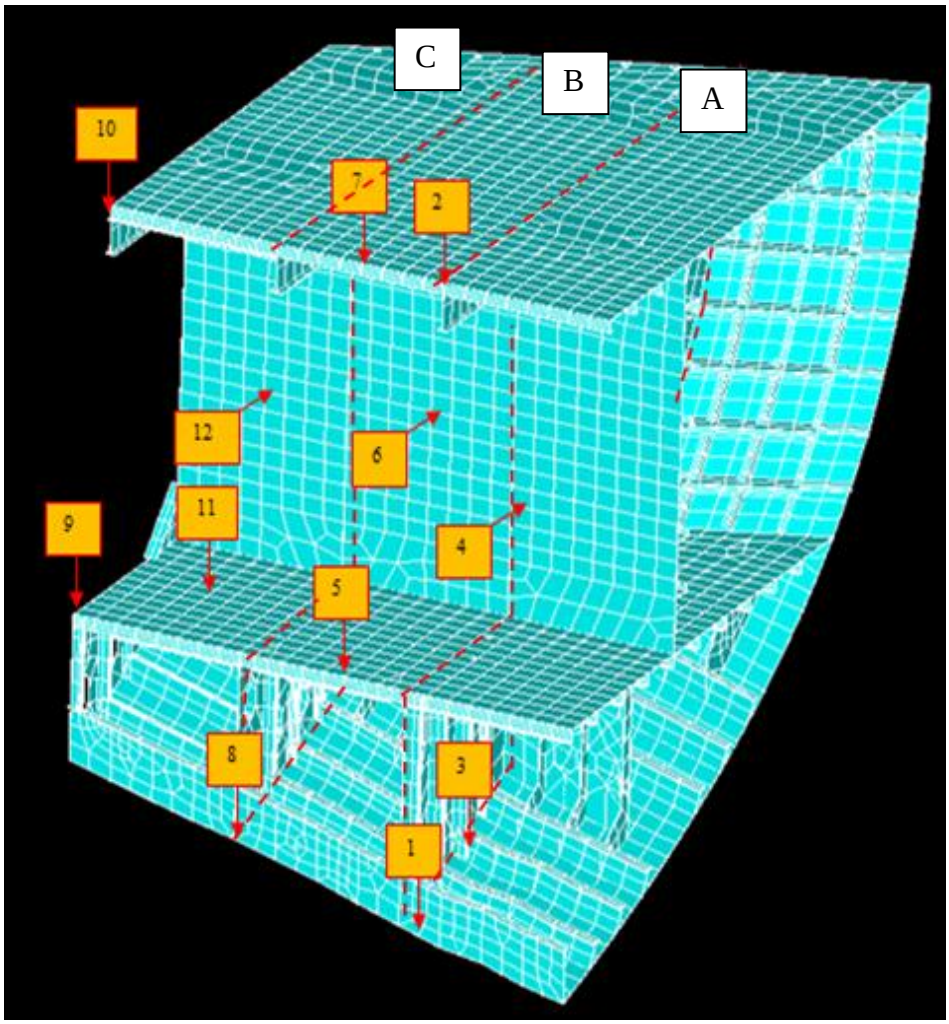

Test model flexible boundary CMS	Number of nodes	Number of modes required	Number of boundary nodes	Number of boundary degrees of freedomnodes	Required CP for calcuating eigenvectors and eigenvalues	Required CP generation pass
PartAfixedcms	1903	25	140	840	9.3	11.8
PartAfreecms		31	140	840	11	14.8
PartBfixedcms	1695	21	140 and 120	1560	9.5	11.8
PartBfreecms		75	140 and 120	1566	11	16.5
PartCfixedcms	1342	16	120	1296	9.1	9.4
PartCfreecms		59	120	1320	9.5	13.42

Reduced test model subdivided into three substructures (A, B and C). Dotted lines show the interface boundaries of the substructures. Model is clamped at the nodes on the far right side of substructure

Free CMS is free interface CMS according to Rubin's method (without residual compensation) and fixed interface CMS is according to Craig-Bamton's method.

For selecting the number of retained normal modes, a cut-out frequency has been applied of 1.5 fmax = 60 Hz

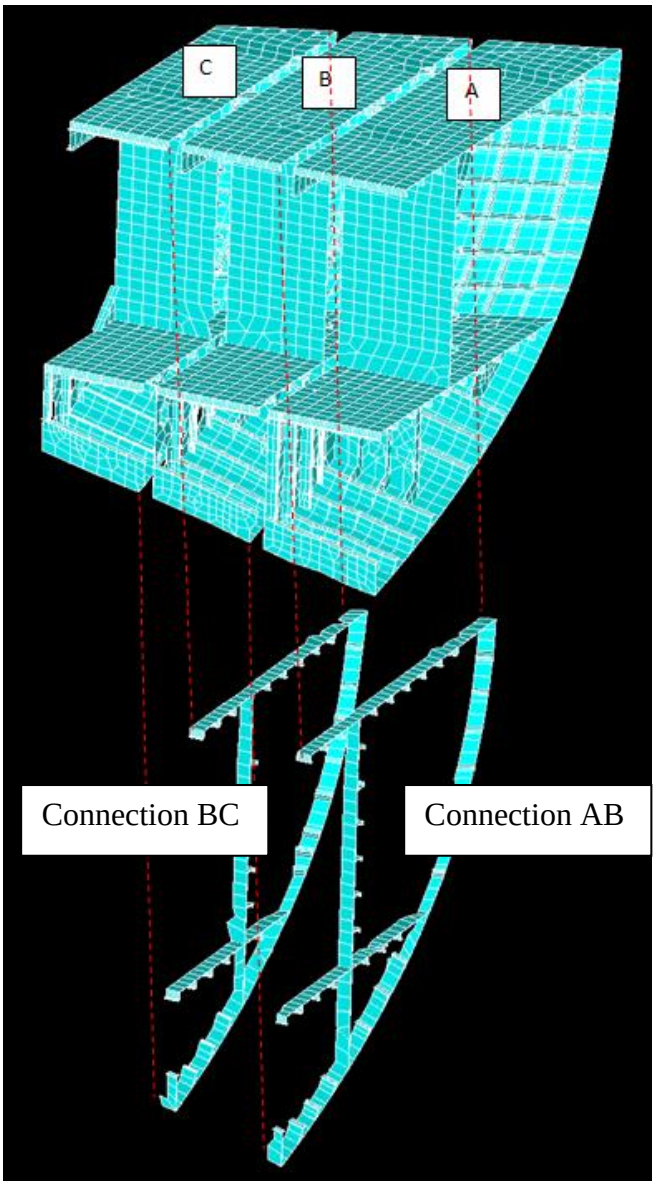

Test model flexible boundary CMS	Number of nodes	Number of modes required	Number of boundary nodes	Number of boundary degrees of freedomnodes	Required CP for calcuating eigenvectors and eigenvalues	Required time generation pass
PartAfreecms	1903	31	140	840	10.2	14.8
PartA Zoet	1903	205	140	840	16.3	18.9
PartBfreecms	1695	75	140 and 120	1560	11	16.5
PartB Zoet	1555	179	141 and 120	1566	13.3	18.3
PartCfreecms	1342	59	120	1296	9.5	13.4
PartC Zoet	1222	148	124	1320	12	17.6

Free CMS is free interface CMS according to Rubin's method (without residual compensation). For selecting the number of retained normal modes, a cut-out frequency has been applied of 1.5 fmax = 60 Hz for Rubin's method, and 3 fmax = 120 Hz for Zoet's method (see section 9.3)

Location 1

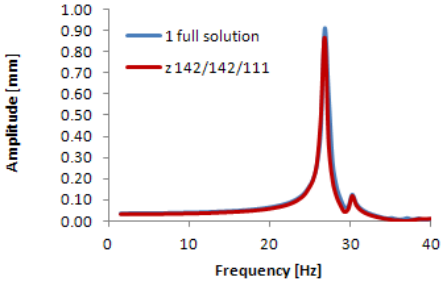

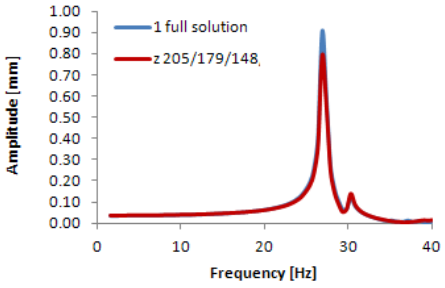

Location 2

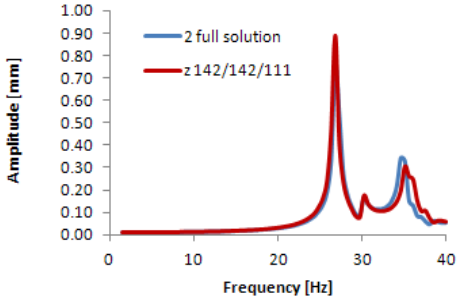

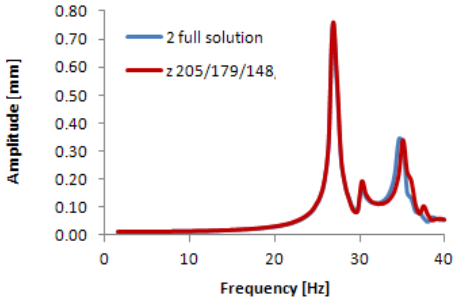

Location 3

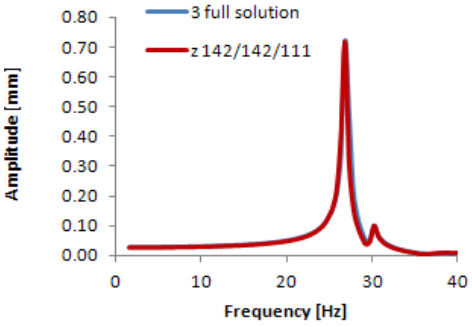

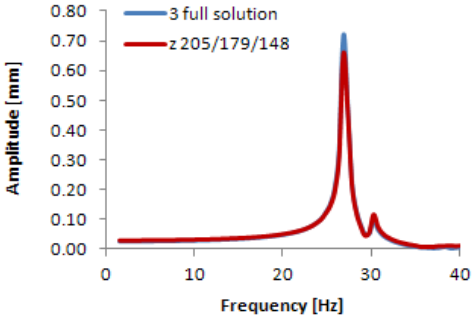

Location 4

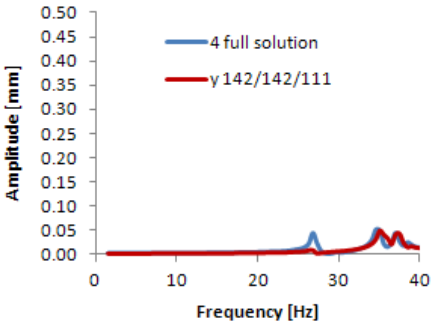

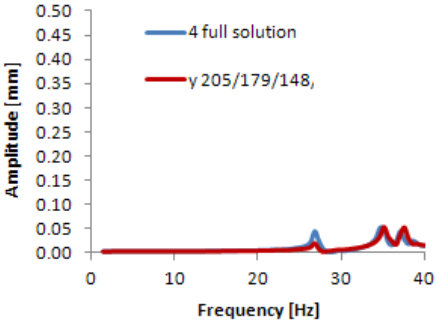

y and z are simulation results obtained in z and y direction respectively by only expanding the normal modes

yc and zc are the simulation results obtained through expanding both normal and static modes in y and z direction respectively

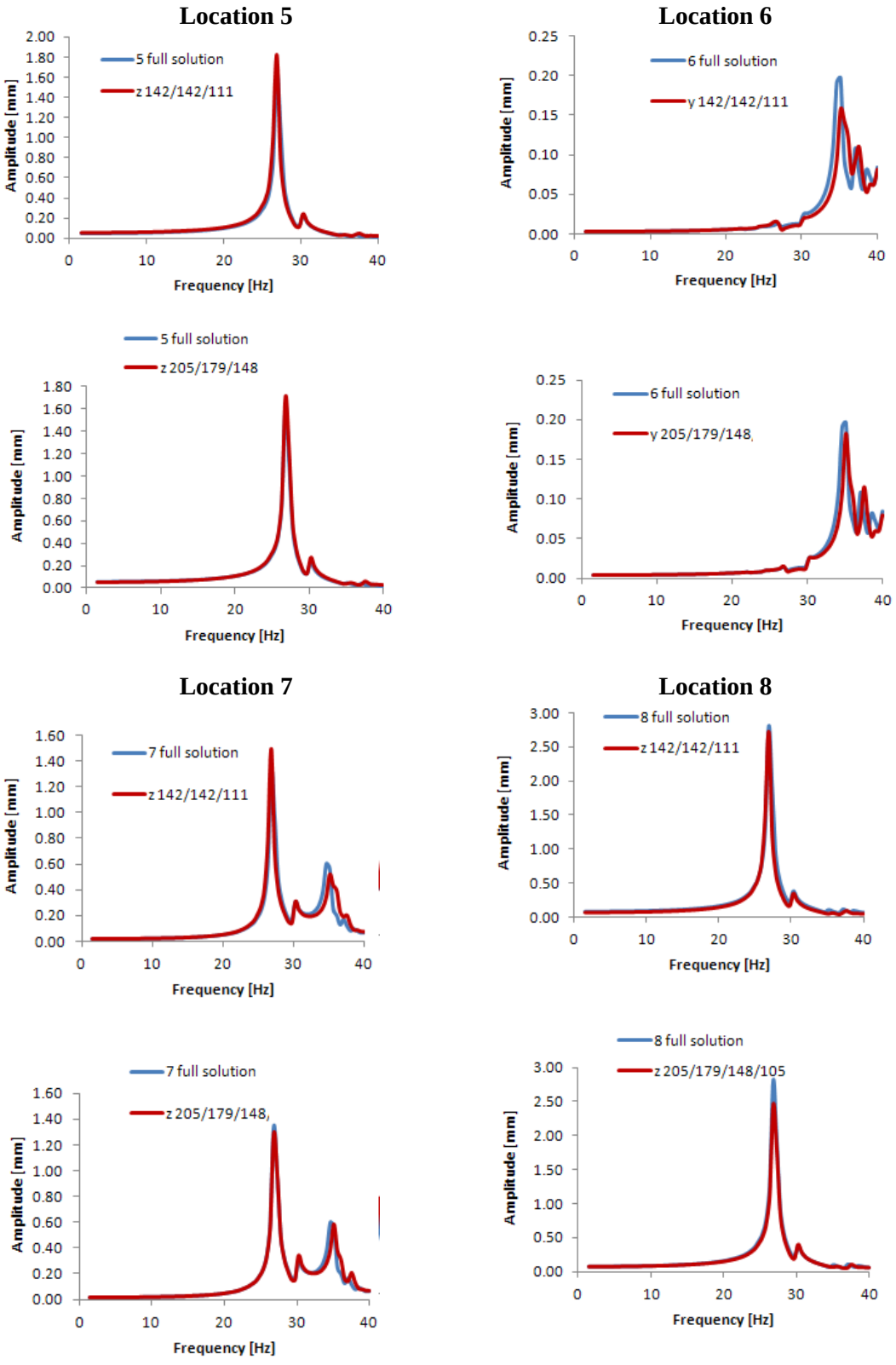

y and z are simulation results obtained in z and y direction respectively by only expanding the normal modes

yc and zc are the simulation results obtained through expanding both normal and static modes in y and z direction respectively

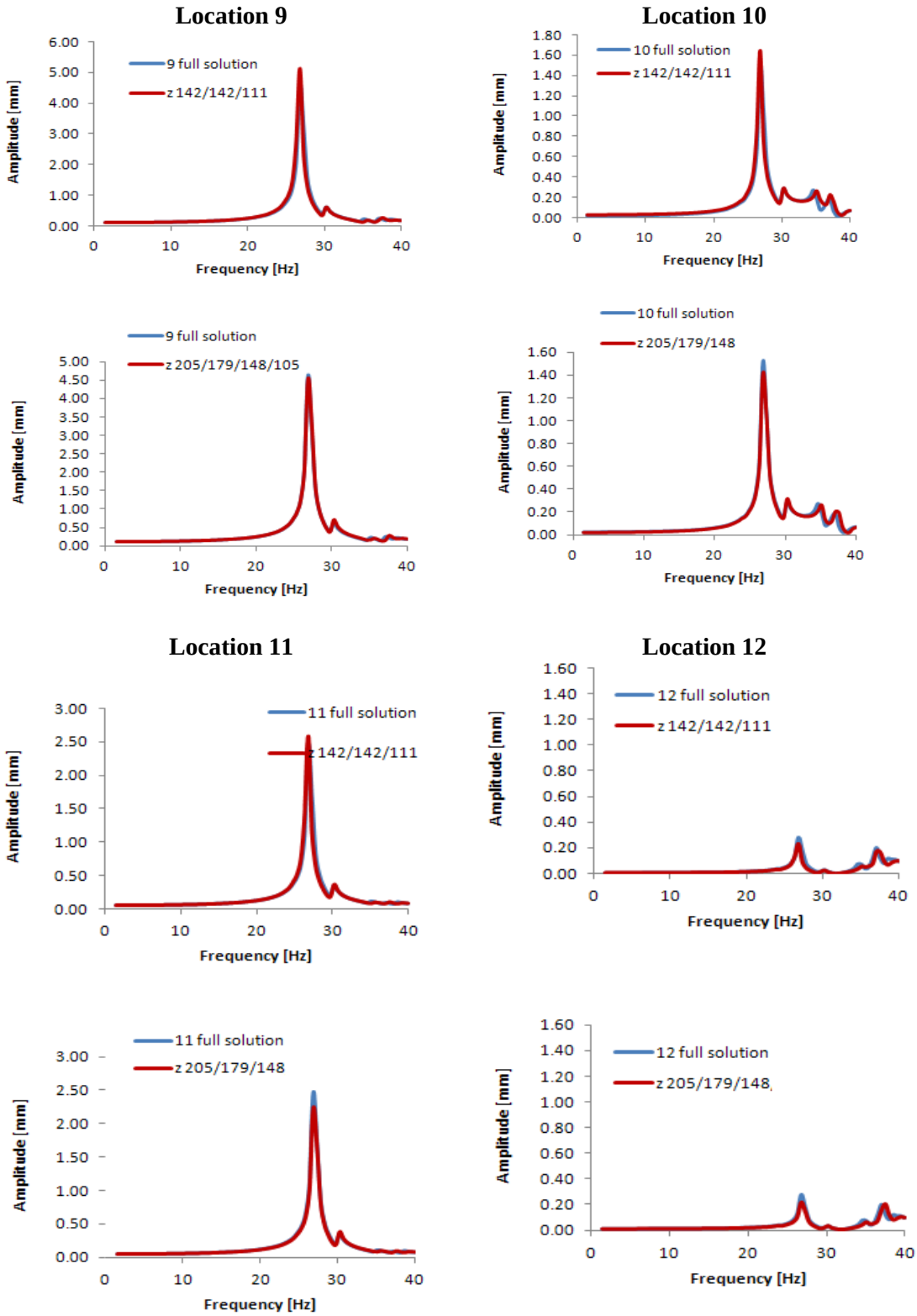

y and z are simulation results obtained in z and y direction respectively by only expanding the normal modesyc and zc are the simulation results obtained through expanding both normal and static modes in y and z direction respectively

Appendix XXX *Rubin's Method With Interface Modes for PHD Test Case*

	Method	Number of nodes	Number of boundary nodes		Number of boundary degrees of freedomnodes	Number of modes required retained	Required CP for calcuating eigenvectors and eigenvalues	Required CP generation pass
Part A	PartAfixedcms	1903	Bounary A-B	140	840	25	9.3	11.8
	PartAfreecms		Bounary A-B	140	840	31	11	14.8
	PartA Zoet and Rubin-Zoet method		Bounary A-B	140	840	205	16.3	18.9
Part B	PartBfixedcms	1695	Boundary B-A	140	840	21	9.5	11.8
			Boundary B-C	120	720			
	PartBfreecms		Boundary B-A	140	840	75	11	16.5
			Boundary B-C	120	720			
	PartB Zoet and Rubin-Zoet method		Boundary B-A	141	846	179	13.3	18.3
			Boundary B-C	120	720			
Part C	PartCfixedcms	1342	Boundary C-B	120	720	16	9.1	9.4
			Boundary C-D	96	576			
	PartCfreecms		Boundary C-B	120	720	59	9.5	13.42
			Boundary C-D	96	576			
	PartC Zoet and Rubin-Zoet method		Boundary C-B	124	744	148	12	17.6
			Boundary C-D	96	576			
part D	PartDfixedcms	1160	Boundary D-C	96	576	15	8.84	9.1
	PartDfreecms		Boundary D-C	96	576	41	8.7	10.7
	PartD Zoet and Rubin-Zoet method		Boundary D-C	95	570	105	10	13.8

Properties of the substructures used as a test case for the Zoet method (see Appendix XXIV and Appendix XXV). Fixed and free CMS is CMS based on the fixed interface approach (Craig-Bampton) and the free interface approach (Rubin's method without residual compensation) respectively.

For all methods a cut-out frequency of 1.5* f_{max} Hz (=60 Hz) has been applied for the selection of the number of normal modes of the individual substructures.
The number of floating point operations has been calculated for applying the Rubin-Zoet method for 80 frequency steps in the range between 1 and 40 Hz.

Cut-out frequency used for the selection of the number of retained interface modes is $3.5 * f_{max}$ = 140 Hz, based on the finding by Tran [41]

Here follow the calculation results of the number of real floating point operations required for each step for obtaining results according to Rubin's method, using interface (boundary) reduction through application of interface modes. No floating point operations have been calculated required for the generation of the mode shapes and natural frequencies. The number of floating point operation required for are estimated through measured CP times and are presented in Appendix XXXI.

See Appendix XVII 'Steps and Estimated Number of Matrix Operations Rubin's Method using Interface Modes' for description of symbols used and equations for estimating floating point operations.

Step 1: Generating constraint modes			Step 1A	Step 1B
PartA	ni	10578	5.96E+09	7.11E+08
boundary A-B	n boundary	840		
PartB	ni	9330	4.64E+09	6.27E+08
Boundary B-A	n boundary	840		
Boundary B-C	ni	9450	4.76E+09	5.44E+08
	n boundary	720		
PartC	ni	7332	2.86E+09	4.22E+08
Boundary C-B	n boundary	720		
Boundary C-D	ni	7476	2.98E+09	3.44E+08
	n boundary	576		
PartD	ni	6384	2.17E+09	2.94E+08
	n boundary	576		
Total number of FLOPS for each step			2.34E+10	2.94E+09
Grand total for calcuating all required constraint modes (Step 1)				2.63E+10
n bandwidth = 40				

Required calculation time for each step 1 and 2 of the Rubin's method using interface reduction through application of interface modes following the IRS method. Calculation times are based on applying a cut-out frequency of 60 Hz for selecting normal modes of individual substructures, and applying a cut-out frequency of 3.5 fmax = 140 Hz for selecting the number of interface modes. Calculation times are based on analysing 80 frequency steps between 1 and 40 Hz.(see Appendix XVII for description calculation time and Appendix XXIV for description geometry test structure)

Step 2: Reducing the Interface Dgrees of Freedom			Step 2A	Step 2B
PartA	ni	10578	1.42E+09	2.99E+10
boundary A-B	n boundary	840		
	n bandwidth	40		
PartB	ni	9330	1.25E+09	2.63E+10
Boundary B-A	n boundary	840		
	n bandwidth	40		
Boundary B-C	ni	9450	1.09E+09	1.96E+10
	n boundary	720		
	n bandwidth	40		
PartC	ni	7332	8.45E+08	1.52E+10
Boundary C-B	n boundary	720		
	n bandwidth	40		
Boundary C-D	ni	7476	6.89E+08	9.92E+09
	n boundary	576		
	n bandwidth	40		
PartD	ni	6384	5.88E+08	8.47E+09
Boundary D-C	n boundary	576		
	n bandwidth	40		
Total number of FLOPS for each step			5.89E+09	1.09E+11
Grand total for calcuating step2				1.15E+11

Step 3: Generating the reduction basis			Step 3A	Step 3B
PartA	ni	10578	5.51E+08	3.28E+05
	n boundary	840		
	nn	31		
	nL	130		
PartB	ni	8610	2.01E+09	6.46E+05
	n boundary	1560		
	nn	75		
	nL	191		
Part C	ni	6756	1.03E+09	3.99E+05
	n boundary	1296		
	nn	59		
	nL	162		
Part D	ni	6384	3.02E+08	2.62E+05
	n boundary	576		
	nn	41		
	nL	62		
Total number of FLOPS for each step			3.90E+09	1.63E+06
Grand total for calculating step 3				3.90E+09

Step 4: Generating reduced mass and stiffness matrices			Step 4A	Step 4B	Step 4C
PartA	n	11418	3.38E+08	1.17E+09	3.62E+06
	nn	31			
	nbandwidth	46			
	na	161			
	nL	130			
	ni	10578			
PartB	n	10170	4.98E+08	2.75E+09	5.18E+06
	nn	75			
	nbandwidth	46			
	na	266			
	nL	191			
	ni	8610			
Part C	n	8052	3.27E+08	1.51E+09	3.41E+06
	nn	59			
	nbandwidth	46			
	na	221			
	nL	162			
	ni	6756			
Part D	n	6960	1.32E+08	2.86E+08	1.39E+06
	nn	41			
	nbandwidth	46			
	na	103			
	nL	62			
	ni	6384			
Total number of FLOPS for each step			1.30E+09	5.71E+09	1.36E+07
Grand total for generating reduced matrices					7.02E+09

Required calculation time for step 3 and 4 of the Rubin's method using interface reduction through application of interface modes following the IRS method. Calculation times are based on applying a cut-out frequency of 60 Hz for selecting normal modes of individual substructures, and applying a cut-out frequency of 3.5 fmax = 140 Hz for selecting the number of interface modes. Calculation times are based on analysing 80 frequency steps between 1 and 40 Hz.(see Appendix XVII for description calculation time and Appendix XXIV for description geometry test structure)

			Step 5A	Step 5B
PartA	nn	31	7.78E+04	7.78E+04
	nL	130		
PartB	nn	75	2.12E+05	2.12E+05
	nL	191		
Part C	nn	59	1.47E+05	1.47E+05
	nL	162		
Part D	nn	41	3.18E+04	3.18E+04
	nL	62		
Total number of FLOPS for each step			4.68E+05	4.68E+05
Grand total for generating reduced matrices				9.37E+05

Forcing compatibility and equilibrium relations			Step 6A	Step 6B	Step 6C	Step 6D
	nLkept	253	2.73E+08	3.16E+08	2.16E+07	3.74E+07
	nLred	292				
	nboundary	2136				
Total number of FLOPS for each step			2.73E+08	3.16E+08	2.16E+07	3.74E+07
Grand total FLOPS for forcing compatibility and equilibrium relations					6.48E+08	

Forcing compatibility and equilibrium relations			Step 7A	Step 7B	Step 7C
	nLred	292	2.36E+08	3.70E+08	5.06E+07
	nNtotal	206			
	nLkept	253			
Total number of FLOPS for each step			2.36E+08	3.70E+08	5.06E+07
Grand total FLOPS for forcing compatibility and equilibrium relations					6.57E+08

Required calculation time for step 5 to 6 of the Rubin's method using interface reduction through application of interface modes following the IRS method. Calculation times are based on applying a cut-out frequency of 60 Hz for selecting normal modes of individual substructures, and applying a cut-out frequency of 3.5 fmax = 140 Hz for selecting the number of interface modes. Calculation times are based on analysing 80 frequency steps between 1 and 40 Hz.(see Appendix XVII for description calculation time and Appendix XXIV for description geometry test structure)

Rubin's Method With Interface Reduction		
number of frequencies		80
Generation Pass		
Step number	Action	Estimated FLOPS
Calculating natural frequencies and modeshapes		1.31E+12
1	Generating constraint modes	2.63E+10
step 2 and 3	Generating reduction basis	1.19E+11
step 4	Generating Reduced mass and stiffness	7.02E+09
Total Flops Generation Pass		1.46E+12
Use Pass		
Step number	Action	Estimated FLOPS
step 5	Compiling reduced dynamic stiffness	9.37E+05
step 6 and 7	Formulating compatibility and equilibrium relations for boundary	1.25E+09
8	Solving the matrix equations	Sparse matrix
a.	Row reduction forward phase	1.55E+10
b.	Row reduction backward phase	5.10E+07
c.	Solving triangular matrix	3.37E+07
Total FLOPS Use Pass		1.68E+10
Grand total		1.47E+12

Summary of calculated required number of real floating point operations for the application of Rubin's method with the application of interface modes following the IRS reduction method. For the selection of the number of normal modes, a cut-out frequency of $1.5 * f_{max}$ = 60Hz has been applied. The number of interface modes retained is based on a cut-out frequency of $3.5 * f_{max}$ following the findings published in [41]

Appendix XXXI *Computation Time for Different Methods PHD Test Case*

	Method	Number of nodes	Number of boundary nodes		Number of boundary degrees of freedomnodes	Number of modes required retained	Required CP for calcuating eigenvectors and eigenvalues	Required CP generation pass
Part A	PartAfixedcms	1903	Bounary A-B	140	840	25	9.3	11.8
	PartAfreecms		Bounary A-B	140	840	31	11	14.8
	PartA Zoet and Rubin-Zoet method		Bounary A-B	140	840	205	16.3	18.9
Part B	PartBfixedcms	1695	Boundary B-A	140	840	21	9.5	11.8
			Boundary B-C	120	720			
	PartBfreecms		Boundary B-A	140	840	75	11	16.5
			Boundary B-C	120	720			
	PartB Zoet and Rubin-Zoet method		Boundary B-A	141	846	179	13.3	18.3
			Boundary B-C	120	720			
Part C	PartCfixedcms	1342	Boundary C-B	120	720	16	9.1	9.4
			Boundary C-D	96	576			
	PartCfreecms		Boundary C-B	120	720	59	9.5	13.42
			Boundary C-D	96	576			
	PartC Zoet and Rubin-Zoet method		Boundary C-B	124	744	148	12	17.6
			Boundary C-D	96	576			
part D	PartDfixedcms	1160	Boundary D-C	96	576	15	8.84	9.1
	PartDfreecms		Boundary D-C	96	576	41	8.7	10.7
	PartD Zoet and Rubin-Zoet method		Boundary D-C	95	570	105	10	13.8

Properties of the substructures used as a test case for the Zoet method (see Appendix XXIV and Appendix XXV). Free interface CMS is carried out according to the classic Rubin's method with no residual compensation taken into account. The fixed interface CMS is carried out according to the classic Craig-Bampton method.

For the classic Craig-Bampton and Rubin method (fixed interface, free interface CMS respectively) all normal modes with natural frequencies between 0 and 60 Hz (1 to $1.5 * f_{max}$) have been retained. f_{max} is the maximum analysed frequency, which is 40 Hz in this case study.

For the Zoet method and Rubin-Zoet method a higher number of mode shapes has been selected in order to reduce the effect of overcompensation of residual flexibility (see section 8.5.3). Therefore all normal modes with natural frequencies between 0 and 120 Hz (1 to $3 * f_{max}$) have been retained. f_{max} is the maximum analysed frequency, which is 40 Hz in this case study.

	Ub AB	Ub BC	Ub CD	aA	aB	aC	aD	
	Number of Columns							
variable	840	720	576	31	75	59	41	number of rows
Ub AB	705600	604800		26040	63000			840
Ub BC	604800	518400	414720		54000	42480		720
Ub CD		414720	331776			33984	23616	576
aA	26040			961				31
aB	63000	54000			5625			75
aC		42480	33984			3481		59
aD			23616				1681	41

Skyline of matrix representing the dynamic stiffness of the total assembled structure composed according to **Rubin's Method** as applied in ANSYS. Coloured cells are full matrix sections. The numbers in the coloured cells show the number of non zeros in these sections. For the selection of the number of normal modes, a cut-out frequency of $1.5 * f_{max}$ = 60Hz has been applied.

	Ub AB	Ub BC	Ub CD	aA	aB	aC	aD	
	Number of Columns							
variable	111	80	62	31	75	59	41	number of rows
Ub AB	12321	8880		3441	8325			111
Ub BC	8880	6400	4960		6000	4720		80
Ub CD		4960	3844			3658	2542	62
aA	3441			961				31
aB	8325	6000			5625			75
aC		4720	3658			3481		59
aD			2542				1681	41

Skyline of matrix representing the dynamic stiffness of the total assembled structure composed according to **Rubin's Method** using **interface reduction** through introduction of interface modes. Coloured cells are full matrix sections. The numbers in the coloured cells show the number of non zeros in these sections. For the selection of the number of normal modes, a cut-out frequency of $1.5 * f_{max}$ = 60Hz has been applied. The number of interface modes retained is based on a cut-out frequency of $3.5 * f_{max}$ following the findings published in [41]. Ub AB, Ub BC and Ub CD are the number of retained normal mode that not have been made redundant in the procedure of coupling the substructures together.

	aA	aB	aC	aD	
	Number of Columns				
Variable	205	179	148	105	Number of rows
aA	42025	36695			205
aB	36695	32041	26492		179
aC		26492	21904	15540	148
aD			15540	11025	105

Skyline of matrix representing the boundary mobility matrix of the total assembled structure composed according to **Zoet Method**. Coloured cells are full matrix sections. The numbers in the coloured cells show the number of non zeros in these sections. All normal modes with natural frequencies between 0 and 120 Hz (1 to $3 * f_{max}$) have been retained.

	aA	aB	aC	aD	
	Number of Columns				
Variable	205	179	148	105	Number of rows
aA	42025	36695			205
aB	36695	32041	26492		179
aC		26492	21904	15540	148
aD			15540	11025	105

Skyline of matrix representing the dynamic stiffness of the total assembled structure composed according to **Rubin-Zoet Method**. Coloured cells are full matrix sections. The numbers in the coloured cells show the number of non zeros in these sections.
All normal modes with natural frequencies between 0 and 120 Hz (1 to 3 $* f_{max}$) have been retained.

Rubin's Method

number of frequencies	80

Generation Pass		
Step number	Action	Estimated FLOPS
Calculating natural frequencies and modeshapes		5.63E+11
1	Generating constraint modes	1.73E+10
2	Generating reduction basis	3.90E+09
3	Generating Reduced mass and stiffness matrices	1.91E+11
Total Flops Generation Pass		7.75E+11

Use Pass		
Step number	Action	Estimated FLOPS
4	Compiling reduced dynamic stiffness matrix total assembled system	3.39E+07
5	Formulating compatibility and equilibrium relations for boundary degrees of freedom	1.52E+09
6	Solving the matrix equations	Sparse matrix approach
a.	Row reduction forward phase	2.02E+12
b.	Row reduction backward phase	1.32E+09
c.	Solving triangular matrix	8.78E+08
Total FLOPS Use Pass		2.03E+12

Grand total	2.80E+12

All modeshapes have been selected with the natural frequencies within the range between 0 and 1.5×fmax
The fmax is the highest frequency in the frequency range for which results have been obtained (= 40 Hz in this case)
Fmax in this case = 40 Hz, modeshapes have been selected over a frequency range between 0 and 60 Hz
Calculation times are based on producing 80 out sets for 80 frequencies evenly distributed between 1 and 40 Hz

Rubin's Method With Interface Reduction		
number of frequencies		80
Generation Pass		
Step number	Action	Estimated FLOPS
Calculating natural frequencies and modeshapes		1.31E+12
1	Generating constraint modes	2.63E+10
step 2 and 3	Generating reduction basis	1.19E+11
step 4	Generating Reduced mass and stiffness	7.02E+09
Total Flops Generation Pass		1.46E+12
Use Pass		
Step number	Action	Estimated FLOPS
step 5	Compiling reduced dynamic stiffness	9.37E+05
step 6 and 7	Formulating compatibility and equilibrium relations for boundary	1.25E+09
8	Solving the matrix equations	Sparse matrix
a.	Row reduction forward phase	1.55E+10
b.	Row reduction backward phase	5.10E+07
c.	Solving triangular matrix	3.37E+07
Total FLOPS Use Pass		1.68E+10
Grand total		1.47E+12

Summary of calculated required number of real floating point operations for the application of Rubin's method with the application of interface modes following the IRS reduction method. For the selection of the number of normal modes, a cut-out frequency of $1.5 * f_{max}$ = 60Hz has been applied. The number of interface modes retained is based on a cut-out frequency of $3.5 * f_{max}$ following the findings published in [41]

Calculation times are based on producing 80 out sets for 80 frequencies evenly distributed between 1 and 40 Hz

Zoet's Method With Residual Compensation		
number of frequencies		80
Generation Pass		
Step number	Action	Estimated FLOPS
Calculating natural frequencies and modeshapes		7.22E+11
1	Generating residual flexibility modes	9.42E+11
2	Formulating boundary mobility matrix	4.87E+10
4	Eliminating boundary degrees of	4.25E+11
Total Flops Generation Pass		2.14E+12
Use Pass		
Step number	Action	Estimated FLOPS
5	Composing Total Assembled System	5.09E+07
6	Solving the matrix equations	
a.	Row reduction forward phase	2.11E+10
b.	Row reduction backward phase	6.38E+07
c.	Solving triangular matrix	6.49E+07
Total FLOPS Use Pass		2.12E+10
Grand total		2.16E+12

All modeshapes have been selected with the natural frequencies within the range between 0 and 3×fmax
The fmax is the highest frequency in the frequency range for which results have been obtained (= 40 Hz in this case)
Fmax in this case = 40 Hz, modeshapes have been selected over a frequency range between 0 and 120 Hz

Calculation times are based on producing 80 out sets for 80 frequencies evenly distributed between 1 and 40 Hz

Rubin-Zoet Method		
number of frequencies		80
Generation Pass		
Step number	Action	Estimated FLOPS
Calculating natural frequencies and modeshapes		7.22E+11
1	Generating constraint modes	2.63E+10
2	Generating reduction basis	1.25E+10
3	Generating Reduced Mass, Stiffness	7.08E+10
4	Generating Reduced Equations of Motion of Coupled Sets of Substructures	1.48E+09
5	Forcing equilibrium and compatibility at the boundary degrees of freedom:	3.68E+09
6	Eliminating boundary degrees of freedom	1.69E+11
Total Flops Generation Pass		1.01E+12
Use Pass		
Step number	Action	Estimated FLOPS
5	Formulating compatibility and equilibrium relations for boundary	5.09E+07
6	Solving the matrix equations	
a.	Row reduction forward phase	2.11E+10
b.	Row reduction backward phase	6.38E+07
c.	Solving triangular matrix	6.49E+07
Total FLOPS Use Pass		2.12E+10
Grand total		1.03E+12

All modeshapes have been selected with the natural frequencies within the range between 0 and 3×fmax
The fmax is the highest frequency in the frequency range for which results have been obtained (= 40 Hz in this case)
Fmax in this case = 40 Hz, modeshapes have been selected over a frequency range between 0 and 120 Hz

Calculation times are based on producing 80 out sets for 80 frequencies evenly distributed between 1 and 40 Hz

Total structure	Number of equations total assembled matrix	Number of non zeros	Normal Modes and Natural Frequencies		Constraint/Residual Attachment Modes and Reducing Matrices		Total Computation Time Generation Pass	
			CP	FLOPS	CP	FLOPS	CP	FLOPS
full solution	33564	1.32E+06	n.a.	n.a.	n.a.	n.a.	n.a.	n.a.
mode superposition (cut out frequency = 1.5 fmax = 60 Hz)	100	1.00E+04	29	4.06E+11	0.2	2.83E+09	29.2	4.09E+11
Craig-Bampton (cut out frequency = 1.5 fmax = 60 Hz)	2213	3.71E+06	36.74	5.14E+11	5.4	7.48E+10	42.1	5.89E+11
Rubin's Method (cut out frequency = 1.5 fmax = 60 Hz)	2342	4.09E+06	40.2	5.63E+11	15.2	2.12E+11	55.4	7.75E+11
Rubin method with interface modes (cut out frequency normal modes = 60 Hz, cut out frequency interface modes = 140 Hz)	459	1.19E+05	93.24	1.31E+12	10.9	1.52E+11	104.2	1.46E+12
Zoet method (cut out frequency = 3* fmax = 120 Hz)	637	2.64E+05	51.6	7.22E+11	101.4	1.42E+12	153.0	2.14E+12
Rubin-Zoet method (cut out frequency = 3*fmax = 120 Hz)	637	2.64E+05	51.6	7.22E+11	20.3	2.83E+11	71.9	1.01E+12

Total structure	Generating Full Assembled Matrix		Solving Full Assembled Matrices		Total Computation Time Use Pass	
	CP	FLOPS	CP	FLOPS	CP	FLOPS
full solution	8.7	6.03E+10	288.0	2.03E+12	296.7	2.09E+12
mode superposition (cut out frequency = 1.5 fmax = 60 Hz)	n.a.	n.a.	0.0	2.24E+08	0.0	2.24E+08
Craig-Bampton (cut out frequency = 1.5 fmax = 60 Hz)	4	1.56E+09	288.0	2.03E+12	292.0	2.03E+12
Rubin's Method (cut out frequency = 1.5 fmax = 60 Hz)	4	1.56E+09	288.0	2.03E+12	292.0	2.03E+12
Rubin method with interface modes (cut out frequency normal modes = 60 Hz, cut out frequency interface modes = 140 Hz)	3	1.26E+09	2.4	1.68E+10	2.4	1.80E+10
Zoet method (cut out frequency = 3* fmax = 120 Hz)	0.13	5.09E+07	3.0	2.12E+10	3.1	2.12E+10
Rubin-Zoet method (cut out frequency = 3*fmax = 120 Hz)	0.13	5.09E+07	3.0	2.12E+10	3.1	2.12E+10

Total structure	Total Computation Time	
	CP	FLOPS
full solution	296.7	2.09E+12
mode superposition (cut out frequency = 1.5 fmax = 60 Hz)	29.2	4.09E+11
Craig-Bampton (cut out frequency = 1.5 fmax = 60 Hz)	334.1	2.62E+12
Rubin's Method (cut out frequency = 1.5 fmax = 60 Hz)	347.4	2.80E+12
Rubin method with interface modes (cut out frequency normal modes = 60 Hz, cut out frequency interface modes = 140 Hz)	106.6	1.48E+12
Zoet method (cut out frequency = 3* fmax = 120 Hz)	156.1	2.16E+12
Rubin-Zoet method (cut out frequency = 3*fmax = 120 Hz)	75.1	1.03E+12

Presentation of the Number of Flops and CP time calculated/measured for the test CMS model according to Appendix XXV. Calculation times are based on producing 80 out sets for 80 frequencies evenly distributed

between 1 and 40 Hz**.** Black numbers have been directly measured (CP time) or calculated (FLOPS). Brown numbers have been calculated through an estimated relation between measured computation time and number of calculated floating point operation.

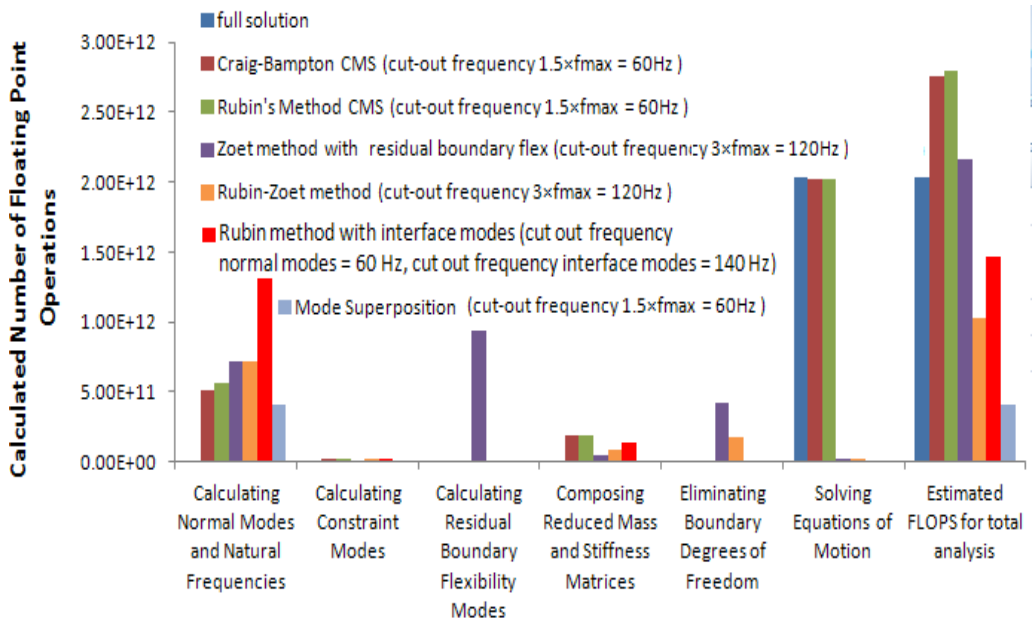

FLOPS for all different stages of the different analysis methods. Calculation times are based on producing 80 out sets for 80 frequencies evenly distributed between 1 and 40 Hz

	Computation Time Difference with Rubin's Method	Computation Time Difference with Full Harmonic Analysis	Computation Time Difference with Rubin's Method with Interface Modes
full solution	-27.5%	0.0%	37.9%
Mode Superposition	-85.4%	-79.8%	-72.2%
Craig-Bampton CMS (cut-out frequency 1.5×fmax = 60Hz)	-1.7%	35.6%	87.1%
Rubin's Method CMS (cut-out frequency 1.5×fmax = 60Hz)	0.0%	38.0%	90.4%
Rubin method with interface modes	-47.5%	-27.5%	0.0%
Zoet method with residual boundary flex (cut-out frequency 3×fmax = 120Hz)	-22.9%	6.4%	46.8%
Rubin-Zoet method (cut-out frequency 3×fmax = 120Hz)	-63.3%	-49.4%	-30.2%

Difference in percentage in computation time relatively to Rubin's free boundary (interface) method (first column), relatively to the full harmonic method (second column) and relatively to the Rubin's method with interface reduction through interface modes according to IRS (third column). Calculation times are based on producing 80 output sets for 80 frequencies evenly distributed between 1 and 40 Hz.

Appendix XXXII *Computation Time for Zoet and Rubin-Zoet Method for the LNG Carrier with Increased Number of Normal Modes*

LNG vessel FE model	Number of nodes	Number of boundary nodes		Number of boundary degrees of freedom	Method	Number of modes required*	Required CP for calcuating eigenvectors and eigenvalues	Required time generation pass
PartH	4991	Boundary H-E	298	2088	CMS fixed	181	18.5	22.8
		Boundary H-G	86		CMS free	257	24.5	52.5
		Boundary H-F	86		Zoet and Rubin-Zoet (frequency range to 3xf max)	586	44	100
PartG	5680	Boundary G-H	86	1536	CMS fixed	373	29.8	40
		Boundary G-F	57		CMS free	419	39	100.8
		Boundary G-E	205		Zoet and Rubin-Zoet (frequency range to 3xf max)	877	85	244
PartF	5680	Boundary F-G	57	1536	CMS fixed	373	29.8	40
		Boundary F-H	86		CMS free	419	39	100.8
		Boundary F-E	205		Zoet and Rubin-Zoet (frequency range to 3xf max)	877	85	244
PartE	8933	Boundary E-H	298	7188	CMS fixed	213	30	46.6
		Boundary E-G	205		CMS free	323	61	174
		Boundary E-F	205		Zoet and Rubin-Zoet (frequency range to 3xf max)	879	122	419
		Boundary E-D	656					
PartD	9833	Boundary D-E	656	6198	CMS fixed	162	29.14	53.6
		Boundary D-C	484		CMS free	336	95	328
					Zoet and Rubin-Zoet (frequency range to 3xf max)	913	202	566
PartC	11965	Boundary C-D	484	5124	CMS fixed	195	38.11	68.13
		Boundary C-B	370		CMS free	335	75	225.7
					Zoet and Rubin-Zoet (frequency range to 3xf max)	1084	215	733
PartB	10044	Boundary B-C	370	3798	CMS fixed	138	29.4	47.7
		Boundary B-A	263		CMS free	231	53	138.3
					Zoet and Rubin-Zoet (frequency range to 3xf max)	752	131	407
PartA	6612	Boundary A-B	263	1578	CMS fixed	91	18.8	25.4
					CMS free	154	24.6	53.3
					Zoet and Rubin-Zoet (frequency range to 3xf max)	502	67	158

Properties of the LNG carrier substructures (according to Appendix IX). Free interface CMS is carried out according to the classic Rubin's method. The fixed interface CMS is carried out according to the classic Craig-Bampton method

For the classic Craig-Bampton and Rubin method (fixed interface, free interface CMS respectively) all normal modes with natural frequencies between 0 and 60 Hz (1 to $1.5 * f_{max}$) have been retained. f_{max} is the maximum analysed frequency, which is 40 Hz in this case study.

For the Zoet method and Rubin-Zoet method a higher number of mode shapes has been selected in order to reduce the effect of overcompensation of residual flexibility (see section 8.5.3). Therefore all normal modes with natural frequencies between 0 and 120 Hz (1 to $3 * f_{max}$) have been retained. f_{max} is the maximum analysed frequency, which is 40 Hz in this case study.

Total structure	Number of equations total assembled matrix	Number of non zeros	calculating Normal Modes and Natural Frequencies		Constraint/Residual Attachment Modes and Reducing Matrices		Total Computation Time Generation Pass	
			CP Time	FLOPS	CP Time	FLOPS	CP Time	FLOPS
full solution	366973	1.49E+07	n.a.	n.a.	n.a.	n.a.	n.a.	n.a.
Mode superposition, f cut-out = 1.5 fmax = 60Hz	1668	2782224	2665	1.24E+14	135	6.28E+12	2.80E+03	1.30E+14
fixed interface CMS (Craig-Bampton), f cut-out = 1.5 fmax = 60Hz	15370	1.25E+08	223.55	1.04E+13	121	5.60E+12	344.2	1.60E+13
free interface CMS (Rubin's Method), f cut-out = 1.5 fmax = 60Hz	16118	1.34E+08	411.1	1.91E+13	762	3.54E+13	1173.4	5.45E+13
Zoet method cut-out frequency 3×f max =120 Hz, **with** residual boundary flex	6470	1.92E+07	829	3.85E+13	5.95E+03	2.76E+14	6780.4	3.15E+14
Rubin-Zoet method cut-out frequency 3×f max = 120 Hz	6470	1.92E+07	829	3.85E+13	1450	6.73E+13	2279.1	1.06E+14

Total structure	Generating Full Assembled Matrix		Solving Full Assembled Matrices		Total Computation Time Use Pass	
	CP Time	FLOPS	CP Time	FLOPS	CP Time	FLOPS
full solution	20	7.71E+10	7600.0	3.56E+14	7620.0	3.56E+14
Mode superposition, f cut-out = 1.5 fmax = 60Hz	n.a.	n.a.	21	9.92E+11	21	9.92E+11
fixed interface CMS (Craig-Bampton), f cut-out = 1.5 fmax = 60Hz	18	6.94E+10	12960.0	5.32E+14	13322.2	5.32E+14
free interface CMS (Rubin's Method), f cut-out = 1.5 fmax = 60Hz	18	6.94E+10	11360.0	5.32E+14	12551.4	5.32E+14
Zoet method cut-out frequency 3×f max =120 Hz, **with** residual boundary flex	1.07	4.11E+09	237.4	1.11E+13	7018.9	1.11E+13
Rubin-Zoet method cut-out frequency 3×f max = 120 Hz	1.07	4.11E+09	238.0	1.11E+13	2518.2	1.12E+13

Total structure	Total Computation Time Generation plus Use Pass	
	CP Time	FLOPS
full solution	7620.0	3.56E+14
Mode superposition, f cut-out = 1.5 fmax = 60Hz	2821.3	1.31E+14
fixed interface CMS (Craig-Bampton), f cut-out = 1.5 fmax = 60Hz	13666.5	5.48E+14
free interface CMS (Rubin's Method), f cut-out = 1.5 fmax = 60Hz	13724.8	5.87E+14
Zoet method cut-out frequency 3×f max =120 Hz, **with** residual boundary flex	13799.3	3.26E+14
Rubin-Zoet method cut-out frequency 3×f max = 120 Hz	4797.4	1.17E+14

Presentation of the Number of Flops and CPU calculated/measured for the LNG carrier model according to Appendix IX. Calculation times are based on producing 80 out sets for 80 frequencies evenly distributed between 1 and 40 Hz**.** Black numbers have been directly measured (CP time units) or calculated (FLOPS). Brown numbers have been calculated through an estimated relation between measured computation time and number of calculated floating point operation.

	aH	aG	aF	aE	aD	aC	aB	aA	
	Number of Columns								
variable	586	877	877	879	913	1084	752	502	number of rows
aH	343396	513922	513922	515094					586
aG	513922	769129	769129	770883					877
aF	513922	769129	769129	770883					877
aE	515094	770883	770883	772641	802527				879
aD				802527	833569	989692			913
aC					989692	1175056	815168		1084
aB						815168	565504	377504	752
aA							377504	252004	502

Skyline of matrix representing the boundary mobility matrix of the total assembled structure composed according to **Zoet Method**. Coloured cells are full matrix sections. The numbers in the coloured cells show the number of non zeros in these sections. All normal modes with natural frequencies between 0 and 120 Hz (1 to 3 $*$ f_{max}) have been retained.

	aH	aG	aF	aE	aD	aC	aB	aA	
	Number of Columns								
variable	586	877	877	879	913	1084	752	502	number of rows
aH	343396	513922	513922	515094					586
aG	513922	769129	769129	770883					877
aF	513922	769129	769129	770883					877
aE	515094	770883	770883	772641	802527				879
aD				802527	833569	989692			913
aC					989692	1175056	815168		1084
aB						815168	565504	377504	752
aA							377504	252004	502

Skyline of matrix representing the dynamic stiffness of the total assembled structure composed according to **Rubin-Zoet Method**. Coloured cells are full matrix sections. The numbers in the coloured cells show the number of non zeros in these sections.
All normal modes with natural frequencies between 0 and 120 Hz (1 to 3 $*$ f_{max}) have been retained.

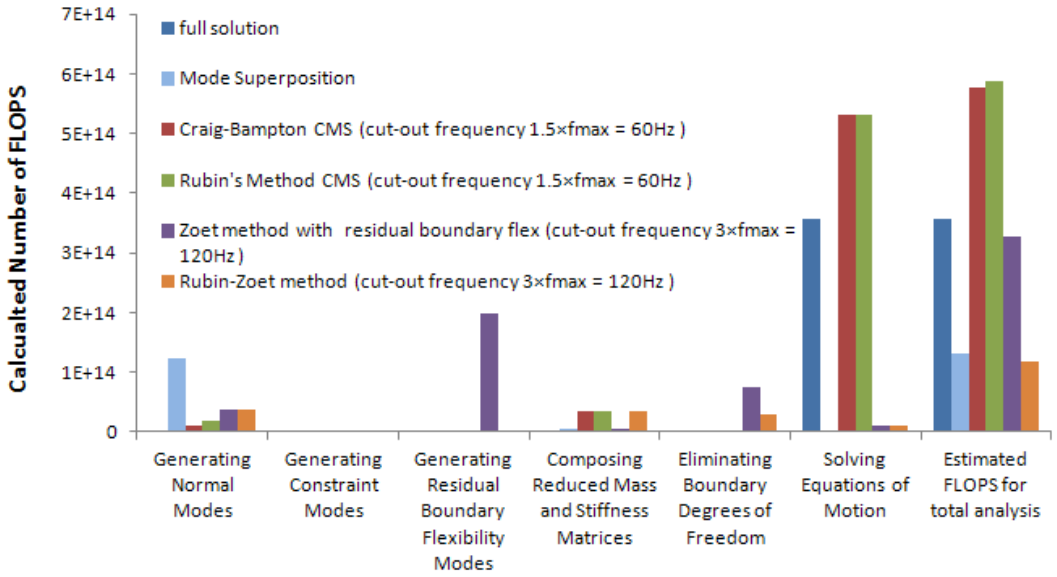

FLOPS for all different stages of the different analysis methods. Calculation times are based

on producing 80 out sets for 80 frequencies evenly distributed between 1 and 40 Hz.

Rubin's Method		
number of frequencies		80
Generation Pass		
Step number	Action	Estimated FLOPS
Calcuating natural frequencies and mode shapes		1.91E+13
1	Generating constraint modes	1.02E+12
2	Generating reduction basis	8.96E+11
3	Generating Reduced mass and stiffness	3.35E+13
Total Flops Generation Pass		5.45E+13
Use Pass		
Step number	Action	Estimated FLOPS
4	Compiling reduced dynamic stiffness	9.68E+08
5	Formulating compatibility and	6.84E+10
6	Solving the matrix equations	Sparse matrix approach
a.	Row reduction forward phase	5.32E+14
b.	Row reduction backward phase	6.24E+10
c.	Solving triangular matrix	4.16E+10
Total FLOPS Use Pass		5.32E+14
Grand total		5.87E+14

All modeshapes have been selected with the natural frequencies within the range between 0 and 1.5×fmax
The fmax is the highest frequency in the frequency range for which results have been obtained (= 40 Hz in this case)
Fmax in this case = 40 Hz, modeshapes have been selected over a frequency range between 0 and 60 Hz

Calculation times are based on producing 80 out sets for 80 frequencies evenly distributed between 1 and 40 Hz.

Zoet's Method With Residual Boundary Flexibility		
number of frequencies		80
Generation Pass		
Step number	Action	Estimated FLOPS
1	Generating residual flexibility modes	1.97E+14
2	Formulating boundary mobility matrix	4.87E+12
4	Eliminating boundary degrees of freedom	7.42E+13
Total Flops Generation Pass		2.76E+14
Use Pass		
Step number	Action	Estimated FLOPS
5	Composing Total Assembled System	4.11E+09
6	Solving the matrix equations	
a.	Row reduction forward phase	1.11E+13
b.	Row reduction backward phase	4.60E+09
c.	Solving triangular matrix	6.70E+09
Total FLOPS Use Pass		1.11E+13
Grand total		2.87E+14

All modeshapes have been selected with the natural frequencies within the range between 0 and 3×fmax
The fmax is the highest frequency in the frequency range for which results have been obtained (= 40 Hz in this case)
Fmax in this case = 40 Hz, modeshapes have been selected over a frequency range between 0 and 120 Hz

Calculation times are based on producing 80 out sets for 80 frequencies evenly distributed between 1 and 40 Hz.

Rubin-Zoet Method		
number of frequencies		80
Generation Pass		
Step number	Action	Estimated FLOPS
Calcuating natural frequencies and mode shapes		3.85E+13
1	Generating constraint modes	2.47E+12
2	Generating reduction basis	2.93E+12
3	Generating Reduced Mass, Stiffness and	3.12E+13
4	Generating Reduced Equations of Motion of	4.32E+10
5	Forcing equilibrium and compatibility at the boundary degrees of freedom:	1.12E+11
6	Eliminating boundary degrees of freedom	3.05E+13
Total Flops Generation Pass		1.06E+14
Use Pass		
Step number	Action	Estimated FLOPS
7	Formulating compatibility and equilibrium	4.11E+09
8	Solving the matrix equations	
a.	Row reduction forward phase	1.11E+13
b.	Row reduction backward phase	4.60E+09
c.	Solving triangular matrix	3.59E+10
Total FLOPS Use Pass		1.12E+13
Grand total		1.17E+14

All modeshapes have been selected with the natural frequencies within the range between 0 and 3×fmax
The fmax is the highest frequency in the frequency range for which results have been obtained (= 40 Hz in this case)
Fmax in this case = 40 Hz, modeshapes have been selected over a frequency range between 0 and 120 Hz

Calculation times are based on producing 80 out sets for 80 frequencies evenly distributed between 1 and 40 Hz.

	Cut out frequency 1.5 fmax = 60 Hz		Cut out frequency 3 fmax = 120 Hz	
	Reduction Factor Computation TimeRelatively to Rubin's Method	Reduction Factor Computation Time Relatively to the Full Harmonic Analysis	Reduction Factor Computation TimeRelatively to Rubin's Method	Reduction Factor Computation Time Relatively to the Full Harmonic Analysis
Full Solution	-39.3%	0.0%	-39.3%	0.0%
Mode Superposition	-77.7%	-63.2%	-77.7%	-63.2%
Craig-Bampton CMS	-1.5%	62.3%	-1.5%	62.3%
Rubin's Method CMS	0.0%	64.8%	0.0%	64.8%
Zoet Method	-59.0%	-32.5%	-44.4%	-8.4%
Rubin Zoet method	-91.5%	-86.0%	-80.1%	-67.1%

Difference in percentage in computation time relative to Rubin's free interface (interface) method (first column) and relative to the full harmonic method (second column). The first set of two columns represent calculation times applying a cut-out frequency of 1.5 fmax = 60 Hz for all methods for the selection of the number of normal modes. The second set of two columns represent calculation times applying a cut-out frequency of 1.5 fmax = 60 Hz for the Rubin and Craig-Bampton method, and applying a cut-out frequency of 3 fmax = 120 Hz for the Zoet and Rubin-Zoet method. Calculation times are based on producing 80 output sets for 80 frequencies evenly distributed between 1 and 40 Hz.